

NASA Technical Memorandum 82385

Reports of Planetary  
Geology Program - 1980

FOR REFERENCE  
NOT TO BE TAKEN FROM THIS ROOM

DECEMBER 1980

NASA





NASA Technical Memorandum 82385

# Reports of Planetary Geology Program - 1980

*Compiled by*

Henry E. Holt and Elisabeth C. Kusters

*NASA Office of Space Science*

*Washington, D.C.*



National Aeronautics  
and Space Administration

**Scientific and Technical  
Information Branch**

1980



This Volume is Dedicated to Dr. Thomas A. Mutch,  
Associate Administrator, Office of Space Science, NASA; Space  
Scientist, Educator, and Friend.





## Foreword

This is a compilation of abstracts of reports from Principal Investigators of NASA's Office of Space Science, Division of Lunar and Planetary Programs Planetary Geology Program.

The purpose is to provide a document which succinctly summarizes work conducted in this program. Each report reflects significant accomplishments within the area of the author's funded grant or contract.

No attempt has been made to introduce editorial or stylistic uniformity; on the contrary, the style of each report is that of the Principal Investigator and may best portray his research. Bibliography information will be included in a separately published document.

Full reports of selected abstracts were presented to the annual meeting of Planetary Geology Principal Investigators at Louisiana State University, Baton Rouge, Louisiana, January 6-8, 1981.

J.M. Boyce  
Discipline Scientist  
Planetary Geology Program



# TABLE OF CONTENTS

	Page
Foreword.....	v
CHAPTER 1-ASTEROIDS, COMETS AND GALILEAN SATELLITES.....	1
New Planet-Crossing Asteroids (1979) .....	3
E.M. Shoemaker, E.F. Helin, S.J. Bus, and Q.R. Passey	
The Rotation of "New" and "Young" Comet Nuclei.....	6
F.L. Whipple	
Theoretical Studies of the Galilean Satellites.....	8
R. Reynolds, P. Cassen, C. Alexander A. Summers, S. Peale	
Global Multispectral Maps of the Galilean Satellites...	10
L.A. Soderblom, T.V. Johnson, J.A. Mosher, G.E. Danielson, P. Kupferman, A.F. Cook and M.E. Davies	
Vertical Dimensions on the Galilean Satellites Progress Report.....	12
D.W.G. Arthur	
Evolution of IO's Volatile Inventory.....	14
J.C. Pollack and F.C. Witteborn	
IO: Atmosphere-Surface-Magnetosphere Interactions.....	16
F.P. Fanale and W.B. Banerdt	
Ejection of Material from IO.....	19
C.B. Pilcher	
Near Surface Flow of Volcanic Gases on IO.....	20
S.W. Lee and P.C. Thomas	
Oblique Impacts and Asteroidal Structure C.R. Chapman, S.J. Weidenschilling, D.R. Davis R. Greenberg.....	23
Thermal Infrared Studies of the Galilean Satellites.....	27
D. Morrison	

## CHAPTER 1-ASTEROIDS, COMETS AND GALILEAN SATELLITES (continued)

Volcanic Eruption Plumes on IO.....	28
R.G. Strom, N.M. Schneider, R.J. Terrile, A.F. Cook and C. Hansen	
IO Plume Dynamics.....	31
N.M. Schneider, R.G. Strom and A.F. Cook	
Morphometry of Craters and Caldera on IO as an Indicator of Eruptive Style.....	34
J.L. Whitford-Stark and P.J. Mouginis-Mark	
IO: Size and Spatial Distributions of Volcanic Vents; Trends of Tectonic Features.....	37
G.G. Schaber and A.L. Dial, Jr.	
IO: Preliminary Mapping of Geologic Units.....	40
G.G. Schaber and D.W.G. Arthur	
Europa Surface Cracking: A Consequence of Thermal Evolution.....	43
A.A. Finnerty, G.A. Ransford and D. Pieri	
Europa's Petrologic Thermal History.....	45
G.A. Ransford and A.A. Finnerty	
Europa: Size-Frequency Distributions of Global Polygons.....	48
D. Pieri	
Preliminary Classification of Lineament Patterns on Europa.....	51
D. Pieri	
The Cratering of Ganymede I: The Dark Terrain.....	55
J.B. Plescia, E.M. Shoemaker and J.M. Boyce	
The Cratering of Ganymede II: Grooved Terrain, Smooth and Gilgamesh.....	60
J.B. Plescia, E.M. Shoemaker and J.M. Boyce	
The Origin of Grooved Terrain on Ganymede.....	64
S.W. Squyres, E.M. Parmentier and J.M. Head	
Domes on Ganymede.....	67
M.C. Malin	



## CHAPTER 1-ASTEROIDS, COMETS AND GALILEAN SATELLITES (continued)

Voyager Photometry of Surface Features on Ganymede and Callisto.....	68
S. Squyres and J. Veverka	
Thermal Evolution of Ganymede and Callisto.....	70
G. Schubert and K. Ellsworth	
Temperature of Amalthea.....	72
D. Simonelli	

## CHAPTER 2-STRUCTURE, TECTONICS AND STRATIGRAPHY

Simulation of Pioneer-Venus Altimetry Using Northern Pacific Ocean Floor Bathymetry.....	77
R.E. Arvidson, R. Batiza and E.A. Guinness	
Evidence for Continental-Style Rifting from the Beta Region of Venus.....	79
G.E. McGill	
Topography of Earth and Venus.....	81
M.D. Malin and P.R. Paluzzi	
Ridge and Trench Systems of Venus and Global Rift Valleys on Earth : A Comparison.....	82
G.G. Schaber and H. Masursky	
Possible Relations Between the Early Martian Geologic Record, Convective Overturn and Core Segregation.....	85
R.E. Arvidson and G.F. Davies	
Gravity-Tectonics and Volcanism: Implications for Earth and Mars.....	88
L.S. Crumpler	
Ridge-Rings on Mars.....	90
A.W. Gifford	
Tectonic Implications of Martian Ridged Plains.....	93
R.S. Saunders and T.E. Gregory	
Martian Valley Orientations and Regional Structural Controls.....	95
M. Ginberg and D. Pieri	

## CHAPTER 2-STRUCTURE, TECTONICS AND STRATAGRAPHY (continued)

Tectonic Heredity of Fracture Systems: A New Method of Testing by Correlation of Domain Boundaries.....	98
T. McCrory and D. Wise	
Mottled Plains of Mars: A Review.....	101
J.R. Underwood, Jr. and N.E. Witbeck	
Mars Stratigraphy: Lowland Plains and Valles Marineris.....	104
D.H.Scott and K.L. Tanaka	
A Possible Origin of the Ridged Plains of Mars.....	107
A. Fernandez-Chicarro and Ph. Masson	

## CHAPTER 3-CRATERING PROCESSES AND LANDFORM DEVELOPMENT

Impact Basins: Implications for Formation from Experiments.....	113
R. Greeley, J. Fink, and D.E. Gault	
The Evolution of Multi-Ringed Basins: Cooling, Thermal Stress and Relaxation of Topography.....	116
S.C. Soloman, S. Bratt, R.P. Comer, J.W. Head	
The Distal Deposits of Lunar Basins at the Apollo 14 and 16 Landing Sites.....	119
B.R. Hawke and J.W. Head	
Complex Impact Craters on the Planets.....	122
R.J. Pike	
Goat Paddock, Western Australia: An Impact Crater near the Simple-Complex Transition.....	125
D.J. Milton, R.F. Fudali, J. Ferguson and L. Jaques	
Macroscopic Hypervelocity Impact Phenomena.....	127
J. Hurren, G. Martelli, P.M. Smith, R. Bianchi, P. Cerroni, M. Coradini, M. Fulchignoni, M. Poscolieri and R. Flavill	
Apparent Crater Depth: Selenographic Distribution....	128
R.A. DeHon and M.X. Furin	
Crater Central Peaks on the Moon, Mercury and Earth...	131
W. Hale and J.W. Head	

## CHAPTER 3-CRATERING PROCESSES AND LANDFORM DEVELOPMENT (contin)

Rampart Crater Ejecta: Experiments and Analysis of Melt-Water Interactions.....	134
K.H. Wohletz and M.F. Sheridan	
An Estimate of Water Content of Some Martian Rampart-Ejecta Deposits Derived from their Pre-Flow Stress Conditions.....	137
A. Woronow	
Distribution of Thermal Gradient Values in the Equatorial Region of Mars Based on Impact Crater Morphology.....	140
J.M. Boyce and N.E. Witbeck	
Large Tectonic Effects of the Caloris Impact on Mercury.....	144
P. Thomas, E. Carey, L. Fleitout and Ph. Masson	
Global Patterns of Primary Crater Ejecta Morphology on Mars.....	147
K.R. Blasius and J.A. Cutts	
Latitudinal Distribution of Flow-Ejecta Morphology Types on the Ridged Plains of Mars.....	150
R.S. Saunders and L.A. Johansen	
Studies of Martian Crater and Basin Deposits.....	152
B.R. Hawke and P.J. Mougini-Mark	
Basin Deposits on Mars: The Role of Ejecta Fluidization.....	155
P.J. Mougini-Mark and B.R. Hawke	
Central Peaks in Martian Craters: Comparisons to the Moon and Mercury.....	158
W. Hale and J.W. Head	
Statistical Analysis of Central-Peaked Craters on Mars.....	161
A.H. Hamdan and F. El-Baz	
Non-Circularity of Martian Impact Craters: Clues to Hidden Structures?.....	164
R.W. Wolfe and M.L. Hutson	

### CHAPTER 3-CRATERING PROCESSES AND LANDFORM DEVELOPMENT (contin)

Depth/Diameter Relationships for Large Martian Craters: Radar Results.....	167
L.E. Roth, G.S. Downs, R.S. Saunders, and G. Schubert	
Laboratory Simulations of Central Pit Craters.....	170
J. Fink, R. Greeley and D.E. Gault	
Martian Cratering Revisited.....	172
M.C. Gurnis	
Cratering Record in the Inner Solar System.....	174
A. Woronow, R.G. Strom and M.C. Gurnis	
Crater Forming Process on Mars, Impact-Energy Coupling and Explosion-Cratering Analogs for Formation of Central Uplifts and Multirings.....	177
D.J. Roddy and L.A. Soderblom	
Martian Impact Craters: Inventory of Three-Dimensional Crater and Ejecta Blanket Parameters.....	180
L.A. Soderblom, D.J. Roddy, D.W.G. Arthur and P.A. Davis	
Martian Channels - A lake Viking Review	
H. Masursky, A.L. Dial, Jr. and M.E. Strobell.....	184

### CHAPTER 4-GEOCHEMISTRY, VOLATILES AND REGOLITH

Low Temperature Phase Changes in Montmorillonite and Nontronite at High Water Contents and High Salt Contents.....	191
D.M. Anderson and A.R. Tice	
Sulfate Production from Photochemical Oxidation of Sulfides: Preliminary Results.....	193
T.R. Blackburn, E.K. Gibson, Jr., F.F. Andrawes and V. Young	
Chemical Weathering on Mars: Carbonate Formation.....	196
M.C. Booth	

## CHAPTER 4-GEOCHEMISTRY, VOLATILES AND REGOLITH (continued)

Dry Valleys of Antarctica: Analogs of the Martian Surface .....	199
E.K. Gibson, Jr.	
Geochemical Changes Produced by Weathering of Soils from the Dry Valleys of Antarctica: A Progress Report.....	202
E.K. Gibson, Jr., B. Ransom and R.E.L. Ingram	
Experimental Alteration of Rocks under "Hydrothermal", Conditions Applicable to Mars and Venus.....	205
J.L. Gooding	
Mineralogical Studies of Terrestrial Analogs of Martian Surface Materials.....	206
J.L. Gooding	
Hawaiian Basalts as Analogs of Martian Surface Materials, 1: Particle-Size Distribution of Soils and Sediments.....	209
J.L. Gooding	
Size-Fraction Analysis of Mauna Kea, Hawaii Summit Soils and their Possible Analogy with Martian Soils.....	212
J.M. Japp and J.L. Gooding	
Mars Fines Atmospheric Pressure Wave Experiment: A Progress Report.....	215
F. Fanale, B. Banerdt, R. Sanger, L. Johansen, P. Diffendaffer and L. Muradian	
Stability of Ferric Oxyhydroxides (FeOOH) to Dehydration in the Presence of UV Radiation: Implications for Weathering on Mars.....	218
R.V. Morris and H.V. Lauer, Jr.	
Mars Soil/Water/Atmosphere Dynamic Interaction Facility Description.....	221
R.S. Saunders, J. Gooding, F. Fanale, L. Johansen, E. Laue, D. Schneider, R. Sanger, P. Diffendaffer and S. Wall	

#### CHAPTER 4-GEOCHEMISTRY, VOLATILES AND REGOLITH (continued)

Cohesion and Angle of Internal Friction of Surface Materials at Viking Landing Sites, Mars.....	225
H.J. Moore, E.M. Dowey, R.E. Hutton, R.F. Scott, R.W. Shorthill and C.R. Spitzer	

#### CHAPTER 5-VOLCANIC PROCESSES AND LANDFORMS

Vertical Structure and Erosion Rates of Pahoehoe Basalt Flows.....	231
J.C. Aubele, L.S. Crumpler and W.E. Elston	
Degradation of Volcanic Landforms on Mars and Earth.....	234
V.R. Baker	
Geology of Kilauea Caldera, Hawaii.....	236
D. Dzurisin and T.J. Casadevall	
Hawaiian Rock Population: Possible Analogs to Mars.....	238
J.B. Garvin, P.J. Mouginis-Mark, and J.W. Head	
A New Technique for Identifying Buried Surfaces.....	241
D.H. Scott and K.L. Tanaka	
Explosive Volcanism: A Possible Source for Aggregate Formation on Mars.....	243
J. Fink, D. Krinsley and R. Greeley	
Pristine Morphology of a Quasi-Flood Basalt Flow: The Bardardalshraun of Trolladyngja, Iceland.....	245
R. Greeley and H. Sigurdsson	
Physical Modelling of Lava Flows.....	247
R. Greeley and M. Womer	
Mud as a Pseudo-Volcanic Rock Magma.....	249
L.A. Johansen	
A Pyroclastic Origin for the Aureole Deposits of Olympus Mons.....	252
E.C. Morris	

## CHAPTER 5-VOLCANIC PROCESSES AND LANDFORMS (continued)

Martian Ignimbrites.....	255
D.H. Scott and K.L. Tanaka	
Regional Volcanic Studies in Elysium Planitia, Mars....	258
P.J. Mouginis-Mark and S.H. Brown	
Small Volcanic Features of the Elysium Region.....	261
J.B. Plescia	
Cinder Cones of Isidis and Elysium.....	263
J.B. Plescia	
Some Martian Volcanic Centers with Small Edifices.....	266
H.J. Moore and C.A. Hodges	
Estimates of Lava Flow Velocities in Channels of the Pu'u Kia'I Flow, Hawaii.....	269
H.J. Moore, R. Kachadoorian and R.B. Moore	
Quantitative morphology of volcanoes; status report....	272
R.J. Pike	

## CHAPTER 6-AEOLIAN PROCESSES AND LANDFORMS

Venus Aeolian Processes/Saltation Studies and the Venusian Wind Tunnel.....	275
R. Greeley, B.R. White, R. Leach, R. Leonard, J. Pollack and J.D. Iversen	
Flux of Windblown Particles on Mars: Preliminary Wind Tunnel Determination.....	278
R. Greeley, K. Malone, R. Leach, R. Leonard and B.R. White	
Parametric Study of Dust Fountains.....	281
J. Kenney, F. Fanale and R.S. Saunders	
Electrostatic Aggregates and their Physical Properties.....	285
D.H. Krinsley, R. Leach, J. Marshall and R. Greeley	
Compression Testing of Electrostatic Aggregates- Analog to Sand Grains on Mars.....	287
J. Marshall, D.H. Krinsley and R. Greeley	

## CHAPTER 6-AEOLIAN PROCESSES AND LANDFORMS (continued)

Field Studies of Aeolian Patterns.....	290
R. Greeley, M. Malin, S. Williams and G. Stewart	
Comparisons of Wind Streak Form in Egypt and on Mars..	292
F. El-Baz and T.A. Maxwell	
Comparison of Knobs in the Cerberus Region of Mars and Eolian Knobs in the Farafra Depression, Western Desert of Egypt.....	295
F. El-Baz and L.S. Manent	
Effects of Topography on Dune Orientation in the Farafra Region, Western Desert of Egypt, and Implications to Mars.....	298
L.S. Manent and F. El-Baz	
The Effects of Minerology and Grain Shape on the Color of Sands from the Western Desert of Egypt, and Possible Applications to Mars.....	301
C.T. Herzog and F. El-Baz	
Thickness of Coatings on Quartz Grains from the Great Sand Sea, Egypt .....	304
D. McKay, J. Constantopoulos, D.J. Prestel and F. El-Baz	
Evolution of Inselbergs in the Hyperarid Western Desert of Egypt - Comparisons with Martian Fretted Terrain.....	307
C.S. Breed, J.F. McCauley and M.J. Grolrier	
Gilf Kebir and the Western Desert of Egypt - Insights into the origin of the North Polar Erg on Mars.....	312
J.F. McCauley, C.F. Breed and M.J. Grolrier	
Field Observations within a Little Known Dune Complex in the Great Sand Sea, Western Desert, Egypt.....	314
R. Giegengack and J.R. Underwood, Jr.	
Climbing and Falling Dunes in the Painted Desert of Arizona: Comparison with Mars.....	317
C.K. McCauley, W.J. Breed, A.S. Cotera, M. Gray, R. Axelrod, and A.P. Johnson	



## CHAPTER 6-AEOLIAN PROCESSES AND LANDFORMS (continued)

Granule-Armored Sand Dunes.....	318
R.S.U. Smith	
Detection of Dune Areas Using the Autocorrelation Structure of Digital Imagery-Earth and Mars Imagery-Space.....	319
R.G. Craig, R.W. Wolfe, B.R. Hoyt, M.S. Schmidt, M. Raymondi and K. Kaufman	
Significance of Large Open Spaces Within the North Polar Dunes on Mars .....	322
R.S.U. Smith	
North-South Asymmetry of Polar Wind Indicators on Mars.....	324
P. Thomas	
Wind Streaks on Mars: Meteorological Control of Occurrence and Mode of Formation.....	327
J. Veverka, P. Gierasch and P. Thomas	
Global Digital Map of Martian Eolian Features.....	330
A.W. Ward, P.J. Helm, N. Witbeck and M. Weisman	
Effect of Wind on Scarp Evolution on the Martian Poles.....	333
A. Howard	

## CHAPTER 7-FLUVIAL, PERIGLACIAL AND OTHER PROCESSES OF LANDFORM DEVELOPMENT

Mudflow Studies on Mount St. Helens.....	339
J. Fink and R. Greeley	
Fluvial History of Mars.....	342
M.H. Carr	
Nirgal Vallis.....	345
V.R. Baker	
Landscape Evolution, Central Arctic Slope, Alaska: An Analog for Proximal Martian Outflow Channels.....	348
J.C. Boothroyd and B.S. Timson	

# CHAPTER 7-FLUVIAL, PERIGLACIAL AND OTHER PROCESSES OF LANDFORM DEVELOPMENT (continued)

Network Patterns as Related to Formation Mechanism of Martian Valleys.....	352
D. Pieri	
Low Energy Cavitation in Martian Floods.....	355
D. Pieri and C. Sagan	
Groundwater Sapping on the Colorado Plateau.....	358
J.E. Laity	
Channel Meandering and Braiding: Are Empirical Equations Based on Terrestrial Rivers Applicable to Mars.....	361
P.D. Komar	
Preliminary Analysis of Energy in the Martian Geomorphic System.....	364
L.A. Rossbacher and S. Judson	
Geomorphic Processes in Iceland's Cold Deserts: Mars Analogs.....	367
M.C. Malin	
The Martian Fretted Terrains: Examples of Thermokarst Labyrinth Topography.....	369
G.A. Brook	
Martian Fractured Terrain: Possible Consequences of Ice-Heaving.....	373
P. Helfenstein	
The Last Picture Show: Small Scale Patterned Ground in Lunae Planum.....	376
N. Evans and L.A. Rossbacher	
Survey of Possible Glacial or Periglacial Features on Orthophotomosaic Subquadrangles of Mars at scale of 1:2,000,000.....	379
B.K. Lucchitta and H.M. Ferguson	
Glacially Grooved Valley Floors on Earth and Mars.....	381
B.K. Lucchitta	

# CHAPTER 7-FLUVIAL, PERIGLACIAL AND OTHER PROCESSES OF LANDFORM DEVELOPMENT (continued)

Inventory of North Polar Ice, Mars.....	383
H. Masursky, A. Dial and M. Strobell	
Mechanics of Flow and Erosion Potential of Rock Glaciers and Glaciers in Compressing Flow.....	384
D.E. Thompson	
Pre-Surge Characteristics and Water Storage in Trapridge Glacier, Yukon, 1980.....	386
D.E. Thompson	
Surging Glaciers as an Oscillatory Stable Flow.....	389
D.E. Thompson	
Geomorphic and Hydraulic Analysis of Catastrophic Flood Features in the Alsek River Valley, Yukon.....	392
D.E. Thompson	
Hillslope Modification and Evolution of the Valles Marineris Wall Scarps.....	394
P.C. Patton and V.R. Baker	
Exhumed Topography - A Case Study of the Stanislaus Table Mountain, California.....	397
D.D. Rhodes	
Rheology of Bingham plastics ad Implications for Mars outflow channels.....	400
D. Nummedal	
Submarine Landslides.....	401
D.B. Prior	
Preliminary Geomorphic interpretation of the Valles Marineris, Kasei Valles and Noctis Labyrinthus regions of Mars.....	402
J. Bodard, E. Pernet, P. Rogeon, B. Bousquet, Ph. Masson	
A Model for the Removal and Subsurface Storage of a PrimitiveMartian Ice Sheet.....	405
S.M. Clifford	

CHAPTER 7-FLUVIAL, PERIGLACIAL AND OTHER PROCESSES OF LANDFORM  
DEVELOPMENT (continued)

Large landslides in Ophir, Candor, and Melas Chasmata, Mars.....	408
K.L. Kaufman and B.K. Lucchitta	

CHAPTER 8-REMOTE SENSING OF PLANETARY SURFACES: INTERPRETIONS  
AND TECHNIQUES

Viking Lander Imaging Experiment - Update and New Observations.....	413
K.L. Jones and S.K. LaVoie	

Spectral Variety of Martian Surface Materials: Comparison of Earthbased and Viking Lander Data.....	416
E.L. Strickland and R.B. Singer	

Spectral Properties of Soils Exposed at the Viking 1 Site.....	417
E.A. Guinness	

Observing Changes with the Viking Lander Cameras.....	420
S.D. Wall and L. Cullen	

The Search for Sun Dogs on Mars.....	423
P. Romani	

Brightness Degradation of Viking Lander Ultraviolet Chips.....	426
A.P. Zent, E.A. Guinness and R.E. Arvidson	

Comparison of Voyager Images of Day and Night Views of IO.....	429
R.J. Terrile and A.F. Cook	

Mariner 10 Color-Ratio Data and the Surface of Mercury.....	431
B. Hapke and B. Rava	

Impact Cratering: Relative Importance to Radar Scattering from Lunar Maria and Syrtis Major.....	432
R.A. Simpson, H.T. Howard and G.L. Tyler	

## CHAPTER 8-REMOTE SENSING OF PLANETARY SURFACES: INTERPRETATIONS AND TECHNIQUES (continued)

Mars Radar: The Search for Radar-Defineable Surface Units.....	435
S.H. Zisk and P.J. Mouginis-Mark	
Radar Backscatter Studies in Northern Arizona: A Progress Report.....	438
G.G. Schaber	
SEASAT Radar Lineament Detection: Testing the Effects of Shadow Illusions.....	439
D.U. Wise	
The Maeti9 Dome Egypt - An Earth Analog Study of Rock Type Discriminability Using Broad-Band Visible and Reflected IR Data.....	442
P. Jacobberger, R. Arvidson and E. Guinness	
Diffuse Reflectance Spectra of Particulate (submicron) Iron Oxides and Selected Mixtures Thereof.....	445
R.V. Morris and S.C. Neely	

## CHAPTER 9-PLANETARY CARTOGRAPHY, GEODESY AND GEOLOGIC MAPPING

Voyager Cartography.....	451
R.M. Batson	
The Control Network of the Galilean Satellites.....	453
M.E. Davies	
Improved Accuracy of Coordinates of Features on Mars.....	454
M.E. Davies	
Mars 1:2,000,000 Mapping .....	456
R.M. Batson and R.L. Tyner	
Topographic Mapping of Mars: 1:2 Million Contour Map Series.....	458
S.S.C. Wu, F.J. Schafer and R. Jordan	
Mars 1:15,000,000 Mapping.....	462
R.M. Batson	

## CHAPTER 9-PLANETARY CARTOGRAPHY, GEODESY AND GEOLOGIC MAPPING (continued)

VOIR Photogrammetry.....	463
S.S.C. Wu, F.J. Schafer and L.A. Barcus	
Paleogeologic Maps of the Far Side of the Moon.....	466
D.E. Wilhelms	

## CHAPTER 10. WORKSHOPS AND SPECIAL PROGRAMS

Planetary Geology Undergraduate Research Program (PGUR).....	471
M.M. Eagan	
Planetary Geology Adjunct Investigators Project: A Progress Report.....	473
R.E. D'Alli	
Planetology in Rome, 1980.....	474
R. Bianchi, A. Carusi, P. Cerroni, A. Coradini, M. Coradini, C. Federico, E. Flamini, M. Fulchignoni, G. Magni, M. Poscolieri and G.B. Valsecchi	
Planetary Nomenclature.....	475
H. Masursky and M. Strobell	
Outer Solar System Nomenclature.....	476
T. Owen	
Planetary Data at the National Space Science Data Center.....	477
R.W. Vostreys	
Frequency-Encoded Storage of Digital Images Data on Videodisks.....	478
L.K. Bolef and R.E. Arvidson	
Viking Orbiter Imaging Mosaic Catalog.....	479
N. Evans	
Location and Plotting of High Resolution Viking Orbiter Image Sequences.....	480
N. Evans and P. Scribner	

## CHAPTER 10-WORKSHOPS AND SPECIAL PROGRAMS (continued)

Viking Orbiter Survey Missions I and II, Coverage and Data Reduction.....	483
N. Evans	
The Second Mars Channel Workshop: A Report.....	486
V.R. Baker and D. Nummedal	
Planetary Geology Activities and Developments in France.....	488
Ph. Masson and J. L. Mercier	

-----

## LATE ABSTRACTS

The Origin of Mare Ridges.....	493
V.L. Sharpton and J.W. Head	
Chemical Weathering the Dry Valleys of Antarctica: Preliminary results of a sem study.....	496
D.S. McKay and D. Prestell	
Cratering Records of Ganymede and Callisto.....	499
R.G. Strom, A. Woronow, and M.C. Gurnis	
Possible Source of the Martian Salts.....	502
R.L. Huguenin	
Quantitative Measurements of the Topography of the North Pole Layered Deposits.....	504
J.A. Cutts and K.R. Blasius	
Status of Planetary Image Processing at Munich.....	507
G. Neukum, J. Henkel, K. Hiller and W. Lüders	
Relative Ages of Olympus Mons Aureole Material.....	509
K. Hiller, R. Lopes, J. Guest and G. Neukum	
Small Lunar Dark-Mantle Deposits of Probable Pyroclastic Origin .....	512

AUTHOR INDEX .....	515
--------------------	-----





## Chapter 1

### ASTEROIDS, COMETS AND GALILEAN SATELLITES



## New planet-crossing asteroids (1979)

by E.M. Shoemaker, E.F. Helin, S.J. Bus, and Q.R. Passey

Eight new planet-crossing asteroids were found in the Palomar Planet-crossing Asteroid Survey in 1979 (Table 1). In addition, we rediscovered the long-lost Apollo asteroid 1947 XC. This high rate of discovery was achieved largely with a limited set of plates from the 122-cm Schmidt telescope at Palomar Mountain, California, and at Siding Spring, Australia. However, discovery of the most striking new asteroid, Apollo object 1979 VA, as well as the rediscovery of 1947 XC, was accomplished with the 46-cm Schmidt at Palomar. Relatively secure preliminary orbits have been obtained for all but one of the new planet-crossers.

Apollo asteroid 1979 VA has an unusual orbit which takes it out closer to Jupiter than any other known Apollo asteroid. It is in an orbit similar to P/Encke and appears to be just stable against strong perturbations by encounter with Jupiter. Results of physical observations from 0.3 - 2.2 $\mu$ m (by E.F. Tedesco, D.J. Tholen, H. Spinrad, J. Stauffer, J. Degewij, and D.P. Cruikshank) show its reflectance spectrum to be consistent with some rare carbonaceous meteorite assemblages. Its orbit and spectral reflectance suggest 1979 VA may be a recently defunct short period comet.

Apollo 1979 XA discovered at 0.32 AU from the earth was found to be identical to 1947 XC discovered by H. Giclas at Lowell Observatory. The asteroid was nearly in the same position in respect to Earth and Sun as it was on initial discovery 32 years earlier. As only two plates were originally obtained by Giclas, the observed arc was insufficient to calculate an orbit adequate to predict future positions. Hence, our reobservation of the fourth known Apollo asteroid was purely accidental. Now numbered (2201), 1947 XA = 1947 XC is the second earth crossing asteroid to have been accidentally rediscovered. UBV observations made by E. Bowell suggest it is an "S" type object.

A third new earth-crosser, 1979 QA, is probably the smallest celestial body ever reported in the IAU circulars. Unfortunately, the object was moving at such a high angular rate and was also so faint that we succeeded in finding it on only two plates with the 122-cm Palomar Schmidt, despite prompt detection and our concerted effort to follow it. Hence, insufficient observations were obtained to compute a meaningful orbit. There is no doubt that it passed extremely close to Earth and belongs to the group of Earth crossers, however. Very roughly, we estimate that 1979 QA probably does not exceed 50 m in diameter.

Amor asteroid, 1979 QB, was discovered on the same 122-cm Schmidt plate as the Apollo 1979 QA. Its moderate retrograde motion at the time of discovery allowed it to be well observed over a two month arc. At apparent magnitude 17 it was slightly too faint for standard photoelectric photometry to be obtained with instruments available at the time of discovery.

Five Mars-crossing asteroids were discovered on plates taken in June on the United Kingdom 122-cm Schmidt telescope at Siding Spring, Australia. Asteroids detected in four plates of a single field were measured and reported to the Minor Planet Center. Follow-up fields were then obtained with the

122-cm Schmidt at Palomar on two lunations and at Siding Spring on one lunation; in addition, other plates obtained by Charles Kowal at Palomar for his survey of distant objects were used to obtain follow-up positions. To date, orbits on positions from two lunations have been obtained for 135 of the new asteroids. It will be possible to double the observed arc for about 110 of these objects with positions obtained on the third lunation and assure that the new asteroids will be recoverable on later apparitions. We will attempt to follow all of these faint asteroids, in future years, and expect to find many of them on 122-cm Schmidt plates taken at Palomar on prior apparitions as well. If we are successful, this group of about 100 faint objects ( $16^m$  to  $20^m$ ) will constitute the first such group of asteroids to be systematically followed until they become numbered. The relatively high precision preliminary orbits will make it possible to obtain photometric and radiometric observations of many of these faint asteroids and to identify IRAS observations for the brighter of these objects.

One of the new faint Mars crossers, 1979 MN4, is a relatively deep crosser. The other four are fairly shallow crossers (Table 1 and Figure 1). The fraction of Mars crossers among the newly discovered objects,  $5/137 = 3.7\%$  is very close to the fraction of Mars crossers among the numbered asteroids. Hence, the proportion of Mars crossers among the faint asteroids probably is close to the proportion observed among the larger bodies. This observation buttresses a previous calculation of the Mars-crossing asteroid population to  $V(1,0) = 18$  (Shoemaker, 1977). Continued search for faint Mars crossers and physical observations of these objects are needed to obtain the data required for a precise calculation of the cratering rate on Mars.

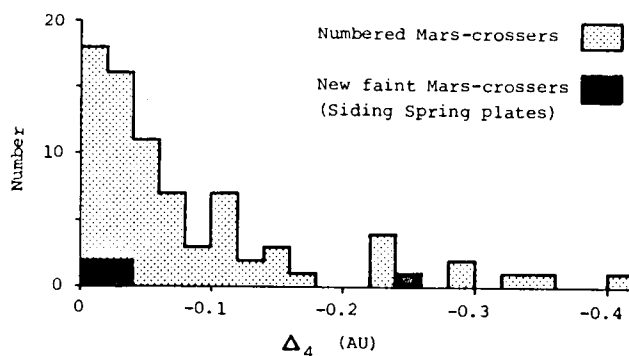


Figure 1. Frequency distribution of  $\Delta_4$  for numbered Mars-crossing asteroids and for new faint Mars crossers.

## References

Helin, E.F., and Gaffey, M.J., in press, 1979 VA, A possible carbonaceous asteroid: Meteoritics.

Shoemaker, E.M., 1977, Astronomically observable crater-forming projectiles in *Impact and Explosion Cratering: Planetary and Terrestrial Implications*, eds. D.J. Roddy, R.O. Pepin, and R.B. Merrill (New York: Pergamon Press) p. 617-628.

Williams, J.G., 1969, Secular perturbations in the solar system: Ph.D. dissertation, University of California at Los Angeles.

Table 1. Planet-crossing asteroids discovered in the Palomar Planet-Crossing Asteroid Survey (including Mars-crossing asteroids discovered in 1979 from plates taken with the U.K. 122-cm Schmidt telescope at Siding Spring, Australia)

	a AU	e	i	q AU	$\Delta_4$ $\frac{1}{\text{AU}}$
<u>Earth-crossing asteroids</u>					
1976 UA	0.84	0.45	5.9°	0.46	
(2100) Ra-Shalom	0.83	0.44	15.8°	0.47	
(2201) 1979 XA = 1947 XC (rediscovery)	2.17	0.72	2.6°	0.61	
(2062) Aten	0.97	0.18	18.9°	0.79	
(2135) Aristaeus	1.56	0.49	22.6°	0.80	
1973 NA	2.43	0.64	68.0°	0.88	
1979 VA	2.62	0.63	2.8°	0.97	
1979 QA	insufficient observations for meaningful orbit				
<u>Amor Asteroids</u>					
1977 VA	1.86	0.39	2.9°	1.13	-0.57
1979 QB	2.33	0.44	3.4°	1.30	-0.42
<u>Mars-crossing Asteroids</u>					
1974 UB	2.12	0.36	36.3°	1.36	$(v_{16}) \frac{2}{\text{AU}}$
(2099) Öpik	2.30	0.36	26.9°	1.46	-0.29
1979 MN4	2.32	0.37	5.3°	1.47	-0.26
(2074) Shoemaker	1.80	0.08	30.1°	1.65	-0.09
1978 VR8	2.30	0.27	1.2°	1.68	-0.13
(2128) Wetherill	2.74	0.38	16.8°	1.69	-0.07
1979 MT3	2.14	0.21	3.2°	1.69	-0.029
1979 MU7	2.25	0.24	4.5°	1.72	-0.011
1979 MC4	2.24	0.23	5.6°	1.72	-0.002
(2143) Jimarnold	2.28	0.24	8.4°	1.75	+0.001
1978 VL4	2.31	0.23	5.0°	1.78	-0.06
(2050) Francis	2.33	0.24	26.6°	1.78	-0.06
1979 MM7	2.20	0.19	3.4°	1.79	-0.036
<u>Mars-grazing Asteroid</u> <sup>3/</sup>					
(1982) Cline	2.31	0.25	6.8°	1.73	+0.006

<sup>1/</sup>  $\Delta_4$  is the closest approach to Mars obtained from Williams' (1969) theory for secular perturbations. A negative  $\Delta_4$  indicates that the asteroid can actually lie closer to the sun than Mars by the amount indicated, at the time it passes through the node on Mars' orbit. Hence, physical collisions with Mars are possible for all asteroids with negative  $\Delta_4$ .

<sup>2/</sup> 1974 UB lies too close to the  $v_{16}$  secular resonance to calculate a meaningful value of  $\Delta_4$ . This object is, without question, a deep Mars crosser. At times during the resonant oscillation of its eccentricity, it probably becomes an Amor ( $q \leq 1.3$  AU).

<sup>3/</sup> Mars-grazing asteroids have very small positive values of  $\Delta_4$ . These asteroids may pass close enough to Mars to be perturbed by Mars into Mars-crossing orbits.

## The Rotation of "New" and "Young" Comet Nuclei

Fred L. Whipple      Smithsonian Astrophysical Observatory

Coma-diameter measures can be interpreted in many comets as halo expansions arising periodically from the emissions by active regions on successive rotations of the nuclei. (Whipple, *Nature*, 273, 134, 1978). From the known average velocity of coma-expansion as a function of solar distance, a diameter measure leads to a "zero date" (ZD) when the emission occurred. The series of ZD's for a comet can be analyzed for the period of nuclear spin. Adequate coma-diameter measures have been found to justify an attempt to determine the rotation periods for some 35 relatively "young" comets, with original periods exceeding  $10^4$  years, 20 of Type I ( $1/a < 50 \times 10^{-6}/\text{AU}$ , where  $a$  is the semimajor axis of the orbit before entry into the planetary region) and 15 of "Type II" ( $50 < 1/a < 2154/\text{AU}$ ). The major data were obtained from the extraordinary series of visual observations made by Max Beyer over nearly 40 years. For Comet Timmers, 1946 I, and for a few diameters of other comets, I have measured plates taken by Henry L. Giclas, kindly provided by the Lowell Observatory. Elizabeth Roemer also gave me access to some plates made at the Yerkes Observatory, and I have measured a number by G. van Biesbroeck.

Over a third of the comets of both types give reasonably well determined periods ranging from 7.8 hours (Reid, 1921 II) to 81.6 hours (Baade, 1922 II). Nearly a third of the remaining comets give some indication of probable period and a similar remainder give no viable solution. Although the data tell almost nothing about the directions of the spin axes, several of the nuclei must have been oriented with axes too near the solar direction for active areas to show periodic emission. Furthermore, the accuracy of measurement precluded the determination of possible very short periods for several.

We may conclude, therefore, that the majority of the newer comets concentrate their activity in single areas. The surfaces of cometary nuclei are thus highly non-uniform for most comets of all classes because I find that sufficiently observed comets of periods less than  $10^4$  yr. are mostly susceptible to spin-period determination by the halo method. The type I and II comets will determine the initial spin-period distribution at the time of comet formation, related to their manner of origin. Comparison of the distribution with that of the shorter period comets should indicate whether sublimation-induced spinup is a significant factor in comet development. The distribution of spin periods for the new comets covers much the same range as that for the poorly sampled spin periods of older comets but appears to show fewer of short period.

No data have indicated previously whether comet splitting is associated with rapid rotation. The minimum rotation period for a sphere of mean density,  $\rho$ , is  $3.3/\sqrt{\rho}$  hours, below which period the centrifugal force at the equator exceeds the gravitational force. Comet Honda, 1955 V shows a somewhat doubtful period of 4.1 hours, rather close to this limit, if  $\rho$  does not greatly exceed  $1.0 \text{ gm/cm}^3$ .

Z. Sekanina (Icarus, 38, 300, 1979) finds that a component of Comet Honda separated 8.2 AU from the Sun, 740 d. before perihelion. B. G. Marsden, Z. Sekanina and E. Everhart (Astr. Jour. 83, 64, 1978) derive an "original"  $1/a$  of  $-284 \pm 289 \times 10^{-6}/\text{AU}$ , suggesting that the comet was probably making its first excursion in from the Oort cloud when it split at this enormous solar distance. Any deviation from sphericity for a comet nucleus rotating, as would be expected, about its axis of maximum inertia, would increase the critical period of rotation. A small irregular mass almost in orbit near the equator of Comet Honda may have been disturbed by sublimation forces and slowly ejected, with an acceleration of only  $4 \times 10^{-7}$  of solar gravity (Sekanina's value). The analysis of Comet Honda data will continue in hopes of clarifying the question as to its period.

### Theoretical Studies of the Galilean Satellites

R. Reynolds, P. Cassen, C. Alexander and A. Summers, NASA-Ames Research Center, Moffett Field, CA 94035. S. Peale, Dept. of Physics, University of California, Santa Barbara, CA 93106

A program of study of the evolution and structure of the Galilean satellites that includes the effects of tidal heating (Peale et. al., 1979) and solid state convection (Reynolds and Cassen, 1979), is continuing. This report outlines some of the results obtained during the past year.

Io - A model has been proposed to explain the source of the driving volatiles for the volcanoes of Io (Reynolds et. al., 1980). The observed lack of impact craters, together with considerable evidence for the presence of sulfur on the surface of Io suggest the existence of a surface layer of sulfur. The high heat flow rates through the surface of Io imply that such a layer would melt at depths of a few hundred meters. Evidence for silicate constructs (Carr, 1979) is also strong, however, and indicates that flows of silicate magma do occur. Contacts between a silicate magma intrusion and the overlying sulfur layer could produce volcanic plumes driven by high temperature sulfur vapor.

Smith et. al. (1979) have proposed a plume model based upon  $\text{SO}_2$  gas, heated by molten sulfur, as the driving volatile. Although energy considerations marginally allow such a model, the inclusion of probable energy losses due to departures from thermodynamic equilibrium, friction, etc., suggest that observational values for plume heights and velocities cannot be met. We have shown that (for silicate magma temperatures of 1200 K or higher) the specific enthalpy available for sulfur vapor, under the conditions of rapid expansion from a subsurface chamber through a restricted pipe or vent to the surface, can easily meet the observationally inferred energy constraints.

It is suggested that high spatial resolution infrared photometry might be able to differentiate between the two models since plume temperatures for the liquid sulfur heated models must be low ( $< 100$  K) while the silicate magma heated sulfur plume should be considerably hotter than the surface temperature.

Europa - Calculations have been presented (Cassen et. al., 1979) which indicated that Europa could retain a liquid water layer beneath a solid ice crust (due to intensive thin shell tidal heating) until the present time; if a molten (or near molten) region had ever existed at an earlier time. There was, however, an error in the estimation of the thin shell heating rate in that work. The correction (Cassen, et. al., 1980a) results in a lowering of the calculated rate of tidal energy production by a factor of  $\sim 8$ . Although the existence of a liquid  $\text{H}_2\text{O}$  region is not ruled out, the likelihood of such a configuration is less than previously supposed.

Ganymede and Callisto - Although similar in bulk properties, there are great differences in the surface morphologies of Ganymede and Callisto. In order to study possible mechanisms for producing this difference (e.g. Cassen et. al., 1980b); two component mathematical models have been constructed using the equation of hydrostatic equilibrium, silicate densities for a constant density core and temperature dependent equations of state for a  $\text{H}_2\text{O}$  mantle which include the numerous high density phases of



ice. Variations in the mean radii of these models have been calculated for a range of thermal profiles corresponding to thermal evolution scenarios using both convective and conductive heat transfer mechanisms. The effects of phase changes upon the stability of thermal profiles to solid-state convection have been investigated. It appears that local differences in the internal temperature profile, due perhaps to convective motions, may be capable under certain conditions of producing local differences in elevation which, in turn, could affect the surface morphology. These possibilities are being studied.

- Carr, M., H. Masursky, R. Strom and R. Terrile (1979). Volcanic Features of Io, Nature, 280, 729-733.
- Cassen, P., R. Reynolds and S. Peale (1979). Is There Liquid Water on Europa? Geophys. Res. Lett., 6, 731-734.
- Cassen, P., S. Peale and R. Reynolds (1980a). Tidal Dissipation in Europa: A Correction. Geophys. Res. Lett., (submitted).
- Cassen, P., S. Peale and R. Reynolds (1980b). On the Comparative Evolution of Ganymede and Callisto. Icarus, 41, 232-239.
- Cassen, P., S. Peale and R. Reynolds (1980c). Structure and Thermal Evolution of the Galilean Satellites. The Satellites of Jupiter (in press).
- Peale, S., P. Cassen and R. Reynolds (1979). Melting of Io by Tidal Dissipation. Science, 203, 892-894.
- Reynolds, R. and P. Cassen (1979). On the Internal Structure of the Major Satellites of the Outer Planets. Geophys. Res. Lett., 6, 121-124.
- Reynolds, R., S. Peale and P. Cassen (1980). Io: Energy Constraints and Plume Volcanism. Icarus (submitted).
- Smith, B., E. Shoemaker, S. Kieffer and A. Cook (1979). The role of SO<sub>2</sub> in volcanism on Io. Nature, 280, 738-743.

GLOBAL MULTISPECTRAL MAPS OF THE GALILEAN SATELLITES,  
L. A. Soderblom, U.S. Geological Survey, T. V. Johnson, J. A. Mosher,  
G. E. Danielson, P. Kupferman, Jet Propulsion Laboratory/California  
Institute of Technology, and A. F. Cook, Smithsonian Astrophysical  
Observatory, M. E. Davies, Rand Corporation.

During the last few days of their approaches to the Jovian system, Voyager 1 and Voyager 2 acquired global multispectral imaging coverage of the four Galilean satellites. Nearly complete longitudinal coverage was systematically acquired with the narrow-angle cameras in four spectral band passes: ultraviolet, violet, blue, and orange filters (central wavelengths of 0.35, 0.41, 0.48, and 0.59 $\mu$ m). Global multispectral mosaics of the four satellites have been prepared, following the scheme described in (1) for Viking approach photography of Mars. For Europa, Ganymede, and Callisto, Voyager 1 and Voyager 2 coverages were combined to yield the best complete global maps. For Io, nearly complete coverage was available from each of the two spacecraft; therefore, two independent mosaics were assembled that can be used to detect changes in surface materials or in plume activity during the 4-month interval between the two encounters. Each Voyager spacecraft carries a diffusely reflecting aluminum target to be used to recalibrate the Voyager cameras in-flight. As a result, the absolute radiometry is thought to be better than 10% and the relative photometry generally better than a few percent. After calibration of the images to produce absolute intensities for each spectral band, a model photometric function--consisting of a Minnaert correction and a global phase coefficient correction--was applied to produce model estimates of normal albedo from each image. These images were then geometrically transformed to normal cylindrical projections either by using geodetic control established by Davies and Katayama (2), or by using spacecraft ephemeris and limb fits to control the geometry. The images were then assembled into digital mosaics; residual seams were suppressed by a technique described in (1).

Preliminary studies of the Voyager 1 and Voyager 2 multispectral maps of Io show that in most places very little change occurred between the two encounters. The remarkable similarity in appearance of most of the planet in these two mosaics is testimony to the fidelity of the camera calibration and processing procedures. In some areas, notably around the large heart-shaped volcanic fallout pattern centered on Pele<sup>1</sup>, major changes did occur in the surface features, reflecting changes in activity of the volcanic plumes. The dark-floored calderas, which appear black in the normal color presentations, are divided into two general categories, based on their multispectral properties: those with steep "red" reflection curves and extremely low ultraviolet reflectance, and those with rather flat spectral curves and high UV reflectance. Preliminary investigations suggest that calderas with high UV reflectance are associated with hot spots or active plumes; the high UV reflectance is evidently caused by condensing gases or airborne particulates as described in (3). Cluster analyses of the multispectral data suggest that the coloration of Io's plains materials can be explained by a variety of forms of sulfur mixed with various amounts of material (now thought to be SO<sub>2</sub> frost). Sulfur forms range from white

through yellow, orange, and red to brown to black; they have monoconically decreasing spectral slopes and extremely low ultraviolet reflectances that is highly reflective at  $.35\mu\text{m}$  (4,5,6). Preliminary analyses of multispectral maps of the three icy satellites indicate that Europa displays three distinct plains units: bright plains, dark plains with low UV reflectance, and dark plains with high UV reflectance. These three units are consistent with ground-based measurements of rotational variations in the integral spectral properties of the satellite. The multispectral maps also allow comparison of the dark ancient cratered terrains on Ganymede and Callisto. Callisto's cratered terrain are systematically darker by a factor of about two. This comparison includes dark background materials as well as the brightest, fresh, rayed craters, suggesting that the difference is due to the intrinsic bulk properties of the materials in the upper few kilometers of the crusts rather than to a simple dusting or aging process. The grooved terrains on Ganymede are similar in albedo to the low-UV dark terrains on Europa.

These global multispectral maps provide a preliminary assessment of the types of information available in the Voyager collection. Higher resolution mosaics (approximately 5 Km per line pair) were acquired for about 40% of the satellite surfaces. Preliminary analyses of the global multispectral mosaics suggest that these high-resolution data will be extremely valuable in understanding the nature of the geomorphic forms found on the surfaces of the satellite systems.

#### REFERENCES

- (1) Soderblom, L. A., Edwards, K., Eliason, E. M., Sanchez, E. M., and Charette, M. P., 1980, Global color variations on the martian surface: *Icarus* 34, 446-464.
- (2) Davies, M. E., and Katayama, F. Y., 1980, Coordinates of features on the Galilean satellites, submitted to *Jour. Geophys. Res.*
- (3) Collins, S. A., 1980, Spatial color variations in Io's Plume 2, at Loki: *IAU Colloquium No. 57, The Satellites of Jupiter*, May 1980, 3-11.
- (4) Kumar, S., 1979, The stability of an  $\text{SO}_2$  atmosphere on Io: *Nature* 280, no. 5725, p. 758.
- (5) Fanale, F. P., Brown, R. H., Cruikshank, D. P., and Clarke, R. N., 1979, Significance of absorption features on Io's IR reflectance spectrum: *Nature*, 280, no. 5725, p. 761.
- (6) Smythe, W. D., Nelson, R. M., and Nash, D. B., 1979, Spectral evidence for  $\text{SO}_2$  frost or adsorbate on Io's surface: *Nature*, 280, no. 5725, p. 766.

## VERTICAL DIMENSIONS ON THE GALILEAN SATELLITES: PROGRESS REPORT.

D.W.G. Arthur, U.S. Geological Survey, Flagstaff, Arizona 86001.

The Galilean satellites of Jupiter differ markedly from one another and from the more familiar surfaces of the Moon, Mars and Mercury. A knowledge of both horizontal and vertical dimensions of the new and unfamiliar landforms on these bodies is essential to constrain theorization. These dimensions are critical in the case of Io because of differing theories of its surface chemistry. The Voyager pictures provide some stereopsis, but do not afford a useful precision for the relatively low objects on the surface of the satellites. Relative heights found from shadow measurements appear to be more precise.

An adequate ( $\pm 10$ -20%) relative height determination using shadows requires both precise measurement and good geometry, that is, in terms of spherical geometry, a well-determined relation between pole, surface feature, and the subpolar point. Such a geometry implies a very definite surface coordinate system in which the positions of sun and surface feature are known with some precision. Unfortunately, this condition does not exist on the Galilean satellites, where the situation is similar to that of the Moon before precise maps were made of that body. In early techniques used for lunar mapping, the surface feature was related to the nearby terminator, thus establishing the solar elevation at the feature without recourse to surface coordinates. This method then involved locating on the picture the true terminator, which is by no means coincident with the apparent terminator. Indeed, the latter's position depends to some extent on enhancement and photographic manipulation of the hard copy.

For Io, objective and definite determinations of the true terminator were made using photometric profiles derived from original spacecraft data tapes. On these profiles, the DN (brightness) values decline steadily to a point at which the curve levels out and stays level at the instrumental zero. This point was identified as the intersect of the image line with the true terminator. Moving averages were used to suppress the effects of noise and jitter and to obtain a more definite result. On Io, this technique located the terminator to within a few pixels. The much rougher surfaces of Ganymede give poorer results: it was more useful to locate the last illuminated star-like points at intervals from top to bottom of the picture and to fit these points to a second-degree curve. This approach is validated by the relatively low magnitude of the positive relief. With surface feature and nearby terminator located, the solar elevation at the feature is computed by simple geometry. The accuracy is variable, but generally better than  $1^\circ$ .

The shadows of surface features on all the satellites are too short for such simple methods as pixel counting. Instead, the integration technique is used: the smooth blurred curve of the shadow in the photometric profile is converted to the theoretical rectangular curve, using the instrumental background value for the true shadow brightness. The curve is treated so that the brightness integral is conserved. This technique estimates shadows to 0.1 pixel.

On Io, the long scarps bounding the layered plains range from 160 m to 2000 m in height, with most in the 300-600 m range. Heights of 2000 m were noted for one set of scarps associated with collapse. Several calderas were found to be about 2000 m deep. The greatest elevation measured on Io, that of a volcanic construct photographed on the limb, is about 9000 m, determined by a more direct measurement. On Europa, the most conspicuous features are cusped ridges of considerable length. They are about 5-6 km across, rise only 200-300 m above surrounding terrain, and slope only 5°. On Ganymede, only the braided grooves have been investigated to date. The larger grooves (10 km across) are about 800 m deep and have interior slopes of about 10°. They are found in all widths down to the resolution limit (< 1 km/line pair), but their depth/width ratio of 0.1 to 0.08 seems more or less constant.

#### REFERENCE

- Arthur, D.W.G., 1979, Precise Mars relative altitudes (abs.):  
Reports of Planetary Geology Program, 1978-1979, NASA Tech. Memo  
80339, p. 397.

## EVOLUTION OF IO'S VOLATILE INVENTORY

James B. Pollack and Fred C. Witteborn, Space Science Division, NASA-Ames Research Center, Moffett Field, CA 94035

As a result of its active volcanism and the large mass loading capability of the inner Jovian magnetosphere, Io is currently losing volatiles at a prodigious rate to the magnetosphere, a situation that has probably occurred over much of its history. Sulfur compounds--especially elemental sulfur and sulfur dioxide--constitute the major compounds of Io's present atmosphere, volcanic plumes, and surface. Because of the strong control exerted by the saturation vapor pressure curve of  $\text{SO}_2$  on the local surface pressure, the exobase may lie at the surface on the night side, thus allowing sputtered material on this side to escape from Io. Despite the low surface pressure even on the day side, the exobase there extends into the magnetosphere on the upstream side due to the high exospheric temperatures realized with an  $\text{SO}_2$  atmosphere, thereby exposing the background atmosphere to the magnetospheric plasma. The high exospheric temperature also implies rapid, diffusion limited escape of light and medium weight atoms, up to atomic mass unit 40. Consequently, the dissociation products of  $\text{SO}_2$  can rapidly escape. Finally, some plumes reach altitudes that lie within the magnetosphere, thus exposing their gases and particulate contents to the magnetospheric plasma.

Observations of the Io torus imply that Io is losing material, principally S and O, at a rate of  $10^{10}$  to  $10^{11}$  molecules/cm<sup>2</sup>/s. According to our calculations there are four processes that make significant contributions to these losses: interaction of plume particles and the background atmosphere with the magnetosphere, sputtering of surface ices, and Jeans escape of the dissociation products of  $\text{SO}_2$ . All but this last process involve interactions with the magnetosphere. Thus, there exist feedback relationships in most of these loss processes, with these being positive or self-amplifying ones. Conceivably, the amount of mass loading may be limited by the response of the magnetosphere to this loading, in the sense that once a limit is passed very rapid diffusion sets in.

Hypothetical paleoatmospheres may have existed in Io's early history, as exemplified by a  $\text{N}_2$  dominated one. If so, they would be characterized by much higher surface pressures, the occurrence of a non-trivial atmosphere on the night side, and much lower exospheric temperatures. Nevertheless, the exobase is expected to extend into the magnetosphere and volcanic plumes are expected to achieve comparable altitudes to those of today. Losses due to Jeans escape and sputtering of surface ices are negligible for these early atmospheres. However, much mass loss can still occur due to the interaction of plume particles and the background atmosphere with the magnetospheric plasma. These losses are sufficiently

high to eliminate the equivalent of the Earth's volatile inventory of  $N_2$  in much less than the age of the satellite or still larger amounts over longer time scales.

There are good cosmogonic reasons for suspecting that Io was endowed with a nontrivial amount of water. The apparent absence of water ice and bound water on the surface of Io today can be attributed to several loss processes that effectively eliminated virtually all of Io's water over its lifetime. During times when silicate volcanism was dominant much water was lost as it was repeatedly recycled between the upper and lower parts of the crust, with water being partially dissociated in each cycle into hydrogen and oxygen. The hydrogen was released to the atmosphere and rapidly escaped to space while the oxygen was taken up by reduced iron compounds in the silicate melt. At later times after the  $SO_2$  dominated atmosphere became established, additional water loss occurred due to sputtering of surface ices by high energy magnetospheric ions. Finally, substantial losses of water may have occurred as high altitude plume ice particles became charged and were swept away by Lorentz forces.

Thus, Io has lost a number of the components of its initial volatile inventory. The fact that Io still has significant quantities of S bearing volatiles at the current epoch is largely the result of these materials constituting a large enough fraction of the planet's total mass to be able to sustain the large loss rates.

## IO: ATMOSPHERE-SURFACE-MAGNETOSPHERE INTERACTIONS

F. P. Fanale, Planetary Geosciences Department, Institute for Geophysics, U. of Hawaii, Honolulu, HI 96822, and W. B. Banerdt, Jet Propulsion Laboratory, California Institute of Technology, Pasadena, CA 91103

The Problem: Sulfur dioxide molecules (in some form) are abundant in Io's atmosphere (Pearl et al; 1979, Kumar et al, 1979) and in Io's surface material (Fanale et al, 1979; Smythe et al, 1979). This knowledge allows us to construct quantitative models for the history of  $\text{SO}_2$  molecules from the time that they are supplied to Io's surface/atmosphere environment by volcanism to the time when they are lost from that environment by supply to the magnetosphere or (possibly) incorporation into other phases. Such models link Io's surface, atmosphere and magnetosphere. We evaluated these models on the basis of how well they explain (1) the lack of total coverage with  $\text{SO}_2$  frost - which is particularly puzzling in Io's near-polar regions, (2) the required rates and geometry with which the ionized torus and Io-surrounding cloud are supplied, including time variations, (3) groundbased and Voyager surface spectral reflectance data, and (4) Earthbased spectroscopic data and Pioneer occultation data on the disc-integrated gaseous  $\text{SO}_2$  abundance and the total gas abundance near the terminators, respectively. The present study is concerned with the development and evaluation of such models. The most telling tests of such models are their ability (1) to explain variations in Io's global properties and those of the torus/cloud and (2) to explain Io's darker near-polar regions. It also appears that the most satisfactory  $\text{SO}_2$  regime model, one involving a transient steady state among volcanic supply, gas migration across Io's disc and loss to the magnetosphere can be used to very severely constrain the mechanism by which Io's post-eclipse brightening must take place, providing that we assume that the phenomenon is real and is related to frost formation at all.

Transient Steady State Model: Specifically, groundbased and spacecraft observations suggest that the surface of Io is largely covered with an anhydrous mix of S allotropes formed at various temperatures. Dissolved, occluded and adsorbed  $\text{SO}_2$  is likely to be abundant, and there is also free  $\text{SO}_2$  frost and gaseous  $\text{SO}_2$  present. Also, some Na- (and K-) containing phase must be a significant component of the surface, and the sulfide salts,  $\text{Na}_2\text{S}$  and  $\text{K}_2\text{S}$ , appear to be the candidate phases most harmonious with the simultaneous constraints imposed by Io's optical properties and Earthbased and in situ observations of Io's neutral cloud and plasma torus. Volatization of neutral Na from magmas may be an important atmospheric Na supply source, however.

Io  $\text{SO}_2$  "meteorology" is emerging as a complex problem which is the key to the balance between supply and loss of  $\text{SO}_2$ . Plasma data argues for an  $\text{SO}_2$  dominated atmosphere and several observations seem nearly compatible with perfect local buffering with  $\text{SO}_2$  frost at ambient ground temperature. Such models, in which Io's atmosphere is considered to be saturated everywhere, are useful for testing, but do not satisfactorily explain why Io does not exhibit a higher whole disc gas abundance than that currently inferred from International Ultraviolet Explorer results,



or why Io's near-polar regions are not very bright. Moreover, they are generally incompatible with preliminary gas migration models. Instead, a "limited SO<sub>2</sub> supply - transient steady state" model is suggested having the following characteristics: (1) the supply of SO<sub>2</sub> is limited, regional and variable, (2) much of the disc is undersaturated with respect to SO<sub>2</sub> much of the time, (3) the net SO<sub>2</sub> flux to the poles is limited by regional SO<sub>2</sub> supply rates, regional cold trapping on unusually high albedo regions, and also gas migration kinetics. Even where saturation is not achieved, the SO<sub>2</sub> may occur largely as an absorbed phase which may also serve as a sputtering target. The sputtered flux to the magnetosphere seemingly must equal or exceed the flux from SO<sub>2</sub> sources toward the polar regions or the polar regions would be bright. The former flux is currently  $\sim 10^{28-10^{29}}$  atoms sec<sup>-1</sup>, but could vary considerably with time. Unlike a saturated atmosphere model, our model explains the accessibility of Io's light side to sputtering, variations in the torus plasma density, and the disc integrated SO<sub>2</sub> abundance as constrained by 1979 International Ultraviolet Explorer observations. It also partly explains Io's failure to develop bright polar regions since it involves a flux SO<sub>2</sub> to the poles no more than one order of magnitude greater than the sputtered flux whereas other models involve a three order of magnitude discrepancy.

Supply of species to the Io surrounding neutral cloud and ionized torus may occur by several mechanisms. Any such proposed mechanism must explain the chemical composition, ionization state, velocity/energy, geometry and intensity of the fluxes coming from Io. No single mechanism seems satisfactory to explain all these and other observational constraints for all neutral and ionized species. In general, hypotheses involving direct plume throwout and thermal escape appear inferior in their ability to satisfy the observations involving magnetosphere interaction. Direct surface sputtering of Na neutrals seems likely, and it is generally presumed that other species are sputtered as well. Atmospheric loss processes are likely to involve magnetospheric interaction as well, and both ionization/field sweeping and atmospheric sputtering seem highly viable candidate processes.

Post Eclipse Brightening: Our transient steady state SO<sub>2</sub> supply and loss model can also lead to inferences concerning the brightening mechanism, provided that certain assumptions are accepted: If Io post-eclipse brightening is caused by frost, then two independent arguments - both based on identification of frozen SO<sub>2</sub> on Io's surface may separately be used to show this condensation must take place within  $\sim 30^\circ$  of the subsolar point upon eclipse emergence. One is based on the equilibrium capacity of the atmosphere for SO<sub>2</sub> and the other on kinetics. They are: (1) If  $\sim 10^{-3}$  g cm<sup>-2</sup> is an optically thick frost, then the only places where frost can appear during eclipse, vs. always being there, are areas where the atmosphere can hold  $\sim 10^{-3}$  g cm<sup>-2</sup> of SO<sub>2</sub> in equilibrium. This is where the ground temperature is  $> 126\text{K}$  or only within  $30^\circ$  of the subsolar point on eclipse entry. (2) Since the time for disappearance of the brightening is only  $\sim 15$  minutes, it is required that  $\sim 10^{-3}$  g/cm<sup>2</sup> of SO<sub>2</sub> sublime in that time. Calculations for SO<sub>2</sub> show that, again, only within  $\sim 32^\circ$  of the subsolar point upon emergence is the sublimation rate nearly

this fast ( $> 1.10 \times 10^{-6} \text{ g cm}^{-2} \text{ sec}^{-1}$ ) corresponding to a ground temperature  $> 125^\circ\text{K}$ . Also, the occurrence of the present volcanic  $\text{SO}_2$  sources near this region on Io, together with the variable nature of brightening and the low whole disc I.U.E.  $\text{SO}_2$  gas abundance suggests to us an  $\text{SO}_2$  regime model where condition one is underfulfilled even in the area of interest during periods of low volcanism. At times of more intense volcanism  $\text{SO}_2$  saturation is approached, the torus grows, the I.U.E.  $\text{SO}_2$  gas observation should increase, and post-eclipse brightening should be observed. Our model explains the only quantifiable aspects of brightening: amplitude, duration, and variability.

#### References:

- Fanale, F. P., R. H. Brown, D. P. Cruickshank and R. N. Clark, Nature, 280, 761-763, 1979.
- Smythe, W. D., R. M. Nelson, and D. B. Nash, Nature, 280, 766, 1979.
- Pearl, J., R. Hanel, V. Kunde, W. Maguire, K. Fox, S. Gupta, C. Ponnampertuma, and F. Raulin, Nature, 280, 755-758, 1979.
- Kumar, S., Nature, 280, 758, 1979.

### Ejection of Material from Io

Carl B. Pilcher, Institute for Astronomy and Department of Physics and Astronomy, University of Hawaii, Honolulu.

During the past year, a large quantity of data was obtained that bears on the problem of determining the mechanisms by which material is removed from Io. These data include both images of the circum-Jovian ring of ionized sulfur that show inhomogeneities that may be related to episodes of sulfur ionization, as well as images of the Io sodium cloud that show complex directional features whose structures vary with time.

At our present stage in data reduction and analysis, we can make the following statements regarding the directional sodium features:

1. They are generally present, although their form varies substantially from night to night.
2. They generally extend out of the Galilean satellite orbital plane toward the north.
3. The extent of the features from Io projected onto the plane of the sky is generally  $\gtrsim 2 R_J$  ( $1.4 \times 10^5$  km).
4. The gravitational potential energy of material in the features requires ejection velocities from Io of at least 4-5 km/sec.
5. Preliminary model studies conducted in collaboration with W. H. Smyth indicate that if the features are caused by jets of sodium leaving the satellite, then ejection velocities of ~10 km/sec may be required.
6. Ejection velocities even as high as those required by the potential energy argument cannot be attained in any reasonable model of volcanic ejection.

Studies aimed at further elucidating the characteristics of and possible mechanisms for the ejection process are in progress.

Some of the sulfur ring images show structure down to the resolution limit of the digitally filtered images (a few arcseconds). Episodic removal of sulfur from Io followed by or coupled with ionization could produce relatively high density regions in the plasma such as those indicated by the data.

NEAR SURFACE FLOW OF VOLCANIC GASES ON IO. Steven W. Lee and Peter C. Thomas, Laboratory for Planetary Studies, Cornell University, Ithaca, New York 14853

Analysis of Voyager 1 images of Io has revealed a series of bright, elongate albedo markings directed radially away from the Pele vent area and located several hundred km distant from the vent. These features strongly suggest that substantial near-surface flow of gas from active vents can occur over large distances on Io. The high mass flow rates inferred to be effective far from the plumes have important implications for volcanic resurfacing rates on that satellite.

Figure 1 is a sketch map showing six bright streamers associated with the Pele vent and one associated with the Loki vent. The streamers lie 150 to 750 km from the vents, are between 15 and 70 km in length, have shapes varying from fan to elliptical, and cross a variety of topographic features without noticeable effect on streamer shape. Sources for the streamers appear to be: 1) bright spots (less than 2 km across); 2) sharp albedo boundaries, convex toward the Pele vent; and 3) a large mountain block. The streamers are not related to the vents directed from the bases of scarps such as those discussed by McCauley et al. (1979).

We interpret the bright streamers to be material on the surface that has been carried "downwind" from small local vents (crudely likened to fumaroles - see Figure 2) based on the following: 1) Several streamers have bright point sources. Other bright spots farther from plumes do not have streamers; 2) The streamers cannot be associated definitely with scarps; 3) The parallelism of groups of streamers strongly suggests regional control of flow directions; 4) Streamers have consistently radial orientations relative to active plume sources. Venting of gas that either carries or condenses solid particles can build constructs around the local vent. A pervasive flow of gas away from a large plume could blow the material discharged from the small vent into a streamer-shaped deposit.

Characteristics of gas flow necessary for suspension and transport of particles injected into the flow from small vents have been modeled. SO<sub>2</sub> "snow" with a density of 0.15 gm/cm<sup>3</sup> and particle sizes of 0.1 to 10  $\mu$ m were considered. The plume gas flow was taken to be SO<sub>2</sub> gas at a pressure of between 10<sup>-5</sup> and 10<sup>-9</sup> bar at a temperature of 130°K. Settling velocities of cm/sec to tens of meters/second were obtained (see Figure 3). Thus, rather modest velocities may be adequate to maintain small particles in suspension. Similar calculations of flow velocities necessary to entrain particles already resting on the surface yield values that are two orders of magnitude larger than the settling velocities. As cohesive effects were

neglected in our models, the results suggest that subsonic winds (at  $10^{-7}$  bar) cannot entrain surface particles. It appears that entrainment of surface particles is not possible, while suspension of small particles injected into the gas flow (as in Figure 2) is reasonable.

Based on our models, the mass flow rates needed for suspension of 0.1 to 10  $\mu\text{m}$  particles at the streamer locations range from  $\sim 10^7$  to  $\sim 10^9$  g/s (for  $\text{SO}_2$  gas). The mass flow rates at the plume vents would equal or exceed these values, but do not require extraordinary conditions at the sources. Assuming the gas vented in the plumes eventually condenses on the surface of Io, our mass flow rates yield a resurfacing rate of about  $10^{-4}$  to  $10^{-2}$  cm/yr. This rate is consistent with that of Johnson, *et al.* (1979), which was based on particulate transport in the Pele plume.

This research was supported by NASA Grant NSG 7156.

#### References

- Johnson, T. V., Cook, A. F., Sagan, C., and Soderblom, L. A. (1979). Volcanic resurfacing rates and implications for volatiles on Io. *Nature* 280, 746-750.
- McCauley, J. F., Smith, B. A., and Soderblom, L. A. (1979). Erosional scarps on Io. *Nature* 280, 736-738.

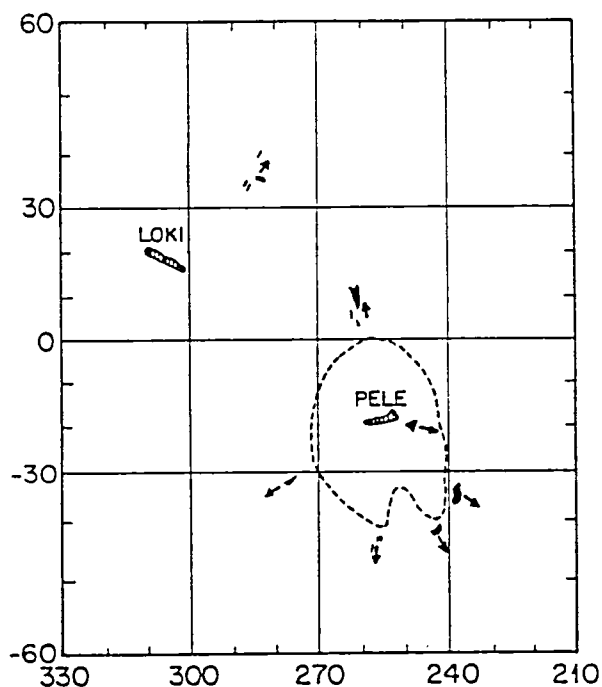


Figure 1. Sketch map (Mercator projection) of bright streaks in the vicinity of Pele and Loki. The arrows indicate the flow direction inferred to cause the streaks.

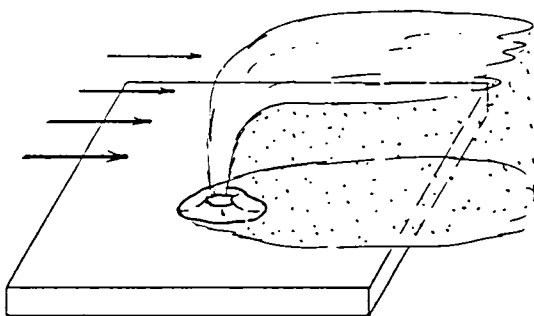
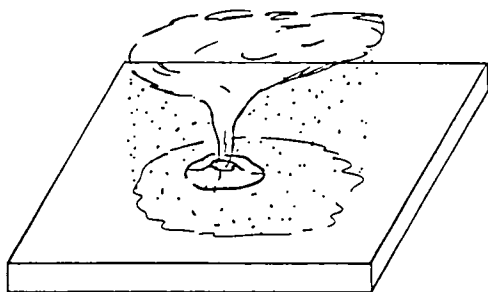
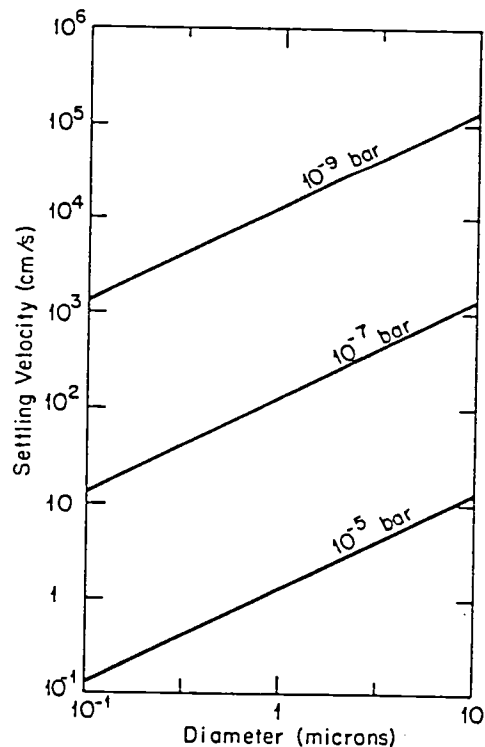


Figure 2. Sketch of fumarole-like source for streamers (horizontal dimension not to scale). Top: During periods with no major nearby plume activity, particulates condensing from the local venting are deposited symmetrically about the vent. Bottom: Gas flowing away from a plume source suspends and transports particulates produced by the local venting. A deposit "down-wind" of the local vent is formed.

Figure 3. Settling velocity versus particle diameter (particle density =  $0.15 \text{ gm/cm}^3$ ) in  $\text{SO}_2$  gas at  $130^\circ\text{K}$ .



## OBLIQUE IMPACTS AND ASTEROIDAL STRUCTURE

Chapman, C.R.; Weidenschilling, S.J.; Davis, D.R.; and Greenberg, R., Planetary Science Institute, Tucson, Arizona 85719

The geological and geophysical properties of asteroids and their collisional evolution are intimately connected. On one hand, asteroids have collided with each other so often that the size distribution of the population, as well as physical and geological properties of most individual asteroids, have probably been shaped chiefly by collisions. On the other hand, the modifications of asteroidal properties resulting from collisions may have dominant effects on outcomes of further collisions (e.g. depending on the degree to which the effective strength of bodies is weakened by fracturing).

Until recently, most studies of collisional evolution have emphasized the energetics of head-on collisions. The known size and velocity-distributions of asteroids yield readily calculable collision frequencies and kinetic energies. It is uncertain how impact kinetic energy is partitioned into rock fragmentation, ejecta velocities, heat, etc., although there is some experimental and theoretical evidence on this matter. Nevertheless, even over wide ranges of possible partition coefficients, useful conclusions about asteroidal evolution have been drawn (e.g. Davis *et al.*, 1979, 1980) because the energy densities involved are so large compared with strengths of geological materials that asteroids must have been badly damaged or altered in one or more ways.

In order to further constrain asteroidal evolution, we have recently begun to consider the effects of another fundamental physical quantity that is conserved in asteroidal collisions: angular momentum. Generally asteroidal collisions are off-center, resulting in changes in angular momentum of a target asteroid. Studies of asteroid spins, in combination with our earlier work concerning head-on collisions, are resulting in surprisingly important conclusions about asteroidal evolution. In particular, many asteroids will spin up to such rapid rates, due to collisions, that their overall geophysical configurations may be grossly distorted and they may disrupt into binary and multiple-asteroid systems.

In order to amplify on Harris' (1979) analytical models of asteroid spin evolution, we have devised a Monte Carlo numerical model, incorporating a detailed simulation of the collision process. Included in our simulation is partitioning of collisional energy and momentum into detailed ejecta mass and velocity distributions, together with the effect of the rotational velocity of the asteroid surface and the variation of ejecta distribution with azimuth. The model computes

changes in mass and angular momentum of a target body resulting from random impacts selected from an appropriate size distribution (Weidenschilling, 1980a). The results are sensitive to choices of ejecta mass and velocity distributions, for which there is a paucity of experimental data. But reasonable assumptions lead to the following conclusions.

Assuming the asteroids are spherical, the random-walk spin-up of moderate- to large-sized asteroids results in some asteroids having very rapid spins ( $\sim 2$  hr.), which are not observed. We now believe we understand why: Our earlier studies demonstrated that many asteroidal collisions may have sufficient energies to fragment asteroids, but insufficient to disperse them. Thus, many asteroids are expected to be structurally weak, gravitationally bound "rubble piles", or they may have developed extensive megaregoliths. Such asteroids would not be sufficiently strong to retain grossly disequilibrium shapes against their own gravity and the centrifugal forces of rapid spin. Instead, the shapes of large, rapidly spinning asteroids would be governed more nearly by hydrodynamic forces than by material strength. Weidenschilling (1980b,c) and Farinella *et al.* (1980) have applied Chandrasekhar's (1969) treatment of equilibrium fluid bodies to the asteroidal case. They find that the larger asteroids spinning with periods shorter than  $6^h$  may be substantially deformed into Maclaurin spheroids or triaxial Jacobi ellipsoids, depending on their spins and bulk densities. Additional angular momentum results in modifications of shape rather than faster spin, explaining the absence of observed spin periods  $< 4^h$  for known asteroids.

Collisional shattering of rapidly rotating asteroids can result in gravitationally bound systems having too much angular momentum to collapse into a single body, resulting in a binary or multiple asteroid. Indeed, observational evidence is accumulating that some asteroids are indeed binary objects: asteroidal satellites may have been detected by stellar occultations (Van Flandern *et al.*, 1980), speckle interferometric data show satellites of Pallas and Victoria (Hege *et al.*, 1980), and some lightcurves seem most compatible with binary systems. For example, Weidenschilling (1980b) has shown that Hektor's lightcurve is compatible with a tidally deformed contact binary. These startling observations may now be understood as the inevitable result (in a statistically significant number of cases) of the natural collisional processes occurring in the asteroid belt. Not only is it common for asteroids to be energetically shattered while the fragments remain gravitationally bound, but in many of these cases the angular momentum of the system will be too large for a single body to reaccumulate. Our collisional simulations suggest that  $\sim 10\%$  of large asteroids will pass through such a binary or multiple-asteroid stage prior to catastrophic destruction (Chapman *et al.*, 1980).

Once a binary object is formed, its subsequent collisional evolution will be somewhat different from what it would have



been as a single body. Each component will be subject individually to the chances of catastrophic destruction by the impacting flux, resulting in shorter lifetimes than would be expected for a single body of the same total mass. Such a speeding-up of asteroid destruction processes is qualitatively counterbalanced by the tendency for off-center collisions to be less efficient at fracturing targets than the head-on collisions previously studied. Fujiwara et al. (1980) have conducted laboratory experiments showing that the mass of the largest fragment in an off-center collision varies as the inverse-cube of the cosine of the impact angle (measured with respect to the surface normal at the impact point). Oblique impacts tend to "chip" off parts of the target body rather than shatter it. It is not known the degree to which these inefficiencies are relevant to the large, structurally weak bodies we are considering, but individual asteroidal fragmentation rates may be somewhat slower than we have previously calculated.

We are currently working on combining our numerical simulations of the evolution of the asteroid size distribution with our more recent models of angular momentum evolution. We hope to learn how the whole population evolves. We will calculate the steady-state distributions of asteroidal spins, shapes, proportion of binaries, and so on to compare with astronomical observations. It is interesting that the concept of asteroidal megaregololiths, which we developed to explain the geological properties of asteroids, is turning out to have fundamental importance in understanding the cosmogony of the asteroidal population and the existence of binary asteroids.

#### REFERENCES:

- Chandrasekhar, S. (1969), Ellipsoidal Figures of Equilibrium  
Yale Univ. Press, New Haven, Conn.
- Chapman, C. R. , Davis, D. R. and Weidenschilling, S. J. (1980),  
BAAS, in press; presented at 12th DPS Meeting, Tucson, Az.
- Davis, D. R., Chapman, C. R., Greenberg, R., Weidenschilling, S. J.  
and Harris, A. L., in Asteroids, T. Gehrels, ed. Univ. of Ariz.  
Press, Tucson, Az.
- Davis, D. R., Chapman, C. R., Greenberg, R. and Weidenschilling,  
S. J. (1980), Reports of the PGPI 1979-1980, NASA TM 81776.
- Farinella, P., Paolicchi, P., Tedesco, E. F. and Zappala, V. (1980),  
submitted to Icarus.
- Fujiwara, A. and Tsukamoto, A. (1980), submitted to Icarus.
- Harris, A. L. (1979), Icarus, 40, No. 1.
- Hege, E. K., Cocke, W. J., Hubbard, E. N., Christov, J. and  
Radick, R. (1980), BAAS, in press, presented at 12th DPS Meeting,  
Tucson, Az.

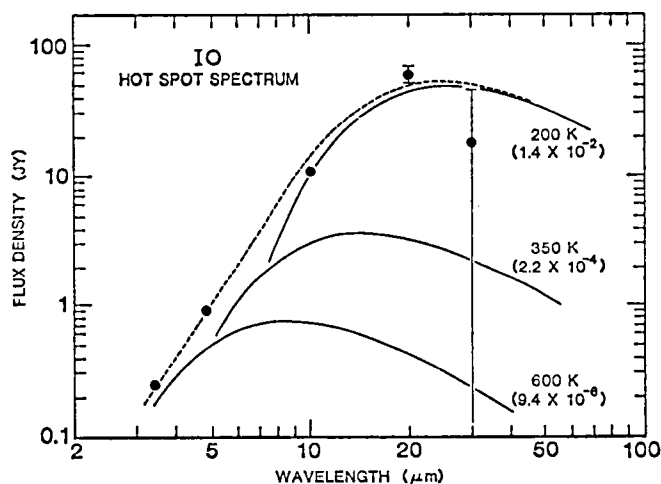
- Van Flandern, T. C., Tedesco, E. F. and Binzel, R. P. (1979), in Asteroids, T. Gehrels, ed. Univ. of Ariz. Press, Tucson, Az.
- Weidenschilling S. J. (1980a), LPSC XI Abstracts, 1231-1233.
- Weidenschilling S. J. (1980b), submitted to Science.
- Weidenschilling S. J. (1980c), BAAS, in press, presented at 12th DPS Meeting, Tucson, Az.

# THERMAL INFRARED STUDIES OF THE GALILEAN SATELLITES

Morrison, David, Institute for Astronomy, University of Hawaii,  
Honolulu, Hawaii 96822

Infrared observations of the Io eclipse of 12 April 1980 in five broad bands from 3 to 30  $\mu\text{m}$  define the thermal emission spectrum both during and after eclipse. A substantial fraction of the emitted radiation during eclipse arises from hot spots; the figure illustrates the hot spot spectrum. The equivalent global average heat flow is  $1.5 \pm 0.3 \text{ W m}^{-2}$ , corresponding to an internal source of  $(6 \pm 1) \times 10^{13} \text{ W}$ . The hot spot spectra can be matched by components with color temperatures of 200-600 K covering 1 - 2% of the surface, as indicated by the model curves in the figure. Comparison with observations over the past 8 years suggests that, while the flux at the hottest temperatures may be highly variable, there is no evidence for major changes in the total heat flow, which is emitted primarily in the 10 - 20  $\mu\text{m}$  spectral region. The internal heat source can be used to constrain the Q of Io to values less than  $\sim 50$ . The total tidal dissipation indicated by these observations exceeds by about a factor of 2 the maximum expected from dynamical theory of the orbital resonance of the Galilean satellites.

The heating curves of the surface of Io were observed at the same eclipse at wavelengths of 10 and 20  $\mu\text{m}$ ; when corrected for the hot spot contribution they indicate a typical global thermal inertia for Io of  $(0.2 \pm 0.1) \times 10^{-3} \text{ cal cm}^{-2} \text{ s}^{-1/2} \text{ K}^{-1}$ , similar to that of the other Galilean satellites. Additional observations of eclipses of several satellites are planned for the 1980 Fall observing season and will be reported on, if successful. The surface properties of the satellites as indicated by their eclipse cooling and heating curves can be compared with large-scale topography and with surface composition to investigate the presence of regolith formation and evolution.



# VOLCANIC ERUPTION PLUMES ON IO,

Robert G. Strom<sup>1</sup>, Nicholas M. Schneider<sup>1</sup>, Richard J. Terrile<sup>2</sup>, Allan F. Cook<sup>3</sup> and Candice Hansen<sup>2</sup>, <sup>1</sup>Lunar and Planetary Laboratory, University of Arizona, Tucson, Arizona 85721. <sup>2</sup>Jet Propulsion Laboratory, Pasadena, California 91103. <sup>3</sup>Center for Astrophysics, Cambridge, Massachusetts 02138.

Nine volcanic eruption plumes were observed over a period of 6 1/2 days during the Voyager 1 encounter with Io. During the Voyager 2 encounter, four months later, eight of these eruptions were still active. The largest plume viewed by Voyager 1 became inactive sometime between the two encounters. However, a major eruption occurred at Surt sometime between the two encounters and deposited an ejecta blanket comparable in size to those associated with the largest plumes. The source area of this eruption was not viewed near enough to the limb on the second encounter to confirm whether or not it was still active. The plumes range in height from about 60 to over 300 km with corresponding ejection velocities of about 0.5 to 1.0 km/sec. Some plumes are symmetrical and umbrella-shaped (Plumes 1 and 3) whereas others are diffuse and more irregularly shaped. Their shape appears to be largely governed by the vent geometry; umbrella-shaped plumes appear to be associated with elliptical to circular vents and diffuse plumes seem to be issuing from long fissures. Where topographic information exists (Plumes 1 and 8), the plume source is located on level plains rather than topographic highs. With the exception of Plume 1 (Pele), the brightness distribution monotonically increases from the core to the top of the plume. The shape, brightness distribution and pattern of the surface deposit of at least Plume 3 (Prometheus) can be simulated by a ballistic model in which the ejection velocity is constant (0.5 km/sec) and ejection angles vary from vertical down to 55 degrees (Figures 1 and 2). The brightness distribution of Plume 1 is probably better explained by a shock front near the top of the plume.

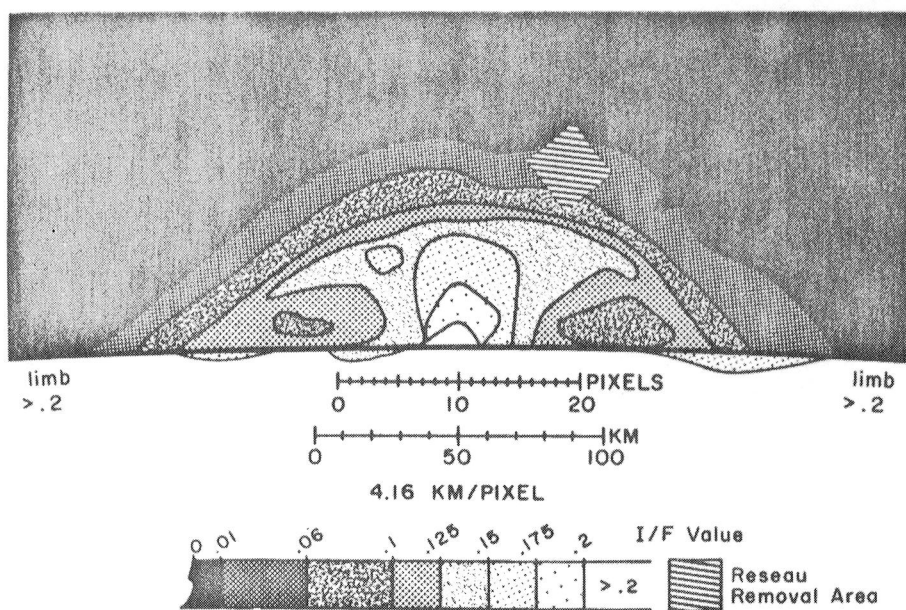
Active eruptions are randomly distributed with respect to longitude but are concentrated within  $\pm 45$  degrees of the equator. Numerous surface deposits similar to those associated with active plumes probably mark the sites of recent eruptions, and they also appear to be concentrated in the equatorial regions. Many small dark diffuse deposits less than 40 km diameter are seen on the highest resolution pictures and are located primarily on the rims of calderas. These also seem to be concentrated in the equatorial regions, and are probably the sites of small recent eruptions some of which may have been active during the Voyager encounters. Furthermore, geological mapping by Schaber (1980) shows that the equatorial zone has six times the number of calderas or vents per unit area as the south polar region. The distribution of calderas and of active and recent eruptions indicates the volcanic activity is more frequent and intense in the equatorial regions than the polar regions. This suggests that the depositional rate is greater and the surface age younger in the equatorial regions. This may account for the darker polar regions which would be subjected to radiation darkening over a longer period of time.

At least eight eruptions have continued at a high level of activity with ejection velocities of  $\sim 0.5$  to  $1.0$  km/sec for at least four months and probably much longer. This indicates that large reservoirs of volatiles are available to continuously supply gases to the vent areas over long periods of time. This, together with the geological setting of certain plume sources, suggests that sulphur volcanism similar to that proposed by Smith, et al. (1979) is responsible for at least the active eruptions. The recent discovery of high temperature hot spots suggests that  $S_2$  vapor may be the primary driving volatile, and that  $SO_2$  may be primarily responsible for the smaller eruptions characterized by small dark diffuse deposits.

#### REFERENCES:

Schaber, G. G. (1980). The Surface of Io: Geologic Units, Morphology and Tectonics, Icarus, in press.

Smith, B. A. et al. (1979). The Role of  $SO_2$  in Volcanism on Io, Nature 280, 733-738.



Smoothed Brightness Contours of Plume 3  
Voyager I Io Encounter FDS 16377.48, Clear Filter

Figure 1

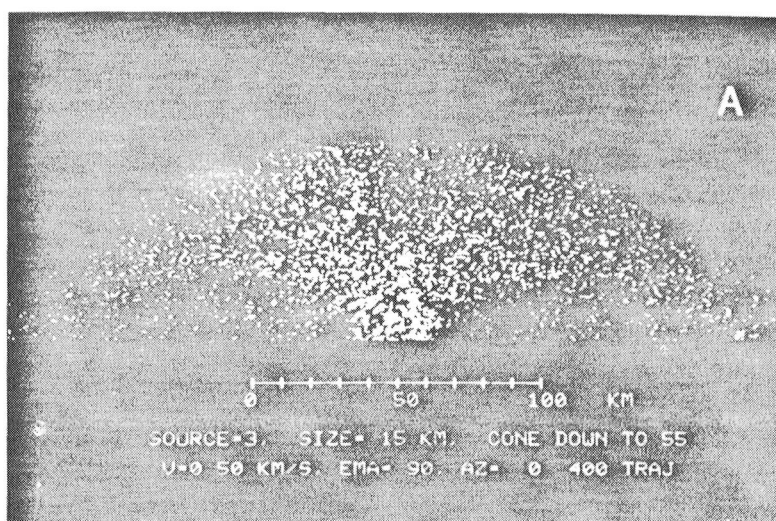


Figure 2

## 10 PLUME DYNAMICS.

N. M. Schneider and R. G. Strom, Lunar and Planetary Laboratory,  
University of Arizona, A. F. Cook, Harvard-Smithsonian Center for  
Astrophysics

Recent analyses of the Voyager images and theoretical models of Io's eruption plumes have led to certain constraints on their dynamics. Preliminary comparisons of the brightness contours of Plumes 1 (Pele) and 3 (Prometheus) have been made with ballistic models and expected characteristics of shock front models. In the ballistic model, material ejected from the vent follows the parabola dictated by a uniform gravitational field. In the shock front model, the trajectories are ballistic until they intersect the dome-shaped shock front. The motion of the particles after this point is dependent on the conditions at the front. The equations of motion have not yet been solved, so we will make the qualitative assumption that after passing through the front, material falls to the surface following the shape of the front.

In an attempt to determine which model best matches the Voyager observations, we compared Monte-Carlo simulations of the ballistic model with brightness contours of Plumes 1 and 3. We varied the vent geometry, limits on ejection angles, angle/frequency distribution, and velocity/frequency distribution to obtain the best match. The three criteria were envelope shape, brightness structure and surface deposit. Figure 1 shows the brightness contours of Plume 3 on the limb. Figure 2A shows a plume simulation with material ejected at a velocity of 0.5 km/sec isotropically from a point source into a cone from  $0^\circ$  to  $55^\circ$  from the vertical. Considering the simplicity of the model, the simulation matches rather closely (1) the roughly parabolic envelope, (2) the monotonic decrease in brightness from the core to the top, and (3) the very dark holes either side of the core. The  $55^\circ$  angle is not precise, but the quality of the match deteriorates significantly as the limiting angle becomes less than  $45^\circ$  from the vertical.

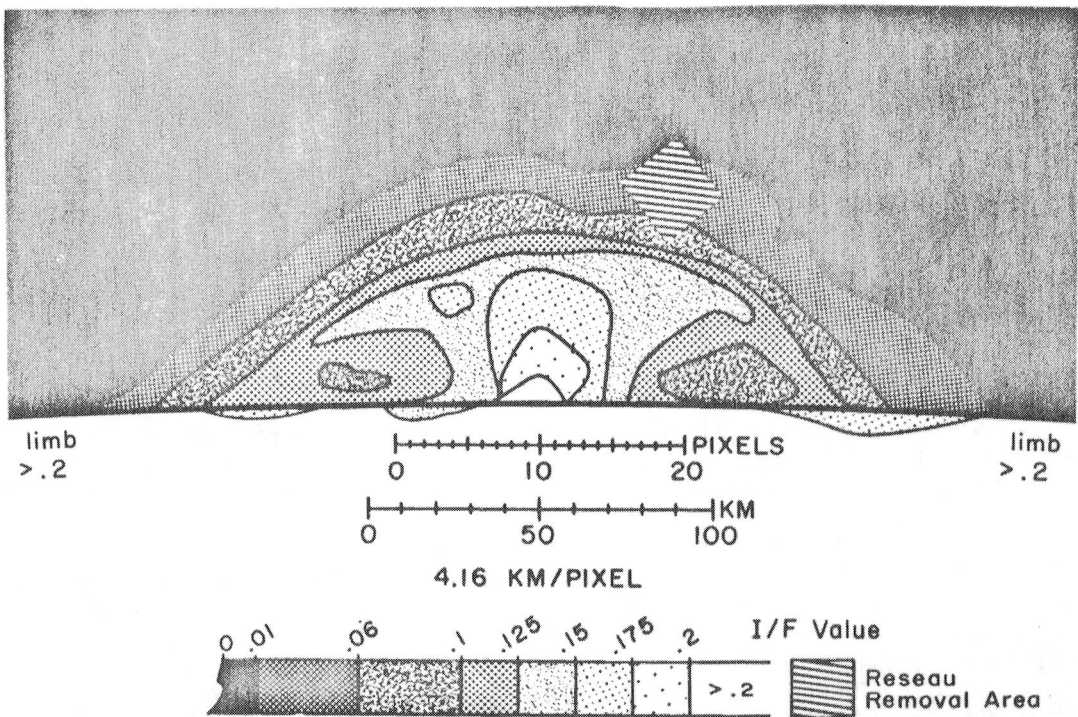
Slight adjustment of the model parameters can improve the match. The introduction of a small velocity dependence on angle ( $\leq 10\%$  of ejection velocity over the  $55^\circ$  range) and a small gaussian velocity distribution ( $\sigma \leq 10\%$  of ejection velocity) will lead to minor improvements in the fit. Not much insight can be gained into the nature of the source region since the lower 7 km of Plume 3 are hidden by the limb. The upper structure is not highly sensitive to vent configuration; the plume from a point source does not differ significantly above 7 km from that created by a 10 km disk-shaped source.

Images of Prometheus against the disk show a ring deposit near maximum range. The simulations also predict this (Figure 2B), as long as the limiting ejection angle is greater than  $45^\circ$  (which gives maximum range in the constant velocity case). The sharp outer cutoff will become diffuse when a velocity dispersion is introduced.

The simulations lead to the following conclusions concerning Plume 3: (1) The ejection velocity is not highly dependent on angle, (2) The velocity dispersion is small, (3) The ejection angle/frequency distribution is close to isotropic, (4) The limiting ejection angle is  $>45^\circ$  from the vertical.

While Plume 1 (Figure 3) exhibits many similarities to Plume 3, the differences make it impossible to match its structure with the same model. The significantly greater height ( $\sim 300$  km vs.  $\sim 80$  km) and intrinsic faintness may be important, but the most radical difference is the bright outer envelope near the plume top. This appears to be the only plume which shows such a structure. This feature has not been reproduced by ballistic simulations which also yield the ring deposit seen around Pélé.

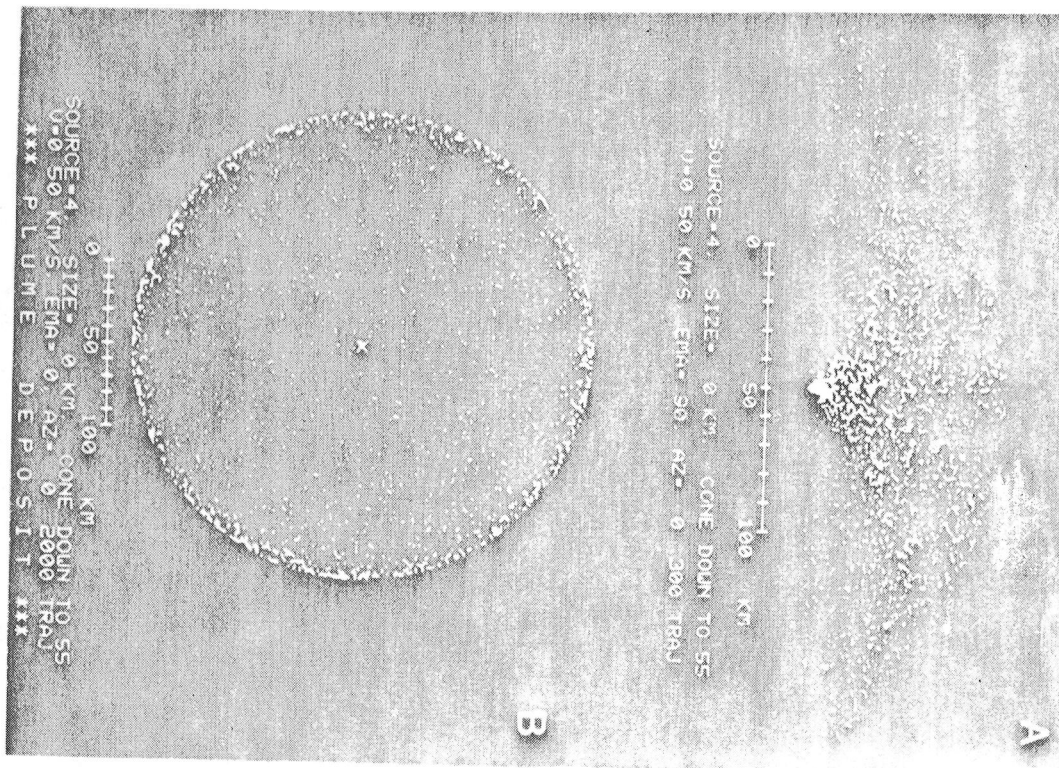
The shock model has not yet been successfully simulated, but qualitatively we would expect the dome-shaped shock shell to appear as a bright outer envelope in projection. The choice of the model for Plume 1 will not be resolved without further simulations of both the ballistic and shock front models.



Smoothed Brightness Contours of Plume 3  
Voyager I Io Encounter FDS 16377.48, Clear Filter

Figure 1

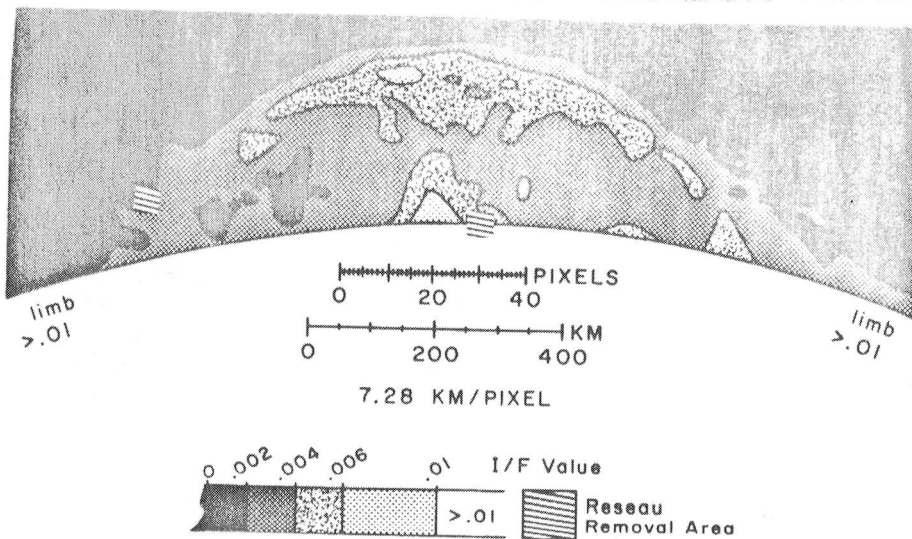




A

B

< Figure 2  
 V Figure 3



Smoothed Brightness Contours of Plume I  
 Voyager I Io Encounter FDS 16368.50, UV Filter

## MORPHOMETRY OF CRATERS AND CALDERA ON IO AS AN INDICATOR OF ERUPTIVE STYLE

J.L.Whitford-Stark\*and P.J.Mouginis-Mark, Dept. Geological Sciences, Brown University, Providence, RI 02912

Io represents an important new environment in which the dynamics of active volcanism can be investigated. As a result, we have initiated a survey of ionian volcanic features in an attempt to identify spatial variations in volcano eruptive style, relative age, and lithospheric thickness. Pike (1,2) has shown that morphometric data for volcanic craters on the terrestrial planets illustrates that variations in eruptive style can be correlated with the dimensions of the volcanoes. Although attempts to interpret the origin of volcanic structures have proved difficult due to possible alternate lava chemistries producing morphologically similar landforms (3), Schaber (4) has proposed that the closest terrestrial analogue to Io craters is the calkalic ash-flow plains caldera. Schaber (4) also suggested that the ionian craters may be characterized by early-stage fissure eruptions. However, by comparison to Mars, volcanic craters on Io may be produced by basaltic-style eruptions (5). Williams and McBirney (6) have listed seven ways in which terrestrial caldera may form, and several different mechanism may be responsible for the formation of caldera on Io. Unfortunately, the use of terrestrial examples is limited for the interpretation of Io craters because only a few small terrestrial caldera have been observed in the process of formation. For example, Mt.St.Helens, Katmai and Krakatau are all less than 10 km (1,7). Other caldera have become enlarged, for example Fernandina (8) and Askja (9). The only apparently unifying characteristic of all terrestrial caldera is that they have been the sites of repetitive volcanic activity for substantial periods of time.

It has been argued (10), on the basis of observed plumes, that the equatorial region of Io is currently more active than the polar regions. The morphology of some high latitude crater deposits suggests to us, however, that if the volcanoes were indeed inactive during the Voyager flybys, then they have only recently ceased to erupt: deposits associated with some 33 craters indicate recent (or current) activity. The difficulty of resolving all eruption locations on the basis of a short observational time can be illustrated by reference to known terrestrial activity. For example, if the average of about 13 volcanic events reported in the SEAN Bulletin each month is broken down into latitudinal positions, it is found that up to the start of 1980, 64% of the reported volcanoes were located within 30° of the equator and 52% occurred within 20°. Were it not for the known distribution of dormant volcanoes, such a

statistic could achieve undue significance.

Major questions concerning ionian caldera exist: for example, how do individual craters form?; how long does it take to form a caldera?; do size and shape variations in the different caldera reflect different eruption styles and/or chemistry?; and do these variations in caldera morphology indicate contrasting magma or crustal conditions? Several authors (11-13) have postulated that the spacing of terrestrial volcanoes is proportional to lithospheric thickness and others (14) have suggested that volcano spacing appears to be correlated with the explosiveness of the eruptions. It is unclear if this relationship for volcano spacing also holds for craters on Io. In an attempt to resolve some of the ambiguities in the interpretation of volcanism on Io, we are currently analyzing morphometric data collected for 179 craters identified on high and medium resolution Voyager 1 images. The distribution of these craters is shown in Fig.1. Apparent from Fig. 1 is the close proximity ( less than 1 crater diameter) of multiple caldera from adjacent volcanic landforms. Together with the observation that many of the same plumes were observed to be erupting during both Voyager flybys, this suggests to us that many of the Io calderas are the product of subsidence rather than explosive eruptions of short duration.

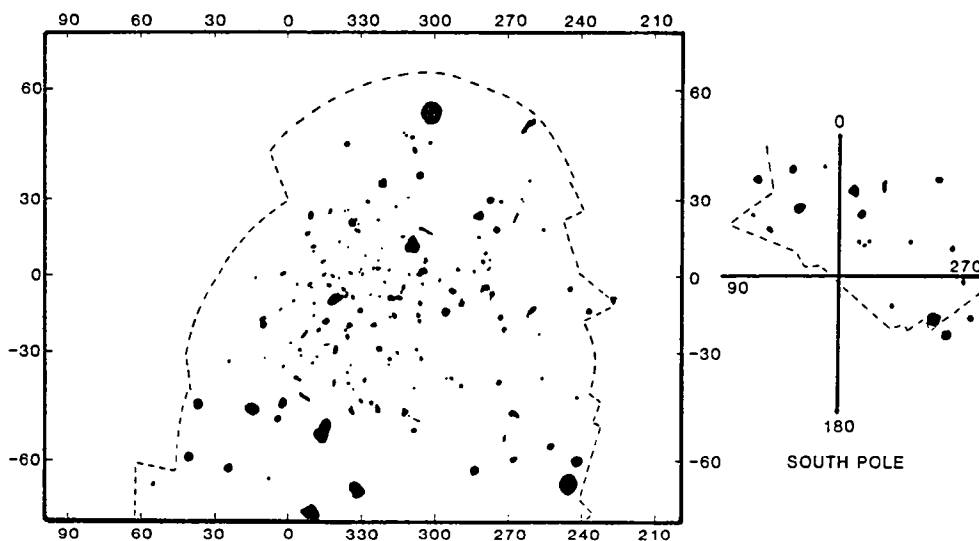


Figure 1: Distribution map of the craters on Io considered in this analysis. Dashed line indicates the limits of the medium resolution images.

A size/frequency plot for the craters on Io (Fig.2) demonstrates that the majority of the craters are less than 50 km in diameter, although caldera 200 km in size can be found. Within the observational limits imposed by the available images, it appears that regional size variations do indeed exist in the dimensions of the volcanoes. As a result, we are currently pursuing the possible association between volcano spacing and position on the satellite, in the hope of identifying regional variations in eruption characteristics or differences in lithospheric thickness.

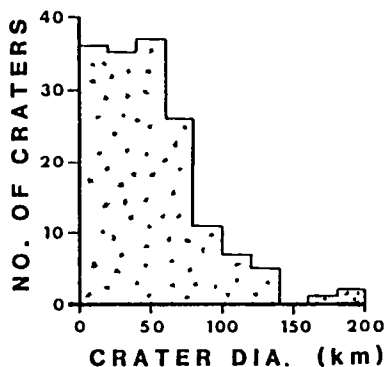


Figure 2: Histogram of the size distribution of craters on Io, bin size is 20 km.

REFERENCES: 1) Pike R.J. (1978) PLPSC 9th, 3239-3273. 2) Pike R.J. (1980) NASA-TM 81776, 192-194. 3) Whitford-Stark J.L. (1980) NASA-TM 81776, 195-197. 4) Schaber G.G. (1980) Icarus in press. 5) Moore H.J. et al. (1979) PLPSC 9th, 3351-3378. 6) Williams H. & McBirney A.R. (1979) Volcanology, Freeman, Cooper & Co., San Francisco, 370 pp. 7) Wunderman R. (1980) Volcano News 4, 7. 8) Simkin T. & Howard K.A. (1970) Science 169, 429-437. 9) Wood C.A. et al. (1977) B.V. Study Project Contrib. #6, Lunar & Planetary Inst. 10) Masursky H. et al (1979) Nature 280, 725-729. 11) Vogt P.R. (1974) Earth Planet. Sci.Lett. 21, 235-252. 12) Mohr P.A. & Wood C.A. (1976) Earth Planet.Sci.Lett. 33, 126-144. 13) Windley B.F. & Davies F.B. (1978) Earth Planet.Sci.Lett. 38, 291-297. 14) Swanson F.J. et al. (1974) Geol.Soc.Amer.Bull. 85, 1803-1810.

\* JLW-S currently at 501, Turner Apt.#5, Columbia, Missouri 65201.

IO: SIZE AND SPATIAL DISTRIBUTIONS OF VOLCANIC VENTS; TRENDS OF  
TECTONIC FEATURES, Gerald G. Schaber and Arthur L. Dial, Jr., U.S.  
Geological Survey, Flagstaff, Arizona.

A total of 170 volcanic vents with diameters  $> 14$  km and 151 lineaments with lengths  $> 50$  km have been mapped within an area representing 26.5% of the surface of Io during preliminary geologic mapping [1]. The area of the volcanic vents was calculated and a cumulative size-frequency distribution plot was prepared (Fig. 1). A perfectly circular outline was assumed for assignment of crater diameters. The curve in Fig. 1 is similar to conventional impact crater size-frequency distribution plots, and, like these plots, attests to a nonrandom distribution of crater diameters and a surplus of small craters.

A total of 587 terrestrial craters (1 to 12 km in diameter) of explosive volcanic origin was shown by Simpson [2] to have a percentage distribution curve that is very similar in shape to those observed for lunar and martian craters. This overall similarity of crater distribution curves led Simpson [2] and other early workers to assume incorrectly a volcanic origin for the majority of the observed craters on the Moon and Mars. The resemblance of impact crater size-frequency and percentage-frequency statistics to those of volcanic craters emphasizes the need to integrate studies of crater origin with crater-count research on solid solar system bodies [3]. Frequencies of both impact and volcanic craters have an excess of small craters with a predictable falloff to larger crater sizes. For impact craters, this phenomenon is a function of the collisional evolution of planetesimals, asteroids and cometary debris, impact velocity, and acceleration of gravity. The size of a volcanic explosion crater is a complex function of magma temperature and gas saturation, overburden strength and density, and the acceleration of gravity.

A total of 21 equal-area bins was established within the mapped area of Io for the purpose of assessing the spatial distribution of volcanic vents (Fig. 2). Regions covered by oblique pictures and areas obscured in part by plume materials were deleted from the count. In each bin shown in Fig. 2 is included the percentage deviation from the mean number of vents expected for a totally random distribution for the area of all 21 bins combined. Note that bins 1 through 6 and 8, near the equator, have excesses from +39% to +148% of the expected values, whereas the six polar bins (16 to 21) have deficiencies of -70% to 101%. The remaining bins (7 and 9 through 15) in the midlatitude zone have both negative and positive deviations (-31% to +16%) from expected values for randomness. No longitudinal asymmetry in vent distribution was found within the mapped area. The equatorial zone, exemplified by bins 1 through 5 and 8, has about twice the concentration of vents as the midlatitude zone and six times the concentration of the south polar zone. Mean vent sizes appear to increase steadily from the equatorial zone (48 km) to the south polar zone (65 km), but standard deviations overlap, suggesting little or no statistical significance.

The meaning of the latitudinal variation in vent sizes on Io is unknown; however, it could be related to the present concentration of tidal stress and resulting volcanic activity within 30° north and south of the equator [4]. The cumulative size-frequency and areal distribution of the vents are preliminary because of the poor control ( $\pm 1-2^\circ$ ) of the airbrush base used; however, they should provide useful interim statistics for those workers interested in assessing models of the eruptive process(es). More precise vent statistics will be forthcoming upon completion of controlled orthophotomosaics by the U.S. Geological Survey of the best available Voyager frames.

Io contains numerous lineaments and grabens despite a very young surface age. Poorly defined lineaments are concentrated in the equatorial zone imaged at high (75°) sun angle. Several fault traces are well documented at lat -8°, long 284°.

South of lat -46°, tectonic features are mainly grabens with medial troughs clearly defined at low sun angles. These tensional structures are concentrated on the layered plains unit and appear to be the controlling factors for the layered plains boundary scarps [1]. Both grabens and lineaments trend dominantly northwest and northeast (Fig. 3); thus they exhibit a common planetary grid pattern (probably resulting from tidal flexing) characteristic of virtually all silicate bodies observed thus far in the solar system. The tectonic structures also exhibit an approximate east-west trend, which is not seen on Mercury and the Moon but is described on Mars and Venus.

The mountain material is the most disrupted by tectonic stresses; virtually every exposure of this unit has at least one nearly orthogonal set of fractures that control the irregular topography characteristic of this material.

#### References

- [1] Schaber, G. G., and Arthur, D. W. G., 1981, Io: Preliminary mapping of geologic units, (this volume).
- [2] Simpson, J. F., 1966, Additional evidence for the volcanic origin of lunar and martian craters: *Earth Planet. Sci. Lett.*, 1, 132-134.
- [3] Greeley, Ronald, and Gault, D. E., 1979, Endogenic craters on basaltic lava flows: Size-frequency distributions: *Proc. 10th Lunar and Planetary Sci. Conf.*, 2919-2933.
- [4] Strom, R. G., Terrile, R. J., Masursky, Harold, and Hansen, Candice, 1979, Volcanic eruption plumes on Io: *Nature*, 280, 733-736.
- [5] Schaber, G.G., 1980, The surface of Io: geologic units, morphology, and tectonics: *Icarus* - in press.

Fig. 1- Cumulative size-frequency plot of Io's volcanic vents compared to conventional impact crater curves for average lunar maria and heavily cratered surfaces on the Moon and other planetary bodies. Total of vents counted is 170. One sigma error bars shown. After [5].

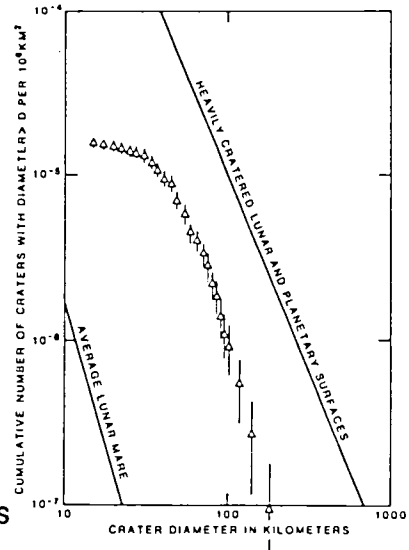
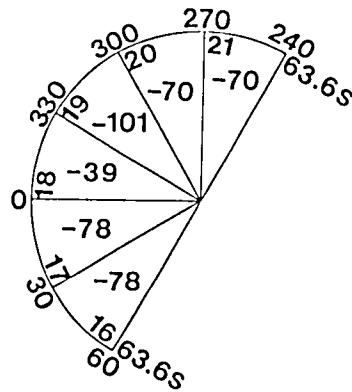
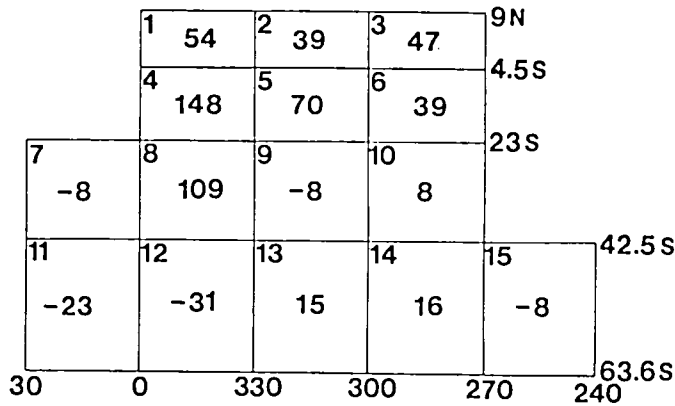


Fig. 2- Location sketch of 21 equal-area bins used for analysis of vent areal distribution statistics for the equatorial, mid-latitude, and south polar zones of Io. Number in center of each bin is percentage deviation from number of vents necessary for total randomness over area of all 21 bins. After [5].

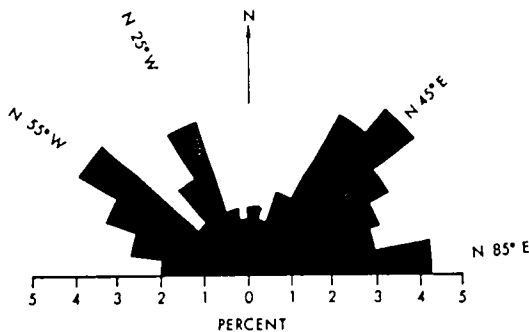


Fig. 3- Tectonic azimuth rosette compiled from lineaments and grabens mapped on Io. Two nearly orthogonal trends occur with 110° separation. Length of lineaments given as percent of total number (151) measured. After [5].

IO: PRELIMINARY MAPPING OF GEOLOGIC UNITS, Gerald G. Schaber, and David W. G. Arthur; U.S. Geological Survey, Flagstaff, Arizona 86001.

A preliminary geologic map (Fig. 1), representing 26.5% of the surface of Io, has been compiled using best resolution (0.5 to 5 km/line pair) Voyager 1 images and (as a base) a preliminary pictorial map of Io. Nine volcanic units are identified, including materials of mountains (1.9% of mapped area), plains (49.6%), crater vents (4.0%), flows (31.1%), and cones (0.1%). The remaining area (13.35%) was obscured by active plume deposits. The mapped area of Io is dominantly reddish orange in color and lies within the longitudinal zone that contains the least amount of SO<sub>2</sub> frost observed by spectral reflectance [1]; thus at least the uppermost microns to meters of the surface are dominated by other sulfurous components. Mountain Unit is thought to be the oldest mapped unit; it is characterized by relief at least as high as  $9 \pm 1$  km and a tectonically disrupted, topographically rugged surface. Its significant relief suggests a composition of primarily silicate volcanic material [2]. The unit is commonly associated with patches of layered plains material and it also occurs in several localities rimming large, shallow circular volcanic depressions within the intervent plains. Numerous pit craters with steep walls on the mountain material unit indicate that the mountains themselves are commonly vent sources. Mountain material appears to be equally well represented in the equatorial and polar regions of Io and its distribution has no obvious longitudinal significance. Intervent Plains Unit covers 39.6% of the mapped area of Io. It is characterized by smooth surfaces, locally developed low scarps, and regionally consistent, intermediate albedo that lies between those of all other mapped geologic units. The unit is thought to consist of stratified materials that originated as frozen fallout from volcanic plumes or as lava flows, probably interbedded with fumarole materials and flow deposits from pit craters, shield craters, and fissure vents. Colors of the unit are dominantly reddish orange, orange, yellow, and orange brown. Layered Plains Unit is characterized by an extensive, smooth, flat surface; straight, curvilinear and scalloped boundary scarps 150 m to 1700 m high; and abundant grabens that are either parallel or transverse to the scarps. The unit covers 9.3% of the mapped area and, although found at diverse latitudes and longitudes, is best developed near the south pole. It is thought to have the same origin and composition as the intervent plains unit, but is bounded by scarps that vary greatly in height. The scarps appear to be caused by SO<sub>2</sub>-sapping processes [3] operating along normal faults and grabens; scalloped or fretted contacts may indicate scarp erosion that has progressed beyond the controlling faults. Eroded Layered Plains Unit: these isolated remnants provide the strongest evidence for SO<sub>2</sub>-sapping or surface devolatilization of the layered plains unit. The unit occupies only 0.7% of the mapped area and appears to be restricted to the south polar region; however, this distribution may well be an artifact of the low sun angles in this region. Vent Wall and Floor Unit includes materials of walls and floors of pit craters, shield craters, and fissures; it is



mapped as a single unit (Fig. 1). The materials composing it, thought to be the same as those of the intervent plains, layered plains, and eroded layered plains units, are strong enough to support steep vent walls more than 2 km high with a notable absence of slumping. The unit is characterized by extreme variation in color from white through shades of orange, yellowish-orange, and brown to black. Multiple-stage floor and wall structures in many of the vents indicate repeated eruption episodes from the same vent structure; similar features are common in terrestrial volcanic craters. Of the vents responsible for the plumes observed by Voyager, more are linear in shape than circular [4], indicating that fissure eruptions may dominate early stages of ionian volcanic activity. Pit Crater Flow Unit is deposited in the immediate vicinity of pit crater vents that appear to lie at the elevation of the surrounding intervent plains; thicknesses of individual flows are unresolvable at Voyager 1 resolution. The unit generally extends from one side of pit crater vents as massive coalescing flows with extreme color and albedo variations within the flows. Flow materials probably have a high sulfur content, but some silicate lavas may be present. Pit crater flow materials can be traced as far as 700 km from individual vents, indicating high eruption rates and/or a very fluid eruptive material; the eruptive styles is certainly less violent than those producing fumarole haloes and active plume ring deposits (not mapped in Fig. 1). The pit crater flow unit covers 20.2% of the mapped region of Io. Shield Crater Flow Unit: is associated with the rims and general vicinity of shield craters that appear to be elevated above the surrounding intervent plains. It is probably similar in origin but is perhaps of slightly different composition, viscosity, and flow history than the pit crater flow unit. Individual narrow, sinuous flow lobes can be traced as far as 300 km; color variation along flow length may be related to quenching of different temperature-dependent sulfur allotropes along the flow path. Length-to-width ratios for the well-defined, 200-km-long flows on Maasaw Patera (Fig. 2) range from 20:1 to 50:1 over unknown surface slopes. Twentieth-century hawaiite lava flows on Mount Etna have similar length-to-width ratios (20:1 to 40:1) for flows 7 to 10 km long extruded onto slopes of approximately 8°. However, no compositional similarities are proposed because of the difficulties in relating flow morphologies, surface slopes, and assumed yield strengths to composition [5]. Fissure Flow Unit: is associated with elongate fissure vents that may have fault control. This type of vent and deposit is rare on Io (1.2% of area). All four exposures of the fissure flow unit shown on Fig. 1 originate from fissures with northwest-southeast orientations.

The best documented example of a fissure flow deposit is just west of Mazda Catena at lat -4°, long 320°. Its source is a raised, dike-like feature 92 km long from which thick flows (not measureable) emanate in both directions normal to the fissure strike. Crater Cone Unit forms raised rims surrounding pit craters and shield craters. Cones appear to be similar in form (but not scale) to common terrestrial pyroclastic cones of silicate ash and cinders. This unit forms only 0.1% of the

mapped area and is best observed associated with the pit crater vent named Amaterasu Patera at lat  $+36^\circ$ , long  $306^\circ$ .

## References

- [1] Nelson, R. M., and Hapke, B. W., 1978, Spectral reflectance of the Galilean satellites and Titan, 0.32 to 0.86 micrometers: *Icarus*, 36, 304-329.
- [2] Masursky, Harold, Schaber, G. G., Soderblom, L. A., and Strom, R. G., 1979, Preliminary geological mapping of Io: *Nature*, 280, 725-729.
- [3] McCauley, J. F., Smith, B. A., and Soderblom, L. A., 1979, Erosional scarps on Io: *Nature*, 280, 736-738.
- [4] Strom, R. G., Schneider, N. M., Terrile, R. J., Cook, A. F., II, and Hansen, Candice, 1980, Volcanic eruptions on Io: *Icarus*, Special issue on Galilean satellites (in press).
- [5] Moore, H. J., Arthur, D. W. G., and Schaber, G. G., 1978, Yield strengths of flows on the Earth, Moon, and Mars: *Proc. 9th Lunar and Planetary Sci. Conf.*, 3351-3378.

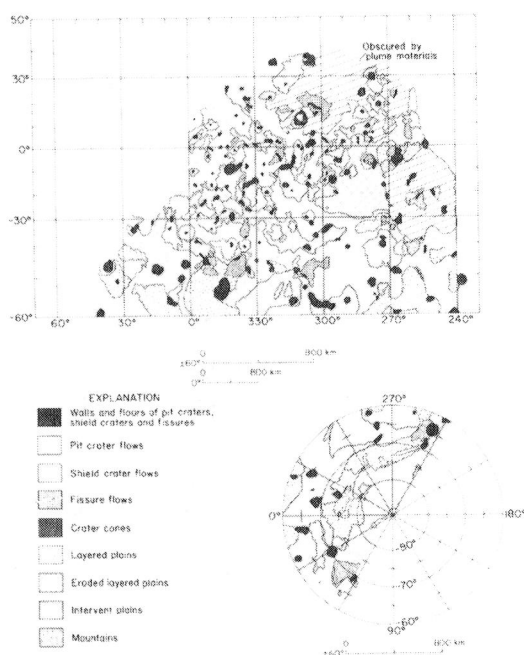


Fig. 1 - Preliminary geologic map of Io showing distribution of nine surface units on 26.5% of the body. Upper map is Mercator projection; lower map is south polar stereographic projection.

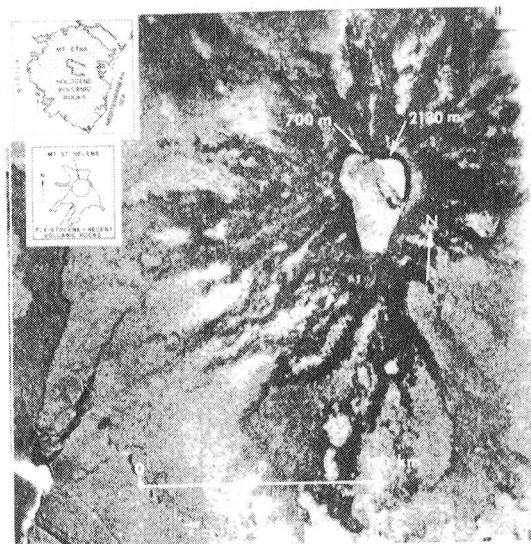


Fig. 2 - Voyager 1 frame 0911J1 showing shield crater vent and radial flows of Maasaw Patera (lat  $-52.6^\circ$ , long  $330.0^\circ$ ). Depths of shield crater wall scarps estimated by D.W.G. Arthur. Insets show (to scale) extent of volcanic flows of Mount Etna and Mount Saint Helens.

## EUROPA SURFACE CRACKING: A CONSEQUENCE OF THERMAL EVOLUTION

Finnerty, A.A., Ransford, G.A., and Pieri, D., Jet Propulsion Laboratory, California Institute of Technology, Pasadena, California 91103.

We have analyzed the mechanical behavior of the petrologic/thermal model for Europa of Ransford and Finnerty (1980), and compared it to the patterns of lineations analyzed by Pieri (1980). In the petrologic model it is suggested that a large core of anhydrous silicates is overlain by a 200-300 km mantle composed of serpentine  $\pm$  chlorite + brucite, and that sufficient water can be contained in such a mantle that only a very thin ice crust is required to satisfy density and volume constraints.

Each of these units have physical properties that are likely to be reflected at the surface of Europa. The anhydrous silicate core is probably at temperatures sufficiently high to induce solid-state convection (Ransford and Finnerty, 1980). The hydrated silicate mantle, on the other hand, is probably very brittle and very weak. Deformation studies of serpentinite and chloritite (e.g. Raleigh and Paterson, 1965; Murrell and Ismail, 1976) show that below the dehydration temperatures (500 to 700°C) they are as strong as granite and brittle. As water is released upon dehydration, or otherwise added to the rocks at lower temperatures, strength declines to  $\sim$  500 - 1000 bars and the rocks become much more brittle. A thin ice crust is also likely to be brittle and deform by fracturing. Deformation studies of water ice show that its behavior mimics that of anhydrous silicates: at a small fraction of its melting temperature it deforms in a brittle fashion (Parameswaren and Jones, 1975), while at high temperatures it deforms plastically by a creep mechanism (Weertman, 1973).

The mean temperature of ice below the diurnal zone on Europa is about 93°K (Gaffney and Matson, 1980). If the ice layer is indeed thin, it will serve as a recorder for any interior or exterior processes that create stresses above 500-1000 bars in the brittle layers. The Voyager images suggest that this is the case. Pieri (1980) has analyzed and classified the lineations on Europa. Of particular interest to us are his Types 1, 2 and 3 lineae, interpreted as great and small circle extensional fractures, and the Types 5, 6 and 7 lineations. The Type 5 features are localized to the anti-Jove region and are interpreted as small scale extensional fractures, while the Types 6 and 7 features occur in a ring located about 70° outside of the anti-Jove region and are thought to be cusped ridges and scarps formed by compression. Inasmuch as tidal forces are unlikely to cause stresses greater than 10 bars in the ice crust, we relate these features to two internal processes: core expansion and convection.

Core Expansion: The volume change of reaction for dehydration of serpentine has been calculated, assuming that water vapor does not escape immediately from the dehydrating region. At 500°C (the dehydration temperature of serpentine), the volume of the dehydration products increases by 26, 16, 9 and 6 percent at 50, 100, 200 and 300 km depth respectively, and becomes nearly zero at the center of Europa. Similar volume changes are probable for chlorite. An initially cool (<500 - 700°C) Europa composed of  $\sim$  40% hydrated minerals in the petrologic model will, as it heats due to radioactive decay, reach the dehydration temperature initially at the core. A dehydration front will coincide with the 500 - 700°C isotherm as it evolves

upwards, because the dehydration temperature is not sensitive to pressure. Water diffusing upwards may decrease the volume of the dehydrated region and increase the degree of hydration in front of this isotherm to 100%, but because the volume change becomes greater with shallower depth, the process always gives a net volume increase. The hydrostatic stress imposed at the bottom of the brittle and weak serpentinite-chloritite layer can cause global scale fracturing, which is transmitted through the thin (consequently cold and brittle) ice layer to cause the great and small circle fracturing evident in the Voyager images. Many of these fractures have high albedo stripes in their centers that may be topographically high (Malin, 1980), and it may be that fresh ice is currently gaining access to the surface from the dehydrating region through these cracks.

Convection: Solid state convection, as proposed by Ransford and Finnerty (1980) for the anhydrous silicate core of Europa, can induce a non-hydrostatic shape in objects such as the Moon (e.g. Cassen et al., 1978) and Europa. A convection pattern with a strong second order component in a satellite would influence the spin-orbit coupling of the satellite with its planet. The sites of upwelling would define the surface positions of the axis of minimum inertia, and would be the sub-Jove and anti-Jove points for Europa. Above a zone of upwelling would be a region under tension. We propose that such tensile stress results in fracturing of the serpentinite-chloritite layer of Europa above the anti-Jove point, and consequently is responsible for the Type 5 fractures in the ice crust imaged by Voyager. Concentrically about the zone of upwelling, the return flow in a second order convection pattern induces compressive stresses, which we suggest are represented on the surface of Europa by the Types 6 and 7 compressional features as classified by Pieri. Unfortunately, the sub-Jove point was not imaged at high resolution by either Voyager spacecraft. If subsequent missions reveal features in the sub-Jove region similar to those observed in the anti-Jove region, our model would be strongly supported.

#### REFERENCES:

- Cassen, P., et al., Geophys. Res. Lett. **6**, 731-735, 1979.  
 Gaffney, E.S. and Matson, D.L., submitted to Icarus, 1980.  
 Malin, M.C., I.A.U. Colloquium No. 57, Kailua-Kona, Hawaii, abstr. 7-2, 1980.  
 Murrell, S.A.F. and Ismail, I.A.H., Tectonophysics **31**, 207-258, 1976.  
 Parameswaren, V.R. and Jones, S.J., J. Glaciology **14**, 305-315, 1975.  
 Pieri, D., Nature, in press, 1980.  
 Raleigh, C.B., and Paterson, M.S., J. Geophys. Res. **70**, 3965-3985, 1965.  
 Ransford, G.A., and Finnerty, A.A., Nature, in press, 1980.  
 Weertman, J., in Physics and Chemistry of Ice, Whalley et al., eds., Royal Society of Canada, Ottawa, 320-337, 1973.

This research was carried out under NASA Contract 7-100.

## EUROPA'S PETROLOGIC THERMAL HISTORY

G.A. Ransford and A.A. Finnerty, Jet Propulsion Laboratory, California Institute of Technology, Pasadena, CA 91103

We have reconsidered the thermal evolution of Jupiter's second Galilean satellite, Europa, from its accumulation from circum-Jovian debris until the formation of surface features imaged by Voyager. By including the petrological sequence that probably accompanied Europa's thermal evolution, a different path of geophysical development from that outlined in earlier studies (1, 2, 3) is indicated, a path which leads to a present geophysical state that seems to be more in concert with the Voyager observations than earlier models. The petrological considerations imply that heat transport within Europa by sub-solidus convection might have been important throughout much of that satellite's history. It is also suggested that a large fraction of the water of Europa is retained in the interior in the form of hydrated silicates.

The total amount of water required to dilute the density of a lunar or Io type body ( $\rho \sim 3.3\text{--}3.5$ ) to Europa's value ( $\rho \sim 3.0\text{--}3.1$ ) is about 5 wt.% (3) compared to about 33 wt.% for Ganymede and 47 wt.% for Callisto. Such a small percentage of water need not have started in Europa as ice, since there are many hydrated minerals that could be stable in a relatively cool planet of chondritic composition (e.g., brucite  $\sim 30$  wt.%  $\text{H}_2\text{O}$ , serpentine  $\sim 14$  wt.%  $\text{H}_2\text{O}$ , chlorite  $\sim 12\text{--}15$  wt.%  $\text{H}_2\text{O}$ , talc  $\sim 5$  wt.%  $\text{H}_2\text{O}$ , micas  $\sim 2\text{--}4$  wt.%  $\text{H}_2\text{O}$ , amphiboles  $\sim 2$  wt.%  $\text{H}_2\text{O}$ ). We will consider the possibility here that water was present in Europa as water of hydration from the start.

There are two reasons to think that Europa might have started its thermal evolution with most, if not all, of its water in the form of water of hydration. The first is a consideration of the likely pressure-temperature conditions in the Europa zone of the circum-Jovian nebula during the condensation of the material that eventually becomes the satellite. All reconstructions that give high temperatures for the condensation conditions at Io's orbit result in conditions of high humidity and moderate temperatures at Europa's distance. Under such conditions, hydrous silicates may condense stably (4).

The second reason for considering water of hydration is if the circum-Jovian nebula considerations cited above are not true, (i.e., if Europa does form as a mixture of ice and silicates), subsequent thermal evolution will melt the ice, which will then hydrate the surrounding silicates. These reactions would occur in the low-to-moderate temperature environment that is presumed for Europa's interior early in its thermal evolution provided the appropriate bulk composition is present within the satellite.

While it is plausible that the water of Europa may at one time have been incorporated in the interior of the satellite as hydrous silicates, it is not obvious that the water may currently exist in the interior after 4.5 Gy of thermal evolution. Using the Moon as an analog because its radius is nearly the same as that of Europa, current thermal models employing convective heat transport models and materials properties

thought to be appropriate for the Earth and the Moon (5, 6, 7) predict temperatures well above those at which hydrous minerals dehydrate over most of the interior (Figure 1). The lithospheres in the models of Figure 1 are about 300-400 km thick. In a convective Moon model with initial post-accretion temperature of 1300°C, Schubert *et al.*, (1979) calculate a lithospheric thickness of 550 km after 4.5 Gy. The upper 200-300 km of the thermal boundary layers or lithospheres in the models cited above are at temperatures below the 600-700°C required to stabilize hydrous minerals. It is apparent, therefore, that the hypothesis that most of the water of Europa is incorporated in a relatively cool lithosphere composed of hydrous minerals, which is situated above a hot convecting interior or anhydrous silicates, is consistent with our current knowledge of planetary thermal evolution.

An alternative model may be considered. Tozer (8, 9) has suggested that the effect of water of hydration on silicate material properties is to decrease the resistance to creep, i.e. to decrease the effective viscosity. A thermal profile for a Moon composed of "water saturated basalt" from Tozer's work is incorporated in Figure 1. If such a model is applied to Europa, it is clear that hydrated silicates can remain stable throughout the interior, because the low-temperature convection transports heat at a rate sufficient to maintain the interior below the dehydration temperatures.

It is expected that some free water gains access to the surface during this evolution, but not in vast quantities. Most of the water present in Europa can be retained in the hydrated minerals in the interior. We would therefore predict that the ice layer on the surface of Europa is much thinner than the 150 km that had been estimated before. A thin (~ 10 km?) ice crust on Europa has important implications for tidal coupling and surface morphology (e.g., cracking) - see (10, 11, 12) for more details.

The cracking patterns on Europa's surface suggest some sort of global deformation mechanism (10, 12, 13) and internal convective activity would certainly provide such deformation. This aspect will be discussed in considerably more detail in Finnerty *et al.* (11). The distortions of the silicate surface that are created by the areas of upwelling and subduction in the convective model can fracture the overlying thin layer of ice, generating crack patterns which can be tested against the observed patterns for various orders of convective activity.

#### REFERENCES:

- (1) Lewis, J.S., *Science*, 172, 1127-11238, 1971.
- (2) Consolmagno, G.J. and J.S. Lewis, *Icarus*, 34, 280-293, 1978.
- (3) Fanale, F.P. *et al.*, in *Planetary Satellites*, 379-405, 1977.
- (4) Grossman, L. and J.W. Larimer, *Revs. Geophys. Space Phys.*, 12, 71-101, 1974.
- (5) Turcotte, D.L. *et al.*, *Proc. Lunar Planet. Sci. Conf.* 10th, 2375-2392, 1979.
- (6) Schubert, G. *et al.*, *Phil. Trans. R. Soc. London*, A285, 523-536, 1977.

- (7) Cassen, P. et al., Phys. Earth Plan. Inf., 19, 183-196, 1979.
- (8) Tozer, D.C., Phys. Earth. Plan. Inf., 6, 182-197, 1972.
- (9) Tozer, D.C., The Moon, 9, 167-182, 1974.
- (10) Pieri, D., Nature, in press, 1980.
- (11) Finnerty, A.A. et al., Nature, in press, 1980.
- (12) Collerson, K.D. et al., Nature, in press, 1980.
- (13) Helfenstein, P. and E.M. Parmentier, Proc. Lunar Plan. Sci. Conf. 11th, in press, 1980.

This research was carried out under NASA Contract 7-100.

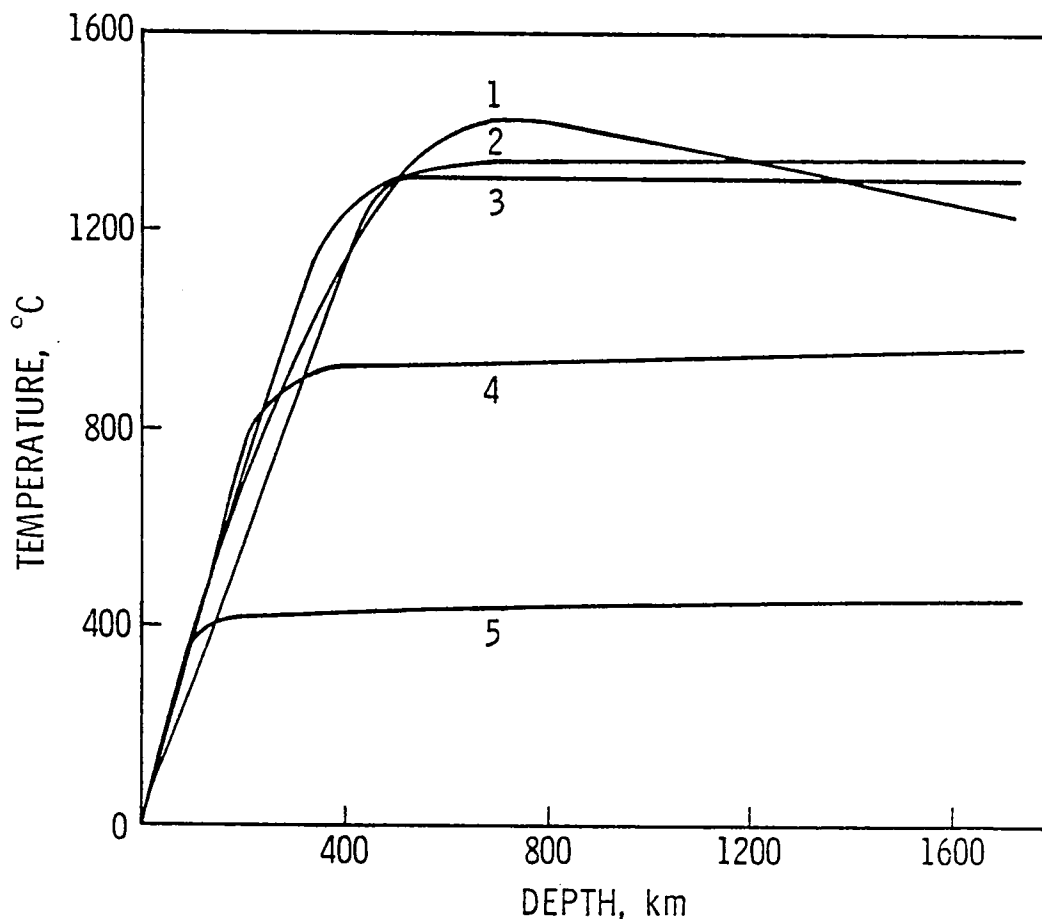


Figure 1: Spherically averaged temperature-depth curves for the Moon. Data are taken from: 1) Turcotte et al. (1972); 2) Cassen et al. (1979b); 3) Schubert et al. (1977); 4) Tozer, 1974 (anhydrous dunite model); 5) Tozer, 1974 (water-saturated basalt model).

## EUROPA: SIDE-FREQUENCY DISTRIBUTIONS OF GLOBAL POLYGONS

David Pieri, Jet Propulsion Laboratory, California Institute of Technology, Pasadena, CA 91103.

Europa displays a perplexing array of intersecting global lineaments which have been studied and classified qualitatively by several authors (Smith et al., 1979); Malin, 1980; Pieri, 1980; Soderblom, 1980) and quantitatively analyzed by a few (Helfenstein et al., 1980; Parmentier et al., 1980; Pieri, 1980; Pieri et al., 1980). We report here on the approach of Pieri (1980) and Pieri et al. (1980) which utilize the quantitative analysis of the frequency distribution of polygons formed by the intersection of the European lineaments.

The statistics of polygons formed by intersecting lines in a plane or on a sphere are well-known (e.g. see Crain, 1976). The intersection of random lines yields the polygon "side-frequency distribution" (i.e. the number of polygons each with a given number of sides) shown in figure 1, a Poisson distribution. Faults or joints in complex geological settings form polygon systems which mimic this distribution, however, the more well-oriented the fault or joint systems are, greater the excess in frequency at the mode (see figure 1). Polygons formed by intersecting fractures formed under isotropic stress conditions tend to follow a distribution similar to the Voronoi distribution (figure 1), first used to describe polygons formed by isotropic growth around random centers (Miles, 1971). Such tessellated surfaces are typical of dessication cracks and fault patterns over salt domes (Crain, 1976; Pieri, 1980). Polygons formed by the intersections of lineament systems on Europa tend to show examples of both distributions (figure 2), mostly as a function of geographical position. This differentiation is consistent with previously mentioned preliminary qualitative classification schemes (see above). Polygons systems on Europa which exhibit a Voronoi distribution (isotropic stress) tend to cluster around the anti-Jove point, whereas the ones which show a more Poisson-like distribution with an excess at the mode (oriented stress) occur about 60°-80° away from the anti-Jove point (Pieri, 1980). These orientations are roughly consistent with models of imposed internal stress due to dehydration, expansion, and solid state convection in a chloritite-serpentinite interior with a thin (~ 10 km) icy crust (Finnerty et al., 1980; Ransford and Finnerty, 1980). Further, since the size of polygon spacing varies with material strength and/or rate of stress imposition (Lachenbruch, 1964), closely spaced reticulate patterns at the anti-Jove point may be indicative of higher imposed stress, or of a weaker (or possibly thinner) icy crust, or both (Pieri, 1980).

### REFERENCES:

- Crain, I.K. (1976) Statistical analyses of geotectonics, p. 3 in Random Processes in Geology, D.F. Merriam ed., Springer-Verlag, N.Y., Heidelberg, Berlin, 168 pgs.
- Finnerty, A.A., G.A. Ransford, and D. Pieri (1980). Europa surface cracking: A consequence of thermal evolution, Nature in press.
- Helfenstein, P., E.M. Parmentier, and J.W. Head (1980), Fractures on Europa, possible indications of tidal deformation, The Satellites of



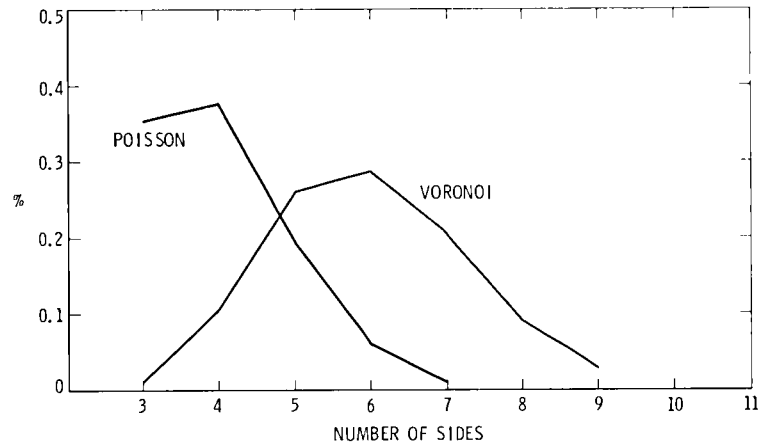
- Jupiter, I.A.U. Colloq. #57, Kailua-Kona, Hawaii, May 13-16, 1980.
- Lachenbruch, A.H. (1962), Mechanics of thermal contraction cracks and ice-wedge polygons in permafrost, G.S.A. Special Paper #70, Waverly Press, Baltimore, 69 pgs.
- Malin, M.C. (1980), Morphology of lineaments on Europa, The Sat. of Jup. I.A.U. Colloq. #57, Kailua-Kona, Hawaii, May 13-16.
- Miles, R.E., (1971), Random points, sets, and tessellations on the surface of a sphere, Sankhya, Ser. A., 33, p. 145-174.
- Pieri, D.C., (1980), Lineaments and Polygon patterns on Europa, Nature, in press.
- Pieri, D., G. Ransford, and K. Collerson, (1980), Quantitative aspects of polygons on Europa, The Satellites of Jupiter, I.A.U. Colloq. #57, Kailua-Kona, Hawaii, May 13-16, abstr.
- Parmentier, E.M., P. Helfenstein, and J.W. Head, (1980), Some implications of fracturing on Europa, XI Lunar Sci. Conference, abstr.
- Ransford, G.A., and A.A. Finnerty, (1980), Europa's thermal history, Nature, in press.
- Smith, B.A., et al., (1979), The Galilean Satellites and Jupiter: Voyager 2 Imaging Science Results, Science, 206, p. 927-950.
- Soderblom, L.A., (1980), Geology of Europa, oral presentation, The Satellites of Jupiter, I.A.U. Colloq. #57, Kailua-Kona, Hawaii, May 13-19.

#### FIGURE CAPTIONS:

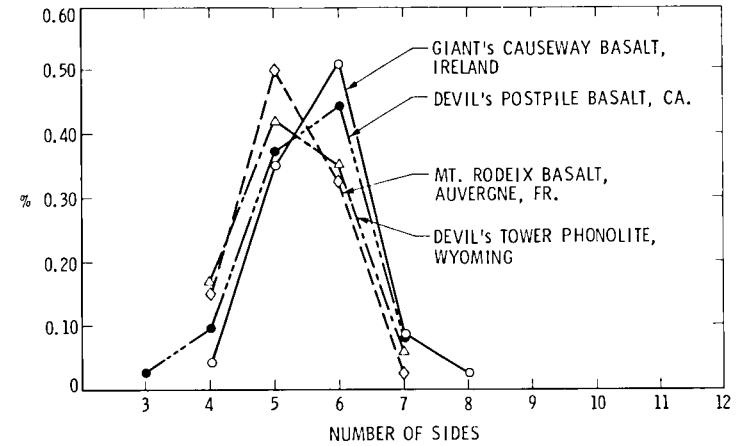
- 1a. Theoretical percent age distribution of polygons with a given number of sides created by random intersections of lines (Poisson) and for equant polygons (e.g. mudcracks) formed under isotropic stress (Voronoi).
- 1b. Polygon side-frequency distributions observed for well-oriented fault systems in various areas.
- 1c. Polygon side-frequency distributions observed in cooling basalt under the most ideal (mode of 6) and less ideal (mode of 5) conditions.
2. Distributions observed on Europa for intersections of "great circles" lineaments (Type 3), reticulate anti-Jove lineament patterns (Types 1, 2, 4, 5), and for the most "polygonal" lineaments (Types 1, 2) abstracted from the general anti-Jove group.

This research was carried out under NASA Contract 7-100.

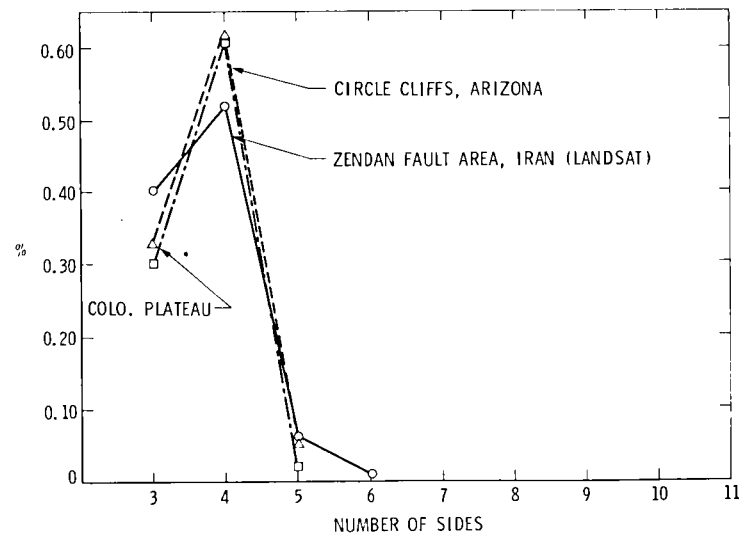
# SIDE FREQUENCY DISTRIBUTIONS



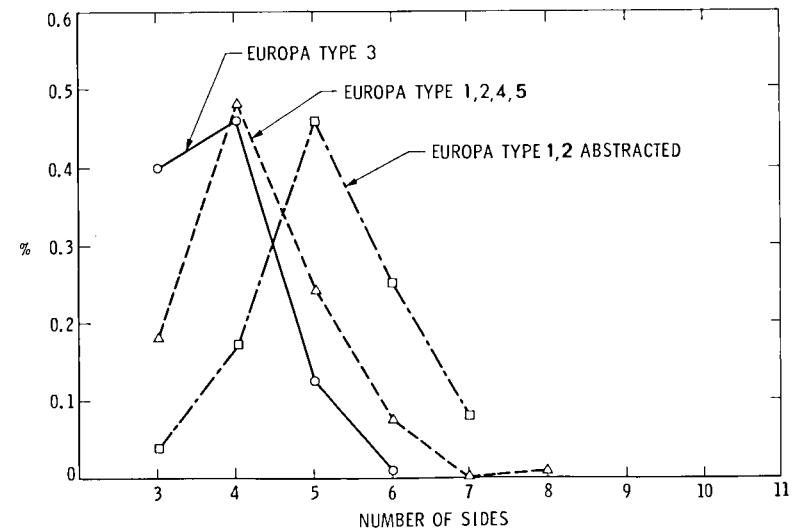
1a.



1c.



1b.



2.

## PRELIMINARY CLASSIFICATION OF LINEAMENT PATTERNS ON EUROPA

David Pieri, Jet Propulsion Laboratory, California Institute of Technology, Pasadena, CA 91103.

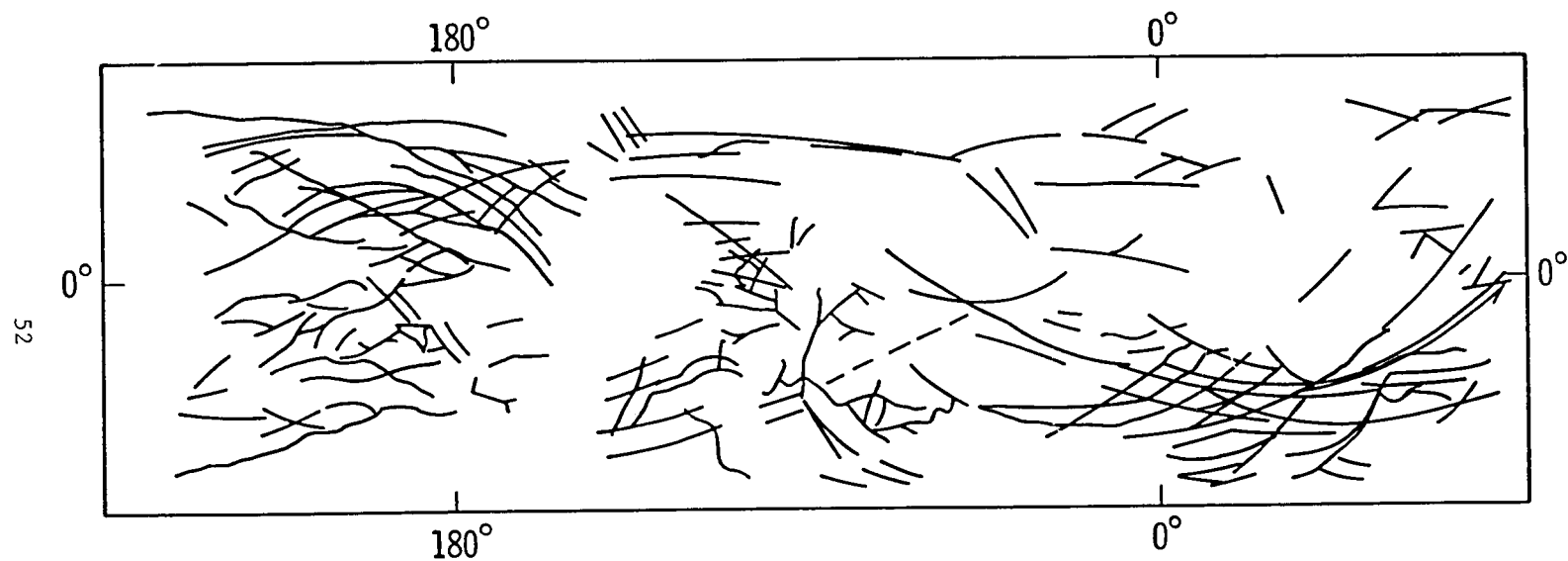
Figure 1 is a low resolution sketch map of global lineament patterns on Europa. The general orientation of large lineaments along great circles is apparent and has been mentioned previously (Plescia, 1979 - personal communication; Smith *et al.*, 1979). Lineaments are seen less frequently in low albedo regions, although this is probably due to loss of contrast across dark areas.

Figure 2 is a series of sketch maps made from the Voyager Europa mercator projection shown in Figure 3 (Pieri, 1980). These lineaments have been divided into 8 groups on the basis of albedo, morphology, orientation, and characteristic geometric style: Type 1, a series of enechelon markings of intermediate albedo; Type 2 are generally short, wedge-shaped markings occurring near the equator; Type 3 are smooth arcuate features which appear to be on great circles; Type 4 are reticulate, faint and difficult to see, and may be ubiquitous in light terrains on Europa; Type 5 are reticulate and are most common near the anti-Jove point; Type 6 are flexi, a complex series of cuapate ridges; Type 7 are rare, high albedo lineaments, and Type 8 may be low, sun-facing scarps. All are discussed in greater detail in Pieri (1980). These lineaments are of several length scales and of at least two basic types: Flexi (type 6) and scarps (type 8) appear as topographic features with little or no albedo contrast; flexi are global features, while it is indeterminate how extensive the low scarps really are. The lineaments appear primarily as albedo features: type 3 is clearly global, types 1, 4, and 7 appear regional in extent, while we may speculate that types 2 and 5 are the result of localized processes.

### REFERENCES:

- Pieri, D.C. (1980) Lineaments and Polygon Patterns on Europa, Nature, in press.  
Smith, B.A. *et al.* (1979), Galilean Satellites and Jupiter: Voyager 2 Imaging Science Results, Science, 206, p. 927-950.

This research was carried out under NASA Contract 7-100.



LINEAMENT PATTERNS ON EUROPA

Figure 1

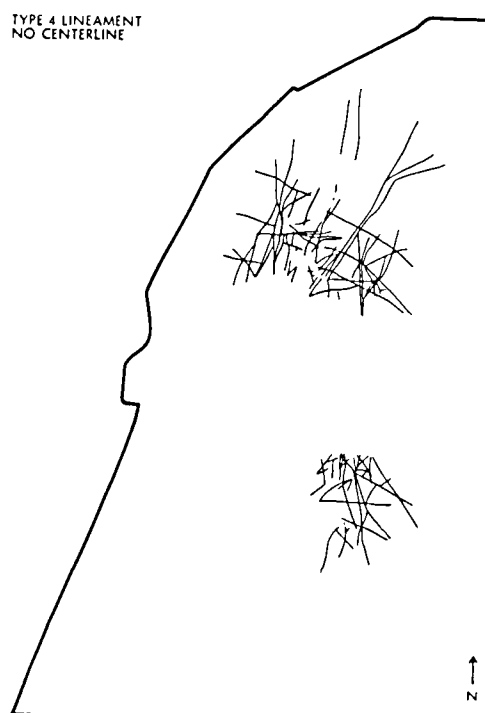
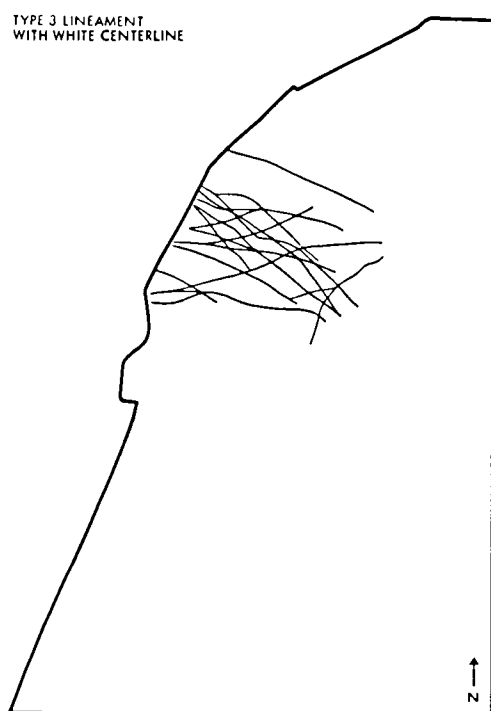
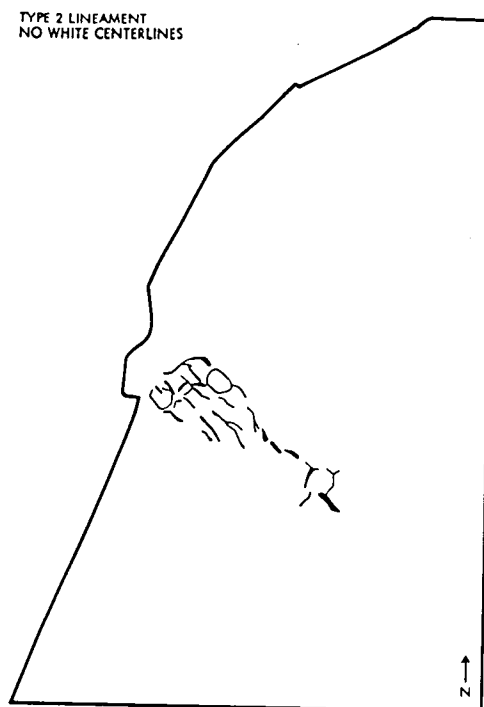
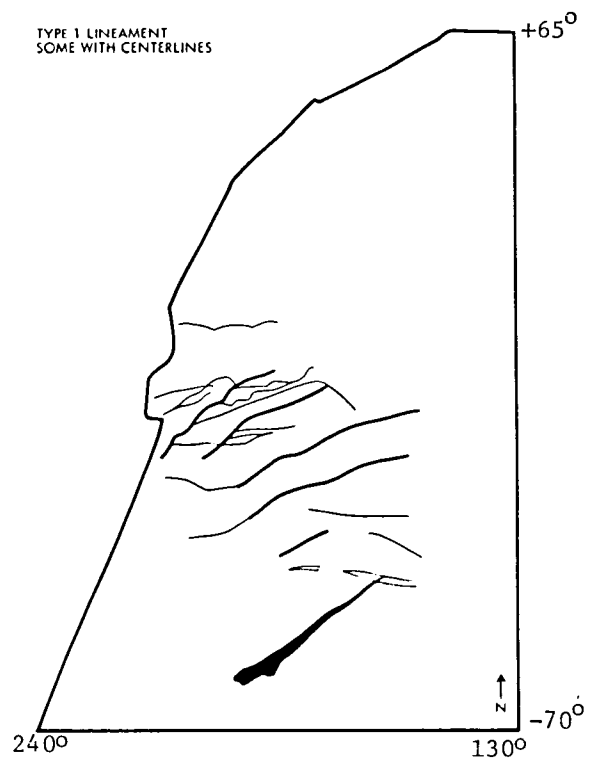
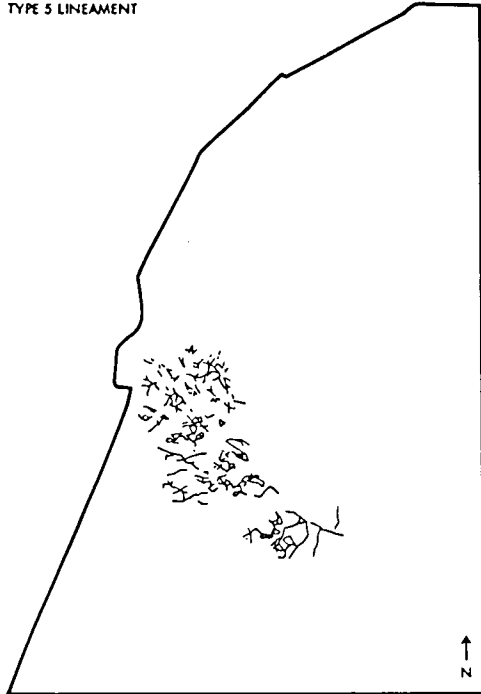


Figure 2

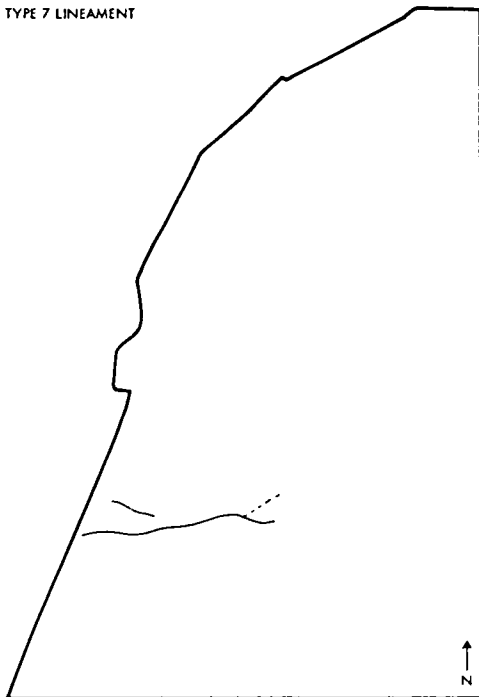
TYPE 5 LINEAMENT



TYPE 6 LINEAMENT



TYPE 7 LINEAMENT



LINEAMENT TYPE 8  
SCARPS

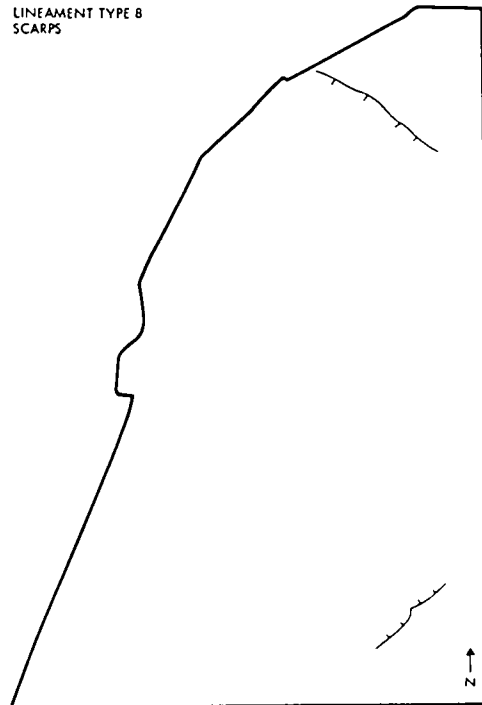


Figure 2 (continued)

## THE CRATERING OF GANYMEDE I: THE DARK TERRAIN

Jeffrey B. Plescia, Jet Propulsion Laboratory, Pasadena,  
California 91103, Eugene M. Shoemaker, U. S. Geological  
Survey, Flagstaff, Arizona 86001, and Joseph M. Boyce, NASA  
Headquarters, Washington, D.C. 20546

The density and size-frequency distribution of craters has been analyzed for each of the major terrain types on Ganymede, for many of the palimpsests, and for various subunits of the basin Gilgamesh. Data for the dark terrain and the palimpsests are reported here; the data for the grooved and smooth terrains and Gilgamesh are reported in an accompanying abstract (Plescia et al., 1980).

Cumulative crater size-frequency curves have been obtained for sample areas that include a large percentage of Galileo Regio and smaller fractions of Nicholson Regio and Barnard Regio. The images used from Voyager I and II have resolutions of 2 to 3 km/line pair. The sample areas counted, average about 120,000 km<sup>2</sup>, but range from as small as 33,000 km<sup>2</sup> to as large 200,000 km<sup>2</sup>.

The dark terrain is the most densely cratered terrain on Ganymede, a result consistent with the preliminary data of Smith et al. (1979a,b). The dark terrain is not uniformly cratered, however. Statistically significant variations in crater density occur among the sample areas, and inflections are present in the cumulative size-frequency curves for some areas. Variations in density are best observed in the 20 to 30 km crater diameter range, where the statistics and resolution are best. At larger crater sizes the statistics of small numbers introduces large uncertainties. At smaller sizes problems of identification of craters become a source of uncertainty.

The crater density to 20 km diameter is 100 to 300 craters/10<sup>6</sup> km<sup>2</sup> in the most densely cratered parts of the dark terrain; to 30 km diameter the density is 50 to 60 craters/10<sup>6</sup> km<sup>2</sup>. The least cratered areas of dark terrain have crater densities to 20 km diameter of 20 to 30 craters/10<sup>6</sup> km<sup>2</sup>, and, to 30 km, from 7 to 10 craters/10<sup>6</sup> km<sup>2</sup>. The range in observed densities is a factor of about 6 to 7 between the most and least cratered parts of the dark terrain (fig. 1).

The observed crater densities on the dark terrain should be viewed as indicative of crater retention ages. Craters on the dark terrain exhibit a range of preservation state. Some craters are sharp-rimmed deep craters with well defined bright rim deposits and rays, whereas others are so degraded so as to be represented only by a barely perceptible annular ridge, the former crater rim. The degradation process appears to be chiefly controlled by cold flow of the icy crust (Johnson and McGetchin, 1973). As shown by the existence of crater palimpsests, the

process of topographic relaxation of craters proceeded to the point where craters disappeared. The relaxation process is a function of crater diameter; large craters relaxed faster than small craters.

In order to obtain relative ages from crater densities, it is necessary to take account of the position of the sample area on the satellite. Because the orbital velocity of the satellite is a substantial fraction of the encounter velocities of the impacting objects, there must have been a significant gradient in flux and in the mean impact velocity of the impacting bodies from the apex to the antapex of orbital motion. Shoemaker and Wolfe (in press) found that the ratio of the cratering rate at the apex to the rate at the antapex on Ganymede, for currently impacting bodies, is approximately 9.6. Thus, for a surface of uniform crater retention age, the crater density at the apex would be 9.6 times higher than at the antapex. Figure 2 illustrates the crater densities at 10 km diameter determined for a number of areas on the dark terrain, plotted as a function of distance (in degrees) away from the apex. Also plotted is the model distribution of crater densities for a surface of uniform crater retention age.

As can be seen from figure 2, the majority of points lie along the modeled curve. Hence, a large part of the observed variation in crater density can be attributed to the gradient in cratering rate. Much of the scatter about the model curve is within the statistically expected variation for random encounter of impacting bodies. Areas of dark terrain near the apex, however, have a lower average crater retention age than the other areas shown.

Passey and Shoemaker (1980) have suggested that the impact of various objects during the growth of Ganymede added significantly to the initial heating of the body. The region near the apex received more initial heat and remained warm for a longer time than the region near the antapex. Hence the lithosphere remained thin and craters relaxed and disappeared at a later time near the apex than near the antapex.

Local variation in age within sample areas is indicated by inflections in the cumulative size-frequency curves. These inflections, where observed on terrestrial planets, have been taken to indicate one or more resurfacing events. All of the observed inflections on Ganymede occur between crater diameters of 10 and 30 km; most occur between 20 and 30 km. Large numbers of small craters apparently have been removed or hidden. Inspection of the areas that exhibit the inflections shows that, in several cases, one or more large craters or a palimpsest is present. Small craters have been buried beneath the rim deposits of larger craters. We infer that this was the primary process of small crater removal, even where the large craters are no longer recognizable.



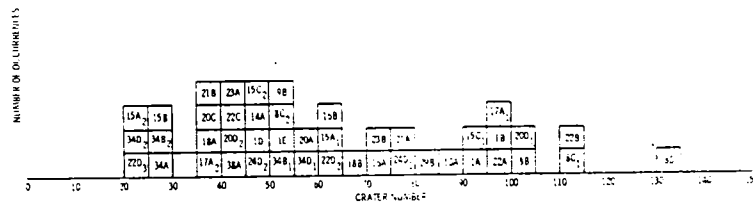
The cumulative size-frequency curves are steeper on the trailing hemisphere of Ganymede than on the leading hemisphere. This reflects a higher ratio of small to large craters on the trailing side relative to the leading side. Earlier cooling of the crust, sufficient to support small craters, could account for the higher proportion of small craters on the trailing hemisphere.

The palimpsests on the dark terrain have crater densities comparable to densities found elsewhere on the dark terrain. The observed crater densities of the palimpsests, to 20 km crater diameter range from 50 to 130 craters/ $10^6$  km<sup>2</sup>.

#### References cited:

- Johnson, T. V., and McGetchin, T. R., (1973) Topography on Satellite Surfaces and the Shape of Asteroids: Icarus, 18, 612-620.
- Passey, Q. R., and Shoemaker, E. M. (in press) Craters and Basins on Ganymede and Callisto: Morphological Indicators of Crustal Evolution, in The Satellites of Jupiter, D. Morrison (ed.), Univ. of Arizona Press.
- Plescia, J. B., Shoemaker, E. M., and Boyce, J. M. (this volume) The Cratering of Ganymede, or a Snowball Really Does Have a Chance in Hell: Grooved Terrain, Smooth Terrain, and Gilamash.
- Shoemaker, E. M., and Wolfe, R. F. (in press) Cratering Time Scales for the Galilean Satellites: in The Satellites of Jupiter, D. Morrison (ed.), Univ. of Arizona Press.
- Smith, B. A., Soderblom, L. A., Johnson, T. V., Ingersoll, A. P., Collins, S. A., Shoemaker, E. M., Hunt, G. E., Masursky, H., Carr, M. H., Davies, M. E., Cook, A. F. II, Boyce, J., Danielson, G. E., Owen, T., Sagan, C., Beebe, R. F., Veverka, J., Strom, R. G., McCauley, J. F., Morrison, D., Briggs, G. A., and Suomi, V. E., (1979a) The Jupiter System through the Eyes of Voyager 1: Science, 204, 951-972.
- Smith, B. A., Soderblom, L. A., Beebe, R., Boyce, J., Briggs, G., Carr, M., Collins, S. A., Cook, A. F. II, Danielson, G. E., Davies, M. E., Hunt, G. E., Ingersoll, A., Johnson, T. V., Masursky, H., McCauley, J., Morrison, D., Owen, T., Sagan, C., Shoemaker, E. M., Strom, R., Suomi, V. E., and Veverka, J., (1979b) The Galilean Satellites and Jupiter: Voyager 2 Imaging Science Results: Science, 206, 927-950.

### DARK TERRAIN 20 KM CRATER NUMBERS



### DARK TERRAIN 30 KM CRATER NUMBERS

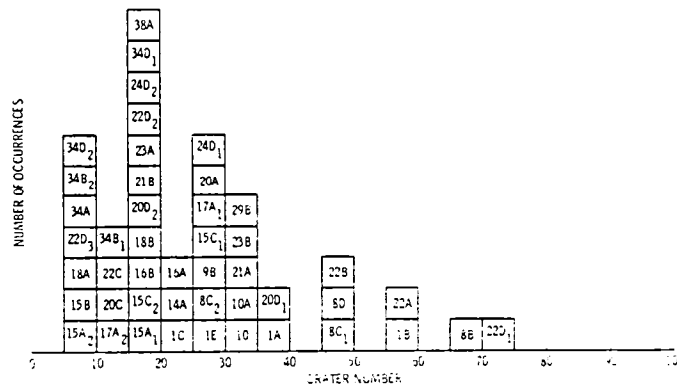


Figure 1. Histograms of density of craters greater than 20 km (top) and 30 km (bottom) diameter per  $10^6 \text{ km}^2$  per plotted 5 crater number increment for the Dark Terrain. Sample numbers are included in each box.

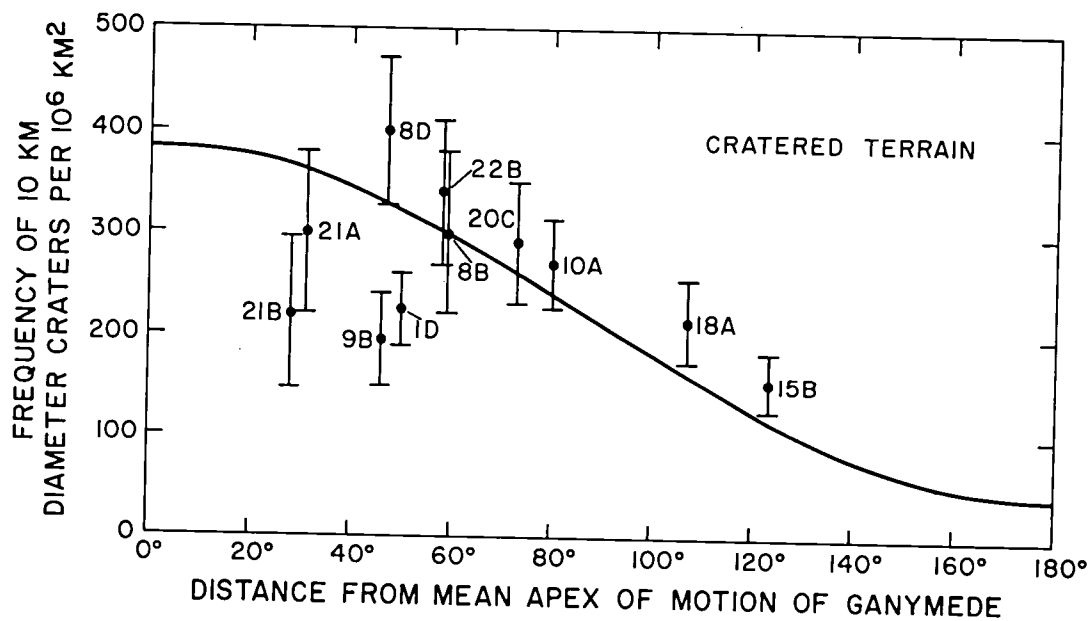


Figure 2. Spatial variation in density of craters on the dark terrain of Ganymede. Error bars are  $\pm$  one standard deviation. Heavy curve is the theoretical distribution of crater density for a surface of uniform crater retention age (based on the spatial variation in cratering rate determined by Shoemaker and Wolfe, in press).

## THE CRATERING OF GANYMEDE II: GROOVED TERRAIN, SMOOTH AND GILGAMESH

Jeffrey B. Plescia, Jet Propulsion Laboratory, Pasadena, California 91103, Eugene M. Shoemaker, U.S. Geological Survey, Flagstaff, Arizona 86001, and Joseph M. Boyce, NASA Headquarters, Washington, D.C. 20546

The grooved and smooth terrains, taken together, are the most extensive terrains on Ganymede. Crater densities are presented here for selected areas of both terrain types and for various parts of the Gilgamesh basin and rim deposit, which is approximately contemporaneous with young grooved terrain. Crater densities were determined from Voyager I and II images with resolutions of 2 to 3 km/line pair. Individual areas of grooved terrain counted average approximately  $100,00 \text{ km}^2$ ; they range from approximately 5,000 to 300,000  $\text{km}^2$ . Areas of smooth terrain counted range from 3,000 to 45,000  $\text{km}^2$ . Crater densities on the grooved terrain, as in the case of the dark terrain, are best determined at the 20 to 30 km diameter size range. Smooth terrain densities are most accurately determined to 10 km. The largest crater observed on the smooth terrain is 15 km in diameter.

A significant range in crater densities was found on both the grooved terrain and the smooth terrain, a result consistent with the preliminary data of Smith *et al* (1979a, b). Crater densities on the grooved terrain are from 5-6 to  $100-200/10^6 \text{ km}^2$  at 20 km crater diameter, and from 2-3 to  $40-50/10^6 \text{ km}^2$  at 30 km diameter. The variation in crater density is greater than a factor of 25 (fig. 1). Some areas of the grooved terrain exhibit crater densities comparable to that on the least cratered areas of dark terrain. Because of the small area and limited number of craters, the crater densities found on the smooth terrain have large statistical errors. The equivalent crater densities to 20 km (derived by extrapolation from 10 km crater densities) are 1-2 to slightly more than  $50/10^6 \text{ km}^2$ , again about a factor of 25 variation (fig. 1).

The craters of the grooved and smooth terrain, although exhibiting a wide range of topographic form, do not appear to have been degraded by cold flow to the point where they have become unrecognizable. Hence, while densities on the dark terrain reflect crater retention ages, the densities for the grooved and smooth terrain are indicative of relative age of formation of these terrains. To determine relative ages, the densities must be analyzed in light of the gradient in cratering rate from the apex to the antapex of orbital motion (Shoemaker and Wolfe, 1980).

Figure 2 illustrates some of the observed densities for the grooved terrain plotted as a function of angular distance from the apex of motion, as well as the model curve for a surface of

uniform age. Most of the variation observed can be accounted for by the gradient in cratering rate determined by Shoemaker and Wolfe (1980). There are, however, some areas (not shown in figure 2) which significantly depart from the model. Grooved terrain near the south pole, which exhibits the most pronounced grooves and ridges, appears to be significantly older than other grooved terrain.

Crater densities on the smooth terrain, while not illustrated, also show a spatial variation that follows the modeled variation in cratering rate. Densities for a few areas of smooth terrain appear to deviate from the model by a statistically significant amount, however, which suggests some variation in age. In general, the smooth terrain appears to be younger than the grooved terrain. This conclusion is supported by stratigraphic relationships between the two units. Smooth terrain is commonly observed to overlap and embay areas of grooved terrain.

The basin and surrounding rim deposit of Gilgamesh has been divided into three regions: 1) the flat-floored basin, 2) an inner humocky rim unit, and 3) an outer radially sculptured rim unit. Crater counts were compiled for each region. Because of the small areas studied and low number of observed craters, statistical uncertainties are rather large. The basin floor has an equivalent crater density to 20 km (derived by extrapolation from the 5 km density) of  $5/10^6 \text{ km}^2$ . The inner and outer rim units both exhibit crater densities to 20 km of 12 to  $15/10^6 \text{ km}^2$ . The basin floor is clearly less cratered and appears younger than the rim units. Part of the difference may be due to secondary craters included in the crater counts on the rim units. A real difference in crater retention age might be due either to flooding of the basin or to topographic relaxation of craters formed on the floor while the lithosphere there remained comparatively thin.

#### References cited:

- Shoemaker, E. M., and Wolfe, R. F. (in press) Cratering Time Scales for the Galilean Satellites, in The Satellites of Jupiter, D. Morrison (ed.), Univ. of Arizona Press.
- Smith, B. A., Soderblom, L. A., Johnson, T. V., Ingersoll, A. P., Collins, S. A., Shoemaker, E. M., Hunt, G. E., Masursky H., Carr, M. H., Davies, M. E., Cook, A. F., II, Boyce, J., Danielson, G. E., Owen, T., Sagan, C., Beebe, R. F., Ververka, J., Strom, R. G., McCauley, J. F., Morrison, D., Briggs, G. A., and Suomi, V. E., (1979a) The Jupiter System through the Eyes of Voyager I: Science, 204, 951-972.
- Smith, B. A., Soderblom, L. A., Beebe, R., Boyce, J., Briggs, G., Carr, M., Collins, S. A., Cook, A. F., II, Danielson, G. E., Davies, M. E., Hunt, G. E., Ingersoll, A., Johnson, T. V., Masursky, H., McCauley, J., Morrison, D., Owen, T., Sagan, C., Shoemaker, E. M., Strom, R., Suomi, V. E., and Ververka, J., (1979b) The Galilean Satellites and Jupiter: Voyager 2 Imaging Science Results: Science, 206, 927-950.

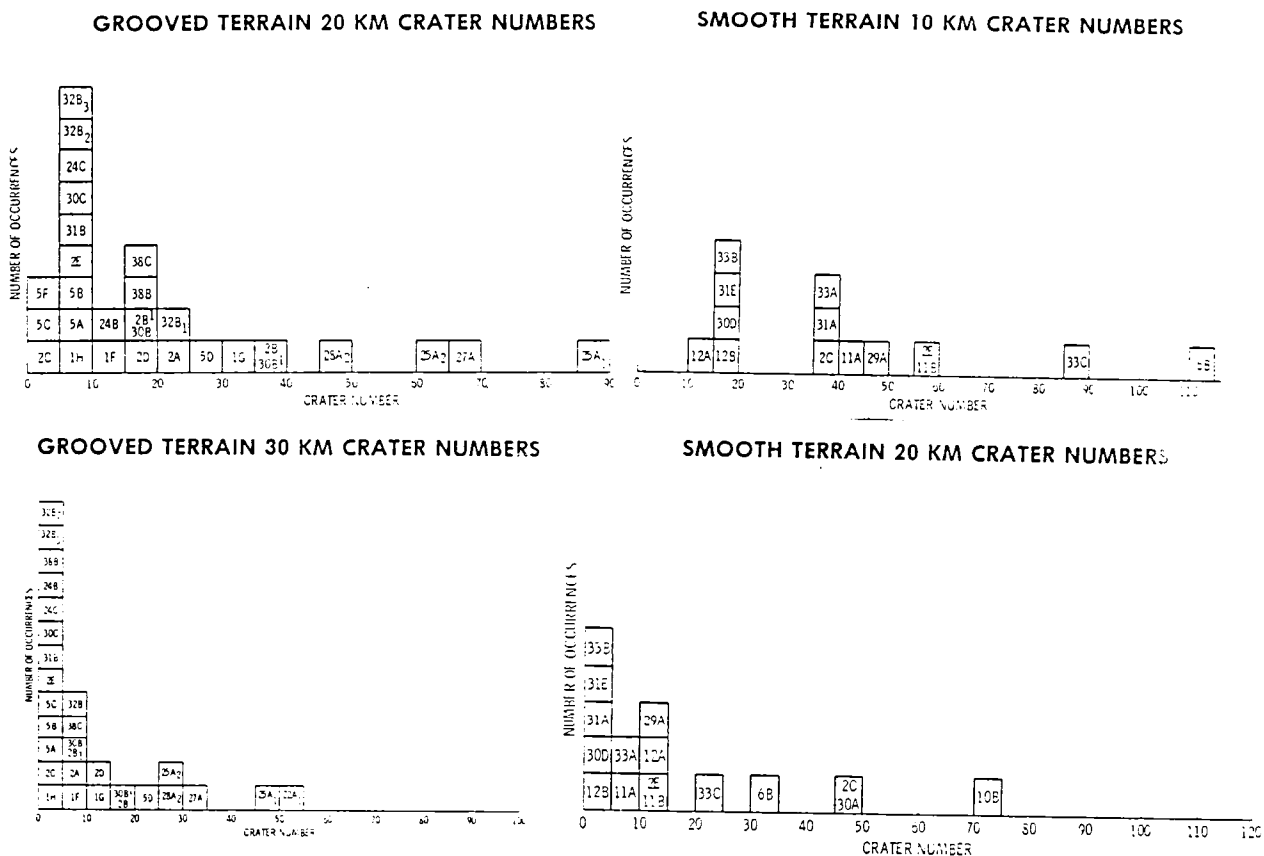


Figure 1. Histograms of density of craters greater than 20 km (top left) and 30 km (bottom left) diameter for the grooved terrain and 10 km (top right) and 20 km (bottom right) diameter for the smooth terrain. All crater densities are per  $10^6 \text{ km}^2$  plotted per 5 crater number increments. Sample numbers are included in each box.

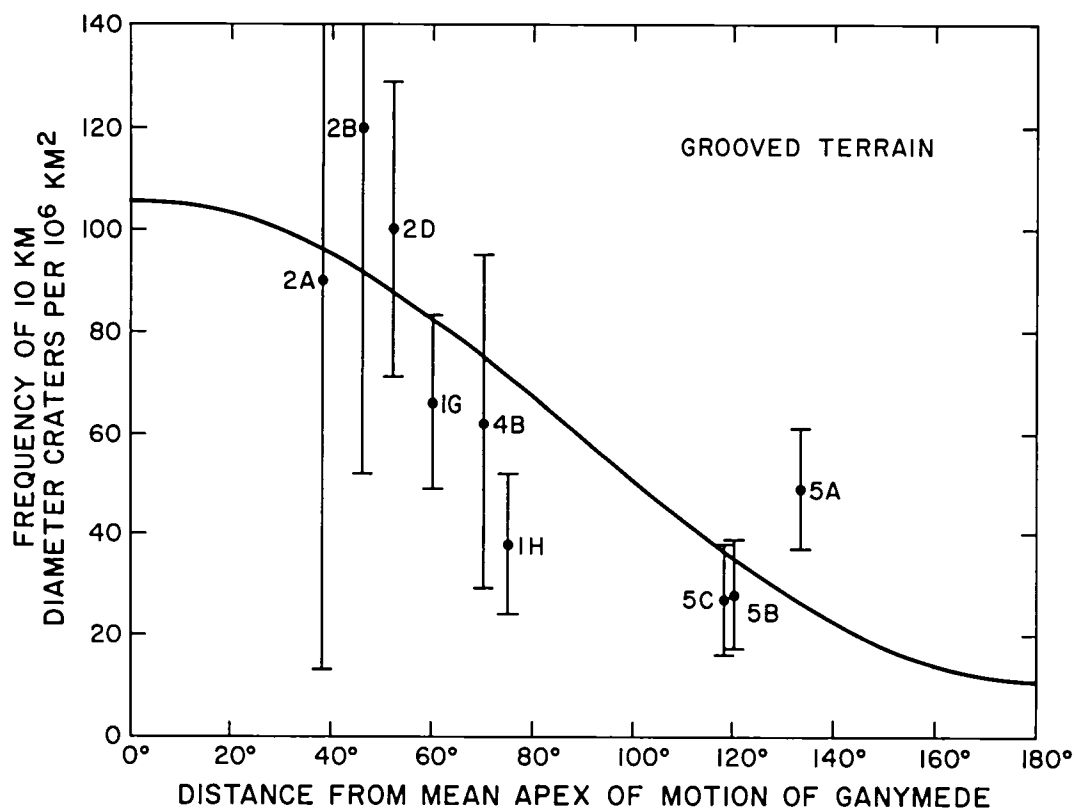


Figure 2. Spatial variation in density of craters on the grooved terrain of Ganymede. Error bars are  $\pm$  one standard deviation. Heavy curve is the theoretical distribution of crater density for a surface of uniform age (based on the spatial variation in cratering rate determined by Shoemaker and Wolfe, in press).

The Origin of Grooved Terrain on Ganymede. S. W. Squyres, Dept. of Geological Sciences and Laboratory for Planetary Studies, Cornell University, Ithaca, NY 14853; E.M. Parmentier and J.W. Head III, Dept. of Geological Sciences, Brown University, Providence, RI 02912

The surface of Ganymede consists of two principal geologic units. One is dark and has undergone only cratering and viscous relaxation, while the other is bright and has undergone complete resurfacing. These units have been termed "cratered terrain" and "grooved terrain", respectively.<sup>1</sup> The names derive from the dominant structural features of the two units. Many bands and broad regions of the bright resurfaced material are very smooth and free of grooves, however. There are also a number of instances where grooves extend into regions of dark terrain. We therefore conclude that two processes have operated: one that creates bands or regions of bright, smooth material, and another that forms grooves. The groove formation process has operated more effectively, but not exclusively, in the bright terrain.

Several lines of photogeologic evidence provide information about the resurfacing process. In several cases the orientation of bright bands with respect to shear offsets implies tectonic extension perpendicular to the trend of the band.<sup>2</sup> The extreme smoothness of many resurfaced regions, in the absence of a reasonable erosional mechanism, suggests emplacement of a highly mobile material. Finally, the high albedo and concentration of bright ray craters in the resurfaced material indicate a higher ice/silicate ratio than in the dark terrain.<sup>3</sup> We therefore favor flooding of broad graben or downdropped rift zones by liquid water as a resurfacing mechanism. Such a situation could result if a thin ice + silicate crust overlying a liquid layer were subjected to extension generated by internal H<sub>2</sub>O phase changes.<sup>2</sup> As faulting and downdropping occurred, displaced liquid would flow to the surface along fault zones, filling the graben in a manner similar to the flooding of terrestrial continental rifts by basaltic lava. The boundaries of a few bright regions are diffuse or in places formed by the rims of truncated craters,<sup>4</sup> suggesting that flooding in some cases overflowed the graben margins.

If grooves were formed by a tectonic process, their morphology may reflect the style of deformation and provide constraints on the nature of stresses that have affected the surface layer. A topographic profile across a segment of grooved terrain is shown in Figure 1. Individual ridges and troughs show no significant asymmetric or scarp-like topography. This argues against compressional deformation by large scale thrust faulting as seen, for example, on Mercury. The negative relief of the grooves instead strongly suggests formation by extension of a brittle surface layer. Extensional deformation may be expressed by the formation of extension fractures or graben bounded by normal faults. Low gravity and low density surface materials on Ganymede result in low lithostatic stresses that favor formation of extension fractures rather than normal faults. The extreme length to width ratio of individual grooves and the parallelism of adjacent grooves also are more consistent with extension fractures.

Viscous relaxation has probably significantly altered the initial topography of the grooves. For a viscosity of  $10^{23}$  poise, a value consistent with the relaxation of large craters to form palimpsests in several billion years, extrapolation of present groove topography backwards in time indicates that several kilometers of relief may have been lost since the grooves formed. The calculations indicate that viscous relaxation would affect the amplitude but not the general form of the short wavelength topography. For example, steep scarps with gentle backslopes would not degrade to the more symmetric ridge and trough-like topography presently observed.

Several trends evident in grooved bands of bright terrain are noteworthy. Grooves forming band boundaries are generally more distinct than other grooves. Many smooth bands are bounded by single grooves on each edge, and a few bands



are bounded by several grooves on each edge and are smooth in the center. Counts of impact craters as a function of scaled distance from the center of a grooved band (distance from center/groove width) show a statistically significant decrease in crater abundance toward the center of bands (Figure 2). These observations suggest that grooves first form along the boundaries of a bright band, where a major material discontinuity and zone of weakness already exist, and subsequently replicate toward the center of the band, forming a parallel pattern.

If the grooves are extension fractures, then replication of the groove pattern may be possible if, once a groove formed, the crustal material along its length were somehow rapidly strengthened so that further extension, rather than continuing to widen the existing groove, would cause formation of an adjacent parallel groove. One possible strengthening process could occur if the original groove were sufficiently narrow and deep. Two-dimensional modeling of heat conduction and radiation from an icy crust shows that heat loss from initially steep groove walls that receive little or no sunlight will cause substantial thickening and strengthening of a cold, brittle near-surface layer in the vicinity of a groove over time scales of  $10^4$ - $10^6$  years. The pattern established by the bounding grooves is apparently only replicated in the bright material, presumably because polycrystalline ice containing inclusions (e.g.-silicate grains) is generally several times stronger than clean ice. The process proposed for formation of a grooved band is summarized in Figure 3.

It is not possible to establish a clear time sequence of resurfacing and groove formation episodes. Grooved bands crosscut and are crosscut by smooth bands, suggesting that the two processes took place intermittently and concurrently. In one instance a grooved band appears to have been downdropped at one end and partially reflooded. The apparent contemporaneity of the resurfacing and groove formation processes supports the idea that they both resulted from the same tectonic regime: global extension for a brief period early in Ganymede's history.

This work was supported by NASA grants NSG 7156 (SWS) and NSG 7605 (EMP and JWH).

#### References

1. Smith, B. A. et al. (1979). The Jupiter system through the eyes of Voyager I, Science 204, 951.
2. Squyres, S. W. (1980). Volume changes in Ganymede and Callisto and the origin of grooved terrain, Geophys. Res. Lett., 7, 593.
3. Squyres, S. W. (1980). Surface temperatures and retention of H<sub>2</sub>O frost on Ganymede and Callisto, Icarus, in press.
4. Allison, M. L. et al. (1980). Grooved terrain on Ganymede: Origin as flooded graben, IAU Colloquium 57, Kailua-Kona, Hawaii.

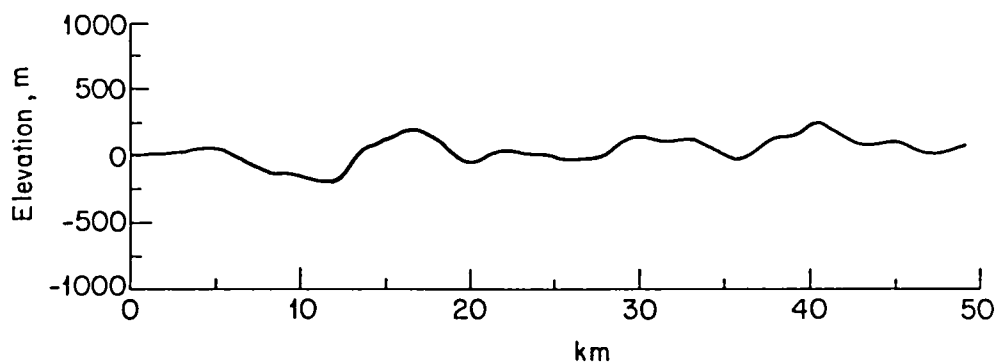


Figure 1. Typical photoclinometric profile across grooved terrain. Vertical exaggeration is 8:1.

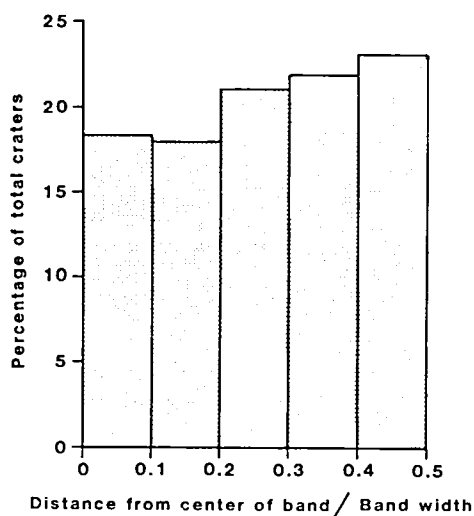


Figure 2. Crater distribution within grooved bands, showing concentration toward band edges. Slope is significant with an error probability of  $<0.005$  (total of 229 craters).

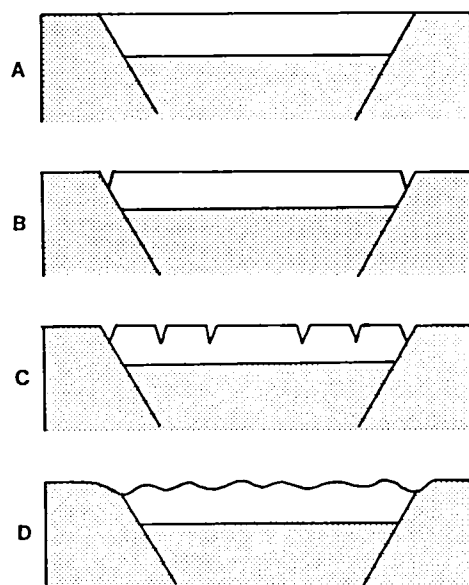


Figure 3. Schematic summary of grooved band formation. A-Creation of ice-filled graben in ice + silicate crust by down-dropping and flooding. B-Development of bounding grooves. C-Replication of groove pattern inward. D-Viscous relaxation of topography over several billion years after extension ceases.

## DOMES ON GANYMEDE

Malin, Michael C., Department of Geology, Arizona State University,  
Tempe, Arizona 85281

Owing to their positive relief, domes are usually the most obvious non-impact crater related features seen on planetary surfaces. In addition, because it is difficult for impact and/or erosional processes to create domes, endogenic processes can be inferred to have participated in their formation (1). Voyager observations of Ganymede reveal domes principally within impact craters, and this association suggests that domes form during endogenic modification of these craters.

Domes under specific study range from about 5 km up to 40 km in diameter, and occupy the interior of craters up to about 120 km diameter. Dome to crater diameter ratios vary from 0.1 for small domes inside central pits to 0.6, with 0.45 representing the mean of a distinct and large subgroup, those that occupy craters without evidence of central pits (the domes may have destroyed or covered these pits). A few larger domes (to 200 km diameter) may be large, impact-basin equivalents of these smaller domes.

Two possible genetic mechanisms may be operating. 1) The domes represent the surface tips of diapirs. In this case, the driving mechanisms might be deep-seated isostatic response to the impact crater, or density differences between a "dirty-ice" crust and an intrusion of purer ice and/or water; 2) the domes may represent extrusive "ice volcanism". In this case, the analogy is best with dacite/rhyolite flows and domes in general morphology, and with glaciers for flow features.

### Reference

- 1) Malin, Michael C. (1978). Surfaces of Mercury and the Moon: Effects of Resolution and Lighting Conditions on the Discrimination of Volcanic Features. Proc. Lunar Planet. Sci. Conf. 9th, 3395-3409.

VOYAGER PHOTOMETRY OF SURFACE FEATURES ON GANYMEDE AND CALLISTO.  
S. Squyres and J. Veverka, Laboratory for Planetary Studies, Cornell  
University, Ithaca, New York, 14853

We have completed our study of the photometric properties of selected surface features on Ganymede and Callisto using Voyager images over phase angles from  $10^\circ$  to  $124^\circ$ , taken with the CLEAR filter (effective wavelength  $\sim 0.5 \mu\text{m}$ ). Normal reflectances on Ganymede average 0.36 for the Cratered Terrain and 0.44 for the Grooved Terrain. The value for the ubiquitous Cratered Terrain on Callisto is 0.19. The photometric properties of these regions are described closely by a simple scattering function of the form  $I = AF(\alpha)\mu_0/(\mu + \mu_0)$ , in which  $A$  is a constant,  $\mu$  is the cosine of the emission angle,  $\mu_0$  is the cosine of the incidence angle, and  $F(\alpha)$  is a function of the phase angle  $\alpha$  only. For these terrains the shape of  $F(\alpha)$  is qualitatively similar to that for the Moon--generally concave upward (Fig. 1). By contrast bright craters on both satellites have  $F(\alpha)$ 's which are convex upward (Fig. 2). The scattering properties of these bright features are definitely not Lambertian, but are described approximately by the scattering law given above. It is noteworthy that the brightest craters on Callisto have reflectances which are only 10% lower than the brightest craters on Ganymede; both have closely similar scattering laws. We estimate that the brightest craters on Ganymede reach normal reflectances of 0.6. Our phase functions yield phase integrals of  $q = 0.8$  and  $0.6$  for Ganymede and Callisto, respectively--in general agreement with earlier radiometric estimates by Morrison (1977) of  $1.0 \pm 0.3$  and  $0.8 \pm 0.4$ .

This research was supported by NASA Grant NSG 7156.

#### REFERENCES

- Morrison, D. (1977). Radiometry of Satellites and of the Rings of Saturn. In Planetary Satellites (J. Burns, ed.). Chapter 12. Univ. of Arizona Press.

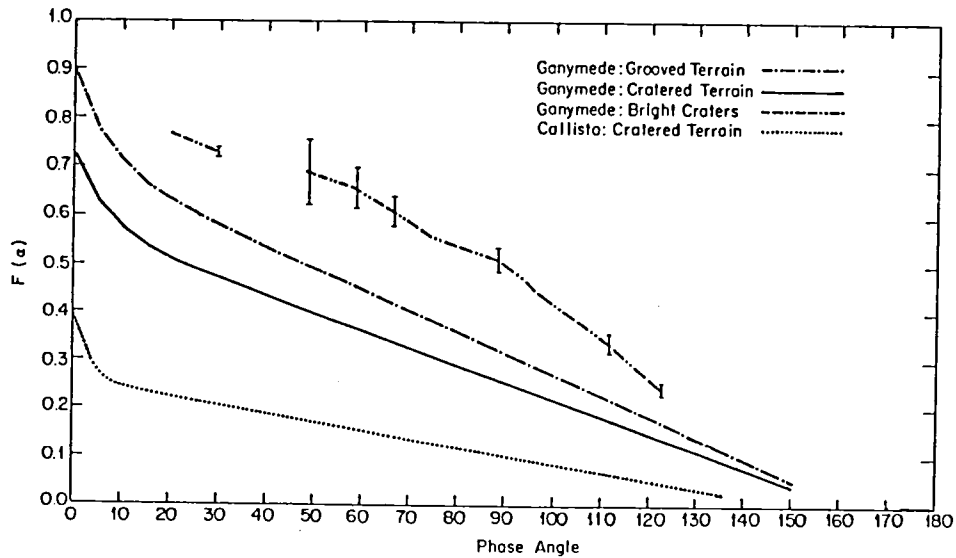


Figure 1. Preliminary best fit phase curves for the grooved and cratered terrains on Ganymede, and for the cratered terrain on Callisto. Beyond  $\alpha \sim 10^\circ$ , the curves are based on Voyager data; the extrapolation to zero phase is based on telescopic disc-integrated measurements. Note that  $F(\alpha)$ , evaluated at  $\alpha = 0^\circ$ , is twice the normal reflectance. Average curve for Ganymede bright craters is also shown.

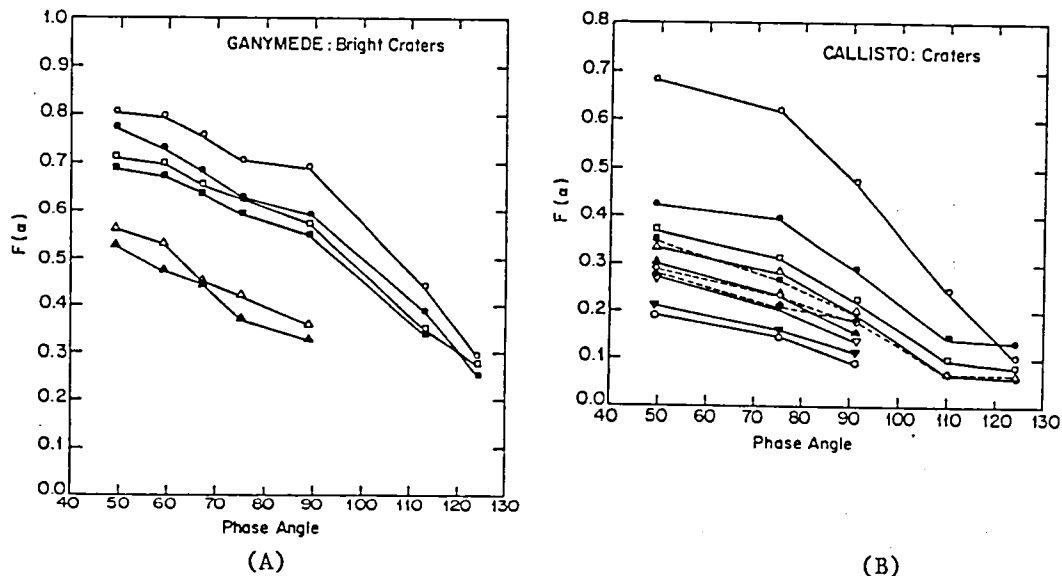
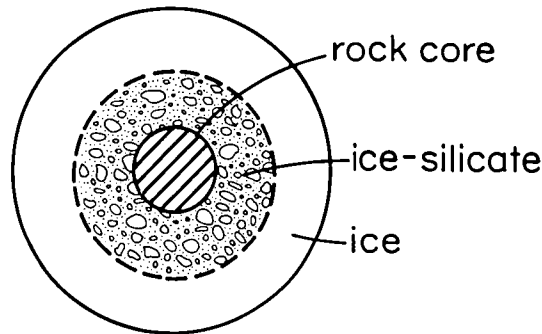


Figure 2. A) Phase curves for selected bright craters on Ganymede.  
B) Phase curves for selected craters on Callisto. (As in Figure 1, the value of  $F(\alpha)$  at  $\alpha = 0^\circ$  is twice the normal reflectance.)

#### THERMAL EVOLUTION OF GANYMEDE AND CALLISTO

G. Schubert and K. Ellsworth, Dept. of Earth and Space Sciences, University of California, Los Angeles, Calif. 90024.

We have proposed (1) that the interiors of Ganymede and Callisto consist of three major regions: 1) a silicate core, 2) an undifferentiated ice-silicate lower mantle, and 3) a predominantly ice upper mantle, as shown in Figure 1.



### Ganymede or Callisto

Figure 1. Model of Ganymede and Callisto

The structure shown above is a consequence of the melting of the outer regions of the icy satellites by accretional heating; the deep interiors of the bodies never melt, however. Silicates sink to the bottom of the melted outer layers and accumulate above the undifferentiated central regions. In the course of geologic time these rocks sink through the solid interior ice-silicate mixture and form a rocky core. The water mantle quickly refreezes (2).

Figure 2 is a sketch of a typical "initial" temperature profile as a function of radius, or the temperature shortly after accumulation, for the structure indicated in Figure 1. The profile of the outer region of the planet is the solidus curve of ice, while that of the inner region is an accretional heating curve. The transition from an accretional temperature profile to a solidus profile occurs at a radius determined by the extent of early melting. This depends on the accretional heat retention factor  $h$ , a parameter which crudely models the complex accretional heating process (3,4). Accretional time scales are so short that radiogenic heating in the silicates cannot significantly modify the 'initial' accretion profile.

Profiles such as the one shown in Figure 2 are used as initial conditions in quantitative studies of the subsequent thermal histories of icy satellite models. The calculations account for radiogenic heating in the ice-silicate interior, subsolidus convection in the ice mantle and

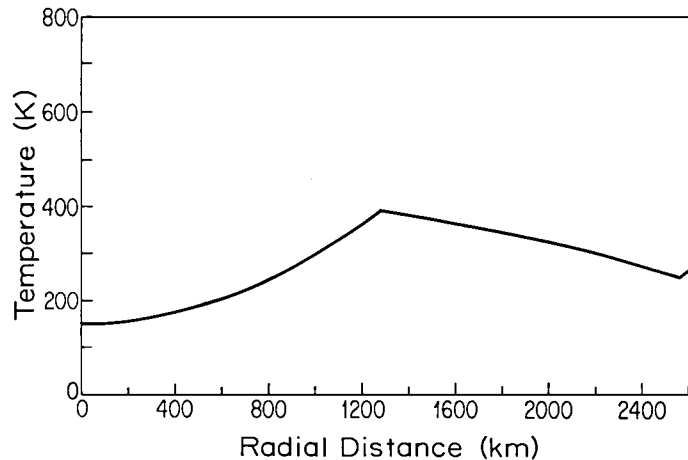


Figure 2. Model initial temperature profile for one of the icy satellites

in the ice-silicate interior as it heats up by radiogenic heating, and conduction in the deep interior until it becomes sufficiently hot to convect. They also account for the temperature and pressure dependences of the effective viscosity of ice and the growth of an ice lithosphere as a consequence of surface cooling. Thermal histories will be presented for different values of the accretional heating parameter  $h$ .

#### REFERENCES

- 1) Schubert, G., D. J. Stevenson, and K. Ellsworth, Internal structures of the Galilean satellites, submitted to Icarus, 1980. Schubert, G., K. Ellsworth, and D. J. Stevenson, Ice in the interiors of Ganymede and Callisto, Abstracts of the Third Colloquium on Planetary Water, Oct. 27-29, 1980, Niagra Falls, New York.
- 2) Cassen, P., S. J. Peale, and R. T. Reynolds, On the comparative evolution of Ganymede and Callisto, Icarus, in press, 1980.
- 3) Safronov, V. F., Evolution of the protoplanetary cloud and formation of the earth and planets, NASA Tech. Transl. TTF-677, 206 pp., 1972.
- 4) Kaula, W. M., The beginning of the earth's thermal evolution, In The Continental Crust and Its Mineral Deposits, D. W. Strangway, ed., Geol. Assoc. of Canada Special Paper 20, in press, 1980.

THE TEMPERATURE OF AMALTHEA. Damon Simonelli, Laboratory for Planetary Studies, Cornell University, Ithaca, New York 14853

The Voyager IRIS measurement of the temperature of Amalthea ( $180 \pm 5^\circ\text{K}$ ; J. C. Pearl, personal communication) is higher than earth-based measurements ( $155 \pm 15^\circ\text{K}$ ; Rieke, 1975) and higher than the equilibrium blackbody temperature from solar heating alone ( $172^\circ\text{K}$ ). Because Amalthea's environment includes intense particle radiation and magnetic fields, thermal radiation and reflected light from Jupiter, we have simulated diurnal temperature history to see if temperatures significantly above the  $172^\circ\text{K}$  equilibrium value can occur.

The diurnal temperature cycle at a point on the surface was calculated using the method of Linsky (1965). We assumed that Amalthea is spherical, has an emissivity of 1.0 and a uniform surface layer with thermal properties similar to those of lunar soil at  $150^\circ\text{K}$  (lunar soil data from Hemingway *et al.*, 1973). The calculation included the following energy inputs: (a) solar insolation, (b) sunlight reflected from Jupiter, (c) Jovian thermal radiation, and (d) heating by charged particles (calculated from Divine, 1979). Heating by charged particles amounts to only  $0.5^\circ\text{K}$ . Jupiter thermal radiation and reflected light, which affect only the Jupiter-facing side of the satellite, increase the maximum surface temperature by  $3^\circ\text{K}$ .

Diurnal temperature curves, calculated including all the energy sources, are given in Figs. 1-3. Fig. 1 shows the temperature cycles of two different locations on the sub-Jupiter longitude ( $0^\circ$ ), and Fig. 2 shows cycles for two points on the anti-Jupiter longitude ( $180^\circ$ ). The temperature curves for  $180^\circ$  longitude vary smoothly; temperatures at the sub-Jupiter longitude drop sharply when Amalthea goes into eclipse near local noon. Fig. 3 compares the diurnal temperature histories of the sub-Jupiter and anti-Jupiter points. At night, the sub-Jupiter point is warmer than the anti-Jupiter point because of incident Jupiter shine and Jupiter thermal radiation, but the anti-Jupiter point is warmer during the day ( $T_{\text{max}} \approx 165^\circ\text{K}$ ) because it is never eclipsed.

A maximum Amalthea surface temperature of  $165^\circ\text{K}$  is consistent with Rieke's measurement but inconsistent with the Voyager IRIS observation. In an attempt to increase the maximum temperature, the emissivity was reduced to .95 (a reasonable value) and the surface was modeled as a thin, low density, low conductivity layer over more conductive material of normal density. The resulting temperature curve for the anti-Jupiter point is shown in Fig. 4. The maximum surface temperature is near  $172^\circ\text{K}$ ; the maximum disc-averaged temperature is still well below  $180^\circ\text{K}$ .

Our calculations demonstrate that disc-averaged temperatures near  $180^\circ\text{K}$  require either (1) the existence of an important energy source not included in our calculations, or (2) that the emissivity of Amalthea is unusually low. Future work will involve modeling the actual shape of Amalthea more realistically and including Joule heating as an energy source. Preliminary calculations show that unless Amalthea is metallic, Joule heating cannot affect its temperature significantly.

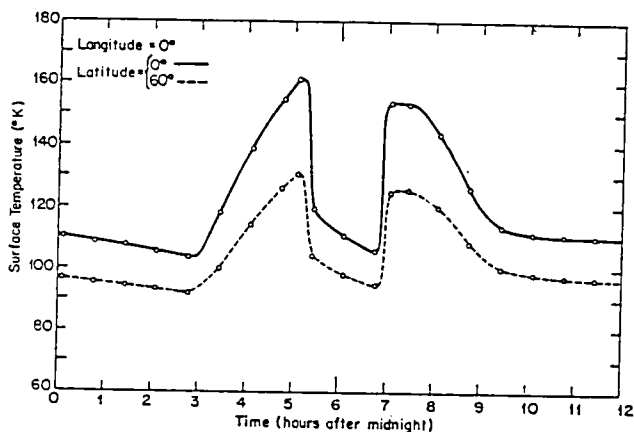


This research was supported by NASA Grant NSG 7156.

#### REFERENCES

- Divine, N. (1979). February 1979 models for the distribution of energetic electrons and protons in Jupiter's radiation belts. JPL Interoffice Memo, 3574-79-51.
- Hemingway, B. S., Robie, R. A., Wilson, W. H. (1973). Specific heats of lunar soils, basalt, and breccias from the Apollo 14, 15 and 16 landing sites, between 90 and 350°K. Proc. Fourth Lunar Science Conf. 3, 2481-2487.
- Linsky, J. L. (1965). A computer program to solve the heat-conduction equation in the lunar surface for temperature-dependent thermal properties. Harvard College Observatory Scientific Report No. 7
- Rieke, G. H. (1975). The temperature of Amalthea. Icarus 25, 333-334.

Figure 1. Diurnal surface temperature history for two locations on the sub-Jupiter longitude ( $0^\circ$ ), assuming a lunar-like surface layer. Note that an eclipse of the Sun occurs once every revolution (between 5 and 7 hours).



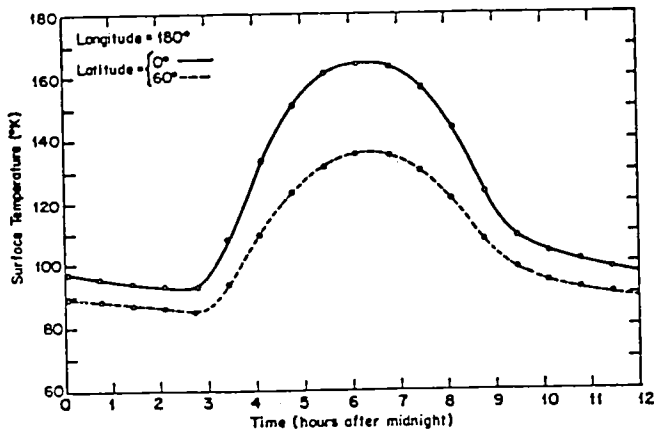


Figure 2. Diurnal surface temperature history for two locations on the anti-Jupiter longitude ( $180^\circ$ ), assuming a lunar-like surface layer.

Figure 3. Comparison of the diurnal surface temperature histories of the sub-Jupiter and anti-Jupiter points.

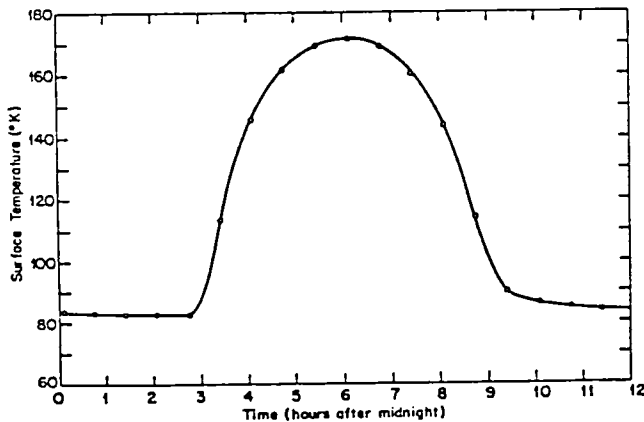
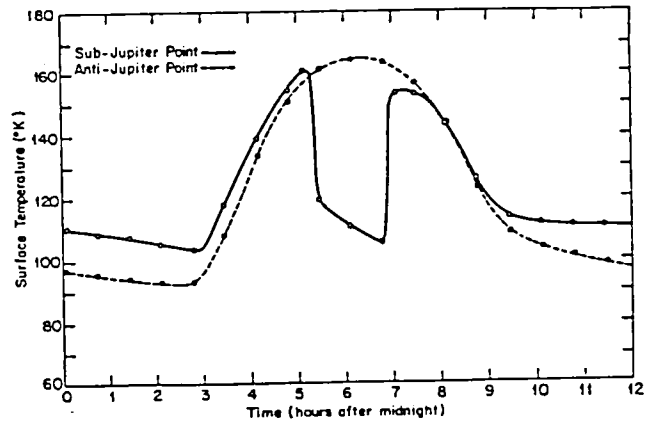


Figure 4. Diurnal surface temperature history for the anti-Jupiter point, assuming a thin, low-density, low-conductivity layer over more conductive material of higher density.

Chapter 2  
STRUCTURE, TECTONICS AND STRATIGRAPHY



# SIMULATION OF PIONEER-VENUS ALTIMETRY USING NORTHERN PACIFIC OCEAN FLOOR BATHYMETRY.

Arvidson, R.E., R. Batiza and E.A. Guinness, Dept. of Earth and Planetary Sciences, Washington University, St. Louis, Missouri 63130

The tectonic and volcanic evolution of the North Pacific are reasonably well understood. Important clues to this understanding were of course provided by bathymetric data. This is because first order tectonic elements such as constructional plate boundaries, collisional boundaries and fracture zones all have clear and characteristic topographic expression. These terrestrial bathymetric features were first discovered by means of surface ship surveys of relatively high resolution. If such features were present on other planetary surfaces, could they be recognized using surveying techniques of lower resolution? In this study we give evidence that for Pioneer-Venus altimeter data, this question can be answered affirmatively.

Figure 1A is a gray-coded elevation map for the Northern Pacific ocean floor. The map is based on estimates of the average depth for 56 x 56 km sections of the ocean floor. The raw data were processed with a 3 x 3 low pass boxcar filter to fill in data gaps. The resulting display has an effective footprint size of about 150 km x 150 km. For reference, the footprint size of the Pioneer-Venus altimeter is about 100 x 100 km (Pettengill et al., 1980). Thus, Figure 1A provides a fair representation of the level of topographic information that could be seen for the sea floor if the data were acquired by the PV altimeter instrument. Figure 1B is a shaded relief map of the data presented in Figure 1A. The sun is coming from the west at an angle of 45 degrees to the horizon. In the case of Figure 1B, the effective footprint size is about 250 x 250 km.

Figures 1A and 1B illustrate that, even with relatively coarse sampling, the systematic structure of the sea floor is evident in the distribution of elevations. All major tectonic features of the North Pacific are clearly evident. The crest and flanks of the East Pacific rise are easily discernable in the equatorial East Pacific. The systematic age-depth relationship on the flanks of the rise are also clear as are the major age-depth offsets across E-W trending fracture zones. The arc-trench system of the North and West Pacific are also very clearly shown. In addition, major volcanic constructs such as the Hawaii-Emperor seamount chain and the large aseismic plateaus as well as lower order tectonic features such as the Emperor trough are clearly visible. Only the higher frequency bathymetric features such as abyssal hills and many seamounts are not detectable. It is likely that given our understanding of terrestrial tectonic processes and associated patterns of crustal elevation, we could detect analogous features on other planetary surfaces if they were present and sampled in a manner similar to the data in Figures 1A and 1B. It is important, therefore, to realize that such a systematic pattern of structure does not appear to exist in the topographic maps of Venus made from PV altimetry data (Pettengill et al., 1980), which cover the same areal extent as Figure 1A and 1B.

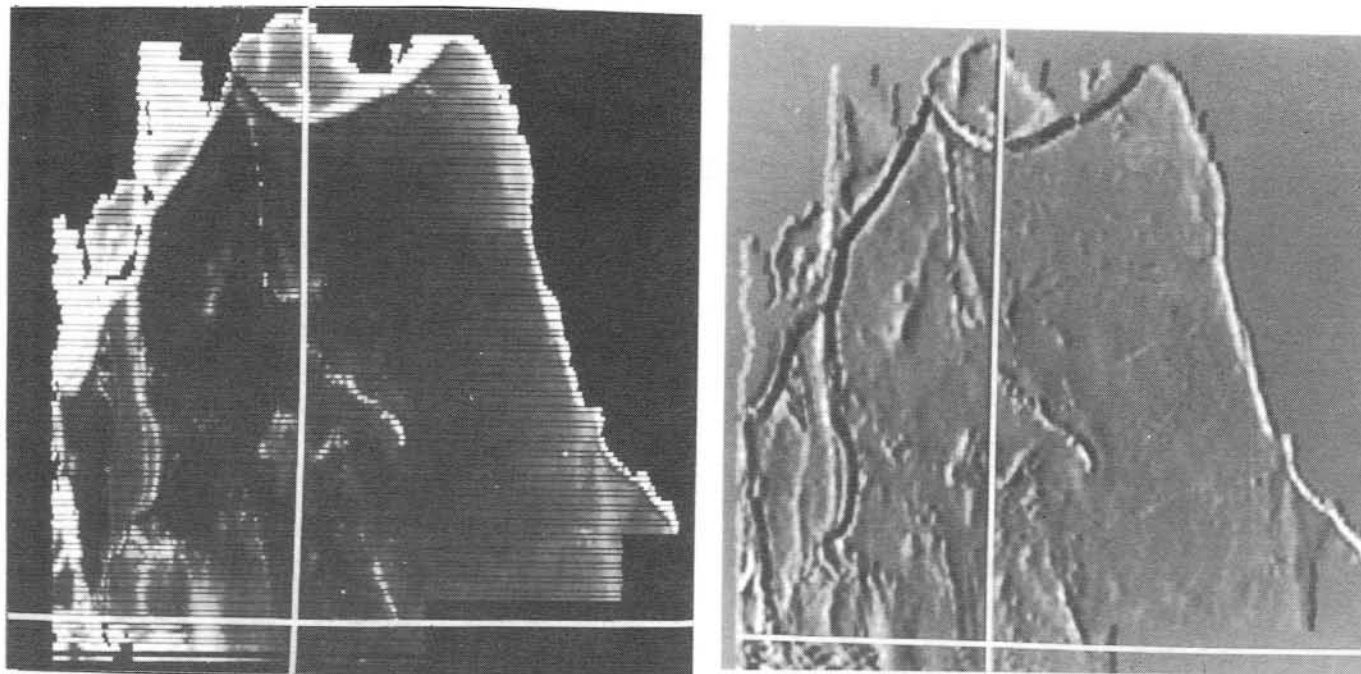


Figure 1A - Gray tone coded depth map for the Northern Pacific. The horizontal white line is the equator and the vertical white line corresponds to 180° W. Longitude. The eastern edge of the map shows the continental shelf of North and South America and the northern edge extends to the Bering Sea. The major tectonic features are readily discernable. Based on 25,000 estimates of the average depth in 56 x 56 km sections of the sea floor. Data from NOAA.

Figure 1B - Shaded relief map version of the data shown in Figure 1A.

## EVIDENCE FOR CONTINENTAL-STYLE RIFTING FROM THE BETA REGION OF VENUS

George E. McGill, Department of Geology and Geography, University of Massachusetts, Amherst 01003

Although the total area of elevated regions on Venus is small, these regions are of great interest because their origin must relate to the global tectonics of Venus. The elevated region named "Beta Regio" (Beta) is particularly interesting because it lies north of and on trend with a long, narrow, linear feature visible on Earth-based radar images as being, on average, rougher at radar wavelengths ( $\sim 10$  cm) than the surrounding surface (Campbell, et al., 1979, 1980). The portion of this linear feature between  $5^{\circ}\text{N}$  and  $5^{\circ}\text{S}$  latitude was shown to be a trough lying within an elevated region (Goldstein, et al., 1976) and thus possibly a rift (Malin and Saunders, 1977). Furthermore, Saunders and Malin (1977) interpreted Beta itself as one or more very large shield volcanoes. Pioneer Venus radar altimetry and imaging data support the existence of a rift, but suggest that Beta is better interpreted as a complex dome with a medial rift, analogous to the domes characteristic of some continental rift zones on Earth.

Beta is a broad elevated region that is moderately elliptical in plan, with the long axis of the ellipse oriented north-south. Its horizontal dimensions are 2000-2500 km by 1500-2000 km, depending on which contour line is selected to define the periphery. Slopes apparently are very gentle, but the wide spacing and large diameters of Pioneer Venus altimeter footprints (Pettengill, et al., 1980) cause slope angles to be significantly underestimated. The total relief of Beta is about 5 km, indicating that average flank slopes are less than  $0.5^{\circ}$ . Extending for almost the entire north-south length of Beta is a series of elongated, linked depressions that define a trough shown by Pioneer Venus altimetry to be 0.5 to 2.5 km below the general upland surface. However, the spacing and size of altimeter footprints also cause an underestimate of the depth of any narrow depression, so this trough must be deeper than indicated.

Many of the topographic features of Beta and its associated rift are similar to structural and topographic features characteristic of the East African rift system. The Venus rift is about 50% longer and is within a factor of 2 of being the same width and depth as the East African rift, and Beta is within a factor of 2 of having the same diameter and relief as the Ethiopian dome. The resolutions of Pioneer Venus altimetry and of all available imagery are not adequate to permit more precise size comparisons. Venera 9 and 10 gamma-ray data (Surkov, et al., 1976) suggesting that rocks on the flank of Beta are basalt also are consistent with this analogy because most of the volcanic rocks on the flanks of the Ethiopian dome are fissure basalts.

The presence of a medial trough on Beta, its association with a major rift, and general similarities of scale and topographic detail suggest that Beta is better interpreted as a complex dome than simply as one or more basaltic shield volcanoes. The analogy suggested here implies that rifting comparable to continental rifting on Earth has occurred or is occurring on Venus. Because the total horizontal spreading associated with known continental

rifts on Earth is modest (e.g., Baker, et al., 1972), the evidence for continental-style rifting on Venus does not necessarily imply a complete global system of plate tectonics.

#### REFERENCES CITED

- Baker, B.M., P.A. Mohr, and L.A.J. Williams, 1972, Geology of the Eastern Rift System of Africa, Geol. Soc. American Spec. Paper 136, 67p.
- Campbell, D.B., and B.A. Burns, 1980, Earth-based radar imagery of Venus, Jour. Geophys. Res., in press for Pioneer Venus special issue.
- Campbell, D.B., B.A. Burns, and V. Boriakoff, 1979, Venus: further evidence of impact cratering and tectonic activity from radar observations, Science, 204, 1424-1427.
- Goldstein, R.M., R.R. Green, and H.C. Rumsey, 1976, Venus radar images, Jour. Geophys. Res., 81, 4807-4817.
- Malin, M.C., and R.S. Saunders, 1977, Surface of Venus: evidence of diverse landforms from radar observations, Science, 196, 987-990.
- Pettengill, G.H., E. Eliason, P.G. Ford, G.B. Lorient, H. Masursky, and G.E. McGill, 1980, Pioneer Venus radar results: altimetry and surface properties, Jour. Geophys. Res., in press for Pioneer Venus special issue.
- Saunders, R.S., and M.C. Malin, 1977, Geologic interpretation of new observations of the surface of Venus, Geophys. Res. Lett., 4, 547-550.
- Surkov, Y.A., F.F. Kirnozov, V.N. Glazov, A.G. Duchenko, and L.P. Tatsil, 1976, The content of natural radioactive elements in Venusian rock as determined by Venera 9 and Venera 10, Kosmicheskie Issledovaniya, 14, 704-709.



## TOPOGRAPHY OF EARTH AND VENUS

Malin, Michael D., Department of Geology, Arizona State University,  
Tempe, Arizona 85281

Paluzzi, Peter R., Jet Propulsion Laboratory, 4800 Oak Grove Drive,  
Pasadena, California 91103

Digital topography has, for some years, been formatted and processed into shaded relief images for specific studies involving land-use, and thermal properties of geologic materials. Recently, a shaded relief image of Venus has been produced in a similar manner to provide a first view of that planet's surface physiography. Views of the Earth have been produced and examined at similar scale and resolution, using the RAND/SIO Global Topographic Data Set. Several important observations can be reported: 1) variations in illumination geometry yield significant changes in the apparent visibility of major topographic features of the seafloor, in particular, the Mid-Ocean Ridges (MORs); 2) in many views, MORs are not as prominent as typically portrayed in artist renditions; 3) the bimodal distribution of terrestrial topography, when viewed without the oceans, shows the continents to be relatively flat-lying plateaus, with the seafloor displaying considerably greater low topographic variability than the continents (i.e. the seafloor is topographically rougher); this latter point can be attributed in part to the relative youth of the seafloor. In comparing these aspects of the Earth's topography with those seen in the Pioneer views of Venus, the following conclusions are tentatively drawn: 1) Ishtar Terra shows many aspects similar to those seen on terrestrial continents, including an abrupt boundary, relatively flat, plateau-like upland with few relief features, surmounted by mountains (e.g. Maxwell) in confined zones across and around the margin of the plateau; 2) the "median plains" on Venus, those that cover the largest areal percentage of Venus, have a gently undulating topography with numerous isolated and clustered mounts; these plains show a morphologic similarity to portions of the terrestrial seafloor; 3) Aphrodite Terra and Beta Regio appear unlike terrestrial continents, except for large rift troughs and valleys oriented along their longitudinal axes. The general aspect of Venus is that of a planet frozen in a period of tectonic evolution not unlike Pangaeon Earth.

RIDGE-AND-TRENCH SYSTEMS OF VENUS AND GLOBAL RIFT VALLEYS ON EARTH: A COMPARISON, Gerald G. Schaber and Harold Masursky, U.S. Geological Survey, Flagstaff, AZ 86001.

We have begun a comparative study of topographic and geomorphic characteristics of global rift valleys on Earth and similar features observed on Venus. Radar altimetry, surface rms slope values and radar-image data returned from Venus by the Pioneer-Venus spacecraft have revealed ridge-and-trench systems that cover  $4 \times 10^7 \text{ km}^2$  south and east of Aphrodite Terra and  $6 \times 10^6 \text{ km}^2$  south of Beta Regio (Fig. 1) [1]. The venusian trenches average about 100 km wide and are as deep as 2.5 km below the surrounding plains. The marginal ridges are commonly of unequal height, ranging from 500 m to 3 km (Figs. 1, 2, 3). Ridge-and-trench features on Venus are almost all restricted to elevated (1.5 to 3 km) platforms or domes suspected to be of regional tectonic origin, whose uplift is thought to be responsible for an extensional origin for the valley features.

After initial differentiation, the crust of Venus was probably uniformly distributed; subsequent redistribution may have been a result of mantle convection [1]. These workers further proposed that the absence of medial ridges and marginal valleys within the venusian lowlands (27% of the planet, occupying surfaces 500 m to 2.5 km below mean radius) suggests that Earth-like plate motions are not operating on Venus. However, the existence of ridge-and-trench systems associated with apparently uplifted segments of a probable sialic crust may indicate regional extensional stresses (and possible volcanism). Associated with these stresses would be thermal perturbations in the mantle that operate beneath thinner segments of an otherwise very thick, unbroken crust. The best terrestrial analogs for both the scale and possible origin of the venusian ridge-and-trench features are the large continental rift valleys: the afro-Arabian rifts are proposed to be extensions of global midoceanic seafloor spreading that operate beneath the African continent [2] (Fig. 4; Table 1). The African rift valleys, like those on Venus, traverse the crests of regions in Kenya and Ethiopia that have been uplifted several kilometers. Continental rifts have long been recognized as having remarkably consistent widths (Table 1); most have raised rims resulting from isostatic compensation for the deficiency of crustal material in the rift. Continental rifts are associated with a wide diversity of volcanic rocks, including silicic-alkalic, ignimbritic and altered basaltic materials, all attributed to partial melts from the mantle and contamination with sialic rocks. Where spreading is slow and encumbered, as in the African rifts, long-term crustal accretion at the base of the continental crust is feasible.

Although many other tectonic mechanisms (including compression) have been proposed for the formation of the rifts, a tensional model has gained the most acceptance. Using a tension model, Meinesz [3] has

shown that continued horizontal stress within a known thickness of crust will produce a graben of predictable width, wall slope, depth and marginal rim height. For a crust 40 km thick, his model predicts a graben with a width of 65 km, maximum depth (with sediment infill) of 2.8 km, and marginal rim uplifts of 640 m. These figures are consistent with observed continental rifts (See Table 1). By applying his equations to the 100-km-wide venusian valleys, a crustal thickness of ~70 km is estimated. Such a thick crust is not totally unacceptable in view of preliminary results from Pioneer-Venus gravity data [4], which infer a depth of isostatic compensation between 75 and 100 km. A detailed report on our comparisons of venusian and terrestrial rifting is being prepared, but confirmational data on the gravity, morphology and tectonic history of the ridge-and-trench features on Venus must await the proposed Venus Orbiting Imaging Radar (VOIR) mission later in the decade.

## References

- [1] Masursky, Harold, Eliason, Eric, Ford, G., McGill, G. E., Pettengill, G. H., Schaber, G. G., and Schubert, Gerald, 1981, Pioneer-Venus radar results: Geology from images and altimetry: Jour. Geophys. Res., in press.
- [2] Baker, B. H., Mohr, P. A., and Williams, L. A., 1972, Geology of the eastern rift system of Africa: Geol. Soc. Amer. Spec. Paper 136, 67 p.
- [3] Meinesz, F. A. V., 1950, Les "graben" africains, resultat de compression ou de tension dans la croute terrestre: Koninkl. Belg. Kol. Inst., Bull., 21, 539-552.
- [4] Phillips, R. J., Kaula, W. M., McGill, G. E., and Malin, M. C., 1981, Tectonics and evolution of Venus: Science, in press.
- [5] Heezen, B. C., 1962, The deep-sea floor, in Runcorn, S. K., ed., Continental drift, Chap. 9, New York, Academic Press, 235-288.
- [6] Girdler, R. W., 1964, Geophysical studies of rift valleys, in Physics and chemistry of the Earth, 5, 122-156.

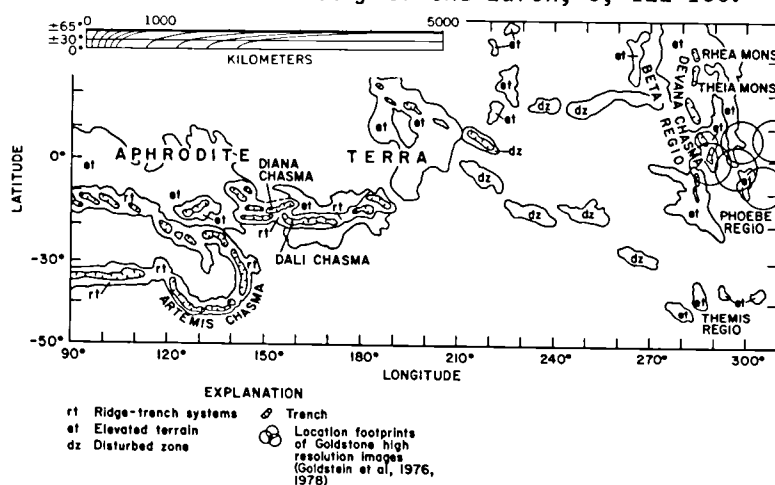


Fig. 1-Tectonic map of Venus showing location of deep trenches, canyons, marginal ridges and other disturbed zones lying between Aphrodite Terra and Beta Regio. Note scale of features. After [1].

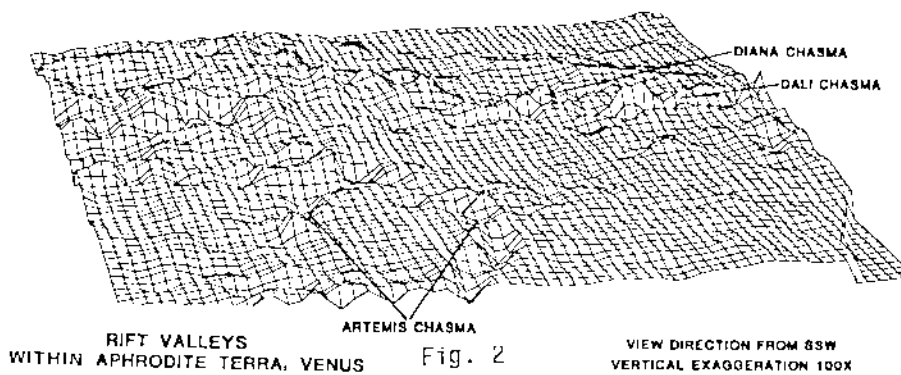


Fig. 2

3-D topographic plot of Venus ridge-and-trench complexes south and east of Aphrodite Terra. After [1].

TABLE 1

	Width (km)	Depth (km)
Gulf of Aqaba	50	1.8 to 2.4
Lake Baikal rift valley	50	2.2
Dead Sea rift valley	35	1.6
East African rift valleys	50	0.2 to 1.9
Midland valley of Scotland	75	0.5
Rhine valley	40	0.6
Gulf of Suez	35	0.8

Mean widths and depths of several large continental rifts. After [6].

profiles across several Venus ridge-and-trench systems. After [1].

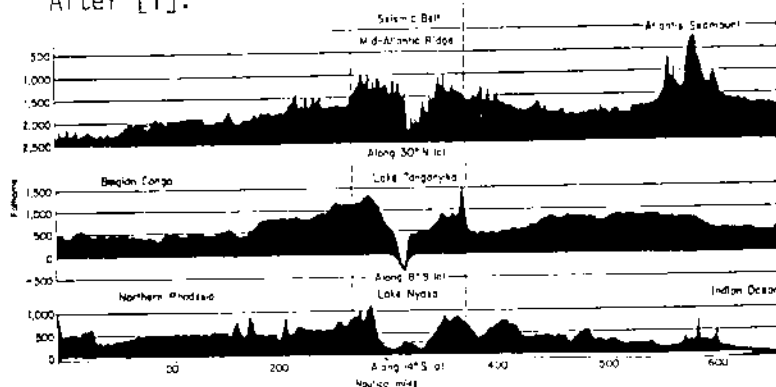


Fig. 4- Profiles of the African rift valleys and the mid-oceanic rift valleys. Note the great similarity in the form of the rift valley and the rift mountains on these three profiles. After [5].

POSSIBLE RELATIONS BETWEEN THE EARLY MARTIAN GEOLOGIC RECORD, CONVECTIVE OVERTURN, AND CORE SEGREGATION.

Raymond E. Arvidson and Geoffrey F. Davies, Dept. of Earth and Planetary Sciences, Washington University, St. Louis, Missouri 63130

A number of workers have pointed-out the geological, geophysical, and topographic evidence for a major hemispheric asymmetry on Mars between the northern, sparsely cratered plains and the southern, densely cratered uplands (Mutch et al., 1976; Malin, 1977; Wise et al., 1979; Arvidson and Davies, 1980). Bills and Ferrari (1978) showed that the center of figure is offset from the center of mass for Mars in a direction that implies that the heavily cratered hemisphere is underlain by a crust that is thicker than the crust underlying the northern plains. Figure 1 is gray-scale coded geologic map of Mars with a perspective simulating that of the Viking Orbiter cameras at a distance of 750,000 km from the center of the planet. The view is centered at the piercing point location of the center figure/center mass offset vector. The map shows that the stratigraphically oldest materials are clustered symmetrically about the center figure/center of mass vector. Thus, it would appear that the heavily cratered hemisphere is not only underlain with a thicker crust; the oldest units are also preserved in greatest abundance.

The vast scale of the asymmetry between the heavily cratered and plains hemispheres argues for an origin by deep interior processes (Lingenfelter and Schubert, 1973). First-order convective overturn, with a rising plume centered over what is presently the plains hemisphere, would tend to place that hemisphere in deviatoric tension, leading to fracturing and volcanism (Wise et al., 1979). Alternatively, asymmetric core formation could lead to similar stress field patterns (Stevenson, 1980). One important aspect of first-order convective overturn is that it would be difficult to maintain after core formation. Mars may thus be unique among the terrestrial planets in preserving a record of events prior to, during, and after core formation.

If a lunar-like cratering rate can be used to date Martian surfaces that have survived from the period of early heavy bombardment, it follows that the asymmetry (and thus the core) formed within the first billion years of geologic time (Neukum and Hiller, 1980). In addition, use of such a cratering history forces about 75% of the equatorial regions to have been resurfaced by copious quantities of volcanic materials soon after formation of the asymmetry (Arvidson et al., 1980). However, use of a lunar-like cratering history early in Martian evolution is somewhat ad-hoc. In fact, some evidence indicates that Mars may have taken up to 2.5 Gy to accrete (Weidenschilling, 1976). Use of such a constraint forces the core to have formed intermediate in geologic time, rather than soon after planetary formation.

An exploratory thermal evolution model for Mars is shown in Figure 2. The free parameters in the model are the characteristic initial planetary temperature, along with the timing and the rate of core segregation. Figure 2 follows the most plausible scenario, i.e. one in

which the core forms within the first billion years of geologic time. Results of the modeling imply that Mars must have been initially hot in order to begin core segregation early. Another result of such a constraint is that the details of core segregation (total time needed, and whether accelerating or constant function of time) control the height and timing of a peak in heat production. Such a pulse, with computed heat fluxes comparable to that characteristic of terrestrial ocean basins, may help to explain the generation of copious quantities of volcanic materials during and immediately after disruption of the northern cratered terrain (Arvidson and Davies, 1980). If this scenario is accepted, then the question can be raised as to why evidence of plate tectonics is missing on Mars for this time period, even though heat fluxes may have comparable to terrestrial ocean basins, which are part of a vigorous convective system.

#### References Cited

- Arvidson, R.E., K.A. Goettel and C.M. Hohenberg, 1980, A post-Viking view of the geologic evolution of Mars, *Rev. Geophys. Space Phys.*, 18, 565-603.
- Arvidson R.E., and G.F. Davies, 1980, Possible relations between the early martian geologic record, convective overturn, and core segregation, *Icarus*, submitted.
- Bills, B.G. and A.J. Ferrari, 1978, Mars topography harmonics and geophysical implications, *J. Geophys. Res.*, 83, 3497-3508.
- Lingenfelter, R.E. and G. Schubert, 1973, Evidence for convection in planetary interiors from first-order topography, *Moon*, 7, 172-180.
- Malin, M., 1977, The nature and origin of the Martian planetary dichotomy, NASA TM-79729, pp. 83-85.
- Mutch, T.A., R.E. Arvidson, J.W. Head III, K.L. Jones and R.S. Saunders, 1976, *The Geology of Mars*, Princeton University Press, 400 pp.
- Neukum, G. and K. Hiller, *Martian Ages*, *J. Geophys. Res.*, in press.
- Scott, D. and M. Carr, 1978, *Geologic Map of Mars*, U.S.G.S. Misc. Inves. I-1083.
- Stevenson, D.J., 1980, Core formation dynamics and primordial planetary dynamos, *Lunar and Planet. Sci. XI*, 1088-1090.
- Weidenschilling, S., 1976. *Accretion of the terrestrial planets II.*, *Icarus*, 27, 161-170.

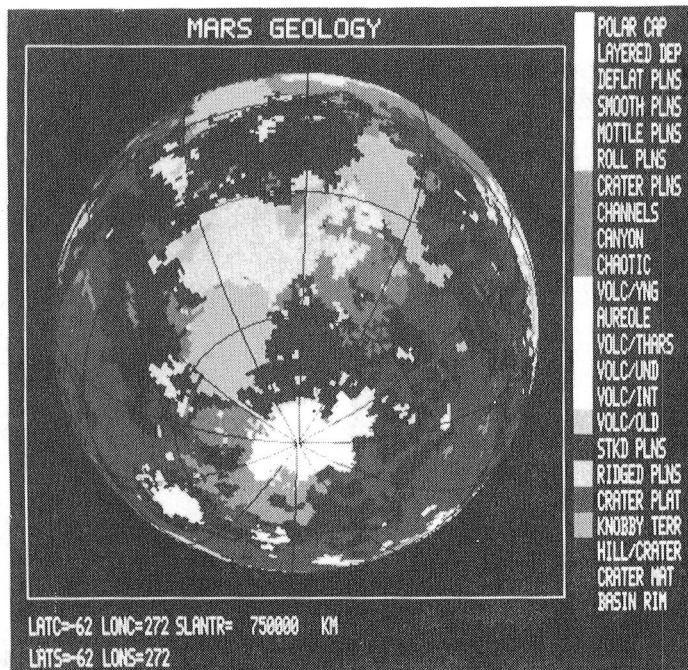


Figure 1 - Gray-coded geologic map of Mars, centered at the center of figure/center of mass offset vector. Units from Scott and Carr (1978). The oldest units are shown as the darkest, i.e. basin rim, cratered materials, and hilly/cratered terrains.

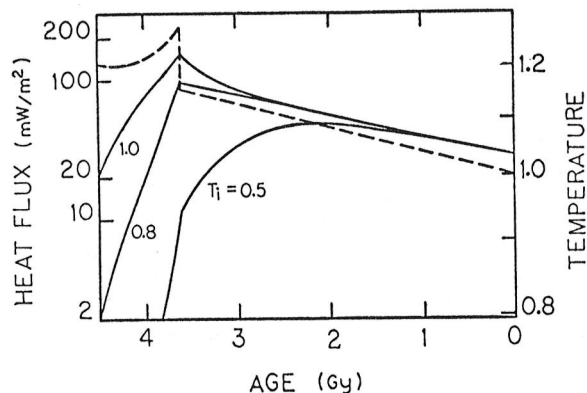


Figure 2 - Calculated thermal histories for various initial temperatures,  $T_i$ , a core segregation time of 0.9 Gy, and an accelerating rate of release of core energy, starting at  $t=0$  (i.e. 4.5 Gy ago) and accelerating exponentially with a characteristic timescale of 300 My. Curves are labelled with normalized initial temperature,  $T_i$ . Dashed line is the heat production curve (expressed per unit surface area). Temperatures are normalized by the steady state temperature corresponding to the present heat generation rate, which means that the temperatures are effectively normalized by the present temperature.

## GRAVITY-TECTONICS AND VOLCANISM: IMPLICATIONS FOR THE EARTH AND MARS

L.S. Crumpler, Department of Planetary Sciences, University of Arizona,  
Tucson, Arizona 85721

Terracing of the upper flanks of Olympus Mons may be a consequence of gravity stresses which result in minor landslipping within the upper flanks of the main shield. Body force-induced deformations of this type may be a fundamental cause of fractures in massive volcanoes, and may result in localized linear to arcuate fissures. The inboard edges of the terraces on Olympus Mons may be the site of such fissure eruptions initiated at the heads of gravitationally unstable segments of the shield. Similar gravity structures may play an important part in the style of eruption in many terrestrial volcanoes as well.

Arcuate fissures, somma-type calderas and amphitheater-shaped calderas occur in all major volcano types on earth, including shield volcanoes and composite cones. Modeling of gravitational body forces in volcanic constructs shows that these and similar features may result from the gravitational deformation in segments or in entire summits of large volcanoes. Two basic types of gravity structure are here recognized in terrestrial volcanoes: (1) Long term unstable gliding of the volcano superstructure, in which continuously rejuvenated eruptions occur from fissures, or isolated vents, marking the heads of glide segments (e.g., Mauna Loa southwest rift); and (2) instantaneous amphitheater formation during paroxysmal eruptions utilizing gravity stress-weakened summits and flanks (e.g., lateral blast eruptions). These stresses will be inherent in any free-standing and elastic mass of conical form. Instability arises when the slopes are overloaded or become over-steepened. In type (1), body forces continually deform the construct and create fractures that can enhance the egress of available magmas. In type (2), body forces are typically stable until dynamic (eruptive) energy creates unstable conditions, particularly during rapid and voluminous explosive eruptions; under these conditions, whole summits may "slump" off.

The gravitational stresses acting on the upper flank of Olympus Mons, may be related to the origin of the aureole deposits, whose origin can be explained as a result of gravity sliding (Lopes, and others, 1980; Harris, 1977). Such aureole thrust sheets would differ from the terraced fissures in that they represent translational gliding of the distal slopes on a weak substratum, and the latter represent minor gravity slipping of the upper slopes of the shield. Here it is proposed that the gravity tectonic sliding of the lower flanks has resulted in the formation of the escarpments which characterize Olympus Mons, and that these escarpments have in turn resulted in loss of lateral support for the more massive upper flanks. As a consequence, long term unstable body forces could be expected to exceed the yield strength of the main shield mass.

Amphitheater-shaped valleys common in many oceanic shield volcanoes (Taylor, and others, 1980; Ridley, 1971), and the Hawaiian-type arcuate fissures may be a result of similar gravity slipping (Swanson, and others, 1976; Lipman and Lockwood, 1977). Gravitational instability can result when the steep unbuttressed subaqueous slopes typical of oceanic shield volcanoes are unable to provide the necessary lateral support for the subaerial mass of the cone during the course of its normal growth.



The continuous eruption of Stromboli may be a special case of type (1) volcano gravity tectonics , in which lateral conveyor belt-like slipping of the Sciara del Fuoco maintains an open conduit through which magmas can be erupted. Without gravity structures, many volcanoes in both deep seismic and aseismic environments might quickly become dormant.

(This report was initially presented in the Department of Planetary Sciences, University of Arizona in February, 1980, and in May, the eruption of Mt. St. Helens provided a spectacular confirmation of the importance of gravity sliding in volcanic eruptions.)

### References

- Harris, S.A., 1977, The aureole of Olympus Mons, Mars. Jour. Geophys. Res., 82, 3099-3107.
- Lipman, P.W. and Lockwood, J.P., 1977, Structure and evolution of Mauna Loa volcano, Hawaii. NASA Tech Mem. TM X - 3511, 129-130.
- Lopes, R.M.C., Guest, J.E., and Wilson, G.J., 1980, Origin of the Olympus Mons aureole and perimeter scarp. The Moon and the Planets, 22, 221-234.
- Ridley, W.I., 1971, The origin of some collapse structures in the Canary Islands: Geol. Mag., 108, 477-484.
- Swanson, D.A., Duffield, W.A., and Fiske, R.S., 1976, Displacement of the south flank of Kilauea volcano; the result of forceful intrusion of magma into the rift zones. U.S. Geol. Surv. Prof. Paper 963, 39p.
- Taylor, P.T., Wood, C.A., and O'Haran, T.J., 1980, Morphological investigations of submarine volcanism: Henderson Seamount. Geology, 8, 390-395.

## RIDGE-RINGS ON MARS

Ann W. Gifford, Center for Earth and Planetary Studies, National Air and Space Museum, Smithsonian Institution, Washington, D.C. 20560.

Ridges on Mars with similarities to lunar mare ridges have been used to model compressive stresses and refine global models (Phillips and Lambeck, 1980; Eppink and Saunders, 1980). The occurrence of ridges in circular rings (here informally termed "ridge-rings") is one exception to the global scale pattern. As part of an ongoing study of various aspects of ridges on all planets, a planet-wide survey of mare-type ridges on Mars is being conducted. The numerous occurrences of ridge rings on Mars may further help in interpreting the mechanism(s) of ridge formation.

Fifty-one ridge-rings have been identified so far in the region from 40°N to 40°S. They range from 10 to 70 km in diameter, and can be divided into several types based on morphology and associations.

One type consists of an incomplete ridge-ring that follows the trace of a crater rim which has been partially buried or destroyed (Fig. 1a). The remaining portions of the crater rims are either continuous or have been degraded into numerous distinct knobs or peaks. The eight examples of this type of ridge-ring seen on Mars are between 40 and 70 km in diameter. The ridges of these rings almost everywhere display the arch/ridge morphology described for lunar ridges by Strom (1972). In plan view, the ridge segments generally lie slightly outside a circle drawn through the remaining rim sections. As is true of all the ring types, the ridge-rings associated with crater rims are found in volcanic plains as well as undifferentiated plains units in cratered terrain.

Circular structures composed of both rim and ridge segments grade to ridge-rings interrupted by only scattered protruding peaks, to rings composed only of ridges. These features form the second major type of ridge-ring on Mars. Rings of ridges, either complete or segmented, range in diameter from 10 to 40 km. They are common in areas which have numerous other ridges, and often interrupt otherwise linear ridge systems (Fig. 1b). Morphologically, the ridges in ring structures usually consist of an arch portion with a crenulated ridge on top meandering from side to side of the arch. Sometimes the crenulated ridge on top is absent and the ring is formed by steep-sided arches.

A third ridge-ring type is an association of rounded and angular polygonal patterns (Fig. 1c). These rings are circular or subcircular in plan view with one or more flattened sides which parallel the trend of other polygonal ridge forms in the same area. This pattern occurs primarily in plains units of limited extent bounded by cratered terrain.

Analogs for most of the ridge-rings on Mars are present on the Moon (Fig. 2). Because of the morphologic similarity of ridges which form rings and other ridge systems, the same mechanisms have been proposed for both. Muehlberger (1974) ascribed ridges which are concentric to basin rims to the effect of drowned inner rings of the original basin structure; similarly, smaller ridge-rings in the lunar maria have been interpreted as pre-mare crater rims which have been draped by mare lavas (e.g. Fig. 2a). Maxwell et al. (1975) mapped several large (140 to 400 km diameter) circular ridge systems on Mare Serenitatis and related them to pre-mare

impact craters. As an alternative hypothesis, smaller scale ring structures have been interpreted to be post-mare extrusions of volcanic material along ring fractures. A combination of these two theories was put forward by Hodges (1973) who suggested that ridges are squeezeups of still-molten material through surface fractures localized by subsidence of a cooled mare crust over underlying topography such as a buried basin rim or crater.

The overlapping ridges in Mare Frigoris on the Moon (Fig. 2c) have been interpreted as individual "plates" thrusting against each other, the plates being cooled crust on the mare surface and driven by subsurface movement of still-molten lava, or overthrust due to subsidence of the mare surface (Schultz, 1976). The ridges in a lava plains unit on Mars (Scott, Morris and West, 1978) display a similar rounded polygonal pattern (Fig. 1c).

The interruption of numerous straight ridge segments by a ridge-ring (e.g. Figs. 1b and 2b) is strong evidence for the deflection of the trend of a compressionally formed ridge around a pre-mare or -plains crater. Muehlberger (1974) favors this mechanism not only for basin-scale concentric ridge systems, but also for the deflection of ridge trends around post-mare crater rims. If the fill is shallow enough, a small pre-mare crater could similarly affect the surface trend of a ridge. On a larger scale, if deflection of compressional ridges is the mechanism of formation, the many polygonal offsets of predominant global trends could be due to deflection of the ridges around other subsurface topographic irregularities. The mainly northwest and northeast trending ridges in the Hesperia Planitia region of Mars show such a pattern, including angular offsets in the main trends as well as circular and semi-circular ridge-rings. For Mars, this is the preferred mechanism of ridge-ring formation.

The other possible mechanism, draping by subsidence, or subsidence and extrusion through resulting fractures, is a possibility in the case of definite underlying topography with known form (i.e. a crater) but it is difficult to visualize this mechanism for areas with numerous long parallel ridges (e.g. Lunae Planum). The mechanism of deformation of compressional ridge trends for the origin of ridge-rings on Mars is also a possibility on Mercury where occurrence of similar-appearing rings in the Caloris smooth plains provides a suggestion of similar surface units and geologic processes occurring there.

#### REFERENCES

- Eppink, J.F. and Saunders, R.S., 1980, NASA TMX-81776; 66-67.  
Hodges, C.A., 1973, NASA SP-330, 31-12 to 31-21.  
Maxwell, T.A., El-Baz, F., and Wood, S., 1975, G.S.A. Bull., 86, 1273-1278.  
Phillips, R.J. and Lambeck, K., 1980, Rev. Geophys. Space Phys., 18, 27-76.  
Scott, D.H., Morris, E.L., and West, M.N., 1978, U.S.G.S. Map I-1111.  
Strom, R.G., 1972, The Moon, 47, 187-215.

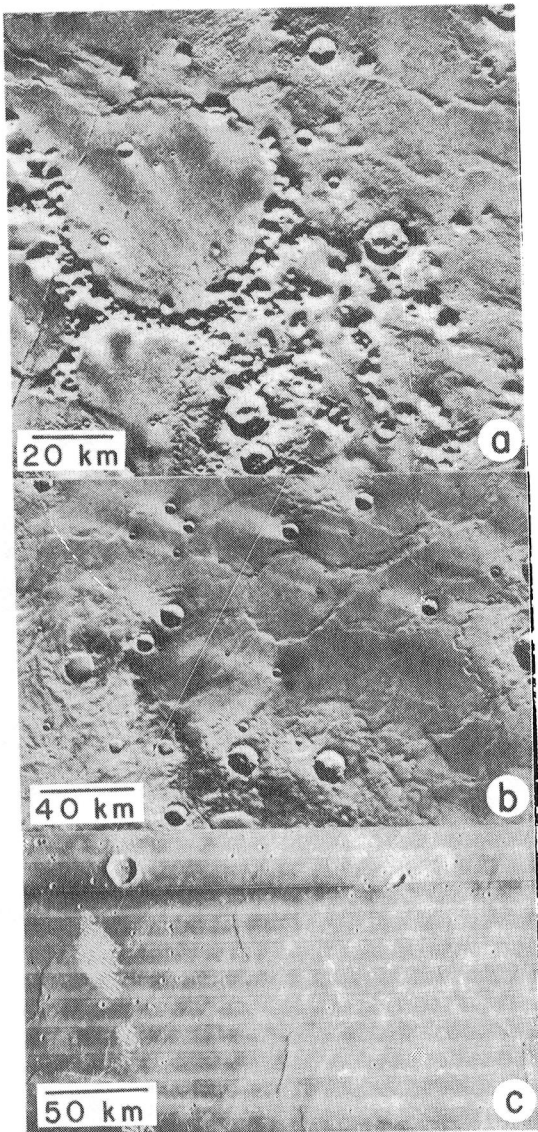


Figure 1(a) Ridge tracing partially absent crater rim in the Cerberus region of Mars; VO 545A50; (b) Ridge-ring interrupting straight ridge segments in Hesperia Planitia; VO 629A05; (c) Circular and polygonal ridge associations; VO 595A72,74.

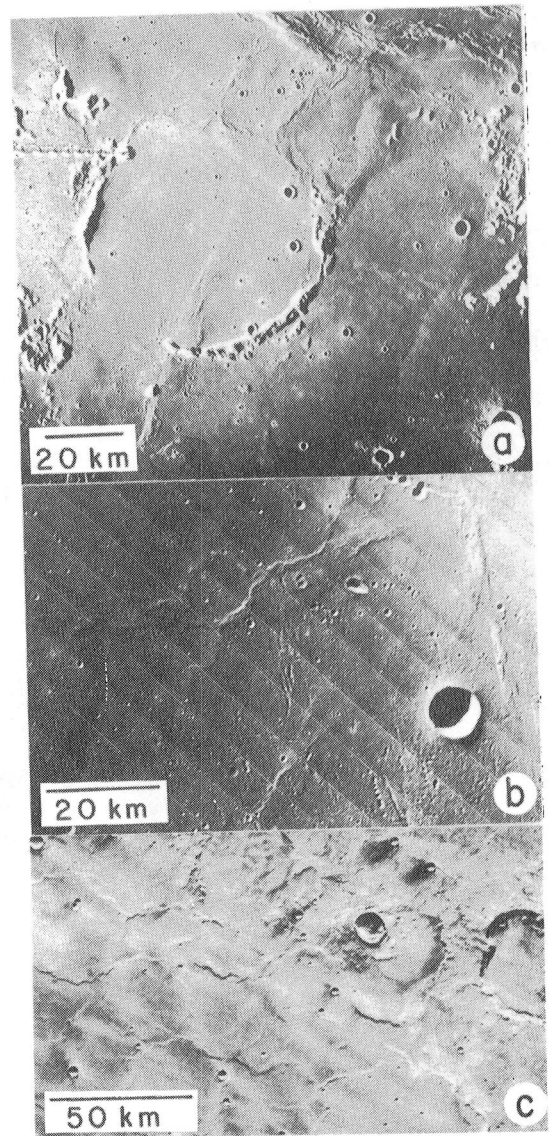


Figure 2(a) Ridge outlining crater rim in southern Oceanus Procellarum AS16-M-2838; (b) Ridge-ring in Mare Fecunditatis, LOI-32M; (c) Polygonal ridge pattern in Mare Frigoris, LOIV-191H3.

## TECTONIC IMPLICATIONS OF MARTIAN RIDGED PLAINS

R.S. Saunders and Therese E. Gregory, Jet Propulsion Laboratory, California Institute of Technology, Pasadena, CA 91103

The oldest wide-spread units on Mars other than the cratered terrains are the ridged plains. The ridges are morphologically similar to lunar mare ridges. They are typically tens to hundreds of km in length and a few hundred meters to ten km wide. Average spacings between ridges in various localities vary between about 15 km and 50 km. Two types of ridge patterns occur, parallel and reticulate. The reticulate patterns are irregular producing a random grid arrangement.

The regions having parallel ridges are nearest to Tharsis. These ridges are remarkably consistent with compressional stresses arising from the load associated with the central Tharsis region (Phillips and Lambeck, 1980) and thus, may be interpreted to be related to the long-term viscous response of crustal rocks to the Tharsis load.

Under this hypothesis, it is appropriate to consider the mean ridge spacing as a dominate wavelength of folding. The theory of folding of viscoelastic media (Biot, 1961) suggests that the ratio of this wavelength ( $L_d$ ) to the thickness of the layer ( $h$ ) is related to the ratio of the viscosity of the layer ( $\eta$ ) and underlying medium ( $\eta_1$ ) by:

$$\frac{L_d}{h} = 2\pi \sqrt[3]{\frac{\eta}{3\eta_1}}.$$

Thus, we need also to estimate the thickness of the plains. This is done using methods developed by DeHon (see for example DeHon, 1979) which involves a relationship between crater rim heights and diameters. The derived parameters are given in Table 1.

The interesting finding is that the ratio of ridge spacing to plains thickness is approximately constant ( $\sim 30$ ) over a range of spacings and widely separated plains units. This implies a viscosity ratio, plains to substrate, of about 500. This finding tends to confirm the hypothesis that ridge spacing is related to dominant wavelengths of folding of the surface materials in response to a load centered at Tharsis. Although the present stresses are low, they may represent a relic of some larger initial stress. Also, folding can occur at very low stresses in a viscous medium.

The observation that the substrate is several orders of magnitude less viscous than the surface may be explained by a variation in temperature or mechanical properties. The plains are underlain by cratered terrain which may best be characterized as megaregolith. The effective viscosity of this largely unconsolidated material may be much less than the plains if the plains are, in fact, extrusive volcanic materials.

In conclusion, there appears to exist a simple linear relationship between the thickness of the ridged plains and mean ridge spacings. This is readily explained in terms of viscoelastic response to the observed compressive stresses associated with Tharsis. The ridged plains and the megaregolith substrate appear to have similar properties over the planet.

# REFERENCES:

- Biot, M.A., 1961, Theory of folding of stratified viscoelastic media and its implications in tectonics and orogenesis: Bull. G.S.A., v. 72, p. 1595-1620.
- De Hon, Rene A., Thickness of the western mare basalts: Proc. Lunar Planet. Sci. Conf. 10th (1979), p. 2935-2955.
- Phillips, R.J. and Lambeck, K., 1980, Gravity fields of the Terrestrial Planet: Long-wavelength anomalies and tectonics: Rev. Geophys. and Space Phys., v. 18, p. 27-76.

TABLE 1 Ridge Spacing and Thickness of Ridged Plains

<u>REGION</u>	<u>THICKNESS, KM (h)</u>	<u>SPACING, KM (L)</u>	<u>L/h</u>	<u>TYPE</u>
Amazonis Planitia	.950	40 ± 20	42	Parallel
W. Lunae Planum	1.500	50 ± 20	33	Parallel
E. Lunae Planum				
& E. Chryse Planitia	1.050	30 ± 15	29	Parallel
W. Solis Planum	1.500	50 ± 15	33	Parallel
E. Solis Planum	.800	20 ± 10	25	Reticulate
Hesperia Planum				
& Syrtis Major Planitia	.866	25 ± 15	29	Reticulate
Noachis-Hellas	.600	15 ± 10	25	Reticulate

## MARTIAN VALLEY ORIENTATIONS AND REGIONAL STRUCTURAL CONTROLS

Marilyn Ginberg, Dept. of Geology, Franklin and Marshall College, Lancaster, PA 17604 and David Pieri, Jet Propulsion Laboratory, Pasadena, CA 91103

Processes ranging from rainfall to basal sapping to surface runoff from seepage zones (Sharp and Malin, 1975) have been proposed to explain the origins of martian valley networks (Milton, 1973; Sharp and Malin, 1975; Pieri, 1976, 1980). Such formational processes, involve the movement of groundwater or surface water which would presumably be facilitated and directed by the existence of zones of structural weakness associated with faults or joints. Strong positive correlations between network orientation and regional joint patterns have been demonstrated for canyons in the Colorado Plateau (Laity, 1980) which are analogous to martian valleys in morphology and perhaps in certain aspects of their origin (i.e. basal sapping) (Baker, 1980; Pieri, 1979; Pieri *et al.*, 1980). Thus, models for valley formation which invoke a lithospheric source (e.g. sapping/seepage) imply that the subsurface control of valley orientation should be strong (Sharp and Malin, 1975; Pieri, 1980).

In an effort to determine whether any correlation exists between valley orientation and structural landforms (e.g. grabens, scarps, mare ridges, lineaments), the orientations and lengths of these features were compared to the orientations and lengths of link segments comprising nearby valley networks (Figure 1). Three regions on Mars were selected on the basis of terrain type: (1) Margaritifer Sinus in the neighborhood of Nirgal Vallis representing Lunae Planum age cratered plains (Figure 1c and b); (2) Sinus Sabaeus near Flaugergues crater representing older heavily cratered terrain (Figure 1e and f); and (3) Sinus Sabaeus proper which is a composite of older heavily cratered terrain and younger intercrater plains (Figure 1e and d). Figure 1 (a through f) is a series of rose diagrams comparing the orientation and lengths of mapped structural features (Figure 1a, c, e) to nearby valley lengths and orientations (Figure 1b, d, f).

Figure 1a clearly displays the strong E-W trend of the numerous graben which exist between Nirgal Vallis and Valles Marineris. A corresponding trend is clear in Figure 1b and is due primarily to the orientation of Nirgal Vallis, generally parallel to the graben system. Also visible is a strong NE-SW structural trend with which there is little correspondence in valley orientation. This lobe corresponds to mare ridges which may be younger than nearby valleys. There is a major N-S trend in valley orientations, with no structural counterpart associated with Ladon Vallis which is quite old as evidenced by clearly superimposed large impact craters.

The heavily cratered terrain of Sinus Sabaeus (1e and f) shows two prominent trends (N 20° - 30° W and N 30° - 40° E) which appear in both valley and structural orientations. Old and perhaps exhumed valleys showing good directional correlation with structural topographic elements may argue for persistent, stable or ancient structural controls.

The region near Flaugergues crater (Figure 1c and d) composed of both cratered terrain and intercrater plains shows two major trends in structure orientation (N 20° - 40° W and N 20° - 40° E) but with only the former expressed in valley orientation. The NE-SW structural trend corresponds to mare ridges in intercrater plains, younger than the subjacent heavily cratered terrain in which the valleys are expressed.

Correlations exist in these data between the trends of structural features and valley orientation, however, in several cases structural elements postdate valley formation and show no correlation with valley orientations. It is felt that sun orientation while probably having a small effect does not

bias the data strongly, particularly since about one-third of the data show clear east-west trends.

While this study is preliminary and of limited scope, it shows the coincidence between the regional orientations of structures such as grabens, scarps, structural lineaments, and mare ridges and valley networks. Further detailed work which addresses the local geological interaction between mare ridges and tributary canyons of Nirgal Vallis is underway. Preliminary geologic and geomorphologic sketch maps have been produced from high resolution ( $\sim 40$  meter per line pair) Viking images, which show the direction of tributary development to be correlated with the presence of mare ridges intersecting the valley at high angles. We conclude that on both regional and local scales subsurface structure has a strong influence on the orientations of neighboring valley networks. This observation is consistent with and suggestive of valley formation by groundwater flow by either seepage or sapping mechanisms.

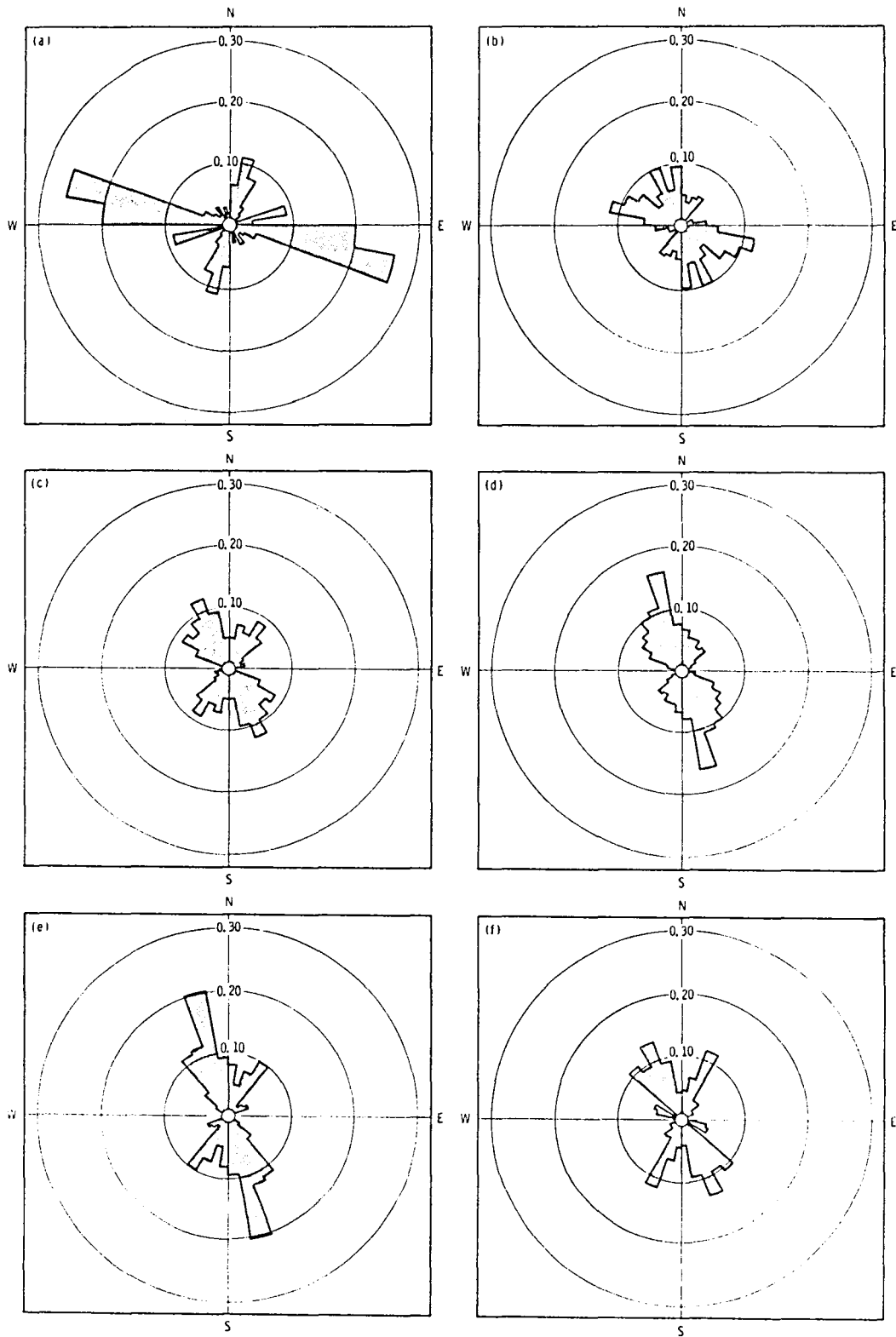
#### Caption, Figure 1

Shown here are the orientations of valley link segments (b,d,f) as compared to the orientations of structural landscape elements (e.g. scarps, grabens, troughs, lineaments) (a,c,e). Locations are defined in the text.

#### BIBLIOGRAPHY

- Baker, V.R., 1980, Some terrestrial analogs to dry valley systems on Mars, p. 286-288 in Report of Planetary Geology Program 1979-1980, P. Wirth, R. Greeley, and R.D'Alli eds. NASA TM-81776, NASA, Wash. D.C., 421 pgs.
- Laity, J.E., 1980, Sapping processes in martian and terrestrial valleys, EOS, 61, p. 286.
- Milton, D.J., 1973, Water and processes of degradation in the martian landscape: Jour. Geophys. Research, 78, pp. 4037-4049.
- Pieri, D., 1976, Distribution of small channels on the martian surface: Icarus, 27, pp. 25-50.
- Pieri, D.C., 1979, Geomorphology of martian valleys, Ph.D. Thesis, Cornell University, Ithaca, N.Y., 280 pgs.
- Pieri, D.C., 1980, Martian valleys: Morphology, distribution, age, and origin, in press, Science.
- Pieri, D.C., M.C. Malin, and J.E. Laity, 1980, Sapping: Network structure in terrestrial and martian valleys, Repts. of Plan. Geol. Prog., 1979-1980, NASA TM-81776, p. 292.
- Sharp, R.P. and M.C. Malin, 1975, Channels on Mars, GSA Bull., 86, p. 593-609.





TECTONIC HEREDITY OF FRACTURE SYSTEMS: A NEW METHOD OF TESTING BY  
CORRELATION OF DOMAIN BOUNDARIES

T. McCrory and D. Wise, University of Massachusetts, Amherst, Mass. 01003

In analysis of the fracture system of planetary crusts, a recurring problem is evaluation of the effect of older fracture anisotropy of basement in controlling the fracture patterns in the overlying rocks. Suggestions of the activity of this tectonic heredity mechanism have been made for a number of terrestrial areas (Hodgson, 1965, for the Grand Canyon; Wise, 1964, for the Northern Rockies) but the methodology of proving or disproving the similarity of two fracture patterns is highly subjective. The inability to test this heredity relationship on most earthbound examples leaves considerable room for doubt on extra-terrestrial extrapolations.

Most previous tests of tectonic heredity have relied on comparing patterns of joint azimuths plotted on equal area nets for stations above and below a basement unconformity. For example, this method was used by McGill (1980) to show that more detailed joint sampling suggests non-correlation of Precambrian versus Cambrian joints in the same area of the Grand Canyon that Hodgson measured to suggest that correlation existed. The difference in interpretation reflects a basic enigma of structural geology: when correlating stations with multiple joint or fracture sets, there is no statistically rigorous test known to place confidence limits on the degree of correlation between two stations.

This paper represents the application of a new method of attacking the problem, a method developed by Wise (unpublished studies of fracturing in eastern Kentucky, 1977) in trying to map the limits of fracture domains. Instead of plotting measurements for specific stations, the data are plotted as diagrams of azimuth versus distance along traverse (Fig. 1). The approach recognizes the existence of several discrete fracture domains in an area and attempts to locate the boundaries of these domains by continuous plotting of the azimuths of fractures along a linear traverse. When parallel traverses are run in basement and in cover rocks, the locations of domain boundaries can be mapped in both stratigraphic units. Simple upward propagation of fracture sets should produce a coincidence of domain boundaries in basement and cover. Non-coincidence of domain boundaries would be evidence against the tectonic heredity influence.

The technique was tested in the Dead Indian Region of northwest Wyoming, about 40 km north of Cody, Wyoming. The area, part of the Bear-tooth Uplift, has excellent exposure of basement and overlying Cambrian Flathead Quartzite. The basement fracture systems in the area have been suggested as models for tectonic hereditary controls (Spencer, 1959; Wise, 1964) but fracture relationships in the overlying quartzite are less certain. A general study of fracture and lineament mechanisms and origins in the area was initiated by the senior author in an attempt to test some of these hypotheses. Fig. 1 and 2 show a small but representative part of the total study. The Cambrian beds are almost horizontal and the joints are near-vertical, permitting their representation by azimuth alone.

Locations along the traverses marking change in character of one or more of the joint sets are indicated by letters on both figures.

The figures show that some of the Laramide faults represent domain boundaries for some joint sets. The plots also indicate a generally higher variability of joint orientation in the Precambrian than the Cambrian. In addition, some joint sets correlate whereas others do not. For example, east-west joint sets are common in the A to D portion of the traverse but are absent or nearly absent in the Precambrian. The pattern from E to F seems to have no counterpart in the adjacent Precambrian. The data argue that either there is no hereditary influence of the Cambrian joints or if present, it is much more complicated than predicted by simple upward propagation.

The method has virtues other than defining or mapping fracture domain boundaries. It permits sampling of relatively pure domains rather than random station sampling which may or may not mix several domains or unwittingly include the disturbance by a fault zone. For example, the zone of no outcrop between M and N may well project to F to create the discontinuity in joint pattern on either side of F. Thus, by obtaining a purer signal the method aids correlation between adjacent areas. It also helps throw some light on the origins of the double maxima which plague many joint studies. For example, Muehberger (1961) proposed a very difficult mechanism of jointing by shear in the near surface environment to explain joint sets of very low dihedral angle. An alternative is an oscillation in strike of a given joint set. Hints of the oscillation appear on either side of the Nazimuth between stations B and D. The effect of random sampling across these oscillations could be the production of a double maximum. In other traverse lines, the oscillations are even more prominent and may include sympathetic oscillation of an orthogonal fracture set.

The method probably has broader application to large scale planetary features. By plotting fracture trends along a series of regional traverses, domain boundaries of the various crustal fracture sets may be determined by inspection and the extent of a domain mapped. Thus, the problem of planetary lineament correlation can be partially moved from the unsatisfactory realm of multiple peak correlation on azimuth frequency histograms to a more tractable problem of correlation of mapped fracture domains with the domains of other mapped geologic elements.

- Hodgson, R.A., 1965, Am. Assoc. Petrol. Geol. Bull., 49, 935-949.  
McGill, G.E., 1980, NASA TM 81776, 80-82.  
Spencer, E.W., 1959, Geol. Soc. Am. Bull., 70, 467-508.  
Wise, D.U., 1964, Geol. Soc. Am. Bull., 75, 287-306.  
Muehberger, W.R., 1961, Jour. Geol., 69, 211-219.

Figure 1: Plot of vertical joint azimuths along two parallel traverses. The traverses are plotted with the northwest end at the top of the page. Letters refer to locations in Figure 2.

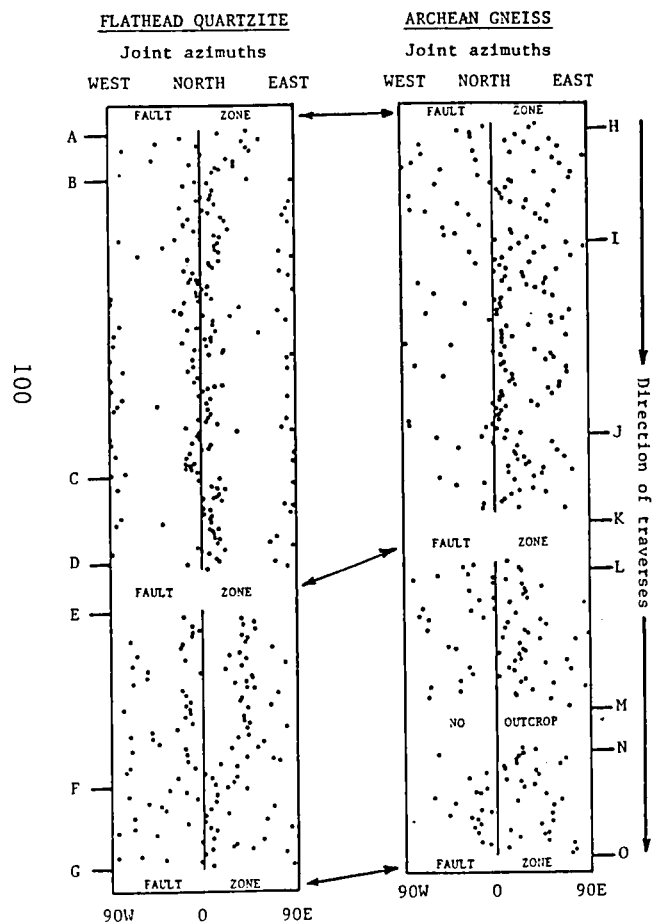
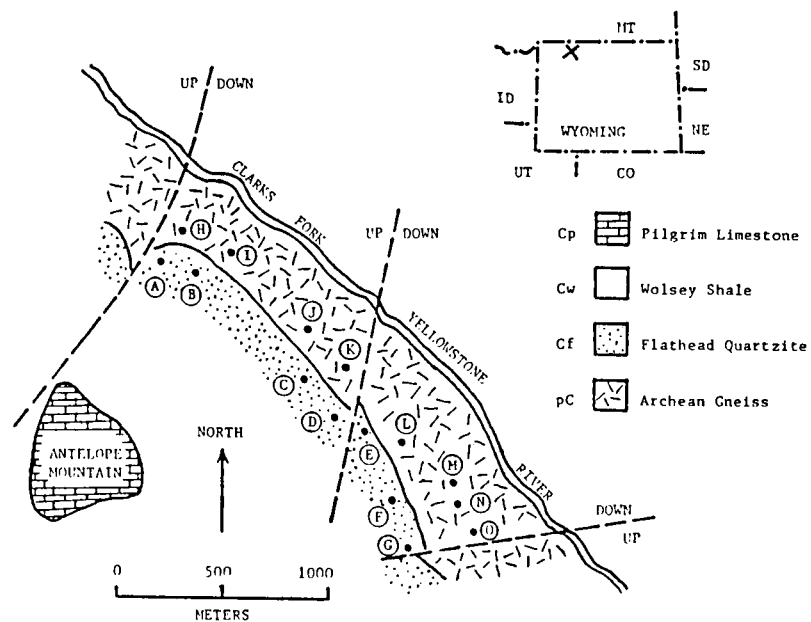


Figure 2: Location of traverses plotted in Figure 1. The location is at 44°48'N, 109°26'W, 4.5 kilometers north of Sunlight Picnic Ground in the Deep Lake Quadrangle, Wyoming.



## MOTTLED PLAINS OF MARS: A REVIEW

Underwood, James R., Jr., and Nanci E. Witbeck, Department of Geology, Kansas State University, Manhattan, KS 66506

One of the unexpected characteristics of Mars revealed by the Mariner 9 mission was the existence in the northern hemisphere of a vast area of relatively smooth plains. The striking dichotomy of the planet, heavily cratered terrain largely in the southern hemisphere and smooth plains mostly in the northern hemisphere, remains one of its most distinctive and least understood features (Malin et al., 1978).

The mottled plains lie south of the north polar plains and north of the smooth plains, in a belt that almost encircles the northern hemisphere mostly between latitudes  $50^{\circ}$  N and  $70^{\circ}$  N. Images of the mottled plains obtained by Mariner 9 were of poor quality because of dust in the atmosphere and because of the high sun angle at which most of the images were recorded. On the 1:25,000,000 geologic map of Mars, Scott and Carr (1978) show mottled plains material as far south as  $30^{\circ}$  N and as far north as  $74^{\circ}$  N latitude. The hiatus in the circumpolar belt of mottled plains material lies between about  $80^{\circ}$  W and  $140^{\circ}$  W longitude where younger smooth and cratered plains material may overlie it. The southern margin of the mottled plains material is parallel or subparallel to the north-facing escarpment of the highlands to the south, except between  $180^{\circ}$  W and  $270^{\circ}$  W longitude. The mottled plains lie in a topographically low circumpolar belt. In the north-central part of the Casius quadrangle, the mottled plains rise to the elevation of the Mars datum; in the northernmost part of Mare Acidalius quadrangle, however, they drop well below the -3 km contour.

Scott and Carr (1978) described the mottled appearance as the result of: "High albedo in and around craters contrasting sharply with dark plains..." They interpreted the mottled plains material to be "cratered lava plains." Although the boundaries of the mottled plains material are recognized by the sharp albedo contrast with adjacent material, thus far the albedo boundary has not been identified, in any significant number of places, to coincide with a topographic feature (Batson et al., 1979).

Members of the mapping teams preparing geologic maps for the Atlas of Mars struggled with the poor quality and with the relative scarcity of images of the mottled plains. For the most part they could only draw the most tentative conclusions about the characteristics of that material. The descriptions and interpretations of the mappers are summarized in Table 1.

Viking orbiter images of the mottled plains are not very numerous or of as high resolution as the region requires for detailed study. Nevertheless, in places Viking images permit the subdivision of the mottled plains into hilly and knobby terrain, fractured terrain, channelled terrain, and so on. Thus far it has not been possible to subdivide

the mottled plains into stratigraphic units that can be traced laterally a significant distance or into units that can be correlated unequivocally with each other or with adjacent stratigraphic units.

Scott (1979) has made the interesting suggestion that the mottled plains may represent lower, deeply eroded remnants of the highlands to the south, remnants ".... that have survived an episode of crustal separation and volcanism, with flood basalts filling the intervening region and forming the smoother plains between the segregated parts." Alternatively, they may represent a very complex history of several episodes of emplacement and erosion of materials.

#### References:

- Batson, R.M., Bridges, P.M., and Inge, J.L., 1979, Atlas of Mars; the 1:5,000,000 series; NASA SP-438, 146 p.
- Elston, W.E., 1979, Geologic map of the Cebrenia quadrangle of Mars: U.S. Geol. Survey Misc. Inv. Map I-1140.
- Greeley, R. and Guest, J.E., 1978, Geologic map of the Casius quadrangle of Mars: U.S. Geol. Survey Misc. Inv. Map I-1038.
- Lucchitta, B.K., 1978, Geologic map of the Ismenius Lacus quadrangle of Mars: U.S. Geol. Survey Misc. Inv. Map I-1065.
- Malin, M.C., Phillips, R.J., Saunders, R.S., 1978, The nature and origin of the Martian planetary dichotomy (is still a problem); NASA Tech. Memo. 79729, p. 83-85.
- Morris, E.C. and Howard, K.A., 1980, Geologic map of the Diacria quadrangle of Mars: U.S. Geol. Survey Misc. Inv. Map (in press).
- Scott, D.H., 1979, Geologic problems in the northern plains of Mars: Proc. Lunar Sci. Conf. 10th, p. 3039-3054.
- Scott, D.H. and Carr, M.H., 1978, Geologic map of Mars, U.S. Geol. Survey Misc. Inv. Series Map I-1083, 1:25,000,000.
- Underwood, J.R., Jr., and Trask, N.J., 1978, Geologic map of the Mare Acidaliu quadrangle of Mars (including the potential Viking landing site Cydonia): U.S. Geol. Survey Misc. Inv. Map I-1048.
- Wise, D.U., 1979, Geologic map of the Arcadia quadrangle of Mars: U.S. Geol. Survey Misc. Inv. Map I-1154.

	Diacria (MC-2)	Arcadia (MC-3)	Mare Acidalium (MC-4)
Descrip.	High-albedo mat'l in and around craters; contrasts w/darker plains mat'l; broad areas of hummocks and knobs; many pedestal craters; crater interiors mostly filled w/high-albedo mat'l; moderate to heavily cratered; small crater (<10 km) population low.	Low albedo; moderate density of 10-km craters; pedestal craters and wind streaks common.	Flat to gently rolling terrain; distinctive circular high-albedo zones surrounding numerous craters 1-10 km diameter; pedestal craters common; many filled or partly filled w/bright mat'l; SE-trending high-albedo wind plumes emanate from numerous craters to NW; distinct NW-SE erosional grain visible on high-resolution images; exhumed terrain well shown in some B frames.
Interp.	Highly eroded lava plains w/eolian covering.	Volatile-rich, high-latitude deposit overlying high-albedo plains mat'l; surficial eolian deposits cause much of streaking; removal of volatiles (water or CO <sub>2</sub> ice) caused active retreat of S and W margins; surface removal of volat'ls except where protected by crater aprons, produced pedestal craters.	Plains lowered by wind erosion, creating pedestal craters and exhuming ancient terrain; windblown mat'l fills or partly fills many craters; interaction of probably thin, shifting eolian mantle and ejecta blankets produces mottled appearance; NW-SE erosional grain produced by prevailing NW wind.
	Ismenius Lacus (MC-5)	Casius (MC-6)	Cebrenia (MC-7)
Descrip.	Shows irregular blotches and mottling of contrasting albedo through obscuring haze, and faint light circular areas; c <sub>3</sub> craters superposed.	Plains of moderate relief; high-resolution images show surface of closely spaced small hills or a reticulate albedo pattern; moderately cratered; linear structure trending N-S; albedo highly varied giving mottled appearance.	Forms circumpolar plains of Mars; highly varied albedo and surface of low relief; craters sparse but w/conspicuous rim deposits.
Interp.	May include several units not recognized because of obscuring haze; faint circles probably old eroded craters; probably similar to plains mat'l, but w/ lower albedo.	Origin and lithology unknown; may be eolian, but region covered w/north-polar winter frost; surface texture may be produced by frost heaving or other frost phenomena.	Sedimentary mat'l that loses cohesion on impact; possibly eolian deposits cemented by permafrost; c <sub>3</sub> craters superposed.

Table 1. Summary of descriptions and interpretations of mottled plains material based on Mariner 9 images. From Elston (1979), Greeley and Guest (1979), Lucchitta (1978), Morris and Howard (1981), Underwood and Trask (1978), and Wise (1979).

MARS STRATIGRAPHY: LOWLAND PLAINS AND VALLES MARINERIS, David H. Scott and Kenneth L. Tanaka, U.S. Geological Survey, Flagstaff, AZ 86001.

Geologic studies using high-resolution Viking Orbiter images show that alluvial processes in the northern plains of Mars are of greater areal extent and significance than had been previously considered. Three areas have been examined where the Viking pictures clearly reveal erosional patterns that result from running water. 1) Deuteronilus Mensae - The fretted terrain (1) in this area consists of dissected plateaus and mesas thought to be formed by melting or evaporation of permafrost. New mapping confirms previous units (2) and indicates that fluvial action has been an important process in the development of the terrain. Shallow tributary channels feed into larger channels and rimless craters, which interconnect and lead to the low-lying northern plains. High-resolution images of channels show scour structures, stream terraces, and braided patterns. Channeling appears to have occurred early in martian history during a long period when surface water removed a considerable volume of plateau material. After water ceased to flow, most channels continued to expand in width by slump of the channel escarpments. Resistant layers in the plateau material capped mesas developed in the outlying terrain and also long, continuous escarpments morphologically analogous to the Mogollon Rim on the south border of the Colorado Plateau. 2) Chryse Planitia - Alluvial channels and their floodplains within the Chryse drainage basin extend farther outward into Acidalia Planitia than previously mapped (3,4). Figure 1 shows the possible extent of these river systems, which suggests that drainage within the highland block encompassing Tempe Fossae may have connected with the outward floodplain of Kasei Vallis. 3) Orcas Patera - Plains immediately east of this large elongate crater show good evidence of erosion by water. The margins of a probable flow channel can be traced from about lat 10° N. to 22° N., where they appear to terminate in Amazonis Planitia. The source of the water has not been determined, but the floodplain is more than 100 km across in places, suggesting contributions from multiple sources over a large area.

Stratigraphic studies within Hebes Chasma (5) have been extended into Ophir, Candor, and Melas Chasmata -- the central and major canyon systems of Valles Marineris. Some of the layers exposed in the canyon wall have distinctive colors, thicknesses, and weathering patterns. These properties, together with similar arrangements in different locations, permit their correlation from place to place.

In conjunction with the geologic mapping of Valles Marineris, preliminary studies were made of gravity profiles across some of the canyons. Although Valles Marineris lies in a gravity low (6), some anomalies associated with individual chasmata are quite small. Also, the low points on the gravity profiles are offset several hundred kilometers to the north of the center lines of the major chasmata and are closer to the smaller, more recently formed canyons. Two profiles across Ius and Tithonium Chasmata show departures of about -5 milligals



from regional slopes, compared with a calculated (theoretical) anomaly value of more than -25 milligals for the larger chasma (Ius) alone. Low points on the profiles lie slightly north of Tithonium Chasma. The three largest chasmata (Melas, Candor, and Ophir) show a combined negative anomaly of about -30 milligals compared to a calculated value of about -65 milligals. A density of  $3.0 \text{ g cm}^{-3}$  was used in these estimations; this figure may be somewhat high for a bulk density of a thick series of stratified rocks, even though volcanic, if weathered layers occur between depositional units. However, a decrease in density to the unlikely figure of  $2.0 \text{ g cm}^{-3}$  is insufficient to account for the discrepancy between observed and theoretical values for these structures. It is also doubtful that a better correspondence would result using improved topographic models of the canyons.

Conceivably, then, these results indicate that some of the larger canyons are partly compensated and that the low points on the gravity profiles more nearly reflect the smaller and less compensated canyons.

#### REFERENCES

- (1) Sharp, R. P., 1973, Mars: Fretted and chaotic terrains: J. Geophys. Res., 78, 4073-4083.
- (2) Lucchitta, B. K., 1978, Geologic map of the Ismenius Lacus quadrangle of Mars: U.S. Geol. Survey Misc. Geol. Inv. Map I-1065.
- (3) Greeley, R., Theilis, E., Guest, J. E., Carr, M. H., Masursky, H., and Cutts, J. A., 1977, Geology of Chryse Planitia: J. Geophys. Res., 82, 4093-4109.
- (4) Scott, D. H., and Carr, M. H., 1978, Geologic map of Mars: U.S. Geol. Survey Misc. Geol. Inv. Map I-1083.
- (5) Peterson, C., 1980, Hebes Chasma - a martian pyroclastic sink (abs.), in Proceedings Lunar and Planetary Science XII (in preparation).
- (6) Sjogren, W. L., 1979, Mars gravity: High-resolution results from Viking Orbiter 2: Science, 203, 1006-1010.



Figure 1. Alluvial channel and floodplain systems of Chryse drainage basin.

## A POSSIBLE ORIGIN OF THE RIDGED PLAINS OF MARS

Fernandez-Chicarro, A., Masson, Ph., Laboratoire de Géologie Dynamique Interne (ERA n° 804-02), Université Paris-Sud, 91 405 Orsay, France.

Due to the existence of extensional stress field previously analyzed in the Valles Marineris region of Mars (Masson, 1980) we aimed to bring some evidence of subsequent compressional features. The only structures which seem to be compatible with such tectonic regime, are the prominent linear features observed in the relatively smooth plains and called "ridges" due to their similarity to the Lunar Maria Ridges. Some detailed studies were conducted in the Coprates quadrangle of Mars, Southward of Valles Marineris.

The observed ridges show the following physiographic characteristics :

- . a length sometimes longer than 100 km for a single continuous element, and up to 5 km wide ;
- . an asymmetrical shape generally continuous and sinuous ;
- . a location restricted to the relatively smooth plains regarded as mare-like filling covered by regolith ;
- . at a large scale, the ridges tend to be parallelly oriented toward the NNE, but locally separate lobes show arborescent patterns ;
- . from the age dating point of view, the ridges are relatively old compared to the surrounding geologic features (old craters, extensional features), but younger than the rigid and fractured nuclei. A nucleus may be defined as an old fractured outcrop which escaped burial by the ridged volcanic plains because of its higher elevation (fig. 1) ;
- . the ridges are faulted and shifted and they seem to be often localized along preexisting fractures ;
- . they are mainly oriented perpendicularly to more recent extensional major structure, e.g. Valles Marineris ;
- . the ridges do not seem to disturb or to distort the older and rigid nuclei ; but on the contrary they show some changements in their NNE original orientation, and they seem to surround these nuclei. In some places, the large NNE pattern is disturbed by crossing ridges of apparently same age ;
- . all the ridges seem to be equally weathered and eroded.

According to these observations a chronology of the local geologic events is proposed. The nuclei considered as the remnants of the oldest geologic unit in this area, are surrounded by volcanic materials which filled the smooth plains where the ridges are now observed. In the southern-central part of Coprates quadrangle, a quasi continuous area of old material shows a semi-circular shaped feature. This feature seems to belong to the eastern and

southern rims of an old crater (500 km in diameter) buried later by volcanic materials, i.e. the ridged plains. Latterly structures related to extensional tectonics (grabens, en échelon faults, cracks) appeared while the meteoritic bombardment and the erosional processes continued.

The comparison of the ridged plains on Mars with the Maria ridges on the Moon and the Caloris ridges on Mercury, shows only their morphologic similarities. The martian ridges appear to be much bigger than the lunar ridges and they seem to follow a directional pattern. The ridges on the Moon and Mercury are restricted to the large basins filled with volcanic materials. On Mars, where a larger variety of volcanic phenomena took place, one can notice that the ridges are not only restricted to the volcanic filling of the interiors of large impact craters and basins (as seen for instance in Huygens or in Schiaparelli), but that they are also associated to volcanic calderas like in the South of Hellas Planitia.

Therefore it seems undoubtedly that the material of the Coprates ridged plains has a volcanic origin which could be :

- . primitive lava flows coming from the Tharsis area, or
- . volcanic fillings coming up to the surface through crustal fractures (possibly subsequent to a huge impact).

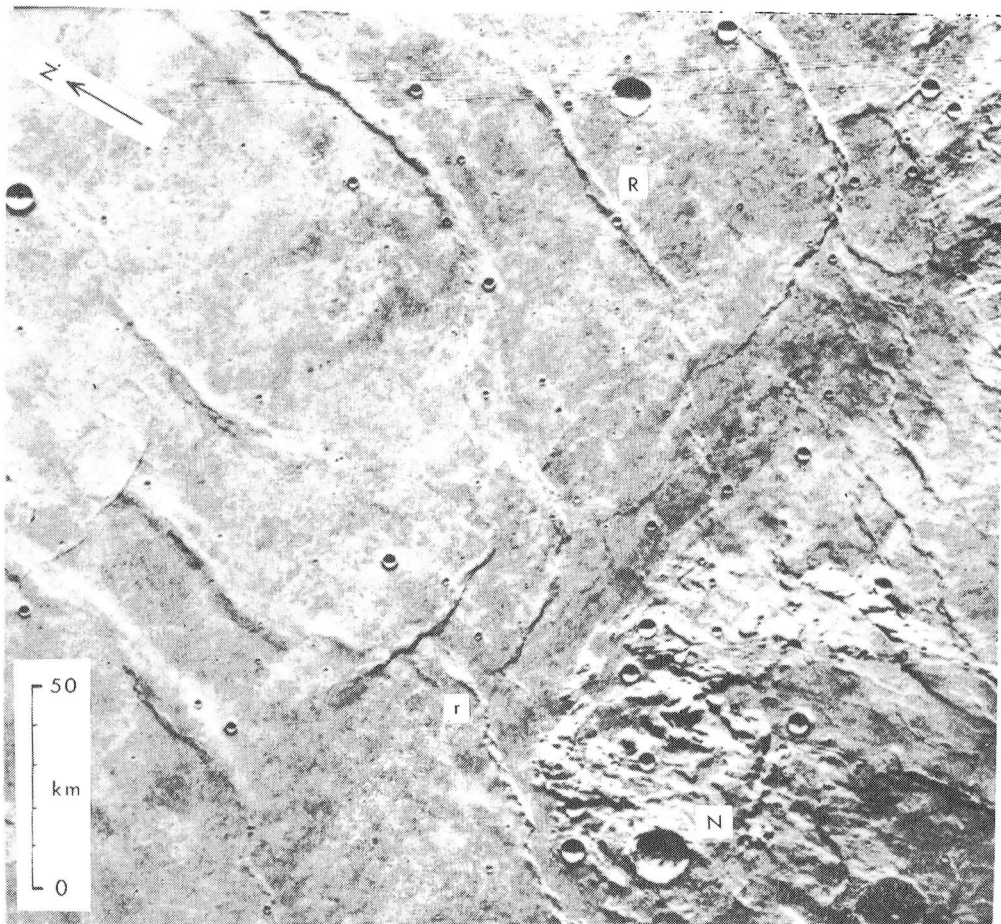
What appears to be a structural pattern of parallel ridges oriented NNE could be interpreted as the result of an E-W compressional movement. This movement could be due to an early updoming phase of the Tharsis bulge. The specific location of the ridges (especially around the nuclei) could be considered as the consequence of the volcanic material relative plasticity compared to the relative rigidity of the remnants of the old geologic materials (nuclei).

In conclusion, the ridges on Mars are always observed in the volcanic terrains. In the Coprates quadrangle where they were analyzed, these ridges could be the consequence of a compressional stress field.

### References

- Guest, J. E., Greeley, R. (1977) - Geology of the Moon. Wykeham Publications
- Mc Cauley, J. F. (1978) - Geologic map of the Coprates quadrangle of Mars, U. S. Geol. Survey Misc. Geol. Inv. Map I-896
- Masson, Ph. (1980) - Contribution to the structural interpretation of the Valles Marineris-Noctis Labyrinthus-Claritas Fossae regions of Mars. The Moon and the Planets 22, p. 211-219
- Scott, D. M., Carr, M. H. (1978) - Geologic map of Mars. U. S. Geol. Survey Misc. Geol. Inv., Map I - 1083
- Wells, R. A. (1979) - Geophysics of Mars. Elsevier.

Fig. 1 - This picture shows the general NNE/SSW trending pattern of Coprates Ridges (R). In the lower right of the picture the ridges (r) surround a nucleus (N). This nucleus shows old structural ENE and WNW directions. The difference of material plasticity between the ridged plains and the nucleus is shown by the change-ment of the ridge directions in the vicinity of the nucleus (Viking Orbiter I, frame n° 608 A 24).





Chapter 3  
CRATERING PROCESSES AND LANDFORM DEVELOPMENT





## IMPACT BASINS: IMPLICATIONS FOR FORMATION FROM EXPERIMENTS

R. Greeley, J. Fink, Center for Meteorite Studies, Arizona State University, Tempe, AZ 85281 and D. E. Gault, Murphys Center of Planetology, Murphys, CA 95247

Impact basins appear to occur on all the terrestrial planets and on some of the Galilean satellites. In some planets, such as the Moon, basins constitute the major structural elements of the surface. Yet, despite their widespread occurrence, obvious importance, and study for more than two decades, a great many questions about basins remain unanswered, particularly in regard to the details of their formation and various structural relationships. Of particular interest are basin-forming impacts into relatively thin lithospheres overlying viscous mantle or core materials, comparable to interiors proposed for icy satellites and the early Moon. To simulate qualitatively such conditions in the laboratory, a series of impact experiments was carried out at the NASA-Ames Vertical Gun Facility involving a thin layer of either bonded or unbonded particles (simulated elastic lithosphere) overlying a substrate of viscous material (simulated mantle/core). Variables in the experiments were: 1) *thickness* of the "lithosphere" (0.6, 1.2, and 1.9 cm); 2) *strength* of the "lithosphere" ( $6.2 \times 10^5$  to  $3.6 \times 10^6 \text{ N m}^{-2}$ ); 3) subsurface material plastic *viscosity* ( $125$  to  $275 \text{ N} \cdot \text{s m}^{-2}$ ) and *yield strength* ( $5$  to  $10 \text{ N m}^{-2}$ ); and 4) impact *energy* (90 to 560 joules).

Impacts into models involving weakly bonded particles (simulated lithosphere) underlain by viscous material yielded the following sequence and relationships: 1) upon initial impact, the surface material was severely fragmented, forming an ejecta plume of disaggregated material; 2) as the transient cavity enlarged, the ejecta consisted of larger pieces of the upper layer plus clots derived from the viscous substrate; the angle of the ejecta plume became steeper as more of the viscous material was excavated. Because the ejecta trajectory was relatively steep, most of

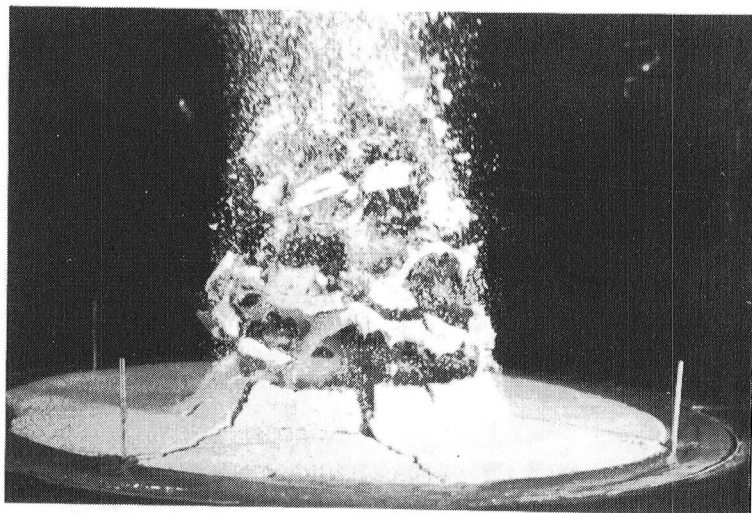
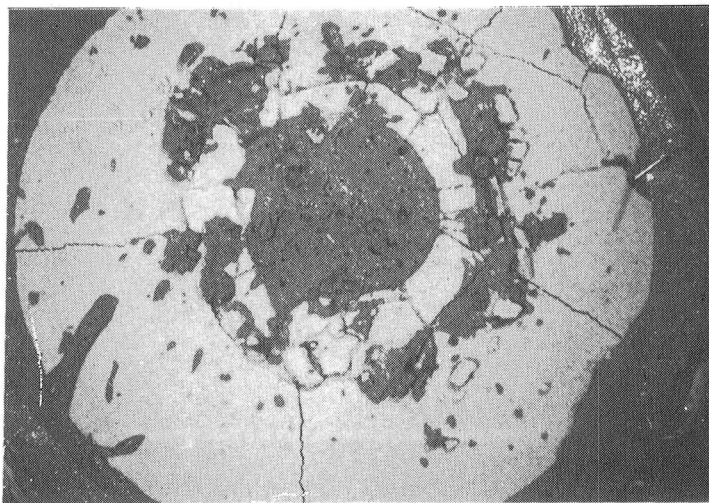


FIGURE 1. Shot 800643 showing impact (energy = 490 joules) into 1.2 cm thick layer of weakly bonded quartz particles underlain by a viscous clay slurry; note the directed ejecta plume, uptilted crustal plates, and fracture pattern (width of target is approximately 1 m).

the material landed within two crater radii (maximum transient cavity) of the point of impact; 3) as the transient cavity grew, a wave passed through the viscous substrate, accompanied by radial and concentric fracturing of the "lithosphere"; 4) as the growth of the transient cavity ceased, the upper elastic layer was too massive to be ejected; 5) in some cases it was simply overturned as the transient cavity collapsed, further fracturing the elastic material and a rising central mound of viscous material was generated; in some experiments, as the central mound collapsed, it sent a surge of viscous ejecta over the fractured plates; 6) the outlines of the fractured plates remained visible; commonly one complete and one partial ring fracture formed; the ratio of the inner rim diameter to the crater diameter increased roughly in proportion to the thickness of the "lithosphere" layer. Although only 13 experiments were conducted involving the bonded particles overlying a viscous substrate, the results suggest that there is a critical balance between the thickness (and/or strength) of the upper layer and the viscosity of the underlying material to produce multiple ring fractures; if the upper layer was too thin (or weak), a palimpsest-like feature formed with very little topographic expression; if the upper layer were too thick (or strong), the impact simply punched into it, leaving a bowl-shaped crater.

In the 16 experiments involving an upper layer of unbonded (hence, very weak) particles, the apparent diameter of the crater increased as the upper layer decreased in thickness. Although it is unlikely that physical modelling of impact basin formation can be applied quantitatively because of the orders of magnitude differences in size between laboratory and full-scale events, such modelling may provide qualitative insight into some of the mechanisms of basin formation.



*FIGURE 2. Vertical view, post-impact, of shot 800643, showing radial and concentric fracture pattern.*

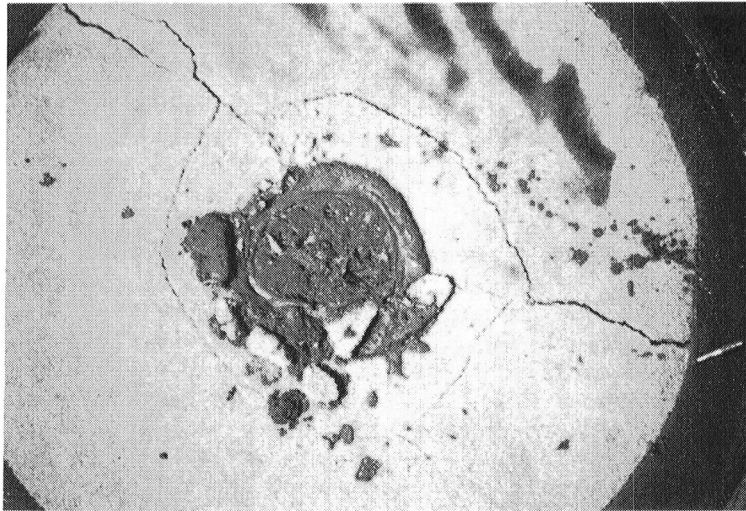


*FIGURE 3. Shot 800646 showing impact (energy 190 joules) into 1.2 cm thick layer of weakly bonded quartz particles underlain by viscous clay slurry; note the more simple fracture pattern than in the more energetic impact of shot 800643.*

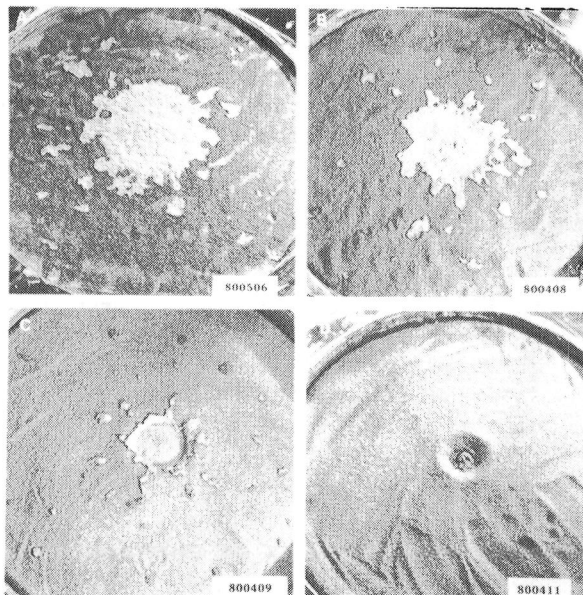


*FIGURE 4. Sequence (A to D) of shots showing the smaller apparent crater diameter of impact into progressively thicker upper layer of particles underlain by viscous medium.*

# THE EVOLUTION OF MULTI-RINGED BASINS: COOLING, THERMAL STRESS, AND RELAXATION OF TOPOGRAPHY

Sean C. Solomon<sup>1</sup>, Steven Bratt<sup>1</sup>, Robert P. Comer<sup>1</sup>, and James W. Head<sup>2</sup>

<sup>1</sup>Dept. of Earth and Planetary Sciences, Massachusetts Institute of Technology, Cambridge, MA 02139; <sup>2</sup>Dept. of Geological Sciences, Brown University, Providence, RI 02912

**Introduction.** Multi-ringed basins on the terrestrial planets show wide variations in their present geometry and structure [1-3]. Some of these variations may be attributed to differences in the initial extent of ring development due to differences in lithospheric properties at the time of basin formation [4,5]. It is likely, however, that many of the presently observed variations reflect different degrees of modification of initial basin geometry or structure by geological processes acting on time scales long compared to those for cavity excavation and ring formation. As a step toward understanding the differences among the basins of the terrestrial planets, we have modeled the effects of two such modification processes: (1) the local thermal evolution of the basin region, including subsidence and thermal stress, and (2) the viscoelastic relaxation of basin topography.

**Thermal evolution.** The impact process leading to the formation of a basin results in a substantial input of heat to the underlying material [6], though the spatial distribution of this heat is not well known. This heat will eventually be lost from the planet by conduction and surface radiation. Two consequences of this heat loss will be thermal contraction and thermal stress in the material underlying the basin relative to adjacent terrain. Under some conditions the thermal contraction will lead to observable subsidence of the basin region and the thermal stress may exert a substantial effect on local tectonics. This stress should be considered in context with stresses associated with later volcanic filling of the basin and with global scale stresses [7,8].

The model for the thermal evolution of a basin is based on the assumption of cylindrical symmetry. It is sufficient for our problem to solve for the case where the initial temperature is uniformly  $T_0$  within a buried vertical cylinder extending from  $r = 0$  to  $r = a$  and from  $z = h_1$  to  $z = h_2$ , and zero elsewhere ( $r$  and  $z$  are horizontal radius and depth, respectively, in cylindrical coordinates). The solution for any circularly symmetric initial temperature distribution may then be adequately approximated by a sum of suitably weighted solutions for uniform cylinders. The solution for the buried cylinder is

$$T(r,z;t) = T_0 \frac{\sqrt{\pi}}{2} P\left(\frac{a}{\sqrt{2kt}}, \frac{r}{\sqrt{2kt}}\right) \cdot \left\{ \left[ \operatorname{erf}\left(\frac{h_2-z}{2\sqrt{kt}}\right) - \operatorname{erf}\left(\frac{h_1-z}{2\sqrt{kt}}\right) \right] - \left[ \operatorname{erf}\left(\frac{h_2+z}{2\sqrt{kt}}\right) - \operatorname{erf}\left(\frac{h_1+z}{2\sqrt{kt}}\right) \right] \right\} \quad (1)$$

where  $I_0$  is a modified Bessel function,  $k$  is thermal diffusivity [9]

$$P\left(\frac{a}{\sqrt{2kt}}, \frac{r}{\sqrt{2kt}}\right) = \frac{1}{2kt} e^{-r^2/4kt} \int_0^a r' e^{-r'^2/4kt} I_0\left(\frac{rr'}{2kt}\right) dr' \quad (2)$$

$$\text{and } \text{erf } x = \frac{2}{\sqrt{\pi}} \int_0^x e^{-\xi^2} d\xi.$$

To obtain the displacement and thermal stress fields, we assume that  $t=0$  is the reference (zero displacements, stress free) state. The vector displacement  $\underline{u}$  is [10]

$$\underline{u}(r, \theta, z; t) = -\nabla \phi_1 - \nabla_2 \phi_2 \quad (3)$$

where

$$\begin{aligned} \phi_1 &= \frac{1}{2} \int_0^\infty \int_0^\infty \frac{\alpha(1-\nu)}{3(1-\nu)} \frac{T(r', z'; t)}{R} r' dr' dz' \\ \phi_2 &= \frac{1}{2} \int_0^\infty \int_0^\infty \frac{\alpha(1+\nu)}{3(1-\nu)} \frac{T(r', z'; t)}{R'} r' dr' dz' \end{aligned} \quad (4)$$

$$R^2 = (r \cos \theta - r' \cos \theta')^2 + (r \sin \theta - r' \sin \theta')^2 + (z - z')^2$$

$$R'^2 = (r \cos \theta - r' \cos \theta')^2 + (r \sin \theta - r' \sin \theta')^2 + (z + z')^2$$

$\nu$  is Poisson's ratio,  $\alpha$  is the coefficient of volumetric expansion, and the operator

$$\nabla_2 = (3-4\nu)\nabla + 2\nabla \left[ z \frac{\partial}{\partial z} \right] - 4(1-\nu) \frac{\partial}{\partial z} \nabla^2 [z].$$

Once  $\underline{u}$  is determined, then the thermal strains  $\epsilon$  and stresses  $\sigma$  follow from standard formulae [11].

The volumetric distribution of initial heat is the primary unknown for the basin thermal evolution problem. For a variety of simply parameterized initial thermal states, we compare the predicted subsidence and thermal stress with available topographic and tectonic information on prominent basins on the Moon, Mars and Mercury.

**Viscoelastic Relaxation.** For basins formed comparatively early in the history of a planet when near-surface temperatures were globally high and the lithosphere was thin, viscoelastic relaxation of initial basin topography may have been important. Viscoelastic relaxation has been invoked to explain the poorly preserved ring structures of older basins on the Moon (e.g., Tranquillitatis) and even for some portions of the rings of large younger basins such as Imbrium [5].

We model the lithosphere of a planet as a thin viscoelastic plate of flexural rigidity  $D$ , thickness  $T$ , and relaxation time  $\tau$ , overlying an

inviscid fluid of density  $\rho$ . We treat the initial basin topography as a load  $q(r) H(t)$ , where  $H(t)$  is a unit step function. The subsidence for  $t \geq 0$  is given by [12]

$$w(r,t) = \frac{H(t)}{\rho g} \int_0^{\infty} \left[ 1 - \frac{\alpha^4 k^4}{1 + \alpha^4 k^4} e^{-t/\tau(1 + \alpha^4 k^4)} \right] q(k) J_0(kr) k dk \quad (5)$$

where  $g$  is the gravitational acceleration,  $k$  is the radial wave number,  $q(k)$  is the Hankel transform of  $q(r)$ , and the flexural parameter  $\alpha$  is given by  $\alpha^4 = D/\rho g$ . Expressions may also be found in [12] for the radial and tangential stresses at the surface of the lithosphere for  $t \geq 0$ . Expression (5) at  $t=0$  is equivalent to the solution for the flexural response of a purely elastic plate [13].

Starting from a model for 'initial' basin topography based on Oriental [14], we calculate topographic and stress profiles as functions of  $t/\tau$ . A comparison of these predicted profiles with observed topography for older basins (after removing the contribution to the topography from both volcanic fill and fill-related subsidence) demonstrates the potential importance of viscoelastic relaxation as a modification process for basins formed on lithosphere sufficiently thin or warm so that the effective relaxation time is comparable to or less than the basin age.

#### References.

- [1] W.K. Hartmann and C.A. Wood (1971) Moon, 3, 3.
- [2] J.W. Head (1974) Moon, 11, 327
- [3] C.A. Hodges and D.E. Wilhelms (1978) Icarus, 34, 294.
- [4] H.J. Melosh and W.B. McKinnon (1978) Geophys. Res. Lett., 5, 985.
- [5] J.W. Head and S.C. Solomon (1980) Lunar Planet Sci XI, 421.
- [6] J.D. O'Keefe and T.J. Ahrens (1977) Proc. Lunar Sci. Conf. 8th, 3357.
- [7] S.C. Solomon and J.W. Head (1979) J. Geophys. Res., 84, 1667.
- [8] S.C. Solomon and J.W. Head (1980) Rev. Geophys. Space Phys., 18, 107.
- [9] H.S. Carslaw and J.C. Jaeger (1959) Conduction of Heat in Solids, Oxford.
- [10] R.D. Mindlin and D.H. Cheng (1950) J. Appl. Phys., 21, 931.
- [11] S.P. Timoshenko and J.N. Goodier (1970) Theory of Elasticity, McGraw-Hill.
- [12] R.P. Comer, S.C. Solomon and J.W. Head (1980) Lunar Planet Sci. XI, 171.
- [13] J.F. Brotchie (1971) Mod. Geol. 3, 15.
- [14] J.W. Head, R.J. Phillips, and E. Robinson (1980) Moon and Planets, to be submitted.

# THE DISTAL DEPOSITS OF LUNAR BASINS AT THE APOLLO 14 AND 16 LANDING SITES

B. Ray Hawke, Hawaii Inst. of Geophysics, Univ. of Hawaii, Hon., HI 96822;

James W. Head, Dept. of Geological Sciences, Brown Univ., Prov., RI 02912.

**Introduction:** The Apollo 14 mission returned material from the Fra Mauro Formation which has been interpreted as a portion of the ejecta blanket deposited during the formation of the Imbrium basin<sup>1,2</sup>. Major controversy has centered on questions of the mode of emplacement of the Fra Mauro Fm., the provenance of materials within the unit, and the source of the range of thermal effects exhibited by the returned samples. Preliminary results of sample studies were thought to be consistent with an Imbrium ejecta origin and the variety of thermal effects was attributed by some to the autometamorphism of a thick, hot ejecta blanket<sup>3,4,5</sup>. Other workers have interpreted the Fra Mauro Fm. as a deposit derived from the Imbrium crater but with the range of metamorphic effects resulting from pre-Imbrian events in the Imbrium target site<sup>6,7,8</sup>. More recently, Oberbeck and co-workers published the results of numerous studies which emphasized the importance of local mixing in the formation of distal deposits of large impact structures<sup>9,10,11</sup>. In light of these findings, Head and Hawke<sup>12</sup> investigated the processes and events which dominated the history of the Apollo 14 region. It was concluded that the Fra Mauro Fm. was formed by a process which included the erosion and excavation of local, pre-Imbrian material by the impact of Imbrium primary ejecta, and the mixing of this Imbrium ejecta with local crater deposits, to produce an ejecta blanket dominated by locally derived material. Similar conclusions have been reached in other studies based on laboratory cratering experiments, theoretical cratering mechanics, and photogeologic analysis<sup>11,13,14,15,16,17,28</sup>.

Similar arguments for local as opposed to distant basin ejecta origin have been advanced for the material sampled at the Apollo 16 site<sup>11,13,18</sup>. According to the hypotheses proposed in these studies, the general stratigraphic sequence at the Apollo 16 landing site is apparently dominated by Nectaris basin deposits and the products of large local cratering events (see Ref. 18, p. 91) and contains relatively minor amounts of primary ejecta from Imbrium and Orientale basins. The local origin hypothesis stands in sharp contrast to suggestions that the material sampled at Apollo 16 (Cayley plains and Descartes Mts.) represents primary basin ejecta from Orientale<sup>19,20</sup> and/or Imbrium<sup>21,22</sup> basin that was emplaced by ballistic or surface flow processes. In a recent publication, Wilhelms and co-workers pointed out alleged deficiencies in the local mixing hypothesis and restated the arguments for primary basin ejecta deposits at the Apollo 14 and 16 landing sites. In light of the continuing uncertainty as to the provenance of the Apollo 14 and 16 samples, we have initiated a variety of studies to aid in the solution of this critical lunar question. The purpose of this paper is to present the preliminary results of our current research and to summarize the recent results of other investigators which have relevance to the origin of Apollo 14 and 16 material.

**Fra Mauro region:** Major controversy has centered around the nature and origin of features radial to Imbrium basin in the Fra Mauro region. We have re-analyzed these radial structures and compared them with analogous features around Orientale basin. Numerous large (4-13 km in width) radial grooves were identified. These grooves appear to be akin to Imbrium sculpature and are clearly erosional as opposed to depositional in origin. These grooves slash topographic features with little regard for pre-existing terrain. The grooves exhibit roughly parallel walls having a scalloped or crater-form aspect. These large radial features are interpreted as Imbrium secondary chains. Where best preserved, individual, clearly defined secondary craters can be identified. The large ridges between the large secondary chains appear to be erosional

remnants modified by the later debris surge. Little evidence was found to support the argument that these large ridges are flows or features resulting from surface flow.

Many smaller radial features have been identified at a variety of scales. One class of such radial features ranging from 0.5 to 5 km in width was mapped by Eggleton<sup>27</sup> and Head and Hawke<sup>12</sup> and interpreted to be secondary crater chains formed by Imbrium ejecta. New mapping has established the existence of these features in the immediate vicinity of the Apollo 14 landing site. A series of very small ridges have been mapped in the Fra Mauro region and appear to be analogous to the braided texture seen in the Hevelius Formation.

An attempt has been made to calculate the percentage of Imbrium primary ejecta actually present in the Fra Mauro Fm. at the Apollo 14 site. Eggleton<sup>27</sup> first noted that some local, pre-Imbrium material was probably incorporated into the Fra Mauro by the impact of Imbrium secondary projectiles but no quantitative estimates were made. Morrison and Oberbeck<sup>13</sup> presented the results of calculations which suggested that the Fra Mauro contained between 15% and 20% Imbrium material. We have made similar calculations based on the equations and assumptions presented by Oberbeck and co-workers<sup>11,13</sup> and using the measured diameters of Imbrium secondaries. As noted above, these secondaries range from about 0.5 km to 13 km in diameter with the larger structures being concentrated in chains 25 to 50 km east of the landing site. The identifiable secondary craters and crater chains in the immediate vicinity of the Apollo 14 site are about 1-2 km in diameter. If impact angles of 15° and 30° from the horizontal are assumed, the calculations yield values of 9.5% to 19% for the amount of Imbrium primary ejecta in the deposits of these secondary impact structures. Values for the surrounding region range from 7% to 32%.

Objections to the local mixing hypothesis have been raised on the basis of the inferred size of basin ejecta fragments and the supposed scarcity of secondary craters<sup>20,29,30,31</sup>. Morgan *et al.*<sup>29</sup> assumed that the bulk of distant basin ejecta was of millimeter to decimeter size. They describe a process in which the first material to arrive mixes thoroughly with the local regolith to a depth on the order of the diameter of the larger fragments (~10 cm) and successive 10 cm layers mix with material containing progressively larger amounts of basin ejecta thus diluting the concentration of local material in the deposit to the degree where it is no longer important. However, recent work has demonstrated that secondary craters from Imbrium basin are much more common than had been previously recognized<sup>32,12,13</sup>. Apparently these craters were formed by either large individual blocks of Imbrium ejecta or by clumps of smaller fragments that are launched on similar trajectories and thus act as a single body in ballistic flight and upon impact with the surface<sup>14,15</sup>. Morrison and Oberbeck<sup>15</sup> reviewed evidence to support the idea that large masses of jointed rocks can remain intact after ejection from the crater.

Additional support for a local as opposed to Imbrium ejecta origin for the Fra Mauro samples has been obtained by analyses of petrologic and geochemical data for the Apollo 14 samples and remote sensing data for the Fra Mauro region. This evidence was discussed in detail by Hawke and Head<sup>16,17</sup>.

Descartes Region: Many of the arguments advanced in support of the local origin of the bulk of the Fra Mauro Fm. also apply to the Apollo 16 site. While it is not our purpose to present a detailed view of Apollo 16 site geology at this time, certain points should be discussed and emphasized.

First, the effect of material ejected by Orientale basin on the Apollo 16 region seems minimal<sup>18</sup>. McGetchin *et al.*<sup>24</sup> predict less than 2 m average thickness at the Apollo 16 site. No Orientale secondaries have been identified in the Apollo 16 region and studies of Orientale basin secondaries and secondaries show a distinct lack of these structures in the quadrant toward the Apollo 16



region. A thin blanket of Orientale ejecta in the central highlands appears to be ruled out by systematic east to west changes in the composition of the central highlands as revealed by the Apollo orbital geochemistry data<sup>17,25</sup>.

The Descartes region was affected by the formation of Imbrium basin. The region is surrounded by a variety of features radial to Imbrium. Imbrium sculpture interpreted to be the product of the impact of Imbrium secondary-forming projectiles, is particularly well-developed NW of the landing site where these radial structures cut the rims of Dollond B and C. More clearly defined Imbrium secondary chains are superposed on Descartes Mts. material north and south of the site. Major quantities of local, non-Imbrium ejecta must have been incorporated into the deposits of these Imbrium secondaries. Morrison and Oberbeck<sup>13</sup> presented the results of calculations based on the measured diameters of Imbrium secondaries in the Descartes region which indicated that deposits emplaced by Imbrium secondary craters at the Apollo 16 site could contain only 13-18% primary Imbrium ejecta. These estimates may overestimate the actual percentages because of effects of surface scour by the subsequent debris surge and the dilution of surface material by material from post-Imbrium impact events. Debris surges resulting from the formation of Imbrium secondaries in the region may have played an important role in the emplacement of Cayley plains material.

The origin the Descartes Mts. material has been the source of considerable controversy. The bulk of the evidence favors an origin as hummocky Nectaris basin deposits which were later furrowed by Imbrium secondaries<sup>e.g. 18,26</sup>. It has been suggested that the Descartes Mt. material represents Imbrium primary ejecta emplaced by surface flow down a long Imbrium-radial trough<sup>23</sup>. As noted above, Imbrium secondaries are superposed on the unit. For reasonable ejection angles (e.g. 15°-30°), the secondary-forming projectiles would have impacted in the Apollo 16 region about 7-13 minutes after ejection. It seems unreasonable that the Descartes Mt. material was emplaced in its final form prior to the arrival of the Imbrium secondary projectiles. An extremely rapid mode of surface transport would be required.

In conclusion, the bulk of the currently available evidence supports the origin of most Apollo 16 material as Nectaris basin ejecta and the products of large craters in the Descartes region.

References: 1) R. Eggleton (1964) Astrogeol. Studies, Ann. Prog., Aug. 1962-Jul. 1963, 46. 2) D. Wilhelms (1970) USGS Prof. Paper 599-F. 3) H. Wilshire and E. Jackson (1972) USGS Prof. Paper 785. 4) J. Warner (1972) PLSC 3, 623. 5) R. Williams (1972) EPSL 16, 250. 6) E. Chao et al. (1972) PLSC 3, 645. 7) M. Dence and A. Plant (1972) PLSC 3, 379. 8) E. Chao (1973) USGS Jour. Res. 1, 1. 9) V. Oberbeck et al. (1973) NASA TM X62-302, 1. 10) V. Oberbeck et al. (1974) PLSC 5, 111. 11) V. Oberbeck et al. (1975) The Moon 12, 19. 12) J. Head and R. Hawke (1975) PLSC 6, 2483. 13) R. Morrison and V. Oberbeck (1975) PLSC 6, 2503. 14) V. Oberbeck (1975) Rev. Geophys. Space Phys. 13, 337. 15) R. Morrison and V. Oberbeck (1978) PLSC 8, 3763. 16) R. Hawke and J. Head (1977) PLSC 8, 2741. 17) R. Hawke and J. Head (1978) PLPSC 9, 3285. 18) J. Head (1974) The Moon 11, 77. 19) E. Chao et al. (1973) LS IV, 127. 20) E. Chao et al. (1975) USGS Jour. Res. 3, 379. 21) C. Hodges (1972) NASA SP-315, sec. 29-D. 22) H. Moore et al. (1974) PLSC 4, 71. 23) D. Wilhelms et al. (1980) LPS XI, 1251. 24) T. McGetchin et al. (1973) EPSL 20, 226. 25) R. Hawke and P. Spudis (1979) Lunar Highland Crust Conf., 53. 26) D. Wilhelms (1972) NASA SP-315, sec. 29-F. 27) R. Eggleton (1970) USGS Map I-708, sheet 2. 28) V. Oberbeck and R. Morrison (1976) PLSC 7, 2983. 29) J. Morgan et al. (1977) Proc. Soviet-Amer. Conf. Cosmochem. of the Moon and Planets, 659. 30) E. Chao (1974) PLSC 5, 35. 31) P. Schultz and M. Mendenhall (1979) Lunar Highland Crust Conf., 143. 32) D. Wilhelms (1976) PLSC 7, 2883.

# COMPLEX IMPACT CRATERS ON THE PLANETS

R. J. Pike, U.S. Geological Survey, Menlo Park, CA 94025

A transition from simple (small) to complex (large) impact craters has been observed on all solid bodies in the solar system that are larger than Amalthea. Differences between the two types of craters have not yet been explained. Several morphologic and structural features of complex craters are summarized schematically in Figure 1. The interpretive and generalized cross section, shown at true scale for Earth, is based on photo-geology of Viking Orbiter images (Pike, 1980a, b) and the composite geology of four complex meteorite craters in horizontal sedimentary rocks on Earth, especially Flynn Creek crater, Tennessee (Roddy, 1979).

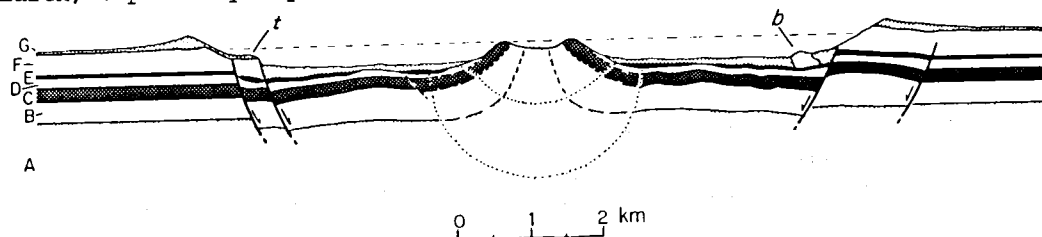


Figure 1

Hypothetical rock units A through G illustrate major points of the interpretation. Units A and B comprise the core of the central uplift, where the rock layers dip vertically. The lowest unit, A, has been displaced more than a kilometer upward. Unit C forms the rim of the peak-pit, a feature that is not found in all complex craters. Thin units D and E have been attenuated and pinch out against the central uplift. Unit F has been stripped out of the crater during impact but forms a slump block (b) and a structural terrace (t) at the base of the rim. The uppermost unit, G, is ejecta on the crater rim and beyond and fallback breccia and shock melt within the crater. Horizontal dashes indicate precrater ground surface. Arrows show downthrown sides of faults, which die out at shallow depths.

Salient features represented in Figure 1 (Pike, 1980b) include the transient cavity: a broad, shallow zone of total brecciation and excavation (within the crater above unit E) and a smaller, deeper central zone (small semicircle) of breccia -- resulting from shallow penetration of the impacting body; a larger and deeper central zone of total disruption, outlined by the large semicircle; uplift of the central peak by rebound; inward movement of the subfloor to compensate for peak uplift; shallow deformation of inner subfloor and peripheral faulting, leading to terracing (t), in response to inward movement of the subfloor; slight downdropping of outer floor edge and uplift of inner floor edge.

The transition from fresh-looking simple craters to complex craters on six planets and satellites may be interpreted in terms of gravitational acceleration,  $g$ , and target characteristics (Fig. 2). Each of the 59 small dots is a statistically derived crater diameter that expresses a different aspect of the transition, such as inflection of the depth/diameter distribution (arrows), frequency or onset of central peaks, and median overlap of simple and complex distributions (Pike, 1980a). For clarity, the dots for Mars are displaced slightly to the right of those for Mercury. There are 23 morphologic aspects for the Moon, 18 for Mercury, 10 for Mars, 8 for Earth, and 1 each (approximate onset of central peaks; see Pike, 1980a) for Callisto (upper square) and Ganymede (lower square). Large circles are centered on geometric means,  $D_t$ , for the 8, 10, 18, and 23 diameters of morphologic aspects for the four planets indicated. Bars show one standard deviation. The solid line, a least-squares fit to four geometric means:  $\log D_t = \log 3300 - 1.00 \log g$ , is interpreted as indicating targets of average strength or degree of stratification. The  $D_t$  value for Earth changes dramatically when craters are subdivided by type of target: upper diamond,  $D_t$  for meteorite craters in crystalline rock only (see shaded rectangles in Fig. 3); lower diamond,  $D_t$  in sedimentary rock only (from Fig. 3). The two dashed lines are extrapolations, down to lower values of  $g$ , of the disparate terrestrial  $D_t$  values for crystalline and sedimentary rock, also with a slope of  $-1.00$ . The upper dashed line is interpreted to represent planets with either resistant or homogeneous target characteristics (e.g., Mercury). The lower dashed line is interpreted to represent planets with either weak or strongly layered targets. Martian data and estimates of  $D_t$  for impact craters on the two Galilean satellites are consistent with weak or layered, volatile-rich, strata.

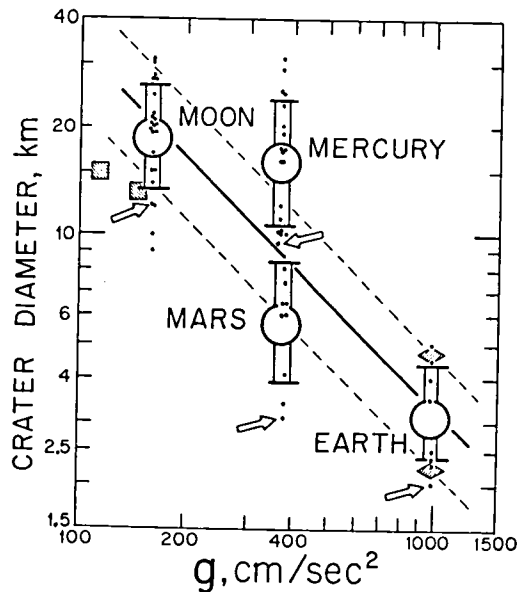


Figure 2

Grieve and Robertson (1979) have shown that the simple-to-complex transition, essentially the presence or absence of a central uplift, in terrestrial impact craters (shaded bars in Fig. 3) depends strongly on target characteristics. Arrays of "proven" and "probable" meteorite craters were compiled from data of Grieve and Robertson (1979).  $N = 80$ . The transition in sedimentary rock (soft) occurs at  $D = 2.25$  km, whereas in crystalline rock (hard) it occurs at  $D = 4.75$  km. The transition from complex

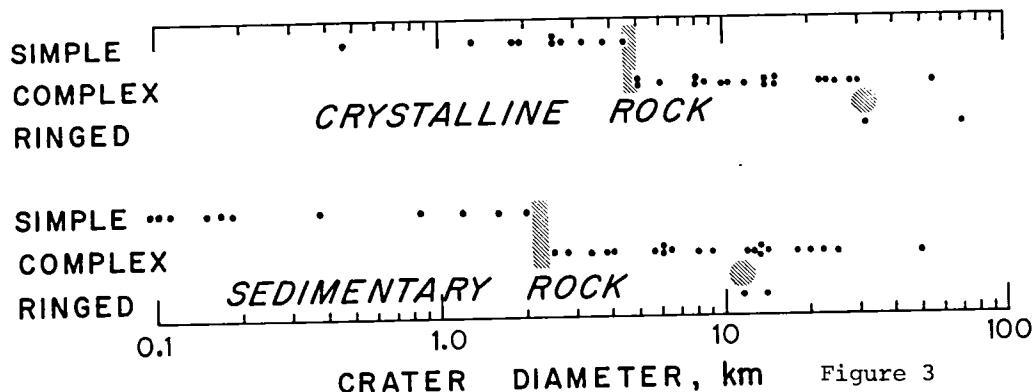


Figure 3

craters to ringed complex craters (shaded circles) shows a similar trend. Comparison with lunar data in Figure 4 suggests that the observed contrast in morphology reflects layering of the sedimentary targets rather than a difference in overall rock strength (Pike, 1980a).

Crater morphology on the Moon also depends upon target characteristics (Wood and Andersson, 1978; Pike, 1980a). Figure 4 summarizes depth/diameter ( $d/D$ ) results for 203 mare craters versus 136 upland craters. To show relations in detail, plotted fields outline only craters  $4.2 \text{ km} \leq D \leq 95 \text{ km}$ ;  $d/D$  equations are given in Pike (1980a). The square (Diophantus) and crosses (with increasing size: Dionysius, Proclus, Kant, Auzout) are craters with a morphology transitional from simple to complex configurations. Simple craters

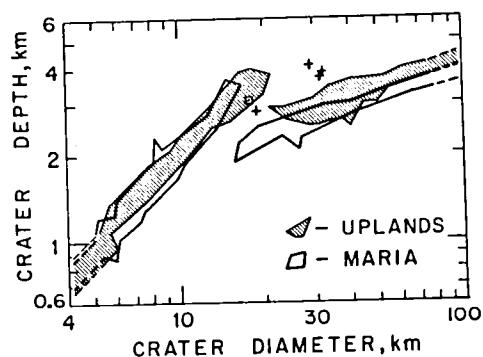


Figure 4

do not differ much in  $d/D$  (0.5%), but upland complex craters average 12% deeper than mare complex craters. The simple-to-complex transition occurs on maria (layered target) in craters about 16 km across, 3 km below the average lunar  $D_t$  value in Fig. 2, whereas it occurs in upland (nonlayered target) craters about 21 km in diameter, 2 km above the lunar  $D_t$  value.

#### References

- Grieve, R.A.F., and Robertson, P.B., 1979, The terrestrial cratering record I. Current status of observations: *Icarus*, v. 38, p. 212-229.
- Pike, R.J., 1980a, Control of crater morphology by gravity and target type: Mars, Earth, Moon Proc. *Lunar Planet. Sci. Conf.*, 11th, in press.
- Pike, R.J., 1980b, Formation of complex impact craters: Evidence from Mars and other planets: *Icarus*, in press.
- Roddy, D.J., 1979, Structural deformation at the Flynn Creek impact crater, Tennessee: A preliminary report on deep drilling: *Proc. Lunar Planet. Sci. Conf.* 10th, p. 2519-2534.
- Wood, C.A., and Andersson, L., 1978, New morphometric data for fresh lunar craters: *Proc. Lunar Planet. Sci. Conf.* 9th, p. 3669-3689.

GOAT PADDOCK, WESTERN AUSTRALIA--AN IMPACT CRATER NEAR THE SIMPLE-COMPLEX TRANSITION

Daniel J. Milton

U.S. Geological Survey  
National Center, MS928  
Reston, VA 22092

Robert F. Fudali

Department of Mineral Sciences  
Smithsonian Institution  
Washington, D.C. 20560

John Ferguson

Lynton Jaques

Bureau of Mineral Resources  
P.O. Box 378 Canberra City, A.C.T. 2601  
Australia

Field work at this crater, in the Kimberley District of Western Australia, was carried out in August 1980 and consisted of geologic mapping on a specially flown set of color aerial photographs, gravity and magnetic profiling along two lines crossing the crater, and collection of specimens for laboratory study. In addition, arrangements were made for aeromagnetism and aeroradioactivity to be flown. All the field data require compilation and at this writing (September 1980) it can best be said that the published description based on the 1979 reconnaissance (Harms *et al.*, 1980) holds up well.

On at least six terrestrial planets and satellites, small craters are simple (bowl-shaped) and large craters are complex, characterized by shallow flat floors, central peaks or pits, scalloped rim crest outlines, and slumped or terraced walls. A sequence of appearance of the features of complex craters with increasing crater size is emerging, but its significance and the causative mechanisms are controversial (Pike, *in press*, a, b). The investigation of Goat Paddock is directed toward the problem of the origin of complexity in craters.

Pending a more definitive profile based on the gravity survey, two drill holes indicate Goat Paddock is flat-floored beneath crater fill sediments and has a depth-diameter ratio ( $d = 0.34$  km,  $D = 5.10$  km) that falls on the line for terrestrial complex craters (Pike, *in press*, a). The crater lacks, however, a central peak, which would be expected in a crater of this size. A bench occurs in at least some sectors at about the level of crater fill, 2/3 of the way from the floor to the rim. It is not evident whether slump was involved in its formation. Melt breccia is exposed at a single locality on this bench.

The upper walls are excellently preserved and exposed. Upright or overturned bedrock, locally brecciated and slumped, is in contact with fragmental breccias and conglomerates. Embayments with a shallow slope scallop the generally steep crater wall. Fragmental materials show a sequence that reflects increasingly lengthy processes of deposition, from breccia of unsorted but vaguely oriented clasts that slumped or

slid down the wall immediately after formation, to poorly sorted talus, to well sorted, oriented and even rounded conglomerate.

No ballistic ejecta has been identified, but breccia is abundant on the rim flank. Much is autochthonous, but schlifffläche at the bedrock-breccia contact indicate radial transport of some breccia. Sharp variations in elevation of the bedrock-breccia contact suggest early postemplacement faulting. One fault, about 3/4 km beyond the wall and dipping 75° craterward, is particularly prominent and may even have been expressed physiographically in the fresh crater as a second rim.

#### References

- J.E. Harms, D.J. Milton, John Ferguson, D.J. Gilbert, W.K. Harris and Bruce Goleby (1980), Goat Paddock cryptoexplosion crater, Western Australia, Nature 286, 704-706.
- R.J. Pike (in press, a), Control of crater morphology by gravity and target type: Mars, Earth, Moon, 11th Lunar and Planetary Sci. Conf. Proc.
- R.J. Pike (in press, b), Formation of complex impact craters: Evidence from Mars and other planets, Icarus.

## MACROSCOPIC HYPERVELOCITY IMPACT PHENOMENA

J Hurren, G Martelli<sup>°</sup> and PM Smith  
University of Sussex - Space and Plasma Physics Group - Brighton, UK

R Bianchi, P Cerroni<sup>°°</sup>, M Coradini, M Fulchignoni and M Poscolieri  
Istituto di Astrofisica Spaziale - Reparto di Planetologia - Roma, Italy

R Flavill  
University of Kent - Space Science Group - Canterbury, UK

We report the results from some recent experiments, carried out at the Detonics Centre of the SNIA VISCOSA - Colleferro, Italy, within the frame of a collaborative programme involving the University of Sussex, the Istituto di Astrofisica Spaziale and the University of Kent. The aims of these experiments, performed both in vacuo and under different atmospheric conditions, were essentially:

1. to refine the techniques, based on the use of explosive hollow charges for the production of hypervelocity (13 - 15 Km/s) macroscopic (0.1 - 1gr) projectiles,
2. to study the processes leading to, and concomitant with, the formation of craters on targets made of different materials (basalt, mud, etc).

This investigation has been devoted mainly to the following:

- a. monitoring the formation of the craters throughout their evolution, using a IMACON fast image intensifier framing camera (up to 20 million frame/s),
- b. study of the morphological parameters of the craters as a function of the velocity and mass of the impacting projectile,
- c. recording the formation of the ejecta as well as measuring their velocity and mass spectra and angular distribution.

These results will be discussed in the light of the current theories of hypervelocity cratering processes, secondary cratering and energy balance of the impact phenomena. Preliminary results from the analysis of the mineralogic changes of the target material after impact will also be presented.

Finally, impact associated magnetic phenomena and magnetic changes in and near the cratered area will also be reported, and an attempt made to explain the observations in terms of the formation and time evolution of the dense hot plasma formed during the impact.

---

<sup>°</sup> Temporary address: Istituto di Astrofisica, Reparto di Planetologia, Rome, Italy

<sup>°°</sup> Temporary address: University of Sussex, Space and Plasma Physics Group, Brighton, UK

APPARENT CRATER DEPTH: SELENOGRAPHIC DISTRIBUTION.  
R. A. De Hon and M. X. Furin, Department of Geosciences,  
Northeast Louisiana University, Monroe, LA 71209.

Introduction. The transition from simple to complex crater morphologies within the 10-20 km diameter range on the moon is well documented (1-4). The significance of the transition remains a point of controversy. The correlation of diameter and depth for complex craters ( $>15$  km in diam.) is less well defined than that of smaller, simple craters (4,5); hence, craters of equal diameter exhibit a wide range of depths. This study is designed to examine the apparent depth of complex lunar craters as a function of selenographic distribution. If apparent depth is a simple function of crater diameter, then the distribution of apparent crater depths on the lunar surface should be random. On the other hand, if the apparent depth of craters is controlled by surface or subsurface characteristics of the target material, then the apparent depths should exhibit some correlation with lunar terrain.

Method. Approximately 160 fresh-appearing, complex craters were identified in regions of LAC and LTO topographic coverage. Data collected for each crater includes the location (longitude and latitude), diameter, mean elevation of the surface, and apparent depth (surface elevation minus mean elevation of the crater floor). Depth and diameter plots were constructed and analyzed for significant trends. Apparent depths were plotted on a lunar basemap for construction of proximal and contour maps.

Results. Apparent crater depths, which range from 0.2 to 3.3 km, exhibit little correlation to crater diameter. The average apparent depth within the region of Apollo photographic coverage (95 craters) is 1.8 km. If divided into mare and highland subgroups, the mean apparent depth of mare craters is 1.4 km, and the mean apparent depth of highland craters is 2.2 km. A contour map of apparent depths (Fig. 1) exhibits sufficient organization to suggest that crater depths are correlated to selenographic location. In general, regions of shallow crater depths ( $<1.5$  km) are associated with basin interiors. Greater depths are associated with highland terrains. The deepest craters ( $>2.5$  km) occur in the topographically highest regions, such as basin rims.



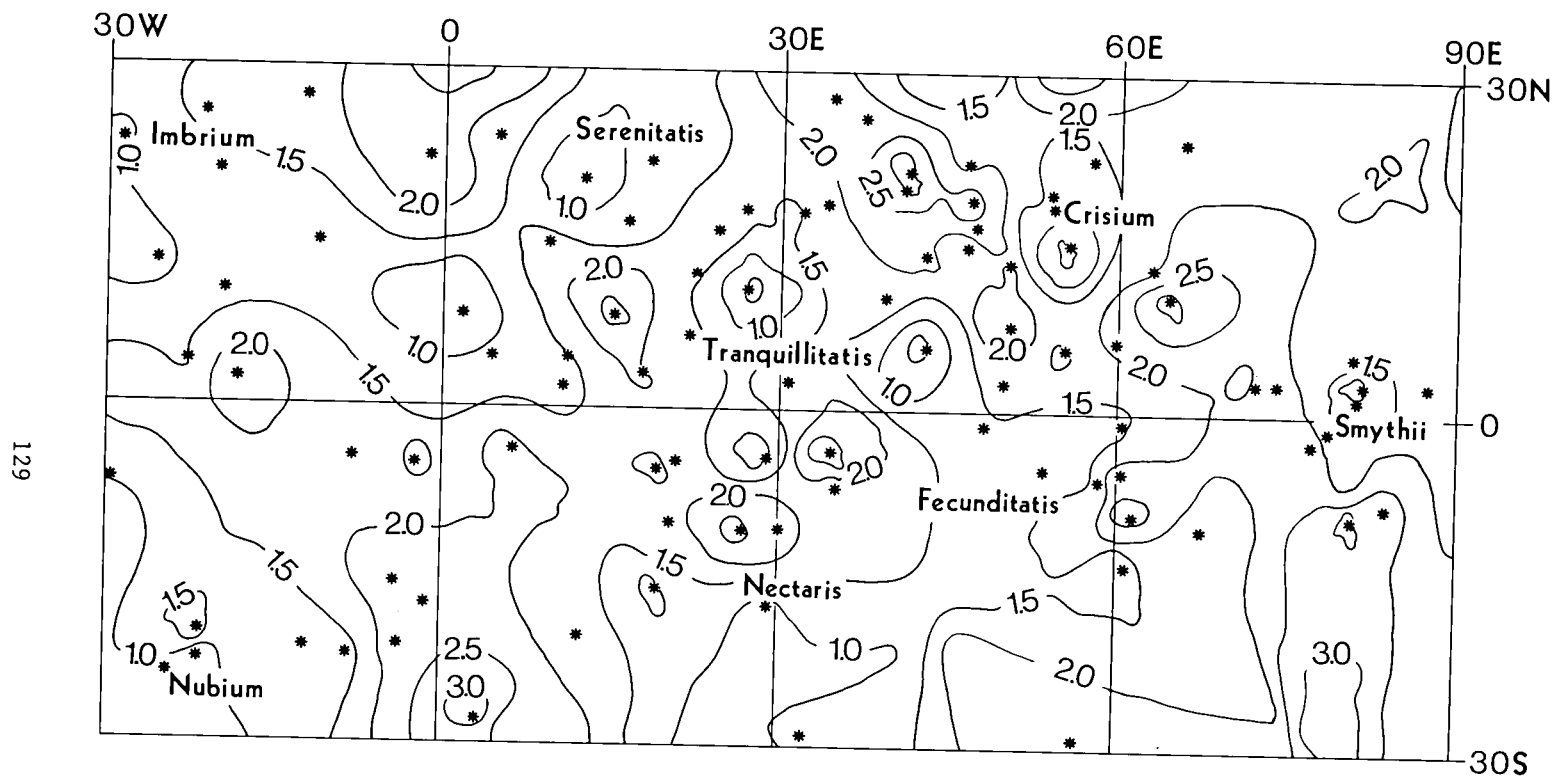


Figure 1. Apparent depths of lunar craters. Low apparent depths occur in regions of basins and low-lying terrain. Greater apparent depths occur on highlands and basin rims. Contour interval is 0.5 km.

Discussion. Crater depths exhibit a strong correlation with terrain characteristics and little relationship to crater diameter. Mean apparent depth of the craters is within the range of estimates for the average thickness of the lunar megaregolith (6-9). If complex craters are the result of restricted excavation at the megaregolith-crystalline rock discontinuity at depth (8-11), then the crater depth map (Fig. 1) provides an estimate of the lateral variations to the base of the megaregolith. The distribution of craters large enough to reach the discontinuity is sufficient to provide reasonable estimate of regional thickness trends; however, the spacing is large and many important local variations are unsampled.

#### References

1. Baldwin R. B. (1963) The Measure of the Moon, Univ. of Chicago Press.
2. Smith E. I. and Sanchez A. G. (1973) Mod. Geol. 4, 51-159.
3. Wood C. A. and Andersson L. (1978) PLPSC 9, 3669-3689.
4. Pike R. J. (1980) PLPSC 11, in press.
5. De Hon R. A. (1980) PLPSC 11, in press.
6. Hartmann W. K. (1973) Icarus 18, 634-636.
7. Short N. M. and Forman M. L. (1972) Mod. Geol. 3, 69-91.
8. Head J. W. (1976) PLSC 7, 2913-2928.
9. Aggarwal H. R. and Oberbeck V. R. (1980) PLPSC 10, 2689-2705.
10. Cintala M. J. et al. (1977) PLSC 8, 3409-3425.
11. De Hon R. A. (1978) Lunar and Planet. Sci. IX, 232-234.

CRATER CENTRAL PEAKS ON THE MOON, MERCURY AND EARTH. Hale, W., and Head, J.W., Dept. of Geological Sciences, Providence, RI 02912

Central peaks are important morphologic features in fresh craters on the Moon and Mercury (1-4). Central uplifts, which appear to represent the eroded roots of central peaks, are also reported in terrestrial impact craters (5-14). Primary morphologic features of impact craters are believed to reflect the partitioning of kinetic energy of the projectile into the target and the target's mechanical response (15). The observed transition from simple, bowl-shaped craters to shallower structures which flat floors and central peaks (1-4) may represent important changes in energy partitioning and/or target response. Thus an understanding of the impact process as a whole depends in part on an understanding of the formation of crater central peaks, a subject of ongoing debate (2,3,4,17-21).

Some workers suggest that central peaks form as a result of deep-seated slumping of the crater cavity during the modification stage of the cratering event (5,16). As such they would consist of intersecting slump toes whose emplacement would represent gravity-driven failure of the target material more than any primary response to impact energy (5,16). Other workers have proposed that central peaks form by dynamic rebound of the target as a primary response to impact-generated shock stresses (11, 17). Studies of fresh lunar and mercurian craters can provide the two-dimensional (surface) data bearing on this controversy. However, no data on the subsurface structure or original stratigraphic position of central peak materials can be derived from the present lunar and mercurian data sets. Such data is needed to determine the nature of peak formational mechanisms. The central uplifts of terrestrial craters (5-14) have been exposed to different levels by the Earth's active weathering system. Drilling and mapping of these has provided a view of the third dimension of central peaks, their structure and stratigraphy.

The purposes of the present work are: 1) delineate and compare the morphology and morphometry of lunar and mercurian central peaks; 2) detail the morphometry and structure of central peaks in terrestrial craters (5-14), summarized in Table 1; and 3) relate these three data sets to the problem of central peak formation.

Morphometry of Lunar and Mercurian Central Peaks-Central peaks occur in 100% of all fresh craters larger than 35 km diameter on the Moon and 40 km diameter on Mercury. Central peak diameter (Dcp) increased as a linear function of crater rim diameter (Drc) on both planets. For the Moon, this relationship is  $D_{cp} = 0.20 D_{rc} + 0.42$  ( $n=175$ ,  $r=0.88$ ) (19), while for Mercury it is  $D_{cp} = 0.17 D_{rc} + 1.97$  ( $n=140$ ,  $r=0.88$ ) (21). These two relationships are statistically indistinguishable within the real scatter of the data (21). Similarly, central peak heights ( $H_p$ ) increase as a function of Drc. For lunar craters  $> 27$  km across, this relation is  $H_p = 0.032 D_{rc} - 0.900$  (15), while for mercurian craters  $> 22$  km across it is  $H_p = 0.118 D_{rc} - 0.545$  (2). The two fits are also indistinguishable within the scatter of the data (22).

Morphology of Lunar and Mercurian Craters-Central peaks on both planets may be classified (under a single system) by complexity (simple, complex) or geometry (linear, symmetric or arcuate) (21). Simple peaks consist of single, coherent massifs while complex peaks consist of peak clusters. Symmetric peaks are roughly circular in plan, while linear or arcuate peaks consist of extended ridges or clusters. Complexity appears unresponsive to substrate variations on both planets, while geometry appears somewhat responsive (14, 21). This is particularly evident in the lunar case, where linear or arcuate central peaks are developed preferentially in highland terrains (20, 21). The elongation directions of these central peaks have a

strong preferred orientation at North-South ( $0^\circ$ ) with secondary trends at  $\pm 20^\circ$ - $30^\circ$  from  $0^\circ$ . These orientations may reflect relict structural fabric in the lunar lithosphere (20). Finally, distributions of peak complexity and geometry as a function of rim diameter on both planets indicate no strong trend towards an increasing frequency of complex, symmetric peaks at large crater diameters (19, 21).

Central Uplifts in Terrestrial Craters-Central uplifts are found in terrestrial craters as small as 3.4 km (13). The best characterized examples of terrestrial central uplift craters are listed in Table 1. The central uplifts consist of tightly to isoclinally folded, faulted and brecciated strata which have been translated inward and upward from their pre-impact positions (10,11). In craters developed in sedimentary targets (Steinheim, Flynn Creek, Sierra Madera, Gosses Bluff) the amount of stratigraphic uplift can be directly measured (9,10,12,13). The ratio of this uplift ( $S_u$ ) to reconstructed crater radius ( $R_c$ ) is  $S_u=0.2R_c$  to  $0.3R_c$  (Table 1). Studies of breccia relationships at Gosses Bluff (12) and Steinheim (13) indicate emplacement of the central peak before the emplacement of fallback ejecta. For  $S_u=3000$  m at Gosses Bluff and a fallback time of 2 minutes for cm-sized blocks, this implies a minimum uplift velocity of 25 m/sec for the central peak. Although all four sedimentary target craters are developed in water-saturated coastal plain environments none show strong evidence of a central pit at present. Gosses Bluff which has been identified as a central pit crater (23), retains a coherent central uplift within its ring, suggesting that explosive evacuation was not a factor here. Gosses Bluff may instead be either a central peak crater or central peak basin, but differential erosion has so altered the original central morphology that an unequivocal classification is not possible.

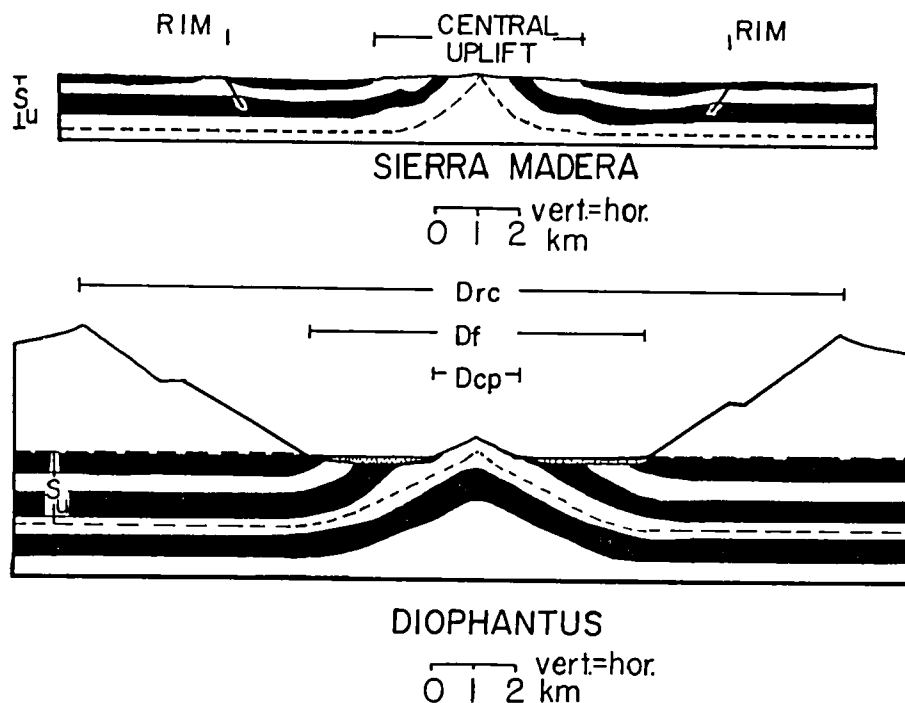
Discussion-Central peaks increase in diameter and height as a direct function of crater rim diameter. These relationships do not vary significantly from the Moon to Mercury. The existence and constancy of these suggest that central peak formation, like crater rim diameter (16) scales directly to the kinetic energy of impact. The tightly to isoclinally folded central uplifts of terrestrial impact craters, showing inward and upward displacements of deep-seated strata at relatively high velocities (25 m/sec), also support this. Therefore dynamic rebound is the favored mechanism for central peak formation. In addition, the lack of any consistent trends toward increasingly complex peaks at large crater diameters indicates that central peaks do not expand in a simple way to form peak rings. The amount of stratigraphic displacement,  $S_u$  of 0.2-0.3  $R_c$  in terrestrial central uplift craters is considered a minimum for uplift in lunar and mercurian craters. For comparison a cross-section of Sierra Madera (10) and a hypothetical crosssection for a lunar crater formed from an equivalent impact, Diophantus ( $D_{rc}=18.8$  km,  $S_u=1880$  m) is shown in Figure 1. This relatively small lunar crater should display peak material originally located 1.8 km below the crater floor. A large crater, such as Copernicus ( $D_{rc}=96$  km) would uplift material from 10 km below its floor. The lack of central pits in terrestrial craters formed in water saturated targets may have important implications for Mars. Here, abundant central pits in craters have been ascribed to explosive decompression of a volatile-rich layer in the substrate during the impact event. However, the presence of water alone seems insufficient to produce central pits. The origin of central pits is the subject of continuing study. References: 1) Baldwin, R.B. (1963) The Measure of the Moon 488 pp.; 2) Hartmann, W.K. and Wood, C.A. (1971) The Moon 3 p 2-78; 3) Cintala et al (1977) PLSC 8 p3409-3425; 4) Wood, C.A. and Andersson (1978) PLSC 9 p. 8267; 5) Dence, M.R. et al (1968)

in Shock Met. in Nat. Mat. p. 3390362; 6) Dence, M.R. (1968) in Shock Met. in Nat. Mat. p. 169-184; 7) Howard, K.A. and Offield, J. N. (1968) Science 162, p. 261-265; 8) Milton, D. J. and Breh, R. (1968) GSA 64th Meeting, p. 82; 9) Roddy, D.J. (1968) in Shock Met. in Nat. Mat. p. 291-320. 10) Nilshire, H.G. and Howard, K. A. (1968) Science 162 p. 258-261; 11) Milton, D. and Roddy, D. J. (1972) IGC sess. 24 p. 119; 12) Milton, D. et al (1972) Science 175 p. 1109-1207; 13) Reiff, W. (1977) in Impact and Explosion Cratering (Roddy et al, eds.) p. 309-320; 14) Roddy, D. J. (1977) in Impact and Explosion Cratering (Roddy et al, eds.) p. 185-246; 15) Pike, R. J. (1977) in Impact and Explosion Cratering (Roddy et al, eds.) p. 589-609; 16) Gault, D. E. et al (1975) JGR 80 p. 2444-1460; 17) Head, J.W. (1978) Lunar Science IX p. 485-487; 18) Hodges, C.A. and Wilhelms D. (1978) Icarus 34, p. 294-323; 19) Hale, W. and Head, J. W. (1979) PLSC 10 p. 2623-2633; 20) Hale, W., (1979) Proc. Lunar Highlands Conf., in press; 21) Hale, W. and Head, J.W. (1980) PLSC 11, in press; 22) Malin, M.C. and Dzurisin, D. (1978) JGR 83, 233-243. 23) Hodges, C.A. (1978) Lunar and Planet. Science IX p. 521-522.

TABLE 1

NAME	LgV Long	Age (m.y)	Drc (km)	Dcp (km)	Su (m)	Su/Radius
Steinheim	48°N, 10°E	14.7	3.4	0.9	340	.2
Flynn Creek	36°N, 85°W	360	3.6	0.9	380	.2
Deep Bay	58°N, 103°N	150	6	2.3	--	--
Lake Nicholson	62°N, 102°W	300 ± 150	12	2.5	--	--
Sierra Madera	30°N, 103°W	--	12	5	1200	.2
Clearwater E.	56°N, 75°W	285 ± 30	15	3.0	--	--
Gosses Bluff	24°S, 132°E	130 ± 6	20	Ring 5.0 L.P 1.25	3000	Ring .2 C.P .3

Figure 1



Rampart Crater Ejecta: Experiments and Analysis of Melt-Water Interactions  
Wohletz, Kenneth H. and Sheridan, Michael F., Department of Geology, Arizona  
State University, Tempe, Arizona 85281

Experiments investigating the interaction of a thermite melt with water have yielded preliminary results bearing upon the emplacement of rampart crater ejecta. The mass ratio of water to melt and confining pressure in the zone of interaction are the principal factors controlling: (1) the efficiency of conversion of thermal to mechanical energy, (2) the degree of melt fragmentation, and (3) the amount of melt-ejecta "fluidization." Analysis of terrestrial volcanic ejecta emplaced by late-stage surface flow/surge of quasi-fluidized materials also give insight into the effect of explosive efficiency, fragmentation, and fluidization upon ejecta emplacement. The deposit morphology is a function of the mean ejecta grain size the availability of water during magma ejection.

The distinctive morphology of ejecta blankets surrounding martian rampart craters is suggested to be a result of emplacement by flow of fluidized materials<sup>1,2</sup> and by atmospheric effects upon ballistic ejecta<sup>3</sup>. Subsurface water and/or ice is vaporized during impact events<sup>4</sup> and can promote fluidization of ejecta during emplacement. Experimental studies<sup>5,6</sup> support the hypothesis that the amount of water contained in target materials greatly effects ejecta emplacement and deposit morphology.

Our experiments<sup>7</sup> have been designed in cooperation with the shock wave physics group of Los Alamos Scientific Laboratory to investigate melt-water explosions. Thermite is used in order to produce large quantities (up to 100 kg) of melt with properties similar to those of basic silicate melts. Various contact geometries have been designed and utilized. Optimum explosive interaction occurs when a confining pressure (inertial, acoustic, hydrostatic, real) is employed. A series of experiments were run in a large (500 kg) steel chamber using different bursting limits to evaluate the effect of confining pressure. The mixing chamber is also designed to cause the entire contents of melt and water to interact so that the effect of mass ratios of water to melt may be evaluated. High speed photo documentation and P and T histories are used to analyze experimental results. The range of experimental parameters are as follows: (1) ejection velocities range from 100 to 200 m/s, (2) static pressures are 20-30 MPa, (3) ejected melt fragments range in size from centimeter to micron diameters, (4) water temperatures vary from 100°C to high levels of super-heating (these are pressure dependent and up to 400° to 500°C), and (5) ejection modes are both ballistic and flow in a turbulent expanding cloud of vapor and fragments.

Optimum explosive efficiency for present designs is achieved for water-melt ratios near 0.3 (Fig. 1) and is accompanied by production of super-heated steam, micron-sized melt fragments, and a high degree of melt dispersion by turbulent expanding vapor supported ejecta flow. Experimental phenomenology suggests that conversion efficiency of thermal

to mechanical energy decreases for water melt ratios that are greater or less than optimum. For small ratios ( $<0.20$ ) pulsating ballistic ejection or centimeter size fragments results. Steady ejection of millimeter and centimeter sized fragments supported in saturated steam cloud results from experiments where water-melt ratios are greater than 1.0.

Preliminary results of experiments compare favorably with field studies of natural (volcanic) melt-water, (hydromagmatic) explosions<sup>8,9</sup>. Eleven localities of hydromagmatism were classified by deposit morphology, and 106 ejecta samples from these deposits were subjected to grain size analysis and scanning electron microscopy with the following observations (Fig.2)

- (1) Deposits emplaced by a high degree ejecta inflation (fluidization) are finer grained and show a greater run out distance than those that are emplaced by poorly inflated flow.
- (2) Fluidized ejecta from highly explosive eruptions to dispersed over a larger area than those from less explosive eruptions resulting in lower profiled deposits.
- (3) Hydrated ejecta is more abundant in the poorly fluidized flow deposits indicating that supporting vapors were condensing on ejecta during transport. Hence, the steam was super heated.
- (4) The degree of ejecta fluidization during emplacement is a function of the amount of water available during eruption.

These results, when combined with preliminary experimental evidence, suggest that quasi-fluidized ejecta transport is a likely result of the interaction of an impact melt with near surface water and/or ice on Mars. The amount of water vaporized in the target and its degree of superheating will determine the level of ejecta fluidization and effect ejecta blanket morphology.

#### References

1. Head, J.W. and Roth, R. (1976) Symposium on Planetary Cratering, 50-52.
2. Carr, M.H., Crumpler, L.A., Cutts, J.A., Greeley, R., Guest, J.E., and Masursky, H. (1977) Jour. Geophys. Res. 82, 4055-4065.
3. Schultz, P.H., and Gault, D.E. (1979) Jour. Geophys. Res. 84, 7669-7687.
4. Kieffer, S.W. and Simonds, C.H. (1980) Rev. Geophys. Space Phys. 18, 143-181.
5. Gault, D.E. and Greeley, R. (1978) Icarus 34 486-495.
6. Greeley, R., Fink, J., Gault, D.E., Snyder, D.B., Guest, J.E., and Schultz, P.H. (1980) Proc. 11th Lunar Plan. Sci. Conf. in press.
7. Wohletz, K.H. (1979) EOS 61 66.
8. Wohletz, K.H. and Sheridan, M.F. (1979) Geol. Soc. Amer. Spec. Paper 180 177-194.
9. Wohletz, K.H. (1979) Geol. Soc. Amer. Abs. Prog. 11 543.
10. Sandia Laboratories (1975) SAND-74-0382 472p.

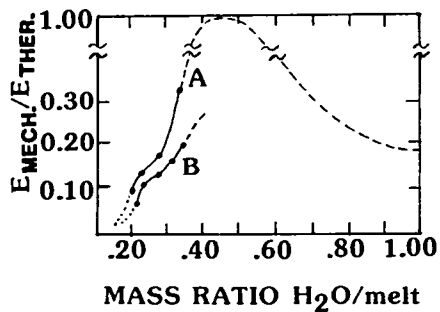


Fig. 1 Efficiency versus mass ratio for melt-water explosion based upon preliminary data. Dashed line shows inferred projection of efficiency curve based upon qualitative observation and the literature.<sup>10</sup> Curve A represents superheating and curve B is for non-superheating.

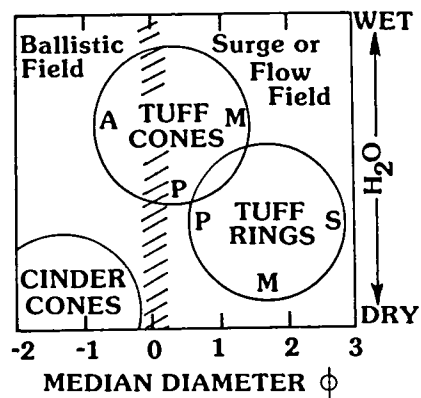


Fig. 2 Relationship of ejecta grain size to geologic environment showing deposit and bed form morphologies.



# AN ESTIMATE OF THE WATER CONTENT OF SOME MARTIAN RAMPART-EJECTA DEPOSITS DERIVED FROM THEIR PRE-FLOW STRESS CONDITIONS.

Alex Woronow, Lunar and Planetary Laboratory, University of Arizona, Tucson, Arizona 85721

Mars possesses several types of distinctive ejecta deposits not encountered elsewhere in the inner solar system. Although the nomenclature of these ejecta types is not standard, this study deals with those broadly termed as "rampart" deposits, that is, those ejecta deposits that appear most likely to have been formed by the viscous flow of the ejecta across the pre-existing surface. The mechanism(s) which initiated the flow are largely a matter of conjecture, but Mutch and Woronow (1980) studying MC-17 and MC 18 constrained the allowable processes to those which produce a uniform, maximum ejecta thicknesses for all rampart ejecta blankets independent of the size of the parent craters. They proposed that the material is initially transported beyond the crater rim ballistically, but if the deposit exceeds a critical thickness, then it fails under its own weight.

If the ejecta blankets fail and flow under the stresses of their own weights, then static stress analyses of the ejecta blankets will determine the conditions that lead to those failures. A finite-element model has been used to determine stress levels and stress trajectories in a homogeneous ejecta deposit. We considered planar stresses only. A two point-gaussian integration is used. The initial ejecta profile (i.e. before failure occurs) is presumed to be that of a ballistically emplaced blanket. We selected the model of McGetchin et al. (1973) for the thickness and the initial rim height from Cinatal (1979) for craters on Mercury (Mercury having about the same gravity as Mars).

Some attributes of the stress conditions are independent of the physical size of the ejecta blanket. That is, the location within the ejecta blanket where a particular condition occurs scales linearly with the size of the ejecta blanket. The two such parameters which we evaluate here are (1) the maximum angle of internal friction, and (2) the direction of maximum shear stress. By "maximum" angle of internal friction, we mean the maximum value that could be attained at any location--not the value necessary to actually cause failure at that location. In order to evaluate the magnitude of the stresses in the ejecta blanket, however, we must decide upon a physical size for the ejecta deposit. We selected an ejecta blanket from a 6 km diameter crater because this size crater is the smallest which commonly has a well-formed rampart-ejecta deposit. Therefore, this size crater should have the minimum stress conditions which commonly caused ejecta flow in MC-17 and MC-18. Although some craters smaller than 6 km diameter have rampart ejecta blankets, those blankets often deviate from the mathematical relationship followed by larger craters (see Mutch and Woronow, 1980).

In order to determine the mechanical properties of the ejecta at failure, we must first determine the height within the ejecta deposit at which failure occurs. The model for uniform-thickness ejecta deposits,

suggested by Mutch and Woronow, must represent the absolute minimum height above ground level at which failure could occur. The value of 40 m height which they derive must be an underestimate because if the ejecta had some internal strength, then it would not flow to form a level surface, as that model assumes, but instead leave a sloping surface with a rim height greater than 40 m. The upper limit of the post-flow thickness comes from Viking Special Products which include contoured images of a rampart crater with both 50 m intervals and 100 m intervals (see 4A90). Using this particular crater in the context of the present study may present some difficulties. But its ejecta extent lies close to the trend for the rampart craters in MC-17 and MC-18. We take this as sufficient reason, given the need, to utilize it in our present analysis. It suggests a value of 100 m as the upper limit on the height at which failure occurs.

Therefore, the following pre-failure stress conditions are implied for rampart ejecta blankets around 6 km diameter craters:

Angle of internal friction 26 to 36 degrees  
Shear stress inclination 45 to 51 degrees  
Deviatoric stress <1000 Kpa  
Shear stress <500 Kpa

Failure probably does not initiate at the surface of the ejecta blanket and propagate inward since the modelling of a "crack" in the ejecta surface, reaching to about the 100 KPa deviatoric stress level does not appear likely to propagate unaided.

The conditions at failure are commensurate with those expected for wet soils. They are not consistent with conditions associated with the failure of indurated rock materials nor of extremely low strength materials. Although we have not, at this time, sufficient data to invert the stress conditions to exactly specify the particle-size distribution and volatile content of the ejecta, we can make some general statements:

- (1) The volatile content is not sufficient to support the entire weight of the ejecta particles during flow.
- (2) The plasticity index was less than 50%, implying that--
- (3) the percentage of clays was less than 30%, the rest being coarser grade.

The last two conclusions are based on the empirical results of studies by Skempton (1960).

If the material properties of the ejecta are dictated by the clay fraction, and the lubricant is water, then we might expect that the water content lies between 18 and 20 weight percent. However, the presence of a considerable fraction of coarser grade material would reduce the void ratio from that for pure clay and render the value of 20% as an upper limit at the level where failure occurs.

#### REFERENCES:

- Clintala, M. J. (1979). Small fresh crater morphometry: A preliminary assessment of the effects of gravitational acceleration and impact velocity (abstract). NASA TM-80339, 176-179.
- McGretchin, T. R., Settle, M., and Head, J. W. (1973). Radial thickness variations in impact crater ejecta: Implications for lunar basin deposits. Earth Planet. Sci. Lett., 20, 226-236.
- Mutch, P. and Woronow, A. (1980). Martian rampart and pedestal crater's ejecta-emplacement: Coprates quadrangle. Icarus, 41, 259-268.
- Skempton, A. W. (1964). Long term stability of clay slopes. Geotechnique, 14, 77-101.

Distribution of Thermal Gradient Values in the Equatorial  
Region of Mars Based on Impact Crater Morphology:  
Joseph M. Boyce, NASA Headquarters, Code SL-4, Washington, DC  
and Nanci E. Witbeck, Kansas State University, Manhattan, KS

Crustal thermal conditions play an important role in the evolution of solid planetary bodies. Boyce (1979) has developed a technique for measurement of the maximum thermal gradient in areas on Mars. We have used this method to map the distribution of thermal gradient values in the equatorial regions of Mars. Work is in progress to extend this map globally.

The method involves the measurement of the smallest diameter rampart crater in an area (called 'onset' diameter). The depth of that crater is estimated using the depth/diameter relationship of rampart craters (modified from Pike, 1980). Boyce (1979) has suggested that this depth corresponds to the minimum depth to the boundary between liquid water and ice in the subsurface water table. This boundary also corresponds to the freezing isotherm for brine water under moderate pressure or about 230°K (Krguskoff 1967). These depth and temperature data can be combined with average surface temperature data (Fanale, 1976) to estimate the maximum thermal gradient,  $T = \frac{dT}{dz}$ , recorded in an area (where T is thermal gradient, t is temperature and d depth).

'Onset' Diameters of rampart craters have been measured in 382 areas in the martian equator region using Viking high and moderate resolution images. The measurements were made in a sample grid with each sample element being 5° sq. The 'onset' diameters ranged from zero, none present, to 21 km, with the average of about 5 km. The onset diameters and the center point location of these sample elements were digitized and transformed into an image array using the technique described by Eliason and Soderblom (1977) and Boyce and Johnson (1978). As part of the transformation the data were interpolated by spatial filtering using 81x81 pixels neighborhood. This 81x81 neighborhood filter size was designed to smooth the data yet retain both statistical significance and high frequency information. The transformed data have been sliced into one kilometer increments and are shown in Figure 1. The image in this figures represents a map of the distribution of 'onset' diameters.

The depths to the water freeze isotherm ( $\sim 2300$  K) have been calculated using the 'onset' diameter data and the modified depth/diameter relationship of Pike (1980) and the

corresponding thermal gradients are shown in table 1. We have assumed that 220° represents an average surface temperature over the narrow latitude distribution of the data and over much of geologic time. Therefore, the map of 'onset' diameter distribution shown in Figure 1 can easily be transformed into a thermal gradient maps by using the data in Table I.

The maps show that there are major thermal gradient provinces in the equatorial region of Mars. The maps show that (1) Hesperia Planum, Sinai Planum, Solis Planum, the Mi'adim Vallis-Al-qahila Vallis region, and the areas near Lassell and west of Schaeberle have relatively high thermal gradients (25°K/km) and (2) Claritas Fossae, Medusae Fossae, the Mangala Vallis region, Gangis Chasma area, the region east of Capri Chasma, and the area northeast of Flaugergues have relatively low thermal gradients ( $\sim 15^\circ$  K/km). Rampart craters of any size are absent in much of the region south of Arsia Mons Ceraunius Fossae and northern Agyre Planitia. There are several possible reasons why rampart craters may not be observed in these areas: (1) a water table was never present in these areas; (2) the surfaces are so young that craters large enough to tap the subsurface water have not formed, or (3) the terrain is so rough that confident identification of the craters is prevented.

Some of the regions with high thermal gradient correspond to areas of extensive volcanism such as Hesperia Planum. Two areas with high thermal gradient correspond to areas that Huguenin (1979) has suggested are present locations of near surface water. However, Huguenin suggests that water may occur within centimeters of the surface and our measurements suggest that significant quantities of water may have existed at a much greater depth (500m).

The average thermal gradient in the equatorial region of Mars is about 20° K/km based on the data presented here. This value is about a third less than for continental regions on earth and about half that for the ocean basins. The relatively low value of Mars could be the result of differences in interior thermal conditions or physical properties of the crustal rock.

The next phase of this study will be to: 1) expand the spatial coverage of the data, and 2) use photogeologic and other remote sensing data to identify regional rock types which can be used for estimates of thermal conductivity. These estimates of thermal conductivity can be coupled with the estimates of thermal gradient to provide global heat flow information.

Table I

Relationship of onset diameter, depth to water table and thermal gradient

<u>Relationship Onset Diameter, km</u>	<u>Depth to Water Table, km</u>	<u>Thermal Gradient °k / km</u>
2	0.22	50
4	0.45	25
6	0.67	16
8	0.90	13
10	1.02	10
12	1.35	8
14	1.57	7

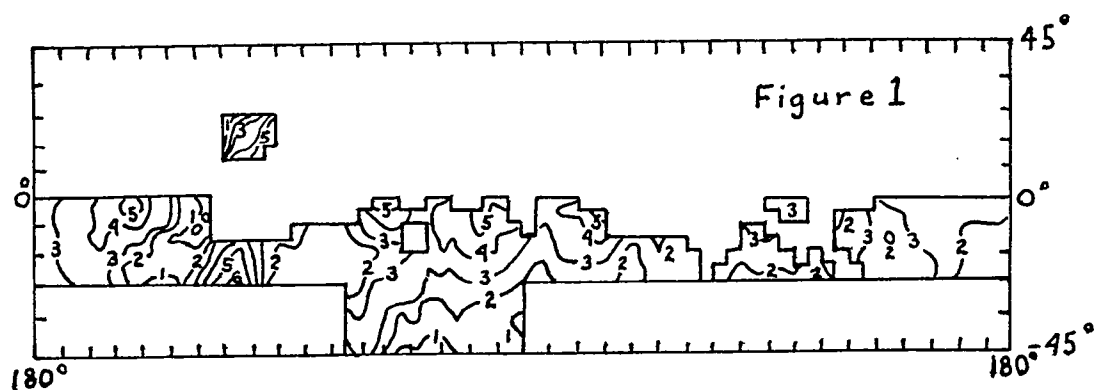


Figure 1. Map of the distribution of 'onset' diameters of rampart craters. Contour interval is 1 km. For conversion of these data to estimates of thermal gradient see table 1.

## Bibliography

- Boyce, J.M., 1979, A method for Measuring Heat Flow in the Martian Crust Using Impact Crater Morphology (Abs): Reports of Planetary Geology Program, 1978-1979, NASA TM 80339, p. 114-118
- Boyce, J.M., and Johnson, D.A., 1978, Age of Flow Units in the Far Eastern Maria and Implications for Basin-Filling History: Pro. Lunar Sci. Conf. 9th, Vol. 3, p. 3275-3283.
- Eliason, E.M., and Soderblom, L.A., 1977, An Array Processing System for Lunar Geochemical and Geophysical data: Proc. Lunar Sci. Conf. 8th Vol. 1, p. 1163-1172.
- Fanale, F.P., 1976, Martian Volatiles: Their Degassing History and Geo-chemical Fate: Icarus, v. 28, p. 179-202.
- Huguenin, R.L., Clifford S.M., Sullivan C.A., and Miller K.J., 1979, Remote sensing evidence for oases on Mars (abs.): Reports of Planetary Geology Program, 1078-1979, NASA TM 80339 p. 208-214.
- Krauskoff, Konrad B., 1967, Introduction to Geochemistry: McGraw-Hill Inc., 721 p.
- Pike, Richard J., 1980, Control of Crater morphology by gravity and target type: Mars, Earth, Moon: Pro. Lunar Sci. Conf. 11th., in press.

## LARGE TECTONIC EFFECTS OF THE CALORIS IMPACT ON MERCURY (+)

Thomas, P. (++) , Carey, E. , Fleitout, L. and Masson, Ph.  
Laboratoire de Géophysique et de Géodynamique Interne (ERA n° 804),  
Université Paris-Sud, 91 405 Orsay, France.

The structural studies conducted on the planet Mercury and described below, are mainly based on the interpretation of the Mariner 10 images. These studies lead us to the conclusion that the Caloris impact and its subsequent consequences (late readjustment) have strongly influenced the structural evolution of the planet.

Since 1975 (1) extensional tectonic structures are known in the Caloris basin internal plains. According to the geometric distribution and to the morphology of the lineaments observed in the Caloris surroundings, many of these lineaments were interpreted as normal faults cutting across the ejecta (2). The area where extensional structures are observed, extends over 500 km from the edge of the basin. These extensional structures can be interpreted as "extrados" tectonic fractures located on a bulge. Caloris basin is surrounded by the large widespread smooth plains unit of probably volcanic origin. These plains which surround the basin, extend over 1000 km from its edge. Assuming that these volcanic plains came from Caloris area, the external limits of these plains could be considered as the bottom of a large topographic low. This hypothesis allows us to suggest the following scenario which explains the formation of the extensional features and of the topographic low : due to the lack of mass inside the basin, an isostatic readjustment produced a bulge surrounded by a topographic low, as demonstrated by the general interpretation of a thin elastic plate deformation (3). A calculation based on the sizes of the areas where extensional structures and volcanic plains are observed, gives a 150 km approximate thickness for this elastic lithosphere (4) (5).

The surface of Mercury covered by Mariner 10 images shows a global pattern of lobate scarps. These structures are interpreted as thrust faults or as reverse faults (6) i. e. compressive structures. These compressive structures could be due to a global contraction of the planet. According to the detailed mapping of these lobate scarps, done in the southern hemisphere of Mercury by W. P. O'Donnell at the London Observatory University (personal communication), and to our geome-



tric analysis of these scarps (4) (5), it appears that the scarps are not randomly distributed. They show statistical orientations mainly parallel. Such orientations seem to be due to a global constriction of the planet. This constriction would be parallel to a submeridian great circle (fig. 1).

The location of Caloris basin nearly perpendicular to the center of the constriction circle suggests the following scenario : after Caloris impact, isostatic readjustment produced an elongation of the planet between Caloris and its antipodes, and a constriction perpendicular to this elongation occurred as a consequence of the elongation (4).

This scenario does not intend to justify all the compressive features observed on Mercury. But, this scenario combined with a global contraction of the planet due to its cooling, would explain the statistical prevalence of some structural directions.

+ INAG Research Contract n° 3727

++ CNES Research Grant n° 77005

#### References

- (1) STROM, R. G., TRASK, J. J., and GUEST, J. E. (1975) - Tectonism and Volcanism on Mercury. J. G. R. 80, pp.2478-2507
- (2) THOMAS, P. (1978) - Two examples of Recent extending tectonics on Mercury. EPGC Symposium on Planetary Geology, Paris, nov. 9-10, 1978.
- (3) COULOMB, J. et JOBERT, G. (1973) - Traité de Géophysique Interne. Masson éd., Paris.
- (4) THOMAS, P. (1980) - Etudes géologiques et structurales de la planète Mercure. Thèse de 3e cycle, Université de Paris XI.
- (5) THOMAS, P. and CAREY, E. - Tectonics of the Caloris area on Mercury (in preparation).
- (6) THOMAS, P. and FLEITOUT, L. - Global tectonics on Mercury : a Caloris effect ? (in preparation).

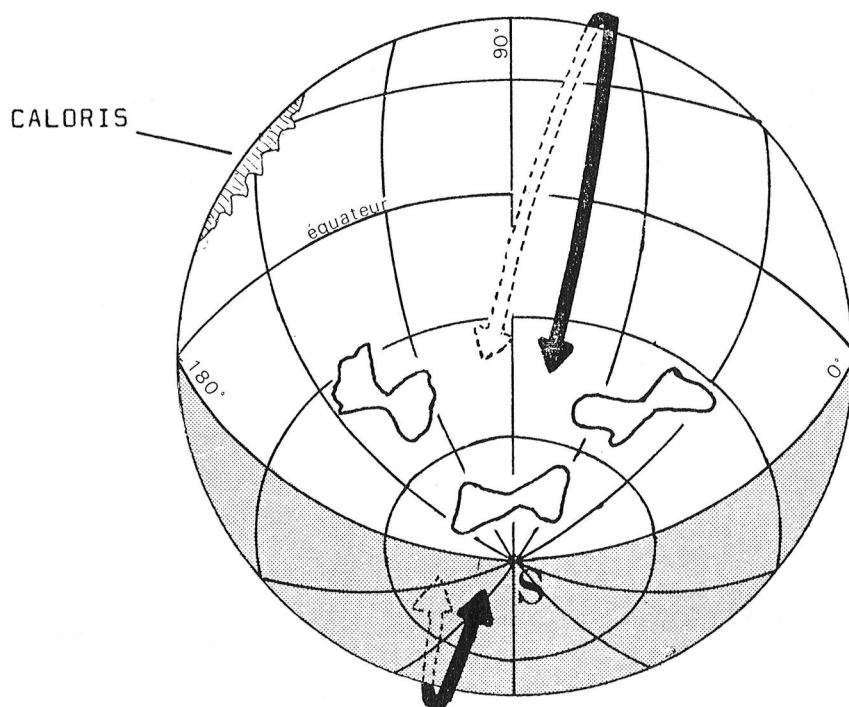


Fig. 1 : Global disposition of the compressive features in the Southern hemisphere of Mercury.



: rose diagram of the scarps'direction



: constriction's great circle

# GLOBAL PATTERNS OF PRIMARY CRATER EJECTA MORPHOLOGY ON MARS

Blasius, K.R. and Cutts, J.A., Planetary Science Institute, 283 S. Lake, Suite 218, Pasadena, CA 91101

A systematic survey of fresh crater ejecta morphology over the entire surface of Mars has been pursued using Viking Orbiter Medium Resolution Mapping imaging (Cutts *et al.* 1979; Blasius *et al.* 1980). Progress gathering data during the summer of 1980 has been rapid. A recent update to the data base showed that 2196 craters had been classified from examination of 162 mosaics covering 47% of the area of Mars (Figs. 1 and 2). Preliminary analyses of a test data base of 1457 craters have been conducted and development of new analytical methods to better handle the large volume and variety of data is underway.

We report here some analyses of the test data base for comparison with the results of studies by Johansen (1978, 1979) and Mouginis-Mark (1979). Figure 3 shows the latitude distribution of four classes of craters recognized by Johansen. Figure 4 is the most nearly comparable plot we could easily construct from our data.

Only the occurrence of Class 2 ("Flower") craters seems to be a similar function of latitude in the two plots. Ejecta flows with terminal ridges, those with the least apparent viscosity according to Johansen, are significantly more common within  $30^{\circ}$  of the equator than at higher latitudes.

Class 1 ("Lunar") craters are present in our test data set in too small numbers to exhibit significant variations with latitude. Class 3 craters with two ejecta flow deposits each show no strong variations in either data set. Class 4 craters, having a single ejecta flow deposit with a terminal scarp, have a distribution which is a strong function of latitude in Johansen's plots, but a similar trend is only suggested by our test data set. Finally, we find 15 to 50% of our craters in each latitude bin cannot be identified with one of Johansen's four classes.

The differences between the results found with the two data sets may be due to one or more of several factors:

- (1) We plot types as fractions of total crater populations while Johansen only plots occurrence in sampling areas on Mars. This almost certainly accounts for our inconclusive results for Class 1.

- (2) Our data set does not include many craters smaller than 6km diameter; Johansen's may.

- (3) Our crater classification scheme allowed for classification of ejecta deposit margins as indistinct in topographic character but clearly non-lunar (not Class 1). For example, a deposit may clearly be composed of multiple flow lobes but the distal margin indistinct. We allowed also for the combination of two ejecta deposits with margin types different from Johansen's "Flower" or "Composite" classes. All but a few percent of our "Other" craters have outer ejecta deposits with "indistinct" margin topography.

- (4) Our test data base does not evenly sample latitudes (Fig. 4). Deficiencies occur near the equator and at high latitudes. Addition of new data has solved this problem.

We have also made a preliminary analysis of the relationship of ejecta

mobility to latitude in our test data set. Figure 5 is reproduced from Mougini-Mark (1979). He notes that the maximum distance ejecta travels from crater center, normalized to crater radius, appears to increase toward higher latitudes. In Figure 6, we plot craters binned by a similar function, mean ejecta radius/crater radius, versus latitude. Since our calculation uses mean rather than maximum ejecta radius, our mobility values are binned somewhat differently from those of Mougini-Mark. We find the same sharp, upward trend in mobility for northern mid-to-high latitudes, but our results for the southern hemisphere are inconclusive.

Considerable progress has also been made toward developing a cluster analysis program for identifying the more abundant combinations of attributes, i.e., crater classes, within our data base. The algorithm now being developed is based on the "Isodata" algorithm of Tou and Gonzalez (1974). With significant changes to the manner in which clusters are initially identified and later split, the program has been successfully tested on latitude and longitude data from our data base.

#### References

- Cutts, J.A., et al., 1979, NASA TM 80339, pp. 111-113.  
 Blasius, K.R., et al., 1980, NASA TM 81776, pp. 93-94.  
 Johansen, L.A., 1978, Proceedings 2nd Colloquium on Planetary Water and Polar Processes, Hanover, N.H., 16-18 October, 1978, pp. 109-110.  
 Johansen, L.A., 1979, NASA TM 80339, pp. 123-125.  
 Mougini-Mark, P.J., 1979, J. Geophys. Res., V. 84, pp. 8011-22.  
 Tou, J.T. and Gonzalez, R.C., 1974, Pattern Recognition Principles, 377 p.

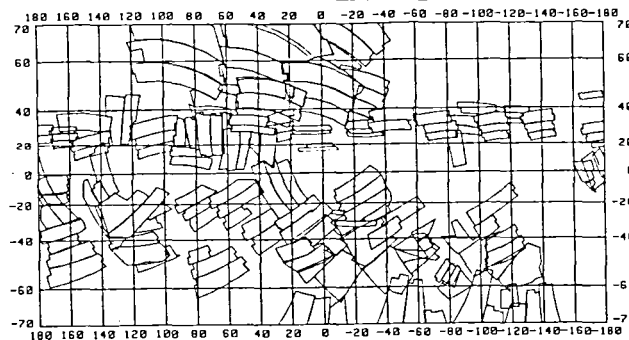
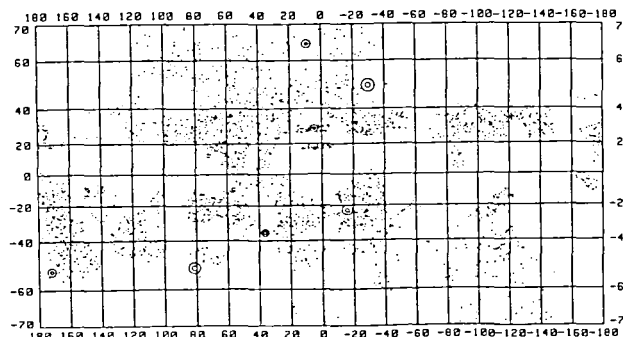


Figure 1. Distribution of mosaic coverage examined.

Figure 2. Distribution of classified craters.



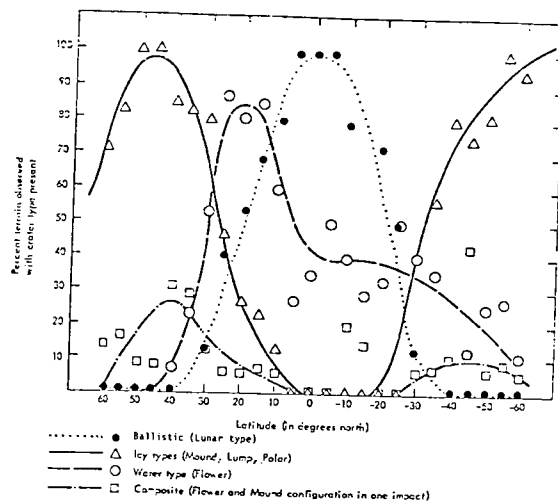


Fig. 3: Distribution of crater ejecta morphology by four types (Johnsen, 1979).

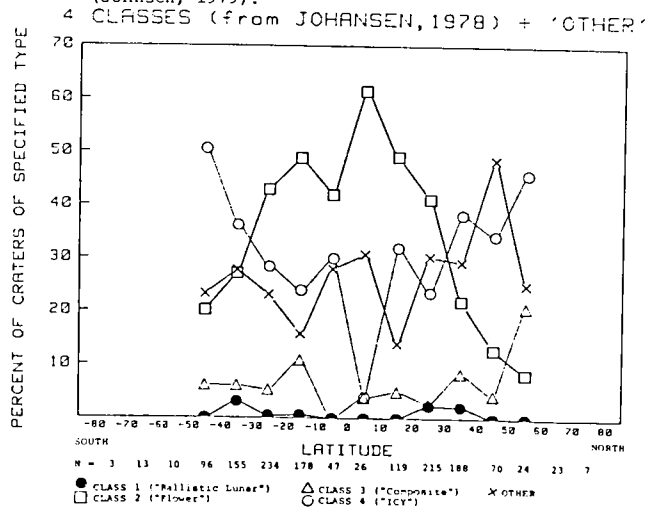


Fig. 4: Distribution with latitude in our test data set of 4 classes of crater ejecta morphology patterned after 4 types of Johnsen. N=number of craters in each latitude bin.

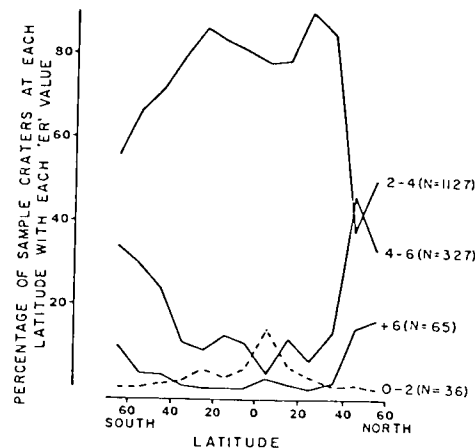


Fig. 5: From Mouginis-Mark (1979). Variability of ejecta mobility with crater latitude. For each crater the maximum ejecta range from the center of the primary is normalized by the crater radius to give the ejecta range ratio ER. The four curves illustrate the incidence of craters with each ER value as a percentage of all craters in any 10° latitude bin. At least 30 craters are represented at each latitude. N is the number of craters at all latitudes with each ER value.

Fig. 5: From Mouginis-Mark (1979).

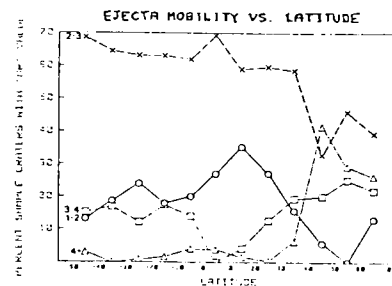


Fig. 6: Ejecta mobility versus latitude as seen in our test data. We detect an enhancement of ejecta range at high northern latitude as reported by Mouginis-Mark (1979).

# LATITUDINAL DISTRIBUTION OF FLOW-EJECTA MORPHOLOGY TYPES ON THE RIDGED PLAINS OF MARS

R. S. Saunders and Laurie A. Johansen, Jet Propulsion Laboratory,  
California Institute of Technology, Pasadena, CA 91103

Many fresh craters on Mars have ejecta that exhibit textures and morphology indicative of flow emplacement. These craters have been described and their distribution and significance discussed by several previous authors (e.g. Mouginis-Mark, 1979). There has been disagreement as to whether the distribution of craters with certain flow-ejecta morphology show latitude dependence (Johansen, 1978) or show no systematic dependence on latitude (Mouginis-Mark, 1979).

In order to further examine the question of latitude dependence, we are in the process of quantifying the size, ejecta type, and latitude of craters on a single terrain type, the ridged plains. Ridged plains were selected because they occupy a wide range of latitudes, are similar in age, and appear to have similar mechanical characteristics as suggested by the ridge morphology common to these plains. The ejecta types that we are considering can be combined to (a) distal-ridge (flower) types having single or multiple thin facies with a slight rise or ridge along the margin, (b) mound types with a relatively thick deposit that terminates abruptly with a steep rounded margin, and (c) composite craters with an inner facies of type b and an outer facies of type a.

An earlier study (Johansen, 1978) suggested that distal-ridge craters are prevalent at low latitudes and rare or absent at greater than  $60^{\circ}$  latitudes. Mound types are prevalent at the higher latitudes and rare or absent below about  $20^{\circ}$ . Composite craters occupy a transitional zone.

Our initial observations in this phase of the study were made on ridged plains in two regions at  $20^{\circ}\text{S}$  latitude and  $60^{\circ}\text{S}$  latitude. The position of the craters (latitude, longitude), diameters, and features are cataloged using a Hewlett-Packard system 45 digitizer and computer.

Preliminary results of the current analysis show that distal-ridge craters are more prevalent at  $20^{\circ}\text{S}$  than at  $60^{\circ}\text{S}$ . Those at  $60^{\circ}\text{S}$  also tend to be larger (greater than 20 km) while the majority of this type at  $20^{\circ}$  are less than 10 km diameter. Mound craters are far more prevalent at  $60^{\circ}\text{S}$  than at  $20^{\circ}\text{S}$ . Most are less than 10 km in diameter in both areas. Composite craters are relatively uncommon in both regions. The total sample was 371 craters.

Although preliminary, the results are consistent with the thesis of Johansen (1978) who examined the relative abundance of crater types on 170 regions of Mars but over a range of geologic units. We are in agreement with the basic interpretation of Johansen that the abundance and nature of subsurface volatiles, in particular water, controls the ejecta morphology. The equatorial regions contain relatively less water in the subsurface and craters tend to have the distal ridge morphology. Nearer the poles, more water is present, most likely as ice, and the mound ejecta type is prevalent.

### References

- Mouginis-Mark, Peter, Martian fluidized crater morphology: Variations with crater size, latitude, altitude, and target material, J. Geophys. Res., 84, 8011-8022, 1979.
- Johansen, L. A., Martian splosh cratering and its relation to water, paper presented at the 2nd Colloquium on Planetary Water and Polar Processes, NASA/AGU/Nat. Acad. of Sci., Hanover, N. H., 1978.

#### STUDIES OF MARTIAN CRATER AND BASIN DEPOSITS

B. Ray Hawke, Hawaii Inst. of Geophysics, Univ. of Hawaii, Hon., HI 96822; P.J. Mouginis-Mark, Dept. of Geological Sciences, Brown Univ., Prov., RI 02912.

**Introduction:** In recent years, considerable attention has been focused on martian crater deposits both because of the unique and enigmatic nature of the deposits themselves and because of the possible information these deposits may provide concerning the existence, thickness, and extent of a proposed subsurface volatile layer. With few exceptions<sup>1</sup>, studies have concentrated on craters less than 55 km in diameter. An effort is underway to investigate the distribution, nature, origin, and mode of emplacement of the exterior and interior deposits associated with large martian craters and small martian basins in the diameter range of 50 to 250 km. This paper presents the initial results of this project. Emphasis is placed on studies of Lyot and Lowell basins and a comparison of the deposits of these basins with those associated with Curie<sup>1</sup> (D=119 km) and Bamberg<sup>1,2</sup> (D=55 km) craters.

**Lyot basin** - Lyot is a relatively unmodified 200 km central peak basin located at 50°N, 330.5°W<sup>1</sup>. From Mariner 9 images, the feature was interpreted to be excavated in cratered plains material<sup>3</sup>. The structure exhibits a central peak and a well-developed peak ring approximately 100 km in diameter. The inner basin floor is relatively flat in contrast to the more rugged outer basin floor. Major portions of the basin interior appear subdued, perhaps by relatively thin eolian debris deposits.

Extremely rugged hummocky rim material completely surrounds the outer ring and is particularly well-developed NE of the basin where it extends almost 40 km from the ring crest. A major expanse of smooth material appears to have ponded to a level surface adjacent to a ring crest low north of the basin. Two dominant continuous ejecta facies were identified. An inner deposit of rough radial material occurs generally within 70 km of the outer ring. This unit exhibits a rough irregular surface texture and is, in part, arranged in large ridges crudely radial to the basin. The distal portion of the continuous deposit is characterized by a smooth though often undulatory surface. In places, distinct flow lobes and distal ridges can be identified. This smooth continuous ejecta unit has overridden and subdued secondary craters and crater chains associated with Lyot. The maximum extent of the smooth continuous ejecta is 187 km (0.94D) but the mean radial extent is approximately 125 km (0.63D). Lyot exhibits a well-developed field of secondary craters. While unmantled secondary craters can be identified within 103 km (0.52D) of the outer ring crest, features interpreted as partly buried secondaries can be identified as close to the basin as 48 km (0.24D).

Evidence was found that both ballistic flight and surface flow were significant processes in the emplacement of Lyot ejecta. Evidence for ballistic transport includes the following: (1) the presence of secondary craters and crater chains demonstrates ballistic transport at large radial distances, (2) the identification of subdued basin secondaries in areas now covered by continuous ejecta and in areas relatively protected from surface flow by obstructions suggests the importance of ballistic flight nearer the basin, (3) textured ejecta deposits have been located on pre-existing topographic highs where it could have only been emplaced in ballistic trajectories, and (4) the more restricted extent of the continuous ejecta deposits (0.63D) compared to those of Bamberg (2.1D)<sup>2</sup> and the much smaller rampart craters (0.2D)<sup>2</sup> suggests a relatively more important role for ballistic as opposed to surface flow processes.

Still, abundant evidence exists for radial flow of material after initial deposition: (1) surface flows appear to have been obstructed in places by large pre-impact topographic highs, (2) what appears to be shadow zones exist



in the lee of some obstacles, (3) in places, secondary craters have been overridden by material which originated nearer the basin rim, and (4) morphologic features (flow lobes, distal ridges) indicative of surface flow have been tentatively identified. As noted above, the continuous deposits of Lyot are relatively less extensive than those at smaller structures with well-developed ejecta flows. Still, the Lyot ejecta deposit extent is far greater than would be expected if ballistic processes alone were responsible. Carr *et al.*<sup>4</sup> pointed out that since the gravity fields of Mercury and Mars are similar, the radial extent of continuous ejecta on both planets should be approximately the same ( $\leq 0.4D$ ) if the ejecta configuration is controlled primarily by ballistic processes. Based on the work of Gault *et al.*<sup>5</sup>, the average radial extent of continuous ejecta around a fresh 200 km mercurian crater would be about 48 km or  $0.24D$ . The average value for Lyot ( $0.63D$ ) determined in the present study is far in excess of that ( $0.24D$ ) predicted for final deposit emplacement by purely ballistic processes. In certain areas, the maximum continuous deposit extent exceeds the values predicted for ballistic processes by a factor of 3.5 to 4!

**Lowell basin** - Lowell is a relatively undergraded 190 km double-ring or peak ring basin centered at  $52.3^{\circ}S$ ,  $81.3^{\circ}W$ <sup>7,8</sup>. The pre-impact target site was dominated by ancient hilly and cratered terrain and cratered plateau material<sup>3,6</sup>. The structure is almost exactly the same diameter (190 km) as Lyot (200 km) but differs in that it does not exhibit a central peak. Lowell does have a well-developed central peak ring ( $D=95$  km) similar to the inner ring of Lyot. The relatively flat inner basin is partly covered by a thick, smooth-textured deposit lobe which is probably sedimentary material of eolian origin. In contrast, the narrow outer basin floor exhibits a somewhat rougher texture but some portions appear to have been subdued by sedimentary material.

A hummocky rim unit, similar to that mapped at Lyot, completely surrounds the outer ring. This unit is extremely rugged near the ring crest and is characterized by numerous outward facing scarps and ridges which are concentric to the basin ring. The rim unit is surrounded by a rough radial unit which is relatively thick and characterized by a rough surface texture and abundant radial features. Since these radial features occur at a variety of scales and exhibit a range of morphologies, multiple origins are likely. Many are clearly secondary crater chains since they are continuous with better defined crater chains at greater distances from the basin. Similar features were identified in the rough radial unit around Lyot but they are more numerous and better-developed at Lowell. As at Lyot, the rough radial material extends at most 70-80 km ( $0.40-0.42D$ ) from the outer ring crest. A distal radially textured unit has also been mapped. This unit is thin, relatively flat (though not necessarily smooth), and exhibits abundant radial lineations at a variety of scales. Several subunits have been defined. A well-developed smooth radial subunit exists SW of the basin. This unit displays a relatively smooth surface with faint radial lineations and is interpreted to have originated by surface flow from a point nearer the basin. Similar but smaller subunits have been identified in other areas. Another major subunit is composed of closely spaced secondary crater chains which have been buried to varying degrees by later material. Outside the limits of the distal radial unit, numerous secondary craters and crater chains can be identified. These features are not so abundant as around Lyot.

**Discussion and Conclusions:** A recent study of martian craters from 15 to 119 km in diameter concluded that increasing crater diameter accentuates variations in interior morphology. Inclusion of Lyot and Lowell in this population suggests that this trend also extends to impact structures 200 km in diameter.

Extensive mapping of Bamberg crater allowed the identification of six

exterior deposit units as well as a secondary crater field<sup>1,2</sup>. A hummocky rim unit similar to the equivalent unit around lunar craters and to the rim unit mapped around larger structures in this study extends completely around the crater rim. At greater radial distances, rough radial and mass flow material are the dominant ejecta deposits. Both rough radial material and mass flow material extend up to 1-1.5D from the crater rim crest and both have appear to have been emplaced as surface flows which have overridden more distal deposits. The distal continuous deposits of Bamberg are dominated by smooth radial material which has commonly overridden secondary craters and crater chains. Less extensive deposits of pitted terrain material and smooth terrain material were mapped. Pitted terrain was not identified at the other impact structures studied in this project.

A comparison of the exterior deposits around Curie with those associated with Bamberg revealed certain similarities but also basic differences. The exterior deposits of both craters were dominated mass flows, lobate flows, and secondary crater fields. Curie deposits differ in both the more restricted radial extent of the ejecta facies from the crater rim, the absence of pitted terrain, and the relative importance of the various ejecta units. Both the lobate flows and mass flows at Curie have been interpreted to be the result of a surface-flow mechanism operative after original deposition at a late stage in the cratering event<sup>1</sup>. Small smooth terrain deposits were identified just outside the northern rim crest of Curie. Similar deposits were located just north of the outer ring of Lyot. The different positions of the smooth terrain deposits at Curie and Lyot relative to similar material at Bamberg make different origins and modes of emplacement possible. On the southern rim of Curie, a slump deposit, morphologically similar to lobate flows, was observed at the foot of a scarp slope on the adjacent mass flow<sup>1</sup>. This deposit extends over 70 km from its apparent source and is quite similar to certain martian landslides. It appears to have formed by the failure of one side of the mass flow after its emplacement. This relationship coupled with the large horizontal distance the material was transported from its source argue for extreme fluidity and the presence of a lubricating agent such as liquid water.

The exterior deposits around the small martian basins described above exhibit many similarities as well as some interesting differences when compared to the deposits of Curie and Bamberg. Deposits with grossly similar features occur in the same relative positions around both large craters and small basins. Differences center around detailed surface morphology and relative radial extent. All of the impact structures exhibit secondary crater fields although they are developed to different degrees. In all cases, some secondary crater clusters and chains can be seen to have been buried by surface flows originating closer to the parent structure. Evidence from the basin deposit study suggests that ballistic ejecta emplacement has been more important at these large structures. Still, a comparison of martian basin deposit extent with what would be expected if ejecta configuration was controlled primarily by ballistics and the morphology of the deposits themselves strongly suggest that radial surface flow has played an important role in the final emplacement of martian basin continuous ejecta deposits.

References: 1) P. Mouginis-Mark and J. Head (1979) LPS X, 870. 2) P. Mouginis-Mark (1979) PLPSC 10th, 2681. 3) D. Scott and M. Carr (1978) USGS Map I-1083. 4) M. Carr et al. (1977) J. Geophys. Res. 82, 4055. 5) D. Gault et al. (1975) J. Geophys. Res. 80, 2444. 6) G. McGill (1978) USGS Map I-1077. 7) C. Wood and J. Head (1976) PLSC 7th, 3629. 8) D. Wilhelms (1973) J. Geophys. Res. 78, 4084.

## BASIN DEPOSITS ON MARS: THE ROLE OF EJECTA FLUIDIZATION

P.J.Mouginis-Mark, Dept. Geological Sciences, Brown Univ., Providence, R.I. 02912; & B.R.Hawke, Hawaii Inst. Geophysics, Honolulu, Hawaii 96822.

The morphological characteristics of fluidized ejecta deposits associated with fresh impact craters on Mars have been intensively investigated in recent years (1-4). Almost unanimously, the lobate nature of these deposits has been attributed, at least in part, to the presence of subsurface volatiles within the target material. Most investigators have concentrated on craters 5-50 km in diameter (where the deposits are most prominent), but craters beyond this size range may also have some fluidized ejecta and can provide information pertinent to the physical characteristics of the martian crust. Boyce (5) and Pike (6) have demonstrated that craters smaller than about 5 km diameter typically possess ejecta that is ballistically emplaced. Similarly, as crater size increases to greater than 40 km, the fluidized ejecta is replaced by more complex deposits, with both ground-flow and ballistically emplaced ejecta observed (2,6).

This influence of target volatiles on intermediate-sized (5-40 km) craters has recently been hypothesized from crater depth/diameter measurements (7). These measurements indicated that intermediate-sized craters are unusually shallow, and may represent the product of cavity enlargement during excavation by the presence of target volatiles (7,8). In order to investigate this size dependence of ejecta deposits, we have initiated an analysis of large craters and basins on Mars (9). Our objectives are to identify the importance of ground-flow versus ballistic ejecta emplacement, and to investigate the areal distribution of martian basin ejecta. Initial observations suggest that even for craters as large as 100 km diameter, scaling relationships for equivalent craters on Mercury (10) would predict a smaller areal distribution than the one that is observed on Mars. This suggests that either ground-flow is still important for large martian craters, and/or that atmospheric effects (11) have to be invoked.

Our preliminary analyses (9) have concentrated on the basins Lyot (190 km, 50°N, 330°W) and Schiaparelli (470 km, 3°S, 343°W), because of the high-resolution Viking images acquired of these basins. Although superficially resembling lunar basins of comparable size (12), both Lyot and Schiaparelli possess complex ejecta deposits which show some evidence for ground-flow emplacement. Lyot (Fig.1) possesses lobate and mass-flow units, together with a secondary crater field, comparable to the 55 km crater Bamberg (13). Unfortunately, due to the greater state of degradation of Schiaparelli, it is unclear what the major



Figure 1: The 190 km basin Lyot ( $50^{\circ}\text{N}$ ,  $330^{\circ}\text{W}$ ) is an excellent example of a small, fresh basin on Mars: prominent are both ballistic and ground-flow ejecta deposits. Part of JPL mosaic # 211-5819.

style of ejecta emplacement was for this basin. A distinctive asymmetry exists in the observable distribution of basin deposits around Schiaparelli, but in general this may be the product of subsequent volcanic and eolian activity that has buried the basin materials. Earth-based radar measurements of basin topography (14), however, indicate that the south east rim is appreciably higher (and hence less mantled) than other parts of Schiaparelli. On the south east rim, a series of grooves radial to the basin center can be identified to a distance in excess of 200 km from the rim crest. Fig. 2 illustrates part of this linearly grooved terrain, which may either represent a large-scale analogue to the scoured rim deposits around Bamberg (9) or to the lineations identified around the lunar basins Orientale (15) and Imbrium (16).

Distinguishing between these two modes of ejecta emplacement for Mars is important for the interpretation of surface materials adjacent to large basins: fluidized ejecta could have a greater aerographic distribution than the equivalent ballistically emplaced material. Basin-sized impact events on the Moon have been shown to be important in the redistribution of crustal materials (15-17), and volatiles within the target materials may increase this phenomenon on Mars. Following the completion of our initial analyses of Lyot and Schiaparelli, we therefore intend to investigate the effects that the formation of the larger martian basins (Isidis, Argyre and Hellas) would have had on the surrounding regions of the planet.

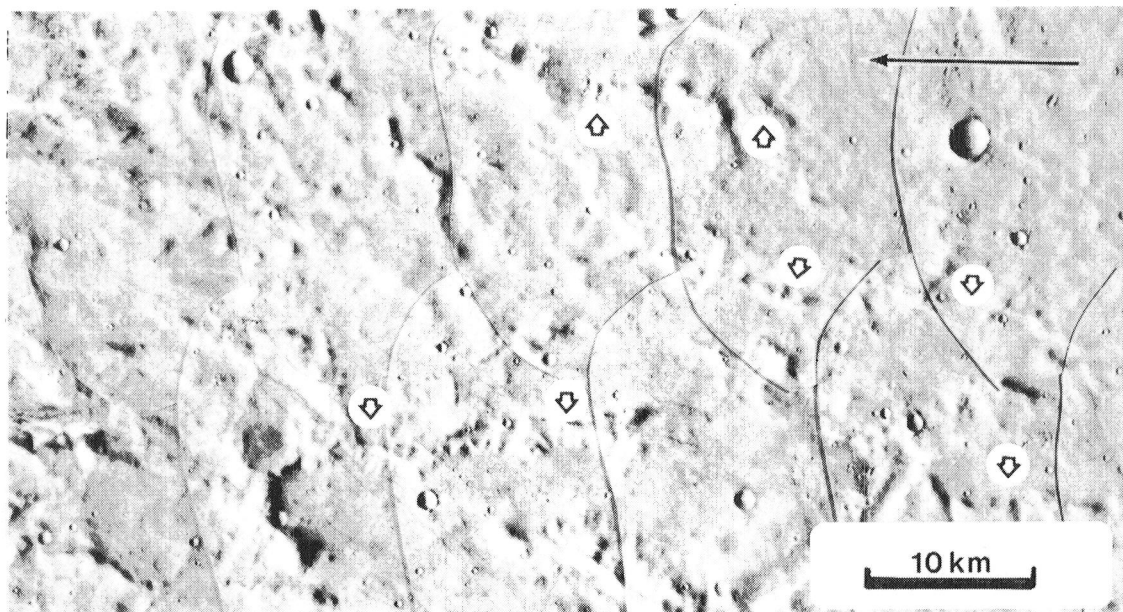


Figure 2: Radially grooved material south east of Schiaparelli at  $6^{\circ}\text{S}, 338^{\circ}\text{W}$  is illustrated here. Black arrow points toward basin center. The small arrows show four radial scarps that are believed to be associated with the basin-forming event. Viking frame nos. 749A01-12.

- REFERENCES: 1) Carr M.H. et al. (1977) J.Geophys.Res. 82, 4055-4065. 2) Mouginis-Mark P.J. (1979) J.Geophys.Res. 84, 8011-8022. 3) Mutch P. & Woronow A. (1980) Icarus 41, 259-268. 4) Greeley R. et al. (1980) PLPSC 11th, in press. 5) Boyce J.M. (1979) NASA-TM 80339, 114-118. 6) Pike R.J. (1980) PLPSC 11th, in press. 7) Cintala M.J. & Mouginis-Mark P.J. (1980) Geophys.Res.Lttrs. 7, 329-332. 8) Boyce J.M. & Roddy D.J. (1978) NASA-TM 79729, 162-165. 9) Mouginis-Mark P.J. et al. (1980) Conf.Multi-Ring Basins (abs.), in press. 10) Gault D.E. et al. (1975) J.Geophys.Res. 80, 2444-2460. 11) Schultz P.H. & Gault D.E. (1979) J.Geophys.Res. 84, 7669-7687. 12) Wilhelms D.E. (1973) J.Geophys.Res. 78, 4048-4095. 13) Mouginis-Mark P.J. (1979) PLPSC 10th, 2651-2668. 14) Downs G.S. et al. (1978) Icarus 33, 441-453. 15) Moore H.J. et al. (1974) PLSC 5th, 71-100. Head J.W. (1976) The Moon 15, 445-462. 17) Head J.W. et al. (1975) PLSC 6th, 2805-2829.

CENTRAL PEAKS IN MARTIAN CRATERS: COMPARISONS TO THE MOON AND MERCURY. Hale, W., and Head, J.W., Dept. of Geological Sciences, Providence, RI 02912

Central peaks are prominent morphologic features in fresh martian craters. Previous workers have established their occurrence as a function of crater diameter and type (1), general substrate type (2) and as a function of specific substrate type, crater altitude (above mean Mars datum) lat/long and ejecta type (3). Martian central peaks may display a summit pit, or be entirely replaced by a centered circular pit (4,2,5,6).

Studies of the morphology and morphometry of fresh craters as defined by Arthur (1963) (7) can yield important data on the impact process as a whole and on the nature of the target materials (8,9,10). Studies of central peaks in lunar and mercurian craters have demonstrated that a linear relationship exists between rim diameter and central peak diameter (11). This relationship does not vary significantly from the Moon to Mercury despite differences in gravitational field strengths and modal impact velocities (12). A similar relationship for peak height also remains statistically constant on both planets (13). Finally central peaks in lunar and mercurian craters may be morphologically classified under the same scheme, and display similar variations in morphology as a function of diameter and terrain type (12).

Central peaks in martian craters differ in at least one aspect from those developed in lunar and mercurian craters--the presence of summit or central pits. These pits have been suggested to result from explosive decompression of a volatile-rich layer in the substrate (14,5,2). Thus the distribution of pits has been suggested as a tool to map the areal extent of subsurface volatiles. Recent studies indicate that pits occur over a wide range of substrate types (6). However, no attempt has yet been made to correlate the number of pitted craters to the number of total central peak craters for different terrain types. The purpose of this study is 1) characterize the morphology and morphometry of central peak and central pits in martian craters; 2) to determine the relationship between these features and terrain type; 3) to compare these to similar ones derived for the Moon and Mercury. The preliminary results presented here consist of data from 145 fresh craters in the western half of Memnonia quad, a region south and west of the Tharsis plateau. This region is mapped as rolling plains and ancient terrain cut by a few channels in the north (15). All data are derived from Viking Orbiter images, U.S.G.S. topographic map series.

Central Peak and Pit Morphometry--of the 145 fresh (3) craters in this study, 137 have central peaks, with or without summit pits. The remaining 8 craters include 6 with central pits only and 2 indeterminants. Of the craters with central peaks (137), 134 (97.8%) display a consistent linear relationship between central peak diameter (Dcp) and rim crest diameter (Drc) defined as  $Dcp = 0.27 Drc - 0.1411$  ( $r = 0.90$ ) for a population diameter range of 5-80 km (Figure 1). A similar relation is identified between Dcp and floor diameter (Df),  $Dcp = 0.45 Df + 0.25$  ( $r = 0.92$ ). The three craters which diverge from this relationship (Nicholson, MC16-Sn, MC16-Rt) display unusual morphologies. Nicholson has a very large central mound with incised channels, while MC16-Sn and ME16-Rt both have small linear peaks which appear to be partially embayed and unusually wide, draped floors. Craters developed in ancient terrains make up 91.1% of this data set, while 7.4% are in rolling plains units and 1.5% occur in channel deposits.

Pits, either alone or as summit pits in central peaks, occur in 39 craters and a linear relationship may also be defined between pit diameter (Dp) and Drc,  $Dp = 0.11 Drc + 0.22$  ( $r = 0.67$ ). The correlation coefficient (r) for this

relationship is low, owing to one crater which has an unusually large, non-circular summit pit. The remaining 38 follow the Dp/Drc relation more closely (Figure 2).

Morphology of Central Peaks and Pits-central peaks in martian craters may be classified by complexity (simple, complex) and geometry (linear, symmetric or arcuate) as was done previously for lunar and mercurian craters (11,12). However, additional categories are required to characterize crater pits. Pits may occur as depressions in the top of central peaks (summit pit craters), which are either circular or elongate, open or closed. Closed, circular pits fit the classic picture of a summit crater, and 75% of the pits are of this type. The rest are either semi-circular summit pits with one section of peak missing, (open circular, 6.25%) or elongate fissures which are either open or closed (18.75%). Pits may also occur in place of central peaks (central pit craters) and these have either raised or flat rims. Six central pit craters are found in West Memnonia, of which 5 have raised rims while only 2 have flat rims.

The distributions of central peak types as a function of substrate type may be seen in Table 1 and 2. Pits (summit or central) are more common on rolling plains units than on ancient terrains, 85-90% of all craters have simple peaks and 62% have symmetric peaks regardless of terrains and arcuate peaks are more favored on the rolling plains units. Both channel craters have indeterminate peak morphology.

Comparisons to Moon and Mercury-the Dcp/Drc relations for the Moon and Mercury are plotted for comparison on Figure 1. The slopes of these relations are statistically indistinguishable from each other (12). However, they are markedly different from that for martian central peak craters. This would suggest that the central peaks of martian craters are larger than those of the Moon and Mercury for similar crater diameters. It should be noted here that these are preliminary conclusions for a restricted region of predominantly high altitudes (>1 km above mean Mars datum) and ancient terrains.

Central peaks with complex form and those of either linear or arcuate geometry are much more common on the Moon or Mercury. Geometry appears somewhat responsive to substrate type on all three planets.

Discussion-Preliminary examination of a restricted region of predominantly ancient terrain in Western Memnonia has suggested the existence of a linear relationship between Dcp/Drc for Mars which is analogous to that defined previously for the Moon and Mercury. However, the slope of the relationship for Mars is much steeper, indicating central peaks on Mars are larger than on the Moon or Mercury for similar crater diameters. Since Mars and Mercury have similar gravitational field strengths, this would suggest some terrain effect for Mars. The existence of pits has been proposed to be a result of a subsurface volatile layer (14,5,2). Volatiles dispersed more generally throughout the target result in a decrease in mechanical strength (16) and could result in proportionally larger central peaks. Morphological data indicate that simple, symmetric peaks are more common on Mars than on the Moon or Mercury although terrain effects on relative distributions of morphologic types are similar on all three planets. Bit distributions have been suggested as a method of tracing the areal extent of subsurface volatiles (2). Although pits occur globally on Mars (6), it appears that the distribution of central or summit pits to unpitted central peaks varies as a function of terrain type (Table 1). Mapping of subsurface volatiles may thus be possible through detailed studies of pit and peak distributions in fresh craters. Preliminary results for a restricted region indicate the importance of planetwide mapping of central

peak and pit crater morphology and morphometry on Mars. Such studies are currently underway. References: 1) Cordell, B.M. et al (1974) *Icarus* 21 p.448-456. 2) Wood, C.A. et al (1978) *PLSC* 9 p.3691-3709. 3) Mouginis-Mark, P.J. (1979) *JGR* 84 p.8011-8022. 4) Smith, E.I. (1976) *Icarus* 28 p.543-550. 5) Hodges, C.A. (1978) *LPS* XI p.521-523 (abst). 6) Hodges, C.A. et al (1979) *LPS* XI p.450-452. 7) Arthur, D.W. et al (1963) *Comm. LPL* 2, p.71-78. 8) Cintala, M.J. (1979) in *Impact and Explosion Cratering* (D.J. Rodely et al eds.), 575-591. 9) Cintala, M.J. et al (1977) *PLSC* 8 p.3409-3425. 10) Pike, R.J. (1979) in *Impact and Explosion Cratering* (D.J. Rodely et al eds.) p.489-509. 11) Hale, W. and Head, J.W. (1979) *PLPSC* 10, p.2623-2633. 12) Hale, W. and Head J.W. (1980) *PLPSC* 11, in press. 13) Malin, M. and Daurisin, D. (1978) *JGR* 83 p.233-243. 14) Smith, E.I. and Hartnell, J.A. (1977) *NASA JMS-3511* p.91-93. 15) Scott, D.H. and Carr, M.H. (1978) *U.S.G.S. Map I-1083*. 16) Kietter, S.W. (1977) *LSVII* p.543-545 (abst.)

Figure 1

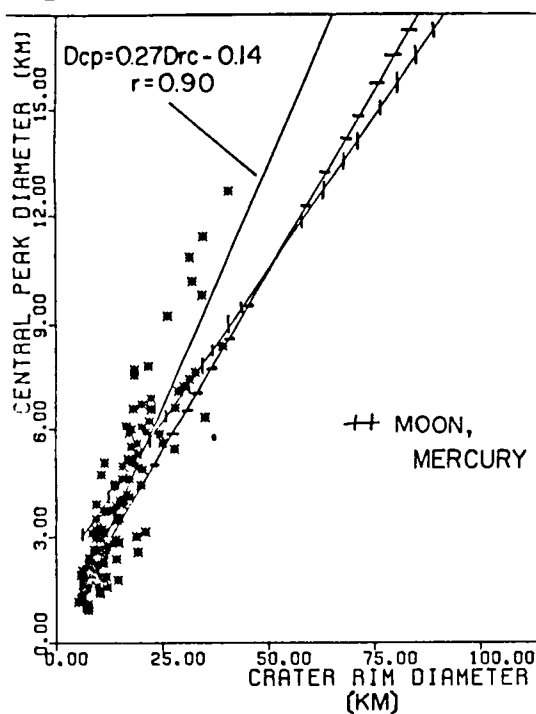


TABLE 2

	ANCIENT TERRAIN	ROLLING PLAINS	CHANNELS
<b>Complexity</b>			
Simple	(116) 87.8%	(10) 90.9%	(0) 0
Complex	(11) 8.4%	(0) 0%	(0) 0
IND	(5) 3.8%	(1) 9.1%	(2) 100%
<b>Geometry</b>			
Symmetric	(83) 63%	(7) 63.6%	(0) 0
Linear	(40) 30%	(2) 18.2%	(0) 0
Arcuate	(4) 3.8%	(1) 9.1%	(0) 0
IND	(5) 3.8%	(1) 9.1%	(2) 100%

Figure 2

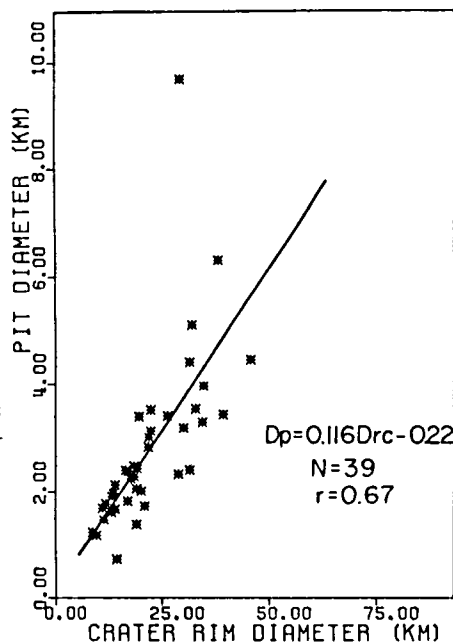


TABLE 1

TERRAIN	PEAK	PEAK & PIT	PIT	IND	% PEAKS ALONE	% PITS
Ancient terrain	99	28	5	0	75%	25%
Rolling plains	7	3	1	0	64%	36%
Channels	0	0	0	2	--	--



## STATISTICAL ANALYSIS OF CENTRAL-PEAKED CRATERS ON MARS.

A. H. Hamdan and Farouk El-Baz, National Air and Space Museum, Smithsonian Institution, Washington, D.C. 20560.

Central peaks, which are common in craters of the terrestrial planets, are attributed to the high stress associated with shock and rarefaction waves concentrated at the sub-impact point during crater formation (1;2). The morphology of central peaks on Mars has been studied and classified into four peak/pit structure categories (3): A) central peak with no pit; B) central peak with relatively small summit pit; C) massive central peak with large summit pit; and D) nearly rimless central pit. Central peaks in craters on Mars are mostly oriented in a northwest direction (4).

The purpose of this study is to examine the frequency distribution of the peak/pit structures on different types of terrain, relate the crater degradation processes to the shape of central peaks, differentiate the size distribution of central-peaked craters, and find out whether there are any preferred orientations in the shape of crater rims, peaks, or pits induced by local or regional forces over geologic time, and on different types of terrain.

Data collected for this study are based on 22 U.S. Geological Survey mosaics at 1:2,000,000 scale. These mosaics cover the Memnonia (MC-16), Phoenicis Lacus (MC-17), Coprates (MC-18), southern half of Margaritifer (MC-19), southern half of Sinus Sabaeus (MC-20), Aeolis (MC-23, except the NE of the quadrangle), and the northern half of Argyre (MC-26) regions.

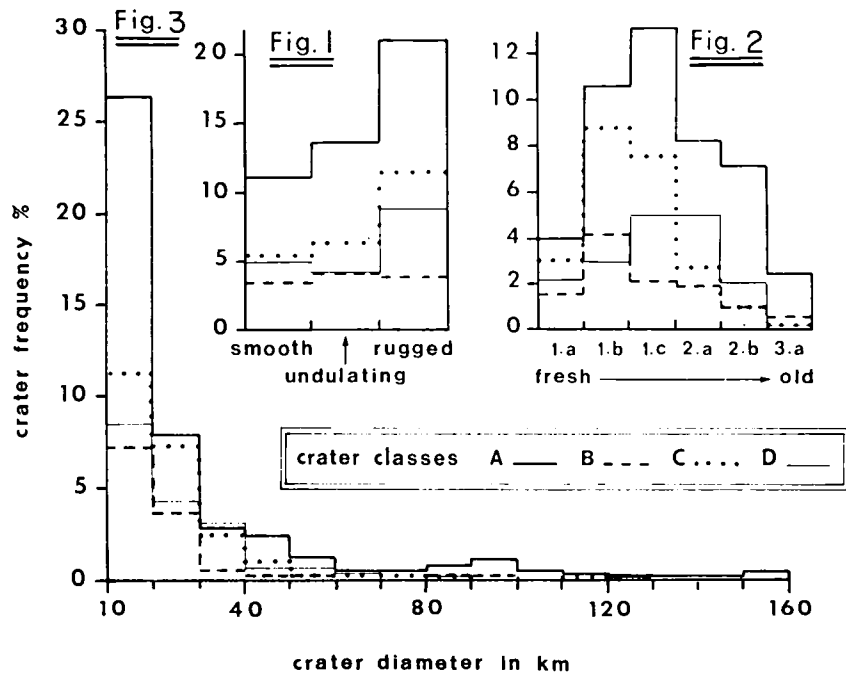
The 595 central-peaked craters studied in the mosaics were examined and classified according to the above-mentioned peak/pit structures. Their ages were assigned according to the same scheme used to classify lunar and mercurian craters (5;6), and the terrain was described as smooth, undulating, or rugged.

From the distribution of peak/pit structures by terrain type (Fig. 1), central-peaked craters are well preserved in the rugged terrain (3), but class B is not. Class A is the most frequent shape in all types of terrain especially in the rugged terrain. Each type of peak/pit structure occurs in the same abundance in the three types of terrains. This indicates that the peak/pit structures are insensitive to substrate type.

The age distribution of craters (Fig. 2) shows that class A has the maximum frequencies in all geologic times and class B has the minimum, except in classes 1.b and 3.a. Class D changes positions with class C; it is less in the fresh craters (1.a, 1.b, and 1.c), and more common in the older ones (2.a, 2.b, and 3.a). This may be due to either the formation of large pits in the older craters or to crater degradation.

The size distribution of the peak/pit structures (Fig. 3) shows that class A is by far the most common in the 10-20 km diameter range. This size range constitutes 53% of the crater population studied and half of these craters are in class A. In the larger craters, class A is also dominant. Craters larger than 130 km in diameter do not show any of the other 3 classes.

From the total number of craters studied, 96 have elongate rims, 172 have elongate central peaks, and 66 have elongate central pits. We also measured 44 elongate rims of craters with no central peaks or pits. The

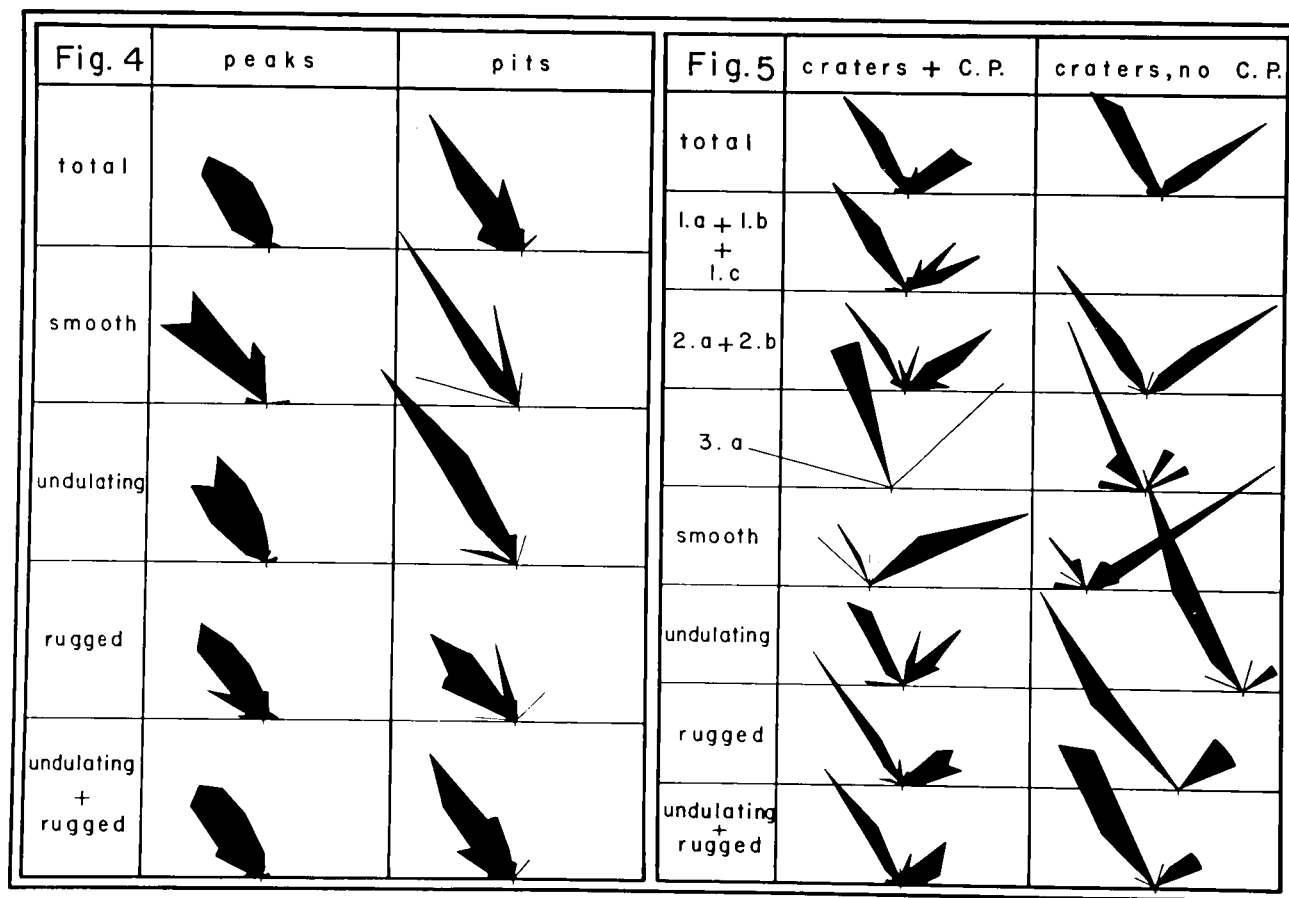


Graphs showing the frequency percent of peak/pit structures in terrain types (Fig. 1), degradation classes (Fig. 2), and crater diameter (Fig. 3).

main orientation of central peaks is  $N20^{\circ}-50^{\circ}W$  (Fig. 4) and this trend prevails in all types of terrain. The central pits have a smaller range of orientation,  $N30^{\circ}-40^{\circ}W$ , with the minor trends of  $N10^{\circ}-20^{\circ}W$  and  $N60^{\circ}-80^{\circ}W$ . This NW direction may be attributed to global structural control. The elongate rims of craters with central peaks or pits have two main perpendicular trends,  $N30^{\circ}-40^{\circ}W$  and  $N40^{\circ}-70^{\circ}E$  (Fig. 5). The old craters (class 3.a) and the craters on the rugged terrain have approximately the same trends  $N10^{\circ}-30^{\circ}W$  and  $N30^{\circ}-40^{\circ}W$  respectively. This is also seen in craters without central peaks, which are oriented  $N20^{\circ}-40^{\circ}W$  and  $N50^{\circ}-60^{\circ}E$ . The old craters (class 3.a) are oriented  $N20^{\circ}-30^{\circ}W$  and the craters on rugged and undulating terrains are oriented  $N20^{\circ}-40^{\circ}W$ . The NW and NE trends of young, elongate craters may be due to the global structural control; the lack of the NE trend in old craters may indicate either a weaker stress in this direction in the planet's early history, or preferential obliquity of impacts.

#### References

1. Head, J.W. (1978) Lunar Sci. 9, p. 485-487.
2. Milton, D. and D.J. Roddy (1972) IGC, Sess. 24, p. 119-124.
3. Wood, C.A. et al. (1978) Proc. LPSC 9th, p. 3691-3709.



Orientations of central peaks and pits (Fig. 4) and of craters with and without central peaks (C.P., Fig. 5)

4. Hamdan, A.H. and F. El-Baz (1980) Lunar Sci. 11, p. 388-390.
5. Wood, C.A. and J.W. Head (1977) Proc. LSC 8th, p. 3503-3520.
6. Wood, C.A. and L.F. Anderson (1978) LPL Catalog, NASA TM-79238.

## NON-CIRCULARITY OF MARTIAN IMPACT CRATERS: CLUES TO HIDDEN STRUCTURES?

R.W. Wolfe, National Air and Space Museum, Washington, D.C. 20560 and M.L. Hutson, University of Minnesota, Minneapolis, MN 55455

### Background

Numerous studies have shown that crater morphology is related, in part, to the nature of the target materials. Layering in the target, for example, has a profound effect on the cross-sectional shape of craters (Quaide and Oberbeck, 1968). Except for very low-oblique impacts, craters are quite circular in plan when formed; subsequent erosion by cratering and mass wasting modify this shape. Deviations from circularity may also be related to lateral discontinuities or inhomogeneities in the target. Meteor Crater is a notable example. Its squared-off sides are parallel to the prominent joint set in the region (Roddy, 1978). Eppler et al (1978) have found that many lunar craters are somewhat elongate and that the directions of these elongations are aligned with structural features in the lunar crust such as mare ridges and rilles.

### Methods

We have analysed the shapes of 817 craters in the south equatorial region of Mars. Crater rim crests were traced from nineteen 1:2,000,000 scale USGS photomosaic maps and the outlines were digitized. All craters with diameters greater than about 12 km were studied, with the exception of those whose rim crests were discontinuous due to modification or to mosaicking flaws.

For each crater outline, a Fourier series of 20 harmonics was computed. The mathematical techniques of these computations for closed shapes is given in Ehrlich et al (1970); a qualitative treatment of the shapes of the various harmonics and their summation to approximate "circular" figures may be found in Eppler et al (1977). The amplitude of the second harmonic may be taken as a measure of the degree of elongation of a crater shape. The phase of this harmonic is the direction of maximum elongation (Eppler, 1978).

For each of the nineteen quadrangles we have prepared circular histograms of crater frequency vs. direction of elongation in 10 degree bins. (Fig. 1). Also displayed are the trends of major structural features, including fossae, dorsa, and valles, generalized from the 1:5,000,000 scale USGS airbrush maps.

## Discussion

For most of the of the map regions comprising the study area, the rose diagrams appear to reveal non-random distributions of the orientations of crater elongation. There is, in general, no strong, overall correlation between crater elongation directions and the trends of major structural features. Some coincidences of alignment, however, do appear to be significant. These include the Al-Qahira, Ma'adim, and Marineris valles; the Medusae, Memnonia, Claritas, and Sirenum fossae; and the Solis, Melas and Felis dorsa.

Few correlations with smaller scale features such as the lineaments mapped by Wilson et al (1973) and Harp (1974) are noted with the exception of those in the region of Vallis Marineris that trend obliquely to the major structural trend. There is, however, a significant coincidence between the major direction of crater elongation (NNW) in the four quadrangles comprising MC-16 and the observations of Hamden and El-Baz (1980) for elongation of crater central peaks in the same region. Apparently craters here have responded in two different ways to a presumably structural influence that is not otherwise manifest.

These data, as presented, are raw and probably somewhat noisy in that there has been no selection or weighting according to how much craters are elongated. It is hoped that such refinement of the data and separating the craters by size (hence depth) will either clarify some ambiguities or point to some hidden structural trends in the south equatorial region of Mars.

## References

- Ehrlich, R. and B. Weinberg, An exact method for characterization of grain shape. Jour. Sed. Pet. 40 (1970) 205-212.
- Eppler, D.T., D. Nummedal, and R. Ehrlich, Fourier analysis of planimetric lunar crater shape— possible guide to impact history and lunar geology. in Roddy, D.J., R.O. Pepin, and R.B. Merrill, eds., Impact and Explosion (1977) 511-526.
- Eppler, D.T., D. Nummedal, and R. Ehrlich, Structural implications of lunar crater elongation. Lunar and Planet. Sci. IX (1978) 294-296.
- Hamden, A.H. and F. El-Baz, Orientation of central peaks in craters on Mars. Lunar and Planet. Sci. XI (1980) 388-390.
- Harp, E.L., Fracture system of Mars. Proc. 1st Conf. New Basement Tectonics (1974) 389-408.

Quaide, W.L. and V.R. Oberbeck, Thickness determinations of the lunar surface layer from lunar impact craters. *J. Geophys. Res.* 73 (1968) 5247-5270.

Roddy, D.J., Pre-impact geologic conditions, physical properties, energy calculations, meteorite and initial crater dimensions and orientations of joints, faults and walls at Meteor Crater, Arizona. *Proc. Lunar Planet. Sci. Conf. 9th* (1978) 3891-3930.

Wilson, R.C., E.L. Harp, M.D. Picard, and S.H. Ward, Chaotic terrain of Mars: A tectonic interpretation from Mariner 6 imagery. *Geol. Soc. Am. Bull.* 84 (1973) 741-748.

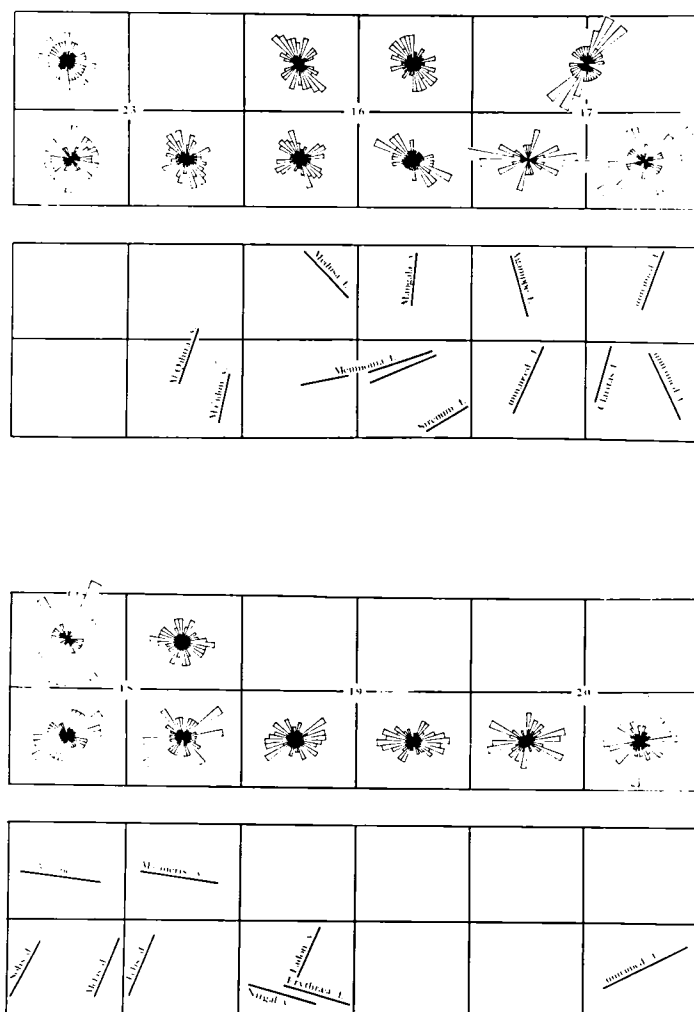


Figure 1.

## DEPTH/DIAMETER RELATIONSHIPS FOR LARGE MARTIAN CRATERS: RADAR RESULTS

L.E. Roth, G.S. Downs, R.S. Saunders, Jet Propulsion Laboratory,  
California Institute of Technology, Pasadena, California 91103;  
G. Schubert, Department of Earth and Space Sciences, University of  
California, Los Angeles, California 90024.

The Goldstone Mars data (Downs *et al.*, 1975) have been used to obtain detailed morphometric information on martian craters. Some qualitative results of this effort have been reported previously (Roth *et al.*, 1978). Radar signatures of a total of 131 impact craters in the diameter range from 20 km to 500 km, all located within a narrow subequatorial belt of martian latitudes, have been recognized. Depths of these craters have been determined with a varying degree of confidence. The data confirm the overall shallowness of the martian craters, an observation made as early as the time of Mariner 4 and since then reproduced by every investigator (Pike, 1971; Burt *et al.*, 1976; Cintala *et al.*, 1976; Malin and Dzurisin 1977; Schubert *et al.*, 1977; Cintala and Mouginiis-Mark, 1980). The measured radar depths of most of the 87 objects comprising the higher-confidence grouping cluster between 1 km and 2 km. Consequently, the least-squares fit to the relationship of the log depth versus the log diameter is markedly less steep than a similar curve derived from the Mariner 9 UVS altimetry (Cintala *et al.*, 1976) (Fig. 1a). Thus the depths of a mixed-age, unevenly degraded, and geographically restricted radar sample of martian craters ( $D_i > 20$  km) are only a weak function of diameter.

If the crater depth measurements are split into two subgroups, one with diameters less than 125 km and the other with diameters greater than 125 km (the dividing diameter of 125 km chosen arbitrarily), and the depth/diameter ratios for each subgroup are fitted in the least-squares sense, a pronounced break in slopes, a "knee," at the junction of both fits can be observed (Fig. 1b). Since the 125 km diameter division was arbitrarily chosen, we cannot be sure that the knee in the depth/diameter relation actually occurs at this diameter. However, these results do suggest that a knee exists somewhere in the diameter range from 100 km to 200 km. It is seen that for  $D_i \geq 125$  km the averaged depths of the sampled martian craters become virtually independent of the crater size. Therefore, a power-law least-squares fit of the depth/diameter relationship for a mixed-age crater population, taken over the full range of diameters as in Fig. 1a, obscures a possibly significant change in the depths/diameter curve for Mars. Clarification of this matter will have to be postponed until more data are available.

Because of the proximity of the radar depth/diameter curve to the lower boundary of the envelope containing the depth/diameter ratios of pre-Imbrium lunar craters (Pike, 1971, Cintala *et al.*, 1976), it has to be concluded that the large martian craters contained in the radar compilation are substantially shallower and hence substantially more modified than the lunar craters of corresponding age and size. This should come as no surprise since the martian craters appear to have been excavated to

shallower depths (Cintala and Mouginis-Mark, 1980), and have unquestionably been exposed to a more erosive environment and a more vigorous gravitational settling. In addition, the radar results show certain large martian craters to be modified by some process that tilted the crater floors relative to the horizontal plane, thus enhancing their shallow visual appearance. Similar crater floor modification has not been detected on the moon. Also, the Apollo Lunar Sounder radar images revealed the centers of the floors of some large lunar craters to be domed upward by several hundred meters (Elachi *et al.*, 1976). No such effect has been observed in the Goldstone Mars data.

The shallow depths of the large martian craters, the modest slope of the depth/diameter curve at large diameters, and the absence of crater floor doming can be interpreted in two ways: (1) Compared to their lunar counterparts, the large martian craters have undergone a more complete post-impact structural adjustment. As a result, the doming, presumably an intermediate phase in such a process, has vanished and the floors of the large martian craters are structurally flat. (2) The large martian craters have retained a structural bulge but it has been obliterated by a blanket of eolian/fluviol/volcanic deposits. If the latter is true, then modification by erosion and deposition is a significant process of landform and crater degradation on Mars.

#### References

- Burt, T., Veverka, T., and Cook, K. (1976). Icarus **29**, 83-90.
- Cintala, M.J., Head, T.W., and Mutch, T.A. (1976). Proc. Lunar Sci. Conf. 7th, 3575-3587.
- Cintala, M.J. and Mouginis-Mark, P.J. (1980). Geophys. Res. Lett. **7** (329-332).
- Downs, G.S., Reichley, P.E., and Green R.R. (1975). Icarus **26**, 273-312.
- Elachi, C., Kobrick, M., Roth, L., Tiernan, M., and Brown, W.E. (1976). Moon **15**, 119-131.
- Malin, M.D., and Dzurisin, D. (1977). J. Geophys. Res. **82**, 376-388.
- Pike, R.J. (1971). Icarus **19**, 384-395.
- Pike, R.J. (1974). Geophys. Res. Lett. **1**, 291-294.
- Roth, L.E., Elachi, C., Saunders, R.S., and Schubert, G. (1978). Lunar and Planetary Science IX, 976-978.
- Schubert, G., Lingenfelter, R.E., and Terrile, R.J. (1977). Icarus **32**, 131-146.



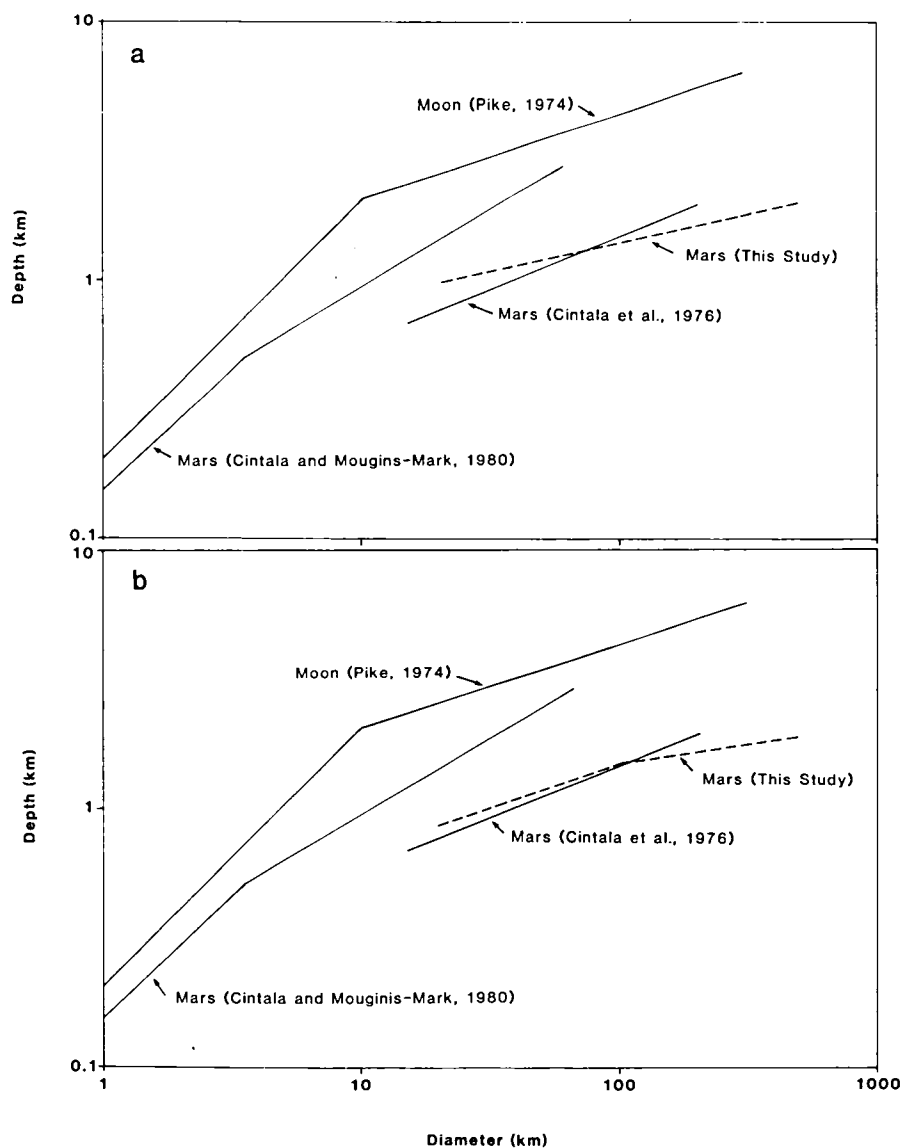


Figure 1. (a) Power-law least-squares fit to the depth/diameter ratios of 87 martian craters in the diameter range from 20 km to 500 km. (b) Similar fits to the same sample subdivided into two subgroups. The curves for the fresh lunar craters (Pike, 1974) and the fresh martian craters (Cintala and Mougins-Mark, 1980) serve as reference.

## LABORATORY SIMULATIONS OF CENTRAL PIT CRATERS

Fink, Jon and Ronald Greeley, Department of Geology, Arizona State University, Tempe, AZ 85281 and Donald E. Gault, Murphys Center for Planetology, Murphys, CA 95247

Among the most puzzling features of impact craters on the Galilean satellites is the predominance of central pits in the larger craters. Analysis of Voyager images of Ganymede shows a strong correlation between crater morphology and diameter in both the old, dark and young, grooved terrains: central peaks form in craters below approximately 13 km in diameter, flat floors predominate in craters 16-25 km and central pits are found in most craters 30 km and larger. To test the hypothesis that these different crater morphologies reflect differences in crustal structure, we performed a series of 64 hypervelocity impact experiments into multilayered targets. Central pits formed in targets comprised of a surface layer of dry shell particles overlying a substrate of mud, if the surface layer was of a critical thickness. If the crust was too thick, the lower substrate was not involved and a bowl-shaped crater formed, completely in the surface layer. For thinner crusts, a central peak of substrate material rose through and spilled over the surface layer. At a critical thickness, a narrow central peak projected through the center of a bowl-shaped crater and then fell directly back, leaving a central depression with a diameter about one fifth that of the crater. Impacts into water overlain by silicon oil (viscosity contrast =  $3 \times 10^4$ ) showed the same process: a central "finger" poked through the viscous surface layer and receded, leaving a pit which, for these strengthless materials, was not preserved. Scaling of the strengths and dimensions of these simulated layers to properties estimated for the crust of Ganymede may allow calculation of the crustal thickness at the time of impact.

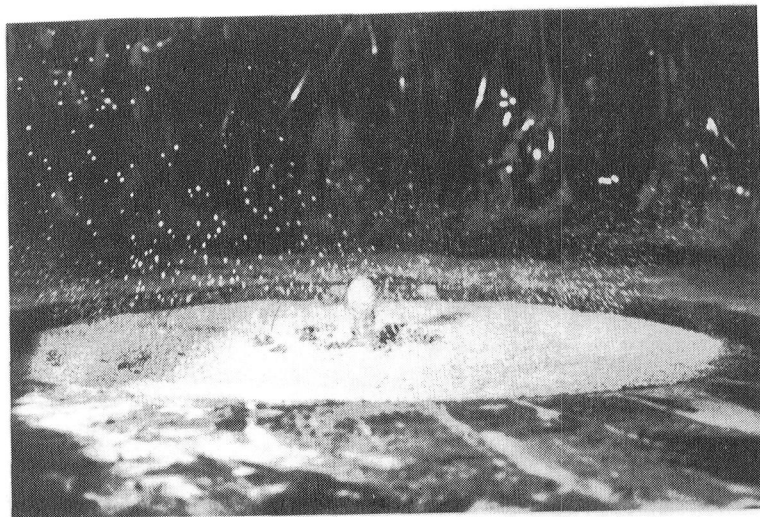


FIGURE 1A. "Stop motion" image of shot 800535 involving impact of pyrex sphere fired at  $1.57 \text{ km sec}^{-1}$  into 25 mm layer of unbonded particles underlain by viscous clay; a very narrow column of viscous material rose, then collapsed, leaving a small, central depression.

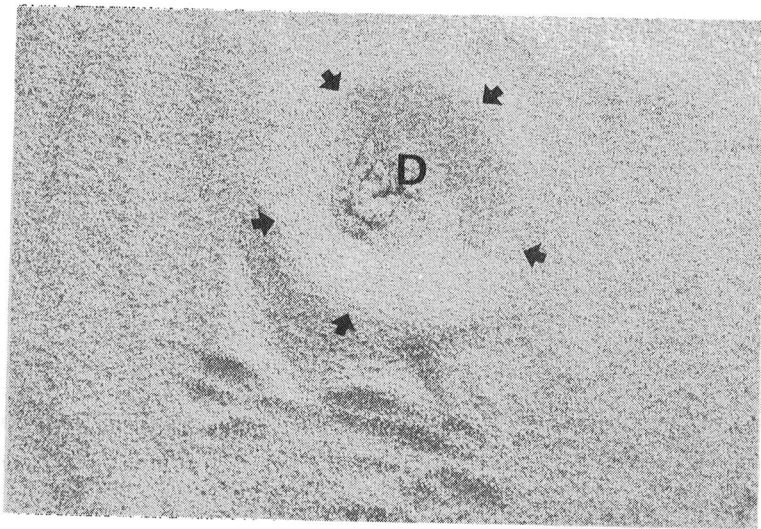


FIGURE 1B. Post-impact vertical view of Shot 800535 (Figure 1A). Arrows outline crater rim, "D" indicates central depression.

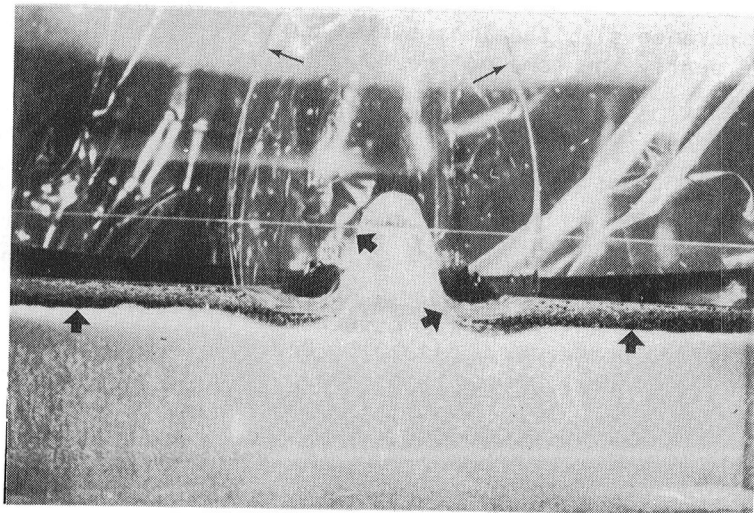


FIGURE 2. "Half space" impact experiment involving an upper layer of viscous silicon oil (above the large arrows) overlying water, showing the development of a central mound derived primarily from the water layer; thin arrows showing edge of ejecta plume.

#### MARTIAN CRATERING REVISITED.

Michael C. Gurnis, Lunar and Planetary Laboratory, University of Arizona,  
Tucson, Arizona 85721

The cratering record of Mars has been a subject of debate. The post-Mariner 9 view of martian history was dictated by hypotheses of planet-wide crater oblitative episodes. These possible episodes were studied by Chapman and Jones (1977) through the statistics of subjectively classed craters. The validity of these studies has been questioned by Woronow (1980). However, up to now data collected from Viking imagery has not been examined to corroborate or disprove these hypotheses. We are currently making the required measurements for craters > 8 km diameter in the martian southern cratered terrain.

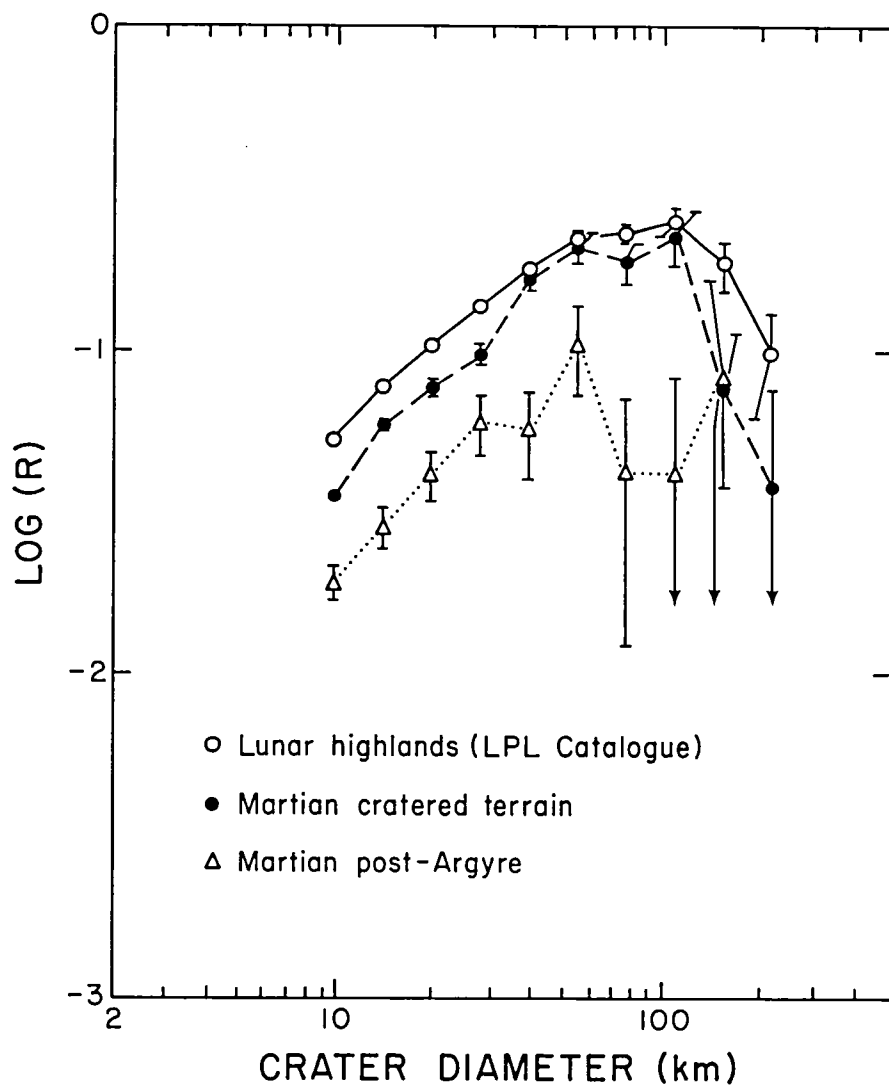
We have now measured craters over parts of MC-22NE, MC-22SE, MC-23SW, and MC-26NC. We have excluded craters on units which are clearly younger plains; such units were identified by the presence of wrinkle ridges and the paucity of superposed craters. The data are presented in Figure 1, along with the average front-side lunar highlands curve.

Overall, we find two similarities between the cratered areas on Mars examined in this study and the lunar highlands' data: 1) the overall crater densities are nearly equal, and 2) they have the same crater diameter distribution function. These two observations strongly indicate that there was no global crater oblitative episode on Mars. Instead, the events which erased martian craters arose from a number of mechanisms that were more regional in their effects.

Hostetler and Drake (1980) have made thermal model calculations showing all the terrestrial planets underwent global melting at about the same time. Because the size-density distribution for martian and lunar craters are so similar, and because both planets started recording impacts contemporaneously, the impact flux during heavy bombardment must have been nearly the same on the Moon and Mars.

#### REFERENCES:

- Chapman, C. R. and Jones, K. L. (1977). Ann. Rev. Earth Planet. Sci. 5, 515.
- Woronow, A. (1980). An analysis of crater classes of the Moon and Mars, Advances in Planetary Geology, in press.
- Hostetler, C. J. and Drake, M. J. (1980). On the Early Global Melting of the Terrestrial Planets, Proc. Lunar Planet. Sci. Conf. XI, in press.



## CRATERING RECORD IN THE INNER SOLAR SYSTEM.

Alex Woronow, Robert G. Strom and Michael C. Gurnis, Lunar and Planetary Laboratory, University of Arizona, Tucson, Arizona 85721

The larger-crater population of the lunar highlands is not at saturation density.

The ramifications of that little-appreciated fact are tremendous: The ancient history of the highlands remains there to be read; the imprint of the size-frequency distribution of the impacting bodies may be recovered from the observed crater distribution; and the impact histories of different terrains and different planets can be meaningfully compared to that preserved in the ancient lunar highlands. In fact, many recently developed lines of evidence support the hypothesis that on some terrains of all of the heavily cratered bodies thus far studied (Moon, Mercury, Mars, Ganymede and Callisto) the observed large-crater populations (craters >8 km diameter) bear a reasonable likeness to their production functions.

Many new insights into the cratering histories, based on new data sets, new simulations, and new theoretical treatments, show: (1) The lunar highlands are not saturated at crater diameters larger than at least 8 km. (2) The observed size-frequency distribution function for the large craters on the lunar highlands is essentially identical to the production function which generated them. (3) Neither the observed size-density function for the larger craters nor their production functions follow a simple power law relationship. (4) Extrapolating information on saturation conditions obtained from small craters to these larger craters is not valid. (5) Extrapolating the larger-crater curve to much smaller diameters by using a simple power law to represent the highlands population grossly misrepresents the highlands data and consequently does not provide a meaningful reference line at the small crater diameters.

Obviously if the lunar highlands are not saturated with craters greater than 8 km, then the mare surfaces also are not saturated at comparable crater diameters. Therefore, the post-mare crater population is a production population in this size range. That crater population has a production function which is significantly different from that of the highlands population over the same diameter range (Figure 1).

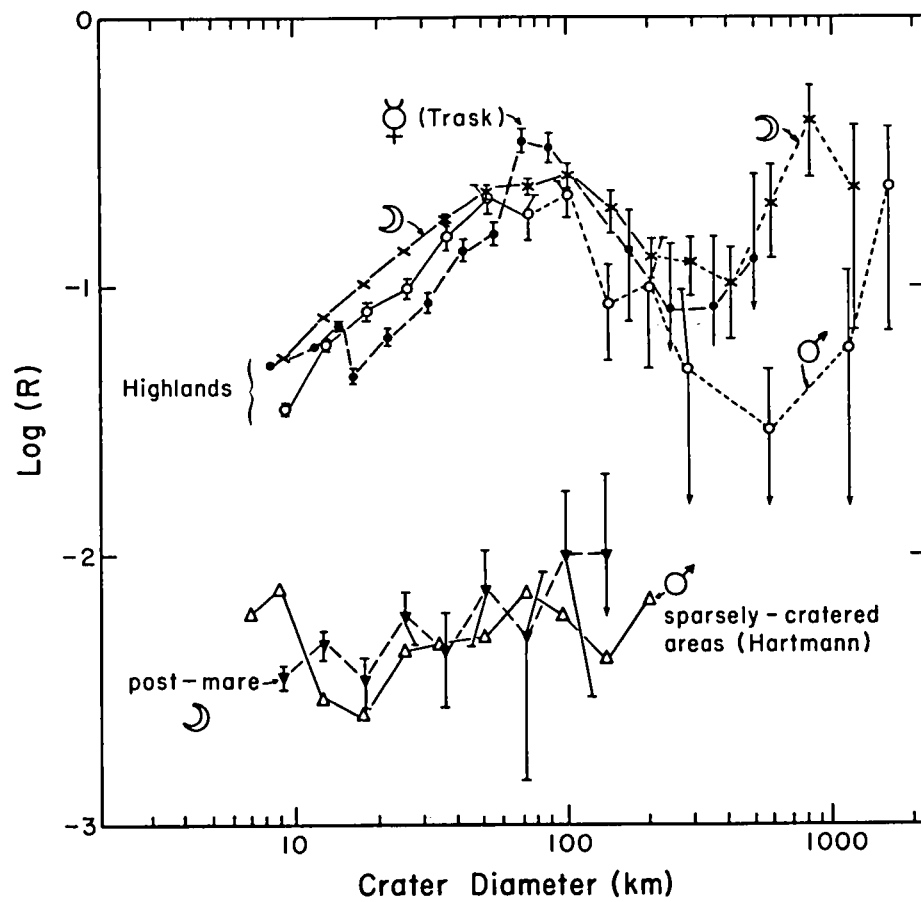
Mercury: The post-Caloris crater curve is virtually identical in both crater density and slope to that of the lunar post-Oriente curve (Strom, 1979; Figure 20), which, in turn, is the same as the lunar highlands curve. This suggests that the ancient production function is very similar, perhaps identical, for both bodies. Furthermore, the most densely cratered terrains on both bodies have similar total crater densities. (Figure 1). To date, a younger crater population similar to the lunar post-mare population has not been recognized on Mercury (Strom, 1979). Perhaps, either it never reached Mercury in numbers large enough to leave a recognizable signature, or the youngest surfaces on Mercury were formed earlier than the lunar maria, when the objects responsible for heavy bombardment of the highlands still dominated.

Mars: In the southern cratered terrain, if one carefully excludes smooth plains units with few superposed craters and with wrinkle ridges, then the size-density distribution on the truly ancient surfaces is virtually identical (Figure 1) to that of the Moon in both crater density and size-frequency distribution function (Gurnis, 1980). The similarity of cratering records between Mars and the Moon extends farther: The northern plains of Mars record an impacting population with a size-frequency distribution function markedly different from that of the ancient terrains, yet almost identical to that found on the lunar maria.

Synthesis: In summarizing the facts now known about the cratering records of the terrestrial planet, we are first confronted by the great similarities they exhibit. The most ancient, most heavily cratered terrains, of the Moon, Mercury and Mars record a complex-shaped crater curve that differs little from one planet to the next in either density or shape. This may be interpreted, in light of studies suggesting that all three bodies underwent crustal melting at about the same time (Hostetler and Drake, 1980), to imply that the same ancient impacting population reached all three bodies with about the same flux rate. A similar relationship holds for the crater populations of the lunar maria and the martian northern plains. But their size-frequency distribution is different from that of the ancient terrains. These data strongly suggest that two populations of objects have impacted the terrestrial planets; one responsible for the period of heavy bombardment early in the history of Mars, the Moon and Mercury, and probably the Earth and Venus as well, and another primarily responsible for the period of crater formation after mare formation on the Moon and plains formation on Mars.

#### REFERENCES:

- Gurnis, M. (1980). Martian Cratering Revisited. Submitted to Icarus.
- Strom, R. G. (1977). Origin and Relative Age of Lunar and Mercurian Inter crater Plains, Phys. Earth & Planet. Interiors, 15, 156-171.
- Strom, R. G. (1979). Mercury: A Post-Mariner 10 Assessment, Sp. Sci. Rev. 24, 3-70.





CRATER FORMING PROCESSES ON MARS, IMPACT-ENERGY COUPLING, AND EXPLOSION-CRATERING ANALOGS FOR FORMATION OF CENTRAL UPLIFTS AND MULTIRINGS

D. J. Roddy and L.A. Soderblom, U.S. Geological Survey,  
Flagstaff, Arizona 86001

Impact cratering on Mars has produced a wide variety of morphological and structural types of craters and ejecta blankets, ranging from simple bowl-shaped craters to giant, flat-floored basins. Recently, studies by a number of workers suggest that the various impact features are functions of a number of different specific impact conditions and target material responses. Certain of these contentions are supported by a series of explosion-cratering experiments, called Snowball, Prairie Flat, and Dial Pack. In these experiments, formation of large, flat-floored craters with central uplift and multiring structures and surface morphologies depended strongly upon several critical initial conditions. In all three cratering trials, the charge type, charge energy, and target media were the same. However, the use of both hemispherical and spherical explosion charges, and the nature of their different energy coupling to the target, had a noticeable effect on the specific morphology and structural deformation developed at each crater. These explosion data imply that a comparable set of morphological and structural effects may occur in large-scale impact events when projectile and target conditions are varied in a scaled manner similar to the changes in explosion conditions.

The three explosion trials were conducted within a kilometer of one another on the Watching Hill Test Site at the Defense Research Establishment Suffield, Alberta, Canada (1,2). Each cratering event was completed in the same stratigraphic units of interbedded clays, silts and sands overlying saturated clay; depth of water table was  $\sim 7$  m. The Snowball Crater, formed by a 500-ton TNT hemisphere lying on the ground, is a flat-floored crater,  $\sim 83$  m in apparent diameter with a large central mound (Figs. 1, 4). The Prairie Flat and Dial Pack Craters were both formed by 500-ton TNT spheres lying tangential on the ground; they are flat-floored craters,  $\sim 60$  m in apparent diameter, with low central mounds surrounded by radial ridges and troughs and multiple rings (Figs. 2, 3, 5, 6).

In the most general sense, both the hemispherical and spherical charges detonated at or near the ground surface formed broad flat-floored craters surrounded by low rims and continuous ejecta blankets. Both types of charges also formed craters with major subsurface uplift and inward movement of deeper water-saturated clay under the entire floor of each crater. The hemispherical Snowball charge formed the largest crater because it was detonated at the center of the charge on the ground surface, i.e., zero height-of-burst. It coupled a high-pressure shockwave directly into the target soils beneath the entire TNT charge. The spherical Prairie Flat and Dial Pack charges formed smaller craters, in part because the detonation point in the center of the charge was above ground. Consequently, the detonation pressure was transferred to the ground only along the contact at the base of the sphere. Beyond the contact area, shock pressures were greatly reduced because of attenuation of the TNT gas pressures prior to interaction

with the ground. Therefore, less total energy was coupled downward because of the shape of the spherical charge and the small contact area with the ground. (S. Schuster, CRT, personal comm., 1980).

Cratering induced by the hemispherical charge with zero height-of-burst produced structural uplift beneath the entire crater floor and the most prominent central mound. Concentric and radial anticlinal/synclinal folds were formed on the flanks of the uplifted clay, but were not uplifted enough to affect the topography of the crater floor. Cratering induced by the spherical charges with a raised height-of-burst also produced uplift beneath the entire crater floor. The uplift, however, contains prominent anticlinal/synclinal folds that form both radial ridges and troughs and multiring topography, surrounding a very low, flat, central mound. These structural and topographic features are a direct consequence of the charge yield, charge configuration, height-of-burst, nature of energy coupling, and highly compressible target soils over less compressible, mobile, water-saturated clay.

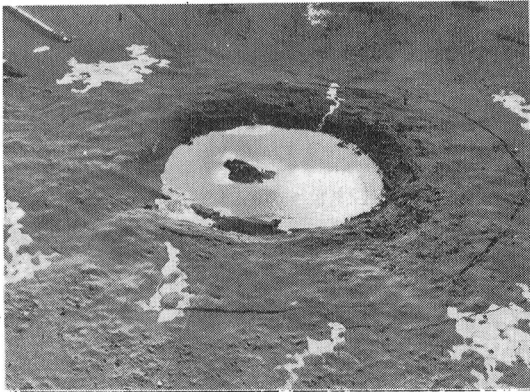


Fig. 1. Snowball explosion crater.

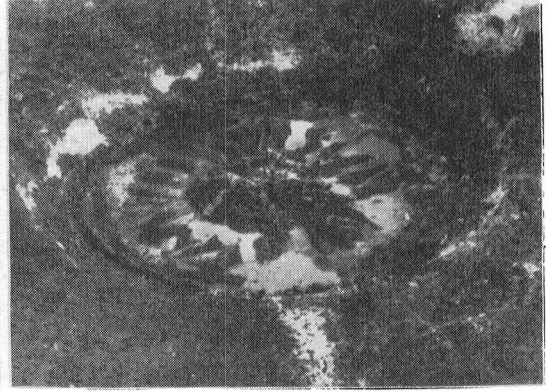


Fig. 3. Dial Pack explosion crater one day after formation with groundwater flooding.

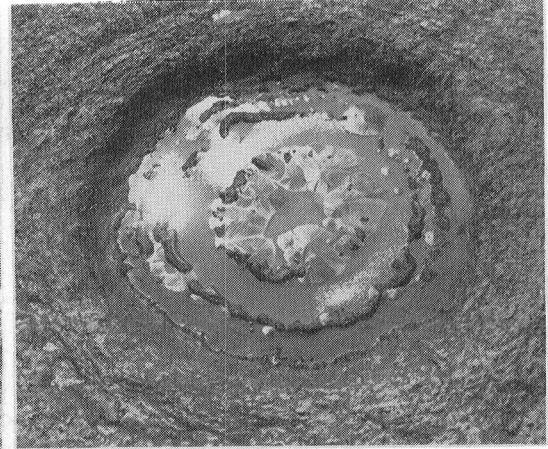
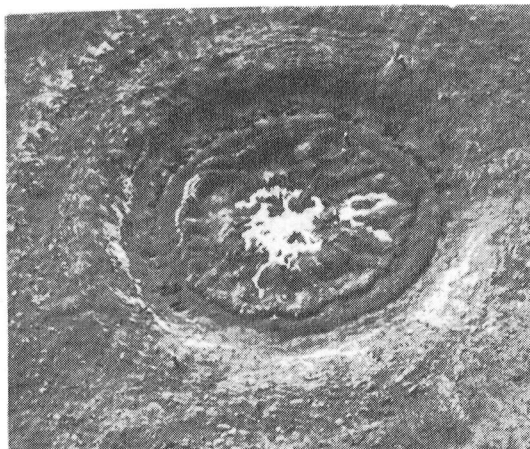


Fig. 2. Prairie Flat explosion crater one hour after formation (a) and one day after formation (b) with groundwater flooding (from 2).

Qualitative application of the explosion analog data suggests that energy coupled by impacting bodies at or near the target surface should be effective in forming central uplift and multiring craters. Furthermore, a narrow range in the height-of-burst appears critical to the development of central peaks versus multiring structure and topography. These explosion analog conditions could be met, in part, by extensive vaporization of the projectile upon impact, thereby insuring maximum surface transfer of energy with minimum target penetration. Such impact conditions are plausible with low-density bodies, such as comets, as suggested in recent calculations by (3) and (4). In addition, layered targets with fluid-like properties, such as those of shallow, hot, mantle rocks, should greatly enhance uplift and multiring structure and topography. The complexity of these conditions, as well as the specific roles of impact energy, impacting body type, layering, target material responses, gravity, and other initial cratering parameters, suggest that numerical code work is essential to studies of the formation of the largest impact craters and basins.

- (1) Jones, G.H.S., 1977, Complex craters in alluvium, in Roddy, D.J., and others, eds., *Impact and Explosion Cratering*, Pergamon, N.Y., 162-184.
- (2) Roddy, D. J., 1977, Large-scale impact and explosion craters: Comparisons of morphological and structural analogs, in Roddy, D.J., and others, eds., *Impact and Explosion Cratering*, Pergamon, N.Y., 185-246.
- (3) O'Keefe, J.D., and Ahrens, T.J., 1980, Cometary impact calculations: Flat floors, multiring and central peaks: *Proc. Lunar Planetary Sci. Conf. 11th*, Abstracts, P. 3, 830-832.
- (4) Roddy, D. J., Kreyenhagen, K., Schuster, S., and Orphal, D., 1980, Theoretical and observational support for formation of flat-floored central uplift craters by low-density impacting bodies: *Proc. Lunar Planetary Sci. Conf. 11th*, Abstracts, P. 3, 943-945.

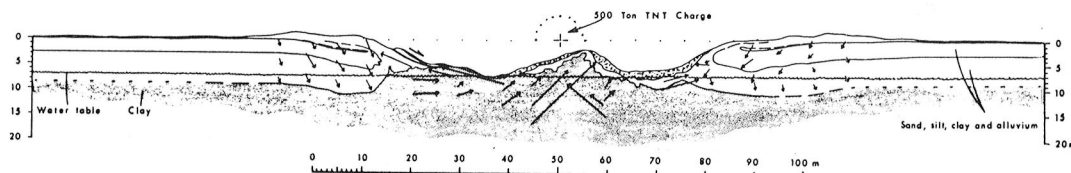


Fig. 4. Generalized geologic cross-section of Snowball explosion crater (2).

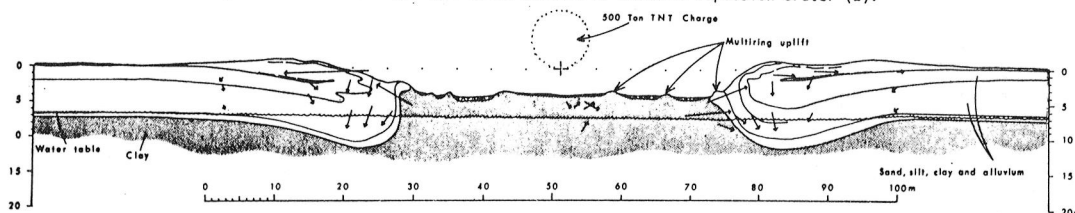


Fig. 5. Generalized geologic cross-section of Prairie Flat explosion crater (2).

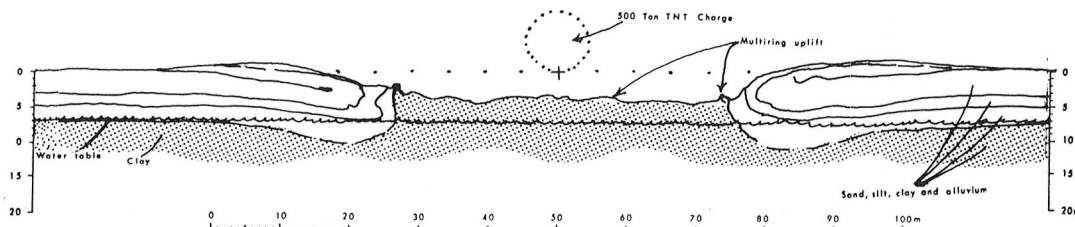


Fig. 6. Generalized geologic cross-section of Dial Pack explosion crater.

MARTIAN IMPACT CRATERS: INVENTORY OF THREE-DIMENSIONAL CRATER AND EJECTA BLANKET PARAMETERS, L. A. Soderblom, D. J. Roddy, D. W. G. Arthur., P. A. Davis, United States Geological Survey, Flagstaff, Arizona.

Impact cratering on Mars has produced a wide variety of morphological and structural types of craters and ejecta blankets. With the acquisition of the first high-resolution Viking photography, it was recognized that the distribution of different types of craters and ejecta blankets appears to reflect many significant aspects in the development of the martian crust, such as cratering rates, types of target material, mantle degassing, history of atmospheric development, and volatile deposition in crustal permafrost zones, to mention a few. A number of workers (1-7), for example, have suggested that the morphologies of the ejecta blankets are strongly influenced by the volatile constituents (water and ice) that can be shock-fluidized in the target rocks. In order to test such concepts, several studies have been initiated to acquire detailed data on the global distribution of martian impact craters and ejecta blankets, their dimensional parameters, and other physical characteristics (3,4,5,7,8). These studies indicate that lobate flow ejecta and pedestal craters may have separable quantitative morphological characteristics, suggesting different origins (5). In fact, studies of the global distribution of "splish" craters (3) suggest that they are concentrated toward the poles, whereas studies of the global distribution of both pedestal and lobate ejecta craters, dominated in number by smaller pedestal craters (5), show a random distribution (4). One of the critical elements of any such inventory, however, is determination of accurate three-dimensional data for rim crest and apparent diameters and depths, ejecta thicknesses, and crater/ejecta profiles. Our current efforts are concentrated on developing interactive computerized photometric techniques that can be applied to radiometrically accurate Viking Orbiter digital images in order to produce a statistically large set of this type of data.

Until recently, three-dimensional information on craters and their ejecta blankets had not been available in high resolution format. Mouginis-Mark and colleagues (7) presented height measurements on the ejecta blanket of the crater Arandas determined from shadow measurements on a Viking Orbiter image with a sun elevation angle of  $\sim 15^\circ$ . Measurements on hard-copy photography, however, present real difficulties in determination of location of true shadow boundaries. Arthur (9) discussed a method of obtaining precise shadow-length/height measurements down to the resolution limits using the raw digital image. His method involves the use of brightness of a shadow that can be used to identify shadowed zones in other parts of the image; by deconvolving the point-spread function at shadow edges, the shadow length then can be precisely estimated. The problem with these methods, in general, is that height measurements are available only for a few discrete points in the images and only on the steepest parts of

the topography. The disadvantage of photogrammetric methods is that stereo pairs with adequate resolution of flow-ejecta blankets are extremely rare. Even the few stereo pairs available are marginal for extraction of the very low relief in the crater ejecta blankets using photogrammetric plotters.

Because our goal is to obtain three-dimensional information on a large number of crater and ejecta blankets, in order to understand the variations with latitude, geologic province and age, neither the shadow nor photogrammetric methods is practical. Consequently, we have developed a numerical method involving an image processing computer interfaced with a digitizer to extract quickly a quantity of profiles from Viking Orbiter images. The method involves a technique termed "photoclinometry", which was used earlier for both the Moon and Mars (10,11). Those attempts were only partly successful for two reasons: 1) the radiometric quality of the data was inadequate and 2) albedo variations were not separable from insolation variations caused by topography. In the case of the Viking data we have been able to circumvent both the radiometric and albedo problems. First, the Viking Orbiter relative radiometric calibration has been repeatedly tested and monitored in orbit, and is thought to be better than a few percent within any given frame. Secondly, techniques have been developed and tested to recognize and eliminate interference from albedo variations. One technique involves the assumption that the albedo and topography of the crater are radially symmetrical. When this condition is met, the digital image is bilaterally symmetrical in the cross-sun direction. After this test is made, the brightness profile in the down-sun direction is folded, or mirror imaged about the center of the crater and ratioed. The ratio is the brightness of corresponding points in the up-sun and down-sun directions. The result is a quantity independent of surface albedo, camera sensitivity, atmospheric transparency, and solar flux. This ratio, therefore, is a function only of the surface topography and the photometric function, if the photometric function is assumed to be independent of albedo. In terms of a specific photometric function, we have determined that both Lambert and Minnaert functions are adequate. The other important aspect that must be recognized and corrected for is the brightness of the martian atmosphere. Even in summer, when the atmosphere is clearest, much more than half of the brightness of the recorded scene may be scattered by the atmosphere. This scattering is severe in scenes less than a few tens of degrees from the terminator (12,13). This atmospheric component, which involves scattering directly to the camera as well as diffuse forward scattering to the surface, must first be subtracted from the calibrated digital files. Preliminary tests using these techniques have been made by comparing shadow height determinations, using the best photogrammetric data from Arthur, with our photoclinometric solutions. Results are in agreement to 90% or better on the comparative data sets.

The procedure for rapid acquisition of a large number of profiles thus involves: 1) selection of moderate resolution mapping frames that

contain craters of interest with a few shadowed features, 2) computer decalibration of the image and subtraction of atmospheric components, 3) use of a digitizer table to locate the specific profiles to be extracted by the computer, 4) location of corresponding symmetrical points on the up-sun and down-sun sides of the profile (i.e. inner and outer edges of the distal edge of the ejecta), 5) extraction by computer of the digital brightness profiles from an on-line disk file, 6) testing the crater image for symmetry, 7) calculation of the topographic profile and 8) storage of the profile data. We are now in the process of extracting and testing several hundred profiles and organizing the data into a computer-accessible global inventory of locations, three-dimensional shape and general characteristics for craters and ejecta.

#### REFERENCES

- ( 1 ) Carr, M.H., Crumpler, L.S., Cutts, J.A., Greeley, R., Guest, J.E., and Masursky, H., 1977, Martian impact craters and emplacement of ejecta by surface flow: *J. Geophys. Res.*, 82, no. 28, 4055-4065.
- ( 2 ) Boyce, J.M., and Roddy, D.J., 1978, Martian rampart craters: Crater processes that may affect diameter-frequency distribution: *NASA Tech. Memo. 79729, Repts of Planetary Geol. Program, 1977-1978*, 162-165.
- ( 3 ) Johansen, L.A., 1978, Martian splosh cratering and its relation to water: *Proceedings of the second colloquium on Planetary Water and Polar Processes*, Hanover, New Hampshire, 109-110.
- ( 4 ) Allen, C.C., 1979, Areal distribution of martian rampart craters: *Icarus*, 38, 111-123.
- ( 5 ) Mutch, P., and Woronow, A., 1980, Emplacement of martian rampart and pedestal ejecta blankets: *NASA Tech. Memo. 81776, Repts of Planetary Geol. Program, 1979-1980*, 96-98.
- ( 6 ) Mouginis-Mark, P.J., 1980, Ejecta emplacement for martian fluidized ejecta craters: *NASA Tech. Memo. 81776, Repts of Planetary Geol. Program, 1979-1980*, 99-101.
- ( 7 ) Mouginis-Mark, P.J., and Carey, D.L., 1980, Crater studies in the northern plains of Mars: Thickness estimates of fluidized ejecta deposits: *NASA Tech. Memo. 81776, Repts of Planetary Geol. Program, 1979-1980*, 105-110.
- ( 8 ) Blasius, K.R., Cutts, J.A., and Roberts, W.J., 1980, A global study of primary crater ejecta morphology on Mars: A progress report: *NASA Tech. Memo. 81776, Repts of Planetary Geol. Program, 1979-1980*, 93-94.
- ( 9 ) Arthur, D. W. G., 1980, Precise Mars relative altitudes: *NASA Tech. Memo 81776, Repts. of Planetary Geol. Program, 1979-1980*, p. 358.
- (10) Watson, K., 1968, Photoclinometry from spacecraft images: *U.S. Geol. Survey Prof. Paper 599B*, B1-B10.
- (11) Wildey, R.L., 1971, Limited-interval definitions of the photometric functions of lunar crater walls by photography from orbiting Apollo: *Icarus*, 15, 93-99.
- (12) Thorpe, T.E., 1977, Viking Orbiter observations of atmospheric opacity during July-November 1976: *J. Geophys. Res.*, 82, no. 28, 4151-4159.

- (13) Pollack, J.B., Colburn, D., Kahn, R., Hunter, J., Van Camp, W., Carlston, C.E., and Wolf, M.R., 1977, Properties of aerosols in the martian atmosphere, as inferred from Viking Lander imaging data: J. Geophys. Res., 82, no. 28, 4479-4496.

MARTIAN CHANNELS - A LATE VIKING VIEW, Harold Masursky, A. L. Dial, Jr., and M. E. Strobbe, U.S. Geological Survey, Flagstaff, Arizona 86001.

Studies of low-resolution Mariner 9 images and medium-resolution images obtained early in the Viking mission have resulted in the theory that martian channels were formed over a long interval of time and by several different processes. This theory has been strongly reinforced by analysis of recent, high-resolution images obtained during the final days of the Viking extended mission.

Various hypotheses have been presented to describe methods of channel-formation on Mars; channeling has been attributed to fluvial action (1,2,3), wind erosion (4), debris flows (5,6), glacial action (7,8) and faulting. Opinions on the time of channel formation have been equally varied. Several authors have proposed that the channels were formed very early in martian history when the atmosphere was still dense (9,10), whereas we have proposed that channeling occurred during several episodes over a longer time span (11). Source of the water, by those who favor a fluvial origin, has been attributed to rainfall, melting of subsurface permafrost, artesian flow, or glacial outbursts similar to those on Earth.

High-resolution contiguous Viking pictures recently obtained have allowed us to make detailed crater density counts of several channel floors, and to distinguish between channels that have not been resurfaced and those whose floors are masked by windblown deposits or debris slides, or degraded by wind. Counts made of these channel floors and nearby volcanic and/or ancient cratered surfaces reaffirm our thesis that channel formation occurred over a long time period. These counts, and relative ages derived from them, are thought to be more valid statistically than earlier determinations based on lower resolution images.

Ancient cratered terrain units and volcanic units that occur as inter-crater plains within the ancient terrain are shown by the new counts to be much older than any of the channels. Volcanic episodes associated with the final stages of volcanism at Tharsis are younger than any of the channels. Other volcanic episodes and the channel formation are intermediate or young in age and occur within the time span bounded by the ancient cratered terrain and the youngest Tharsis flows.

Crater densities for channel floors are tabulated in Table 1; volcanic centers and volcanic plains of young and intermediate age are shown in Table 2; ancient cratered terrain units and ancient volcanic units are shown in Table 3. Relative ages derived from crater densities at the 1-km intercept are shown for some of these units in Figure 1; the value at 1 km was determined in order that the surfaces can be "dated" (Fig. 1) by comparison to the models of Soderblom *et al.* (12) and Neukum and Wise (13) (Figure 1). In some cases where the counts are derived from very high or very low resolution photographs, it was necessary to



project to the 1-km position. These projections are uncertain because most of the crater curves show significant perturbations from linearity caused by resolution or incompleteness of the data set (particularly in large-diameter craters); also, segments of the curves may reflect geologic processes that modify the counts. We established the slope of the "production function" segment of the curve, which is close to the ideal -3 value near the 1-km value. Segments of the curve reflecting smaller and larger crater depart significantly from this slope (see Tables 1, 2, 3). We then projected along the parts of the curves with appropriate slopes to the 1-km position. (The 1-km intercept and Soderblom model are used as a shorthand convenience.) We have found that families of curves in the same area have parallel slopes. By contrast, our relative ages are based on the whole crater curve plotted and compared. We have counted craters in many terrains on Mars, the Moon, Mercury, Phobos, Deimos, Venus and the Galilean satellites. The curves fall nicely into groups and are clearly interpretable, but choice of the 1-km intercept as the only comparison point is inadequate.

The megachannels that rise in highland terrain south of Chryse Planitia originate in complex chaotic collapsed areas; they probably formed when subsurface ice melted. Volumes of collapsed areas and longitudinal slopes, and cross profiles to determine flow rates and volumes for these large channels are being determined from ground-based radar altimetric data combined with stereophotogrammetric analysis of Viking photographs. Photomosaic and geologic maps of these and other channels that debouch into Chryse Planitia are being constructed. Intermediate-sized channels that have multiple tributaries in their headwater regions, such as Mangala and Maja Valles, probably formed by melting of subsurface ice, and/or by "artesian" flow. Small dendritic networks of channels form on slopes and have "theatre-headed", U-shaped cross sections. They may have formed from subsurface flow that encouraged headward sapping; however, runoff from rainfall may be an alternative and, to us, more attractive hypothesis for their formation.

The channels fall into four roughly defined time periods. Based on the Soderblom *et al.* (1974) curve, the intermediate-sized channels Vedra and Reull Valles are 0.2 BY old; counts for these channels were made from medium-resolution frames. (The remaining channels were counted on high resolution frames.) Tiu and Ares Valles, two of the megachannels located at Chryse, are shown (fig. 1) to be about 0.5 BY old; the broad portion of the Kasei mega-channel is about 2 BY in age. Ma'adim Valles, an intermediate-sized channel that cuts the ancient highland terrain, was found to be about 3 BY old.

Volcanic episodes occurred before, during, and after the channel-cutting episodes. At least three stages of volcanism, represented by materials of the intercrater plains (pc), ridged plains (pr) and Tyrrhena Patera volcanics, are recognized at Terra Tyrrhena in the vicinity of Hesperia Planum and the two ancient volcanic centers, Hadriaca and Tyrrhena Paterae. A similar stratigraphic sequence of volcanic flows is

recognizable in the Lunae Planum-Tharsis region; in this area the channels were cut after materials of the intercrater plains (pc) and ridged plains (pr) were extruded. Channeling occurred concomitant with the earliest stages of shield construction at Tharsis; the large Chryse channels were formed while the Arsia Mons shield was being constructed. Thus only the Chryse channels may be related in time and process to augmented geothermal heatflow in the Tharsis region.

#### REFERENCES

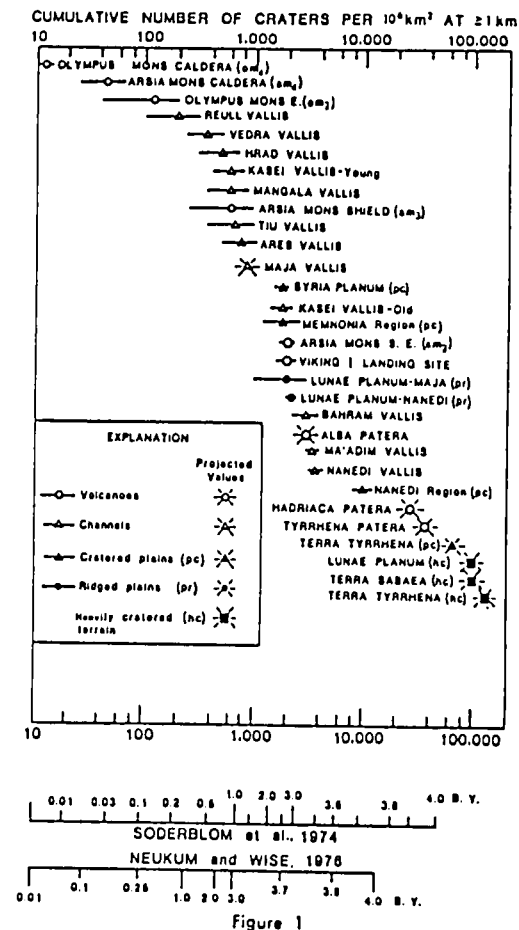
1. Masursky, Harold, 1972, in Driscoll, E., Mariner views a dynamic, volcanic Mars, Sci. News 101, 106-107.
2. Baker, V.R., and D. J. Milton, 1974, Erosion by catastrophic floods on Mars and Earth: Icarus, 23, p. 27-41.
3. Sharp, R. P., and M. C. Malin, 1975, Channels on Mars: Geol. Soc. Amer. Bull., 86, p. 593-609.
4. Cutts, J.A., 1977, The origin of the channels of the Chryse basin region: Paper presented at the 7th Lunar Science Conference, Lunar Sci. Inst., Houston, Tex., March 15, 1977.
5. Thompson, D. E., 1980, Mars catastrophic flooding analog: Analysis of debris transport in variable viscosity fluids, NASA Tech. Memo. 81776, Repts. of Planetary Geol. Program, p. 174.
6. Nummedal, D., 1980, Debris flows and debris avalanches in the large martian channels, NASA Tech. Memo. 81776, Repts. of Planetary Geol. Program, p. 289.
7. Hargraves, R. B., 1976, Informal communication.
8. Lucchitta, B. K., and D. M. Anderson, 1980, Martian outflow channels sculptured by glaciers, NASA Tech. Memo. 81776, Repts. of Planetary Geol. Program, p. 271.
9. McElroy, M. B., Y. L. Yung, and A. O. Nier, 1976, Isotopic composition of nitrogen: Implications for the past history of Mars atmosphere: Science, 194, p. 70-72.
10. Pieri, D., 1976, Martian channels: Distribution of small channels on the martian surface: Icarus, 27, p. 25-50.
11. Masursky, Harold, Boyce, J. M., Dial, A. L., Schaber, G. G., and Strobell, M. E., 1977, Classification and time of formation of martian channels based on Viking data: J. Geophys. Res., 82, no. 28, p. 4016-4038.
12. Soderblom, L. A., R. A. West, B. M. Herman, T. J. Kreidler, and C. D. Condit, 1974, Martian planet-wide crater distribution: Implications for geologic history and surface processes: Icarus, 22, p. 239-263.
13. Neukum, G., and D. U. Wise, 1976, A standard crater curve and possible new time scale: Science, 194, p. 1381-1387.

CHANNELS	TABLE 1 CUMULATIVE NUMBER OF CRATERS PER $10^6 \text{ km}^2$		SLOPE OF CRATER CURVE
	$\geq 0.5 \text{ km}$	$\geq 1 \text{ km}$	
REULL VALLIS	1600 $\pm$ 400	200 $\pm$ 100	-3.0*
VEDRA VALLIS	2800 $\pm$ 600	360 $\pm$ 120	-2.8
KASEI VALLIS, YOUNG	3600 $\pm$ 800	600 $\pm$ 200	-2.6
HRAD VALLIS	5000 $\pm$ 1800	500 $\pm$ 200	-3.0
MANGALA VALLIS	5000 $\pm$ 2000	600 $\pm$ 250	-1.7
TIU VALLIS	5000 $\pm$ 1800	650 $\pm$ 300	-2.8
ARES VALLIS, YOUNG	4800 $\pm$ 800	750 $\pm$ 250	-2.6
MAJA VALLIS	-	750 $\pm$ -	-3.2
KASEI VALLIS, OLD	11000 $\pm$ 1000	1800 $\pm$ 400	-2.5
VIKING 1 LANDING SITE	13500 $\pm$ 1500	2000 $\pm$ 400	-2.95
BAHRAM VALLIS	14000 $\pm$ 4000	3000 $\pm$ 800	-2.3
NAIEDI VALLIS	13000 $\pm$ 5000	3600 $\pm$ 250	-2.5
MA'ADIM VALLIS	18000 $\pm$ 6000	3400 $\pm$ 200	-2.4

VOLCANIC CENTERS AND VOLCANIC PLAINS	TABLE 2 CUMULATIVE NUMBER OF CRATERS PER $10^6 \text{ km}^2$		SLOPE OF CRATER CURVE
	$\geq 0.5 \text{ km}$	$\geq 1 \text{ km}$	
OLYMPUS MONS			
YOUNG CALDERA	120 $\pm$ -	12 $\pm$ -	-3.3*
ARSIA MONS CALDERA ( $\alpha_4$ )	500 $\pm$ 250	45 $\pm$ 20	-3.6
OLYMPUS MONS E. ( $\alpha_2$ )	1000 $\pm$ 200	120 $\pm$ 90	-3.0
ARSIA MONS SHIELD ( $\alpha_3$ )	5500 $\pm$ 1000	600 $\pm$ 350	-3.0
SYRIA PLANUM (pc)	5600 $\pm$ 400	1800 $\pm$ 200	-2.1
MEMNONIA (pc)	6500 $\pm$ 1500	1800 $\pm$ 800	-2.0
ARSIA MONS S.E. ( $\alpha_2$ )	-	2000 $\pm$ 200	-2.9
LUNAE PLANUM - NAIEDI (pr)	7500 $\pm$ 500	2200 $\pm$ 200	-1.7
VIKING 1 LANDING SITE	13500 $\pm$ 1500	2000 $\pm$ 400	-2.95
LUNAE PLANUM - MAJA (pr)	16000 $\pm$ 4000	2000 $\pm$ 1000	-3.6
ALBA PATERA	15000 $\pm$ 5000	3000 $\pm$ -	-2.3
NAIEDI (pr)	70000 $\pm$ 5000	10000 $\pm$ 2000	-2.5

HEAVILY CRATERED TERRAIN AND ANCIENT VOLCANIC MATERIALS	TABLE 3 CUMULATIVE NUMBER OF CRATERS PER $10^6 \text{ km}^2$		SLOPE OF CRATER CURVE
	$\geq 1 \text{ km}$	$\geq 10 \text{ km}$	
LUNAE PLANUM (pr)	2200 $\pm$ 200	420 $\pm$ 100	-1.7*
HADRIACA PATERA	((28000))**	15 $\pm$ 10	-3.6
TYRRHENA PATERA	((38000))	30 $\pm$ 10	-3.6
TERRA TYRRHENA (pc)	((65000))	180 $\pm$ 30	-2.0
TERRA SABAEA (hc)	((100000))	1000 $\pm$ 200	-2.0
LUNAE PLANUM (hc)	((100000))	1000 $\pm$ 200	-2.0
TERRA TYRRHENA (hc)	((140000))	1400 $\pm$ 250	-2.1

\*Single parentheses enclose symbols of geologic map units on USGS map I-896.  
\*\*Double parentheses enclose projected values.





Chapter 4  
GEOCHEMISTRY, VOLATILES AND REGOLITH



## LOW TEMPERATURE PHASE CHANGES IN MONTMORILLONITE AND NONTRONITE AT HIGH WATER CONTENTS AND HIGH SALT CONTENTS.

Duwayne M. Anderson, Faculty of Natural Sciences and Mathematics, State University of NY at Buffalo, Buffalo, NY 14260 and Allen R. Tice, U.S. Army Cold Regions Research and Engineering Laboratory, Hanover, NH 03755

The existence of phase changes below the temperature of initial freezing of clay water mixtures was first established by low temperature differential thermal analysis, (Anderson, 1967 and Anderson and Tice, 1971). These phase changes occur in the unfrozen water still present in ice containing, clay water mixtures at temperatures ranging from  $-5^{\circ}\text{C}$  to about  $-50^{\circ}\text{C}$ . The quantity of unfrozen water present in a frozen sample depends primarily on temperature and electrolyte concentration. It is high for mineral material which has high specific surface areas and low for those that have low specific surface areas, other factors being held constant. The unfrozen water contents are relatively high at high electrolyte concentrations compared to those characteristic of clay water mixtures containing no electrolytes.

The relationship between unfrozen water content for a given material and temperature in degrees below freezing is called the phase composition curve. Phase composition data for a number of materials have been published, (Williams, 1964, Anderson and Hoekstra, 1965, Anderson and Morganstern, 1973, Tice, et. al., 1978). Detailed analysis of published phase composition data indicates the existence of more than one domain for the unfrozen, interfacial water.

The phase changes revealed by low temperature differential analysis were made evident by the appearance of relatively small exotherms between  $-35^{\circ}\text{C}$  and  $-50^{\circ}\text{C}$ . The exotherms observed were independent of total water (ice) content but were obviously related to clay mineral type and the specific exchangeable cations present. Kaolinite and halloysite yielded single exotherms at  $-37^{\circ}\text{C}$  and  $-39^{\circ}\text{C}$  respectively. The lithium, sodium and calcium forms of montmorillonite each yielded three low temperature exotherms, at  $-33^{\circ}\text{C}$ ,  $-35^{\circ}\text{C}$  and  $-43^{\circ}\text{C}$ . The magnitude of these exotherms was determined to be of the order of 0.1 cal/g clay. It was concluded tentatively that they result from a sudden release of the unfrozen, interfacial water from the adsorption fields of the clay surfaces and its migration from two or more characteristic water domains to adjacent, growing ice crystals where it then adds on and freezes. Other explanations are possible, however,

In an effort to learn more about the low temperature behavior of the unfrozen interfacial water, we have employed the technique of scanning calorimetry in a specially arranged Perkin-Elmer Model DSC-2 differential scanning calorimeter. In this paper, we report the results of determinations on montmorillonite and nontronite clay water mixtures at high water contents and at high salt contents. Montmorillonite and nontronite clays were selected for this investigation for two different reasons: Montmorillonite had been extensively investigated earlier by differential thermal analysis. Nontronite, a clay mineral similar in many respects to montmorillonite, was selected in order to provide experimental data useful in interpreting the diurnal temperature fluc-

tuations observed by the Viking Mars Landers 1 and 2, (Moore, 1978). Nontronite clay has been suggested as a probable constituent of the finally divided particles observed by the Viking Landers at two widely separated locations on Mars.

The presence of electrolytes at high concentration is shown to have a very marked effect. The low temperature phase changes are completely absent at high electrolyte concentrations in these clay water systems. The presence of electrolytes also was observed to have a distinctive effect on the shape of the initial freezing peak associated with ice segregation.

#### REFERENCES

- Anderson, D. M., 1967. Ice Nucleation and the Substrate-Ice Interface. *Nature*, 216: 563-566.
- Anderson, D.M. and Tice, A. R., 1971. Low Temperature Phases of Interfacial Water in Clay Water Systems. *Soil Sci. Soc. Am. Proc.* 35 : 47-54.
- Williams, P. J., 1964. Unfrozen Water Content of Frozen Soils and Soil Moisture Suction. *Geotechnique* 14 : 213-246.
- Anderson, D. M. and Hoekstra, P., 1965. Migration of Inter Lammellar Water During Freezing and Thawing of Wyoming Bentonite. *Soil Sci. Soc. Proc.*, 29 : 498-504.
- Anderson, D. M. and Morganstern, N., 1973. Physics, Chemistry and Mechanics of Frozen Ground. In *North American Contribution 2nd International Conference on Permafrost*, National Academy of Sciences, Washington, DC, 1973.
- Tice, A. R., Burrous, C. M. and Anderson, D. M., 1978. Determination of Unfrozen Water in Frozen Soil by Pulsed Nuclear Magnetic Resonance. *Proceedings 3rd International Conference on Permafrost*, Edmonton, Alberta, Canada, 1978, pp. 149-155.
- Tice, A. R., Burrous, C. M. and Anderson, D. M., 1978. Phase Composition Measurements on Soils at Very High Water Contents by the Pulsed Nuclear Magnetic Resonance Technique. *Moisture and Frost/Related Soil Properties*, Transportation Research Record 675, pp. 11-14.
- Moore, Henry, 1978. Personal Communication.



## SULFATE PRODUCTION FROM PHOTOCHEMICAL OXIDATION OF SULFIDES: PRELIMINARY RESULTS

Thomas R. Blackburn, St. Andrews Presbyterian College, Laurinburg, NC  
Everett K. Gibson, Jr., SN7/Geochemistry Branch, NASA-JSC, Houston, TX  
Fikry F. Andrawes, Lockheed, 1830 NASA Road 1, Houston, TX  
Vaneica Young, Chemistry Department, Texas A&M University, College Station, TX

### INTRODUCTION

Clark and Baird (1979) have reviewed the possibilities for a sulfur-rich Martian lithosphere on the basis of the Viking XRF finding of high sulfur abundances in regolith samples and of McGetchin and Smyth's (1978) model of a high-density mantle, possibly including FeS. Reduced sulfur, including Fe(II) sulfides, is thermodynamically unstable under the oxidizing conditions prevalent on the surface of Mars (Gooding, 1977). Further, the Viking GEX result (Oyama and Berdahl, 1977) indicates that species more oxidizing than the equilibrium oxygen fugacity are present there. Therefore, the thermodynamic end products of sulfide weathering are of less interest than alteration rates and mechanisms and the kinetically determined product set--for example, whether production of  $\text{FeSO}_4$  will prevail over production of  $\text{Fe}_2\text{O}_3 + \text{S}$  (Gooding, 1977).

The present work was undertaken to model the photochemical weathering of three iron sulfides, troilite (FeS), pyrrhotite ( $\text{Fe}_{1-x}\text{S}$ ), and pyrite ( $\text{FeS}_2$ ) under Martian surface ambient conditions. Evidence of surface alteration and indications of its chemical nature were obtained by X-ray photoelectron spectroscopy (XPS) and pyrolysis gas chromatography (PGC).

### EXPERIMENTAL CONDITIONS

Samples were located on a liquid nitrogen-cooled sample tray in 3.3-liter stainless steel irradiation vessel (Fig. 1). They were prepared as flat chips (for XPS) and powders (for PGC). Chips 0.80 mm thick were prepared with a diamond saw, cleaned by ultrasonication in ultra-high purity freon followed by a  $110^\circ\text{C}$  bakeout, and polished with fine SiC paper under argon. Powders were produced by grinding bulk minerals under argon. All samples remained under  $\text{CO}_2$ , Ar, or  $\text{N}_2$  atmospheres from the time of preparation until post-irradiation analysis. Irradiations were carried out without the introduction of water vapor ("dry irradiations") and in the presence of water vapor in equilibrium with ice at  $200\text{--}260^\circ\text{K}$  ("humid irradiation"). The water content of the  $\text{CO}_2$  gas was less than 0.01%. During the humid irradiation, samples became coated with a frost that from its vapor pressure we conclude to have been either a mixed  $\text{H}_2\text{O}\text{--}\text{CO}_2$  frost or  $\text{CO}_2\text{--H}_2\text{O}$  clathrate; the temperature and  $\text{CO}_2$  pressure in the chamber during humid irradiation were well within the stability field of the clathrate (Miller, 1974).

Duplicate samples of chips and powders were located in the direct UV beam ("in-beam" samples) and on the sample tray, but out of the direct beam ("out-of-beam"). Thermocouples were directly embedded in the sample in the UV beam and the temperatures of in-beam and out-of-beam samples did not differ by more than  $10^\circ\text{K}$ . Ultraviolet irradiation was supplied by a

deuterium discharge lamp operated at 30 W. The atmosphere during irradiation was high-purity dry  $\text{CO}_2$  at a pressure of 6 torr. The dry irradiation continued for 160.3 hours, and the humid irradiation for 40.0 hours.

## RESULTS

XPS spectra (Fig. 2) indicate significant oxidation of the sulfides to sulfate for both in-beam samples and out-of-beam samples in the humid irradiation, but only on in-beam samples during dry irradiation. Thus, we conclude that gas-phase photochemical products are important in the alteration of these minerals if water vapor at modest abundance is available; doubtless the photochemical pathways begin with the photolysis of water molecules to hydroxyl radicals and hydrogen atoms (Bates and Nicolet, 1950). There is also some XPS evidence for the oxidation of Fe(II) to Fe(III) under humid conditions, but not under dry irradiation.

Pyrolysis gas chromatography (PGC) of powders (Fig. 3) indicates traces of  $\text{SO}_2$  present after dry irradiations, but almost none detected after humid irradiation. However, the sensitivity of the PGC technique for detecting sulfur species is considerably less than the XPS for the amount of alteration products produced on the surfaces of the samples. And the failure to detect  $\text{SO}_2$  by PGC for the humid samples does not confirm the absence of sulfates. Although  $\text{SO}_2$  is a pyrolysis product of sulfates (Collins et al., 1974), the XPS results indicate that sulfates are not the source of this  $\text{SO}_2$  (no sulfates are formed on out-of-beam samples during dry irradiations). Pyrolysis release temperatures of 1000-1350°C indicate that this  $\text{SO}_2$  is not simply trapped or adsorbed  $\text{SO}_2$ ; thus we conclude that it is chemically absorbed, but at too low a surface coverage to register during XPS of the low-area chips (less than 10% of a monolayer. Samples of  $\text{CaCO}_3$  powder placed in the irradiation chamber show increased  $\text{SO}_2$  release during PGC, indicating that at least some gas-phase  $\text{SO}_2$  was formed during irradiation (cf. Clark et al., 1979).

The preliminary experimental results have important implications for Martian surface processes and the behavior of volatiles which may be stored or trapped within the regolith. It has previously been shown that carbonate production is possible within the Martian regolith materials (Booth and Kieffer, 1978). In light of the sulfate production from photooxidation of primary sulfides, the opportunity exists for the volatile phases (e.g.,  $\text{CaCO}_3$ ) produced during cold-environment weathering to act as a very effective scrubber for the removal of volatiles (e.g.,  $\text{SO}_2$ ) produced during UV irradiation of the planetary surface.

## References

- Bates, D.R. and Nicolet, M. (1950) J. Geophys. Res. **55**, 301.  
Booth, M.C. and Kieffer, H.H. (1978) J. Geophys. Res. **83**, 1809-1815.  
Clark, B.C. and Baird, A.K. (1979) J. Geophys. Res. **84**, 8495-8503.  
Clark, B.C. et al. (1979) J. Mol. Evol. **14**, 91-102.  
Collins, L.W. et al. (1974) Thermochimica Acta **9**, 15-21.  
Gooding, J.L. (1977) Icarus **32**, 483-513.  
McGetchin, T.R. and Smyth, J.R. (1978) Icarus **34**, 512-536.  
Miller, S.L. (1974) In Natural Gases in Marine Sediments, ed. I.R. Kaplan, Plenum, NY, pp. 151-177.  
Oyama, V.I. and Berdahl, B.S. (1977) J. Geophys. Res. **82**, 4669-4676.

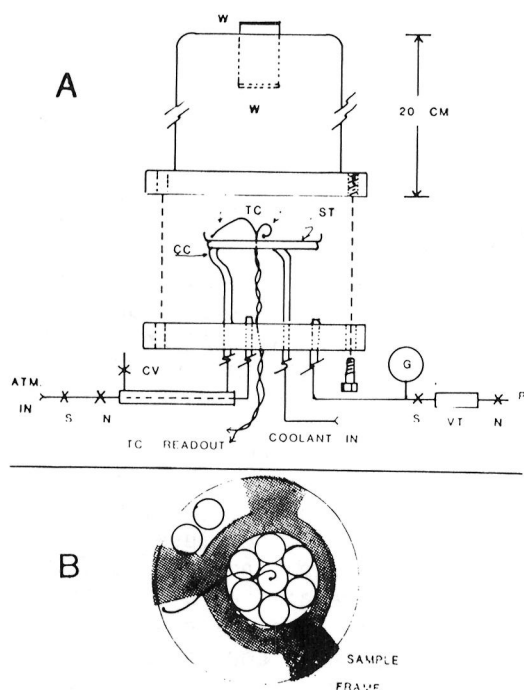


Fig. 1(A). Schematic of irradiation chamber. UV from deuterium lamp enters through window W.

Fig. 1(B). Sample tray. Seven samples in interior ring are "in-UV-beam"--other samples are "out-of-beam."

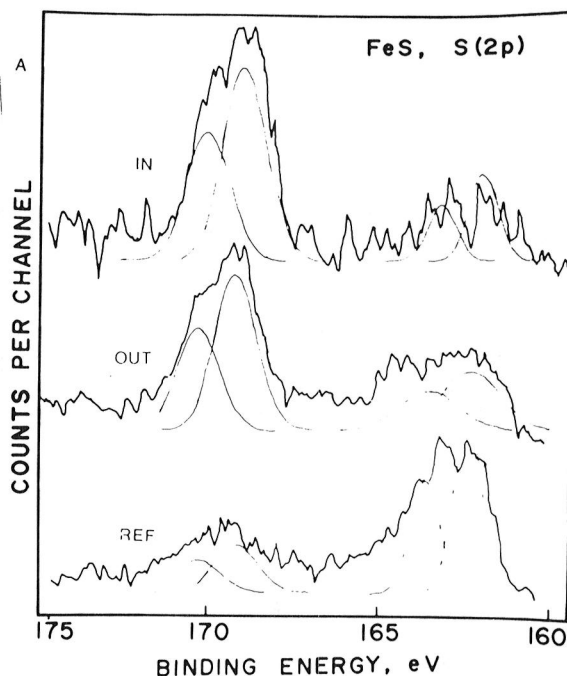


Fig. 2. X-ray photoelectron spectroscopy of troilite. The S(2p) region examined for sulfate production. Sulfate region 169-170 eV; sulfide region 163 eV. Note the production of sulfates for the "in" samples in the 170 eV region as compared to the reference samples.

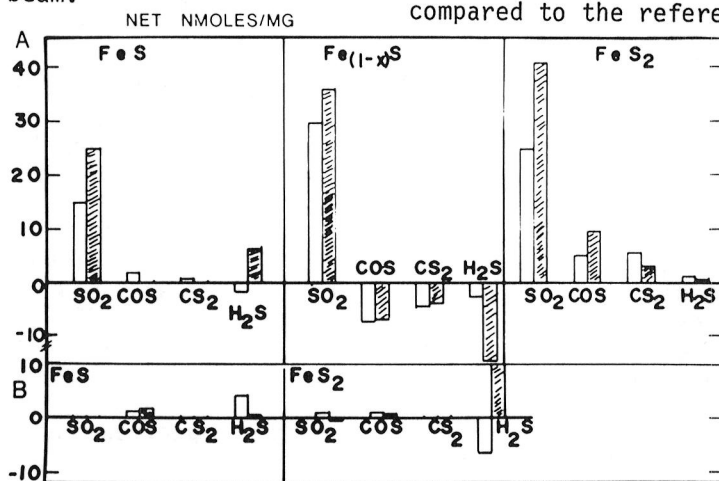


Fig. 3. Pyrolysis gas chromatography (PGC) data for "dry" and "humid" irradiated powders. Values are relative to reference samples. Run A = "dry;" Run B = "humid." Open bars represent samples "in-beam;" dashed bars represent samples "out-of-beam."

## CHEMICAL WEATHERING ON MARS: CARBONATE FORMATION

Michael C. Booth, SN7/Geochemistry Branch, NASA-JSC, Houston, TX 77058

As a first step in the development of an understanding of Martian chemical weathering phenomena, an experimental laboratory study was made of carbonate formation in simulated Martian environments. Reported initially by Booth and Kieffer (1978), carbonate growth was examined as a function of the partial pressures of  $\text{CO}_2$  and  $\text{H}_2\text{O}$ , total water content, ultraviolet irradiation, illumination/temperature cycling frequency, soil composition and temperature maxima, and duration of experiments. Rates of carbonate growth on olivine tholeiite were found to be  $1.0 \times 10^{11}$  to  $1.5 \times 10^{12}$  molecules  $\text{m}^{-2} \text{sec}^{-1}$ .

The environmental system was capable of providing temperatures, atmospheric pressures and compositions, and UV fluxes appropriate to the Martian surface (Fig. 1). Diurnal temperature cycling of experimental soils additionally were able to simulate any diurnal temperature environment of the Martian surface. Illumination cycling was synchronized with temperature cycling by means of an automatically operated dark slide in the light tunnel of the environmental chamber. The physical state of water and the abundance of water vapor was continuously controlled to avoid formation of a liquid phase. Water frosts formed on experimental soils during temperature minima ( $T_{\min} = 180 \text{ K}$ ) were induced to sublime from surfaces during gradual soil warming while values of  $p\text{H}_2\text{O}$  were maintained at a constant value ( $5 \times 10^{-5}$  or  $10^{-3}$  mbar). A high pressure mercury arc ultraviolet source provided up to 50 times the anticipated solar flux at the Martian surface, with a lower end cutoff of  $\sim 2300 \text{ \AA}$ .

Rock material of five types were used in experiments: Mauna Ulu basalt, olivine, two compositions of augite, and enstatite, all of which were crushed to powders having surface areas of 1-5  $\text{m}^2/\text{cc}$ . These powders were subjected to a variety of experimental environments including  $p\text{CO}_2$  values in the range of 20-150 mbars, water vapor pressures of either  $5 \times 10^{-5}$  or  $10^{-3}$  mbar and total water content of 0-60 precipitable micrometers  $\text{H}_2\text{O cm}^{-2}$ , illuminated, nonilluminated, or indirectly illuminated conditions,  $T_{\max}$  values of 240, 260, 270, or 297 K, and diurnal cycles of 3, 6, or 12 hours. Experiments ranged between 18 and 114 hours in length.

Carbonate analysis of all experimental soils was performed on a vacuum system having a high precision manometer capable of measuring volumes in the range  $0.160$  to  $0.700 \pm .005 \text{ ml}$ . Carbonate was decomposed to form  $\text{CO}_2$  gas by reaction of experimental powders with 100% phosphoric acid in vacuo after soil degassing at  $300^\circ\text{C}$ . Carbon dioxide was subsequently separated from accompanying gases before final measurement. Additional techniques used in the study were gas chromatography for the analysis of chamber gases and X-ray photoelectron spectroscopy (XPS) for the identification of the  $\text{CO}_3$  species.

Experimental studies revealed the following characteristics of non-aqueous carbonate formation in simulated Martian environments:

1. With  $p_{H_2O} = 10^{-3}$  mbar, carbonate growth is directly proportional to  $p_{CO_2}$  and water content; at  $p_{H_2O} = 5 \times 10^{-5}$  mbar, however, carbonate growth is proportional to water content but independent of  $p_{CO_2}$  above  $p_{CO_2} = 30$  mbar. A limiting value in carbonate growth is approached with time (Figs. 2,3, and 4).

2. Illumination of samples enhances carbonate growth but is not required for reaction to occur. Indirect illumination of samples has no effect on carbonate growth.

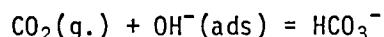
3. Carbonate formation occurs in environments having temperature maxima as low as 240 K (Fig. 5).

4. Carbonate growth is dependent upon temperature cycling while independent of the period of exposure at  $T_{max}$ .

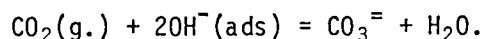
5. Olivine, olivine tholeiite, and augite all exhibited measureable carbonate growth on surfaces with the greatest growth occurring on olivine (Figs. 6a, 6b). Enstatite and subcalcic augite showed no measureable  $CO_2$  fixation.

6. The carbonate species was found to be thermally stable at  $400^\circ C$  when  $p_{CO_2} = 10^{-4}$  mbar.

From experimental results, gaseous  $CO_2$  is indicated to react at silicate surfaces with hydroxyl ions derived from the dissociation of adsorbed "unfrozen" water (Anderson, 1967) to form either  $HCO_3^-$  or  $CO_3^{=}$  ions by either



or



Ultraviolet irradiation is concluded not to play a role in the chemical weathering activity examined, with growth enhancement effects more likely attributable to minor surface heating of samples. The rate of reaction is mineral selective and quickly approaches a limiting value in drier environments studied. Unless impeded by competing chemical reactions, carbonate formation should be an important form of chemical weathering on Mars.

#### References:

Booth, M.C. and Kieffer, H.H. (1978) J. Geophys. Res. **88**, 1809.

Anderson, D.M., Gaffney, E.S., and Low, P.F. (1967) Science **155**, 319.

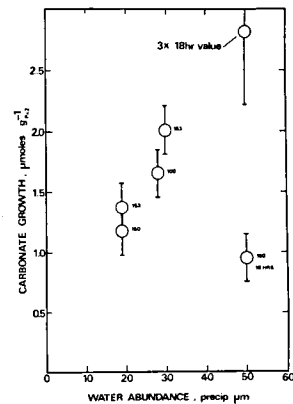
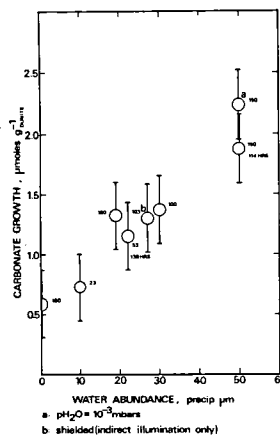
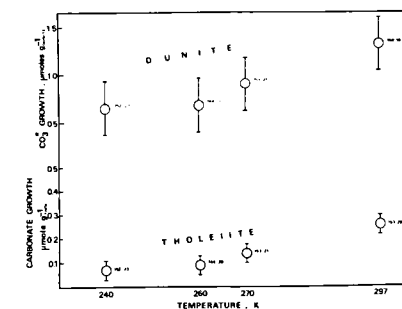
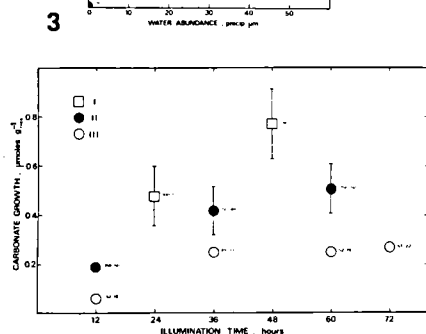
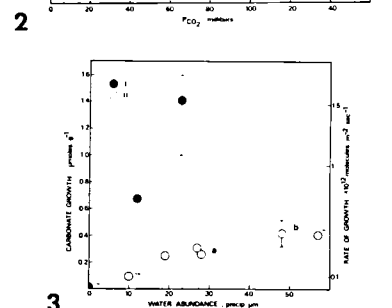
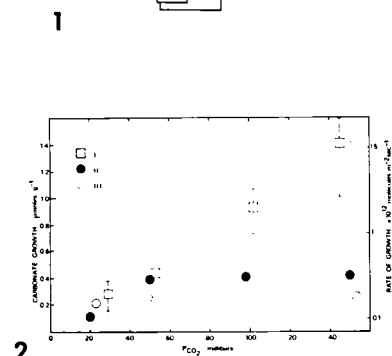
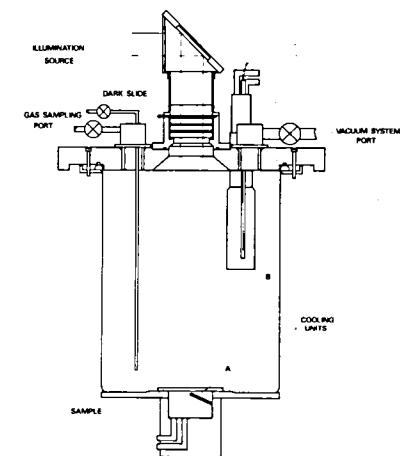
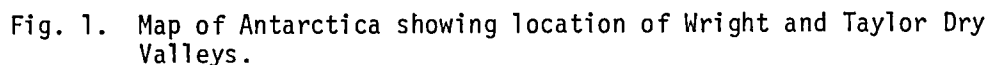


Fig. 1. The environmental chamber.  
 Fig. 2.  $\text{CO}_2$  growth versus  $p\text{CO}_2$  in tholeiite for 66-hr. experiment.  
 I:  $\text{pH} = 10^{-1}$  mb, total water = 20 precip  $\mu\text{m cm}^{-2}$ ;  
 II:  $\text{pH} = 5 \times 10^{-2}$  mb, total water = 50 precip  $\mu\text{m cm}^{-2}$ ;  
 III:  $\text{pH} = 5 \times 10^{-3}$  mb, total water = 30 precip  $\mu\text{m cm}^{-2}$ .  
 Fig. 3.  $\text{CO}_2$  growth versus  $\text{H}_2\text{O}$  in tholeiite for 66-hr. experiment.  
 I:  $\text{pH} = 10^{-1}$  mb,  $p\text{CO}_2 = 150$  mb; II:  $\text{pH} = 5 \times 10^{-2}$  mb,  
 $p\text{CO}_2 = 100$  mb.  
 Fig. 4.  $\text{CO}_2$  growth versus time. I:  $p\text{CO}_2 = 100$  mb,  $\text{pH} = 10^{-1}$  mb,  
 total water = 55 precip  $\mu\text{m cm}^{-2}$ ; II:  $p\text{CO}_2 = 150$  mb,  $\text{pH} = 5 \times 10^{-2}$  mb,  
 total water = 50 precip  $\mu\text{m cm}^{-2}$ ; III:  $p\text{CO}_2 = 50$  mb,  
 $\text{pH} = 5 \times 10^{-3}$  mb, total water = 20 precip  $\mu\text{m cm}^{-2}$ .  
 Fig. 5.  $\text{CO}_2$  growth versus  $T_{\text{max}}$  for dunite and tholeiite in 66-hr.  
 experiment for  $p\text{CO}_2 = 150$  mb, total water = 20 precip  $\mu\text{m cm}^{-2}$ ,  
 $\text{pH} = 5 \times 10^{-3}$  mb.  
 Fig. 6.  $\text{CO}_2$  growth results in olivine (A) and augite (B). Numbers  
 accompanying points provide  $p\text{CO}_2$  of 66-hr. experiments.

Everett K. Gibson, Jr., SN7/Geochemistry Branch, NASA-JSC, Houston, TX

In order to better study the properties of planetary regoliths, a large suite of soils, rocks, and cores were collected from Taylor and Wright Dry Valleys located in southern Victoria Land, Antarctica (Fig. 1). The suite of samples were collected using techniques and tools developed for the collection of the lunar samples. Samples were returned to JSC frozen and their initial characterization is presently underway. Preliminary results from the chemistry and mineralogy study of the soils is presented in Gibson et al. (3).



Ample evidence exists within the Dry Valleys to show the effects of cold weather alteration processes. Among the most striking freeze-thaw features are the patterned grounds displayed in the form of polygons, which have diameters from 10 to 15 meters. These polygons are favored by the presence of a water-rich active zone immediately beneath the surface (Fig. 2).

Photography from the Viking missions indicated the presence of boulder strewn fields which resembled terrestrial ventifacts (4). Within the Dry Valleys ventifacts are the predominant rock form. Ventifacts are shaped by abrasion of wind-driven sand. Wright Valley contains areas around Don Juan Pond which are identical to features observed on the Martian surface by Viking. The flanks of Don Juan Pond (Fig. 3) are the best example and are suggestive of the same surface features observed at the V1 and V2 sites. Similar features have also been observed in the deserts of southwestern Egypt (5).

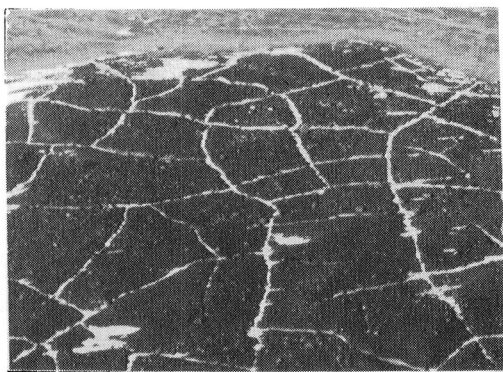


Fig. 2. Patterned ground, Taylor Valley. Diameter of polygons is 10-15 meters. Photo taken from 500 ft. altitude. Frozen lake at top of photograph.

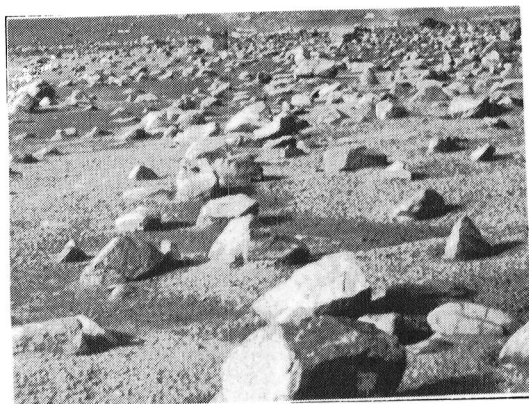


Fig. 3. Martian surface analog located near Don Juan Pond, South Fork, Wright Valley. Areas between boulders represent evaporite-salt deposits.

Duricrust as seen by Viking has been observed throughout the Wright Valley and a typical example is shown in Fig. 4. The duricrust is only 1 to 5 mm thick and results from cementation of surface soil layers by salts which have deposited by percolating water as it moves toward the surface prior to evaporation. The salts remain behind after evaporation and act as a sealant to the tops of the soils. Aeolian action produces the abrasion and removal of the salts at the edges of the duricrust regions. Immediately beneath the surfaces of the soils (1 to 5 cm depth) in the Dry Valleys and surrounding the evaporite ponds, deposition of salts has occurred from percolation of water. Trenches dug at numerous sites has shown the presence of the salt-rich layers (Fig. 5). The salt-rich layers are typically lighter in color and are typically composed of sulfur-rich minerals (3).





Fig. 4. Duricrust, Don Quixote Pond, North Fork, Wright Valley.

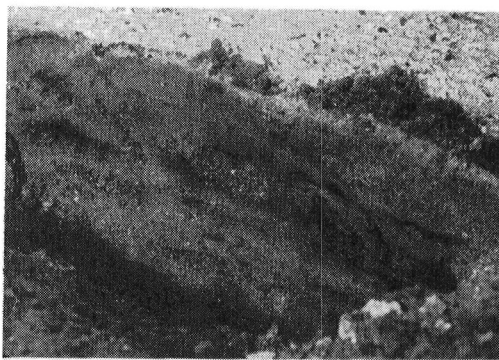


Fig. 5. Trench from edge of Don Juan Pond, South Fork, Wright Valley. Salt-rich layer located within top 2 cm of surface.

It is obvious that within the Antarctic Dry Valleys there are numerous features identical to those seen by the Viking landers on Mars, and the detailed study of geological weathering processes in cold environments may assist in our understanding of regolith processes operating on other planets and satellites.

#### References

- (1) Horowitz, N.H. et al. (1972) Microbiology of the Dry Valleys of Antarctica. Science 176, 242-245.
- (2) Morris, E.C. et al. (1972) Possible analogs of Martian surface features. U.S.G.S. Interagency Report: Astrogeology 52, 156 pages.
- (3) Gibson, E.K., Jr. et al. (this volume) Geochemical changes produced by weathering of soils from the Dry Valleys of Antarctica: A progress report. Reports of Planetary Geology Program, 1980-81.
- (4) Binder, A.B. et al. (1977) The geology of the Viking Lander 1 site. J. Geophys. Res. 82, 4439-4451 and Mutch, T.A. et al. (1977) The geology of the Viking Lander 2 site. J. Geophys. Res. 82, 4452-4467.
- (5) McCauley, J.F. et al. (1979) Pitted rocks and other ventifacts in the western desert of Egypt. Reports of Planetary Geology Program, 1978-79, NASA TM-80339, pp. 286-287.

## GEOCHEMICAL CHANGES PRODUCED BY WEATHERING OF SOILS FROM THE DRY VALLEYS OF ANTARCTICA: A PROGRESS REPORT

Everett K. Gibson, Jr., SN7/Geochemistry Branch, NASA-JSC, Houston, TX  
Barbara Ransom, Lunar and Planetary Institute, Houston, TX (now at the  
Geology Department, Louisiana State University, Baton Rouge, LA)  
Robert E. L. Ingram, Arizona Western College, Yuma, AZ

The Dry Valleys of Antarctica have been considered as terrestrial analogs of weathering processes operating on the Martian surface (1-3). In both locales, mechanical weathering predominates over chemical weathering processes (4). Even though chemical alteration is a secondary weathering process, it is still present and plays an important role in the modification of parent materials. To better understand the Viking Lander data and its relationship to the regolith formation and alteration, a suite of systematically sampled soils, rocks, and cores from the valleys and brine ponds of Taylor and Wright Dry Valleys in Antarctica are being investigated. Samples were collected during the 1979-80 austral summer by E.K. Gibson and are being studied as a portion of a consortium centered at NASA-JSC. The purpose of the study is to understand the chemical and mineralogical alterations produced during cold-environment weathering processes which operate in the Antarctic and relate these processes to Mars. This progress report will discuss the abundances of the volatile elements  $H_2O$ , total C and S, along with water soluble cations and anions (e.g., Ca, K, and Cl).

The majority of previous investigations which have related to evaporite sequences and to weathering processes have been carried out with sea waters or closed basins associated with hot, dry climates; but the study of Thompson and Nelson (5) considers the depositions of salts at temperatures as low as  $-45^{\circ}C$ . The order and mineralogy of precipitated salts from frigid seawater is considerably different from the classical evaporation sequence from warm seawater. In the latter, calcite then gypsum and lastly halite crystallize leaving behind a brine enriched in Mg and K. A frigid sequence crystallizes calcite and then sodium chloride dihydrate, leaving K and Mg salts to precipitate last, resulting in a Ca-rich brine. Figure 1 shows the frigid seawater precipitation sequence and the temperatures of crystallization on a diagram showing the major cations of seawater. Along with this data, the brine compositions of four evaporite ponds in the Dry Valleys are plotted (DJ, DQ, LV, and TV) (6). The coincidence of the theoretical path and the pond compositions indicates that this is a good model to start analysis of the Dry Valley brines and their evolutions as represented by the evaporite mineralogy and water soluble cations and anions in the soils collected. The data obtainable may be applicable to interpretation of the Martian regoliths which may represent a previous "wet-period."

Although the solution chemistry studies are incomplete, knowledge of prospective minerals and an evaporative sequence allows some general interpretations of the data. Sets of systematically collected soils were analyzed by selective ion electrodes along with total water, carbon, and sulfur abundances and distributions. Several distinctive weathering trends are obvious from the data.

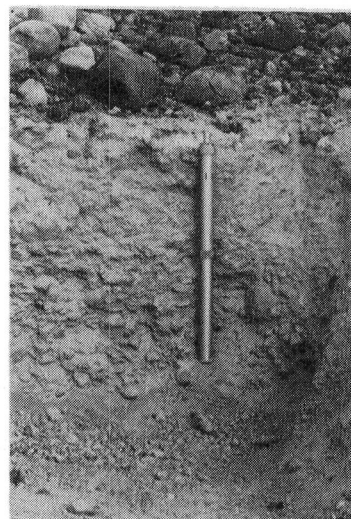
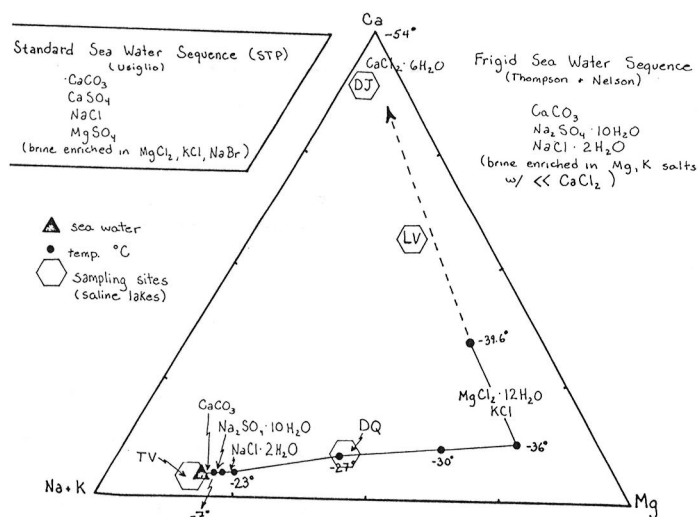


Fig. 1. Frigid seawater evaporation sequence after (5). DJ = Don Juan Pond; LV = Lake Vanda; DQ = Don Quixote Pond; TV = Taylor Valley brine compositions (6).

Fig. 2. Soil pit on Prospekt Formation near Lake Vanda, Wright Valley. Length of core is 70 cm. Note salt layer at top of core tube.

In a 1 meter deep soil pit near Lake Vanda in Wright Valley (Fig. 2), a whitish salt layer was found at 2-4 cm depth. Analysis of soils from this trench is shown in Table 1. Correlative with the white layer are high sulfur concentrations and increased chlorine abundances. This zone appears to be depleted of carbon as compared to the top 2 cm of soil. The S and Cl enrichments are associated with a gypsum and halite deposit. At a depth of 24 cm a sharp depletion of Ca, Cl, K, and S was found. The surficial depletion of chlorides is probably due to aeolian and other mechanical reworking or dilution of the top portion of the soil profile with volatile depleted materials (e.g., Si-rich sands). The enriched sulfur abundances (up to 2.21%) are similar to those observed at the Viking Lander sites and have been interpreted as salt deposits (7).

As progress is made in this study, a geochemical model for the volatile element behavior and distributions for the Dry Valleys of Antarctica can be developed. This model would determine sources and processes involved in modifying mechanically weathered soils at low temperatures and low humidities. The knowledge of the behavior of the evaporites and their compositions allow the possible determination of how an aqueous fluid phase behaves or exists in an environment with a mean annual temperature of  $-18^{\circ}\text{C}$ . The study of chemical weathering effects in the Dry Valleys can then be correlated with the Viking Lander data and possible processes for the formation of the regolith and salt deposits on Mars. It will also give a better background on which to evaluate geochemical processes operating in the Martian regolith when the data becomes available (e.g., future missions) and to assist in planning future sampling of the unusual Martian regolith.

Table 1. Wright Valley - Soil Pit

Sample Number	Depth cm	H <sub>2</sub> O, Percent				Water Soluble Fraction		
		-40 <sup>0</sup> to+27 <sup>0</sup> C	27 <sup>0</sup> to110 <sup>0</sup> C	C ppm	S ppm	Ca <sup>++</sup> ppm	K <sup>+</sup> ppm	Cl <sup>-</sup> ppm
219	Top 2	0.034	1.16	970	10600	2400	240	5790
238	2-4 (Salt layer)	0.16	1.62	185	22150	1600	1240	99800
215	4-6	0.14	1.79	245	4700	1220	1020	43780
216	6-8	0.10	2.00	380	4510	1760	1050	36970
217	8-12	0.06	1.54	230	2160	1180	1200	25970
218	12-16	0.01	1.93	320	1810	1040	980	18170
T R A N S I T I O N      Z O N E								
220	24-28	0.15	1.51	675	330	170	200	4190
214	32-36	0.27	1.98	805	195	170	125	3460
221	44-48	0.48	2.51	1230	410	90	100	3390

#### References

1. Horowitz, N.H. et al. (1972) Science 176, 242-245.
2. Morris, E.C. et al. (1972) U.S.G.S. Interagency Report: Astrogeology 52, 156 pages.
3. Gibson, E.K., Jr. (1981) this volume.
4. Ugolini, F.C. (1963) Ph.D. Dissertation, Rutgers Univ., N.J.
5. Thompson, T. and Nelson, K. (1956) Am. J. Sci. 254, 227-238.
6. Torri, T. et al. (1977) Memoirs of National Inst. for Polar Res., Special Issue 13, 22-32.
7. Clark, B.C. (1979) J. Mol. Evol. 14, 13-31.

EXPERIMENTAL ALTERATION OF ROCKS UNDER "HYDROTHERMAL" CONDITIONS  
APPLICABLE TO MARS AND VENUS

J.L. Gooding, Planetology Section, Jet Propulsion Laboratory, California Institute of Technology, Pasadena, CA 91103.

INTRODUCTION. Chemical weathering under current Martian surface conditions has been examined both theoretically (1, 2) and experimentally (3, 4) and preliminary calculations have been performed for Venusian surface conditions (5, 6). However, neither the alteration reactions expected to occur during magma/ice interactions (7) and impacts into water-bearing strata (8) on Mars, nor those reactions expected to occur at the surface of Venus have been investigated experimentally. Accordingly, an experimental study of rock alteration under appropriate "hydrothermal" conditions ( $P \leq 150$  bars,  $T \leq 500^{\circ}\text{C}$ ) has been initiated and will be supported by parallel studies based on calculational models.

MARS. The alteration behavior of both crystalline and glassy basalts and individual minerals is being studied as a function of temperature, pressure, and "fluid" composition ( $\text{CO}_2$  and  $\text{H}_2\text{O}$  with traces of  $\text{O}_2$ , sulfur-bearing species and electrolyte salts) using an externally heated, gas-pressurized bomb reactor. Since the identity of the Martian regolith volatile reservoir is unknown ( $\text{CO}_2$  ice,  $\text{H}_2\text{O}$  ice,  $\text{CO}_2 \cdot 6\text{H}_2\text{O}$  clathrate, etc.), a range of  $\text{CO}_2/\text{H}_2\text{O}$  "fluid" ratios are being investigated. Well-established mineralogical techniques (9) are used to determine the identities and relative abundances of alteration products.

VENUS. Experimental apparatus and procedures are similar to those used for Mars except for modifications to higher temperatures ( $450\text{--}500^{\circ}\text{C}$ ) and different gas compositions ( $\text{CO}_2$  with variable  $\text{H}_2\text{O}$ ,  $\text{SO}_2$ ,  $\text{H}_2\text{SO}_4$ , etc.) appropriate for Venus. Both mafic and feldspathic rocks are being studied in order to investigate the possible formation of both "basaltic" (Veneras 9, 10) and "granitic" (Venera 8) regolith materials (10) by decomposition of igneous bedrock.

This research was carried out under NASA Contract 7-100.

REFERENCES:

- (1) J.L. Gooding (1978): Icarus, 33, 483.
- (2) J.L. Gooding and K. Keil (1978): Geophys. Res. Lett., 5, 727.
- (3) R.L. Huguenin (1974): J. Geophys. Res., 79, 3895.
- (4) R.V. Morris and H.V. Lauer, Jr. (1980): Geophys. Res. Lett., 7, 605.
- (5) I.L. Khodakovsky, V.P. Volkov, Yu. I. Sidorov, M.V. Borisov, and M.V. Lomonosov (1979): Icarus, 39, 352.
- (6) J.S. Lewis and F.A. Kreimendahl (1980): Icarus, 42, 330.
- (7) C.C. Allen (1979): J. Geophys. Res., 84, 8048.
- (8) H.E. Newsom (1980): Lunar Planet. Sci. XI, 806.
- (9) J.L. Gooding (this volume).
- (10) M.V. Keldysh (1977): Icarus, 30, 605.

## MINERALOGICAL STUDIES OF TERRESTRIAL ANALOGS OF MARTIAN SURFACE MATERIALS

J.L. Gooding, Planetology Section, Jet Propulsion Laboratory, California Institute of Technology, Pasadena, CA 91103.

INTRODUCTION. As discussed elsewhere (1), currently observed Martian surface materials are probably derivatives of mafic or ultramafic igneous rocks. Unfortunately, elemental, but not mineralogical, analyses were performed by the Viking landers so that detailed mineralogical studies of terrestrial analog materials remain an essential part of efforts to understand the evolution of the Martian surface.

SAMPLES AND METHODS. Materials selected for study include weathered basalts and weathered stony meteorites. To date, work has emphasized rocks, soils, and sediments from the Kilauea/Ka'u and Mauna Kea summit areas of Hawaii, and chondritic meteorites recovered from the weathering environment of Antarctica. Each sample has been studied by optical and scanning electron microscopy, thin-section petrography, x-ray diffraction (XRD), differential thermal analysis (DTA), visible/near-infrared (VIS/NIR) reflectance spectrophotometry, and electron microprobe analysis (EMPA).

RESULTS. Preliminary results for Mauna Kea samples are presented elsewhere (2) and work is in progress for six ordinary chondrites from Allan Hills, Antarctica (ALHA-76006, 76008, 77155, 77270, 77272, 77296).

Typical results can be illustrated using the Kilauea/Ka'u samples described elsewhere (1). For silt-sized ( $< 63 \mu\text{m}$ ) fines, colors range from orange-yellow (sample 2B) to red-brown (6A, 11A) to various shades of gray (7B, 8, 9A). Dark materials usually contain greater abundances of basalt glass and/or primary igneous minerals than do light materials which are composed mostly of weathering products. Mineralogical composition commonly varies with particle size as exemplified by Ka'u dune sand (8) which shows decrease of glass and lithic fragment abundances but increase of plagioclase and magnetite/chromite/ilmenite abundances with decreasing particle size.

Alteration and weathering products include hematite but only very minor to trace amounts of clay minerals. Poorly crystallized smectites or "allophane" dominate the weathering products of some samples. Fumarolic soil 2B, for example, shows clear evidence for bound water (Fig. 1) but is mostly amorphous with respect to XRD (containing calcite as the only well-crystallized phase) and exhibits DTA behavior which is clearly different from that of a well-crystallized smectite (Fig. 2). Altered glass is apparently the dominant soil-forming component.

APPLICATION TO MARS. Weathering of basalts on Mars should be expected to produce a wide variety of soil-forming components. Weathering of glass may be an important process (3, 4) but may produce poorly crystallized materials which can be identified only by careful laboratory analysis. Variation of composition with particle size may seriously handicap efforts to deduce the bulk regolith composition from analyses of surface fines.

# REFERENCES:

- (1) J.L. Gooding (this volume).
- (2) J.M. Japp and J.L. Gooding (this volume).
- (3) J.L. Gooding and K. Keil (1978): Geophys. Res. Lett., 5, 727.
- (4) C.C. Allen, J.L. Gooding, M. Jercinovic, and K. Keil: Icarus (in press).

This research was carried out under NASA Contract 7-100.

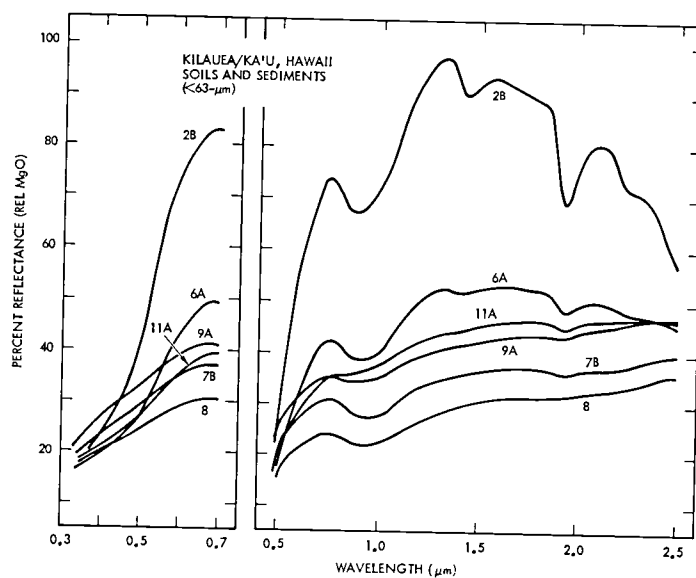


Figure 1. VIS/NIR reflectance spectra of silt-sized Hawaiian basaltic materials. Absorptions at  $\sim 1.4$  and  $\sim 1.9 \mu\text{m}$  are attributed to bound water and those at  $\sim 0.9 \mu\text{m}$  to oxidized iron.

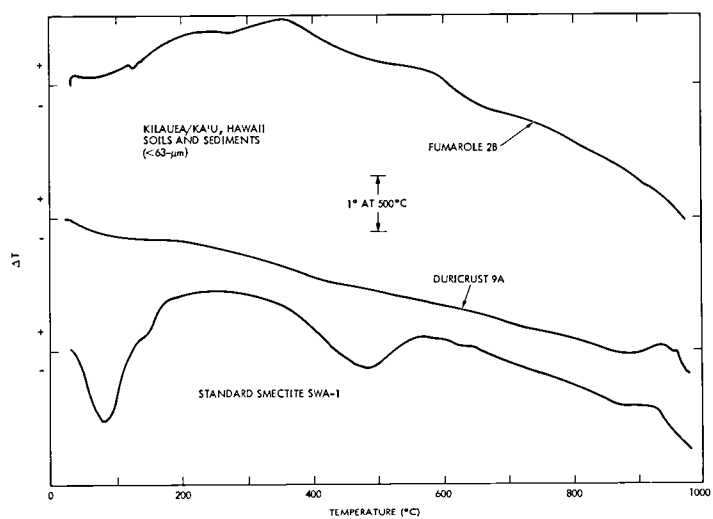


Figure 2. DTA curves for selected basaltic soil/sediment compared with a standard nontronite. All samples were run under vacuum vs.  $\text{Al}_2\text{O}_3$  at  $10^\circ\text{C}/\text{min}$ .



HAWAIIAN BASALTS AS ANALOGS OF MARTIAN SURFACE MATERIALS, 1:  
PARTICLE-SIZE DISTRIBUTIONS OF SOILS AND SEDIMENTS

J.L. Gooding, Planetology Section, Jet Propulsion Laboratory, California Institute of Technology, Pasadena, CA 91103.

INTRODUCTION. Earth-based spectral reflectance studies (1) and x-ray fluorescence analyses by the Viking lander spacecraft (2) strongly suggest that Martian surface materials have evolved from parent rocks of mafic or ultramafic composition. Evidence for basaltic-style volcanism is abundant (3) although erosion and weathering have probably formed soils from many of the primary igneous rocks (4). Consequently, careful study of various terrestrial basalt lithologies from different weathering environments should provide valuable information on the range of properties to be expected among Martian soils.

SAMPLES AND METHODS. Documented sediments and soils were collected from the Kilauea caldera and Ka'u Desert areas of Hawaii. Each was dried in vacuum (25°C), re-equilibrated with laboratory air (~ 50% R.H.), and sieved (~ 20-40 g aliquots) using an L3P Sonic Sifter with woven-wire stainless steel ASTM sieves. Mineralogical studies of these and other samples are reported elsewhere (5). Sample 2B: upper ~ 10-cm soil currently developing on active fumarole (1974 flow) within caldera; 6A: outer ~ 10 -cm soil, S wall of caldera; 11A: upper ~ 6 -cm soil developed on lower Kilauean (6) flow, Hilina Pali Rd.; 7B: outer ~ 10 -cm sandy ash, ~ mid-sequence 1790 (?) pyroclastics, SW rift zone; 8: upper ~ 12 -cm dune sand, Mauna Iki trail; 9A: platy, friable duricrust stratigraphically below 8.

RESULTS. Inman (7) plots (Figs. 1, 2) show that all samples except dune sand contain major amounts of pebble-sized particles and exhibit graphical median diameters of  $\leq 1 \phi$ . The duricrust sample, though composed mostly of fine sand and silt, displays a particle (clod)-size distribution which mimics that of a poorly sorted soil.

PARTICLE SIZES OF MARTIAN SOIL. Most Kilauea/Ka'u samples are significantly more coarse ( $M_d \leq 1 \phi$ ) than the < 1-cm portions of the lunar regolith ( $M_d \approx 3 - 4 \phi$ ; 8). Although ~ 50% of each sample is composed of particles below the best nominal size resolution (2.5 mm) of the Viking lander images (9), < 20% of each falls within the dominantly < 100 - $\mu$ m range deduced for Martian surface fines (10). Thus, Martian fines, if derived from basaltic source materials, may not accurately reflect the particle-size distribution of the bulk regolith but may represent minor fractions of more poorly sorted bulk soils or sediments.

REFERENCES:

- (1) R.B. Singer, T.B. McCord, R.N. Clark, J.B. Adams, and R.L. Huguenin (1979): J. Geophys. Res., 84, 8415.
- (2) P. Toulmin III, A.K. Baird, B.C. Clark, K. Keil, H.J. Rose, Jr., R.P. Christian, P.H. Evans, and W.C. Kelliher (1977): J. Geophys. Res., 82, 4625.
- (3) M.H. Carr (1973): J. Geophys. Res., 78, 4049.

- (4) J.L. Gooding (1978): Icarus, 33, 483.
- (5) J.L. Gooding (this volume).
- (6) D.W. Peterson (1967): Geol. Map Kilauea Crater Quad., Hawaii, U.S.G.S. - 1971 - G67093.
- (7) D.L. Inman (1952): J. Sed. Petrol, 22, 125.
- (8) D.S. McKay, R.M. Fruland, and G.H. Heiken (1974): Proc. Fifth Lunar Conf., 887.
- (9) F.O. Huck, H.F. McCall, W.R. Patterson, and G.R. Taylor (1975): Space Sci. Instr., 1, 189.
- (10) R.W. Shorthill, H.J. Moore, II, R.F. Scott, R.E. Hutton, S. Liebes, Jr., and C.R. Spitzer (1976): Science, 194, 91.

This research was carried out under NASA Contract 7-100.

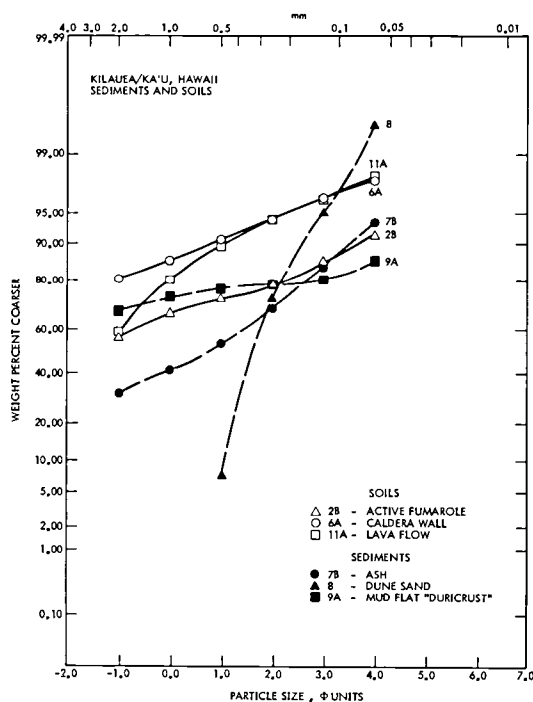


Figure 1. Particle-size distributions of Kilauea/Ka'u bulk soils and sediments.

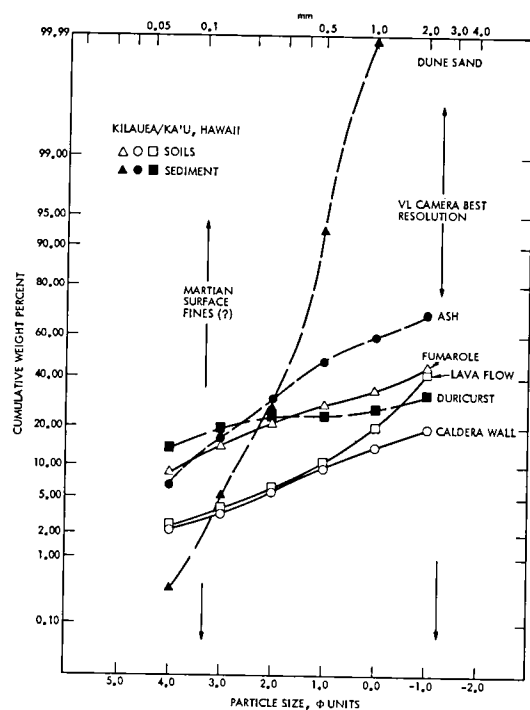


Figure 2. Particle-size distributions of < 2-mm fractions of Kilauea/Ka'u soils and sediments, compared with observational limits for Martian surface soils.

SIZE-FRACTION ANALYSES OF MAUNA KEA, HAWAII  
SUMMIT SOILS AND THEIR POSSIBLE ANALOGY WITH MARTIAN SOILS

J.M. Japp\* and J.L. Gooding, Planetology Section, Jet Propulsion  
Laboratory, California Institute of Technology, Pasadena, CA 91103

INTRODUCTION. The Viking lander x-ray fluorescence spectrometers gave elemental analyses which suggest derivation of surface fines from mafic or ultramafic igneous parent rocks (1), such that soils developed on terrestrial basalts under dry, nearly abiotic conditions might serve as reasonable analogs of Martian soils. Ugolini(2) proposed soils from the summit region of the Mauna Kea, Hawaii volcano as such analogs.

SAMPLES AND METHODS. Two samples were selected from surface (upper ~ 12 cm) soils developed, respectively, on volcanic and glacially/fluviially re-worked deposits near the Mauna Kea summit. The first (5B) was taken from Puu Poliahu, a tephra cone within the Waikahalulu Formation of the Laupahoehoe Group (3,4). The second (3B) was collected from a Makanaka Formation (also Laupahoehoe Group) deposit which is interpreted as outwash material (3,4) possibly produced by catastrophic flooding precipitated by melting of glacial ice.

Each bulk soil was separated into size fractions using a sonic sifter and ASTM sieves. After optical microscopic examination, portions of each fraction were crushed to pass a 30- $\mu$ m sieve and analyzed by x-ray diffraction (XRD) and visible/near-infrared (VIS/NIR) reflectance spectrophotometry.

RESULTS AND INTERPRETATION. Sieve analyses (Fig. 1) show that soil 3B (outwash plain) contains appreciably more fine material than does 5B (tephra cone). However, < 5 weight percent of either sample falls within the apparent silt-size range of Martian surface fines analyzed by the Viking landers (5).

XRD indicates that both soils contain similar relative abundances of primary igneous minerals (plagioclase, olivine, pyroxene, and spinels). Soil 5B also contains substantial amounts of secondary minerals including smectites and hematite. Furthermore, at least three XRD peaks from 5B show systematic increases in intensity with decreasing particle size (Fig. 2), indicating concentration of some (mostly secondary) minerals into small particles. In contrast, 3B shows no pronounced variation of mineralogy with particle size.

Two NIR absorption bands (1.4, 1.9  $\mu$ m) of 5B (Fig. 3) are attributable to hydrous phyllosilicates (6) although 3B exhibits only incipient bands at the same wavelengths as would be characteristic of an unweathered basalt (7). Color differences between the soils (yellow-brown, 5B; gray-black, 3B) are substantial with 3B composed mostly of crystalline rock fragments and 5B composed of tephra fragments coated with weathering products as well as individual particles of secondary minerals (Fig. 4).

\*NASA Planetary Geology Intern, Summer 1980. Now at Dept. of Geology,  
Univ. of Nebraska, Lincoln, NE 68508

CONCLUSIONS. Significant mineralogical differences can arise between soils developed on genetically and temporally related but depositionally distinguished basaltic substrates. Fluvially re-worked but little-weathered silt may be mineralogically similar to its parental material although unworked but significantly weathered materials may produce silt which is mineralogically distinct from its source. Consequently, compositions of silt-sized Martian soils, in general, should not be expected to reflect the compositions of their parental bulk soils or source rocks unless chemical weathering has not occurred. Most likely, a variety of soil types occur on Mars, representing a wide range in degree of weathering.

REFERENCES. (1) P. Toulmin III, A.K. Baird, B.C. Clark, K. Keil, H.J. Rose, Jr., R.P. Christian, P.H. Evans, and W.C. Kelliher (1977) J. Geophys. Res., **82**, 4625. (2) F.C. Ugolini (1976) In Int'l Colloq. Planet. Geol. Proc., Geol. Romana, **15**, 521. (3) S.C. Porter (1979) Geol. Soc. Amer. Bull., **90**, 980. (4) S.C. Porter (1980) Geol. Soc. Amer. Map MC-30. (5) H.J. Moore, R.E. Hutton, R.F. Scott, C.R. Spitzer, and R.W. Shorthill (1977) J. Geophys. Res., **82**, 4521. (6) J.D. Lindberg and D.G. Snyder (1972) Amer. Mineral., **57**, 485. (7) G.R. Hunt, J.W. Salisbury, and C.J. Lenhoff (1974) Mod. Geol., **5**, 15.

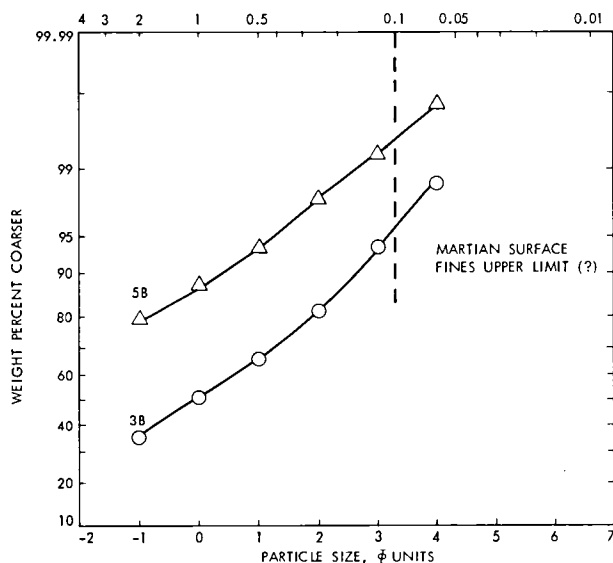


Figure 1. Particle-size distributions of two Mauna Kea summit soils compared with estimated (5) particle size of Martian surface fines. Upper horizontal scale is in mm.

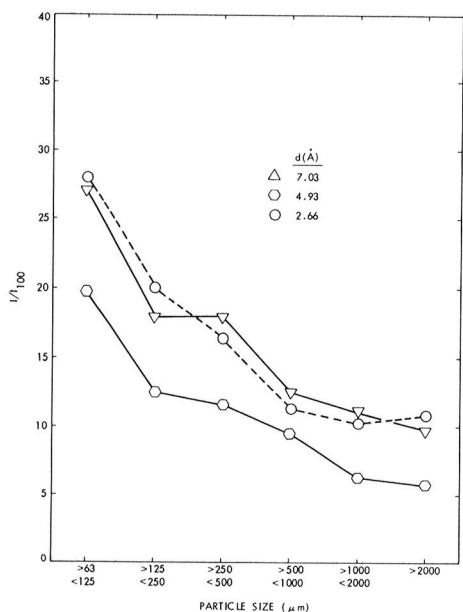


Figure 2. Normalized relative intensities of selected XRD peaks (7.03, 4.93, illite (?); 2.66, plagioclase or hematite) as a function of particle size in Mauna Kea soil 5B.

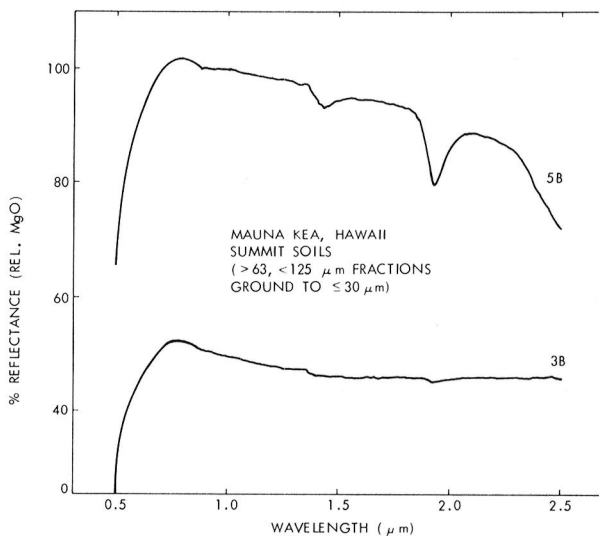


Figure 3. VIS/NIR reflectance spectra of Mauna Kea soils 3B and 5B (>63, <125-μm fractions).

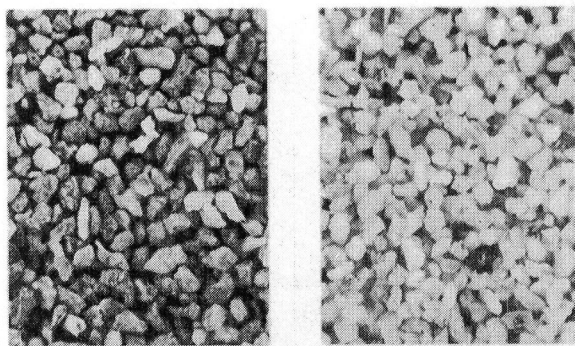


Figure 4. Photomicrographs of the >63, <125 - μm fractions of Mauna Kea soils 3B and 5B.

MARS FINES ATMOSPHERIC  
PRESSURE WAVE EXPERIMENT  
A PROGRESS REPORT

Fraser Fanale, Planetary Geosciences Department, University of Hawaii, Honolulu, HI; Banerdt, B.; Sanger, R.; Johansen, L.; Diffendaffer, P., All of Jet Propulsion Laboratory, California Institute of Technology, Pasadena, CA 91103 and Muradian, L., Massachusetts Institute of Technology, Cambridge, MA.

The Mars regolith may possibly act as a  $\text{CO}_2$  source-sink on some time scale to modify the amplitude of atmospheric pressure variations. This could happen if such pressure variations were transmitted isothermally through the regolith to sufficient depth, since an increase in atmospheric pressure could cause an increase in adsorbed  $\text{CO}_2$ , whereas a decrease in atmospheric pressure might cause the regolith to disgorge  $\text{CO}_2$ . This "isothermal buffering" requires substantial penetration. If it is found that the "pressure wave" does not penetrate much farther into the regolith than the thermal wave, then the regolith may still play a role. In this case, its response would be that of a thermally controlled reservoir rather than an isothermal buffer.

The primary arguments against buffering of Mars' seasonal atmospheric pressure wave have been based on indications that the pressure wave cannot penetrate deeply enough to provide a sufficiently large reservoir of  $\text{CO}_2$  (1). However, theoretical calculation of the characteristic depth of penetration is hampered both by lack of knowledge of Martian soil parameters and by the complexity of calculating the diffusion rate of a gas through a porous, highly adsorbing medium (2, 3, 4, 5, 6, 7). Therefore, we have constructed an apparatus to study the diffusion of  $\text{CO}_2$  through candidate Martian soils under conditions of temperature ( $-80^\circ\text{C}$ ) and pressure ( $\sim 5$  mb. to 8 mb.) appropriate to the Martian surface.

A stainless steel cylinder, containing about  $.25 \text{ m}^3$  of soil is surrounded with cooling coils and heater units and is enclosed within an insulating box. Temperatures within the soil are controlled independently at various depths. Stainless steel probes for sensing pressure and temperature extend from the wall of the cylinder to the center at various depths from 5 cm. to 75 cm. This experimental apparatus is described in more detail in another abstract for this meeting. The soil used in our preliminary runs was composed primarily of a fine montmorillonite. This soil provided a reasonably good fit to the constraints imposed by Viking lander data with the exception of bulk density, which was found to be too low after the dehydrating and sizing processes were completed. This discrepancy will be corrected in later runs.

In our experiments, the pressure in the ullage volume is changed as a step function from  $\sim 5$  mb to  $\sim 7.5$  mb. Pressure is then recorded as a function of time at each depth. Figure 1 shows the raw data from a typical run.

The characteristic depth for a sinusoidal pressure variation (i.e. the depth at which the pore pressure variation amplitude has dropped to  $1/e$  of the surface amplitude) is given by

$$d = \frac{2D}{\omega} \quad (1)$$

where  $D$  is a diffusivity and  $\omega$  is the angular frequency of the variation. As a first approximation for obtaining  $D$ , we will assume that adsorption effects can be combined together with diffusion effects into a single diffusivity. We obtain this diffusivity by comparing our data with the theoretical expression for the pressure in a half space subjected to a step function increase at the surface

$$P(x, t) = P_f - \Delta P \operatorname{erf} \left( \frac{x}{2 \sqrt{Dt}} \right) \quad (2)$$

where  $P_f$  is the final pressure at  $t = \infty$ ,  $\Delta P$  is the magnitude of the pressure increase, and  $x$  is the depth. We obtain a least squares fit to the six different depth curves simultaneously in order to get the best value for  $D$  in each run.

In addition to the  $\text{CO}_2$  runs, several experiments using  $\text{N}_2$  have been run. Since  $\text{N}_2$  is relatively poorly adsorbed, this data, along with our measurements of the volume of gas used in each experiment, should allow us to separate the effects of diffusion and adsorption.

Once we know what  $D$  is for  $\text{CO}_2$  as a function of soil mineralogy, grain sized distribution, packing, and temperature, we can then calculate the capacity of the regolith column to buffer any periodic externally imposed oscillation in atmospheric pressure as a function of the amplitude and period of that imposed variation. We will then know whether the presence of a highly adsorbing regolith on Mars affects atmospheric pressure fluctuations or whether Mars' atmospheric pressure history is effectively the same as if Mars possessed only an atmosphere and caps, but no regolith.

#### REFERENCES:

- 1) Toon, Pollack, Ward, Burns, and Bilski (1980) The astronomical theory of climate change on Mars, Icarus, in press.
- 2) Davies, Farmer, and LaPorte (1977) Behavior of volatiles in Mars' polar areas: A model incorporating new experimental data: J. Geophys. Res., 82, 3815.
- 3) Davis (1969) Some speculations on adsorption and desorption of  $\text{CO}_2$  in Martian bright areas: Icarus, 11, 155.
- 4) Fanale and Cannon (1971) Adsorption on the Martian regolith: Nature, 230, 502.
- 5) Fanale and Cannon (1974) Exchange of adsorbed  $\text{H}_2\text{O}$  and  $\text{CO}_2$  between the regolith and atmosphere of Mars caused by changes in the surface insolation: J. Geophys. Res., 79, 3397.
- 6) Fanale and Cannon (1979) Mars: Adsorption and capillary condensation on clays - significance for volatile storage and atmospheric history: J. Geophys. Res., 84, 8404.
- 7) Hess, Henry, Leoby, and Tillman (1977) Meteorological results from the surface of Mars: Viking 1 and 2: J. Geophys. Res., 82, 4559.
- 8) Pollack (1979) Climatic change on the terrestrial planets: Icarus, 37, 479.

This research was carried out under NASA Contract 7-100.



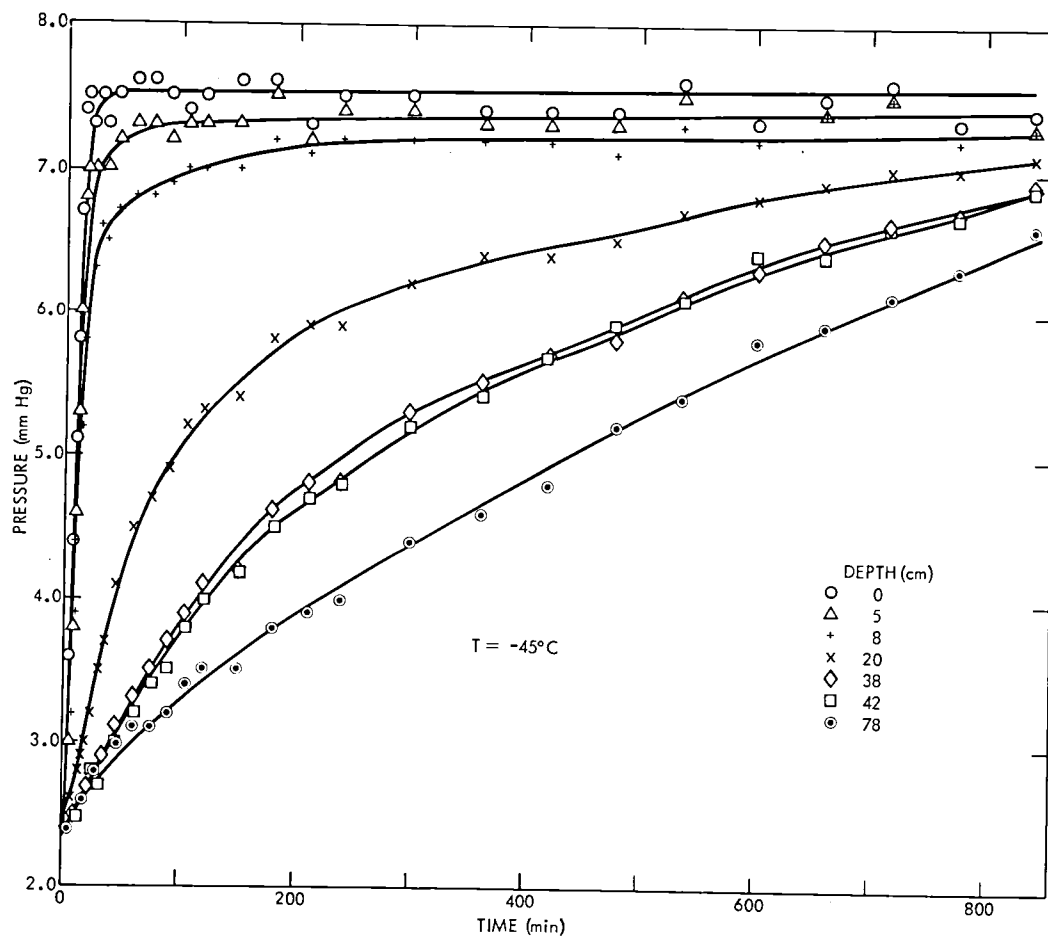


Figure 1. Example of data from a preliminary experiment using CO<sub>2</sub> at -45° C.

# STABILITY OF FERRIC OXYHYDROXIDES (FeOOH) TO DEHYDRATION IN THE PRESENCE OF UV RADIATION: IMPLICATIONS FOR WEATHERING ON MARS

Richard V. Morris, SN7/Geochemistry Branch, NASA-JSC, Houston, TX 77058  
H. V. Lauer, Jr., Lockheed, 1830 NASA Road 1, Houston, TX 77058

## INTRODUCTION

In their summary paper on Martian surface composition from reflection spectroscopy, (1) attribute certain features in the reflectance spectra of the bright areas of Mars to the presence of about 6-8 wt. % ferric oxide. In addition, they consider that dehydrated goethite is the dominant ferric oxide phase. Presumably, this view is based on (2) who report that in laboratory experiments goethite ( $\alpha$ -FeOOH) is efficiently dehydrated when exposed to UV radiation having  $\lambda < 0.28 \mu\text{m}$  and consequently infer that this process occurs naturally on the surface of Mars. However, (2) do not give experimental data to support their position for this potentially important surface process. Since we have found (3) that radiant heating, which if sufficiently intense would dehydrate goethite, can be significant in this type of experiment, we have conducted laboratory experiments to investigate the stability of ferric oxyhydroxides (FeOOH) to dehydration in the presence of UV radiation. In this abstract, we report the results for goethite ( $\alpha$ -FeOOH) and lepidocrocite ( $\gamma$ -FeOOH).

## EXPERIMENTAL PROCEDURES

The irradiational facility is described by (3). For the experiments reported here, we employed Xe(A) and Xe(B) radiations. Their irradiances in the near-UV, visible, and near-IR are given in Table 1; given for comparison is the solar irradiance at 1.5 AU, the orbit of Mars. All irradiations were performed in an atmosphere of dry  $\text{O}_2$  at 100 torr total pressure. Temperature was measured by a shielded thermocouple in intimate contact with the particulate samples.

The water content of irradiated and unirradiated samples was measured with a moisture evolution analyzer. Two water fractions were measured. The parameter  $(-)\text{H}_2\text{O}$  represents the quantity of  $\text{H}_2\text{O}$  removed at room temperature by the dry He stripping gas and is the concentration of adsorbed  $\text{H}_2\text{O}$ . The parameter  $(+)\text{H}_2\text{O}$  represents the quantity of  $\text{H}_2\text{O}$  evolved by subsequent heating to  $650^\circ\text{C}$  and is the concentration of structural  $\text{H}_2\text{O}$ .

## STARTING MATERIALS

We used as starting materials three particulate goethites ( $\alpha$ -FeOOH; GTS1, GTS2, and GTS3) and one particulate lepidocrocite ( $\gamma$ -FeOOH; LPS2). These synthetic materials were obtained as commercially available reagents. The particle shape and mean grain size of the ferric oxyhydroxides were determined from TEM photomicrographs. The values of those parameters as well as the values of  $(-)\text{H}_2\text{O}$  and  $(+)\text{H}_2\text{O}$  are compiled in Table 2. All the ferric oxyhydroxides are acicular in shape and submicron in mean grain size ( $M_z$ ).

Since radiant heating is inherent to any experiment utilizing an electromagnetic energy source, we performed thermogravimetric analyses

(TGA) on the ferric oxyhydroxides to ascertain when thermal dehydration might be expected. TGA curves for GTS2 and LPS2 are given in Figure 1. Both ferric oxyhydroxides evolve  $H_2O$  rapidly around  $200^\circ C$ . However, 0.5 to 1.5 wt. % of the total sample weight is lost in the 50 to  $100^\circ C$  temperature range. The TGA results demonstrate that thermal effects are present even at relatively modest temperatures.

#### RESULTS AND DISCUSSION

The results of the irradiations of the goethites and the lepidocrocite under Xe(A) and Xe(B) are given in Figure 2 as plots of normalized  $(+)H_2O$  versus the square root of the irradiation times; data reported earlier (4) is also included. Normalized  $(+)H_2O$  is the ratio of the value of  $(+)H_2O$  after a given irradiation time to its initial value.

By  $\sim 4$  hours irradiation under Xe(A), the value of normalized  $(+)H_2O$  decreased to plateau values (within the scatter of the data) of  $\sim 0.06$  for the goethites and, with limited data,  $\sim 0.02$  for the lepidocrocite. The thermocouple temperature for these experiments was  $\sim 540^\circ C$ , so the 94 to 98%  $(+)H_2O$  loss is consistent with thermally stimulated dehydration (cf., Fig. 1). However, UV photodehydration could be masked by a kinetically much more rapid thermally stimulated dehydration.

Under Xe(B) radiation, no perceptible change in normalized  $(+)H_2O$  was observed for the goethites within the  $\sim 3\%$  error in the measurement of  $(+)H_2O$ . The limited data available for lepidocrocite indicate a slight decrease in normalized  $(+)H_2O$  to 0.97. However, the magnitude of the decrease is on the same order as the experimental error, so it may not be significant. Also, the apparent decrease is not incompatible with thermally stimulated dehydration since the TGA results indicate  $H_2O$  evolution greater than can be accounted for by just  $(-)H_2O$  at the  $60^\circ C$  thermocouple temperature for the ferric oxyhydroxides under Xe(B). Therefore, we conclude no perceptible UV photodehydration occurred for the ferric oxyhydroxides under Xe(B). The null result with Xe(B) also implies that the dehydration observed under Xe(A) was predominantly thermally stimulated since Xe(A) and Xe(B) have the same irradiances in the near-UV to within a factor of  $\sim 2$ .

Our results, therefore, do not corroborate the effect reported by (2) that goethite is efficiently dehydrated by UV radiation. Since they give no experimental data, it is difficult to attempt a reconciliation of the seemingly contradictory results. However, a plausible explanation, based on the disparate behavior of the ferric oxyhydroxides under Xe(A) and Xe(B) in our experiments, is that the dehydration reported by (2) was thermally stimulated by radiant heating.

#### CONCLUSIONS AND IMPLICATIONS FOR MARTIAN WEATHERING

We found no perceptible UV photodehydration of particulate ferric oxyhydroxides (goethite and lepidocrocite) having submicron mean particle sizes. We can extrapolate our results under Xe(B) to obtain an estimate of the time for an equivalent exposure on Mars such that no perceptible UV photodehydration of ferric oxyhydroxides would be expected. From (5), the flux at  $0.30 \mu m$  at  $50^\circ N$  on the Martian surface in the spring is  $\sim 7 \times 10^{16}$  photons/cm<sup>2</sup>/day/A. Since the flux of Xe(B) at  $0.30 \mu m$  is  $\sim 2.5$  w/cm<sup>2</sup>/ $\mu m$ , our longest irradiation of  $\sim 250$  hours under Xe(B) is equivalent

to  $\sim 10$  Martian years of irradiation at the Martian flux. Thus we conclude that, although the possibility that UV photodehydration of ferric oxyhydroxides actually occurs cannot be totally eliminated, there is as yet no experimental basis for inferring the process occurs naturally on the surface of Mars as an efficient weathering process on a time scale of at least  $\sim 10$  Martian years. While this is an extremely short time scale, geologically speaking, it is long enough to indicate that ferric oxyhydroxides are not efficiently dehydrated under Martian conditions.

Table 1. Irradiances in  $\text{W}/\text{cm}^2$

Radiation	NUV: .25 $\rightarrow .4\mu\text{m}$	VIS: .4 $\rightarrow .7\mu\text{m}$	NIR: .7 $\rightarrow 1.0\mu\text{m}$
Xe(A)	1.68	5.80	6.56
Xe(B)	0.77	0.080	0.30
Solar, 1.5AU	0.0054	0.025	0.017

Table 2. Selected properties

Prop.	Unit	GTS1	GTS2	GTS3	LPS2
$M_z$	$\mu\text{m}$	.03x.3	.05x.4	.1x.7	.03x.9
(+)H <sub>2</sub> O	wt. %	9.92	10.02	9.74	9.84
(-)H <sub>2</sub> O	wt. %	0.60	0.58	0.20	1.08

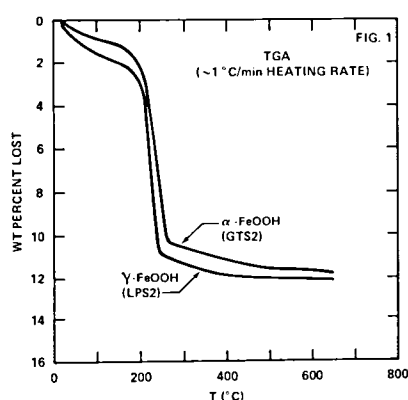
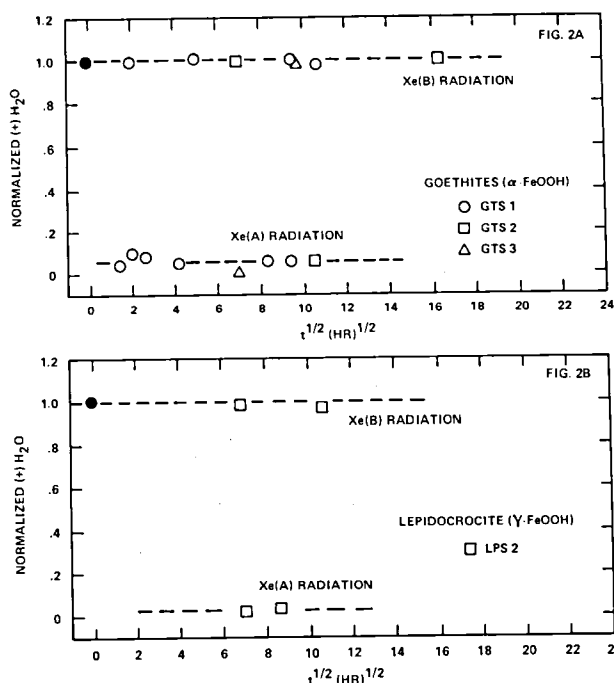


Fig. 1(above). TGA curves for GTS2 and LPS2.

Fig. 2(right). Normalized (+)H<sub>2</sub>O versus square root of the irradiation time for goethite (upper) and lepidocrocite (lower).



REF.: (1) Singer et al. (1979) JGR **84**, 8415; (2) Andersen and Huguenin (1977) BAAS **9**, 449; (3) Morris and Lauer (1980) GRL **7**, 605; (4) Morris and Lauer (1980) NASA TM 81776, 138; (5) Kuhn and Atreya (1979) J. Mol. Evol. **14**, 57.

MARS SOIL/WATER/ATMOSPHERE  
DYNAMIC INTERACTION FACILITY  
DESCRIPTION

Saunders R. Stephen; J. Gooding; F. Fanale; Laurie Johansen; Eric Laue; Don Schneider; Rick Sanger; Paul Diffendaffer; Stephen Wall, All of Jet Propulsion Laboratory, California Institute of Technology, Pasadena, CA 91103.

CHAMBER DESCRIPTION:

The Mars Mud Chamber at the Jet Propulsion Laboratory is a cylindrical stainless steel tank 2 feet in diameter and 6 feet long with heating, cooling and pressure control (Fig. 1).

The candidate soil, typically, fills half the chamber. Inlets at the bottom of the tank allow the soil to be fluidized with  $\text{GN}_2$  for drying, lowering its density, or mixing. A vibrator mounted on the cover of the chamber can toss the soil to eliminate discontinuities and can compact the soil to achieve the desired density.

MARS ENVIRONMENT SIMULATION:

Temperature is controlled using  $\text{LN}_2$  and heater coils around the tank's outside diameter. Differential thermostats compare temperatures at the chamber's wall with those at the center and control heaters to eliminate any difference, thus minimizing thermal gradients and simulating an infinite surface.

Pressure in the chamber can be controlled by an automated pressure feedback system.

A copper shroud with a nichrome wire grid above the test soil provides radiant thermal energy equivalent to a Martian solar constant.  $\text{LN}_2$  coils provide a radiation sink equivalent to the Martian night sky. Thus, martian diurnal and seasonal cycles of temperature can be reproduced in the chamber.

INSTRUMENTATION:

Six probes extend into the soil at different depths. Each measures temperature and pressure at the center of the tank and temperature at the wall. Temperatures are recorded on a strip chart and pressures are recorded by means of a time lapse camera aimed at a multitube manometer. This film also photographs the time, the absolute pressure in the tank's ullage, and the rate of gas flow into the chamber.

Additional ports which can be used to extract soil samples, endoscopically examine the soil or measure water content. A window and interior light provide a view of the surface of the soil and of the ullage space above it.

MARS SOIL SIMULANT DEVELOPMENT:

The material used to simulate Martian soil was selected as a compromise between observational constraints based on data from Mars and

practical limitations experienced in obtaining sufficient volumes of well-characterized commercially available materials. Mixtures dominated by Fe-rich smectites have been advocated as reasonable matches to the Viking XRF elemental analyses (Baird et al., 1976; Toulmin et al., 1977). Unfortunately, acquisition of the required material (i.e., several m<sup>3</sup> of well-characterized nontronite) for the simulation chamber has not been possible. Consequently, we resorted to the use of a commercially available smectite product (Montmorillonite BP, Georgia Kaolin Co.) as a close approximation to the Viking model. In order to more closely simulate the estimated bulk density (~ 1.0 - 1.6 g/cm<sup>3</sup>; Moore et al., 1977) and observed VIS/NIR spectral reflectance (Huck et al., 1977; Singer et al., 1979) of Martian surface fines, the clay product was mixed with pulverized basalt and commercial-grade rouge (Fe<sub>2</sub>O<sub>3</sub>) in the weight proportions 1:1:1. Detailed physical and mineralogical characterization of each component and the resultant mixture is in progress.

#### WATER SENSORS CHARACTERIZATION:

Three candidate transducers are under investigation to determine their response to Martian environmental conditions and characterize their suitability for measuring the content of free and bound water in Martian and other planetary soils. These sensors are currently being used in the Mars soil/water/atmosphere dynamic interaction investigations to monitor the soil simulant water content.

1) A commercial aluminum oxide, conductivity type sensor (Panametrics) changes resistance with changes in absorbed water in direct relationship to the vapor pressure of water in the vicinity of the sensor.

2) A solid polymer electrolyte (sulfonated Teflon "nafion" cell electrically disassociates water. This coulometric measurement provides the potential for an absolute determination of the vapor pressure of free water in the vicinity of the sensor.

3) A soil electrical impedance sensor changes the output frequency and waveshape of a free running multivibrator as a function of the density and free moisture of the soil between two perforated plates. Since these plates are electrically in parallel with the multivibrator, both the resistive and capacitive impedance of the material between the plates affect the output frequency and wave shape. This sensor, when combined with either of the other two sensors, may provide the ability to measure the free and bound water content of the soil and the soil density.

These water sensing instruments are being used in the performance of the "Mars soil/water/atmosphere dynamic interactions investigations." They are also candidate "landed" instruments for future space exploration missions to near Earth asteroids, Mars and the Galilean satellites.

A comparison of the space relevant features of these water sensors and other water sensors (previously studied under earlier programs) is being prepared. This comparison will be useful to mission planners in choosing the appropriate water sensor technology.

# REFERENCES:

- Baird, A.K.; Toulmin, P; Clark, B.C.; Rose, H.J.; Keil, K; Christian, R.P.; and Gooding, J.L. (1976) Mineralogic and petrologic implications of Viking geochemical results from Mars: Interim report, Science 194, 1288-1293.
- Huck, R.O.; Jobson, D.J.; Park, S.K.; Wall, S.D.; Arvidson, R.E.; Patterson, W.R.; and Benton, W.D. (1977) Spectrophotometric and color estimates of the Viking Lander sites, J. Geophys. Res. 82, pp. 4401-4411.
- Singer, R.B. (1979) Mars: Petrologic analysis of near-infrared spectra of dark regions: Bull. Am. Astron. Soc. 11, 574 (Abst).
- Tolumin III, Priestley et al., A.K. Baird; B.C. Clark; Klaus Keil; H.J. Rose, Jr. R.P. Christian; P.H. Evans, W.C. Relliher, Geochemical and mineralogical interpretation of the Viking inorganic chemical results, Journal of Geophysical Research, Sept. 30, 1977, Vol. 82, No. 28, pp. 4634.



# MARS ATMOSPHERE REGOLITH SIMULATION FACILITY

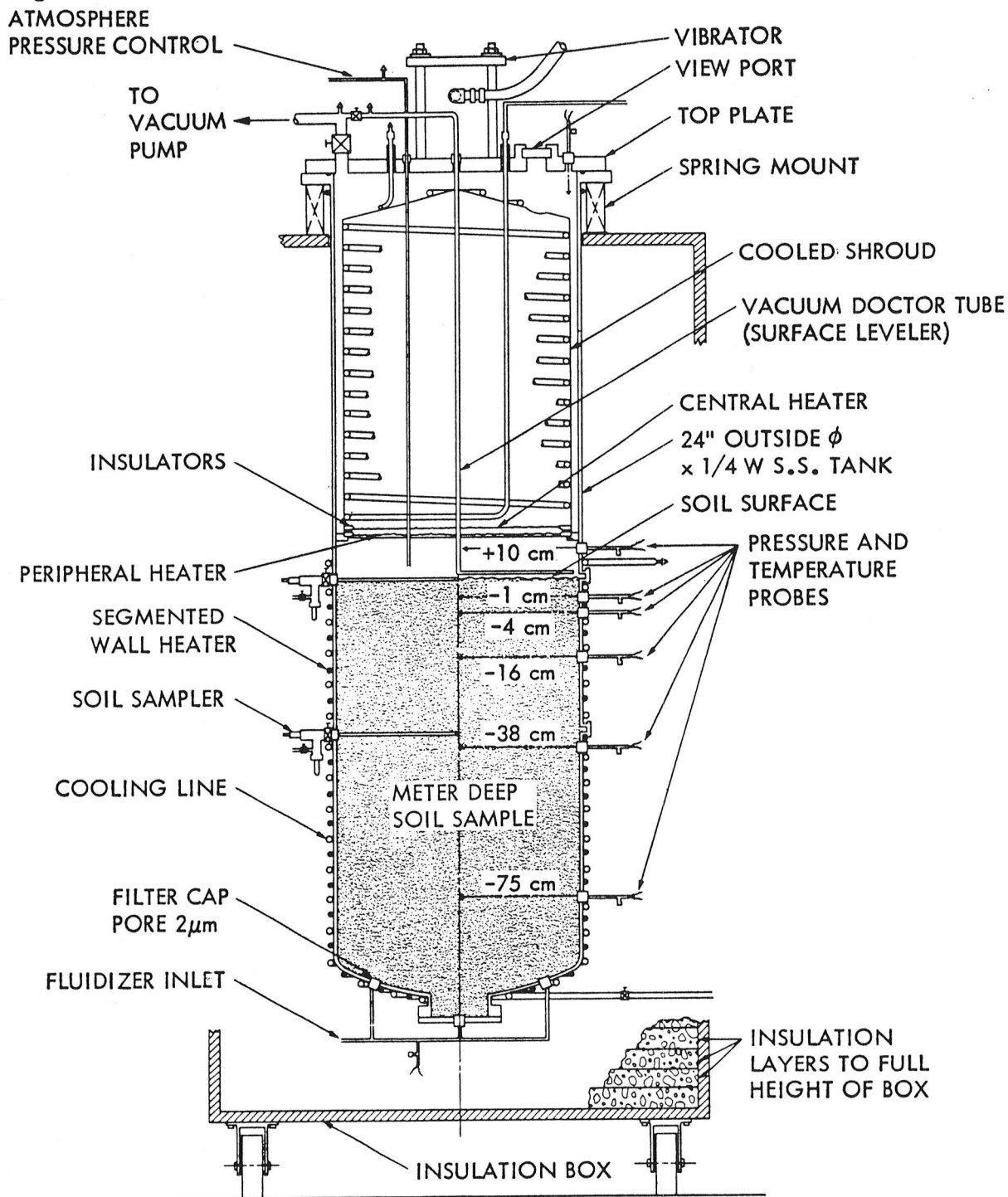


Figure 1



COHESION AND ANGLE OF INTERNAL FRICTION OF SURFACE MATERIALS AT VIKING  
LANDING SITES, MARS

Moore, H.J. and Dowe, E.M., U.S. Geological Survey, Menlo Park, CA 94025;  
Hutton, R.E., 1501 Palos Verde Dr., Harbor City, CA 90710; Scott, R.F.,  
Dept. Engr. and Appl. Sciences, Calif. Inst. Tech., Pasadena, CA  
91125; Shorthill, R.W., Univ. of Utah Res. Inst., Salt Lake City, UT  
84108; and Spitzer, C.R., NASA Langley Res. Ctr., Hampton, VA 23665

Surface materials at the Viking landing sites have been grouped into four categories: (a) drift material, (b) crusty to cloddy material, (c) blocky material, and (d) rocks (1,2). A fifth category includes disturbed materials or tailings from trenches. Backhoe touchdowns, surface bearing tests, and trenching operations performed by the Surface Samplers of Viking Lander 1 (VL-1) and Viking Lander 2 (VL-2) provide data for estimates of cohesion and internal friction of these surface materials. The rocky and variable nature of the surface materials result in variable and gradational values of cohesion at both sites.

In the backhoe touchdowns, penetrations of the backhoes in the martian surface materials are measured on images and compared with penetrations of the backhoe of the Science Test Lander in lunar nominal test material, for which cohesions have been estimated with a shear vane. A force of about 10 N is exerted on the backhoe during a touchdown. Estimates of cohesions using backhoe touchdowns are listed in Table 1.

In the surface bearing tests, the collector heads with the upper jaws closed are inserted in the surface materials at a steep angle ( $\approx 39.5^\circ$ ) and extended until the Surface Sampler motor decouples so that forces near 200-225 N are exerted by the Surface Sampler. The geometry of the surface deformation and collector head positions are established by stereometric mapping and Surface Sampler data. Angles of internal friction are estimated using logarithmic spirals in the azimuthal planes that are fit to the trench depth and the horizontal distance to limit of surface deformation; the spirals are centered on the intersection of the projected original surface and the collector head in the azimuthal plane. Cohesions are then calculated using plowing theory (3). Estimates of cohesions and angles of internal friction from surface bearing tests are listed in Table 1.

During trenching operations, the collector heads with the upper jaws open extend through the surface materials to collect samples and behave like plows. The geometry of the trenches and collector head positions are established by stereometric mapping and Surface Sampler data. Angles of internal friction are estimated from the limit of surface deformation. Cohesions are estimated using forces inferred from motor current records and equations for estimating plowing forces (4,5). Estimates of cohesions and angles of internal friction are listed in Table 1.

The rocky, layered, and variable nature of the surface materials at the Viking sites hamper interpretations of cohesions. The cohesions obtained fall in a continuous, gradational sequence that is probably real. Our best estimates of the cohesion and angle of internal friction for each type of material are listed in Table 1.

Our estimates of cohesion and density from the X-ray Fluorescence Experiment are consistent with clay-like surface materials. Kaolinite has cohesions of 0.9 to 3 kN/m<sup>2</sup> when the density is 1,100 to 1,260 kg/m<sup>3</sup> (6). These values are comparable to our cohesions for drift material and densities of fines (1,100+150 kg/m<sup>3</sup>) estimated by the X-ray Fluorescence Experiment (7). For lunar nominal surface material simulants, corresponding densities are higher (1,380 to 1,650 kg/m<sup>3</sup>). Individual fragments of material from blocky material have densities from 1,140 to 1,880 (8), so that larger cohesions are possible and a range of densities is probable. Crusty to cloddy material has cohesions comparable to kaolinite at bulk densities of 1,300 to 1,400 kg/m<sup>3</sup>, and blocky material has cohesions comparable to kaolinite at bulk densities of 1,420 to 1,510 kg/m<sup>3</sup>. Tailings have cohesions less than 0.6 kN/m<sup>2</sup>, which corresponds to kaolinite with a density less than 1,050 kg/m<sup>3</sup>.

#### References

- (1) Moore, H.J., Hutton, R.E., Scott, R.F., Spitzer, C.R., and Shorthill, R.W., 1977, Surface materials of the Viking landing sites: Jour. Geophys. Res., v. 82, p. 4497-4523.
- (2) Moore, H.J., Spitzer, C.R., Bradford, K.Z., Cates, P.M., Hutton, R.E., and Shorthill, R.W., 1979, Sample fields of the Viking Landers, physical properties, and aeolian processes: Jour. Geophys. Res., v. 84, B-14, p. 8365-8377.
- (3) McKyes, E. and Ali, O.S., 1977, The cutting of soil by narrow blades: Jour. Terra Mechanics, v. 14, p. 43-58.
- (4) Wismer, R.D. and Luth, H.J., 1972, Performance of plane soil cutting blades in clay: Trans. Amer. Soc. Agri. Engrs., v. 15, p. 211-216.
- (5) Luth, H.J. and Wismer, R.D., 1971, Performance of plane soil cutting blades in sand: Trans. Amer. Soc. Agri. Engrs., v. 14, p. 255-262.
- (6) Ko, Hon-Yim, 1971, Soil Properties Study: Martin Marietta Document VER-181, October 15, 1971, 43 p., 6 figs.
- (7) Clark, B.C. III, Baird, A.K., Rose, H.J. Jr., Toulmin, P. III, Christian, R.P., Kelliher, W.C., Castro, A.J., Rowe, C.D., Keil, K., and Huss, G.R., 1977, The Viking X-ray Fluorescence experiment: analytical methods and early results: Jour. Geophys. Res., v. 82, p. 4577-4594.
- (8) Weldon, R. and Castro, A.J., 1978, written communication.

Table 1. Preliminary estimates of cohesions and angles of internal friction of surface materials at the Viking landing sites

Material	Site	<u>Backhoe TD</u>	<u>Surface bearing tests</u>		<u>Selected trenches</u>		<u>Best estimate</u>	
		Cohesion (kN/m <sup>2</sup> )	Cohesion (kN/m <sup>2</sup> )	Friction angle (degrees)	Cohesion (kN/m <sup>2</sup> )	Friction angle (degrees)	Cohesion (kN/m <sup>2</sup> )	Friction angle (degrees)
Drift	VL-1	1-2	*	6-7	1.6+0.5	10+5	1-3	10+5
	VL-1	---	---	---	2.9+0.5	---	---	---
Crusty to cloddy	VL-2	5-8	5+1	20	3.8-5.8	35+5	4-8	30+10
	VL-2	---	4+1	30	5.0-7.2	---	---	---
Blocky	VL-1	10-12	13-17**	25	4.8+1.1	25+5	10-12	25+5
	VL-1	---	---	---	6.1+1.1	---	---	---
	VL-1	---	---	---	10-12	---	---	---
Rocks	VL-1	>>20	---	---	---	---	>>20	---
	VL-2	>>20	---	---	---	---	>>20	---
Tailings	VL-1	< 0.6	---	---	---	---	< 0.6	---
	VL-2	< 0.6	---	---	---	---	< 0.6	---

\* Collector head moved small rock and may have reached hard substrate; apparent cohesion 10-13 kN/m<sup>2</sup>.

\*\* Motor current record can be interpreted in two ways; one interpretation leads to a cohesion of 2 kN/m<sup>2</sup> and the other 13-17 kN/m<sup>2</sup>.



Chapter 5  
VOLCANIC PROCESSES AND LANDFORMS



## VERTICAL STRUCTURE AND EROSION RATES OF PAHOEHOE BASALT FLOWS

Jayne C. Aubele<sup>1</sup>, Larry S. Crumpler<sup>1</sup>, Wolfgang E. Elston, University of New Mexico, Albuquerque, NM 87131

In an earlier paper (Elston, et al. 1976) we described the vertical zoning pattern of terrestrial pahoehoe basalt flows. Within a single climatic zone, it is possible to estimate the age of basalt surfaces by determining the amount of vertical erosion. The rate is about  $1 \text{ m}/10^6$  years in the semiarid climate of New Mexico and decreases thereafter. With caution, this method can be extrapolated to minimum erosion rates of lava surfaces on Mars, on the assumption that climate is even more arid (and the erosion rates slower) than in New Mexico. In this paper we attempt to quantify earlier observations.

Mathematical models of physical processes that result in zoning (cooling, vesiculation, solidification) make some simplifying assumptions: Motion of lava flow is neglected, as is the formation of the glassy and frothy crust. The crust is short-lived (100–200 years in wet tropical Hawaiian climate, a few millenia in New Mexico). Models agree well with field observations on simple non-cavernous flows  $< 10 \text{ m}$  thick.

Three vertical zones can be characterized as follows (Fig. 1):

1. Upper vesicular zone: Vesicles closely packed, 1–10 mm, near the top; gradually become less abundant and larger (max.  $\leq 20 \text{ mm}$ ) near the base. Texture microcrystalline, flow banding may be present. Thickness is about half of total flow thickness.
2. Middle massive zone: Vesicles rare, isolated, typically  $\leq 10 \text{ mm}$ ; rare pipe vesicle columns. Texture diabasic or holocrystalline.
3. Lower vesicular zone: Vesicles irregular to subelliptical,  $\leq 10 \text{ mm}$ , density less than in upper vesicular zone. Basal rubble minimal or absent (unlike aa flows).

Vesicles form, grow, and rise continually through the flow, until trapped and overtaken by solidification fronts. Initially, vesicle distribution is random. As cooling progresses, increasing viscosity decreases the rate of vesicle growth (Sparks, 1978) and ascent (Fig. 1). This explains the increase in vesicle density, and decrease in vesicle size, toward the top of the upper vesicular zone. Near the base of the flow, there is a plane below which ascending vesicles are overtaken and trapped by the solidification front, forming the lower vesicular zone. Above this plane, the rate of ascent is greater than the advance of the solidification front, leaving a middle massive zone depleted in vesicles.

As downward cooling progresses, tensile stresses are relieved by vertical joints. Spacing of joints is roughly equal to their depth (Lachenbruch, 1961); as the solidification front advances, joints become deeper but more

---

<sup>1</sup> Current address: Department Planetary Sciences, University of Arizona

widely spaced (Fig. 2). The amount of a flow that has been eroded can therefore be estimated by (1) the spacing between joints at the eroded tops of flows, which is roughly equal to the amount removed, and (2) the distance between the base of the flow and the base of the upper vesicular zone, which is about half the original thickness of the flow. This method cannot be easily applied to flows  $>10$  m thick, which tend to develop closely spaced columnar joints and in which the distribution of vesicles may be complicated by multiple lava pulses.

This method is most useful in terrestrial ground applications, when applied to dated lava flows. The erosion rates so determined can be extrapolated to extraterrestrial bodies, with due caution. Its usefulness in direct interpretations of extraterrestrial high-altitude images is severely limited by problems of scale and cover. Under ideal conditions and optimum resolution, down to the meter range, spacing of joints in lava flows at the tops of cliffs could indicate the amount of vertical erosion. On plains, jointed lava flows tend to erode to blocky surfaces; the greater the depth of erosion the larger the blocks. The maximum size of blocks indicates maximum spacing of joints and approximate depth of erosion. In images from planetary landers, variations in size and density of vesicles in blocks distributed around impact craters could give clues to underlying basalt stratigraphy.

#### REFERENCES CITED:

- Elston, W.E., Aubele, J.C., Crumpler, L.S., and Eppler, D.B., 1976, Influence of tectonic setting, composition, and erosion on basaltic landforms: New Mexico and Mars: NASA Tech. Memorandum TM X-3364, p. 129-132
- Lachenbruch, A.H., 1961, Depth and spacing of tension cracks: Jour. Geophys. Research v. 66, p. 4273-4292
- Sparks, R.S.J., 1978, The dynamics of bubble formation and growth in magmas: A review and analysis: Jour. Volcanol. & Geothermal Research, v. 3, p. 1-37



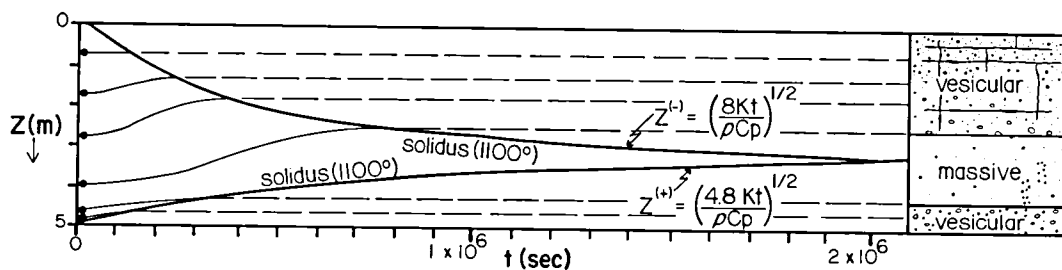


FIGURE 1. Mathematical model of the cooling history of a pahoehoe basalt flow 5 m thick (right). Solidus (1100°C isotherm) corresponds to the solidification front.  $Z$  = thickness in meters,  $K$  = conductivity,  $t$  = time in seconds,  $\rho$  = density,  $CP$  = heat capacity. Dots on left side are initially formed vesicles, solid lines plot positions during buoyant ascent, dashed lines their position after solidification.

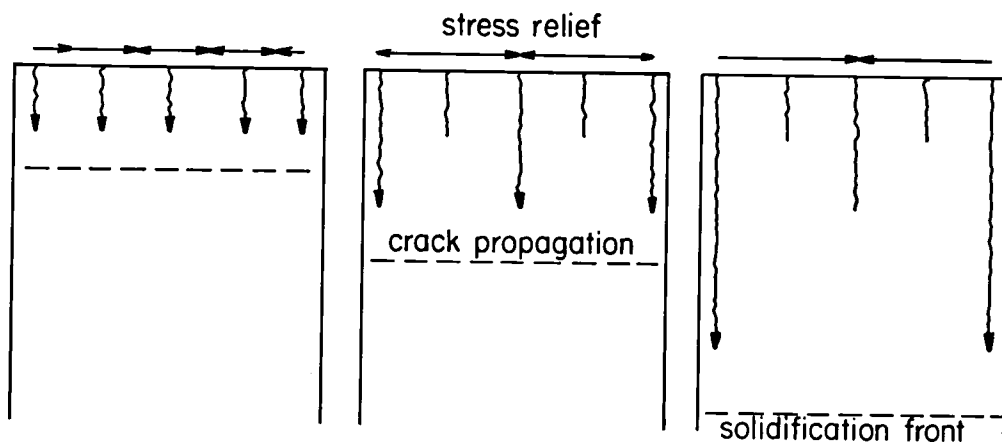


FIGURE 2. Downward propagation of tension joints in a cooling basalt flow. As the cooling front advances, joints become deeper and more widely spaced.

Degradation of Volcanic Landforms on Mars and Earth.

Victor R. Baker, Dept. Geological Sciences, The University of Texas at Austin,  
Austin, Texas 78712

Constructional aspects of volcanic landforms have received intense recent study for the purpose of comparative planetology. In contrast, the degradation of volcanic landforms has received very little serious geomorphic study since the descriptive physiographic work of the early part of this century. Similarly the degradational aspects of volcanic landforms on Mars have not been as fully described as primary features, such as lava flow morphology, caldera forms, structural deformation, and various secondary vents.

Tyrrhenum Patera is typical of the very ancient volcano landforms on Mars. It displays a central caldera, ringlike fracture systems, and an outward radiating system of troughs. The largest trough is about 5 km wide and can be followed from the central caldera through a second caldera and another 200 km down the volcano flanks. This trough is broad and flat-floored, and it narrows slightly with distance from the central caldera zones. Numerous other troughs dissect the distal flanks of the volcano. These distal troughs widen downgradient and are transitional into isolated remnants of the volcano which are similar to fretted terrain. Several of these troughs have distinct theater-like valley heads, i.e. they terminate headward at abrupt canyon walls. Several large rampart craters overlie the troughs, and others were apparently eroded by the trough-forming process. The heads of the longest troughs appear to be overlain by a mantling deposit, which is, in turn, cut by younger troughs. Additional troughs are developed along ring fracture systems that surround the calderas.

These relationships are not easily resolved by a simple hypothesis of lava erosion combined with tectonic collapse. The radial troughs have no apparent volcanic source, and their apparent dissection of the old volcanic form also is not consistent with lava erosion. The development of fretted terrain and theater-like valley heads is similar enough to the fretted channels that a similar process may be implied. The hypothesis of sapping erosion, probably associated with ice-rich permafrost, is more consistent with the morphology. The sapping may have largely occurred before an explosive eruption phase that produced the mantling unit. The two troughs cutting this mantling deposit are headed at the ring fracture complex or in the central calderas.

The northwestern flanks of Elysium Mons and nearby Hecates Tholus show a series of very unusual sinuous valleys. Like the outflow channels (1, 2) these valleys head at discrete source areas, contain streamlined uplands, and erode diverse terrains. However, their source areas are structurally controlled zones of collapse on volcano flanks, not chaotic terrain zones as in the outflow channels. The Elysium channels locally comprise anastomosing complexes.

Viking imagery of the Elysium channel area shows that the channels are associated with a transition from constructional lava plains to fretted, mantled, and channeled plains. Fretted terrain, rampart craters, and chaotic terrain all indicate that ice-rich permafrost may have been important in the development of these distal plains.

The northern flanks of Hecates Tholus also show evidence that the material beneath its lava flows may have had unusual physical properties. The margins of the shield volcano terminate in a highly irregular scarp. In several huge alcoves the upland terrain is broken into large angular blocks. Smaller blocks or mesas occur on the lowland plains to the north. The terrain appears somewhat similar to the

chaotic terrain south of the Chryse Basin, but there are important differences. Most apparent is the small size of the rotational slump blocks and the apparent small amount of vertical subsidence involved. Rather, the blocks appear to have dispersed by lateral displacement toward the plains to the north.

The Elysium channel region probably experienced a history of equilibrium/disequilibrium in ice-rich permafrost induced by volcanism. Permafrost dissipation may at times have been relatively slow, producing chaotic terrain margins of the original plains and the remnant upland of fretted terrain. Alternatively local zones of permafrost may have occasionally melted catastrophically or perhaps released water from confined aquifers (3). Slope channels on Hecates Tholus may have resulted from explosive volcanic density currents. These currents might be generated when rising magma intersected a thick layer of ice-rich permafrost (4). The melting of ground ice provided water for base surge activity.

Large troughs, dissecting inactive shield volcanoes, are very well developed in the Hawaiian Islands (5). Ground water is very important in the growth of the large valleys that occur on the older Hawaiian shield volcanoes. Major valleys grow at the expense of others because they tap larger supplies of groundwater. Chemical disintegration is favored at the water table, and this leads to steep valley walls (6). The characteristic valley form for the older Hawaiian volcanoes is U-shaped in cross section, and the valley terminates in an abrupt theater-like head. Valley sides are steep-walled and subjected to soil avalanches, slumps, and other mass movement processes (7). Because of the very high permeability of the lava flows, only the deeper valleys maintain perennial streams, even in high-rainfall regions. Headward valley growth occurs by spring sapping. Hanging valleys may be created when deep, headwardly receding valleys intersect and capture perched fluvial valleys (8).

On the island of Maui chemical weathering and volcanic ash falls have allowed considerable fluvial dissection of valleys. West Maui shows the huge theater-headed valleys that characterize the more mature erosional stage of Hawaiian volcanoes. The most interesting of these, from the viewpoint of comparative planetology, are those with large springs at their heads. The springs form in especially deep valleys that have eroded back into the dike complex of the volcano to tap groundwater held in interdike compartments. The sapping of these springs results in rapid headward valley growth. This rapid erosional rate combines with a dominance of mass wasting and soil avalanches to yield very steep valley walls.

On Haleakala Volcano (eastern Maui) a large caldera has been breached by two theater-headed valleys. The relationship of valleys to the caldera is somewhat similar to that described for Tyrrhenum Patera on Mars. On Haleakala the valleys were partly filled with lava flows by subsequent eruptions of the volcano. This relationship is also instructive for Martian situations. The Haleakala lavas partly fill a valley created by non-volcanic erosional processes, and similar interactions between constructional volcanic processes (lava flows and ash falls) and erosional processes (sapping, permafrost wastage, and mass movements) probably account for the unusual relationships observed for the Elysium channels.

References. (1) Baker V. R. (1978) Proc. Lunar Planet. Sci. Conf. 9th, 3205-3223. (2) Baker V. R. and Kochel R. C. (1979) J. Geophys. Res. 84, 7961-7983. (3) Carr M. H. (1979) J. Geophys. Res. 84, 2995-3006. (4) Riemers C. E. and Komar P. D. (1979) Icarus 39, 88-110. (5) Baker V. R. (1980) N.A.S.A. Tech. Memo. 81776, 286-288. (6) Wentworth C. K. (1928) Jour. Geology 36, 385-410. (7) Wentworth C. K. (1943) Geol. Soc. America Bull. 54, 53-64. (8) Macdonald G. A. and Abbott A. T. (1970) Volcanoes in the Sea: The Geology of Hawaii, University of Hawaii Press.

## Geology of Kilauea Caldera, Hawaii

Daniel Dzurisin and Thomas J. Casadevall, U.S. Geological Survey, Hawaiian Volcano Observatory, Hawaii Volcanoes National Park, Hawaii 96718

We began a reconnaissance study of the geology of Kilauea caldera in 1979 and have expanded it along several lines during the past year. We have measured a 135 m-thick stratigraphic section at Uwekahuna Bluff and sampled it in detail; 63 flow units and 2 ash deposits have been sampled for thin sections and chemical analyses. The uppermost 14 units are distinguished by their lenticularity and by the presence of plagioclase as a phenocrystic phase. Macroscopic plagioclase is rare in historic Kilauea summit lavas; interpretation of its significance in the late-prehistoric suite of caldera flows awaits laboratory analysis and further mapping. An intriguing possibility which is subject to chemical testing is that some of the flows exposed in Kilauea caldera may have been derived from neighboring Mauna Loa volcano.

The plagioclase-bearing upper units at Uwekahuna Bluff are separated from underlying flows by a zone of significant oxidation. The suggestion that such oxidation may represent a pause in accumulation of the section is supported by a corresponding petrographic discontinuity. Units below the oxidized zone contain little or no macroscopic plagioclase but are remarkably rich in olivine. Individual flow units within the olivine-rich suite are laterally more continuous than overlying plagioclase-bearing units, suggesting a change in source or eruption mechanics after the interval of oxidation.

The prevalence of olivine as a phenocrystic phase ends abruptly below the Uwekahuna Ash. At the base of Uwekahuna Bluff, this distinctive marker bed drapes a steep slope tentatively interpreted as an ancient caldera wall segment. Below the ash, flow units are generally aphyric and seemingly more rounded in outcrop than above.

The remote sensing implication of petrographic discontinuities in the Kilauea caldera section is currently being explored in collaboration with T. McCord and R. Singer of the Hawaii Institute of Geophysics (HIG). An attempt to extend the measured Uwekahuna section laterally, using multispectral imaging techniques available at HIG, is scheduled for late 1980. One goal of this collaborative project is to refine multispectral imaging techniques for future planetary applications.

In addition to the stratigraphic study described above, we are also involved in topical studies of the Uwekahuna Ash and of intrusive bodies exposed in the wall of Kilauea caldera. Results of the ash study reaffirm the potential for violent phreatomagmatic eruptions at Kilauea, and perhaps by analogy at the martian shield volcanoes as well. At Kilauea, interaction between ground water and the magmatic plumbing system is presumably responsible for explosive ash-producing eruptions. On Mars, the presumed existence of widespread subsurface ice or permafrost may have been adequate to trigger comparable explosive eruptions at the Tharsis volcanoes, for example. Implications of potential tephra blankets on Mars have been addressed by M. C. Malin, D. Dzurisin, and R. P. Sharp in a related study at Kilauea.

To date, we have sampled 16 dikes in the west wall of Kilauea caldera, one of which has been traced to the paleosurface at the base of the 1790

A.D. Keanakakoi Ash. In general, dikes that reached the surface display morphologic characteristics which distinguish them from dikes that failed to vent. False or drain-back dikes can also be distinguished on the basis of morphology. Future work on intrusive rocks at Kilauea will include analyses of volatiles (S, Cl) to help assess the importance of shallow intrusions in volcanic outgassing.

The NASA Guest Investigator program at the Hawaiian Volcano Observatory (HVO) was hampered this year by a limitation on government-supported travel. However, R. P. Sharp was able to spend 2 weeks at HVO working with us on caldera stratigraphy and Uwekahuna Ash problems. Since its inception in 1977, the Guest Investigator program has supported Hawaiian field projects by six visiting planetary geologists. Every attempt will be made to maintain the program's viability during 1981. Other plans for 1981 include the acquisition of multispectral images of the west caldera wall by McCord and Singer, preparation of a geologic map of the caldera wall, and publication of results from studies of caldera stratigraphy, the Uwekahuna Ash, and caldera intrusive rocks.

## HAWAIIAN ROCK POPULATIONS: POSSIBLE ANALOGUES TO MARS

J.B.Garvin, P.J.Mouginis-Mark, and J.W.Head, Dept. Geological Sciences, Brown University, Providence, RI 02912.

Following the successful Viking Lander missions to Mars, considerable debate has focused on the possible lithologies and mode(s) of emplacement of the observed block fields (1,2). However, based on the morphology, color, and size distribution of the rocks, recent attempts to distinguish between, for example, vesicular volcanic rocks and fluted sedimentary rocks have so far proved unsuccessful (3,4,5). One of the major causes of this uncertainty has been the lack of a detailed understanding of terrestrial rock populations that might represent possible analogues to Mars. Consequently, as part of our continuing analysis of the Viking Lander data (2,5), we have initiated a series of field investigations of terrestrial boulder fields produced by known geological processes in order to form a framework for interpreting the martian sites.

The first of these field investigations was conducted in September 1980 on the Island of Hawaii. This location was chosen for its geological similarity to Mars (6,7), the monolithologic (volcanic) nature of the rocks, and the variety of known surface processes that have produced the numerous boulder fields. A series of ten field sites were investigated. Table 1 lists the volcanic environments that were studied, while Fig. 1 shows their distribution on the Island.

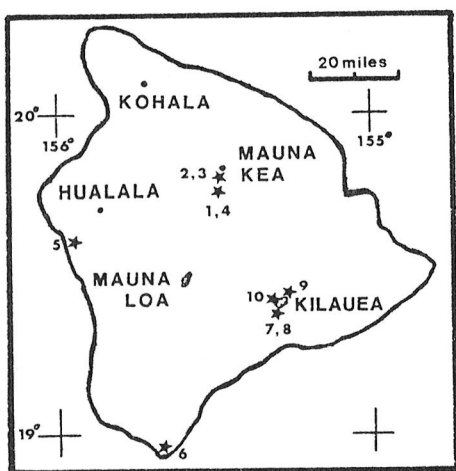


Fig.1: Location map for the ten field sites visited in September 1980. See Table 1 for descriptions.

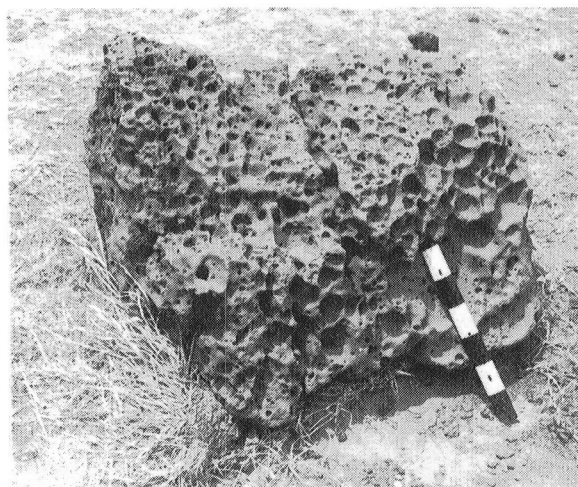


Fig.2: 65 x 37 cm lava block at Site 6, showing pitting similar to that observed at Viking Lander 2. Large pits on this rock occur exclusively on windward side, suggesting subaerial erosion.

For each site, a variety of analyses were conducted in order to provide morphological and morphometric data with which to compare to our martian measurements (5). At each location, individual rocks superficially resembling their martian counterparts (e.g. Fig.2) were photographed under known viewing conditions. Six sites (nos. 1-4,7,8) were also studied in greater detail: multiple stereo images under various lighting conditions; the spatial distribution of the rocks; size/shape measurements on all rocks larger than 1 cm diameter; and substrate samples were acquired for  $\sim 16 \text{ m}^2$  areas.

Although at an early stage in our interpretations, it is apparent that variations in the emplacement mechanism and weathering process can be correlated with specific features of the hawaiian rocks. For example, Fig.3 illustrates part of the boulder field created by the 1924 phreatic explosion of Halemaumau (8) that has many similarities to the rocks at the Viking Lander 1 (VL-1) site in Chryse Planitia. Rock shape, degree of faceting and, at site 10, the eolian features around the rocks on the rim of Halemaumau suggest that VL-1 could represent primarily ballistically emplaced ejecta from the numerous nearby impact craters (9). In order to determine if this comparison is valid, extend our analyses to VL-2, and to assess the importance of such parameters as lighting geometry, rock occultation, and image resolution, our efforts in the coming year will concentrate on collecting and interpreting our morphometric measurements from the images of the hawaiian sites.

TABLE 1: HAWAIIAN BOULDER FIELD SITES, SEPTEMBER 1980

SITE NO.	LOCATION	PROCESS/MORPHOLOGY
1 & 4	Flank of Mauna Kea (Puu Kalepeamo)	Pyroclastic bombs & scoria.
2 & 3	Summit of Mauna Kea (nr. Lake Waiau)	Glacially transported and eroded lava blocks.
5	Kona coast	Surf eroded blocks: littoral.
6	South Point (Ka Lae)	Wind and spray eroded blocks.
7 & 8	S.E. rim, Halemaumau pit crater, Kilauea	Explosion ejecta from 1924 phreomagmatic eruption.
9	N. wall, Kilauea	Talus blocks from caldera wall.
10	S.W. rim, Halemaumau	Wind scour around partially ash buried blocks.

REFERENCES: 1) Binder A.B. et al. (1977) J.Geophys.Res. 82, 4439-4451. 2) Mutch T.A. et al. (1977) J.Geophys.Res. 82, 4452-4467. 3) McCauley J.F. et al. (1979) J.Geophys.Res. 84, 8222-8232. 4) Strickland E.L. (1979) PLPSC 10th, 3055-3077. 5) Garvin J.B. et al. (1980) LPS XI, 317-319. 6) Greeley R. (1974) NASA CR 152416, 257 pp. 7) Carr M.H. & Greeley R. (1980) NASA SP-403, 211 pp. 8) Jaggar T.A. & Finch R.H. (1924) Amer.Jour.Sci. 208, 353-374. 9) Morris E.C. et al. (1978) Icarus 34, 548-555.

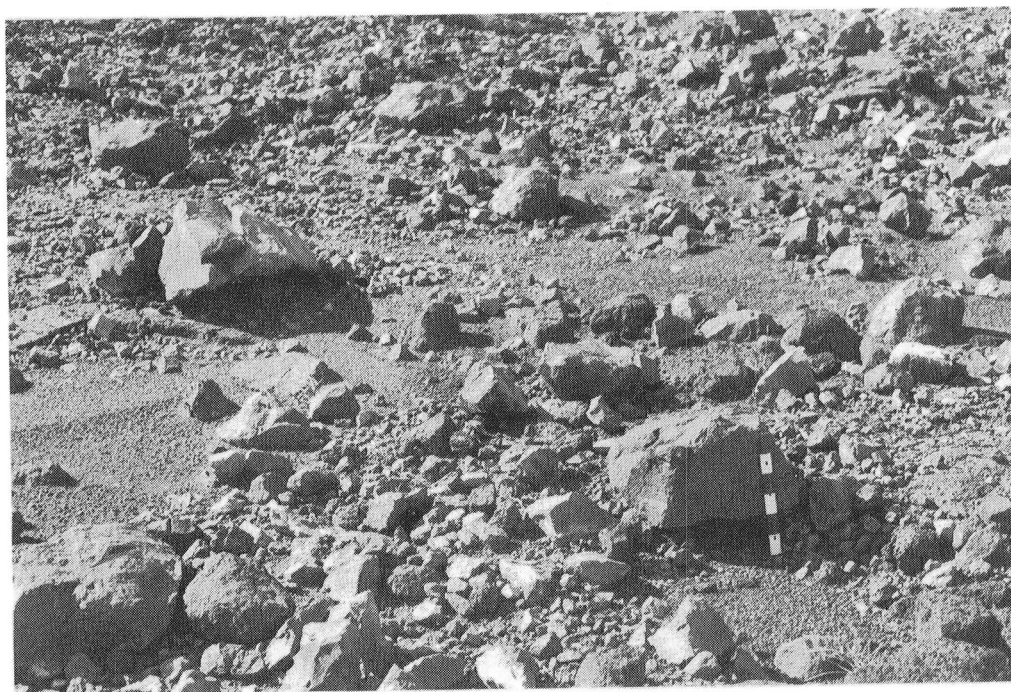


Fig.3: General view of the boulder field created by the 1924 phreomagmatic eruption of Halemaumau (8). Scene located near Sites 7 & 8. Fragmental pieces of vent material from the old crater walls may be good analogues to the rocks seen at Viking Lander 1, which may represent ejecta from nearby impact craters. Image acquired with 50 mm lens, rule divided into 5 cm intervals.



A NEW TECHNIQUE FOR IDENTIFYING BURIED SURFACES, David H. Scott and Kenneth L. Tanaka, U.S. Geological Survey, Flagstaff, AZ 86001.

In the course of mapping the lava flows in and around the Tharsis region of Mars, a technique was developed that allows the identification of buried geologic units (1). The method is similar to that used in the determination of the relative ages of surface units by crater counts. For buried surfaces, however, craters must be selected in size ranges large enough to permit measurement of their rim crest diameters, whether partly exposed or completely mantled by overlying material. In the Tharsis region, individual flow units are relatively thin (tens of meters to a few hundred meters thick) and little erosion appears to have taken place between eruptive events (2). Therefore, craters larger than about 5 km across are measureable, even though they may be buried or partly buried by lava flows or fluvial materials (Fig. 1).

In application, the frequency distributions of buried craters for a given diameter, or range of diameters, are added to the counts of the same size craters on the surface material. Curves plotted from the total size-frequency distributions characterize the buried rock units. Curves so obtained from selected locations throughout an area can then be correlated with those previously constructed for known surface units in the same crater size range. In practice, it was found that some of the curves for buried units lie between those of the known surface materials. This type of placement is probably caused by a thin series of lava flows underlying the exposed unit, allowing craters on several older units to project through to the surface. In such cases, however, a correlation between unknown and known units can commonly be determined from a general knowledge of stratigraphic relations within the area.

In some areas where image quality and resolution are good, craters smaller than 5 km can be used in the determination, thus providing more overlap between the curves being compared and increasing the confidence level of the correlation. However, embayment versus superposition relations become more difficult to ascertain in the smaller size craters, decreasing the certainty as to their relative time of emplacement with respect to surrounding flows.

#### References

- (1) Scott, D. H., and Tanaka, K. L., 1980, Mars: Paleostratigraphic restoration of buried surfaces. (Submitted to *Icarus*).
- 2) Scott, D. H., Schaber, G. G., Tanaka, K. L., Horstman, K. C., and Dial, A. L., Jr., 1980, Map series showing lava flow fronts in the Tharsis region of Mars. U.S. Geol. Survey Misc. Geol. Inv. Maps I-1266-1280 (in press).

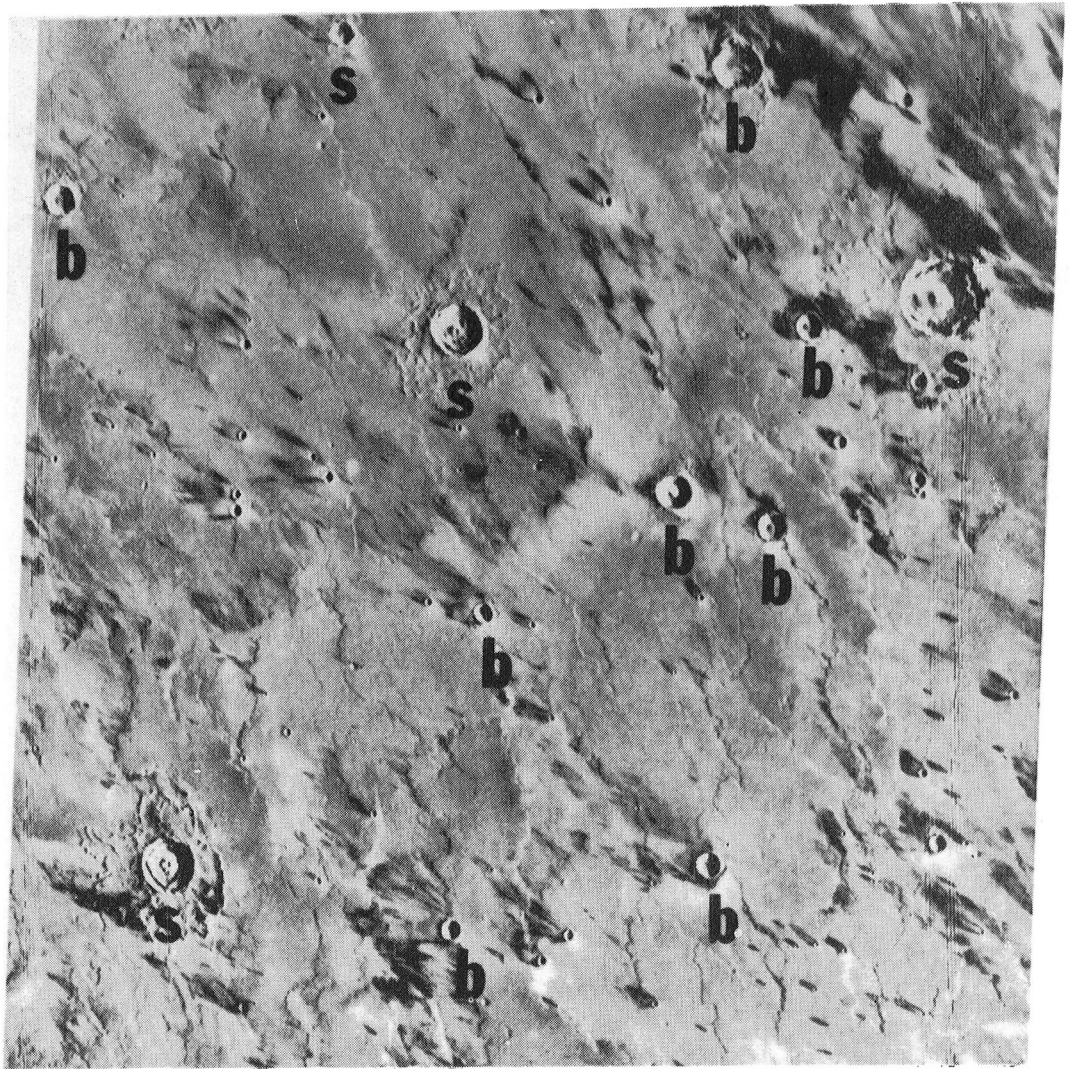


Fig. 1. Lava flows from Arsia Mons showing the distribution of the more prominent craters superposed on the flows (s) and partly buried (b). Viking image 639A36.

Explosive Volcanism: A Possible Source for Aggregate Formation on Mars  
Jonathan Fink, David Krinsley and Ronald Greeley, Dept. of Geology,  
Arizona State University, Tempe, AZ 85281.

The recent eruptions of Mount St. Helens illustrate the important effects which large volumes of volcanic ejecta may have on the opacity of the atmosphere, which in turn could effect climate. The magnitude of this effect is related to the amount of time the particles remain in suspension, which in turn depends on their size. Hence any process which modifies grain size will strongly influence atmospheric dispersal, as well as effecting subsequent near surface eolian transport.

During the ash fall in Portland, Oregon which accompanied the June 12 eruption of Mount St. Helens, large particles were observed which broke up into smaller grains upon impacting the ground. This suggests that the large particles were composed of smaller ones, loosely bonded together. The presence of such loosely bonded groups, called aggregates, has been used to explain several eolian phenomena on Mars (Greeley, 1979; Krinsley and Leach, 1979). Theory (Sagan, et al., 1977), observations at the Viking Lander sites (Moore, et al., 1977), and laboratory experiments (Krinsley and Leach, 1979) all suggest that the sand sized fraction on Mars may be depleted by mechanical abrasion. However, it is generally accepted that sand sized particles are necessary for the formation of dunes (Bagnold, 1954; Smalley and Krinsley, 1979) which are common on Mars. A proposed solution to this problem is the creation of electrostatically bonded aggregates by mechanical abrasion. Such aggregates have been formed in the laboratory using starting materials of quartz, basalt, olivine and augite (Greeley, 1979; Krinsley and Leach, 1979).

Aggregate formation has been attributed exclusively to eolian abrasion; however, the mechanical disintegration of particles required to produce aggregates also occurs during explosive volcanic eruptions. Recent observations from Mount St. Helens suggest that eruptions may indeed produce electrostatic aggregates, although since their formation is reduced by atmospheric water (Krinsley and Leach, manuscript), less of these large particles would be expected to form in a damp terrestrial climate than in the relatively arid Martian environment. Volcanically derived aggregates dispersed by global wind patterns could significantly increase the population of sand sized particles to the level necessary to form the extensive dune fields on Mars. Large concentrations of fine grained, unconsolidated materials near Martian volcanoes such as in the aureole of Olympus Mons (Morris, 1979) could be made of sand sized aggregates rather than smaller ash particles.

Sampling of ash fall material from future eruptions of Mount St. Helens and other volcanoes may indicate the prevalence of volcanic electrostatic aggregates on Earth, and laboratory experiments may help determine their likelihood on Mars.

#### References:

- Bagnold, R.A. 1954. The Physics Of Wind Blown Sand And Desert Dunes. Methuen, London.
- Greeley, R. 1979. Silt-clay aggregates on Mars. A model for the formation of "Sand." J. Geophys. Res. 84, 6248-6254.
- Krinsley, D. H. and Leach, R. 1979. Simulated Martian aeolian abrasion of glassy basalt and augite. Repts. Planet. Geol. Program. 1978-1979, NASA TM 80339, 311-312.
- Moore, H.J., Hutton, R., Scott, C., Spitzer, C., and Shorthill, R. 1977.

- Surface materials of the Viking landing sites. J. Geophys. Res. 82, 4497-4523.
- Morris, E.C. 1979. The aureole of Olympus Mons. Repts. Planet. Geol. Program. 1978-1979. NASA TM 80339, 239-240.
- Sagan, C., Pieri, D., Fox, P., Arvidson, R., and Guinness, E. 1977. Particle motion on Mars inferred from the Viking Lander cameras. J. Geophys. Res. 82, 4430-4438.
- Smalley, I. and Krinsley, D. H. 1979. Aeolian sedimentation on Earth and Mars: Some comparisons. Icarus 40, 276-288.

## PRISTINE MORPHOLOGY OF A QUASI-FLOOD BASALT FLOW: THE BARDARDALSHRAUN OF TROLLADYNGJA, ICELAND

Greeley, Ronald, Department of Geology, Arizona State University, Tempe, AZ 85281 and Haraldur Sigurdsson, Grad. School of Oceanography, Univ. of Rhode Island, Kingston, R. I. 02881

Lunar and planetary exploration has demonstrated that basaltic volcanism has played an important, and in some cases, dominant, role in the evolution of the terrestrial planets. Although various central vent constructs such as shield volcanoes are impressive features, various types of basaltic plains are by far the most important in terms of volume and areal extent. Basaltic plains can be subdivided into two broad categories: 1) massive flood or plateau units composed of relatively thick (~30 m) colling units which often "pond" in topographic depressions, typified by the Columbia River Plateau of the Pacific northwest and 2) complex, thin ( $\leq 10$  m), multiple cooling units emplaced typically as tube-fed and channel-fed flows, as in the Snake River Plain, Idaho. Although there are abundant "fresh" (i.e., having primary surface morphologies) examples of the latter category of basalt flow, a review of the literature shows that "flood" basalt flows *sensu stricto* having preserved primary surface morphologies are extremely rare. Because the study of planetary volcanism is based mostly on photogeology, the establishment of identifying surface features for various types of volcanic units is critical, and because flood basalts may be prevalent on the terrestrial planets, fresh Earth analogs are particularly important. Unfortunately, most flood basalts (such as the Columbia River Plateau) are of Tertiary age and their primary surface features are eroded. However, the Bardardalshraun flow of northern Iceland appears to be a candidate analog. The flow is the second longest flow in Iceland and is an olivine-tholeiite basalt (Sigvaldason, 1974) typical of the shield volcanoes in northern Iceland. The sequence of shield-building in Iceland begins with massive fissure-fed eruptions; with time, the rate of effusion diminishes and the vent focuses to a point source(s) on the fissure, eventually forming the shield (van Bemmelen and Rutten, 1955, and others). The Bardardalshraun flow is considered to represent the initial basal flood eruption leading to the growth of Trolladyngja shield volcano that covers more than 850 km<sup>2</sup>. The flow can be traced northward more than 100 km toward the sea; it has been dated as older than the H<sub>5</sub> ash layer (older than 6600 years), but is younger than 9000 years and is post-glacial. Thus, although in some places the surface of the flow has been scoured by the Skjalfandafljot River, its primary surface morphology is preserved. In two localities, at Godafoss and Barnafoss, the river has incised the flow, exposing it in cross section where cooling units exceeding 10 m in thickness can be seen. Although the flow units are not as thick (at least where exposed) as more typical flood basalts, its surface features may shed light on the general morphology of high volume eruptions. Parts of the flow in several areas exhibit a ridge/rib pattern consisting of ridges parallel to the flow direction that are up to 30 m wide, 7 m high, and nearly a km long; flow "ribs" developed transverse to the flow direction and resemble "mega" festoons that are typically convex down-flow. The "ribs" have spacings of more than 100 m and are up to 5 m high. This type of pattern resembles course festoons observed on more silicic lava flows (e.g., Glass Mountain, California); their presence on the basaltic Bardardalshraun may provide insight into the rheological properties of the flow, and of the mechanisms of emplacement. Other primary surface features include "auto dikes", spinous projections of lava several meters high, and smooth, flat surfaces formed where lava was ponded in local topographic depressions. Erosional surface features (where the Skjalfandafljot River

has scoured the flow) includes polygonal fractures (polygons are several meters across) that may be related to cooling patterns within the lava flow.

Although the Bardardalshraun flow is not as thick as "typical" flood basalts, it does represent a massive, high volume eruption; most of its primary surface features are preserved, and at the same time, parts of the flow are exposed in cross section to permit study of the relationships of some of the surface features with interior structure. Future work includes photogeological analysis of the entire flow to determine its surface morphology, and petrographic study of the flow.

## PHYSICAL MODELLING OF LAVA FLOWS

Greeley, Ronald and Michael Womer, Department of Geology, Arizona State University, Tempe, AZ 85281

In an effort to gain some knowledge on the emplacement of lava flows in impact basins and to place constraints on various theoretical models, a series of laboratory simulations was undertaken, utilizing carbowax and techniques for physically modelling dynamic processes (Greeley and Womer, 1980, Womer et al., 1980, Womer and Greeley, 1980). These experiments involved filling a 3m square topographic model of a multi-ringed basin (stylized from the 300 km diameter lunar basin Schrodinger) with simulated lava (carbowax, an industrial medium with well defined rheological properties). A complex experimental matrix was derived in which the following parameters are varied: 1) viscosity, 2) rates of effusion, 3) placement of vent in relation to the basin, 4) configuration of the vent, 5) duration of eruption. Although not all combinations have been run, enough results are available to draw some tentative conclusions: 1) *The rate of effusion* has a major effect on the final morphology of the accumulation of lava, much more than the viscosity, as proposed by Walker (1973) in his analysis of lava flows on Earth. Hawaiian rates of effusion lead to the formation of shield volcanoes (as one would expect!), flood eruptions produce large expanses of "ponded" lavas, a result that lends credence to the theories that some lunar mare units were the result of flood eruptions. 2) *The effect of topography* is shown quite distinctively in Figure 2; initial eruptions in the simulation produced thin sheets of lava that gradually extended toward the first ring; as soon as the ring was encountered, the lavas began to "pool", with a marked change in surface features. Thus, even though all other parameters were held constant (viscosity, rate of effusion, etc.), there was a change in surface expression related solely to the underlying topography. 3) *"Pseudovents"* developed in several runs in which simulated lava would break through crusted flows, emitting lava flows and lava channels, and give the appearance of being a primary vent.

Although these results are preliminary and the conclusions are tentative, the type of data that are being produced should enable better photogeological interpretations of volcanic features on planetary surfaces through the ability to isolate the effects that various eruptive parameters have on surface morphology.

## REFERENCES

- Greeley, R. and M. B. Womer, 1980. Mare basin filling: Laboratory simulations (abs), Lunar and Planetary Science, XI, 362-364.
- Womer, M. B. and R. Greeley, 1980. Scale model simulations of mare basalts (abs), PGPI NASA TM 81776, 210-212.
- Womer, M. B. et al., 1980. Scale model simulations of lava flows (abs) PGPI, NASA TM 81776, 207-209.

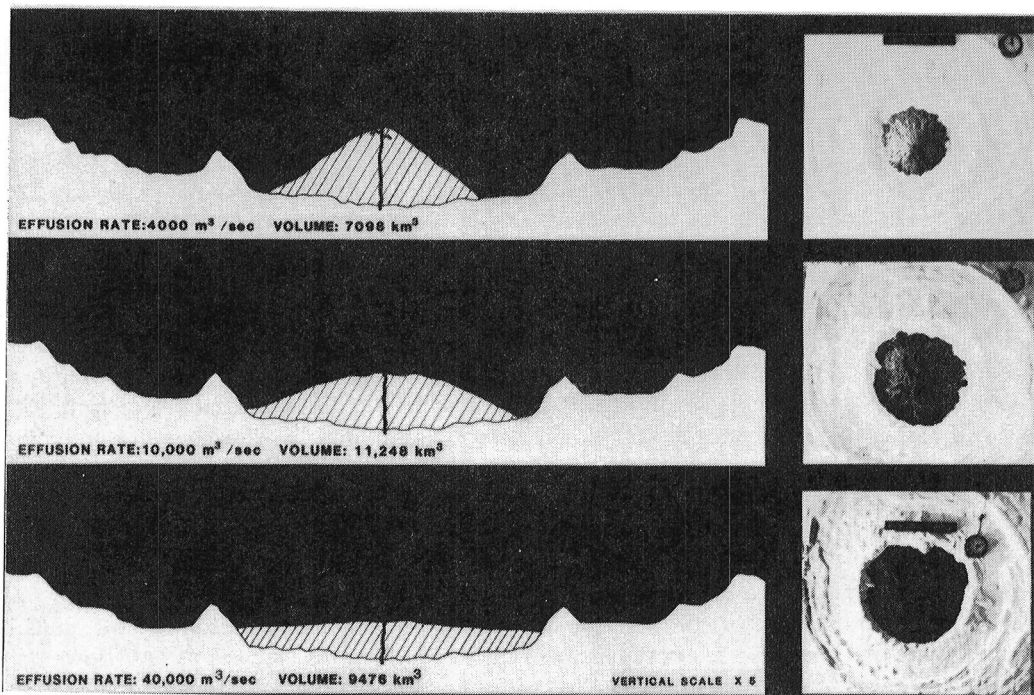


FIGURE 1. Effect of rate of effusion on volcano morphology; profiles on left cut across a stylized multi-ringed basin, cross-hatched areas show the "volcano", images on right are plan views of the model and the accumulated "lava"; experiment shown on top resulted from "Hawaiian" rate of effusion, leading to a volcanic shield (note 5X vertical exaggeration), experiment shown on bottom is a "flood" rate of effusion producing flat surface.

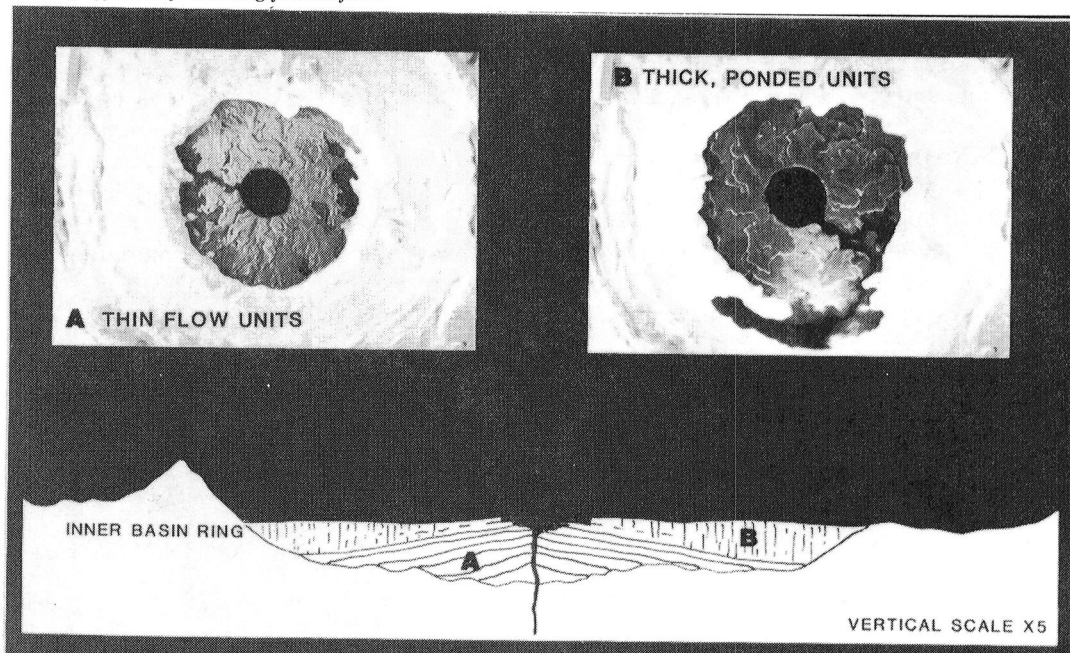


FIGURE 2. Effect of topography on morphology; initial eruptions (A) produced thin, narrow flow units, until inner basin ring was reached, where flow began to "pond"; note change in surface morphology (B); all eruption parameters were held constant.



## MUD AS A PSEUDO-VOLCANIC ROCK MAGMA

Laurie A. Johansen, Jet Propulsion Laboratory, California Institute of Technology, Pasadena, CA 91103

A meteorite impact under the Martian conditions of low atmospheric pressure and subsurface water with an overburden of sediment or volcanic materials, may result in the formation of hard vesicular rocks composed of salt-cemented fines (see photo). Rocks which appear similar to these are found at the Viking lander sites. Collapse features, chaotic terrain, catastrophic flooding, and vesicular rock fragments such as are found on Mars would be consistent with such an association.

Vesicular rocks can be formed by suddenly decompressing mixtures of sediments and water. We added epsomite ( $\text{MgSO}_4$ ) and ferric oxide to mixtures of varying grain size (from clay to coarse silt size), and decompressed them from earth atmospheric pressure to 3 mb. The decompression causes a "rising" of the mud at approximately 30 mb as vesicles formed. As the vesicles form, the material becomes more fluid. Simultaneously, sub-millimeter ice crystals permeate the rock. The ice is then removed by subsequent sublimation. This process takes overnight at 3 mb pressure for a 50 ml rock. Larger rocks take longer. The resultant rock varies in strength and bulk density depending on the composition of the fines, and the concentration of salt and ferric oxide composing the rock. If epsomite is present, it cements the sediment into a rock-like state. Slow drying tends to make the rock stronger than quick drying. Large vesicles tend to weaken the rock somewhat. The bulk density varies between .09 and .20 g/cc for a pure montmorillonite clod. Terrestrial soils with more conventional mineralogy and size distribution and those with salt cement vary between 0.5 and 0.8 g/cc. Contact with liquid water causes the vesicular rock structure to collapse within seconds into a mud. Exposure of the rock to atmospheric moisture will also substantially weaken the rock. No vesicles are formed without the presence of liquid water; ice merely sublimates without producing vesicles, fluidizing the material, or cementing the rock. Low amounts of water either cause the mud to explode, or to form a rock resembling a volcanic tuff.

During an impact event on Mars, muddy ejecta may be thrown from high subsurface pressures to the low atmospheric pressures of Mars. It is hypothesized that this rapid drop to a low pressure would cause the water within the mud to change to a gas and thus form vesicles. Vesicle formation increases the ejecta's fluid nature substantially and would thus aid in mobilization of the material. After outgassing, the ejecta would form a cemented strata which would appear similar to a lava flow.

The rock's vulnerability to water suggests that subsurface liquifaction could result in crustal collapse, chaotic terrain and catastrophic flooding. A later impact event in this strata would scatter ejecta fragments of vesicular rock. The Viking lander sites are both in areas suggested to be underlain by muddy material (Johansen, 1979). The Viking 1 lander is in an outwash plain which has experienced catastrophic floods (Masursky *et al.*, 1977). The muddy material in the flood would be expected to form this kind of rock if there is some salt in solution. It

has been suggested that groundwater on Mars would be expected to contain large amounts of dissolved salts (Hugenin, 1979). Both VL 1 and VL 2 sites may contain some fragments of this nature.

#### REFERENCES:

- 1) Johansen, L.A., Martian splosh cratering and its relation to water, an abstract in NASA Conference Publication 2072, Second International Colloquium on Mars, p. 44, Jan. 15-18, 1979, and in Second Colloquium on Planetary Water and Polar Processes, Oct. 16-18, 1978, p. 109.
- 2) Masursky, H., J.M. Boyce, A.L. Dial, G.G. Schaber and M.E. Strobell, Classification and time of formation of Martian channels based on Viking data: J. Geo. Res., 4016, 1977.
- 3) Hugenin, R., Remote sensing evidence for oases on Mars, NASA-TM 80339: Reports of the Planetary Geology Program, 1978-1979, p. 208.

This research was carried out under NASA Contract 7-100.

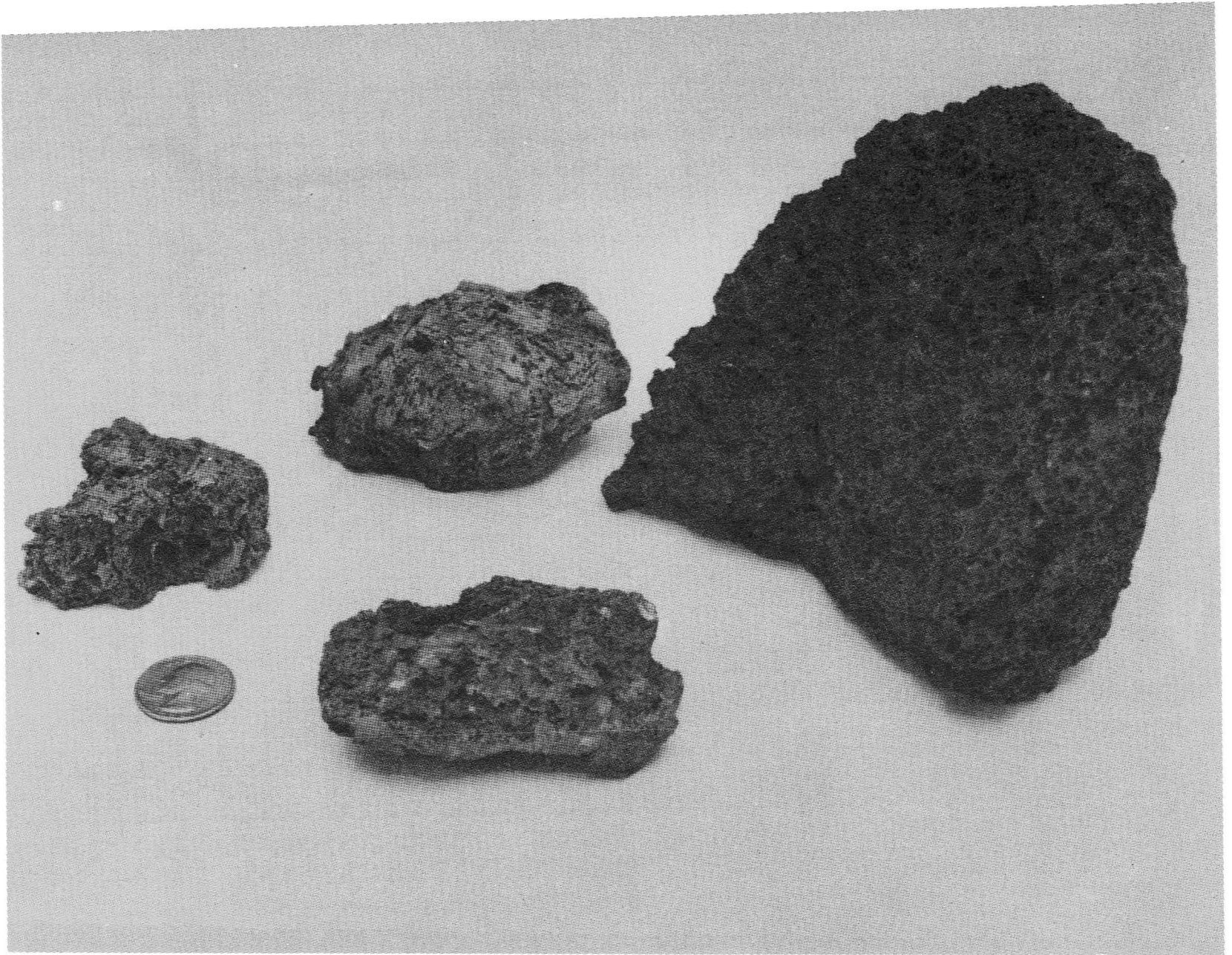


Figure 1. Suddenly decompressed mixtures of clay, iron oxide, powdered basalt, epsomite, and water produce vesicular pseudo-volcanic rock.

## A PYROCLASTIC ORIGIN FOR THE AUREOLE DEPOSITS OF OLYMPUS MONS.

E. C. Morris, U.S. Geological Survey, Flagstaff, Arizona.

Many origins have been proposed for the aureole of grooved terrain that surrounds Olympus Mons (McCauley et al., 1972; Carr, 1973; Blasius, K.R. written communication, 1974; Harris, 1977; Hodges and Moore, 1979; Lopes et al., 1979). However, few adequately explain conditions for emplacement of the great volume of material in the aureole (over  $6 \times 10^6 \text{ km}^3$ ), overlapping relations of the various deposits, formation of the ridge-and-valley structure of the grooved terrain, the anomalously low crater population on the aureole, and the strong gravity anomaly that exists over the greater part of the aureole. A pyroclastic origin explains most observed conditions and relations of the aureole deposits, of which the following are significant:

1. The aureole deposits consist of several thick (up to 1.5 km) overlapping sheets of great areal extent. On Earth, the largest volcanic deposits in terms of volume and areal distribution are pyroclastic flows (ignimbrites)--thick overlapping sheets (cooling units) that cover many hundreds of square kilometers (Fig. 1).
2. The aureole deposits have a ridge-and-valley structure similar to and characteristic of pressure ridges that form on flowing viscous material. The lobate forms of the distal edges of the aureole deposits also indicate that the material was viscous during emplacement. Terrestrial pyroclastic flows are very fluid and travel at high velocities until the entrained volatiles that provide fluidization are depleted and the whole mass collapses and comes to rest. After collapse, momentum of the solid particles causes the mass to flow viscously for a short distance. In the martian environment, viscous flow of the pyroclastic deposits probably continued for a longer period, during which time viscosity increased due to cooling and compaction, and pressure ridges developed due to frictional resistance at the base of the flows.
3. The deposits are composed of easily erodible material, as evidenced by an anomalously low number of craters and the development of secondary ridges (yardangs). Terrestrial ash flows commonly are composed of welded and unwelded zones. Unwelded pyroclastic material is soft and easily eroded. The martian flows may contain a greater percentage of unwelded material than terrestrial ash flows. High-resolution pictures show the aureole material to be unbedded with some indurated zones distributed throughout.

High-resolution pictures also show the aureole material to contain randomly distributed large dark blocks whose weathering products form dark streaks in the talus on the flanks of ridges (Fig. 2). Terrestrial ash flows commonly contain xenoliths or randomly distributed exotic blocks derived from the walls of the conduit through which the material erupted.

4. The ridge-and-valley patterns of the aureole deposits are broken by fractures and sets of intersecting long linear grooves considered to be grabens. The grabens and fractures, confined to individual flow units, resulted from tensional forces that developed during cooling and compaction (Fig. 1 and 2a)

5. Eruptions of the flows were near the centers of the semicircular deposits or near centers established by the intersection of lines drawn normal to the pressure ridges or margins of the deposits. The eruption centers of the two youngest deposits ( $au_3$ ,  $au_4$ ) are offset north and northwest of Olympus Mons. The older deposits are more nearly centered on the site of Olympus Mons. At least six major eruptions and several surges may have occurred.

6. The aureole deposits dip inward to a basin that surrounds Olympus Mons. The basin is probably the subsidence structure resulting from the extrusion of the great quantity of volcanic material that makes up the aureole deposits ( $6 \times 10^6 \text{ km}^3$ ) and forms Olympus Mons ( $2 \times 10^6 \text{ km}^3$ ). Large pyroclastic eruptions on Earth are generally associated with caldera collapse or very large subsidence structures (Smith, 1960). The basin surrounding Olympus Mons subsided after emplacement of the aureole. The aureole deposits are partly covered by lava flows and eolian deposits that have subsequently filled the basin.

7. The largest gravity anomaly on Mars (344 mgal) exists over Olympus Mons and the aureole deposits (Sjogren, 1979). The broadening of the anomaly northwestward over the aureole deposits may define a near-surface magma chamber or source of the pyroclastic eruptions.

#### REFERENCES

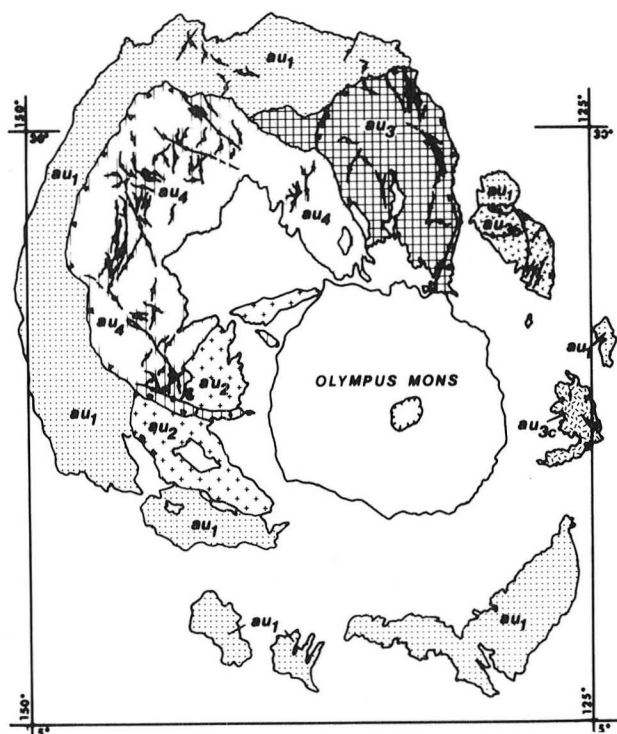
- Carr, M. H., 1973, Volcanism on Mars: J. Geophys. Res. 78, 4049-4062.  
 Harris, S. A., 1977, The aureole of Olympus Mons, Mars: J. Geophys. Res., 82, 3099-3107.  
 Hodges, C.A., and Moore, H. H., 1979, The subglacial birth of Olympus Mons: J. Geophys. Res., 84, 8061-8974.  
 Lopes, R. M., Guest, J. E., and Wilson, C.J.N., 1979, Origin of the Olympus Mons aureole and perimeter scarp, in Reports of Planetary Geology Program, 1979-1980, NASA Tech. Memo. 81776, 176-178.  
 McCauley, J.F., Carr, M.H., Cutts, J.A., Hartmann, W.K., Masursky, Harold, Milton, D.H., Sharp, R. P., and Wilhelms, D.E., 1972, Preliminary Mariner 9 report on the geology of Mars: Icarus, 17, 289-327.  
 Sjogren, W.L., 1979, Mars gravity: High-resolution results from Viking Orbiter 2: Science, 203, 1006-1010.  
 Smith, R. L., 1960, Ashflows: Bull. Geol. Soc. America, 71, 795-842.

#### FIGURE CAPTIONS

- Figure 1.(a) Shaded relief map of Olympus Mons and aureole.  
 (b) Geologic map of the Olympus Mons aureole deposits.  
 Stratigraphic sequence from oldest to youngest:  $au_1$ ,  $au_2$ ,  $au_3$ ,  $au_{3b}$ ,  $au_{3c}$ ,  $au_4$ .
- Figure (2) High-resolution (300-km altitude) Viking Orbiter pictures of ridge-and-valley structure of the youngest aureole deposit ( $au_4$ ). Picture width approximately 10 km.  
 (a) Ridge-and-valley structure cut by northwest-trending fault. No bedding is evident. Note blocky, knobby appearance of ridges and their flanks and apparent hard resistant zones and layers (441B15).  
 (b) Blocks of dark material several meters in size, are distributed throughout the deposits. Arrows point to dark streaks in talus formed from weathering of blocks (441B02).



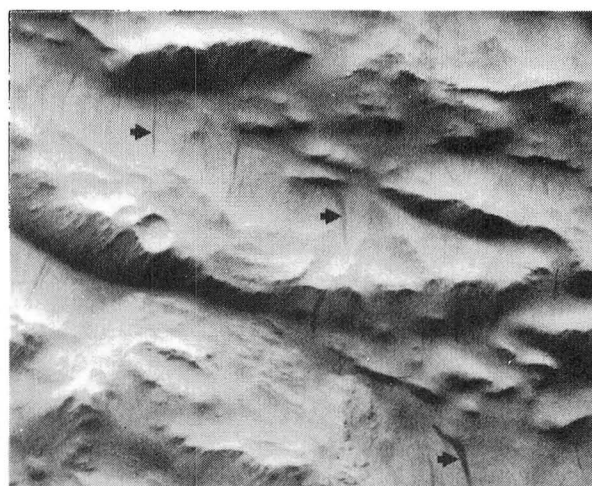
1a



1b



2a



2b

MARTIAN IGNIMBRITES, David H. Scott and Kenneth L. Tanaka, U.S. Geological Survey, Flagstaff, AZ 86001.

The occurrence of ignimbrites (ash-flow deposits) on Mars has been postulated to explain the basal escarpment of Olympus Mons (1) as well as the unusual morphology of the aureole surfaces surrounding this volcano (2). Malin (3) interpreted deposits in the Apollinaris Patera-Tharsis volcanic zone to be ash-fall and ash-flow units. Other investigators have mentioned the possible occurrence of ash-flow materials in places as alternatives to lava flows, eolian deposits, etc.

The regional geologic mapping of Mars at 1:15-million-scale has disclosed large areas in the plains west of the Tharsis region and adjacent to the southern highlands that resemble terrestrial ignimbrites (Fig. 1). They form extensive, relatively flat surfaces that are layered in places but without the lobate and crenulated margins commonly observed in martian lava flows. Superficial similarities, however, can be misleading and definitive evidence was sought that might lead to a more positive identification of these materials. To this end, Landsat and aerial photographs of known ignimbrite flows were acquired and examined for primary forms and flow patterns as well as secondary features such as erosional and structural variations that individually, or together, might aid in the recognition of such deposits. The ignimbrites studied range in age from Oligocene to Recent; most are in the western United States but photographs of some very young ash-flows in New Guinea were obtained through the courtesy of the Royal Australian Air Force.

Individual flows of terrestrial ignimbrites are commonly distinguished by erosional patterns developed along fracture and joint systems as well as by variations in surface expression between welded and nonwelded units. Color or tonal variations associated with differences in mineral composition may also allow some photogeologic discrimination between units. Terrestrial ash-flows do not appear to have some characteristics common to lava flows, such as pressure ridges, lava channels with levees, etc. Perhaps the best criterion for their recognition on a planet such as Mars, where volcanic flows prevail over sedimentary deposits, is the very absence of features characteristic of lava flows.

The martian deposits have several positive features in common, however, with terrestrial ignimbrites. Their surfaces, for example, are flat to gently undulating where they appear to follow, but subdue, the underlying topography. They vary from smooth to grooved and corrugated, possibly reflecting ease of erosion due to their degree of welding. In places, they consist of six or more alternating hard and soft layers that represent either separate flows or several cooling units with welded and nonwelded zones. Like many of the flows in the Basin and Range Province, they are relatively light in color compared with the adjacent terrain; possibly they are more silicic than most of the other volcanic materials on Mars. As in many terrestrial ignimbrites, joints



form conjugate or complimentary sets that have been eroded into linear and crisscross patterns; these patterns do not everywhere follow the prevailing wind directions indicated by streaks and plumes around topographic obstacles. In several places the margins of the deposits are broadly curved with relatively steep convex fronts, whereas in other areas they are thin, tapering to feather edges.

At the present stage of mapping, the martian deposits that are provisionally classified as ignimbrites, cover more than one million square kilometers in the Amazonis, Memnonia, and Aeolis quadrangles. Crater counts and stratigraphic relations suggest that they were emplaced over a considerable time span, but they all appear to postdate the possible ignimbrites forming the aureoles around Olympus Mons (2).

#### REFERENCES

- (1) King, J. S., and Riehle, J. R., 1974, A proposed origin of the Olympus Mons escarpment: *Icarus*, 23, 300-317.
- (2) Morris, E. C., 1980, A pyroclastic origin for the aureole deposits of Olympus Mons: *Icarus* (in press).
- (3). Malin, M. C., 1979, Mars: Evidence of indurated deposits of fine materials (abs.), in *U.S. National Aeronautics Space Administration Pub. 2072, Second International Colloquium on Mars*, p. 54.



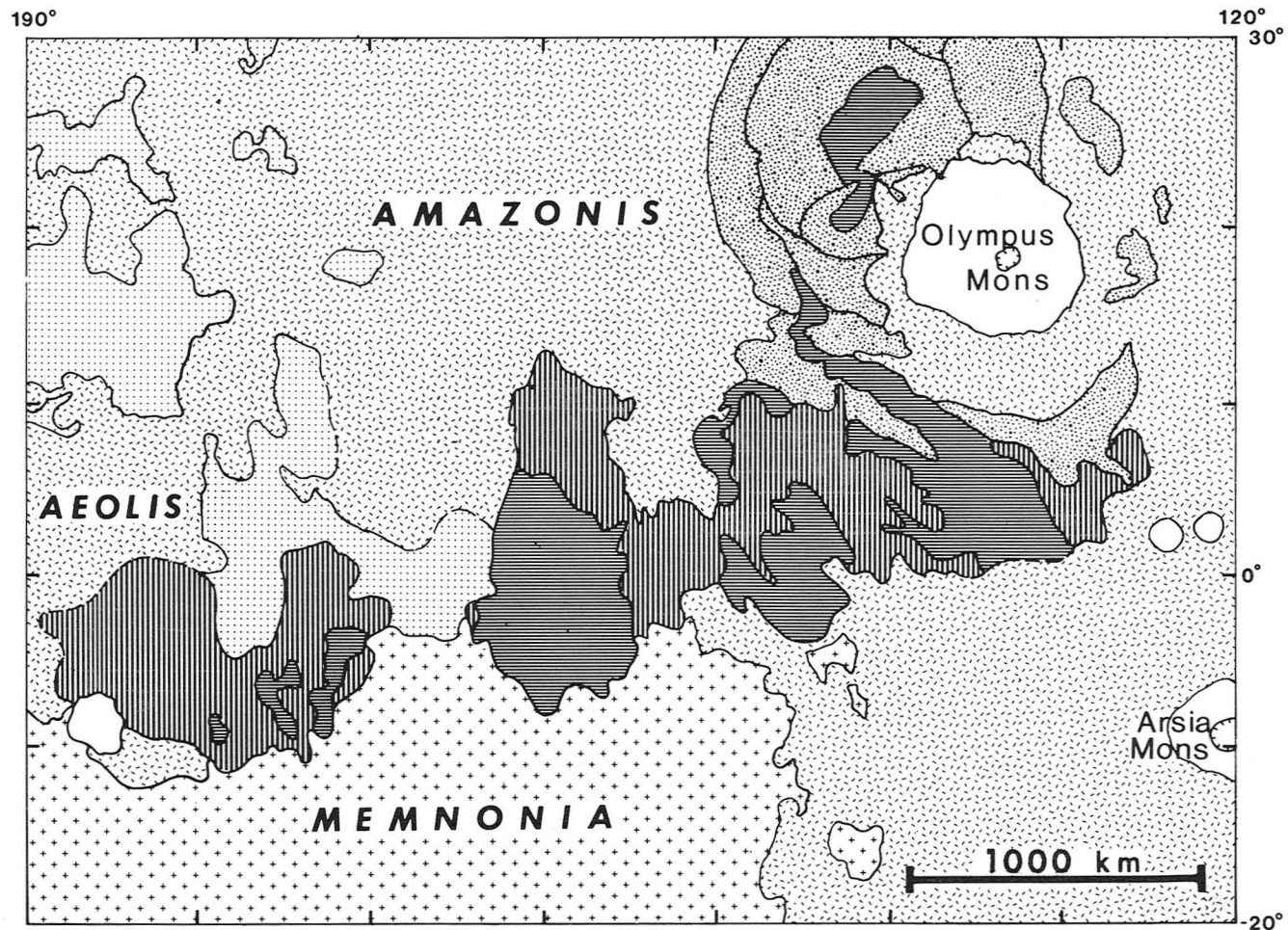


FIG. 1 INDEX MAP; highland terra, knobby terrain, volcano, Olympus aureole, lava plain, lower ignimbrite units, upper ignimbrite units.

## REGIONAL VOLCANIC STUDIES IN ELYSIUM PLANITIA, MARS.

P.J.Mouginis-Mark and S.H.Brown, Dept. Geological Sciences, Brown University, Providence, RI 02912.

Elysium Planitia (200-230°W, 15-40°N) represents the second largest constructional volcanic province on Mars (1,2). It is characterized by three individual volcanoes (Hecates Tholus, Elysium Mons and Albor Tholus) that stand atop a broad dome-shaped rise comparable to the Tharsis Dome (1-5). Unlike Tharsis, however, volcanism in the Elysium Region has been only partially investigated, primarily using Mariner 9 images (2,6). From Viking data (Fig.1), it is apparent that Elysium Planitia is significantly different from Tharsis in terms of volcano morphology (7-9), eruptive style (8,10), and morphometry of associated sinuous channels (11,12).

In order to investigate the regional characteristics of Elysium Planitia, we have initiated an analysis designed to determine: A) the variety of volcanic features and geologic history of the area; B) the influence that different surface materials have had on impact crater morphology; and C) the mode(s) of origin of the channel systems within Elysium Fossae. To date, the regional geology (Fig.2A) and areal distribution of three different crater ejecta morphologies (Fig.2B) have been identified, together with a preliminary analysis of channel morphometry (Figs. 2C-E).

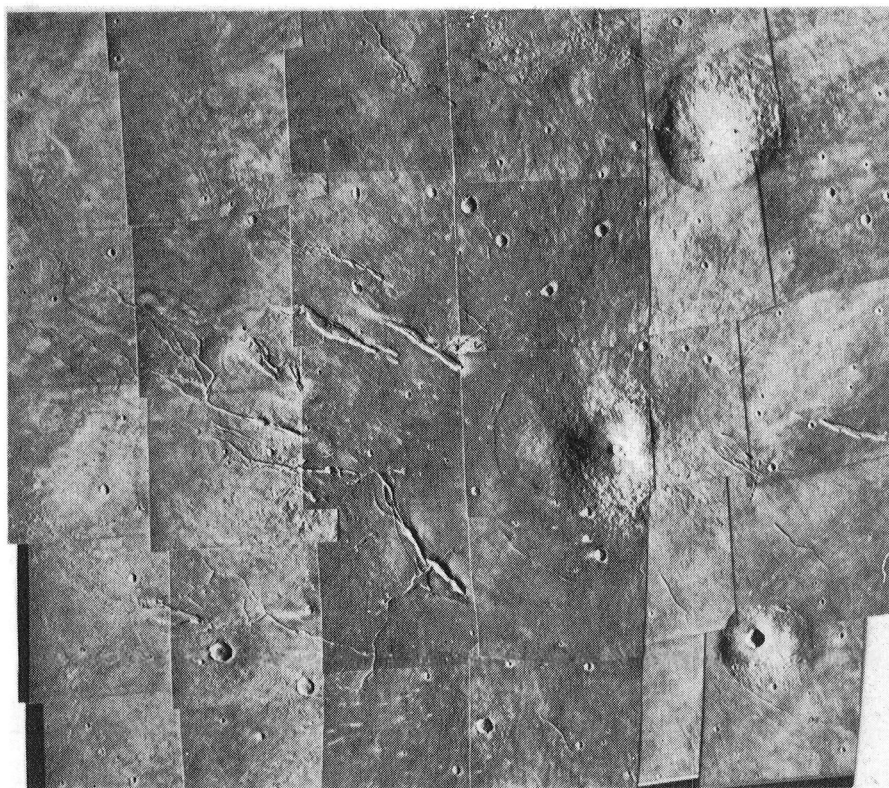


Fig.1: Photomosaic of Elysium Planitia, showing the principal features identified in Figs. 2A-C. Viking frames 844A13-22, 37-46 and 846A13-22.

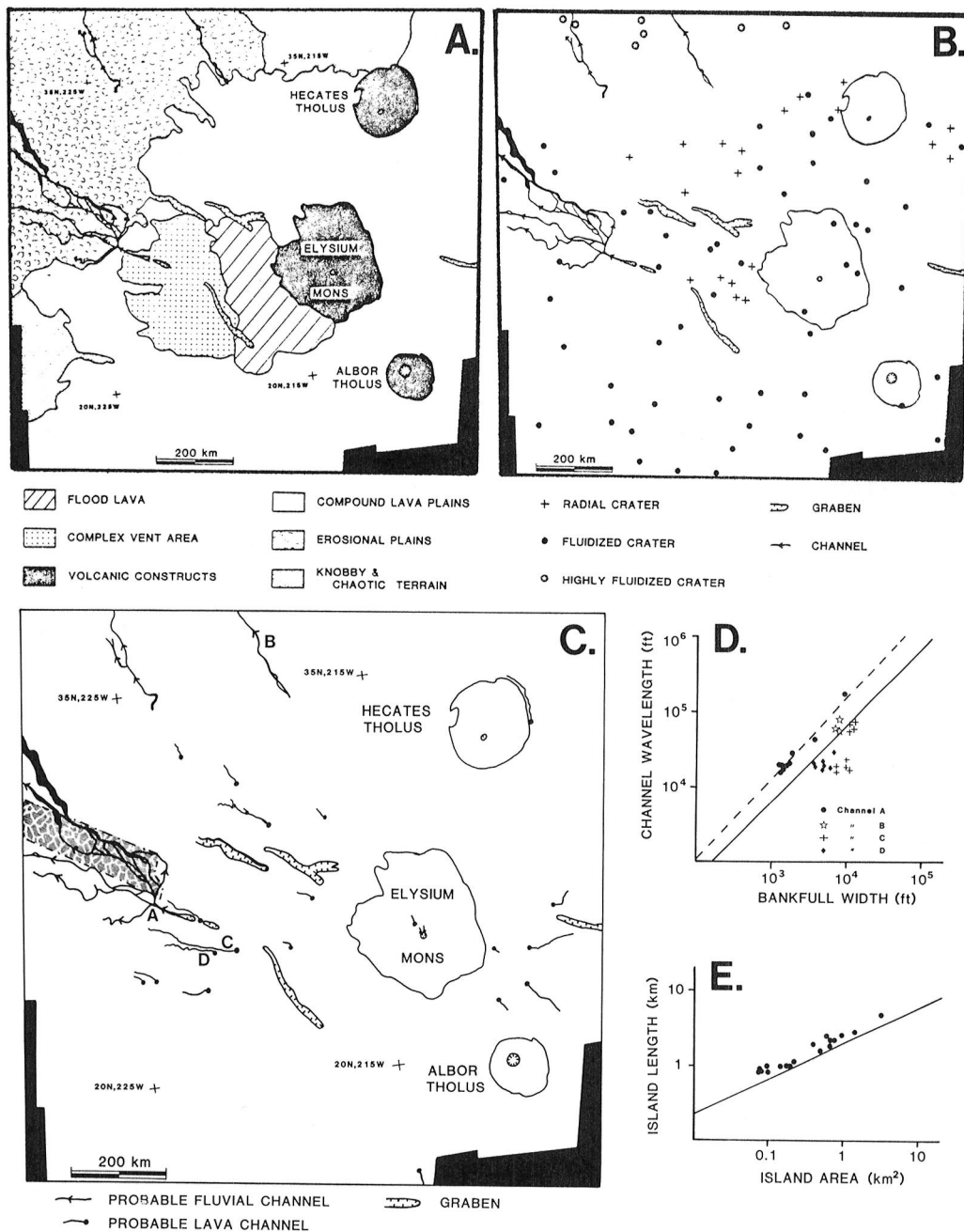


FIG.2: A) Major geological units identified from Fig.1. B) Principal morphologic features and distribution of the three main kinds of crater morphology (all craters greater than 5 km dia.). C) Distribution of channels within Elysium Planitia. Four channels (A-D) considered in Fig.2D are identified. Hatched area shows location of mosaic (Viking frames 649A01-18) from which streamline measurements (Fig.2E) were made. D) Analysis of width vs. wavelength for channels in Fig.2C. Dashed line after ref. 21, solid line ref. 22. Channels which fit Baker's (23,24) model for fluvial origin plot above solid line, sinuous rilles (18,19) plot below, implying a possible fluvial origin for channels A & B, and volcanic for C & D. E) Morphometry of streamlined islands (within hatched area, Fig.2C) compared to analysis of ref.24. Close correlation between two data sets suggests that Elysium channels were produced by fluvial rather than volcanic processes.

Although the constructs have markedly different morphologies from the volcanoes in Tharsis (1,2,7,9), multiple compound lava flows, comparable to Schaber's (4) unit H, constitute the most areally extensive surface material in Elysium. A complex region of vents, domes, flows and sinuous channels, together with a relatively young series of flood lavas, make up the other main volcanic units (Fig.2A). Two areas of knobby and chaotic terrain (13), and an area of subdued (probably mantled) topography to the NW, have also been recognized.

Three main impact crater morphologies are present in Elysium (Fig.2B), and are similar to the fluidized (Type 1 or 3; single or multi-lobed) and radial (Type 4) craters described by Mouginis-Mark (14). In addition, areally extensive ejecta deposits from highly fluidized craters (primarily Type 2; twin-lobed) comparable to those observed in Acidalia Planitia (15) occur to the north within the knobby and chaotic material. Some correlation exists between the occurrence of the radial texture craters and the flood lavas, but this is not a unique association and the crater distribution is currently under investigation with respect to the possible effects that target stratification (16,17) may have on the ejecta.

Multiple modes of origin appear likely for the channels within Elysium Fossae (Fig.2C). We have identified numerous sinuous features that we believe were formed by lava (18,19), while others have the characteristic braided morphology usually attributed to fluvial processes on Mars (11,12, 20). In an attempt to quantify the differences between these two channel types, we have begun a series of measurements of channel morphometry. Fig. 2D compares the width and wavelength of four channels in Fig.2C, using criteria developed in refs. 21, 22. Fig.2E presents data on streamlined islands from the shaded area in Fig.2C (mapped from Viking frames 649A1-18). Based on comparisons with the work of Baker (23,24), we believe that channels A and B in Fig.2C are fluvial in origin, whereas channels C and D, together with many of the others shown in Fig.2C, are lava channels.

Currently, we are continuing more detailed mapping of the Elysium region to identify spatial variations in eruptive style, pursuing the role of substrate characteristics on impact crater ejecta morphology, and extending our analyses of channel morphometry to determine the volumes of lava and water required to produce the observed channels.

- REFERENCES: 1) Carr M.H. (1973) J.Geophys.Res. 78, 4049-4062. 2) Malin M.C. (1977) Geol.Soc.Amer.Bull. 88, 908-919. 3) Scott D. & Carr M.H. (1978) USGS Map I-1083. 4) Schaber G.G. et al. (1978) PLPSC 9th., 3433-3458. 5) Carr M.H. et al. (1977) J.Geophys.Res. 82, 3985-4015. 6) Greeley R. (1973) Geology 1, 175-180. 7) Pike R.J. (1975) PLPSC 9th., 3239-3273. 8) Reimers C. & Komar P. (1979) Icarus 39, 88-110. 9) Pike R.J. (1980) NASA-TM 81776, 192-194. 10) Carr M.H. & Greeley R. (1980) NASA-SF 403, 211pp. 11) Trevena A.S. & Picard M.D. (1978) Icarus 35, 385-394. 12) Baker V.R. (1978) PLPSC 9th., 3205-3223. 13) Carr M.H. (1980) Space Sci. Rev. 25, 231-284. 14) Mouginis-Mark P.J. (1979) J.Geophys.Res. 84, 8011-8022. 15) Mouginis-Mark P.J. & Carey D.L. (1980) NASA-TM 81776, 105-107. 16) Head J.W. (1976) PLSC 7th., 2913-2929. 17) Pike R.J. (1980) PLPSC 11th., in press. 18) Carr M.H. (1974) Icarus 22, 1-23. 19) Hulme G. (1974) Geophys.J.Rov.Astron.Soc. 39, 361-383. 20) Baker V.R. & Milton D.J. (1974) Icarus 23, 27-41. 21) Leopold L.B. & Wolman M.G. (1957) Geol. Surv.Prof.Paper 292-B. 22) Yalin M.S. (1972) Mechanics of Sediment Transport, Pergamon London. 23) Baker V.R. (1979) J.Geophys.Res. 84, 7985-7993. 24) Baker V.R. & Kochel R.C. (1979) J.Geophys.Res. 84, 7969-7983.

## SMALL VOLCANIC FEATURES OF THE ELYSIUM REGION

J.B. Plescia, Jet Propulsion Laboratory, California Institute of Technology, Pasadena, CA 91103

The high resolution Viking images of Mars have allowed the identification of a number of areas which are characterized by small volcanic features many of which appear to be pyroclastic cones. However, several regions exhibit structures that resemble low shields, similar to those seen on the Snake River Plains and in Hawaii (Greeley, 1977). Hodges (1980) and Plescia (1980) have described one of these occurrences in Tempe that is a close analogue for the Snake River Plains. Greeley and Theilig (1978), Wood (1979), and Hodges (1979) have identified a number of other areas characterized by low shields, cones and other small volcanic features. This report briefly describes localities in the Elysium region in which a variety of small volcanic structures occur. Generally the most numerous are low shields. These have been recognized in two areas; along the southwestern flank of Elysium Mons ( $24^{\circ}\text{N}$ ,  $216^{\circ}\text{W}$ ) and northeast of Hecates Tholus ( $33^{\circ}\text{N}$ ,  $215^{\circ}\text{W}$ ).

In the first area, southwest of Elysium Mons, low shields occur on the plains along the contact with the steeper slope of the volcano. This is along the trend of the concentric fractures that surround Elysium Mons. The vents are elongate averaging approximately 3 kilometers in length, and are 300 to 400 meters wide. The orientation of the vents appears to be controlled by circumferential fractures, with the vent orientation changing from  $\text{N}45^{\circ}\text{W}$  to  $\text{N}5^{\circ}\text{W}$  around the western side of the volcano. The low shields near Elysium are characterized by extremely low slopes and surfaces less cratered than adjacent regions. There is a suggestion of radial texture caused by lava flows extending away from the summit crater. Atmospheric haze has, however, prevented positive identification of lava flows.

The second area is northwest of Hecates Tholus. Here low shields have formed along the contact between the plains and the irregular, rough terrain to the north. The vents of the low shields here are considerably larger than those near Elysium Mons. They are elongate ranging from 12 to 29 km in length and average about 700 - 800 meters to over 1.5 km in width. Like the low shields of other regions these have low slopes and a radial texture that is the result of clearly identifiable lava flows extending away from the summit crater. All of the vents are strongly aligned along a trend of  $\text{N}35\text{--}45^{\circ}\text{W}$ .

Also occurring in the same general region, to the northwest of Hecates Tholus, are long ridge-like features. At many locations lava flows can be observed to extend away, which in places, have formed plateaus around a vent, that can be several kilometers across. The ridges have a sort of granular texture, suggesting that they may not be a single continuous feature. Perhaps they are analogous to fractures on Hawaii where spatter cones have built up and formed irregular linear features. These ridges appear to average about 300 meters in width. These features follow the same trend as the low shields of the area,  $\text{N}40^{\circ}\text{W}$ .

The volcanic features near Elysium Mons appear to have been controlled by the stress system and fractures around the volcano. The structures near Hecates Tholus do not appear to be systematically related to that volcano and apparently reflect a regional stress system. The dominant orientation of fractures in the Elysium region is N65°W (Scott and Allingham, 1976), hence the trend of the volcanic structures must reflect a different system. The volcanic features appear relatively young compared to the other volcanic features and may reflect a younger, different, stress system than that which dominated Elysium earlier in its history. The features observed across the Elysium region are similar to those seen in other regions of Mars, particularly in the Tempe area. Here in Elysium, however, the most recent development did not progress to the point where a volcanic province analogous to the Snake River Plains has formed, as in Tempe. That is, in Tempe the volcanics show numerous coalesced flows and shields of considerably larger total volume in contrast to the more solitary occurrences that make up the most recent activity of the Elysium area.

#### REFERENCES:

- Greeley, R., 1977, Basaltic "Plains" volcanism (Chapter 3) in Volcanism of the Eastern Snake River Plains, Idaho: A Comparative Planetology Guidebook. NASA Cr-154621, p. 23-44.
- Greeley, R. and Theilig, E., 1978, Small volcanic constructs in the Chryse Planitia region of Mars: Repts. Planet. Geol. Program 1977-1978. NASA TM 79729. p. 202
- Hodges, C.A., 1979, Some lesser volcanic provinces on Mars: Repts. Planet. Geol. Program, 1978-1979 NASA TM 80339 p. 247-249.
- Hodges, C.A., 1980, Tempe-Mareotis volcanic province of Mars: Repts. Planet. Geol. Program, 1979-1980. NASA TM 91776, p. 181-183.
- Plescia, J.B., 1980, The Tempe volcanic province: An analog to the Eastern Snake River Plain?: Repts. Planet. Geol. Program, 1979-1980, NASA TM 91776, p. 189-191.
- Scott, D., and Allingham, J.W., 1976, Geologic map of the Elysium quadrangle of Mars: U.S. Geological Survey Misc. Inv. Series I-935
- Wood, C.A., 1979, Monogenetic volcanoes of the terrestrial planets: Proc. Lunar and Planet. Sci. Conf. 10th, p. 2815-2840.

This research was carried out under NASA Contract 7-100.

## CINDER CONES OF ISIDIS AND ELYSIUM

J.B. Plescia, Jet Propulsion Laboratory, California Institute of Technology, Pasadena, CA 91103

Although the large volcanoes of the Tharsis region and other areas dominate in terms of size, the small scale features certainly dominate in terms of numbers of volcanic features on Mars. West (1974), has suggested that a number of locations are characterized by pyroclastic cones. Hodges (1979), Wood (1979) and Woronow (1980) have all commented on the occurrence of cinder cones in other localities as well.

Data presented here comes from two areas imaged at high resolution by the Viking Orbiters. Both areas appear to be dominated by cinder cones. One area, imaged during 647A, lies in the eastern Elysium Planitia region at  $25^{\circ}\text{N}$  and  $237^{\circ}\text{W}$ . The second area occurs within the Isidis Basin between  $10^{\circ}$ - $19^{\circ}\text{N}$  and  $272^{\circ}$ - $180^{\circ}\text{W}$ , and selected regions were imaged by a series of survey revs; 142S, 143S, 148S, 150S, and 151S. Both areas were imaged at resolutions of approximately 20 - 30 m/pixel.

Numerous features observed in both regions strongly resemble cinder cones. These are generally circular in outline and are topographically high. Each is capped by a depression, interpreted to be a summit crater. They occur as both isolated features and in chains. In cases where they occur in chains, they may retain their individuality, or they may coalesce into ridge-like features. The objects in Elysium have been observed only to occur as individuals, while those in Isidis occur as both individuals and in chains and ridges.

In order to compare the martian and terrestrial features in a more quantitative manner, the ratio of crater diameter ( $W_{\text{cr}}$ ) to basal diameter ( $W_{\text{co}}$ ) was determined. These ratios were then compared to those calculated for terrestrial cones. The data for the terrestrial cinder cones come from the extensive data set of Pike (1978).

The martian objects examined here were generally less than 600 to 700 meters in diameter, and all were less than 1 kilometer. The sampling was biased, in that only those features with clearly defined summit craters were included. The process which limited clear identification in most cases was atmospheric haze. Many features which appeared to have summit craters were excluded because reliable measurements could not be made. Additional bias came from resolution effects which limits the identification of features at the small end of the size range.

The data obtained from this study is illustrated in Table I. along with the data for terrestrial cones. Included are the image numbers, location, number of data points (N), the mean ratio of crater to basal diameter ( $W_{\text{cr}}/W_{\text{co}}$ ) with its standard deviation, the equation of a line from a least squares fit to the data, and the mean basal diameter of the features.

From the data it can be seen that the martian features have a slightly larger crater diameter/basal diameter ratio, compared to the terrestrial features, although all ratios are within 1 sigma of each

other. The average basal diameters of the martian cones is also less than the terrestrial examples.

Wood (1979) has suggested that terrestrial, lunar and martian cones have similar crater diameter to basal diameter radius. From a limited data set Wood concluded that the ratio for martian features was  $W_{cr} = 0.41W_{co}$ . The average ratio determined for all the martian cones have is 0.437. This is slightly larger than that determined by Wood, although not inconsistent.

McGetchin et al. (1974) studied the dynamics of the formation of cinder cones on Mt. Etna and made comparisons to the Moon and Mars. They calculated the shapes lunar and martian cones would have if erupted under similar conditions to those which produced Northeast crater on Mt. Etna. While the absolute dimensions of the martian cones were much larger than terrestrial examples, the ratio of crater diameter to basal diameter remained approximately the same.

McGetchin et al. concluded that martian crater diameter/basal diameters would be 1.40 times larger than terrestrial ratios. The average ratio for the martian features examined here is 0.547 and is 1.37 times larger than the ratio obtained from the terrestrial data of Pike (1978) (0.326). That result is consistent with the model of McGetchin et al

Hence, in terms of both morphology and dimensional ratios the martian features appear to be cinder cones. The generally smaller size of the martian cones may simply reflect a shorter eruption period. The occurrence of many of the features in chains or coalesced ridges may reflect concentration along fracture zones or subsurface faults, as has occurred along fractures in Hawaii.

#### REFERENCES:

- Hodges, C.A., 1979, Some lesser volcanic provinces on Mars: Rept. Planet. Geol. Program, 1978-1979, NASA TM 80339, p. 247-249.
- McGetchin, T.R., Settle, M., and Chouet, B.A., 1974, Cinder cone growth modeled after Northeast crater, Mount Etna, Sicily: J. Geophys. Res., v. 79, p. 3257-3272.
- Pike, R.J., 1978, Volcanoes on the inner planets: Some preliminary comparisons of gross topography: Proc. Lunar Planet. Sci. Conf. 9th, p. 3239-3273.
- West, M.N., 1974, Martian volcanism: Additional observations and evidence for pyroclastic activity: Icarus, v. 21, p. 1-11.
- Wood, C.A., 1979, Monogenetic volcanoes of the terrestrial planets: Proc. Lunar and Planet. Sci. Conf. 10th, p. 2815-2840.
- Woronow, A., 1980, Small volcanic constructs in Utopia Planitia: Rept. Planet. Geol. Program, 1979-1980. NASA TM 81776, p. 187-188.

This research was carried out under NASA Contract 7-100.



TABLE I

IMAGE NUMBER	LOCATION	N	$W_{cr}/W_{co}$	LINEAR FIT	MEAN $W_{co}$
142S 12/13 - 143S 2/3/13	10°N 273°W	64	$0.452 \pm 0.093$	$Y = 92.26 + 0.25X$	467
148S 8/14/15	19°N 273°W	49	$0.416 \pm 0.084$	$Y = 64.33 + 0.30X$	578
150S 1/5/6	14°N 280°W	35	$0.465 \pm 0.078$	$Y = 33.78 + 0.39X$	469
150S 22/24	16°N 276°W	98	$0.454 \pm 0.097$	$Y = 54.14 + 0.35X$	521
151S 16/18/20-24	16°N 279°W	103	$0.415 \pm 0.085$	$Y = 67.31 + 0.27X$	487
647A 40-48	25°N 237°W	77	$0.419 \pm 0.087$	$Y = 1.89 + 0.42X$	703
TERRESTRIAL		57	$0.326 \pm 0.077$	$Y = 41.84 + 0.28X$	1093

## SOME MARTIAN VOLCANIC CENTERS WITH SMALL EDIFICES

H. J. Moore and C. A. Hodges, U.S. Geological Survey, Menlo Park, CA 94025

In addition to the large volcanoes on Mars, there are less spectacular volcanic centers that are characterized by low shields, domes, pits, flows, and fissure eruptions. Some of these have received little attention. Eight such centers and their locations (Table 1) are briefly discussed here. A search for additional centers is in progress, and about 10 known centers are not reported here.

The Syria Planum center lies near the crest of the Syria Planum rise where flows radiate downslope from a filled caldera (25x35 km). Additional volcanic features include: (a) fissure eruptions similar to those of King's Bowl, Snake River Plains (1); (b) cratered cones 0.75 km across; (c) lava flows; (d) crater chains; (e) slotted vents; and (f) peculiar polygonal tumescences ( $\approx 35$  km).

Northwest of Olympus Mons, the southwest part of a volcano-tectonic collapse (2) has been covered by later flows. In the exposed part of the structure, lava flows appear to issue from concentric graben and extend radially away from the center of the structure. Near the center of the structure, two cones ( $\approx 1.2$  km across) are surrounded by radial lobes that may be flows.

The Ceraunius Fossae center is similar to that of Mareotis-Tempe Fossae (3). Here, small shield volcanoes are scattered among northerly striking graben, and flows from the shields are superposed on the graben, locally obscuring them. The shields ( $\approx 12$  km across) have centrally located craters (0.3 to 1.2 km across).

The center just north of Uranus Patera is characterized by flows and low domes (2x5 km) with summit craters.

In the Mareotis-Tempe Fossae area, low shields are scattered among northeasterly striking graben, and both the shields and flows are superposed on the graben (3). One edifice on the northeast edge of the area is unique because of the unusually thick flows that radiate from it (Fig. 1). A summit caldera with a central peak occurs at the center of the volcano, which is superposed on a northeast-trending graben. The elliptical caldera (5.5x9.4 km) is elongate in a northwest direction. A mesa, similar in size, is adjacent to the northeast side of the caldera. Flank deposits of flows and, probably, pyroclastic material surround the caldera and mesa. Flows clearly post-date the graben in some places but are displaced by faults in others. Flows with typical widths of 1.6 to 3.9 km and thicknesses of 60 to 180 m radiate from the structure but are most extensive in the northwest and southeast directions where tips of flows occur 81 to 125 km away from the caldera. Flows 60 to 180 m thick are uncommon on Mars. Yield strengths of these flows, calculated from estimated thick-

nesses and widths (5), are of the order of  $10^4$  to  $10^5$  Pa. If the gradients here are small, as they appear to be, silica contents of the flows may be high ( $> 58\%$ ).

Small edifices in the Chryse Planitia center (4) differ from others in that some of them appear to be extensively eroded, leaving remnants of volcanic necks, dikes, and low shields. Some flows also appear to be eroded. Some cinder cones and flows, however, are well preserved.

Several small shields are present on the floor of the caldera of Arsia Mons. Elongate vents,  $0.25 \times 1.0$  km, occur at the apices of shields. Basal dimensions of the shields are about  $3.5 \times 7.0$  km to  $10 \times 14$  km. Elongations strike in a northerly direction.

Lava flows occur near crater Lassell. Sources of the flows, which attain widths near 20 km, appear to be wrinkle ridges a few kilometers wide. This volcanic center is somewhat unusual in that there are no apparent shields, calderas, cones, or domes associated with it.

Table 1. Some volcanic centers with small edifices.

Name	Location (degrees)	Elevation (km)	Relative Age Craters/km <sup>2</sup> with D>1 km	Selected Viking Photos
Syria Planum	14S, 104W	9-10	$1.3(+0.7) \times 10^{-3}$	643A59-63
near Olympus Mons	28N, 127W	1-2	$3(+1.5) \times 10^{-3}$	623A29-33
Ceraunius Fossae	24N, 112W	3-6	$0.8(+.2) \times 10^{-3}$	038B53
near Uranus Patera	28N, 90W	2-3	---	224A68
Mareotis-Tempe Fossae	35N, 85W	0-2	$\approx 1 \times 10^{-3}$ (6)	627A21-30,41
Chryse Planitia	20N, 48W	(-) 3-1	$\approx 10^{-3}$	003A01,02,18
in Arsia Caldera	9S, 120W	25	$0.1 \times 10^{-3}$	422A15,35
near Lassell	25S, 64W	5-6	$5.1(+0.8) \times 10^{-3}$	610A03,21

#### References

- (1) King, J.S. and Greeley, R., 1980, Morphologic remnants of a lava lake, eastern Snake River Plain: Lunar and Planet. Sci. XI, part 2, p. 555-556.
- (2) Plescia, J.B. and Saunders, R.S., 1979, The chronology of the martian volcanoes: Proc. Lunar Planet. Sci. Conf. 10th, p. 2841-2859.
- (3) Hodges, C.A., 1980, Tempe-Mareotis volcanic province of Mars: Reports of Planet. Geol. Program, 1979-1980, NASA TM 81776, p. 181-183.
- (4) Greeley, R., Theilig, E., Guest, J.E., Carr, M.H., Masursky, H., and Cutts, J.A., 1977, Geology of Chryse Planitia: Jour. Geophys. Res., v. 82, p. 4093-4109.

- (5) Moore, H.J., Arthur, D.W.G., and Schaber, G.G., 1978, Yield strengths of flows on the Earth, Mars, and Moon: Proc. Lunar Sci. Conf. 9th, p. 3351-3378.
- (6) Plescia, J.B., 1980, The Tempe volcanic province: an analog to the eastern Snake River Plains: Reports of Planet. Geol. Program 1979-1980, NASA TM 81776, p. 189-191.

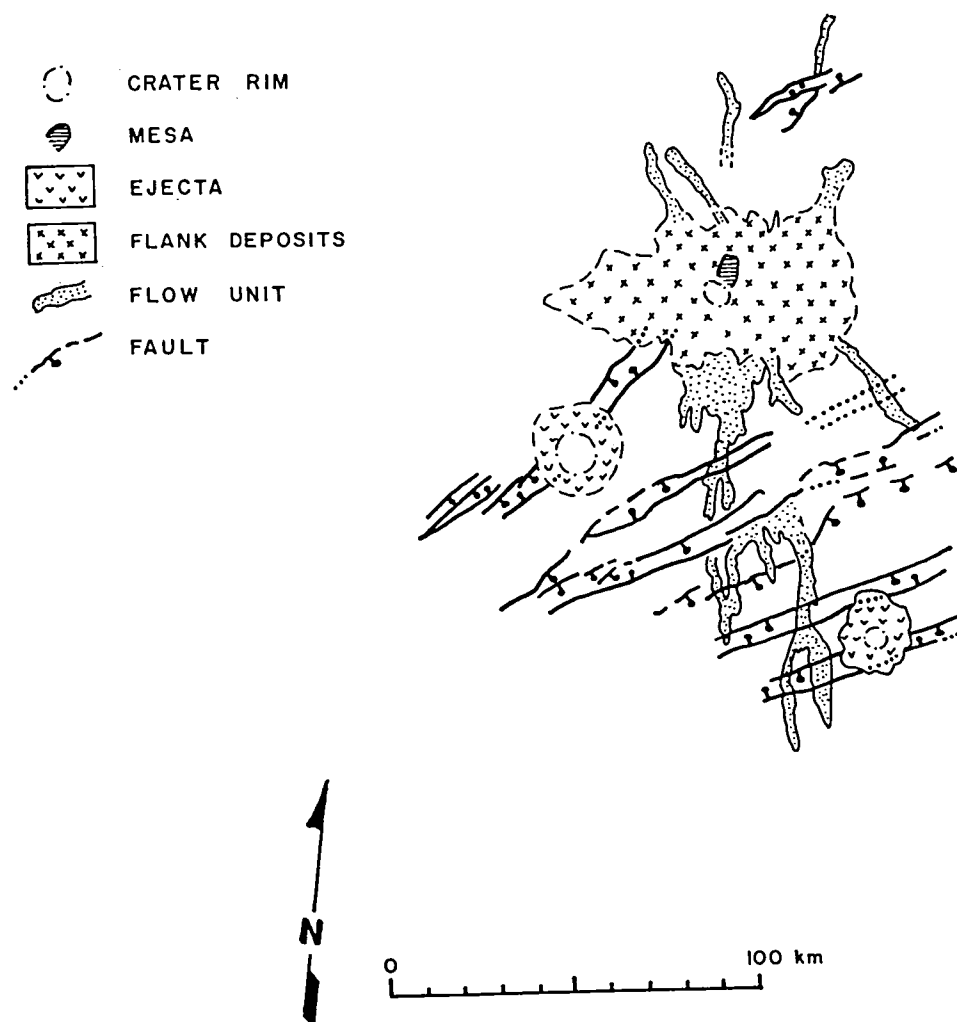


Figure 1. Geologic sketch map of volcano on northeast edge of Mareotis-Tempe Fossae area (76W 39N, Viking Orbiter frame 519A15).

ESTIMATES OF LAVA FLOW VELOCITIES IN CHANNELS OF THE PU'U KIA'I FLOW,  
HAWAII'I

Moore, H.J., Kachadoorian, R., U.S. Geological Survey, Menlo Park, CA  
94025, and Moore, R.B., U.S. Geological Survey, H.V.O., Hawaii Natl.  
Park, HI 96718

Peak flow velocities of lava flowing in channels can be calculated from the geometry of the channels, pressure gradients, and flow thicknesses. We assume that the flow behaved as a Bingham plastic and that channel depths do not arise from ponding due to surges or damming in the downstream flow. Nearby flow lobes and, sometimes, the channels can be used to estimate present-day thickness and yield strength ( $\tau_y$ ) (1). A plastic viscosity ( $\eta_p$ ) can be obtained using an assumed model relating yield strengths and plastic viscosities to the volume fraction of solids (1). The maximum thickness at the time of flow ( $H_f$ ) is taken as the sum of the present-day thickness ( $h_y$ ) and the channel depth ( $d$ ) (fig. 1) and, when combined with the estimated density of the flow ( $\rho$ ), the topographic gradient ( $\sin \theta$ ), and the acceleration of gravity ( $g$ ), permits calculation of the stress at the base of the flow ( $\tau_b$ ). Using reasonable values of these parameters, maximum average velocities at peak flow and the peak velocity of the upper slab-like part of the flow can then be calculated (1). This procedure is similar to that proposed for estimates of lava flow velocities using lava trees (2).

We have applied these concepts to the flow of lava in channels of the Sept. 1977 Pu'u Kia'i flow of Hawaii'i (3) with mixed results. Yield strengths increase from 0.4 kPa near the source to 15 kPa near the tip, and plastic viscosities increase from 2 to 13 kPa\*sec. These increases occur when either the local or total pressure heads are used, but the increase is more uniform when the total head is used. Yield strengths and plastic viscosities are typically larger than those calculated for the July 1974 Keanakako'i flow (0.6 kPa and 2 kPa\*sec) (2) and clearly larger than those measured in Makaopuhi lava lake (0.1 kPa and 0.7 kPa\*sec) (4).

Calculated velocities of the flows in the channels appear, in part, reasonable although some are probably too large. Calculated peak slab velocities (fig. 2) are always larger than the average velocities by variable factors that increase with the increase of the modified Reynold's number (1). At A and B, slab velocities (2 to 5 km/hr at A and 3 to 4 km/hr at B) are smaller than the observed 11.5 km/hr upstream (fig. 2). In a similar calculation using a plastic viscosity and yield strength of the Makaopuhi lava, laminar flow slab velocities would be 16 to 25 km/hr, but turbulent flow may occur (av. velocity 26 km/hr). Downstream, peak slab velocities as great as several km/hr are possible, but those exceeding 10 km/hr are improbable and require explanation. The problem becomes more severe when flows with Makaopuhi yield strengths and plastic viscosities are used; flow becomes chiefly turbulent with average velocities 24 to 64 km/hr at peak flow.

The high velocities in our calculations could be the result of a number of factors. A very probable factor would involve variable behavior of the flow with temporary ponding caused by damming and channel clogging with debris from channel wall failures and the sporadic movement of the front and low lava flow rates to yield deep channels and then followed by increased flowage as the channel debris clears or the ponding front moves downslope. Alternatively, variable flow rates might produce surges of lava and deep channels that are only periodically filled to the levee crest.

Another factor could be underestimates of yield strengths and plastic viscosities. For example, crude continuity considerations combined with channel and flow dimensions at 0 (fig. 2) require average channel velocities near 1 km/hr in order to achieve a front velocity of 0.3 km/hr. This requirement could be accomplished by increasing the yield strengths and plastic viscosities by a factor near 2, which results in reductions of average velocities from about 5 km/hr to 1 km/hr and slab velocities from about 24 km/hr to 4 km/hr.

Another factor may be the model used -- perhaps the Bingham plastic model needs to be modified to include internal friction, or the relation between viscosity and yield strength may be in error (1).

The velocities calculated here, although too high in places and perhaps too low in others, are not unrealistically high, and the larger yield strengths and plastic viscosities are consistent with the observations that the 1977 lava is one of the most differentiated ones that Kilauea has ever produced and that it was relatively cold and degassed (3).

#### References

1. Moore, H.J. and Schaber, G.G., 1975, An estimate of the yield strength of the Imbrium flows: Proc. Lunar Sci. Conf. 6th, p. 101-118.
2. Moore, H.J. and Kachadoorian, R., 1980, Estimates of lava-flow velocities using lava trees: Reports of Planet. Geol. Prog. 1979-1980, NASA TM 81776, p. 201-203.
3. Moore, R.B., Helz, R.T., Dzurisin, D., Eaton, G.P., Koyanagi, R.Y., Lipman, P.W., Lockwood, J.P., and Puniwai, G.S., 1980, The 1977 eruption of Kilauea Volcano, Hawaii: Jour. Volcanology and Geothermal Res., v. 7, p. 189-210.
4. Shaw, H.R., Peck, D.L., Wright, T.L., and Okamura, R., 1968, The viscosity of basaltic magma: an analysis of field measurements in Makaopuhi lava lake, Hawaii: Amer. Jour. Sci., v. 226, p. 225-264.

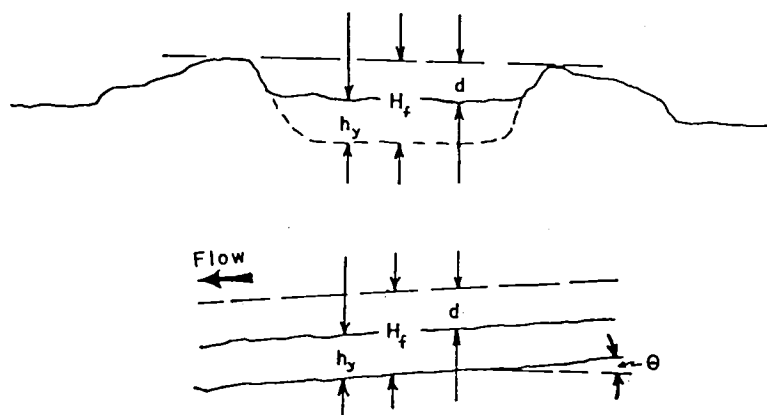


Figure 1. Diagram illustrating measured and estimated dimensions used in calculating flow velocities: A is a cross-sectional profile perpendicular to the direction of flow, and B is parallel to the direction of flow (arrow indicates direction of flow).

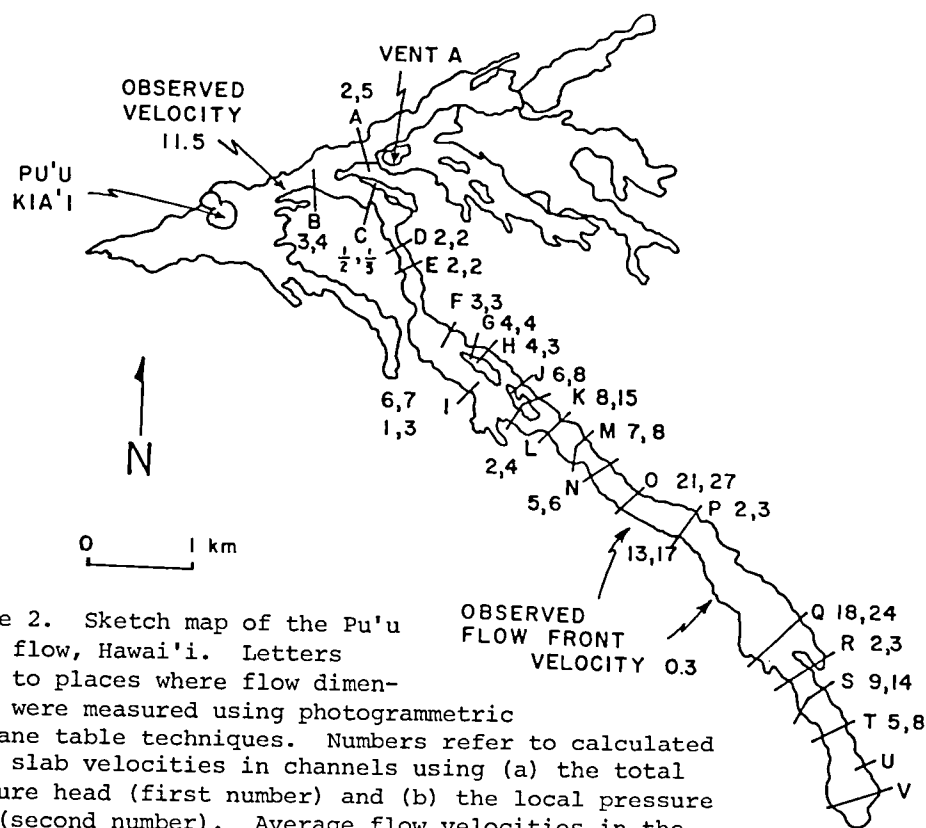


Figure 2. Sketch map of the Pu'u Kia'i flow, Hawai'i. Letters refer to places where flow dimensions were measured using photogrammetric or plane table techniques. Numbers refer to calculated peak slab velocities in channels using (a) the total pressure head (first number) and (b) the local pressure head (second number). Average flow velocities in the channels are less than the slab velocities.

## QUANTITATIVE MORPHOLOGY OF VOLCANOES: STATUS REPORT

R. J. Pike, U. S. Geological Survey, Menlo Park, CA 94025.

The last batch of Viking-Orbiter photogrammetric data, which describe the topography of approximately half a dozen large volcanoes on Mars, is in the final stage of preparation in Flagstaff. The measurements were not completed in time for inclusion in this report. ~~However~~, an analysis of these and complementary data will be ready for oral presentation at Baton Rouge in January.



Chapter 6  
AEOLIAN PROCESSES AND LANDFORMS



## VENUS AEOLIAN PROCESSES: SALTATION STUDIES AND THE VENUSIAN WIND TUNNEL

R. Greeley, Dept. of Geology, Arizona State University, Tempe, AZ 85281; B. R. White, Dept. of Mech. Engr., Univ. Calif./Davis, CA 95616; R. Leach and R. Leonard, Dept. of Physics, Univ. Santa Clara, CA 95053; J. Pollack, Space Sciences Div., NASA-Ames Research Center, Moffett Field, CA 94035; J. D. Iversen, Dept. Aerospace Engineering, Iowa State Univ., Ames, IA 50011

Measurements of the near-surface winds on Venus by the Venera spacecraft (Florensky et al., 1977) and estimates of wind speeds extrapolated from Pioneer-Venus probe measurements yield values of 1 to 2 m s<sup>-1</sup> (Counselman et al., 1979). These values are well within the ranges predicted for particle threshold (Iversen et al., 1976) that are based on theory and wind tunnel experiments extrapolated to venusian conditions. Thus, there is a strong likelihood that aeolian processes occur on Venus at present and may have occurred in the geological past. In general, windblown particles are transported by saltation (from the Latin *saltare*, "to jump, or leap"; the grains bounce, hop and skip along the surface), by surface creep, and by suspension; both surface creep and suspension result primarily from the impact of saltating grains. Thus, saltation is of primary consideration in the analysis of any aeolian regime, including Venus. Using models describing the dynamics of saltating grains, we have derived saltation trajectories as functions of wind speeds and particle diameters under venusian conditions (Fig. 1). In general, the particle saltation height and length are about a factor of 10 less on Venus than for Earth under comparable dynamic conditions (i.e., grain sizes most easily moved, windspeeds slightly higher than threshold). Thus, for particles 0.1 to 1.0 mm in diameter and near-surface wind speeds of 1 to 3 m s<sup>-1</sup>, saltation path lengths range from a few mm to about 17.5 mm, and saltation path heights range from a few mm to about 12.5 mm.

This result has potential significance for future high resolution radar imaging of aeolian bedforms on Venus. It has been demonstrated that the radar return from various sand deposits, including dunes, is enhanced by the presence of ripples (Elachi and Blom, 1980), at least for SEASAT radar wavelengths and for typical ripple wave lengths and heights on Earth. However, because ripple geometry is at least partly a function of saltation trajectory, sand ripples on Venus may have quite different dimensions than ripples on Earth, and their radar signatures may also be different.

In addition to the smaller sizes of ripples on Venus in comparison to Earth, calculations show that the rate of movement of windblown particles on the surface is substantially less on Venus; we estimate that for comparable dynamic conditions, the flux would be  $3 \times 10^{-4}$  less on Venus than on Earth. This suggests that rates of erosion and rates of change for possible "variable" features would be greatly reduced on Venus in comparison to Earth and Mars.

We emphasize that these results are based on numerical modelling involving very poor knowledge of flow dynamics under venusian conditions. In order to obtain the kind of data required for predicting various aspects of aeolian processes on Venus, we are currently fabricating a high pressure wind tunnel at NASA-Ames Research Center, to be operated in conjunction with the Martian Wind Tunnel facility. Because a 1:1 simulation of the surface pressure and temperature on Venus would require a facility that would be prohibitively high in cost, a slightly different approach is being taken than was the case

for the Martian Wind Tunnel. The same primary fluid properties as for the surface of Venus can be achieved at a working pressure of  $\sim 35$  bar and "ambient" Earth temperatures. The apparatus will be a closed-circuit tunnel (Fig. 3) about 6 m long, having a test section cross section of about  $700 \text{ cm}^2$ . The tunnel will be used primarily to conduct threshold experiments, to study saltation dynamics, and to study the fundamental physics of particle movement in the venusian environment.

#### REFERENCES

- Counselman, C. C. et al. (1979), *Science*, 205, 85-87.  
Elachi, C. and R. Blom, *Lunar and Planetary Science Confr.* (1980), LPI Contr. 399, 8-9.  
Florensky, C. D. et al. (1977), *Geol. Soc. Amer. Bull.*, 88, 1537-1547.  
Iversen, J. D., R. Greeley, and J. Pollack, (1976), *J. Atomic Sci.* 33, 2425-2429.

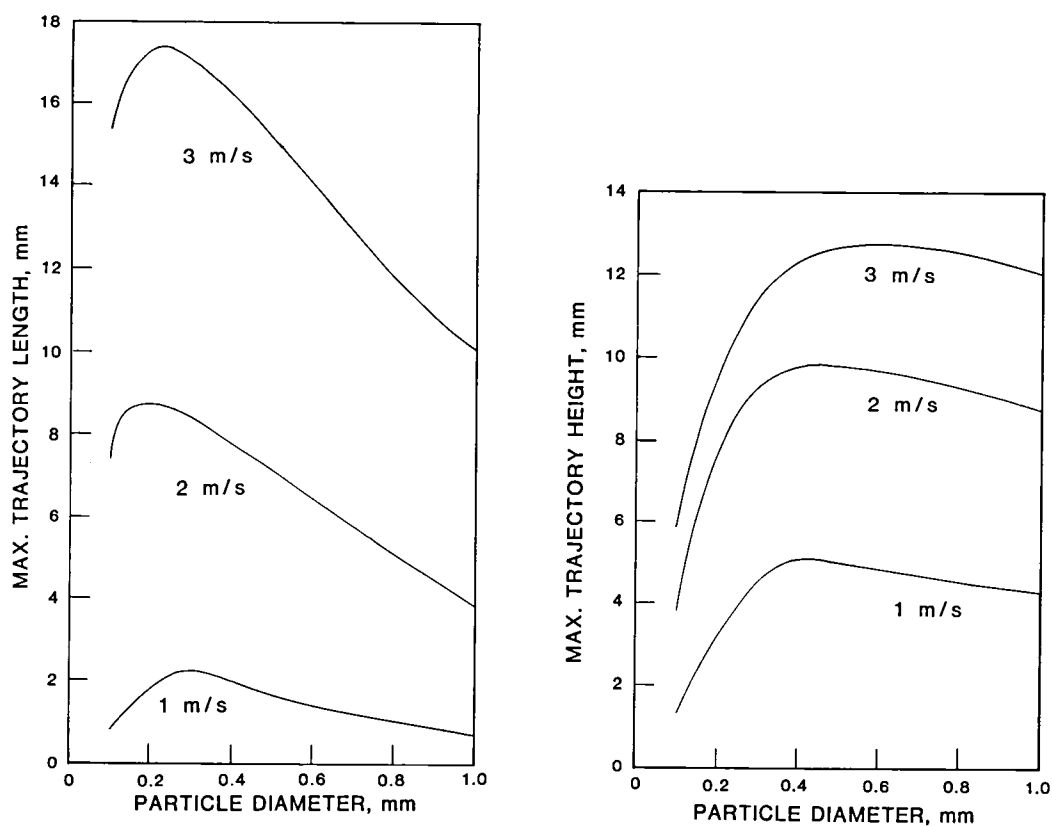


FIGURE 1. Calculated saltation trajectories (left side) for maximum path length and (right side) for maximum path height for particles 0.1 to 1.0 mm in diameter, at speeds of 1, 2, and 3 m/s on the surface of Venus.

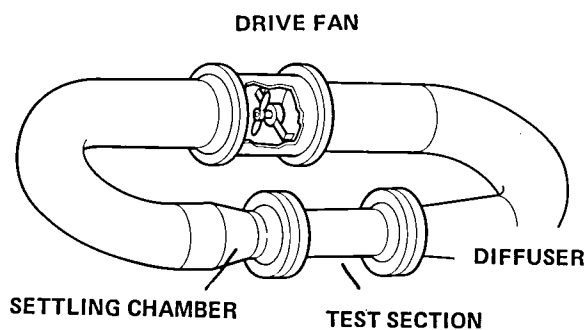


FIGURE 2. Perspective sketch of Venustian Wind Tunnel currently being fabricated; tunnel will operate at simulated Venustian surface conditions and will be used for studying the physics of wind-blown particles.

## FLUX OF WINDBLOWN PARTICLES ON MARS: PRELIMINARY WIND TUNNEL DETERMINATION

Ronald Greeley and K. Malone, Dept. of Geology, Ariz. State Univ., Tempe, AZ 85281; R. Leach and R. Leonard, Dept. of Physics, Univ. of Santa Clara, CA 95053; and B. R. White, Dept. of Mech. Engr., Univ. Calif. at Davis, Davis, CA 95616

Fundamental to the understanding of the aeolian regime on Mars is knowledge of particle flux in terms of particle size distributions and velocities as functions of free-stream wind speed and height above the surface. This knowledge is required for many problems dealing with the evolution of the martian surface, including the determination of rates of aeolian erosion. Although various theoretical approaches have been applied to the problem (White et al., 1979), an experimental approach is desirable in order to check theoretical results and to provide a broader data base for other studies of aeolian processes. Consequently, a general study of particle flux was initiated several years ago using the MARSWIT, the Martian Surface Wind Tunnel. Initial work involved perfection of various particle collectors that would be effective, yet not interfere with the flow of air and of the particles. Trial-and-error wind tunnel tests led to the design of triangular-shaped collectors, open at the apex ( $1 \text{ cm}^2$  collecting area), with flow-through  $40 \text{ }\mu\text{m}$  screens at the back and retainers to prevent particles from escaping; multiple collectors can be stacked to about 2 m high. Although some problems remain, the collectors allow a good assessment of particle size and number distribution as a function of height and free-stream wind speed. The second part of the problem involves the determination of particle velocity. Although high speed motion pictures provide some data, this approach is costly, time consuming for the amount of data returned, and the results are of marginal quality. Another approach uses a *particle velocimeter*; this device was originally developed by the U. S. Forest Service to measure velocities of blowing snow (Schmidt, 1977) and the design was modified for use in our wind tunnel. The velocimeter consists of a light source that produces a light beam perpendicular to the wind-stream, and two light-sensitive semi-conductors that detect the shadow of any intersecting particle as it crosses two separate portions of the light beam. A voltage is produced as each beam is interrupted; thus, particle velocity is derived from the time interval between the two pulses and the distance between the two light sensors. This distance was calibrated using wires of various radii spinning on a motor at known velocities.

An experimental matrix was developed involving: (1) *particle diameter* (760  $\mu\text{m}$ , or "common" sand size and 92  $\mu\text{m}$ , or the size most easily moved by lowest strength winds); (2) *atmospheric pressures* of 1 bar ("Earth" case) and 6.6 mb ("Mars" case); (3) *free-stream wind velocities* of  $65 \text{ m s}^{-1}$  (minimum Mars threshold) and  $115 \text{ m s}^{-1}$  (strong Mars storm) and  $11.1 \text{ m s}^{-1}$  (mild Earth storm) and  $6.9 \text{ m s}^{-1}$  (threshold "Earth" case); and (4) *height above surface* of 29, 71, 161, and 240 mm. Although not all combinations of variables have been run, enough experiments have been completed to show some interesting trends. Figure 1 shows the general increase in particle velocity with height above the surface, reflecting increasing wind speeds through the boundary layer, for the nominal Mars "sand" storm case. Note, however, that most of the particles have velocities *less than 20 percent of the free-stream wind speed*; similar runs for "Earth" conditions show that particles generally achieve velocities much closer to free-stream than on Mars (Fig. 2). Thus, although much greater wind velocities occur (and are required for threshold) under martian conditions, the coupling of the particles with the wind is much less, and the effectiveness of wind erosion would be decreased. Preliminary results for

particle flux as a fraction of free-stream velocity under "Earth" conditions are shown in Figure 3, for two particle sizes. At the time of writing, insufficient data were collected for "Mars-cases" for comparison. However, using some preliminary results for flux in combination with the information on the velocity distributions and knowledge of wind strengths/frequencies from the Viking Landers enables estimates to be made for rates of aeolian erosion. These experiments will continue through the next fiscal year.

Kathleen Malone was supported for work on this project through the Planetary Geology Intern Program, 1980.

#### REFERENCES

- Schmidt, R. A., 1977. A system that measures blowing snow: U. S. Dept. Ag., Forest Service Res. Pap. RM-194.  
 White, B. R., 1979. Soil transport by winds on Mars, Jour. Geophys. Res. 84, 4643-4651.

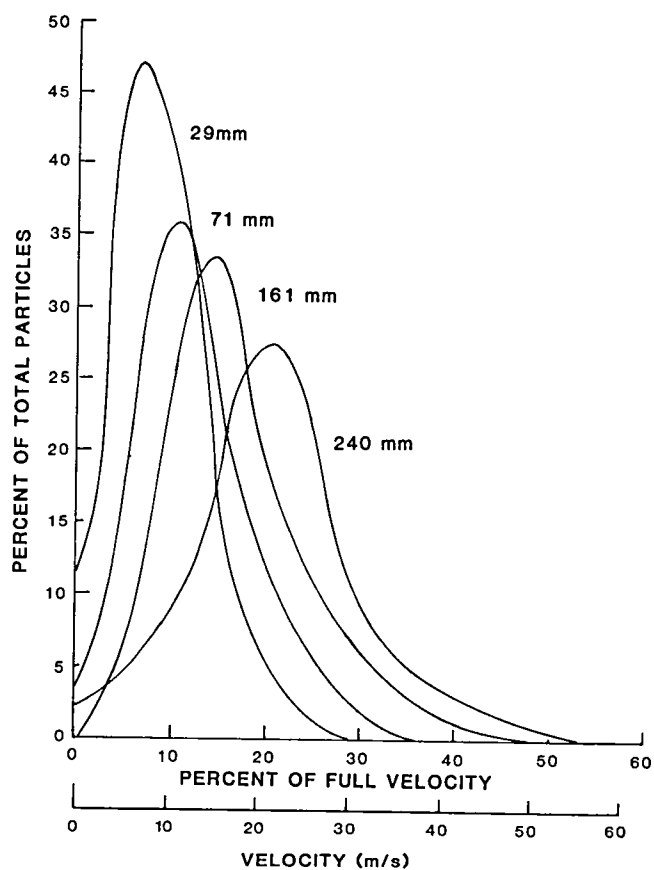


FIGURE 1. Velocity distribution for saltating particles under low pressure (Martian surface) conditions for four heights (29, 71, 161, and 240 mm) above the surface; velocities are shown as both percentage of full "free-stream" speed, and as actual speed in meters per second.

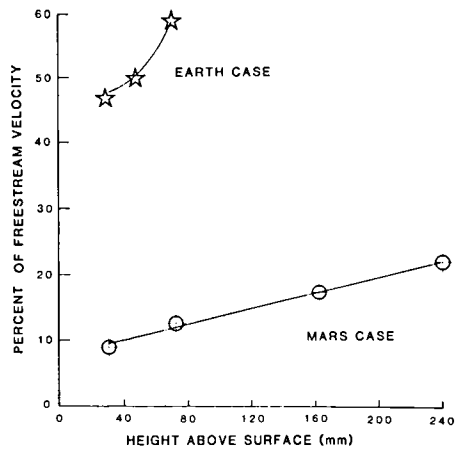


FIGURE 2. Particle velocity shown in percentage of free-stream velocity for "Earth-case" and "Mars-case" as a function of height above the surface; note that particles are more closely coupled to the wind on Earth than on Mars.

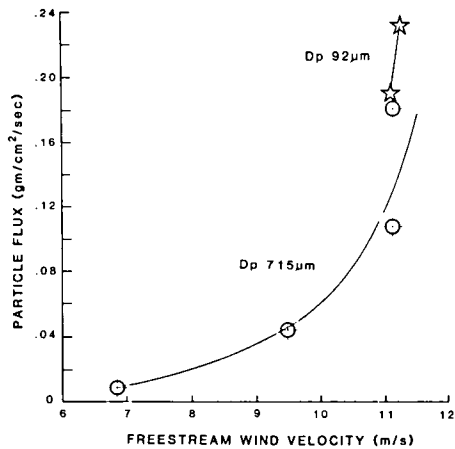


FIGURE 3. Particle flux for "Earth-case" for two sizes of particles as a function of free-stream wind speed.



## PARAMETRIC STUDY OF DUST FOUNTAINS

Jeffrey Kenney, Planetary Geology Summer Intern, Jet Propulsion Laboratory, California Institute of Technology, Pasadena, CA 91103, Fraser Fanale, Institute of Geophysics, Univ. of Hawaii, Honolulu, Hawaii, R. Stephen Saunders, Jet Propulsion Laboratory, California Institute of Technology, Pasadena, CA 91103.

During the "Mars soil/water/atmosphere dynamic interaction investigations," currently being performed at the Jet Propulsion Laboratory, dust fountaining phenomenon were repeatedly observed. The investigations (also reported at this meeting) involved the measurement of "pressure waves" as they pass into and out of deep (1 meter) columns of simulated Martian soil fines. Under Martian environment conditions of pressure and temperature, it was observed that whenever a large upward flow of gas was induced, by changes in pressure or temperature, dust fountains would occur.

Theoretical analysis and experimental observations were undertaken by the author as a planetary geology summer internship task to investigate the possibility that this phenomenon could be the mechanism that inducts soil fines into the atmosphere to produce the Martian dust storms.

Observations of dust fountains in a small chamber (25cm by 40cm by 3cm) with a clear plexiglass wall (like a small ant farm) were made in order to understand the interrelationships of the parameters affecting the channels and fountains, and the potential for fountain formation on Mars. Dust fountains form when the pressure gradient across certain types of soil become great enough to form channels in the soil. Gas flow becomes concentrated in the channels, and shoots particles up above the surface in a fountain (see Figure 1). The channeling phenomenon is one type of fluid flow through a porous medium. When the inertial effects of the gas become significant, channels are formed in the porous medium. There are two ways a pressure gradient could form in the Martian soil: by a change in the atmospheric pressure, or by desorption of  $\text{CO}_2$  by clay minerals (as suggested by Fanale and Cannon 1,2). Because adsorption is a function of temperature and pressure, an increase in surface temperature or a decrease in atmospheric pressure will cause the soil to outgas creating a pressure gradient that could cause channels to form.

Observations seem to indicate four types of behavior in the montmorillonite, and montmorillonite/basalt mix studied as the pressure gradient across it is increased. The first two may be understood without considering the inertial effects of the gas, the latter two cannot. The first behavior is that of normal flow through a porous medium. The second occurs when the hydrostatic pressure difference between some point in the soil and the surface is just greater than the overlying mass pressure. At this point, horizontal cracks appear and the soil surface is upraised.

Channeling with subsequent fountaining is the third type. The subsurface gas pressure becomes great enough to force soil out of the way

and create a path to the surface. Once a channel is formed, the gas flow widens the channel and straightens it out (i.e. makes it more vertical).

The fourth regime is that of fluidized particle movement. When the gradient becomes very great, the soil particles are pushed upwards with the gas in a fluid-like flow. This results in a "bubbling" at the surface, which is quite different from the distinct fountain events, and does not send particles up as high.

The inertial effects of the gas have not been studied yet in detail, but it would seem that a low permeability explains the connection between the cracks and the channeling. A highly permeable soil allows a greater gas flow, and would enter the fluid flow regime before building up great pressures at depth. Thus, a low permeability is a requirement for channel formation. To this we may add two other requirements. The soil particles must be small enough to move under the influence of a concentrated gas flow. And, the soil particles must not stick together with any appreciable force.

The physical dimensions of a channel are dependent upon the mass flow through it. A channel will deepen until the mass flow at its bottom is no longer large enough to elevate the particles. Gas will expand until its upward velocity near the wall of the channel is no longer fast enough to remove particles.

What are the chances for fountains on Mars? Ignoring desorption effects, consider a diurnal atmospheric pressure variation of 5 to 7mb. Suppose that the pressure at a depth of one meter remains at 7mb when the atmospheric pressure has dropped to 5mb. Comparing the overlying mass pressure ( $\rho = 1.2$ ) to the hydrostatic pressure differential, it is found that the mass pressure is greater than the gas pressure at all depths. Thus, if channeling occurs only when the pressure differential is greater than the mass pressure, no fountain activity would be expected on Mars from diurnal pressure variations.

On the other hand, if Mars contains CO<sub>2</sub>-adsorbing clays as Fanale suggests, fountains seem more likely. He calculates that a 10 meter depth of nontronite would release 10 gm when heated from -110°C to -77°C (2). If the top 20cm of soil released one tenth this much gas over a ten hour period, the mass flow would correspond to an isothermal, steady-state pressure distribution (3) of 20+ mb, much greater than the overburden pressure of 11mb. While these are only rough calculations, they indicate that the potential for fountain formation on Mars exists if there are low permeability, gas adsorbing minerals in the regolith. The problem is much more complicated because of the fact that once material begins to move toward the surface through a channel, gas is drawn from a volume and the corresponding flow could be higher by at least a factor of ten.

REFERENCES:

1. Fanale, F.P., and W.A. Cannon, J. Geophys. Res., 83, 2321-2325, 1978.
2. Fanale, F.P., and W.A. Cannon, J. Geophys. Res., 84, 8404-8414, 1979.
3. Muskat, Morris, The flow of homogeneous fluids through porous media, J.W. Edwards Co., Ann Arbor, Michigan, 1937.

This research was carried out under NASA Contract 7-100.

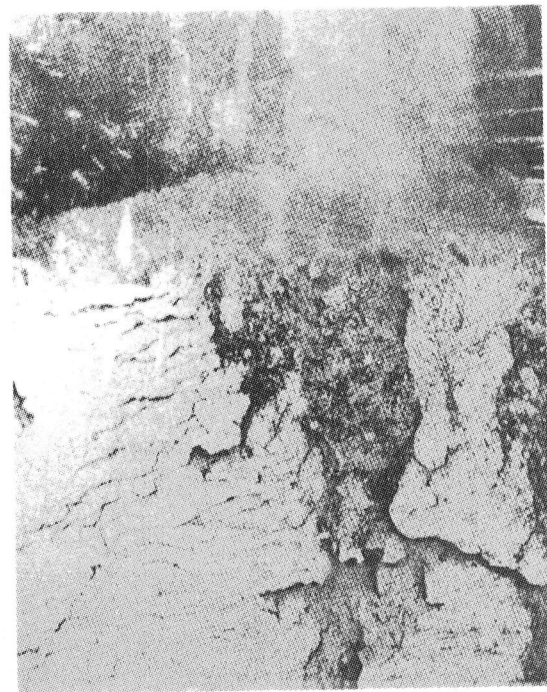
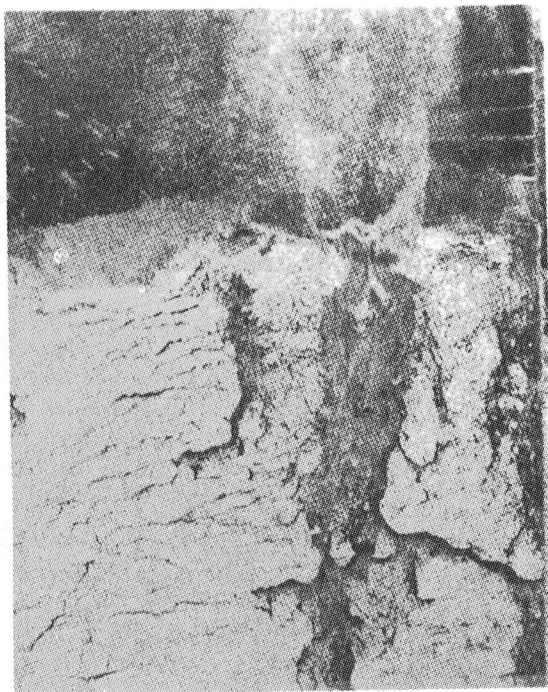
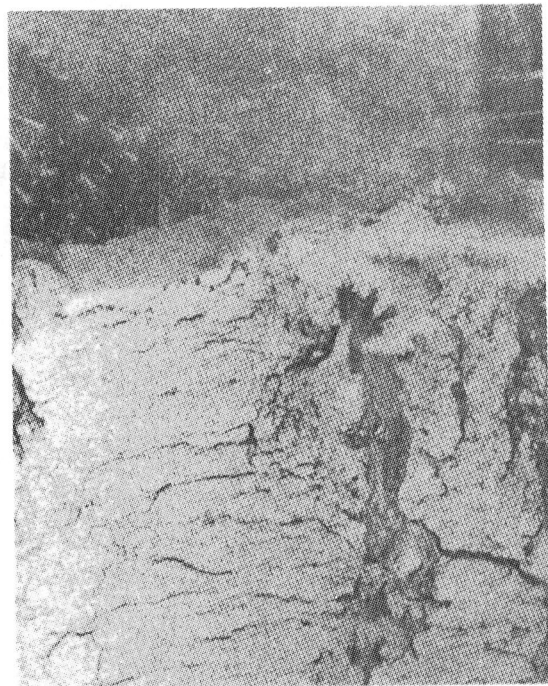
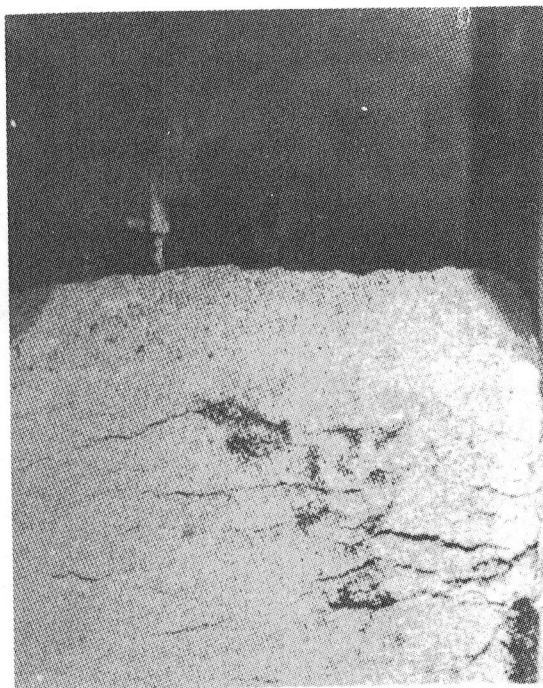


Fig. 1 Dust fountain channel formation sequence (full scale)

### Electrostatic Aggregates and their Physical Properties

D. H. Krinsley, Dept. of Geology, Arizona State University, Tempe, AZ 85281,  
R. Leach, Dept. of Mechanical Engineering, Stanford University, Stanford, CA  
94035, J. Marshall, and R. Greeley, Dept. of Geology, Arizona State University,  
Tempe, AZ 85281.

The presence of dunes and other eolian features on Mars suggests a supply of sand and winds capable of eroding, saltating, and depositing sand sized particles. Experiments indicate that at the high wind velocities characteristic of portions of the Martian surface, sand-sized particles will break down to silt and clay, but further experiments show that these smaller particles will inevitably form sand-sized electrostatic aggregates (Greeley, 1979; Krinsley and Leach, 1979). It seems possible that aggregates could substitute for sand grains on Mars (Greeley and Leach, 1978); thus it is of some importance to characterize the properties of aggregates produced in the laboratory under Martian conditions.

Crushed Hawaiian basalt and olivine were sieved to sand size (125-250 $\mu$ m diameter) and abraded in the Mars Erosion Device (MED) [Krinsley, et al., 1979] at Martian pressures. Runs were made at 8, 20, 30 and 40 m sec<sup>-1</sup> for one hour, the material carefully removed from the MED and shaken in a sonic sifter for about five minutes. A few aggregates were present in the three highest velocity samples upon removal from MED, but there were none in the 8 m sec<sup>-1</sup> sample. Upon shaking, most of the fine grained silt and clay formed aggregates in the three highest velocity samples. Abrasion in MED and shaking in a sonic sifter may well be similar to erosion in a Martian storm and final deposition by waning winds. Following the above procedure, the samples were studied with binocular and scanning electron microscopes.

Apparently the ratio of charge to particle weight must be sufficiently large for aggregates to form, but this does not seem to have happened until sand was abraded at velocities of about 20 m sec<sup>-1</sup> for at least an hour. Aggregates will not form until a threshold quantity of material less than about 37 $\mu$ m in diameter has been produced. As abrasion velocity increases, our experiments have shown that the material less than 37 $\mu$ m diameter also increases, as does the percentage of aggregates.

Electrostatic charges on aggregates may last for at least a year-and-a-half in sealed containers; however, some samples do show charge dissipation after this period of time. Since even after charge dissipation, aggregates retained their size and shape, it is suggested that moisture replaces electrostatics. Due to the thin atmosphere and relative lack of water on Mars, electrostatic aggregates should last a good deal longer than on Earth, but the charges will eventually leak off. It is presumed that water or some form of mineral cementation would substitute for electrostatics; Moore, et al. (1977) describe aggregates or clods held together by what is apparently some form of cementation other than electricity.

Aggregates are usually spheroidal in shape, and become more elongated with increasing size. This property among others, should differentiate their erosive properties from sand grains, as it should change their rate of spin. Very little is known about the relation between spin and erosion; this is a subject that should be studied. In addition, aggregates tend to be layered, with inner portions more tightly bound than outer layers; thus the strength of smaller aggregates should be greater than the larger ones.

Aggregates, broken down mechanically during abrasion, will reform, assuming that their charges have not been dissipated. Additionally, the size-

frequency distribution of the small particles that make up aggregates is an important parameter, as the presence of coarse silt and fine sand-sized grains may lead to instability in the larger aggregates. However, as long as charges are still present on the individual particles, and some agitation occurs, the particles will again form aggregates. Whether these newly formed specimens will be of the same size and shape as the originals is unknown.

Aggregates have a wide range of diameters, from 60  $\mu\text{m}$ , approximately the limit of fine sand size, to over 600  $\mu\text{m}$  in diameter. The upper limit is considerably greater than normally expected for dune sands. However, El Baz, et al. (1979) have shown that the grain size mode for sand sheet deposits in a portion of the Western Desert of Egypt is about 1300  $\mu\text{m}$  as compared to 250  $\mu\text{m}$  for the dune sand in that area. Thus the presence of a wide aggregate size range is not incompatible with dunes and sand sheets on Mars.

One of the major problems in working with aggregates is the difficulty in handling them; they fall apart and reform very quickly. In addition, it seems probable that aggregates made of different materials have varying properties. Thus experimentation with one or a group of minerals to form aggregates may not be characteristic of other types of substances. However, the important point to remember is that at velocities of greater than 20 m  $\text{sec}^{-1}$ , in any kind of erosion device, sand-sized particles of all types of minerals break down almost completely to silt and clay; aggregates then proceed to form under almost all conditions. Thus, given strong winds on Mars, the formation of aggregates is almost a precondition.

#### References

- El-Baz, F., Breed, C., Grolier, M. and McCauley, J., 1979. Eolian features in the Western Desert of Egypt and some applications to Mars. J. Geophys. Res. B14, 84, 8205-8221.
- Greeley, R. and Leach, R., 1978. A preliminary assessment of the effects of electrostatics on aeolian processes. Repts. Planet. Geol. Program 1977-78. NASA TM 79729, 236-237.
- Greeley, R., 1979. Silt-clay aggregates on Mars. A model for the formation of "Sand." J. Geophys. Res. 84, 6248-6254.
- Krinsley, D. H., and Leach, R., 1979. Simulated martian aeolian abrasion of glassy basalt and augite. Repts. Planet. Geol. Program 1978-79. NASA TM 80339, 311-312.
- Krinsley, D. H., Greeley, R., and Pollack, J., 1979. Abrasion of windblown particles on Mars-Erosion of quartz and basaltic sand under simulated martian conditions. Icarus 39, 364-384.
- Moore, H., Hutton, R., Scott, C., Spitzer, C., and Shorthill, R., 1977. Surface materials of the Viking landing sites. J. Geophys. Res. 82, 4497-4523.

## Compression Testing of Electrostatic Aggregates - Analogs to Sand Grains on Mars

J. Marshall, D.H. Krinsley and R. Greeley, Dept. of Geology, Arizona State University, Tempe, Arizona 85281.

Sand-sized electrostatic aggregates were produced in an eolian erosion device at  $40\text{m sec}^{-1}$  from sand-sized crushed basalt (Krinsley, et al., 1979). A standard soil compression test was performed to determine the change in volume of aggregate material with simulated increase in soil depth.

For compression testing, the material (dry and non-compacted) was placed in a brass ring and confined on the top and bottom by porous materials permitting escape of air from the sample during compaction. The following loads were applied: 0.02, 0.05, 0.1, 0.2, 0.5, 1.0, and  $2.0\text{ kg.cm}^{-2}$ . For each load, the volume of the material was determined as a percentage of the initial volume. Readings were also taken during unloading at the following loads: 1.75, 1.50, 1.25, 1.0, 0.5, 0.2 and  $0.1\text{ kg.cm}^{-2}$ . Unloading readings were more closely spaced for the higher loads in order to detect elastic recovery. During the loading part of the compression cycle, the material was allowed to settle under the applied loads for at least one hour before a reading was taken.

The change in specimen volume with increase in load is shown in Fig. 1. It can be seen that there are two distinct sections to the loading curve: a steep slope representing a dramatic decrease in volume in the initial loading stage (for loads between 0.0 and  $0.3\text{ kg.cm}^{-2}$ ) and a gentle sub-horizontal slope representing very little volume change with load increment once the material had been compacted to approximately 82% of its initial volume (for loads between 0.3 and  $2.0\text{ kg.cm}^{-2}$ ). Under the maximum load of  $2.0\text{ kg.cm}^{-2}$ , the material compacts to 78% of its initial volume.

Unloading produces a total rebound of 0.28% (of initial volume) which probably represents the elastic recovery of individual particles rather than any attempt by the material to electrostatically regenerate aggregates. As a first step to understanding the behavior of aggregate material during eolian activity, it is necessary to know how easily the material could be lifted from the Martian surface. This would partly be a function of the density of the material. Since aggregates can be considered for all practical purposes to have no volume recovery (at least for unloading from  $2.0\text{ kg.cm}^{-2}$ ), an erosional surface would retain the density it reached during burial. Thus it is useful to know the density of the material for any given depth of burial; the density was calculated for soil depths of from 0.0 to 14.4 meters (Fig. 2).

Under terrestrial gravity an aggregate surface layer has an uncompacted bulk density of  $\sim 1.10\text{ g.cm}^{-3}$ . Since in this case the layer is composed of basaltic material with a density of  $\sim 3.30\text{ g.cm}^{-3}$ , then 66% must be void space. This is an extremely high value; spheres packed to maximum density have a void space of 26% while those packed to minimum density contain void spaces of 47.6%. Ordinary loose sand has a porosity of about 35%. Single aggregate density would be  $2.11\text{ g.cm}^{-3}$  with a porosity of about 35% (midway between the maximum and minimum porosity of packed spheres); the density of the material in bulk would be  $1.35\text{ g.cm}^{-3}$  if aggregates were packed in the same way as the particles composing them. This value approaches the observed one.

Whether or not the above assumptions about the structure of the material are accurate, the density change during loading implies a very open structure for unconsolidated material. Since only 3 meters (simulated terrestrial) overburden is sufficient to reduce the initial volume by nearly 20%, this open structure must be very weak. The abrupt change in compaction resistance below 3 meters depth implies that a new structure has developed from collapse of the open one. This new form compacts much less easily, but the volume reduction is not a function of elastic

compression as indicated by the almost total lack of volume recovery during unloading. Compaction must be due to the re-orientation of individual particles and perhaps some crushing of sharp particle corners and edges.

Under a load of  $2.0 \text{ kg.cm}^{-2}$  (simulated 14 meters depth), the material has a density of  $1.42 \text{ g.cm}^{-3}$  giving a void space of 57%. This is still a high value, suggesting that the particles have difficulty in adjusting to a different packing arrangement as a result of their irregular and angular nature. The behaviour of the material during compaction is probably not a function of electrostatic charges on the particles; many types of fine-grained particulates have open structures in their uncompacted states.

If sand were loaded to  $2.0 \text{ kg.cm}^{-3}$  by burial and then unloaded by erosion, its resistance to eolian entrainment would probably be much the same as initially. On the other hand, for aggregate material, the change in density at this load may render entrainment more difficult. Thus entrainment would become progressively more difficult as deflation continues and this may be one of the reasons for 'shutting down' of Martian dust storms. In addition, on the assumption that there is a relationship between resistance to entrainment and density, there may be great variation in the susceptibility to erosion of different regions on Mars as a result of variation in aggregate 'age'. Recent deposits would be more susceptible to erosion, while older denuded materials would be more resistant simply as a function of burial history.

The high porosity of the material, even down to 14 meters depth means that large quantities of water could be stored within the structure. In fact, since the porosity is  $>50\%$ , the resulting sediment would be effectively a body of water with particles in it rather than the reverse. If the water were in the form of ice, the sediment would be a heavily laden ice layer and on even the gentlest slopes might be capable of flowing slowly. Certainly, the ability of the material to store large quantities of ice would help in explaining the large scale permafrost features observed on Mars.

Aggregate material has a low penetration resistance and like other materials of this nature, it has a concomitant ability to absorb the energy of an impacting body. Kinetic energy input is converted into motion of particles. It is not returned to an impactor by elastic recovery which means that particles cannot saltate on its surface. This implies that dune formation on Mars from aggregates would be difficult even if aggregates were themselves able to saltate without disintegration. Even though aggregate material may not be able to form dunes, its deposition in a dune region might influence dune behavior. Even a thin mantle of the material over active dunes would inhibit dune migration by shielding the saltating layers from the wind and by damping particle motion.

It should be stressed that Martian gravity is considerably less than terrestrial gravity. This would not affect the load/density relationships established here but it would necessitate increasing soil depth to achieve comparable compaction and density values.

#### References

- Krinsley, D.H., Greeley, R., and Pollack, J. 1979. Abrasion of windblown particles on Mars-Erosion of quartz and basaltic sand under simulated Martian conditions. *Icarus* 39, 364-384.



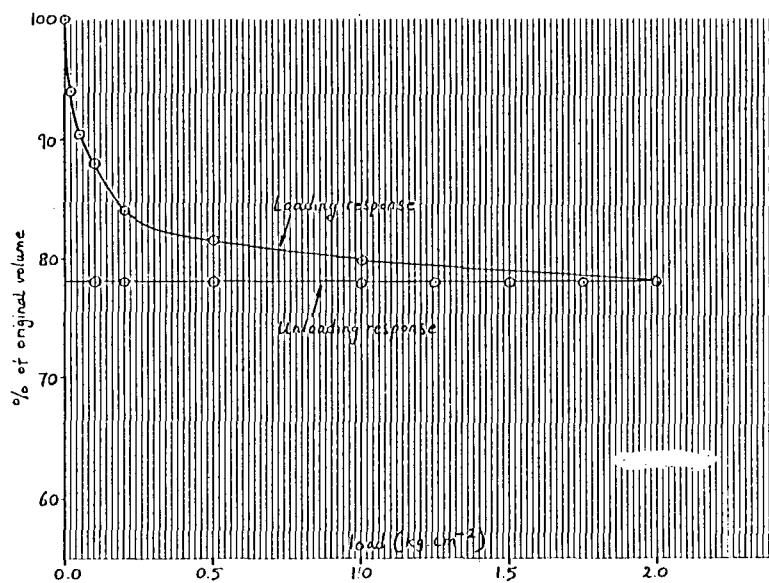


Figure 1

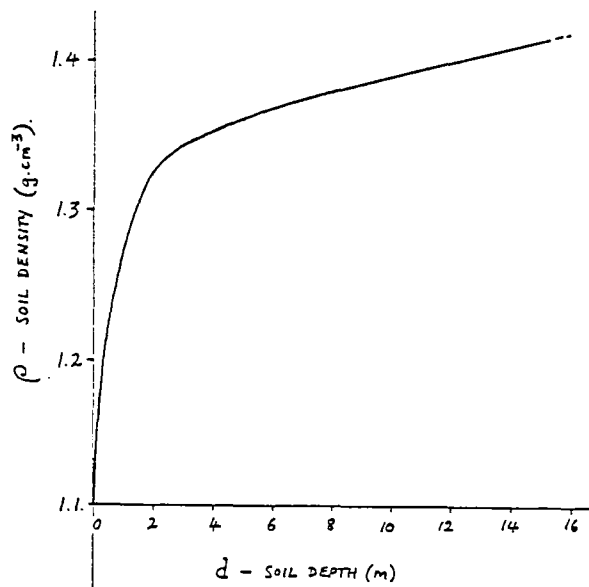


Figure 2

## FIELD STUDIES OF AEOLIAN PATTERNS

Greeley, R., M. Malin, S. Williams and G. Stewart, Department of Geology, Arizona State University, Tempe, Arizona 85281

"Variable features," first defined from Mariner 9 images and observed in high resolution on Viking Orbiter pictures, constitute one of the primary classes of martian aeolian features, and include various light and dark albedo patterns that change on time scales as short as a few days, and which are often associated with craters and other topographic structures. Various models have been derived to explain the albedo patterns in terms of particles of different sizes and/or composition that are subjected to sorting by the wind. As part of a general study of wind erosion and deposition patterns involving wind tunnel simulations, spacecraft data analysis, and field analog studies, we have examined active aeolian sediments to determine their characteristic "signatures" and mode(s) of formation. Two areas where field work is in progress include Amboy, California, and Vikursandur, Iceland. Amboy has been an aeolian test site for several years. It is a young basalt flow/cinder cone situated on an alluvial-fill valley in the Mojave Desert that is swept by prevailing northwesterly winds. Aeolian features include small dunes, ventifacts found in the basalt, and desert pavement surfaces that form distinctive "wind streaks" related to the topography. Our objective is to determine the mechanism of formation for the desert pavement surfaces within the windstreak. The formation and preservation of desert pavement is a common process in arid regions. The two primary theories are 1) upward migration of large particles to the surface, perhaps by a swelling clay process and 2) removal of fines by aeolian activity, leaving the coarser material behind. To test these ideas, two desert pavement test sites were prepared: One test site was adjacent to the cinder cone, the second is in the "wake" of the cone within the "streak" zone. Each site consisted of two plots. In one, the desert pavement grains were removed by raking, in the other, the grains were "stomped" into the underlying fine-grained material. The sites were monitored on a monthly basis. It was found that the "stomped" plot was almost totally restored in a few months while the raked plot showed no restoration apart from some grains being washed in from the sides by rainwater. The "stomped" plots at both sites, however, were modified; one quarter of each plot was "re-stomped" and one quarter was covered with a layer of locally derived aeolian material. Subsequent observation shows that the re-stomped part is restored quickly and that windblown material is removed. The plot in the "wake" of the cinder cone shows a streak of material extending from the plot that implies a wind direction consistent with that predicted for air flow in the cone wake. The results of this experiment imply that the dominant mechanism for the formation of desert pavement is the removal of fine-grained material from the surface, lowering larger grains until an armored surface is formed. The results do not prohibit the alternate mechanism (the upward migration of larger chips to the surface), but may indicate that the latter process occurs at a much slower rate.

The second area is Vikursandur, a vast, windblown, basaltic plain southeast of the Askja volcanic complex of Iceland. During recent volcanic field work in the region, mega ripples were found that have an average wave length of 5 to 6 m and an amplitude of about 20 cm. Windblown particles constituting the ripples are of two primary types: Type 1 are basaltic fragments (hence, dark) with an average diameter of about 10 mm; Type 2 are silicic pumice (hence, light-toned) fragments averaging about 25 mm in diameter; although the basaltic particles are smaller in size, they occupy the crests of the ripple, just the opposite of "normal" quartz granule ripples involving homogeneous particles in which the largest particles form the crest. Although not confirmed, we interpret the basaltic particles to behave as "large" particles by virtue of their greater density;

thus, in the formation of ripples, it is not the particle size alone that governs development, but the *effective* wind threshold speed that appears to be a combination of density and grain surface area. Knowledge of the dynamics of the light and dark particles in the formation of the ripples will provide data in understanding the role that differences in composition and grain size have in the formation of light and dark aeolian patterns.

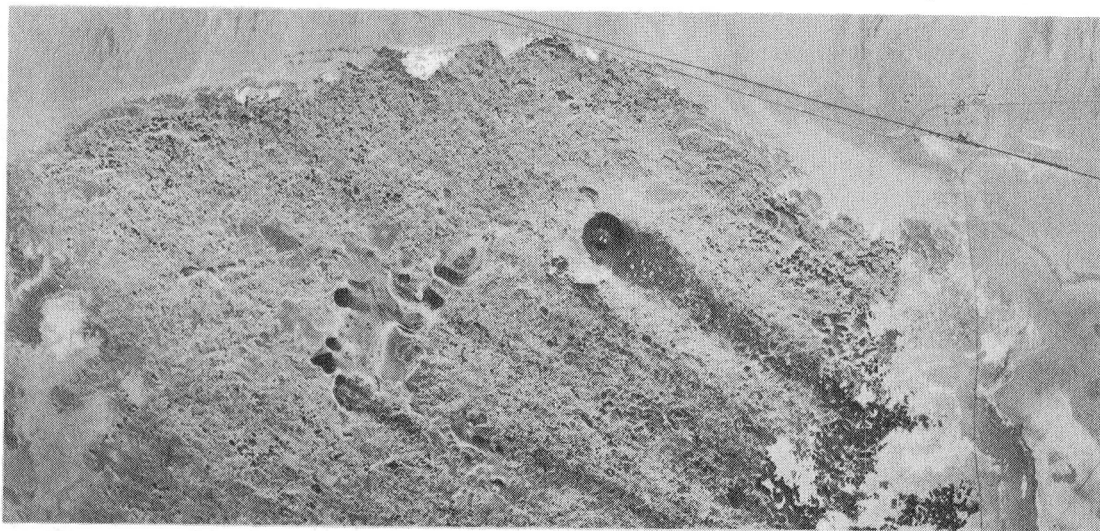


FIGURE 1. Amboy lava field, Mojave Desert, California, showing windswept, basaltic surface and various aeolian features. Dark wind streaks are a combination of non-mantled basalt and desert pavement. The desert pavement is composed of basaltic particles up to 4–5 cm across. Area shown is about 13 km by 8 km.



FIGURE 2. Aeolian megaripples in the Vikursandur region, northern Iceland; ripples are formed of  $\sim$ cm-sized basaltic particles (dark) and larger pumice particles (light-toned). Vehicles indicate scale.

## COMPARISONS OF WIND STREAK FORM IN EGYPT AND ON MARS.

Farouk El-Baz and T.A. Maxwell, National Air and Space Museum, Smithsonian Institution, Washington, D.C. 20560.

It is evident in orbital photographs and images that wind-dominated landforms are the most abundant features throughout northern Africa and particularly in the Western Desert of Egypt. Both bright- and dark-toned wind streaks occur in the Western Desert. Bright streaks are composed of sand dunes and dune belts, sand sheets, and lag deposits of light-colored bedrock, whereas dark-toned streaks are predominantly local lag fragments and desert pavement (1). As seen from orbit, the dark streaks in the Western Desert occur in the lee of topographic obstacles to the predominant northerly winds, and create streamlined patterns similar to those in the lee of craters and knobs on Mars.

In the southern part of the Western Desert, knobs of protruding bedrock and associated wind streaks form an irregular line between the Kharga depression and the Gilf Kebir plateau region (Fig. 1). The bedrock exposures are composed of highly resistant, Fe-rich sandstones and conglomerates of the Nubia series, although east of the Bir Tarfawi region, the protruding knobs consist of outcrops of granite. The linear nature of the Nubia sandstone outcrops is created by the gently northward dipping attitude of the beds, which has been partially submerged by sand driven from the north. It is possible that these linear outcrops mark the positions of low cliffs retreating northward and partly subdued by eolian sand.

For comparison of streak form, the martian streaks were measured from enlarged Viking Orbiter images of the Cerberus region at a scale of 1:425,000. Martian crater and knob streaks range up to 36 km in length and 17 km in width, and the maximum area of 179 knob streaks is 450 km<sup>2</sup>, whereas that of 62 crater streaks is 342 km<sup>2</sup>. The 239 knob streaks in southwestern Egypt, as studied using Landsat false color images at 1:250,000 scale, range up to 21 km<sup>2</sup> in area, and are up to 12 km long and 5 km wide. Because of the less distinct outline of the larger Egyptian streaks, only those smaller than 100 km<sup>2</sup> were used for shape comparisons.

A plot of the maximum width and length of martian crater and knob streaks and Egyptian knob streaks indicates that all three streak types follow the same general curve, although the degree of scatter increases from crater to knob streaks. Knob streaks in the southwestern corner of Egypt exhibit the greatest scatter ( $r = 0.618$ ) and are generally narrower than their martian counterparts. The relatively small width of the Egyptian streaks is also indicated by a plot of streak length versus total area. As shown in Figure 2, the total area of the Egyptian streaks is much less than that of martian streaks. In both cases, however, the range of values is similar for streaks less than about 50 km<sup>2</sup> in area.

In order to compare the degree of streamlined shape versus length for streaks on both planets, we have chosen a dimensionless shape parameter (K) used by Chorley (2) to analyze the shape of drumlins, and more recently by Baker (3) for loess islands in the channeled scablands of Washington. The value of K indicates the deviation of the observed form from that of a circle:  $K = l^2 \pi / 4A$ , where  $l$  is the length of the form, and  $A$  is the area. Thus, a circle would have a value of  $K = 1$ . For streamlined forms in the

channeled scablands,  $K$  varies between 2 and 5, and may be related to the calculated Reynold's number for maximum scabland flood flows (3).

For crater streaks on Mars, values of  $K$  range from 0.6 to 4, and can be correlated with the length of the streak (Fig. 3); the longer the streak, the greater the degree of streamlining. Although this relationship holds for knob streaks on both planets, there is a significant difference in the slope of the regression curve between martian and Egyptian knob streaks. Values of  $K$  for the Egyptian streaks range from 0.3 to 9, and have a greater ratio to streak length than that of the martian streaks, indicating the relatively higher degree of streamlining for the Egyptian knob streaks. Elongation of the Egyptian streaks most likely results from their mode of formation by the southward movement of sand by near-surface winds that deviate around topographic obstacles. This style of transport and deposition has resulted in the build-up of more than a meter of sand deposits surrounding the dark, lag-composed streak in the lee of Garet El-Maiyit hill (4). This suggests that locally-derived material from the hill forms the dark streaks, whose boundaries are defined by the wind-transported materials.

#### REFERENCES

1. El-Baz, F. and T.A. Maxwell (1979) Proc. LPSC, 10th, p. 3017-3030.
2. Chorley, R.J. (1959) J. Glaciology, v. 3, p. 339-344.
3. Baker, V.R. (1978) The Channeled Scablands, NASA, p. 81-115.
4. El-Baz, F. et al. (1980) Geogr. Jour., v. 146, pt. 1, p. 51-93.

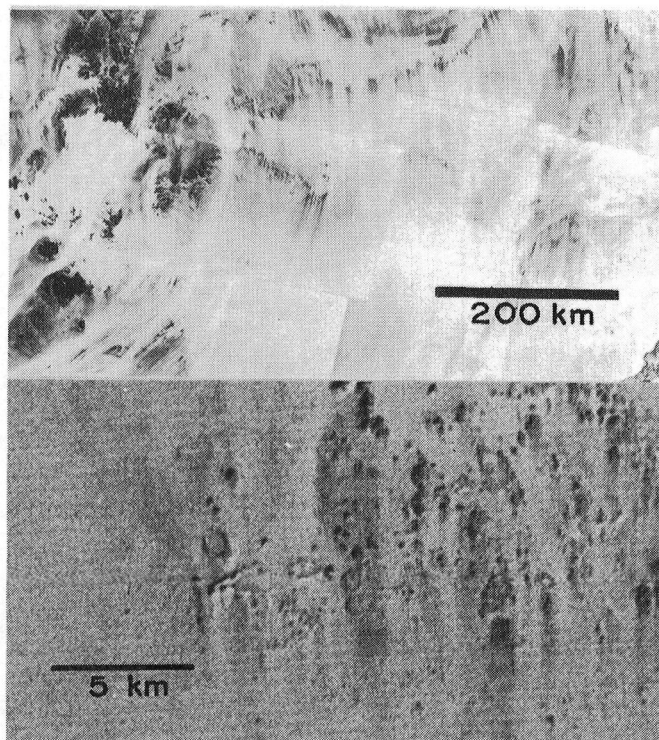


Figure 1.

(A) Landsat mosaic of southwestern Egypt showing prominent wind streaks in the lee of hills and mountains.

(B) Close-up view of dark knob streaks in Egypt. Note composite streak in center of image, formed by several hills.

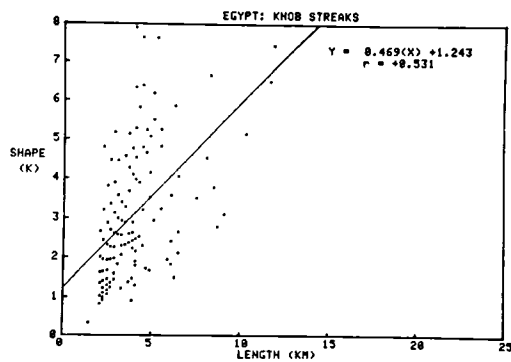
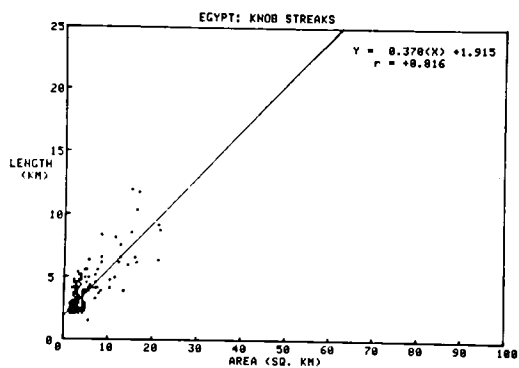
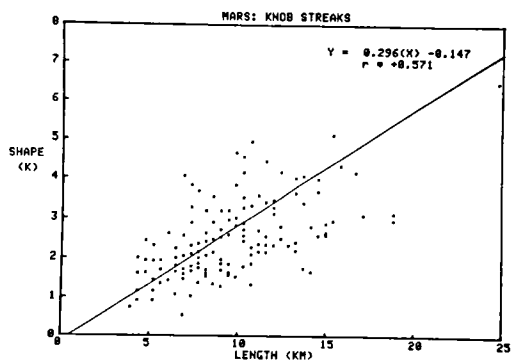
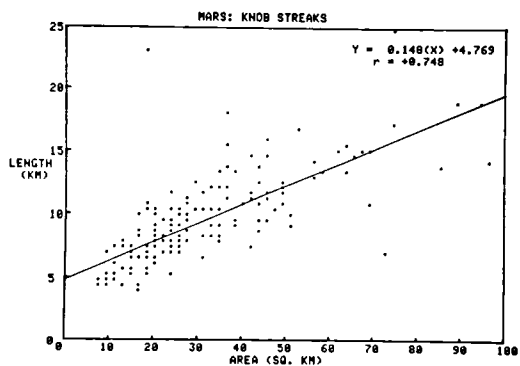
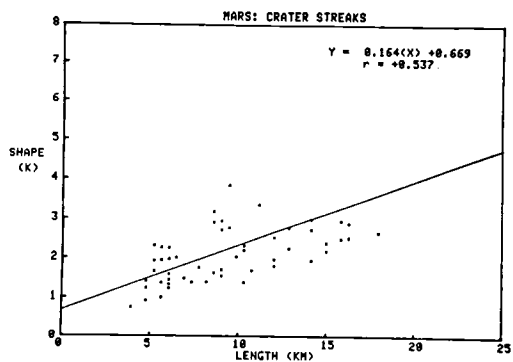
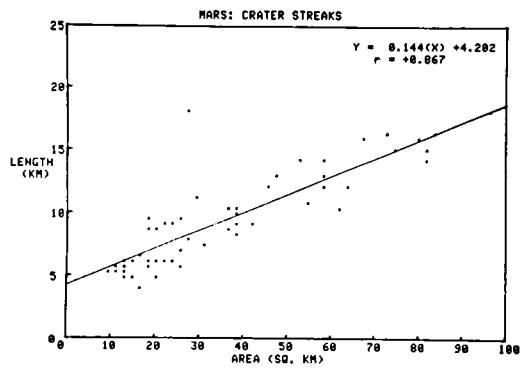


Figure 2. Length vs. area for martian and Egyptian wind streaks.

Figure 3. Shape parameter (K) versus length for martian and Egyptian wind streaks.



COMPARISON OF KNOBS IN THE CERBERUS REGION OF MARS AND EOLIAN KNOBS IN THE FARAFRA DEPRESSION, WESTERN DESERT OF EGYPT.

Farouk El-Baz and L. S. Manent, National Air and Space Museum, Smithsonian Institution, Washington, D.C. 20560.

Knobby material on Mars is found planet-wide and is generally located along or near boundaries between plains and plateau units. The relationship between streaks and knobs, as well as craters, on Mars has been studied by Chaikin et al. (1). Both knobs and craters affect the path of the wind, and therefore, affect the erosion and deposition of particulate material on the martian surface. The purpose of this study is to characterize the knobs in the Cerberus region of the Elysium Quadrangle of Mars, and compare them to similar features in the Farafra depression in the Western Desert of Egypt.

Streaks indicate that the prevailing winds in the Cerberus region, are toward the southwest but in the north and northwest area of Elysium Mons the winds are toward the southeast (2). There appears to be a local effect of the winds around a topographic obstacle, namely Elysium Mons. Knobby materials extend in an arc from the south-central to the north-eastern part of the Elysium quadrangle. Most original craters have been highly degraded and only remnants of their original form remain. The rocks that formed these craters have been reshaped by tectonic and erosional processes into knob-like hills that resemble inselbergs, which display a landscape type that is rather common in the Western Desert of Egypt. This knobby material is not everywhere associated with crater-forms. In some areas, isolated knobs protrude through the plains material. The knobs are probably shaped by fracturing, faulting and/or wind erosion.

In the Cerberus region (Fig. 1a) the knobs range from about 0.65 km

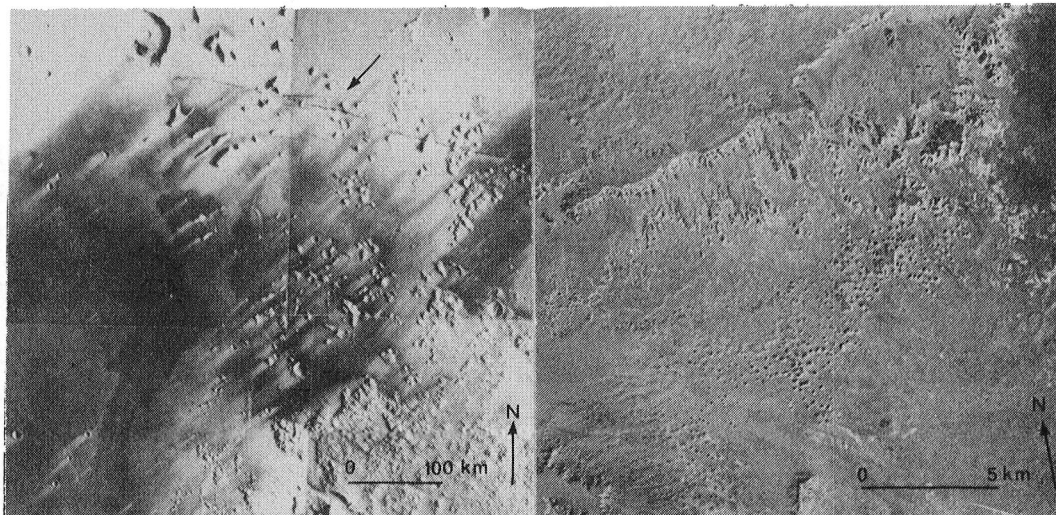


Figure 1a. Knobs in the Cerberus region of Mars. Note linear fracture.

Figure 1b. Knobs in northern part of the Farafra Depression.

to 16.1 km in width and 0.88 km to 27.6 km in length (Figs. 2a and b). The average width to length ratio of 150 knobs in this area is 0.63. The orientations of these knobs show two directions:  $N60^{\circ}E$  and  $N26^{\circ}W$ . The knobs which are oriented in the northeast direction have streaks in the lee and are more dominant, whereas the northwest-oriented knobs are not associated with streaks. These northwest-oriented knobs are possibly crater ring remnants that were eroded by an earlier wind regime. There is a linear fracture that is oriented  $N70^{\circ}W$  to the south of these knobs that may also have had an effect on them (Fig. 1a).

Similar knobs exist in the northern part of the Farafra depression in the Western Desert of Egypt. Aerial photographs were used to characterize the knobs that are below the northern scarp and northeast of El-Quss Abu-Said plateau (Fig. 1b). These knobs range from 4.1 m to 18.4 m in width and 7.1 m to 44.3 m in length (Fig. 2c). The average width to length ratio is 0.69. They are oriented in a  $N59^{\circ}W$  direction. Linear ridges associated with the knobs, possibly of erosional nature, are oriented in a  $N36^{\circ}W$  direction. The wind, measured at the Farafra Oasis, blows to the south and southeast, producing the northwest orientation of the knobs.

Ground measurements of yardangs just north of the Farafra Oasis and in the middle of the depression range from 0.41 m to 10.2 m in width and 0.87 m to 14.4 m in length (Fig. 2d). The average width to length ratio is 0.60. From a total of 26 yardangs measured, 14 are oriented  $N62^{\circ}W$ , 8 are oriented  $N72^{\circ}E$  and 4 are oriented  $N8^{\circ}E$ . The yardangs and knobs in the Farafra region that are oriented in a northwest direction probably have been eroded by the winds from the N-NW and may also be affected somewhat by fractures. The yardangs oriented to the northeast are possibly produced by a cross fracture pattern in the area.

The knobs and yardangs of the Farafra depression and the knobs of the Cerberus region show some similarities and differences. The knobs on Mars measure in kilometers whereas in Farafra region, they measure in meters. The average width to length ratio on Mars is 0.63 and in the Farafra region is 0.65. Although, the knobs on Mars are one hundred times larger than those in Farafra, they have the same relative dimensions. The wind erodes and shapes them in the direction it is blowing with the fracture pattern having a minor effect on their orientation.

#### References

1. Chaikin, A.L. et al. (1976) NASA TM 80339, p. 279-281.
2. Scott, D.H. et al. (1976) U.S. Geol. Survey, Geol. Series Map I-935 (MC-15).



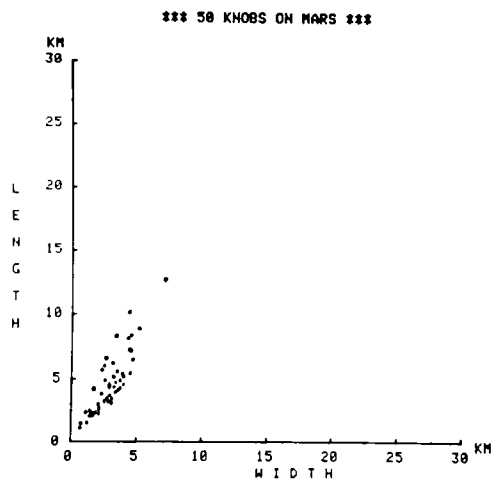
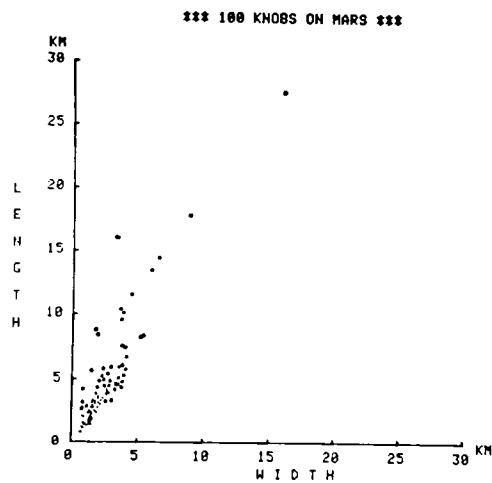


Figure 2a. Length vs. width of 100 knobs in the Cerberus region of Mars from N13° to N18° and E200° to E197°.

Figure 2b. Length vs. width of 50 knobs in the Cerberus region of Mars from N17° to N20° and E184° to E182°.

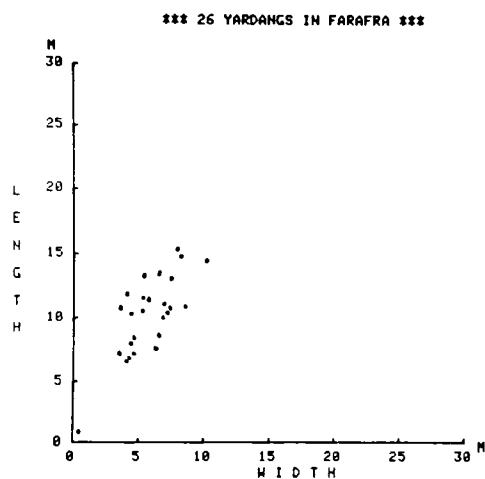
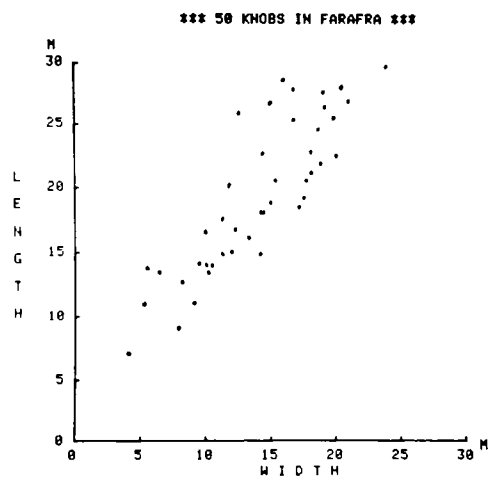


Figure 2c. Length vs. width of 50 knobs in the Farafra Depression, northeast of El-Quss Abu-Said Plateau.

Figure 2d. Length vs. width of 26 yardangs in the Farafra Depression, north of the Farafra Oasis.

EFFECTS OF TOPOGRAPHY ON DUNE ORIENTATION IN THE FARAFRA REGION, WESTERN DESERT OF EGYPT, AND IMPLICATIONS TO MARS.

L. S. Manent and Farouk El-Baz, National Air and Space Museum, Smithsonian Institution, Washington, D.C. 20560.

In the Western Desert of Egypt, general dune orientations change from N-NW in the northern part to N-NE in the southwest. Many dunes are intimately associated with scarps that bound numerous depressions (1). This relationship is believed to result from the interaction between sand-carrying winds and scarps and other topographic features (2). We have selected the Farafra depression for detailed study because of the similarity of some of its features to those of Mars, particularly the distribution, shape and orientation of knob-related streaks.

The Farafra depression is located in the west-central part of the Western Desert of Egypt (Fig. 1). It is bounded by three scarps creating a roughly triangular shape. It is enclosed on the northern side by a low scarp and on its eastern and western sides by higher scarps; the width of the depression continually increases to the south where it meets the Dakhla depression 200 km away. The distance between the east and west cliffs at the latitude of the Farafra Oasis,  $N27^{\circ}$ , is about 90 km. The El-Quss Abu-Said plateau west of the oasis is oriented  $N45E$  with its long axis about 63 km in length, and its width about 28 km (Fig. 1). The plateau is topped by Lower Eocene limestone and Esna shales and is underlain by Upper Cretaceous clays and white chalk. The chalk covers much of the floor of the depression.

The Great Sand Sea west of the Farafra depression is composed of whaleback dunes with longitudinal dunes superimposed on top (3). The dunes vary in orientation, between N-S to  $N26W$ , with an average orientation of

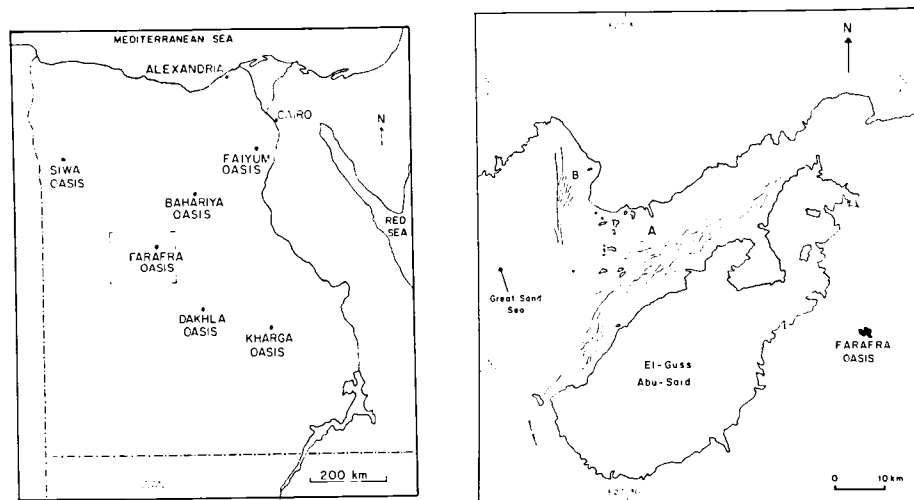


Figure 1. Location of study area in the west-central part of the Western Desert of Egypt, (left) and dunes north of El-Quss Abu-Said plateau (right).

N13W (Fig. 2). The average length of the dunes is 70 km and the average width is 2.5 km. East of the Great Sand Sea in the Farafra region is a smaller dunefield between El-Quss Abu-Said plateau and the northern escarpment (A in Fig. 1). Within this dunefield, the size and orientation of dunes are different from those of the Great Sand Sea. Here, the dunes are smaller, with an average length of 7 km and an average width of 0.2 km. They converge and taper to the northeast and are more widely spaced to the southwest. The orientation of the northern scarp is N58°E and of Abu-Said plateau is N45°E. The resultant direction of these two scarps is N52°E, which is close to the orientation of the dunes, being N50°E.

West of this area is another smaller dunefield that is oriented N6°E (B in Fig. 1). It is surrounded by two scarps, one oriented N50°E and the other N38°W. The resultant direction of these two scarps is N6°E, which is parallel to the orientation of the dunefield.

Comparison of the size and orientation of the Great Sand Sea dunes and those in the Farafra depression dunefields suggests that the topography is affecting the direction and strength of the wind in the formation of dunes within the depression.

We have studied the available wind direction data to correlate them with the dunes in the Farafra region. The data used were derived from surface wind N-summaries recorded in the Farafra oasis between 1958 and 1966, and were compiled and prepared by the Environmental Technical Applications Center of the U.S. Air Force. The wind speed was recorded in knots to the nearest 10° of direction at 3-6 hour intervals. During this nine year period, a total of 11,844 observations were recorded, of which 2,683 were calm winds (less than 1 knot). The rest were calculated into percentages of the total amount of wind and then organized by month. Each month was broken up into sixteen directional sources which were grouped into five categories of velocity.

In order to determine sand-moving winds and drift potentials, at a given height, a threshold wind velocity must be known. The threshold wind velocity at that height is the minimum velocity at which the wind will

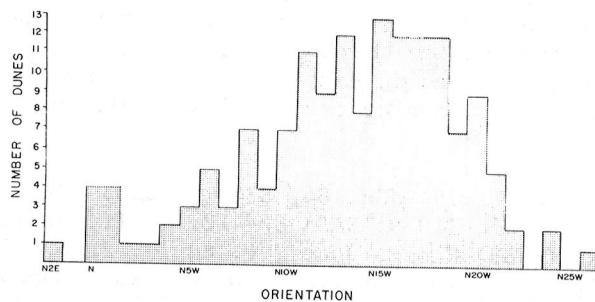


Figure 2. Cumulative graph of orientation of dunes in Great Sand Sea just west of the Farafra region.

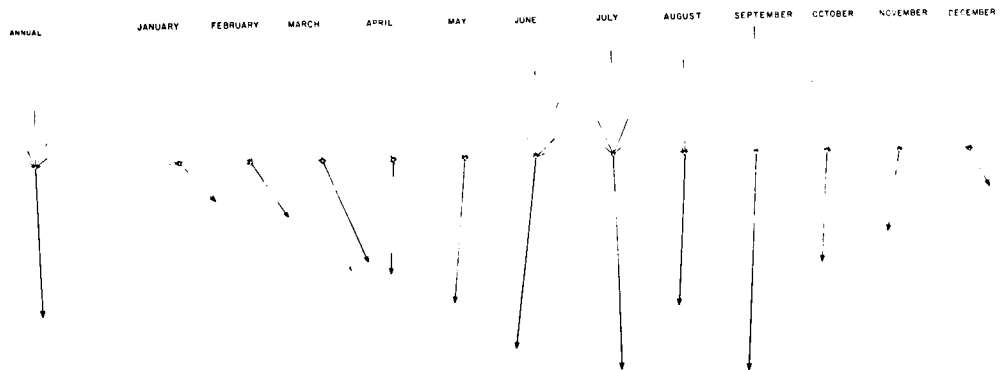


Figure 3. Direction of sand moving potential as computed from Farafra Oasis wind data.

set the grains in motion. This value, as calculated from Bagnold's equation (4), is 11.6 knots. This falls into the 7-16 knot velocity category on the N-Summaries. In order to find the amount of winds above the threshold wind velocity at ten meters high, a percentage of the amount of wind in each direction in the velocity category 7-16 knots and 2/3 of the 7-16 knot velocity category was calculated to plot the frequencies of sand-moving winds (5). These were plotted by sand rose diagrams in monthly, seasonal and annual summaries.

The annual summary when plotted for sand-moving winds gives a northerly direction (Fig. 3). This can be misleading. When sand-moving winds are plotted by season and month (Fig. 3), changes in wind direction are apparent throughout the year, and agree with the dune patterns in the Great Sand Sea. However, there is not a single month with wind blowing in the direction of the dunes within the Farafra depression. Therefore, the scarps must affect the orientation of the dunes by deflecting the wind. The resultant directions of the scarps that bound the two smaller dune-fields are nearly the same as the orientations of the enclosed dunes. Because of this relationship, the possible effect of topography on winds on Mars should be considered in cases where sand dunes are enclosed in depressions, such as inside a crater, vallis or chasma.

#### REFERENCES

1. El-Baz, F. et al. (1979) JGR, 84, B14, p. 8205-8221.
2. Gifford, A.W. et al. (1979) NASA SP-412, v. II, p. 219-236.
3. Bagnold, R.A. (1933) Geogr. Jour., v. 82, n. 2, p. 121.
4. Bagnold, R.A. (1941) The Physics of Blown Sand, London, p. 104.
5. Fryberger, S.G. (1979) USGS Prof. Paper 1052, p. 137-169.

THE EFFECTS OF MINERALOGY AND GRAIN SHAPE ON THE COLOR OF SANDS FROM THE WESTERN DESERT OF EGYPT, AND POSSIBLE APPLICATIONS TO MARS.

C. T. Herzig, Geology Department, Dickinson College, Carlisle, PA 17013; and Farouk El-Baz, National Air and Space Museum, Smithsonian Institution, Washington, D.C. 20560.

Documented visual observations by the astronauts of the Apollo-Soyuz mission indicate that the color of desert surfaces varies on both a regional and local scale (1). Reasons for these variations include compositional changes in the sand (2). The Western Desert of Egypt was selected as a test site for the analysis of sand samples because of the similarity of many of its features to those of Mars (3).

The Western Desert is covered by sandstones in the south and limestones in the north encompassing two-thirds of Egypt. There are seven major depressions in the desert and two topographic highs, the Gilf Kebir and Gebel Uweinat, in its southwestern corner. Overlying the bedrock are bundles of sand dunes, with the largest accumulation, the Great Sand Sea, in the west-central part of the desert. There are several types of dunes and the large, N-S trending longitudinal dunes are the most common.

Sand samples were collected from several locations in the Western Desert, but only five sites were selected for detailed study based on results of previous mineralogical analyses (2). The five representative samples are from the oases of Dakhla, Faiyum, Kharga, and Siwa and the Great Sand Sea (Fig. 1). These sand samples were sieved and separated into quarter phi units (0.00 to 4.00 + pan) and a representative part of each size fraction was mounted in Lakeside 70 (~ 1.54). The grain mounts were examined using a polarizing microscope and 100 grains were counted per mount.

Twenty-two components were identified in the studied samples:

*Apatite* is rare and occurs as rounded bluish grains.

*Biotite* is also rare and is restricted to the smaller size grains (4.00 phi)

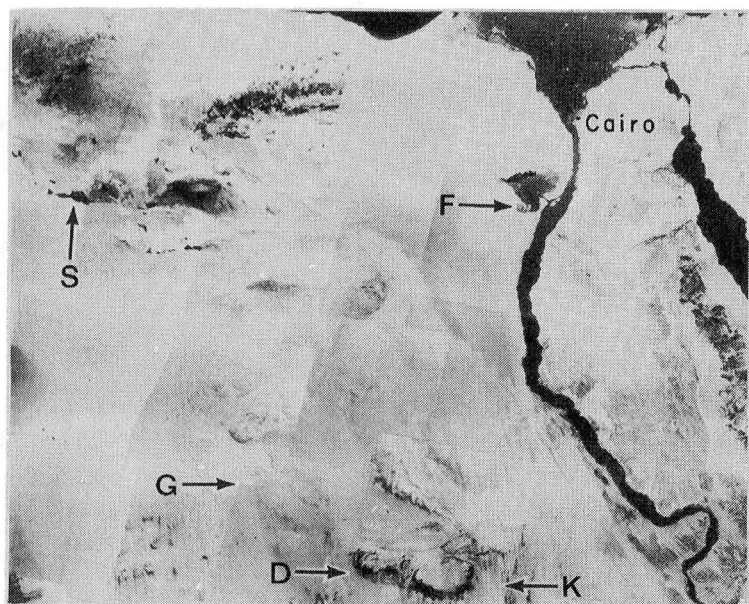


Figure 1. Location map of sand samples:

D: Dakhla depression  
F: Faiyum depression  
G: Great Sand Sea  
K: Kharga depression  
S: Siwa depression

The overall transport direction of sand in the Western Desert of Egypt is towards the south. Advancing quartz sands from the north acquire an iron stain and become mixed with local components. Width of field in this mosaic of Landsat images is approximately 800 km.

exhibiting brown color and biaxial acute bisectrix figure.

*Calcite* is common and occurs as both rounded and euhedral grains; some are coated similar to quartz grains. Some exhibit an anomalous biaxial negative figure, which indicates that they have been subjected to strain. This feature could be useful in a provenance study.

*Carbonates* are generally milky white to dirty brown or red in color, are rounded to hackly in shape, and have interference colors similar to calcite. This class includes marl, chalk, and other types of carbonates.

*Epidote* is identified by its pistachio-green color, weak pleochroism, and biaxial optical axis figure with a very high 2V. It occurs both as rounded and angular, broken grains.

*Feldspar* constitutes usually subrounded grains that could be identified by their low refractive index, twinning, and low birefringence.

*Garnet* is easily identified by its reddish tint (Almandine) and its isotropism. It is fairly common as both rounded and angular grains.

*Gypsum* is identified with difficulty by its monoclinic habit and its tendency to speckle when turning the stage under polarized light.

*Hornblende* occurs both as rounded and angular, greenish grains, sometimes together in the same sample and displays pleochroism and prismatic habit.

*Kyanite* is easily identifiable due to its elongated habit and cleavage, being clear and usually subrounded.

*Microcline* grains show low refractive index and the presence of gridiron twinning and are usually subrounded.

*Opaques* include such minerals as magnetite, hematite and pyrite, but the samples contain mainly ilmenite, sometimes altered to leucoxene.

*Orthoclase* usually subrounded grains with Carlsbad twinning.

*Plagioclase* occurs as subrounded grains with albite twinning.

*Pyroxene* occurs rarely, and its identification is uncertain. It is generally subrounded, clear, and with a prismatic habit.

*Quartz* is easily identifiable because it is the most common species present. Thus, it was subdivided by the degree of angularity, the presence and type of inclusions, and the presence or absence of coatings.

*Rock fragments* are generally restricted to the coarser size fractions and are identified by using incident light.

*Rutile* is identified by its prismatic habit, color and uniaxial optic axis figure. The grains range from euhedral crystals to rounded fragments, with two distinct colors, which may be useful in a provenance study.

*Staurolite* occurs as angular and rounded grains, with numerous inclusions. It is identified by its orange-yellow color and weak pleochroism.

*Tests* or carbonate grains that appear to have some skeletal structure are mostly *globigerina*.

*Tourmaline* is easily identifiable by its intense pleochroism in euhedral crystals to rounded grains. Several varieties of tourmaline occur in the samples, including schorl, dravite, and elbaite.

*Zircon* as identified by crystal form, high index of refraction, and lack of color. The degree of rounding of this resistant mineral would be a good indicator of transport distance or origin. Also, a zircon crystal was observed with coatings similar to those on quartz grains.

We performed statistical analyses of the frequency distribution of these components as shown by the examples in Figure 2. The amount of quartz grains remains consistently high in the larger phi size units 0.00 to about 2.50. Very gradually, quartz diminishes until it falls off sharply at grain

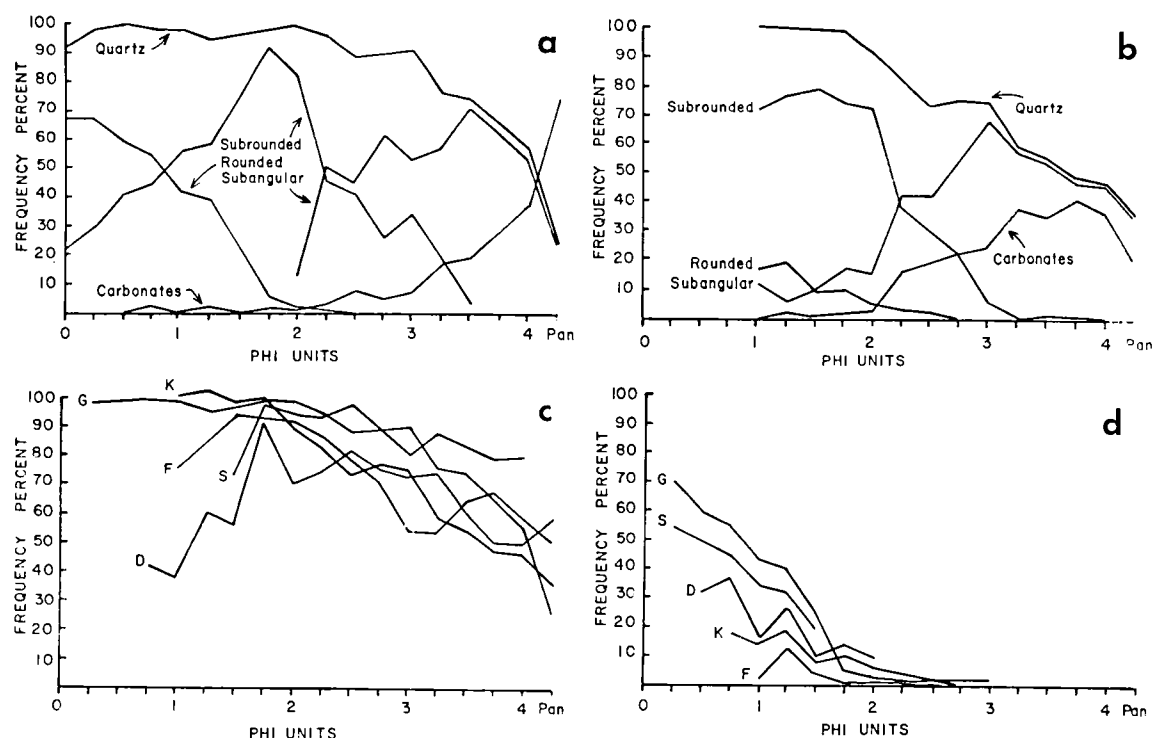


Figure 2. Grain size distribution in sand from the Great Sand Sea (a) and Kharga (b); all quartz grains (c); and rounded quartz grains (d).

sizes smaller than 3.50 phi; the exact opposite is shown by carbonate grains (Fig. 2). The rounded grains decrease in amount gradually from 0.00 to 1.75 phi, where they become negligible (Fig. 2). Subrounded grains appear to peak at 1.75 phi.

The analyses establish a prolonged time of eolian transport and show that the longer the transport distance the more prevalent the rounded and subrounded quartz grains. They also show that samples taken from depressions that enclose the Western Desert oases have less quartz grains and more carbonates and other components as compared to the Great Sand Sea sample. This mixing also reduces the overall degree of roundness of the samples, but has little effect on overall color.

Our studies show that the reddening observed in the southernmost parts of the desert can basically be attributed to the kaolinite/hematite coatings on the grains (4) rather than to the composition of the sands. Such reddening may be analogous to the causes of reddish color, due to iron oxides (5), on the surface of Mars.

#### REFERENCES

1. El-Baz, F. (1978) Photogramm. Eng. Rem. Sens., v. 44, p. 69-75.
2. El-Baz, F. et al. (1979) NASA SP-412, v. 2, p. 219-236.
3. El-Baz, F. et al. (1979) JGR, v. 84, n. B14, p. 8205-8221.
4. Prestel, D.J. et al. (1979) NASA TM-81776, p. 238-240.
5. Huck, F.O. et al. (1977) JGR, v. 82, p. 4401-4411.

## THICKNESS OF COATINGS ON QUARTZ GRAINS FROM THE GREAT SAND SEA, EGYPT

D. McKay, Geology Branch, NASA Johnson Space Center, Houston, TX 77058  
J. Constantopoulos, Calif. State Univ., Northridge, CA  
D. J. Prestel, LOCKHEED, NASA Johnson Space Center, Houston, TX 77058  
Farouk El-Baz, National Air and Space Museum, Smithsonian Institution,  
Washington, DC 20560

### INTRODUCTION

The presence of a thin coating on the surface of quartz sand grains is very common in terrestrial environments and imparts the reddish color to aeolian sand. These coatings have been studied in some detail in Simpson Desert sands by Folk (1), in Libya by Walker (2) and in the Western Desert of Egypt by our own group (3, 4). All workers agree that the coating contains both clay minerals and iron oxides. This coating strongly influences the spectral reflectance properties of these sand grains. We are investigating the characteristics of such coatings in order to assess whether they might be important on Mars and might influence the spectral reflectance data from Viking and from earth-based telescopic observations.

### METHOD

We have determined coating thickness on quartz sand grains from two samples with the Great Sand Sea of the Western Desert of Egypt (Fig. 1). Both samples were taken from active dunes, approximately 400 km apart. One purpose of the study was to establish whether coating thickness varied with location and whether it increases with the distance of aeolian transport (5).

We fractured a number of representative quartz grains from each sample, cleaned them ultrasonically, and examined them with the Scanning Electron Microscope (SEM). Stereo photography was used to position fractured grains so that the fractured edge of the coatings was oriented normal to the view direction. The thickness of the coatings was then measured at from one to eleven locations on each grain.

### THICKNESS RESULTS

Figure 2 shows a typical coating in cross section. Thickness results are presented as histograms (Fig. 3). Distribution of thicknesses could be roughly described as log normal although the Siwa sample shows a superimposed bimodal tendency. Thicker coatings were associated with depressions on the grain; thinner coatings were sometimes associated with areas which appeared to be relatively freshly fractured. None of the grain surfaces was free of coating material. Coating on samples from area B (Fig. 1) are slightly thicker (log mean of 0.8 micrometers) than those on samples from area A (log mean of 1.2 micrometers). This difference correlates with travel distance from source rocks which is greater for sand at location B.

### TEXTURE AND COMPOSITION

The coating usually displayed a clear sharp contact with the underlying quartz grain (Fig. 2). In some cases the coating fills in rough topography producing a smoother outer surface. The coatings on grains used in this study tended to be massive rather than porous when viewed in cross section.



At lower magnification, the coatings appeared to be smooth and slightly dimpled, similar to the "turtle-skin" texture described by (1) for Simpson Desert sands. However at very high magnification the surface of the coating could usually be resolved into individual grains, many of which are platelets. The texture and morphology suggests a coating made up of a network of clay mineral platelets, usually oriented approximately parallel to the surface.

In some cases the platelets appear to be interlocking and to have grown around or on top of other platelets. The texture is not compatible with a simple detrital origin of the coating particles. If these particles were originally detrital they have recrystallized on the quartz grain surfaces. An amorphous silica component may be present in the coating (1) but it is not the primary component and may simply help cement clay minerals and iron oxide grains.

Energy dispersive x-ray analyses shows that the major elements in the coating (other than Si) are Al and Fe. For Siwa samples, K is an important component and Mg is usually present, but for Great Sand Sea samples (Location B), K and Mg are much less abundant and Al is more abundant. These results are compatible with a coating made of a mixture of clay minerals and an iron oxide. The Siwa composition suggests that illite, montmorillonite, and hematite may be present whereas the Great Sand Sea composition is compatible with a coating made mostly of kaolinite and hematite. This mineralogy was found on sand grains from Gilf Kebir farther to the south of the Great Sand Sea (3, 4).

In conclusion, the quartz sand grains which we have studied have a ubiquitous coating apparently consisting of clay minerals and an iron oxide. The coating thickness has an approximate log normal distribution with a mean of about one micrometer. The texture is not detrital and clearly shows signs of recrystallization, or of authigenic growth of minerals. Mineralogy apparently varies from place to place. These coatings clearly influence spectral reflectance signature of the sands (R. Morris, unpublished data). It is significant that these complex coatings are forming in the driest region on earth. Our preliminary data show that sand grains in the Dry Valleys of Antarctica also have complex coatings. These results support our contention that mineral grains on Mars are likely to be covered with complex coatings which may strongly influence the physical and spectral properties of the Martian regolith.

#### REFERENCES:

- (1) Folk R. L. (1976) Jour. Sed. Petrol. 46, p. 604-615.
- (2) Walker T. R. (1979) U.S.G.S. Prof. Paper 1052, p. 61-81.
- (3) Prestel D. J., Wainwright J. E., and El-Baz F. (1980) NASA TM 81776, p. 238-240.
- (4) El-Baz F. and Prestel D. J. (1980) Lunar Planet. Sci. XI, p. 254-256.
- (5) El-Baz F. (1978) Photogramm. Eng. Rem. Sens., 44, p. 69-75

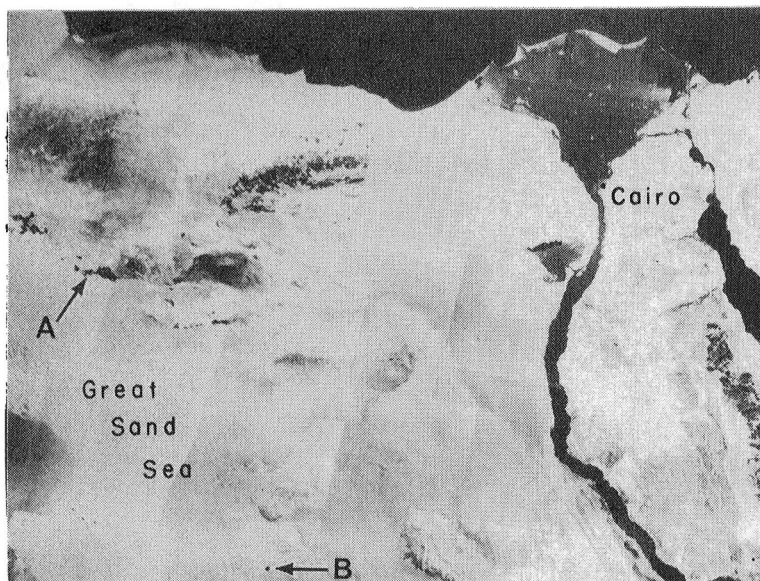


Figure 1. Location map of two sand samples from the Great Sand Sea in the Western Desert of Egypt. Sample A was collected from a complex, barchanoid dune just south of Siwa Oasis. Sample B was taken from the crest of a seif dune atop a whaleback dune southwest of Abu Minqar, which is at the southern entrance of the Farafra depression and on the eastern margin of the Great Sand Sea. Straight line distance between two locations is about 400 km.

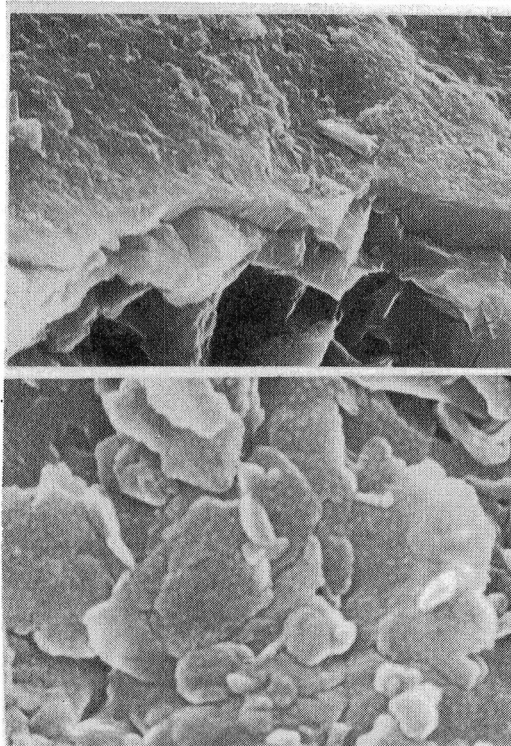


Fig. 3 (top) Coating and coating contact with underlying fractured quartz grain. Width of field is 16 micrometers.

Fig. 3 (bottom) Closeup of typical coating showing platy clay minerals, some of which are euhedral. Width of field is 1.3 micrometers.

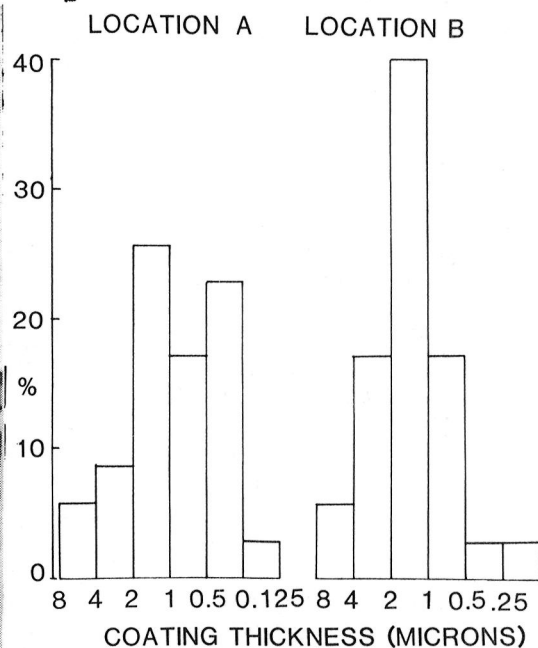


Fig. 2 (above) Histogram of coating thickness on quartz sand grains from areas in Fig. 1

EVOLUTION OF INSELBERGS IN THE HYPERARID WESTERN DESERT OF EGYPT --  
COMPARISONS WITH MARTIAN FRETTED TERRAIN  
C. S. Breed, J. F. McCauley and M. J. Grolier, U.S. Geological Survey,  
Flagstaff, Arizona 86001

Steep-sided conical or flat-topped hills that rise abruptly from surrounding plains are common landforms in terrestrial deserts, and are generally referred to as inselbergs. Unlike yardangs, which owe their relief to excavation of intervening troughs by wind erosion, inselbergs owe their relief to dissection of highlands, usually by stream erosion. On Earth, inselbergs commonly evolve from dissected plateaus capped by resistant, nearly horizontal bedrock. When the caprock disappears, the irregular buttes and mesas gradually become conical hills standing in groups, chains, or in isolation.

The shapes of inselbergs evolving in hyperarid deserts differ significantly from those in arid to semiarid deserts, because slope-forming processes vary in relative effectiveness under different climatic conditions. In semiarid deserts, undercutting of caprock occurs by weathering, spring sapping, and slopewash; comminuted debris is removed mainly by running water, and wind erosion plays a subordinate role. Inselbergs in semiarid deserts are typically bounded by pediments graded to valleys of nearby ephemeral streams. The pediments are veneered by alluvium, and debris aprons are common.

In the hyperarid Western Desert of Egypt, where annual precipitation is less than 1 mm, running water is now virtually absent. Wind erosion and deposition have erased most traces of fluvial topography except in areas of high relief, such as the Gilf Kebir Plateau. There, broad but dry wadis are deeply incised in the caprock. Flat-topped interfluvial areas of the dissected surface are now being reduced to inselbergs mostly by dry mass wasting and wind erosion, but with rare and sporadic episodes of spring sapping and slopewash. These processes result in the erosional detachment of conical segments from the wadi side-slopes and spurs (fig. 1a). Once partly detached, these segments have greatly diminished catchment areas for sporadic rainfall, and no longer collect amounts sufficient to recharge springs or to carve gullies on their slopes. In the absence of collected runoff, wind becomes the dominant agent for removal of slope debris comminuted by weathering, wind abrasion, and mass wasting.

Backwearing further isolates the conical segments from the parent scarps, until each hill stands as an individual outlier on the surrounding plain or on the broad, flat wadi floor. Larger inselbergs that have not been eroded to this stage commonly retain a caprock and have flat tops, but smaller, more isolated outliers from which the caprock has been removed attain an almost perfect conical form. Some of the inselbergs in and near the Gilf Plateau (fig. 1a) retain the imprint of earlier fluvial erosional and depositional processes, which were highly effective during Quaternary intervals of subhumid climatic

conditions (1). These hills have more complex slopes, including pediments, gullies, debris aprons, and fans, than the hills on the open plains, where the imprint of earlier fluvial episodes has been almost entirely erased by the wind (fig. 1b).

Outside the Gilf Kebir Plateau is an essentially flat desert plain, 120,000 km<sup>2</sup> in area, on which no traces of running water remain. Rising sharply from the plain are myriads of isolated, steep-sided, conical hills. Although they almost certainly owe their initial relief to regional down cutting by long-vanished streams (2), (3), these hills lack gullies, pediments, and debris aprons (fig. 1b). Most have developed symmetrical shapes that are forms of dynamic equilibrium under present climatic conditions. Wind and dry mass wasting are now the dominant slope-forming processes, and running water plays almost no role.

A key concept for inselberg evolution under hyperarid climatic conditions is that wind, unlike water, is not confined to downslope movements; wind transports the fines of comminuted slope debris up and away in suspension, not simply down onto the surrounding floor. Winds carrying coarser grains abrade grooves in exposed bedrock floors but do not cut pediments. The steep (typically 35°-40°) slopes that rise directly from the flat plains are maintained while inselbergs are reduced in size from hills tens of meters high to small nubbins. Slope debris, comminuted by weathering, mass wasting, and wind abrasion, is removed rapidly, without accumulating on the floor around the base of the hills. The isolated hills appear to act as centers of vorticity from which material is almost continually deflated. Although windblown debris mantles the plains, it typically does not accumulate in drifts behind individual conical hills.

The fretted terrain (4) in the Ismenius Lacus region of Mars includes numerous mesas and conical hills that are outliers of caprock plateaus (fig. 1c). The plateaus are dissected by broad, dry martian "wadis" which, like those that dissect the Gilf Plateau, debouch onto plains. Larger inselbergs that retain caprocks are irregular-shaped mesas, but many inselbergs without caprocks have conical shapes (5). Surrounding the base of the plateau scarp and its outliers are wide debris aprons that overlap rather than grade into the surrounding floor. The complex slopes and various shapes of the martian inselbergs suggest that they, like the inselbergs of the Western Desert, evolved under episodically varying climatic conditions during which different kinds of slope-forming processes dominated.

Outliers of the martian plateaus appear to have been dissected, at least initially, by the martian wadis, in much the same way as outliers of the Gilf Plateau were initially dissected by now-vanished streams. Since the disappearance of running water from Mars, some of the inselbergs have lost their caprocks and developed steep-sided, conical slopes in their upper parts. These slopes, as in Egypt, may be

explained by dry mass wasting and wind erosion under hyperarid climatic conditions. However, the wide debris aprons at the base of the martian hills and scarps have no counterpart in the Egyptian desert, and cannot be accounted for by these processes. They may result from effects of ground ice on mass-wasting processes (4), (6), (7). Whatever the mechanism of downslope movement of these debris flows, their movements were in response to, and not the cause of, the initial dissection of the plateau that provided the relief required for mass wasting to begin. This initial dissection may well have been by streams whose upstream portions are preserved as incised wadis within the martian plateau.

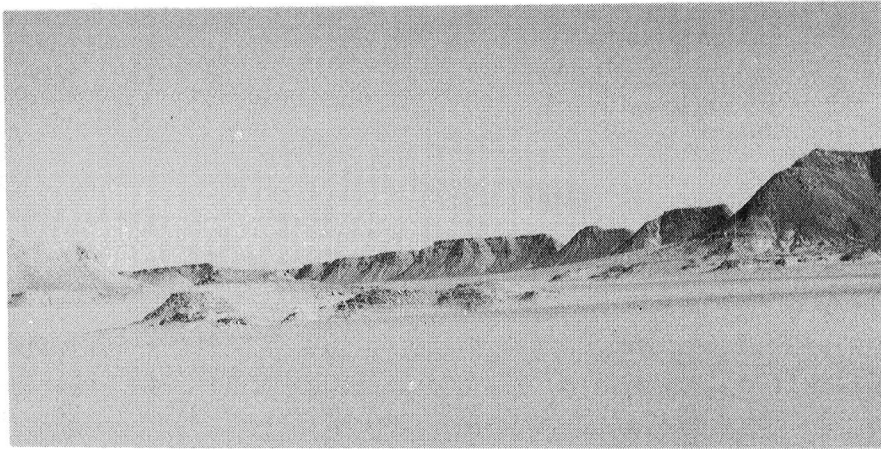
Inselbergs standing in groups on the plains outside the martian plateau appear to be remnants of divides between valleys that are continuous with the incised wadis within the plateau. Similar groups of hills beyond the margin of the Gifl Plateau in Egypt (fig. 1d) mark the positions of the interfluvies between once-vigorous, integrated streams that extended at least 100 km beyond the present plateau scarp (2), (3). The valleys between the martian inselbergs are now occupied by debris flows that may be rock glaciers (7), but this relation does not preclude their initial dissection by running water. If the Gifl drainage analogy is valid, then the patterns of inselbergs near the martian plateau may be useful for tracing ancient watercourses beyond the present margin of the densely cratered uplands, through the fretted terrain, and onto the low northern plains.

#### REFERENCES:

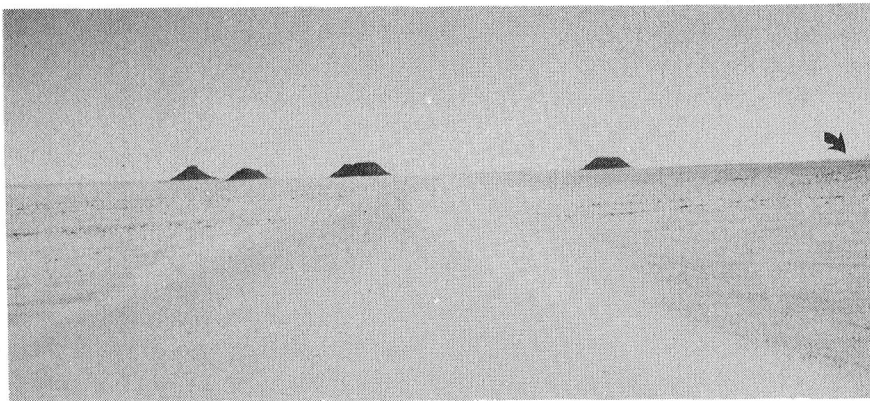
- (1) Haynes, C. V., 1978, The Nubian Desert: a product of Quaternary climate change: Abs. for Planet. Geol. Field Conf. on Aeolian Processes: NASA M-78,455, 22-23.
- (2) McCauley, J. F., Breed, C. S., and Grolier, M. J., 1980, The Gifl Kebir and the Western Desert of Egypt - insights into the source of the north polar erg on Mars: this volume.
- (3) McCauley, J. F., Breed, C. S., and Grolier, M. J., in press, The interplay of fluvial, mass-wasting, and eolian processes in the Gifl Kebir region (southwestern Egypt), in El-Baz, Farouk, and Maxwell, T. A., eds., Contributions to Planetary Geology: Desert Landforms of Southwestern Egypt; to be published by NASA.
- (4) Sharp, R. P., 1973, Mars: fretted and chaotic terrains: Jour. Geophys. Res., 78, 4073-4083.
- (5) Lucchitta, B. K., 1978, Geologic map of the Ismenius Lacus quadrangle of Mars: U.S. Geol. Survey Misc. Inv. Series, I-1065.
- (6) Carr, M. H., and Schaber, G. G., 1977, Martian permafrost features: Jour. Geophys. Res., 82, 4039-4054.
- (7) Squyres, S. W., 1978, Martian fretted terrain: flow of erosional debris: Icarus, 34, 600-613.

FIGURES:

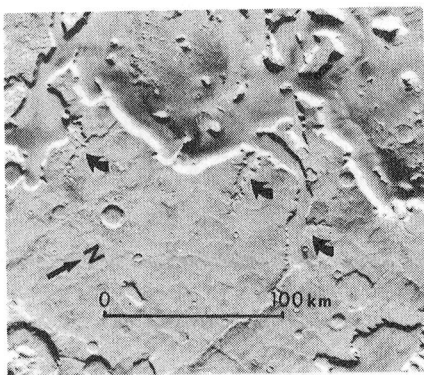
- Figure 1. Relations of inselbergs to plateau margins and wadi systems in Egypt and in the fretted terrain, Mars:
- a. Dissected wadi walls with semi-detached conical segments and isolated inselbergs retain imprint of fluvial dissection within the Gilf Kebir Plateau. Walls are about 100 m high.
  - b. Isolated flat-topped and conical inselbergs, about 15-20 m high, mark position of an old interfluvium on the flat plain outside the distant Gilf Kebir Plateau (arrow). View south (downwind) from crest of migrating linear dune.
  - c. Plateau scarp and outliers in the Ismenius Lacus region of Mars; arrows point to martian "wadis" that debouch onto the adjacent plain (V0675B66,67).
  - d. Plateau scarp and outliers in the Gilf Kebir region, southwestern Egypt; arrows point to wadis that debouch onto the adjacent plain (part of Landsat image 1131-08141).



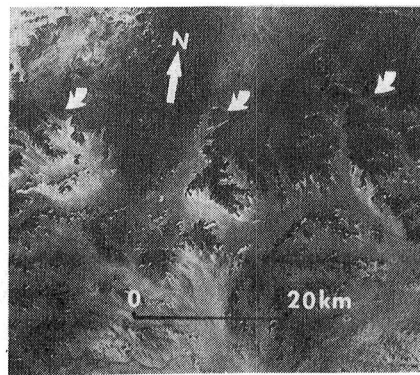
a



b



c



d

Figure 1.- Breed and others.

THE GILF KEBIR AND THE WESTERN DESERT OF EGYPT -- INSIGHTS INTO THE  
ORIGIN OF THE NORTH POLAR ERG ON MARS

J. F. McCauley, C. S. Breed, and M. J. Grolier, U. S. Geological Survey,  
Flagstaff, Arizona 86001

The sources of the materials that make up the polar dunes on Mars remain problematic. Suggestions concerning the composition of these "sands" range from aggregated atmospheric dust to local volcanic and impact debris. On Earth, where the overall erosional regime is far more intense than on Mars, most erg sand is from fluvial sources: fluvial processes, often in conjunction with coastal marine processes, provide the preconditioning necessary for later eolian transport and accumulation.

The Gilf Kebir Plateau of southwestern Egypt and surrounding parts of the Western Desert provide some interesting clues as to how the north polar erg may have originated. The Gilf Kebir lies within the core of what is now the most arid part of the Earth. Remarkable similarities to the fretted terrain on Mars are present within the plateau and along its deeply eroded margins (1, fig. 1). In and around the Gilf, wind, mass-wasting and spring-sapping of scarps have severely altered landscapes whose basic patterns were first established by fluvial activity during Tertiary time, when the region was far more humid than now. Relict drainage basins, reconstructed on a Landsat image of the Gilf region, formerly contained integrated, mature stream networks. These networks conform to Horton's Law of Stream Numbers for drainages developed under humid to semiarid climatic conditions (2, 3). Energetic streams of probable mid- to late-Tertiary age drained the Gilf highlands to the north, east, west, and south; their patterns indicate that this region was formerly a major North African drainage divide.

Distribution of relict interfluves clearly shows that wadis incised in the plateau were continuous with watercourses now barely recognizable on the pediplane beyond the present plateau. One of these, the newly recognized Eight Bells system, drained at least 3,400 km<sup>2</sup> of the southern Gilf region and discharged as a master stream to the south. This and other streams may have fed into the Chad Basin, an internal depression about the size of that occupied by the north polar erg of Mars (3).

Analysis of Landsat imagery combined with ground reconnaissance observations in October, 1978 reveal numerous large, throughgoing elongate sand sheets moving south and southwestward from the Gilf. These mobile sheets are a complex mix of barchanoid, transverse and linear dunes migrating in the direction of the regional south-blowing winds. Although wind processes have obliterated almost all traces of former integrated drainages on the pediplane of western Egypt and northern Sudan, migrating sand bodies generally follow the apparent courses of these ancient drainages, and are now moving en masse downhill toward the Chad Basin.

Along the northern margin of the cratered highlands of Mars (from about longitude 0° to 270°) is an arc of major channel outlets and "fretted terrain" that closely resembles the terrain in and around the



Gilf Kebir (1, fig. 1, c,d). The martian "diluvian" channels (4) debouch onto the smooth, flat northern plains where little or no trace of former fluvial activity can now be seen. Analysis of Viking pictures suggests postdiluvian volcanic flooding and later partial mantling of the plains with eolian debris. Farther north, around the north polar ice cap, these relatively featureless plains grade into the polar erg. The erg contains vast fields of barchanoid and transverse dunes that are seasonally overlain by the "ice" cap.

We suggest that the sand of the martian erg, as in terrestrial ergs, is mostly from fluvial sources. Some time after the diluvian interval on Mars, sand deposited on the northern plains by streams that issued from the highlands was deflated and carried downhill to the polar lowlands by north-blowing winds. This regional circulation pattern differs from that now observed around the north pole (5); it implies that the polar ice cap was not present when the erg accumulated (6).

In North Africa, winds are still transporting debris from old watercourses across the open desert plains to inland basins that are presently filling with windblown sand. On Mars, the eolian transport of sand from old fluvial deposits, and its deposition in the north polar erg seem to be essentially complete (7). The plains have been largely depleted of sands capable of saltation, leaving behind stable, coarse lag surfaces and a few fields of transverse dunes trapped in low-lying areas. The dust blankets that mantle the plains result from more recent suspension transport. The "eolian thoroughfares", typical of actively migrating sand in the Western Desert of Egypt (3), have on Mars been either swept clean of their sands or buried by younger volcanic or eolian deposits.

#### REFERENCES:

- (1) Breed, C. S., McCauley, J. F., and Grolier, M. J., 1980, Evolution of inselbergs in the hyperarid Western Desert of Egypt -- comparisons with martian fretted terrain: this volume.
- (2) Horton, R. E., 1945, Erosional development of streams and their drainage basins: Hydrophysical approach to quantitative morphology: Geol. Soc. America Bull., 56, 275-370.
- (3) McCauley, J. F., Breed, C. S., and Grolier, M. J., in press, The interplay of fluvial, mass-wasting, and eolian processes in the Gilf Kebir region (southwestern Egypt), in El-Baz, Farouk, and Maxwell, T. A., eds., Contributions to Planetary Geology: Desert landforms of Southwestern Egypt; to be published by NASA.
- (4) Baker, V. R., and Kochel, R. C., 1979, Martian channel morphology: Maja and Kasei Valles: Jour. Geophys. Res., 84, 7961-7983.
- (5) Ward, A. W., Helm, P. J., Witbeck, N. and Weisman, M. 1980, Digital map of martian eolian features: this volume.
- (6) McCauley, J. F., Breed, C. S., Grolier, M. J., and Collins, P. S., 1979, The eolian features of the north polar region of Mars (abs.): NASA Conf. Pub. 2072, 55.
- (7) Breed, C. S., Grolier, M. J., and McCauley, J. F., 1979, Morphology and distribution of common "sand" dunes on Mars: comparison with the Earth: Jour. Geophys. Res., 84, 8183-8204.

FIELD OBSERVATIONS WITHIN A LITTLE-KNOWN DUNE COMPLEX IN THE GREAT SAND SEA, WESTERN DESERT, EGYPT.

Giegengack, Robert, Geology Department, University of Pennsylvania, Philadelphia, Pennsylvania, 19104.

Underwood, James R., Jr., Department of Geology, Kansas State University, Manhattan, Kansas, 66506.

The Great Sand Sea is an extensive sheet of blown sand where a broad range of dune morphology is well developed in the vicinity of the Libyan-Egyptian border, between lat  $29^{\circ} 30' N$  and lat  $24^{\circ} 30' N$ . Since Bagnold's pioneering study that led to his classic 1941 book The Physics of Blown Sand and Desert Dunes, this region has only rarely been visited by individuals able to make detailed observations on the configuration of the major dune elements and the surficial processes that maintain their striking regularity. We describe here our observations made in the course of a week-long reconnaissance expedition to the distribution area of the Libyan Desert Glass, at the extreme southwestern limit of the Great Sand Sea.

It was possible to identify with some precision the limits of individual dunes on the several series of Landsat (ERTS) images (1972; 1976) that we carried into the field; we were impressed by the fact that the relative positions of dune terminations to the SSE are not different from the configuration shown on the map produced in 1934 by Clayton, Little, and Spencer (Spencer, 1939). Thus, we conclude that any changes that may have occurred in the configuration of dunes at the limit of the Great Sand Sea in the last 45 years are smaller than the limit of resolution of our Landsat images.

The present configuration of the Great Sand Sea is thought to be maintained by prevailing NNW winds that carry sand from various alluvial accumulations in the northern Sahara to localities farther south. We cannot estimate the residence time of any particular sand grain in any particular dune form, but we believe that time to be far shorter than the survival time of the dune itself as a topographic feature, or of the Great Sand Sea as a geomorphic province.

At the southern end of the Great Sand Sea, and for some 50-80 km NNW, interdune corridors are free of extensive accumulations of blown sand; bedrock is exposed up to the margins of individual dune ridges; topographic relief is considerable (up to 150 m adjacent to the largest dunes); and the topography of dune crests is complex, and separable into identifiable components of individual dune features. In the northern portion of the Great Sand Sea, linear interdune corridors are floored by blown sand of unknown thickness; total relief is of the order of 25-40 m, and the dune crests typically lack any systematic clear demarcation between

stoss and slip faces.

We formed the impression (shared by earlier observers) that the Great Sand Sea is advancing to the SSE. We have adopted the working hypothesis that, regardless of the duration of residence of individual sand grains, the Great Sand Sea as a first-order geomorphic feature is youngest at its distal (downwind) limit. It follows, then, that the dune geometries and surficial processes we observe at the limit of the Great Sand Sea prevailed in an earlier period at localities to the NNW. We may be observing a developmental sequence spread out along a spatial gradient from SSE to NNW.

Near the southern termination of the parallel longitudinal dunes we observed:

1. The western margin of each dune is a sharp line parallel to the long axis of the dune. The western edge of each dune is underlain by soft, loosely packed sand that slopes gently up toward the crest of the dune.
2. The eastern margin of each dune is irregular, and consists of a series of left-side distal horns of individual barchan dunes that have coalesced, each marching up the gently sloping stoss face of the dune ahead. There are thus many sharp re-entrants in the eastern margin of each dune ridge; sand at the margin is tightly packed on individual barchan stoss faces but loose within re-entrants, where slip faces of coalescing barchans directly abut the bedrock desert floor.
3. Each individual dune ridge is an enormously complex topographic feature, on which both stoss and slip faces can be identified as components of individual barchan forms. A characteristic topographic feature within the dune masses is a well-defined semi-conical depression, more or less 50 m in diameter, consisting of slip faces on the west, north, and east, and a more gently sloping stoss face (of the next barchan south) to the south.
4. Each longitudinal dune form terminates distinctly to the SSE; in several examples we observed isolated circular masses of sand (compare dome dunes of Breed and Grow, 1979, and Breed *et al*, 1980), more or less aligned as beads on a string as continuations to the SSE of the long axes of individual dunes; in at least one case the northernmost dome dune had already developed the characteristic form of a small barchan. The dome dunes are smaller than the limit of resolution of our satellite images.

While we do not have the benefit of either a series of sequential observations or adequate meteorological data to support it, we have drawn the inference that the Great Sand Sea originated, and continues to be propagated to the SSE as a first-order topographic feature, by the process of coalescence of individual barchans from NNW to SSE. Coalescence presumably occurs when one barchan runs up against another whose rate of downwind migration is reduced by falling within the wind shadow of the approaching barchan. Such a scenario might best occur as a sand supply increases with time, a circumstance that characterizes the leading edge of a systematically encroaching dune field. With time (and through space, to the NNW in this instance), the morphology of individual converging barchans is lost, as the mass of sand itself becomes large enough to interfere directly with the geometry of air-flow patterns near the ground. With sand supply increasing, the amount of sand that spills down either side of the dune ridge eventually exceeds the capacity of the wind to sweep it into existing dune forms, and the interdune corridors become covered with sand as well. We are at a loss to identify the mechanism that concentrates barchan bundles in parallel linear wave forms of such uniform size and regular spacing.

We know of no other instance in which such an evolutionary sequence has been postulated, but on the Serengeti Plain in NW Tanzania one of us (RG) has examined an analog in which at least a part of the reverse sequence has occurred (see also Hay, 1976, p. 166-174). There, a sand-size sediment supply diminished and is about to disappear entirely, causing a dune field to evolve from a large number of interacting barchans to isolated barchans to isolated domes.

The absence of any developmental data for Martian dune features prevents us from comparing our inferred sequence of events to circumstances on Mars, but, since wind deposits in the hyperarid deserts of Earth are being intensively studied as possible analogs to Martian topographic elements, we feel that these observations should be brought to the attention of those involved in such comparisons.

- Bagnold, R.A., 1941: Methuen & Co., Ltd., London, 265 p.  
Breed, C.S., Embabi, N.S., El-Atr, H.A., and Grolier, M.J., 1980, Geog. Journ., v. 146, p. 88-90.  
Breed, C.S., and Grow, Teresa, 1979: in McKee, E.D., U.S. Geol. Survey Prof. Paper 1052, p. 253-304.  
Hay, R.L., 1976, Geology of the Olduvai Gorge: Univ. Calif. Press, 203 p.

CLIMBING AND FALLING DUNES IN THE PAINTED DESERT OF ARIZONA:  
COMPARISON WITH MARS.

McCauley, Camilla K. and William J. Breed, Museum of Northern Arizona, Flagstaff, Arizona, 86001; Augustus S. Cotter and Morgan Gray, Department of Geology, Northern Arizona University, Flagstaff, Arizona, 86001; Russell Axelrod, Museum of Northern Arizona, Flagstaff, Arizona, 86001; and Anthony P. Johnson, Georgia Southwestern College, Americus, Georgia.

Dune fields on Earth and Mars appear to respond similarly to variations in local wind regimes caused by topographic disturbances. On Mars, climbing and falling dunes occur within craters and on the slopes of crater rims. Dunes also occur in other types of topographic depressions where strong winds are locally channeled.

In order to better understand the changes in wind velocity and direction caused by topography and the resulting modification of dune morphology, an instrumented field study is being conducted in the Painted Desert of northern Arizona where climbing and falling dunes are common along the Red Rock Escarpment.

The climbing dunes are fed by a large field of barchan dunes which occurs between the escarpment and the source of the sediments at the floodplain of the Little Colorado River, 16 km distant. As the dunes near the cliffs, they lose their distinctive barchanoid forms and assume a complex morphology, in some places forming echo dunes which are separated from the base of the nearly vertical cliffs by V-shaped moats. In other places, where former water courses have created more gentle slopes, the sand is funnelled into climbing dunes and ridges that surmount the escarpment.

Wind recording machines were set up in various locations within the dune field to monitor local wind regimes. Recording sites were selected both above and below the 60 meter high escarpment, and measurements were made simultaneously on three machines. These machines are capable of recording wind gusts every two seconds as well as hourly average velocities and directions. In addition, two types of sand traps have been installed within 10 meters of the wind recording machines to measure sand flux as related to wind velocity and direction and height above the dune surface. Computer data analysis of the results of this study are now in progress, however preliminary results indicate a complex wind regime, with reversing winds occurring locally.

### Granule-Armored Sand Dunes

Roger S. U. Smith, Geology Department, University of Houston,  
Houston, TX 77004

It is important to be able to distinguish between ordinary active sand dunes and those stabilized by an armor of granules because the two types can represent very different eolian conditions. Granule-armored dunes are those covered by a veneer of grains too large to saltate but small enough to creep, and their occurrence implies that: 1) Underlying sand is protected from transport and attrition while the veneer persists; 2) New sand grains need not form or become available quickly to replace grains lost by attrition; 3) Armor may preserve dune forms aligned with an ancient wind regime that may differ from the modern regime; and 4) Surfaces upwind of armored dunes have probably been stripped of sand-sized debris but may continue to shed granules when strong winds blow. Thus, wherever granule-armored dunes occur on Mars (or other bodies), they may signify different conditions than do unarmored dunes.

Granule-armored dunes cover large parts of some terrestrial deserts and display distinctive appearance on both aerial and orbital photographs. Bagnold (1941) noted granule armoring of the plinth along seif (longitudinal) dunes, one to three kilometers wide and up to 300 kilometers long, and mentioned vast areas of subdued, undulatory, armored eolian topography elsewhere in the eastern Sahara Desert. Warren (1972) described armored dunes (zibar) in the Ténéré Desert of Chad, where they cover large areas with a spacing on the order of 100 meters and a height of three to seven meters; despite their lack of slip faces, these are surmounted by widely-spaced seif dunes. Similar features cover vast areas of Mali and Mauretania and local areas of the California desert. These features all display a distinctive photo pattern of wavy, alternating dark and light bands, representing, respectively, ridgecrests of darker granules and interridge hollows of finer, lighter sand.

Granule-armored surface can develop quickly and some clearly are fed from the desert floor, not by deflation of mixed sand and granules. Granules prevail along the flanks of barchans, where deflation is slight, not just at their windward toes, where net deflation is greatest. Near Beverly, Washington, relations between armored surfaces and underlying tephra from the 18 May 1980 eruption of Mt. Saint Helens clearly show encroachment of granules across the surface, not deflation. Despite the development of this armored surface within a month's time, the process may be slow elsewhere. The areal extent of granule-armored surfaces along the west edge of the Algodones dune chain, California, seems little changed during the 40 years since the first air photos of them were taken in 1940. However, the pattern of individual ridges on that surface has changed markedly during this period; whether this represents migration or evolution is not known yet.

### References Cited

- Bagnold, R.A., 1941, The physics of blown sand and desert dunes:  
London: Methuen, 265p.
- Warren, Andrew, 1972, Observations on dunes and bi-modal sands in the  
Ténéré Desert: *Sedimentology*, v. 12, p. 37-44.

DETECTION OF DUNE AREAS USING THE AUTOCORRELATION STRUCTURE OF  
DIGITAL IMAGERY - EARTH AND MARS

Richard G. Craig, Robert W. Wolfe\*, Brian R. Hoyt, Martin S.  
Schmidt, Michael Raymondi, and Kathy Kaufman. Dept. of  
Geology, Kent State University, Kent, Ohio 44242; \*National  
Air and Space Museum, Washington, DC, 20560

We have analyzed digital imagery for dune fields on the Earth (Landsat) and Mars (Viking 2) and compared these to non-dune areas. The basis for comparison is the degree of autocorrelation between adjacent pixel values. In addition, a large number of traverses of topography of dune and various non-dune areas have been made, and they form a base for comparison with digital imagery data. Such a comparison is important because good topographic data is not generally available for Mars and the other planets, nor for most dune fields of Earth. Necessarily, therefore, studies of this sort must use digital or other imagery data.

Results of the topographic analysis strongly suggest that dune and non-dune areas can be distinguished on the basis of their autocorrelation structure. It has been found that, for Landsat data, the autocorrelation structure arises from the autocorrelation structure of the landform being sensed and is not a machine artifact (Craig and Labovitz, 1980). We conjecture that this may also hold true for the Viking imagery and, if so, this will form a basis for the automated detection and recognition of various terrain types such as dunes on Mars.



Figure 1. Dune fields on Earth [left] and Mars [right].  
a. Algodones b. North polar region

The autocorrelation function represents the Pearson Product Moment correlation of  $N$  observations of a variable with itself  $K$  lags removed where  $K$  ranges from 0 to  $N/4$ . It ranges from -1 to +1 and the pattern it follows is diagnostic of a particular recursive model that, in most cases, affords a quite parsimonious representation of the observations. Such a model belongs to the class of autoregressive-integrated-moving-average models (ARIMA(p,d,q)) of Box and Jenkins (1976).

For the Earth-based dune study, the Algodones Field in southern California (Fig. 1a) was chosen for several reasons. This field has been the subject of numerous investigations and is well studied. In addition, both a good set of topographic maps at 1:24,000 scale and digital Landsat imagery are readily available. In shape of the field, nature of constituent duneforms, and perhaps topographic setting, the Algodones field may be a close analog of at least one dune field in the north polar region of Mars (Fig. 1b).

The Algodones dune field is located on the Glamis, California 7 1/2' USGS quadrangle and adjacent quadrangles. Three traverses of elevation parallel to the long axis of the dune field were recorded at a 48 m spacing with about 1200 observations each. From these the autocorrelation function (ACF) to 96 lags was computed (Fig. 2a). The decay of the ACF followed a pattern that suggested an exponentially damped sine wave. This indicated an ARIMA(2,0,0) model and such a model indeed fit the data well.

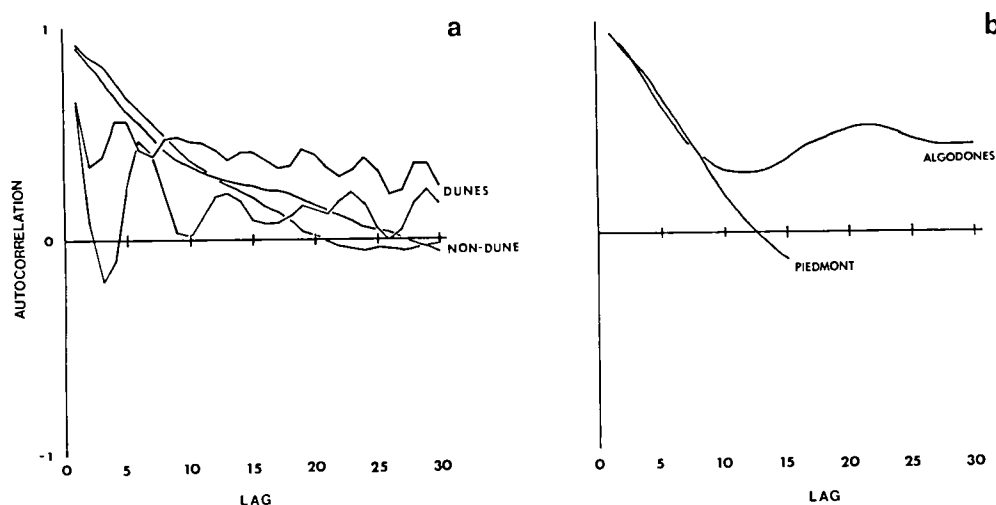


Figure 2. Autocorrelation functions--dune and non-dune areas  
 a. Algodones from topographic data. The non-dune area is from the Piedmont in the Washington West, MD, DC, VA 7 1/2' quadrangle.  
 b. Mars north polar region.



For the same area, a Landsat scene was obtained and geometrically rotated to bring the scan lines parallel to the long axis of the dune field. Autocorrelation functions for scan lines over the dune field show a similar pattern to that obtained from analysis of topography. This result is reasonable and not surprising. In the Algodones and most other dune fields, albedo variations are slight, even over wide distances. Contrast variations in imagery are related to the degree of illumination of slopes and are, therefore, closely related to topography.

For four traverses of Viking-2 image 560B41 (Fig. 1b) the ACF was computed. Two traverses (lines 710 to 910, element 150 and lines 810 to 1010, element 270) were parallel to the long axis of a dune field located near 81.5N, 83.2W. These displayed a mixed sinusoidal-exponential decay remarkably like that observed for topographic traverses of the Algodones dune field. This pattern indicates that the pixel values follow an ARIMA (2,0,0) model similar to the terrestrial field (Fig. 2b).

Two traverses (from lines 100 and 101 elements 102 to 306) in a non-dune area (valley floor) showed a definite pure exponential decay at approximately 25 lags. This indicated an ARIMA (1,0,0) model with the parameter  $\text{PHI}(1)$  equal to 0.92, not unlike that observed for erosional terrains on the Earth (Craig, 1981 and Fig. 2a). We therefore tentatively conclude that it is possible to distinguish dunal areas on the basis of the autocorrelation structure of digital imagery.

Future work is to be directed towards: 1) Topographic analysis of martian dune fields; 2) Addition of other dune fields on Earth and Mars; 3) Examination of the physical meaning of the ARIMA(2,0,0) equation in dune field formation.

### References

- Box, G.E.P. and G.M. Jenkins, Time Series Analysis, Forecasting and Control. Holden-Day, San Francisco, 1976, 550p.
- Craig, R.G., Optimal digital terrain models, in Craig, R.G. and J.C. Croft, eds., Appl. Geomorph. (1981) in press.
- Craig, R.G. and M.L. Labovitz, Sources of variation in Landsat autocorrelation, Proc. 14th Inter. Symp. Remote Sens. (1980) 1755-1168.

Significance of Large Open Spaces within the North Polar Dunes on Mars  
Roger S. U. Smith, Geology Department, University of Houston,  
Houston, TX 77004

A variety of large open spaces, much larger than the spacing between dune ridges, occurs within the extensive circumpolar dune fields in the northern hemisphere of Mars. Study of Viking Orbiter imagery thus far suggests that many of these open spaces are centered about hills and that their form can either be concentric to the hill or elongate but fixed by the position of the hill. These anchored open spaces display even size of dune ridges on their margins; others that exhibit distinctly-larger dune ridges along one margin may not be controlled by topography but represent breakup of dunes within the space and accumulation of the released sand into a single transverse ridge downwind. Studies of open spaces within terrestrial dune fields, both on Landsat and aerial imagery, suggest that these unanchored open spaces may be common where dune fields have been flooded intermittently, eg, on the floors of closed desert basins, but that the anchored open spaces occur about hills within fields of transverse dunes. Most large open spaces on Earth seem to be of a third sort, interconnected interdune flats separating discrete dune fields or isolated composite forms, but this sort seems rare on Mars.

If large open spaces are devoid of dunes, they must either 1) have formed at or before the time of dune accumulation (eg, hills); 2) represent an environment where dunes are destroyed and their constituent sand dispersed (eg, flooded shallow basins on Earth); or 3) represent an environment across which sand moves without forming dunes. If open spaces formed after the enclosing dunes, the bulk of the sand that once covered them must either have 1) been fixed within the open space; 2) escaped by wind action; or 3) been added to the mass of dunes downwind. The margins of some open spaces on Earth and Mars clearly show the last alternative in a conspicuous "rolled up" margin, taller and broader than adjacent dune ridges ("ramparts" of Breed, Grolier & McCauley, 1979). Unlike longitudinal dune systems, the continuous transverse ridges so common on Mars would prevent downwind escape of ordinary sand grains. Except where "rolled-up" margins occur, it seems likely that most open spaces are controlled by features that predate the development of the dune fields in their present form. Some are clearly anchored by raised crater rims, producing equant to oval open spaces; others show just a faint trace of higher ground in their cores, but shaped concentrically within the open space.

Tsoar, Greeley and Peterfreund (1979) attributed some open spaces anchored by crater rims to scour around the craters. On Earth, such scour "tails" behind hills seem most common within fields of longitudinal dunes, whereas open spaces in the north polar region of Mars occur within fields of dunes generally acknowledged to be transverse (Cutts et al, 1976; Breed et al, 1979; Tsoar et al, 1979). On Earth, a hill within a field of transverse dunes generates a dune-free "moat" that mimics the hill's form, so round hills (eg, crater rims) generate round open spaces.

Thus many elongated open spaces require some explanation; perhaps they represent elongation in the resultant direction of the dominant wind in a reversing wind regime, such as the regime proposed by Tsoar et al (1979). If so, these features may prove useful in assessing wind dominance over much longer time spans than can be inferred from the orientation of barchan dunes. Further investigation of terrestrial open spaces is needed to verify this conjecture.

The character of open spaces localized by hills within transverse dune fields constrains the origin and migration of these dunes during their present cycle of development. Open spaces that are concentric about their central hill imply strongly that the dunes have undergone little net migration since they formed because it is difficult for long, straight transverse dune ridges to reform downwind of a hill. The dunes' constituent sand could in part have accreted slowly into the field, but most dunes were probably built from an existing blanket of sand of fairly uniform thickness, perhaps brought into the area by non-eolian processes. These concentric open spaces probably represent sites where opposing winds balance one another; such balance could explain the remarkable continuity and linearity of some martian transverse dunes, forms considered inherently unstable by Bagnold (1941) in unidirectional wind regimes.

#### References Cited

- Bagnold, R.A., 1941, The physics of blown sand and desert dunes: London: Methuen, 265p.
- Breed, C.S., Grolier, M.J., and McCauley, J.F., 1979, Morphology and distribution of common "sand" dunes on Mars: comparison with the Earth: Jour. Geophys. Research, v. 84, p. 8183-8204.
- Cutts, J.A., Blasius, K.R., Briggs, G.A., Carr, M.H., Greeley, Ronald, and Masursky, Harold, 1976, North polar region of Mars: Imaging results from Viking 2: Science, v. 194, p. 1329-1337.
- Tsoar, Haim, Greeley, Ronald, and Peterfreund, A.R., 1979, Mars: the north polar sand sea and related wind patterns: Jour. Geophys. Research, v. 84, p. 8167-8182.

Independent studies of wind indicators in the northern and southern polar latitudes have shown significant differences in the kinds and directions of eolian features (Cutts, 1973; Tsoar *et al.*, 1979; Wolfe, 1979; Thomas and Veverka, 1979). A north-south asymmetry has been attributed to the present asymmetry of seasons: global dust storms and generally strong circulation in southern summer (Haberle *et al.*, 1979; Toon *et al.*, 1980; French and Gierasch, 1979), and more gentle circulation in northern summer. Such asymmetry depends upon the eccentricity of Mars' orbit and the present southerly position of sub-solar latitude at perihelion (SSLP). Its  $\sim 51,000$  year cycle should thus tend to induce geologically rapid changes in the preferred orientations of some eolian features. A detailed study of streak distribution, orientation, and variability in both polar regions is important for documenting the extent of any north-south asymmetry and for assessing the geological significance of the changing wind patterns.

A catalogue of crater-related wind indicators poleward of  $+40^\circ$  has been compiled from Viking images. It includes bright streaks, dark erosional streaks, dark depositional streaks, crater splotches, dunes in crater splotches, winter and summer frost streaks, ice-sediment streaks and dune shadow streaks. Extensive published data exist for north polar dunes outside craters (e.g., Tsoar *et al.*, 1979). Viking Orbiter Survey Mission images filled a critical gap in coverage of north polar frost streaks. Although a variety of parameters have been recorded, this study concentrates on the distributions and orientations of the wind markers.

#### RESULTS:

- 1) North polar summer frost streaks show a retrograde outward flow (Fig. 1a). North polar winter frost streaks show a prograde, outward flow, nearly symmetric with that in the south (Fig. 1b).
- 2) Splotches and splotch streaks in the north show a predominantly prograde outward wind flow and only a minor retrograde outward component (Fig. 1c).
- 3) Splotches, splotch streaks, and dunes in splotches in the south all show retrograde, outward flow (Figs. 1d, 1e, 1f).
- 4) Flow toward the north pole is largely documented north of  $75^\circ$  by dune shadow streaks, ice sediment streaks, and dunes (cf. Tsoar *et al.*, 1979). The few comparable features at southern latitudes greater than  $75^\circ$  do not show a significant inward component. Poleward flow in the south is shown by a few erosional streaks at  $50-70^\circ\text{S}$ , which formed during late southern spring and early summer.

#### INTERPRETATIONS:

- a) Polar wind indicators overwhelmingly follow the flow that occurs during southern spring and summer. These markers include

substantial dune fields as well as highly variable streaks. There are few relict features that could be attributed to strong northern summer circulation, which last occurred  $\sim 15,000$ – $30,000$  years ago.

b) Winter winds in polar areas can be effective in moving non-frost materials. In the north these winds are the strongest of the year and leave a permanent record; in the south the spring winds are strongest and completely dominate surface markings.

c) If the symmetry of the splotch and streak patterns reflects the winds of the present cycle of the SSLP, then splotches have been reoriented in the time since the SSLP was at the equator ( $\sim 11,000$  years). The time during which flow was significantly stronger in the southern summer would be even less. Could splotch reorientation occur on this time scale ( $5,000$ – $10,000$  years)?

Typically such movement would require the translation of a  $150$  m high dune front some  $10$  km (ignoring problems of net sediment balance). Using the results of White (1979), and assuming a  $V_{*t}$  of  $1.6$  m/s and  $V_{*s}$  of  $1.75$  to  $4.0$  m/s for one-fourth of every martian year, reorientation times range from  $760$  to  $32,000$  (terrestrial) years. Although some saltation appears to occur in both polar regions (Tsoar *et al.*, 1979; Thomas and Veverka, 1979), extremely vigorous saltation for a full quarter year probably is a great overestimate. Present knowledge of wind velocities, threshold velocities, and modest streak changes all suggest that winds only marginally above threshold occur for much less than a quarter martian year. Reorientation of the splotches may thus require long times on the order of tens of thousands of years.

The coincidence of polar wind markers with the direction of currently strongest winds, combined with the difficulty of reorienting some of them so rapidly, suggests that the above estimates of the saltation rates on Mars are very conservative, or that the orientations derive from longer cycles and are by chance coincident with present flow. While the latter possibility appears ad hoc, the cycle of wind strengths would not be symmetric for each cycle of SSLP because the changes in eccentricity and obliquity follow different, longer cycles and may create very long period cycles of polar wind strengths. Further modeling of changes of polar winds over periods of  $10^6$  years, and their cumulative effects, is warranted.

This research was supported by NASA Grants NSG 7546 and 7156.

#### REFERENCES:

- Cutts, J.A. (1973). J. Geophys. Res. **78**, 4211–4221.  
French, R. G., and Gierasch, P. (1979). J. Geophys. Res. **84**, 4632–4644.  
Haberle, R.M., Leovy, C.B., and Pollack, J.B. (1979). Icarus **39**, 151–183.  
Thomas, P., and Veverka, J. (1979). J. Geophys. Res. **84**, 8131–8146.  
Toon, O.B., Pollack, J.B., Ward, W.R., Burns, J.A., and Bilski, A. (1980). Icarus, in press.  
Tsoar, H., Greeley, R., and Peterfreund, A.R. (1979). J. Geophys. Res. **84**, 8167–8180.  
White, B. R. (1979). J. Geophys. Res. **84**, 4643–4651.  
Wolfe, R. W. (1979). 10th Lunar Sci. Conf. Abstr. 1363–1365.

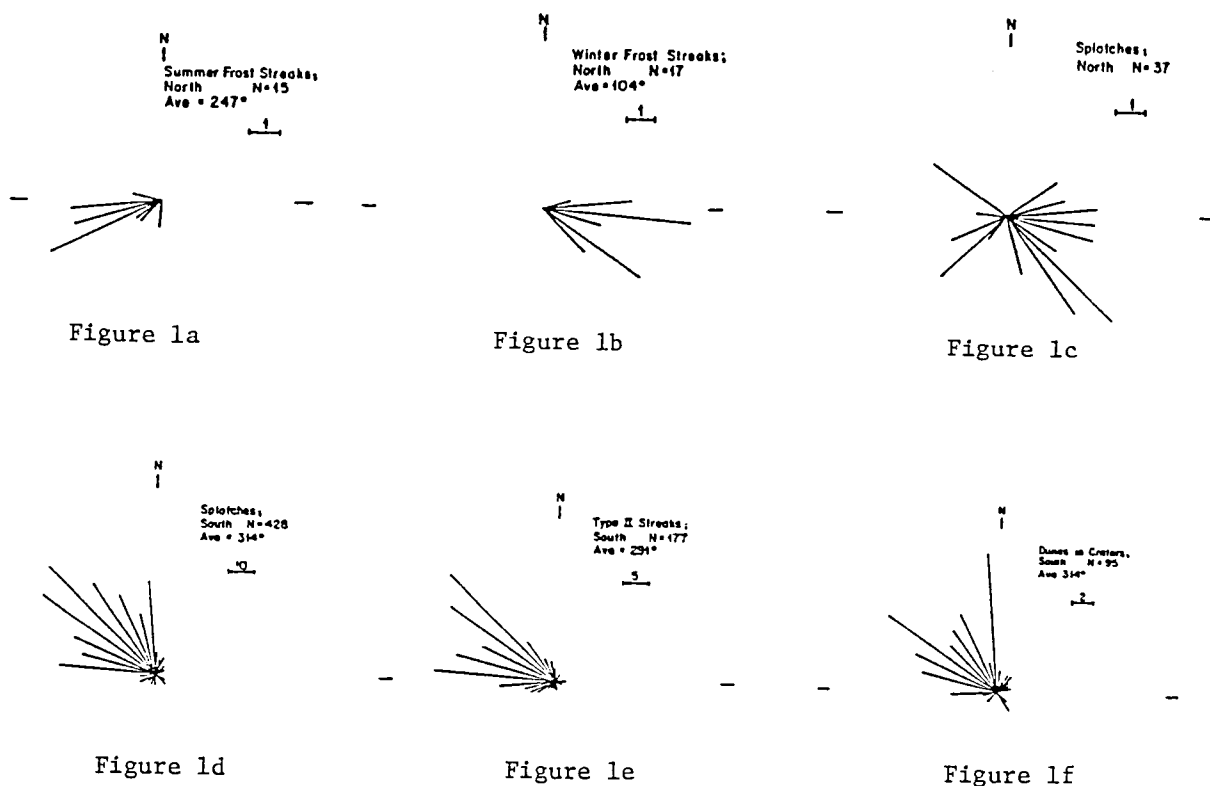


FIGURE 1. Wind directions from several different features in polar latitudes. N is number of features; Ave. is vector sum of directions (not given for 1 c because of scatter). Length scale is for number of samples in each 10° azimuth bin. Features at latitudes > 75° were recorded from all available images; those between 40-75° were taken from images with ranges > 15,000 km to insure even coverage. Dune orientations (1f) were obtained from best images, and include only those with a clear preferred orientation. Splotch directions recorded only for those with clear orientations (37 of 98 in north, 427 of 763 in south).

- 1a: Summer frost streaks in north polar region (edge of permanent cap)
- 1b: Winter frost streaks in north polar region (55-78°N)
- 1c: Crater splotches, 40-90°N. Prograde outward and retrograde outward dominate.
- 1d: Splotches in craters, 40-90°S.
- 1e: Streaks from splotches, 40-90°S.
- 1f: Dunes in craters, 40-90°S.

WIND STREAKS ON MARS: METEOROLOGICAL CONTROL OF OCCURRENCE AND MODE OF FORMATION. J. Veverka, P. Gierasch, and P. Thomas, Laboratory for Planetary Studies, Cornell University, Ithaca, New York 14853

Positive topographic features on Mars interact with windflow to produce either depositional or erosional streaks. Depositional streaks form largely during global dust storms in a zone 30°S to 30°N (Fig.1). Erosional streaks form after global dust storms (usually after  $L_S \sim 310^\circ$ ) mostly between 25°S and 40°S. There is no evidence that crater morphology determines the type of streak (erosional or depositional) formed. Since some craters form both kinds, a meteorological explanation is indicated. Atmospheric stability appears critical in determining whether erosion or deposition occurs downwind of obstacles. A stable atmosphere associated with the lower surface temperatures and higher atmospheric temperatures during dust storms should produce blocking of the mean flow by crater rims and 'wind shadowing' over distances adequate to form bright streaks by dust deposition. As the atmosphere clears after the dust storms, surface heating becomes more vigorous, stability is reduced, and blocking is not expected. Wind flow over obstacles can then increase surface stress downwind by enhanced eddy viscosity and/or wave phenomena, and encourages the formation of erosional streaks.

Local effects such as topography, small scale roughness, albedo contrast effects on winds, and frost precipitation/sublimation can cause exceptions to the general pattern discussed above. Especially important in this context are the erosional streaks formed by downslope winds in the Tharsis and Syrtis Major areas (Veverka et al., 1977; Thomas et al., 1980).

However, from a global point of view, the latitudinal concentration of the bright streaks (Fig. 1), their directions, and inferred times of formation are all consistent with the expected extent of the equatorial Hadley cell regime during dust storm conditions.

Outside of the + 30° latitude belt, the atmosphere may have the stability to form depositional streaks at the dust storm seasons, but the wind directions no longer have the coherence that exists within the equatorial Hadley cell, which we believe is necessary to the formation of discernable depositional bright streaks. Also, the dust content of winds at high northern latitudes at this season is low (Pollack et al., 1979).

The most likely reason why a belt of erosional dark streaks does not occur at northern latitudes is that wind velocities are too low at these latitudes at the appropriate season.

The concentration of erosional dark streaks in a narrow belt in the southern hemisphere may be understood in the following terms. At the appropriate season ( $L_S \sim 310^\circ$ ), wind velocities near 30°S are

increasing as one moves toward the pole; at the same time, the static stability of the atmosphere increases because one is moving away from the sub-solar latitude. Thus, it is only in a narrow belt--apparently near 30°S--that wind velocities are high enough, and the stability is low enough, for erosion behind craters to occur. There is good evidence that even under these circumstances the wind stress at these latitudes is barely enough to move dust; erosion is observed only downwind of craters and other topographic obstacles. Thus even in this latitude belt, in which conditions for erosion are optimized, the general winds are too weak to move dust unless accelerated by interaction with topography.

Atmospheric conditions under which depositional and erosional streaks form are summarized and contrasted in Table 1. It should be noted that the "dust storm" conditions described in the table refer to the late waning stages of a dust storm, when bright streaks are suspected to form (Thomas and Veverka, 1979). The generation of the dust storms clearly involve different conditions (cf. Pollack et al., 1979).

This research was supported by NASA grants NSG 7546 and NSG 7156.

#### REFERENCES

- Pollack, J. B., Colburn, D. S., Flasar, F. M., Kahn, R., Carlston, C. E., and Pidek, D. (1979). Properties and effects of dust particles suspended in the martian atmosphere, J. Geophys. Res., 84, 2929-2945.
- Thomas, P. and Veverka, J. (1979). Seasonal and secular variations of wind streaks on Mars: An analysis of Mariner 9 and Viking data. J. Geophys. Res., 84, 8131-8146.
- Thomas, P., Veverka, J., Lee, S. and Bloom, A. (1980). Classification of wind streaks on Mars. Icarus, in press.
- Veverka, J., Thomas, P. and Greeley, R. (1977). A study of variable features on Mars during the Viking Primary Mission. J. Geophys. Res., 82, 4167-4187.



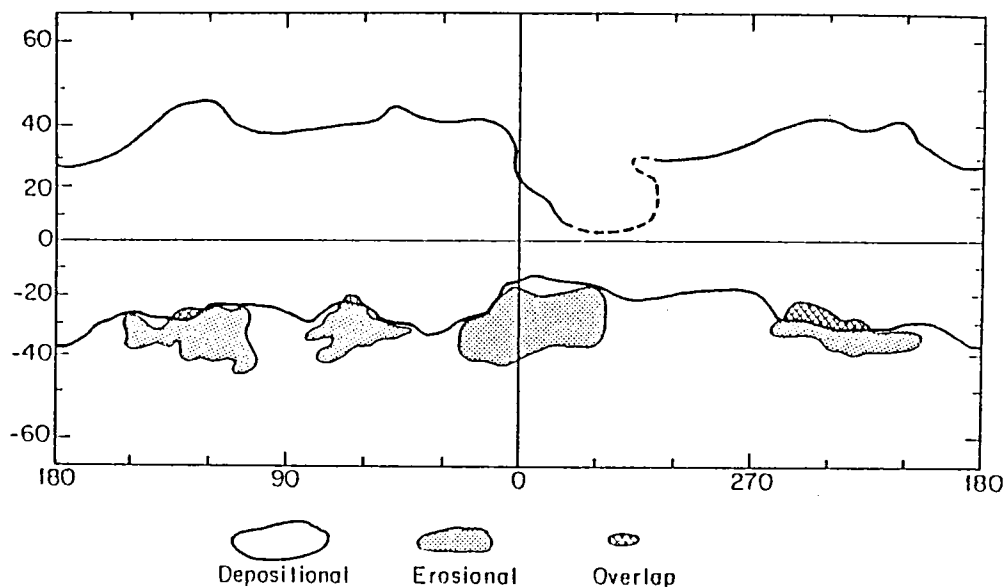


Figure 1. Location of bright depositional streaks (Type 1b), crater-related dark erosional streaks (Type 1d), and regions in which both types do occur. Most bright streaks occur within the equatorial belt bounded by the heavy lines. Dashed line shows uncertain boundary. The streak classification is that of Thomas *et al.* (1980).

TABLE 1

	Dust Storm		Non-Dust Storm	
	Equatorial	Non-Equatorial	Equatorial	Non-Equatorial
Conditions	1. Dust fallout 2. Stable atmosphere 3. Coherent wind directions	1. Less dust 2. Intermediate stability 3. Extremely variable wind directions	1. No dust fallout 2. Low wind velocity 3. Atmosphere unstable only near subsolar point	1. No dust fallout 2. High winds in southern hemisphere decreasing toward low latitudes 3. Atmosphere unstable near subsolar latitude
Bright Streaks	Blocking of flow allows deposition of dust forming bright streaks.	Lesser amounts of dust and variable wind direction prevent formation of bright streaks.	Lack of dust and lack of blocking prevent bright streak formation.	Lack of dust and highly unstable atmosphere (in places) prevents formation of bright streaks.
Dark Streaks	Dust fallout and stability of atmosphere prevent erosion. No dark streaks form.	Wind velocity too low and stability too high to promote erosional streak formation.	Low wind velocities and modestly stable atmosphere prevent erosion. No dark streaks form.	Winds high enough and atmosphere unstable enough for formation of erosional streaks, but only in small latitude band.

## GLOBAL DIGITAL MAP OF MARTIAN EOLIAN FEATURES

A. W. Ward, P. J. Helm, N. Witbeck, and M. Weisman, U.S. Geological Survey, Flagstaff, Arizona 86001

Martian eolian features such as light (including snow) and dark streaks, transverse and barchan dunes, pits and deflation hollows, yardangs and grooves, and sand sheets were mapped at 1:5 million scale from Mariner 9 and Viking orbiter images. These features were also digitized as part of the Mars Data Consortium. They were recorded with their geographic location,  $L_S$  observed, and orientation. We made comparisons of feature distribution vs. thermal inertia.

The dominant global pattern derived from eolian ephemeral features (streaks and dunes) is simple and orderly, reflecting a global wind regime rather than scattered local systems or even hemispheric patterns (1). The overall pattern is of east and northeast winds in the northern hemisphere (except near the pole) and east and southeast winds in the southern hemisphere. These orientations correspond to both Coriolis deflection and to wind directions at perihelion. Southern hemisphere storm winds moving toward the equator (with a Coriolis deflection) produce large features with southeast and east upwind orientations. Conversely, in the northern hemisphere, dominated by winter storm winds, large landforms trend upwind to the east and northeast. Only a few features (e.g., snow streaks) reflect winds of the opposite seasons, no doubt because these are weaker winds.

Two minor exceptions are found to the effective storm wind patterns. The first is in the low southern latitudes. Most light streaks in the region occur in Syria Planum and Sinai Planum, the south-sloping plateaus near Valles Marineris. Most of the streaks show northwest winds, which apparently flow downslope. Similarly oriented light streaks are found in Hesperia Planum, but here slope-controlled winds are less apparent.

Another exception is the wind features between  $80^\circ\text{N.}$  and about  $40^\circ\text{--}50^\circ\text{N.}$  Within this belt, most streaks and dunes trend counterclockwise.

With consideration given to north polar (2), south polar (3);(4), and global (5) models, the following theses are proposed: 1) The north polar dunes are currently active, but only during certain seasons (6). 2) The dunes nearest the pole (and perennial ice cap) record Coriolis-type winds, winds high in angular momentum controlled by equatorial winds descending at the pole. 3) Dunes well away from the pole show a counterclockwise trend, and may reflect winds without angular momentum, showing no Coriolis trend. They are likely storm winds locally generated from the thermal contrast produced by the sublimating ice cap, therefore springtime ( $L_S$  0-90) features. 4) Farther south ( $40^\circ\text{--}50^\circ\text{N.}$ ), where the trend returns to clockwise (NE wind) circulation, a significant new factor may be a high-pressure band, wherein more equatorial air masses high in angular momentum may be descending. Polar winds need not seemingly reverse again; in fact, few may reach this far south. A less likely alternative is that, due to the thinness of the seasonal cap at its southern limits, strong winds needed to override southwest-flowing polar trends may not develop.

Assuming the  $40^\circ\text{--}50^\circ\text{N.}$  downwelling cell controlling wind features in those latitudes, this model addresses the polar features and their associated winds. Cold air is always descending on and near the ice cap. Therefore, the dunes nearest the pole will show a dominantly Coriolis trend. In fact the dunes and streaks as far south as  $70^\circ\text{N.}$  may have a seasonal clockwise (NE wind) orientation, even when covered by the seasonal frost cap. However, as the

cap sublimates in spring, shrinking inwardly, strong thermal winds with CO<sub>2</sub> parcels deficient in angular momentum will create counterclockwise (NW) winds. Accordingly, dunes (especially the transverse dune slipfaces) exposed northward from 70°N. probably will be reversed. This reversal may continue poleward until the seasonal cap is removed and the dominant polar downwelling cell near the perennial cap is encountered.

The north polar dunes are active over a short period of time annually. ("Active" does not necessarily mean migrating, only changing.) The dunes farther away from the pole are active only when the seasonal frost cap encroaches or recedes. Those nearest the pole are active for a longer time because strong winds (of constant direction) are almost always present. None of the dunes are active when covered by the seasonal cap. The dunes are trapped between opposing, seasonal wind regimes, but physical movement in addition to slipface changes has not been recognized.

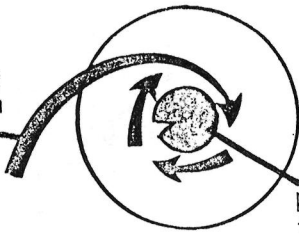
#### References:

- (1) Thomas, P., Veverka, J., Lee, S., and Bloom, A., Classification of wind streaks on Mars: *Icarus* (in press).
- (2) Tsoar, H., Greeley, R., and Peterfreund, A. R., 1979, Mars: The north polar sand sea and related wind patterns: *Jour. Geophys. Res.*, 84, 8167-8180.
- (3) French, R. G., and Gierasch, P. G., 1979, The martian polar vortex: *Jour. Geophys. Res.*, 84, 4634-4642.
- (4) Thomas, P., Veverka, J., and Campos-Marquett, R., 1979, Frost streaks in the south polar cap of Mars: *Jour. Geophys. Res.*, 84, 4621-4633.
- (5) Haberle, R. B., Leovy, C. B., and Pollack, J. B., 1979, A numerical model of the martian polar cap winds: *Icarus*, 39, 151-183.
- (6) McCauley, J. F., Breed, C. S., Grolier, M. J., and Collins, P., 1979, The eolian features of the north polar region of Mars: *NASA Conf. Pub.*, 2072, 55.

# Winds

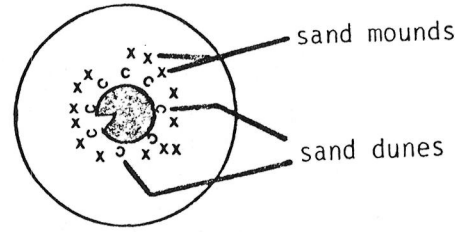
# Dunes

descending  
polar air from  
equator

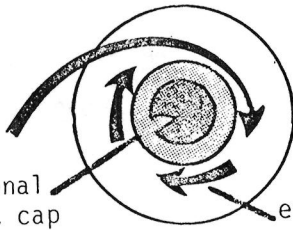


perennial  
ice cap

Summer

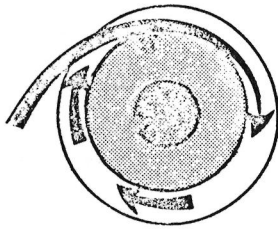
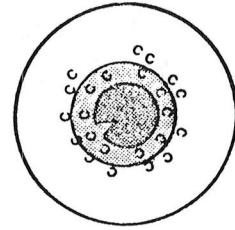


seasonal  
frost cap

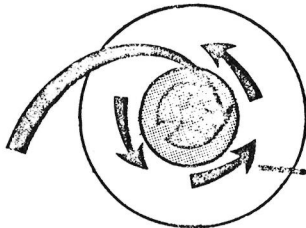
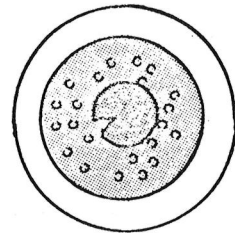


effective  
surface winds

Fall

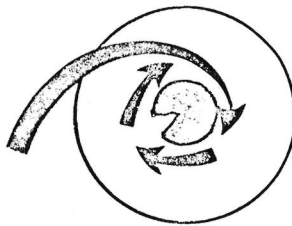
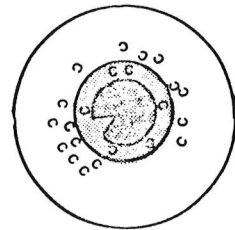


Winter

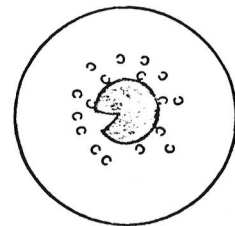


sublime  
winds

Spring



Summer



# EFFECT OF WIND ON SCARP EVOLUTION ON THE MARTIAN POLES

Howard, A. D., Department of Environmental Sciences, University of Virginia, Charlottesville, Virginia 22903.

Wind plays a major role in surface processes of the polar regions, as evidenced by dunes, frost streaks, and presumed wind scour features (1-7). The role of the wind in areas of layered deposits and perennial ice is less clear than in areas covered by dunes, because frost and dust deposition and ice ablation clearly play a major role in creating the polar cap landscape (8-11). Wind directions inferred from streaks in the frost cover and from grooves in the ice and layers were mapped from summer Viking imagery (Ls 130-170) and were compared with the orientation of the polar troughs. The frost streaks are the most common feature, and they are clearly superficial (and presumably ephemeral), for they do not appear in the early spring coverage (Ls 30-50) which revealed subtle undulations in the polar flats (9,11). Although most streaks show a clear wind alignment, the sense is ambiguous. However, a sufficient number are unambiguous to indicate that the strong north polar cap winds are southeasterlies.

Wind direction and scarp orientation were digitized and summarized by latitudinal and longitudinal boxes (Figs. 1,2). Wind directions were expressed by deviation from local south, and scarp orientations were expressed by the dip direction of the terraces slopes, and were likewise referenced to local south. The winds producing the frost streaks are nearly perpendicular to the strike of the scarps, although the scarps consistently face more southerly than the wind direction. The covariance of the wind and scarp orientations is in large part due to both being affected by the large-scale slope of the polar cap, although the deviation from southward orientation indicates a bias away from the regional slope (8, Fig. 2) for both the scarps and the wind. The bias in the wind is clearly due to the coriolis acceleration of wind moving away from the pole (5,12), but the cause of the scarp bias (leading to the spiral pattern) is less certain, since a southward-facing scarp receives most insolation, and scarps retreating due to ablation would tend to orient their strike perpendicular to the direction of most rapid retreat (8,10).

Because scarp orientations are intermediate between the wind direction and south, it may be that the scarp orientation is affected by both the wind and ablational processes. This possibility is enhanced by the clearly covariant change of mean scarp and wind orientations with latitude (Fig. 1). Variations in scarp and wind orientations over the north polar cap correlate with  $r=.65$ . Thus it appears that, neglecting ablation, the preferred orientation of the scarps is perpendicular to the strong polar winds.

The mode of interaction of the polar winds and the ablational processes forming

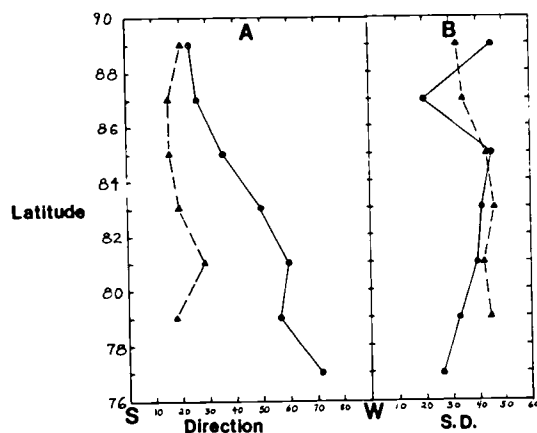


Fig. 1. Direction and standard deviation of wind direction (solid line) and scarp orientation (dashed line) on the north polar cap as a function of latitude.

the scarps and troughs is uncertain. Continued retreat of the scarps by ablation requires removal of the codeposited dust by the wind. At the large scale of the scarps and with their low relief (width of several kilometers and slopes of a few degrees) the interaction must be subtle. Perhaps the acceleration of the dense katabatic flows over the scarps enhances erosion, because this would be at a maximum for scarps oriented perpendicular to the wind. On a more speculative note, it may be that the low undulations on the polar cap, oriented generally parallel to the scarps and lying dominantly southward of them (11) may be due to an interaction between wind erosion and/or ablation with atmospheric gravity waves set up within the off-pole flow by the scarps and troughs. Such an interaction would explain the wavelike superimposition of undulations of different orientation (either due to primary interference among the waves or secondarily due to different waves for wind from slightly different directions).

Surface winds show strong katabatic convergence into several broad valleys (Borealis Chasma and smaller ones) at the margin of the polar cap in a manner similar to patterns in Antarctica and Greenland (2,3,13-15). It is likely that these valleys have been shaped over the long run by the enhanced erosional potential of the stronger convergent wind. The localization of the valleys at the polar cap edge suggests that carving of valleys requires a threshold combination of regional slope and a sufficient upslope "drainage" area.

Zones of wind streak convergence over the cap are in general also zones of scarp convergence (Fig. 3), with the valleys being a marked example. Wind-scoured features, such as scoop-like oversteepened scarps with associated dunes (16) are more common in areas of wind streak convergence. The orientation of the polar scarps often changes abruptly along the strike, often in a coordinated way among adjacent scarps. Some of the mutually parallel bends among scarps suggest that they may mark poorly formed divides and shallow valleys shaped by katabatic flows.

The zones of wind convergence shown in Fig. 3 generally show bimodal distribution of frost streak directions. One set indicates nearly southerly wind, probably katabatic winds off local slopes (minimal coriolis effects), which alternate with easterlies originating from the large-scale outflow off the polar caps. The bimodal wind pattern also tends to be associated with greater irregularity in scarp orientation and a greater number of oversteepened scarps, again suggesting strong influence of the wind in scarp development.

The streaks probably originate during the spring maximum of off-pole winds during maximum CO<sub>2</sub> ablation, which is consistent with the southeasterly flow (5,12). Strong, winter on-pole westerlies are also predicted in atmospheric circulation models (5,12). These seem to have little influence on the development of north polar cap frost streaks, but they may interact subtly with the polar topography by preferentially depositing frost on the northward-facing trough walls, enhancing trough migration rather than widening.

REFERENCES: (1) Cutts, J. A., J. Geophys. Res. 78, 4211 (1973); (2) Wolfe, R. W., Lunar and Planetary Sci. X, 1364 (1979); (3) Leach, J.H.J., NASA Conf. Publ. 2072, 52 (1979); (4) Botts, M.E., NASA TM 81979 (1979); (5) French, R.G. & Gierasch, P.J., J. Geophys. Res. 84 4634 (1979); (6) Thomas, P.J. et al., J. Geophys. Res. 84, 4621 (1979); (7) Cutts, J.A. et al., Science, 194, 1329 (1976); (8) Howard, A.D., Icarus, 34, 581 (1978); (9) Cutts, J.A. et al., J. Geophys. Res. 84, 2975 (1979); (10) Toon, O.B. et al., Icarus, in press; (11) Squyres, S.W., Icarus, 40, 244 (1979); (12) Haberle, R.M. et al., Icarus, 39, 151 (1979); (13) Tsoar, H. et al., J. Geophys. Res. 84, 8167 (1979);

- (14) Yoshino, M.M., Climate in a Small Area, U. Tokyo Press, 273 (1975);  
 (15) Schwerdtfeger, W., in Climates of the Polar Regions, S. Orvig (ed.),  
 Elsevier, 291 (1970); (16) Howard, A.D., NASA TM 80339, 103 (1979).

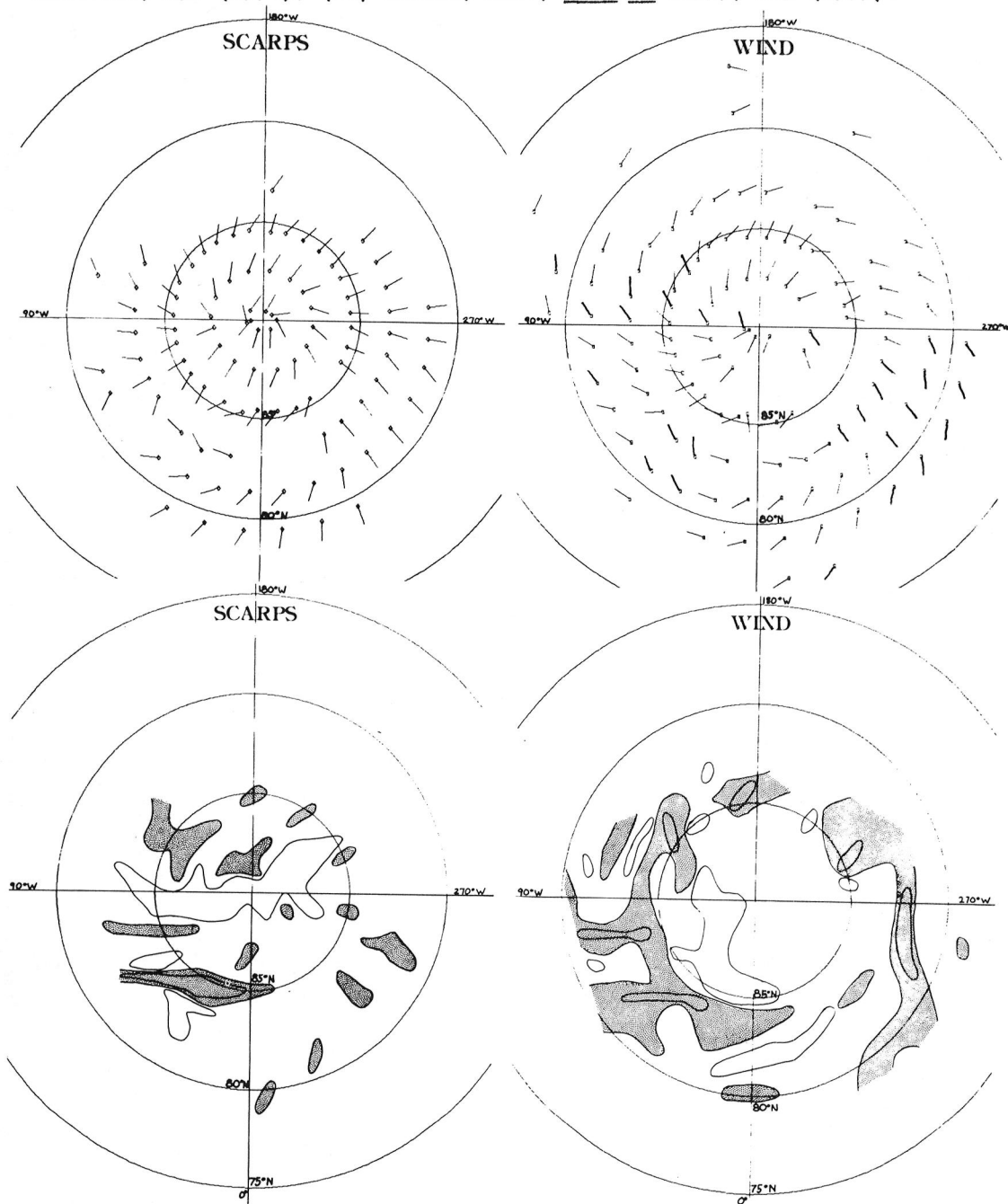


Fig. 2 (top). Mean wind and scarp orientations. Vectors centered over area covered. Fig 3 (bottom). Areas of convergence of scarp and wind vectors (patterned). Extra lines show areas of strong convergence or divergence.





## Chapter 7

### FLUVIAL, PERIGLACIAL AND OTHER PROCESSES OF LANDFORM DEVELOPMENT



## MUDFLOW STUDIES ON MOUNT ST. HELENS

Fink, Jonathan and Ronald Greeley, Department of Geology, Arizona State University, Tempe, AZ 85281

Mudflows associated with the recent eruptions of Mount St. Helens provide unusual opportunities to study the mobilization and subsequent movement of dry or damp materials when they are rapidly mixed with groundwater and/or ice. Such processes may be similar to those occurring during meteor impact into a volatile-rich planetary surface, formation of martian patera, or modification of features such as the Olympus Mons aureole. Here we report on rheological and structural studies of several mudflows formed at or near the time of the eruptions on May 18, May 25, and June 12, 1980 (Fink et al., in press).

Field work was conducted in July and September, 1980, primarily along a branch of Pine Creek which flows from a glacier, between several blocky andesite flows, to a broad area of confluence with the Muddy River, all on the southeast side of Mount St. Helens (Fig. 1). Analysis of photographs taken throughout the early eruptive cycle indicates that the initial mudflows formed on May 18 when thick ash deposits on the steep upper slopes of the volcano became saturated with water derived from the melting of the glacier. The flows cascaded down pre-existing channels, picking up boulders up to 3 m in diameter and depositing them in outwash areas several kilometers downstream. Mudflows formed during the smaller May 25 and June 12 eruptions were much less voluminous than those of May 18.

Smaller mudflows continued to form throughout the summer as glacial meltwater soaked into nearby ash deposits, causing their strength to decrease below that required for slope stability. Slope failure was followed by mixing of the ash/pumice block/water slurry as it proceeded downslope. Many of these small flows (depth  $\leq 1$  meter) were observed and one was recorded on videotape. Depending upon the water content, these flows ranged from laminar to turbulent. Surge waves formed and moved through the channel periodically.

Deposits left by different mudflows had distinctly different textures and appearance. One of our aims was to characterize the material properties both of the deposits, which consist of dacitic ash, rounded lapilli-sized pumice fragments, andesite blocks up to 3 m in diameter, and water, and of the flows when they were active. The flows are modelled as Bingham materials having yield strengths and plastic viscosities, which is appropriate for slurries of fine-grained materials (Caldwell and Babbitt, 1941). Similarities with deposits left by basalt flows, which also have Bingham behavior (Hulme, 1974) include levees, concentric ridges, cracks, and lobate margins (Figure 2).

Rheological properties of the mudflows in Pine Creek were determined using techniques originally applied to debris flow deposits (Johnson, 1970). Yield strengths and velocities of the flows were calculated based on the geometry of their deposits. Field evidence indicated that deposition occurred during a laminar flow regime, so the modified Reynold's number,



*FIGURE 1. West branch of Pine Creek showing deposits from several mudflows. Mount St. Helens in background.*

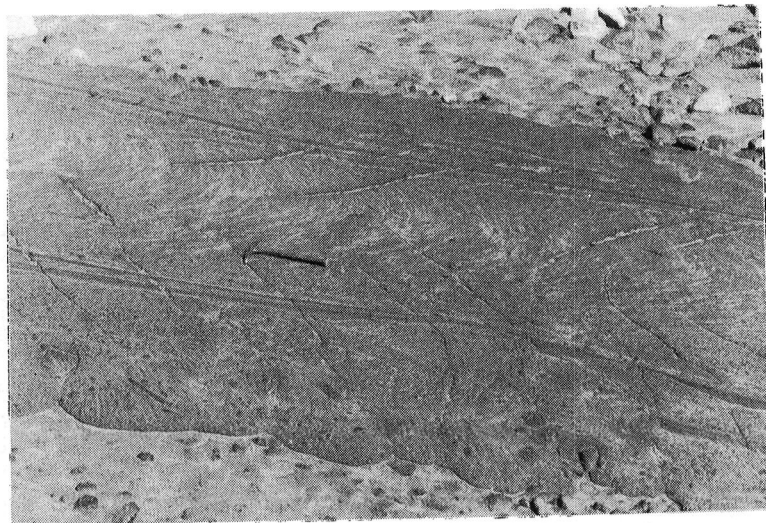


*FIGURE 2. Mudflow stream showing features commonly found on basaltic lava flows: levees, compressional ridges, extensional cracks, and lobate margins. Flow moved from left to right.*

$$R_m = \frac{2}{\frac{\eta}{\rho V H} + \frac{\tau}{\rho V^2}}$$

(where  $\eta$  = plastic viscosity,  $\tau$  = yield strength,  $\rho$  = density,  $V$  = flow velocity, and  $H$  = flow depth) must have been less than 2000 (Moore and Schaber, 1975). Using measured and calculated values of yield strength, velocity, density and flow depth, this relation allowed us to place an upper bound on the plastic viscosity of the active flows. Calculated yield strengths of 1100, 1000 and 400 Pa, mean flow velocities of 10 to 31 m/s, volumetric flow rates of 300 to 3400 m<sup>3</sup>/s and plastic viscosities of 20 to 320 Pa-s (200 to 3200 poises) all compare favorably with measured and estimated values cited in the literature. These values may be used in future scaling of impact experiments into Bingham targets which strive to simulate the formation of rampart craters.

Laboratory studies are currently in progress to determine how the cohesion of ash deposits varies with water content. Results will be applied to the problems of slope stability and drainage development on steep ash-covered terrains. This information may also suggest ways to determine the presence of large areas of ash deposits photogeologically.

#### REFERENCES

- Caldwell, D. H. and Babbitt, H. E. (1941) Flow of muds, sludges, and suspensions in circular pipe. *Indust. Eng. Chem.* 33, 249-256.
- Fink, J. H., Malin, M. C. D'Alli, R. E. and Greeley, R., Rheological properties of mudflows associated with the Spring 1980 eruptions of Mount St. Helens Volcano, Washington, *Geophysical Research Letters*, in press.
- Hulme, G. (1974) The interpretation of lava flow morphology. *Geophys. J. Roy. Astron. Soc.* 39, 361-383.
- Johnson, A. M. (1970) *Physical Processes in Geology*. Freeman, Cooper and Co., San Francisco, 577 pp.
- Moore, H. J. and G. G. Schaber (1975) An estimate of the yield strength of the Imbrium flows. *Proc. Lunar Sci. Conf.* 6th, 101-118.

## FLUVIAL HISTORY OF MARS

Michael H. Carr, U.S. Geological Survey, Menlo Park, CA 94025

As part of a program to outline the fluvial history of Mars, all martian channels visible at a resolution of 150-300 m have been mapped at a scale of 1:5,000,000. The runoff channels have been digitized and placed in the Mars Consortium format (figure 1) to permit correlations with other planet-wide data such as color, elevation, and albedo. In addition, crater counts have been made on dissected and undissected terrains, and on all the large outflow channels.

As anticipated, nearly all runoff channels are in the densely cratered terrain, both in the crater-saturated areas and in the intercrater plains. Channels in the oldest parts of this terrain have a wide range in preservation, from those that are barely visible to some that are relatively fresh appearing. Runoff channels in the intercrater plains all tend to be crisp in appearance. Plains outside the densely cratered terrain are almost completely devoid of runoff channels although they are dissected by outflow channels. Possible exceptions are some tributaries to Valles Marineris. The pattern of dissection of the densely cratered terrain (figure 2) suggests an immature drainage system. Interfluves are undissected, drainage basins are widely spaced, and most tributary systems are relatively short (<300 km). It appears that runoff was not sufficiently sustained for single streams to develop and dominate drainage over large areas. Many stream characteristics, such as cirque-like terminations to tributaries, undissected interfluves, and trunk streams which end within craters, suggest origin by sapping, but surface runoff cannot be ruled out. Restriction of runoff channels to the densely cratered terrain suggests that the runoff channels are ancient. A possible alternative is that the old terrains are more erodable. Supporting the "old channel" hypothesis are the intercrater plains which resemble other plains in every respect except age. The dissection of the intercrater plains and the lack of dissection of the younger plains suggests that the channels did indeed form only very early in Mars' history. The youngest extensively dissected unit is the intercrater plains, and this has around 3300 craters  $> 1 \text{ km}/10^6 \text{ km}^2$  (figure 3), suggesting an age in excess of 3.5 billion years. Apparently the conditions under which runoff channels could form were not sustained after this time. Even previous to this time, the rate of formation must have been extremely slow or episodic for mature drainage systems never developed. Preliminary correlation of the location of runoff channels with other surface characteristics suggests that the runoff channels are preferentially located in areas with low albedo, low pre-dawn temperatures, and elevations between 2.5 and 5 km.

Outflow channels can be divided into two broad categories, those that scour broad regions (unconfined) and those that are restricted to discrete channels (confined). Most unconfined channels occur to the north and east of the canyons where the transition from canyons to chaos to outflow channel is repeated several times. The regions of Chryse scoured by the



Figure 1.

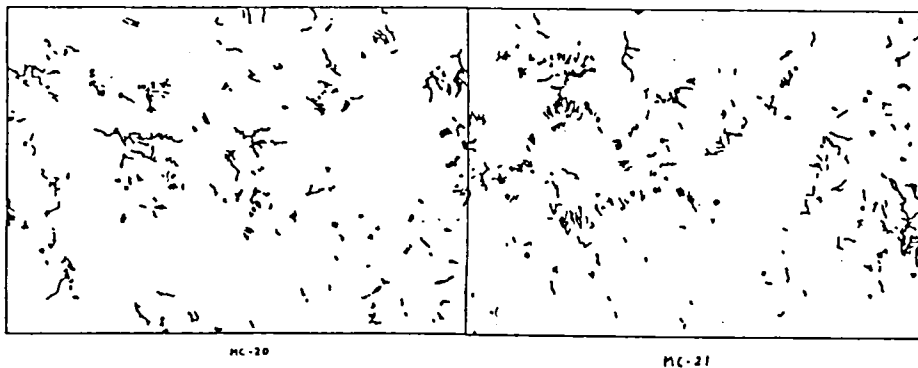


Figure 2.

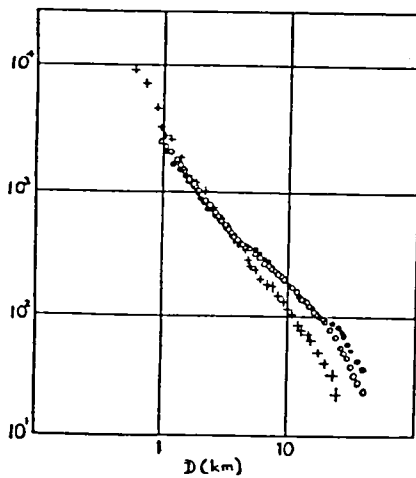


Figure 3.

Figure 1. Distribution of runoff channels between  $\pm 65^\circ$ . Outlined areas have no data.

Figure 2. Samples of individual MC quads showing distribution of runoff channels.

Figure 3. Counts of craters on dissected (closed circles) and undissected (open circles) old cratered terrain are identical. The counts for the inter-crater plains (crosses) represent the youngest unit on Mars that is extensively dissected by runoff channels.

Kasei, Maja, Tiu, Simud and Ares Valles have 1,500 to 2,500 craters  $> 1 \text{ km} / 10^6 \text{ km}^2$ , placing their formation in mid-martian history. Other unconfined channels are found in Amazonis and Memnonia. Mangala Vallis in Memnonia has 1200-1400 craters  $> 1 \text{ km} / 10^6 \text{ km}^2$ , making it one of the youngest outflow channels. It starts from a graben, in contrast to the chaos origin of most of the circum-Chryse channels. Within the scoured regions of Kasei Vallis and Ares Vallis are some deep channels with flat, sparsely cratered floors. Ghost craters on the floors show that they have been partly filled, probably by non-fluvial processes after formation of the main channel. Densities of the larger "ghost craters" are identical to the densities on the adjacent scoured regions; the densities of smaller craters are less within the inner channel as a result of partial infilling.

Most confined outflow channels occur northwest of Elysium and around the Hellas basin. In both areas the channels start full born adjacent to volcanoes. At the time of writing, these channels had not been systematically dated.

Fretted channels are common in both hemispheres between the  $40^\circ$  and  $55^\circ$  latitudes. In these latitude belts, mass wasting features are common around features with any significant relief. Mass wasting appears also to have played a major role in the formation of fretted channels. Most contain features that suggest flow of debris away from the channel walls, then down the valleys. By this process former runoff channels have been widened to form the presently observed flat-floored fretted channels whose walls commonly intersect craters as though by escarpment retreat. Crater counts in these channels thus date the mass wasting processes which may still be continuing.



### Nirgal Vallis

Victor R. Baker, Dept. Geological Sciences, University of Texas at Austin, Austin, Texas 78712

The discovery of branching, coalescing valley networks on Mars, first depicted on Mariner 9 images, led to immediate speculation that these were analogous features to terrestrial drainage networks. The paleoclimatic implications of surface runoff from rainfall are profound for Mars, but in retrospect, this conclusion was premature. Recent monographs on the channels and valleys of Mars (1, 2) conclude that Martian network systems formed by basal sapping in which ground water acted to undermine support in layered rocks. The networks developed by headward extension and bifurcation of the seepage zones, such as occur in valleys of the Colorado Plateau (3, 4).

Nirgal Vallis (Figures 1 and 2) provides a striking illustration of a Martian valley system that probably developed by a sapping mechanism. The western half (Figure 1) displays a tributary pattern, while the eastern half is a tightly sinuous, deeply intrenched valley (Figure 2). The valley debouches into a very wide, slightly sinuous trough named "Uzboi Vallis". Another sinuous channel-like feature lies 80 km northwest of Nirgal Vallis. It flows about 100 km along a similar trend to Nirgal before disappearing abruptly along a zone of structural lineaments. Nirgal Vallis has a total length of about 700 km.

Nirgal Vallis is developed in a cratered plateau upland with Uzboi Vallis acting as a baselevel for the valley system. Wrinkle ridges on the cratered plateau upland suggest that mare-like basalts occur near the surface. Probably the basalt flows are underlain by impact breccia of the megaregolith. This is implied by the partially buried craters of the cratered plateau and by the exposure of probable megaregolith in the lower portions of canyon walls in the Valles Marineris, about 500 km to the north.

Studies of Nirgal from Mariner 9 imagery produced the suggestion that the valley developed through partial melting in the Martian permafrost zone (5), that it was a large tension fracture (6), that it was analogous to a meandering river (7), and that it formed by sapping (8). One remarkable study even employed empirical relationships from terrestrial rivers to calculate expected mean annual discharges of a terrestrial river with comparable dimensions to Nirgal Vallis (7). This approach is highly suspect because of the use of valley width, rather than true fluid-channel width, in the various empirical equations.

The geomorphic maps of Nirgal Vallis (Figures 1 and 2) were compiled from high-resolution Viking imagery. The images show that incision was relatively shallow upstream. Tributaries are very short and terminate at steep-walled, cusped valley heads. Such valleys are sometimes called "amphitheater-headed valleys", indicating a similarity to classical theaters because of their flat floors and steep surrounding slopes. Cirques, which form at the heads of glaciated valleys are a terrestrial example, but amphitheater-headed valleys are also well known in tropical landscapes, such as Hawaii (9, 10). The terminology is not precise, because a true amphitheater would be a closed oval, not a feature open at one end. A more appropriate term would be "theater-headed valley" (11).

The so-called "meandering reach" of Nirgal Vallis is considerably wider than the 2-km average upvalley width. Width in this reach averages 5 km. The valley is deeply incised, and short, stubby tributaries occur along the steep valley walls. The downstream portion of Nirgal Vallis has a valley width of up to 15 km, and it is clear that much of the valley widening has occurred by landsliding. A hanging

valley in this section shows that entrenchment was favored on one local branch of the valley system. The hanging valley is highly degraded in appearance, while the main valley shows more pristine wall morphology.

Nirgal Vallis is clearly a very different kind of valley from the common dendritic valleys of fluvial landscapes on Earth. On Mars it probably represents a relatively well-preserved end member of a spectrum of elongate valley types that are deeply incised and have theater-headed tributaries (1). The lack of dissection of adjacent uplands by these valley systems, the relatively short accordant tributaries with width and depth equal to the main trunk channels, and various morphometric properties provide strong arguments against the formation of such valleys by rainfall and surface runoff (3).

**References.** (1) Pieri D. (1979) Geomorphology of Martian Valleys: Doctoral Thesis, Cornell Univ., (2) Baker V. R. (in press) The Channels of Mars: The University of Texas Press, (3) Pieri D., Malin M. C., and Laity J. E. (1980) N.A.S.A. Tech. Memo. 81776, 292-294, (4) Baker V. R. (1980) N.A.S.A. Tech. Memo 81776, 286-288, (5) Milton D. J. (1973) J. Geophys. Res. 78, 4037-4047. (6) Schumm S. A. (1974) Icarus 22, 371-384, (7) Weihaupt J. G. (1974) J. Geophys. Res. 79, 2073-2076. (8) Sharp R. P. and Malin M. C. (1975) Geol. Soc. America Bull. 86, 593-609. (9) Hinds N. E. A. (1925) Jour. Geology 33, 816-818, (10) Wentworth C. K. (1928) Jour. Geology 36, 385-410, (11) Bloom A. (1980) written communication.

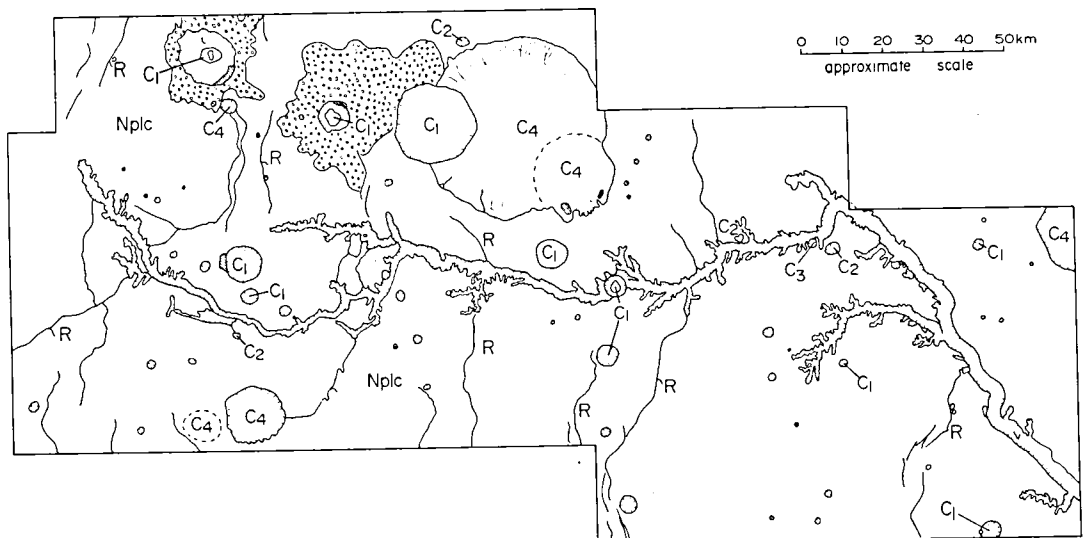


Figure 1. Geomorphic map of upper Nirgal Vallis. The explanation for mapping symbols is given in Figure 2.

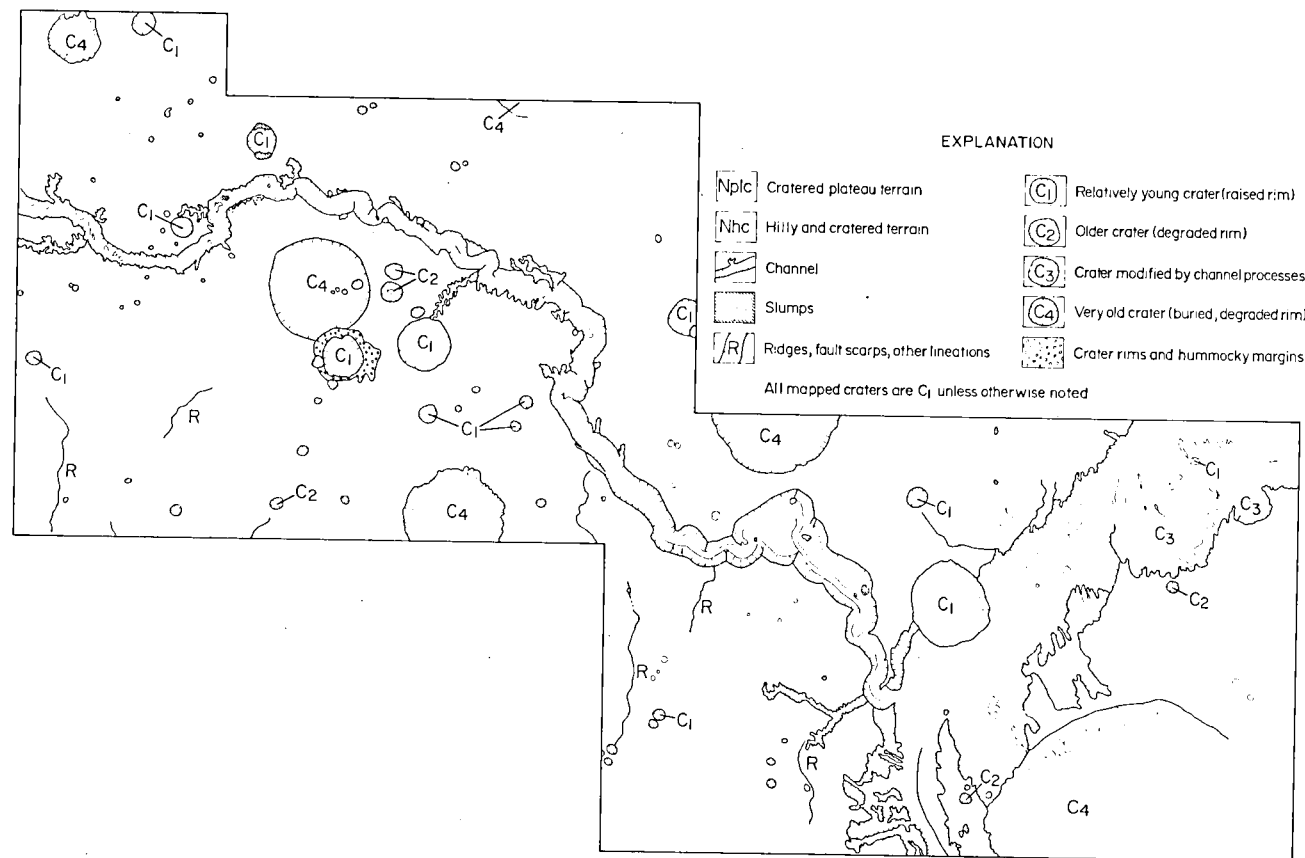


Figure 2. Detailed geomorphic map of the eastern portion of Nirgal Vallis.

## LANDSCAPE EVOLUTION, CENTRAL ARCTIC SLOPE, ALASKA: AN ANALOG FOR PROXIMAL MARTIAN OUTFLOW CHANNELS.

Jon C. Boothroyd, Department of Geology, University of Rhode Island  
Kingston, RI 02881; Barry S. Timson, The Mahoosuc Corporation  
Augusta, ME 03240

Continued detailed geomorphic mapping of the Central Arctic Slope region of northern Alaska, coupled with field studies, has led to the identification of a complex set of geologic processes active in the area. The method of study is to utilize Landsat imagery at a scale of 1:1,000,000 (Fig. 1) to identify terrain that has similar appearing features to selected areas of proximal outflow channels and chaotic regions on Mars. The Landsat images are then enlarged to a scale of 1:250,000 and geomorphic maps constructed (see Boothroyd and Timson, 1980). U-2 photography (scale 1:125,000) is used to further refine the maps (Fig. 2). Selected accessible areas are field-checked to study the geologic processes responsible for the geomorphic features (Fig. 3).

Figure 2 is a geomorphic map of the Franklin Bluffs area of the Arctic Slope; Figure 1 gives the general location, and Figure 3 a low-level aerial view across the southwest corner of the Bluffs. The first-order remnant and channel topography was carved by various courses of the Sagvanirktok and other rivers during Quaternary time. The Sag fluvial system ( $F_A$ ) is still actively cutting the Franklin Bluffs remnant. Other portions of the Sag channel system are inactive ( $F_I$ ) or have been recently abandoned ( $F_B$ ). Relict fluvial systems exist as terraces elevated 10-30 meters above the active river. Bar and channel topography is still identifiable in places ( $E_R$ ), but much of this terrain contains a lake/pond plain ( $E_P$ ) of wind-aligned lakes developed in the active layer of the continuous permafrost. Immediately adjacent to the terrace scarp is an eolian levee ( $E_L$ ) composed of silt and fine sand derived from the active fluvial system. Still older surfaces, such as the upper surface of the Franklin Bluffs remnant, are low-relief plains dominated by solifluction processes ( $C_{SI}$ ). Younger, moderate-relief slopes are also dominated by solifluction processes ( $C_{SM}$ ); whereas steep slopes are subject to ground-ice melting, collapse, and debris flow ( $C_D$ ).

The topography discussed above, as well as other areas adjacent to the Brooks Range subject to glacial processes, appear similar to parts of Martian proximal out-flow channels in, and adjacent to, chaotic terrain. Some specific areas are: Capri Chasma (MC-19) (5S,35W); Hydasois Chaos/Tiu Vallis (MC-11) (3N,27W) (5N,30W); and Iani Chaos/Ares Vallis (MC-11) (2N, 18W).

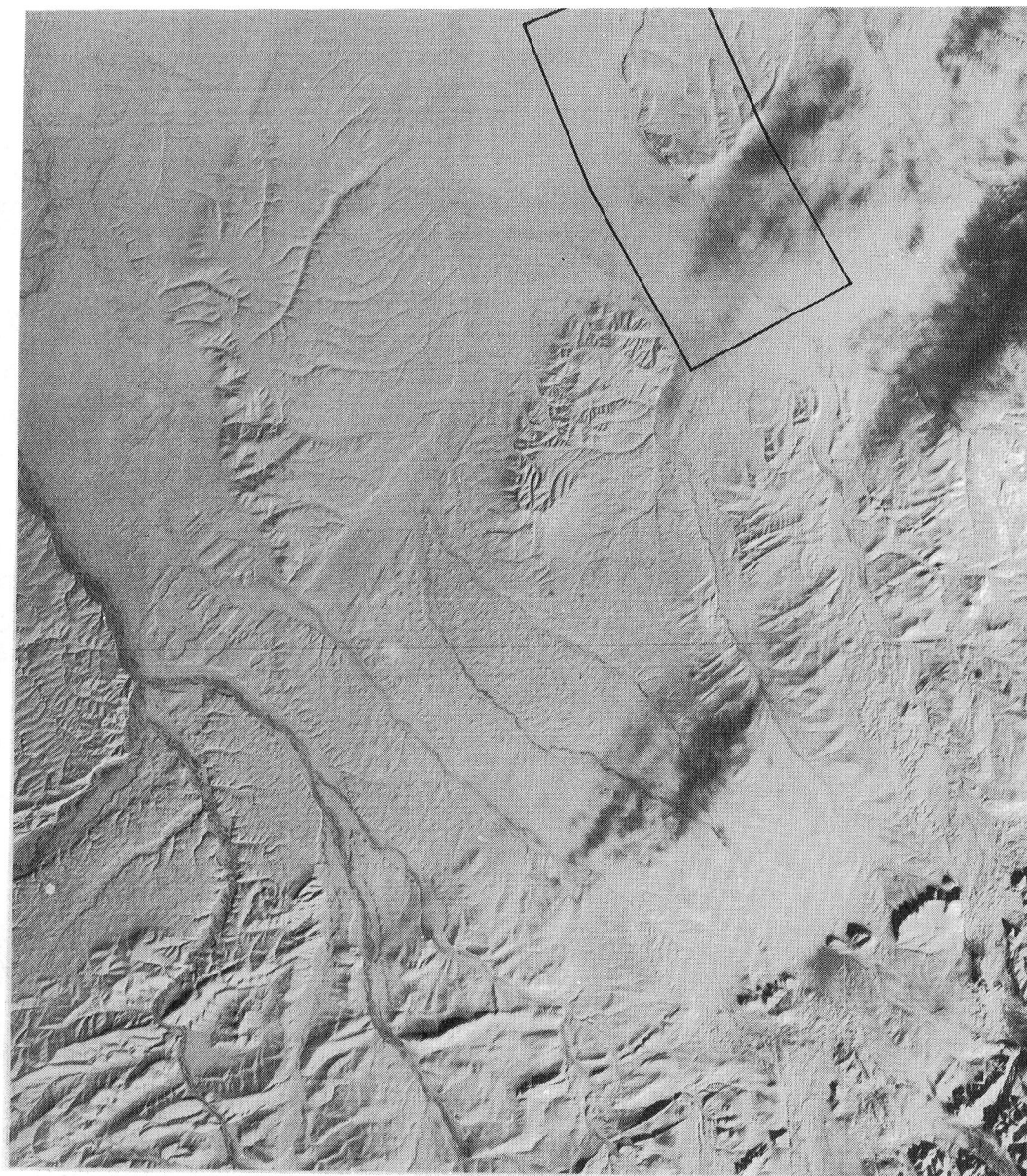


Figure 1. Landsat Band 5 image of Central Arctic Slope, Alaska.  
Box encloses map area of Figure 2. Scene E-1217-21235-501,  
Feb. 25, 1973, Scale: 1:1,000,000.

# GEOLOGIC ENVIRONMENTS FRANKLIN BLUFFS AREA

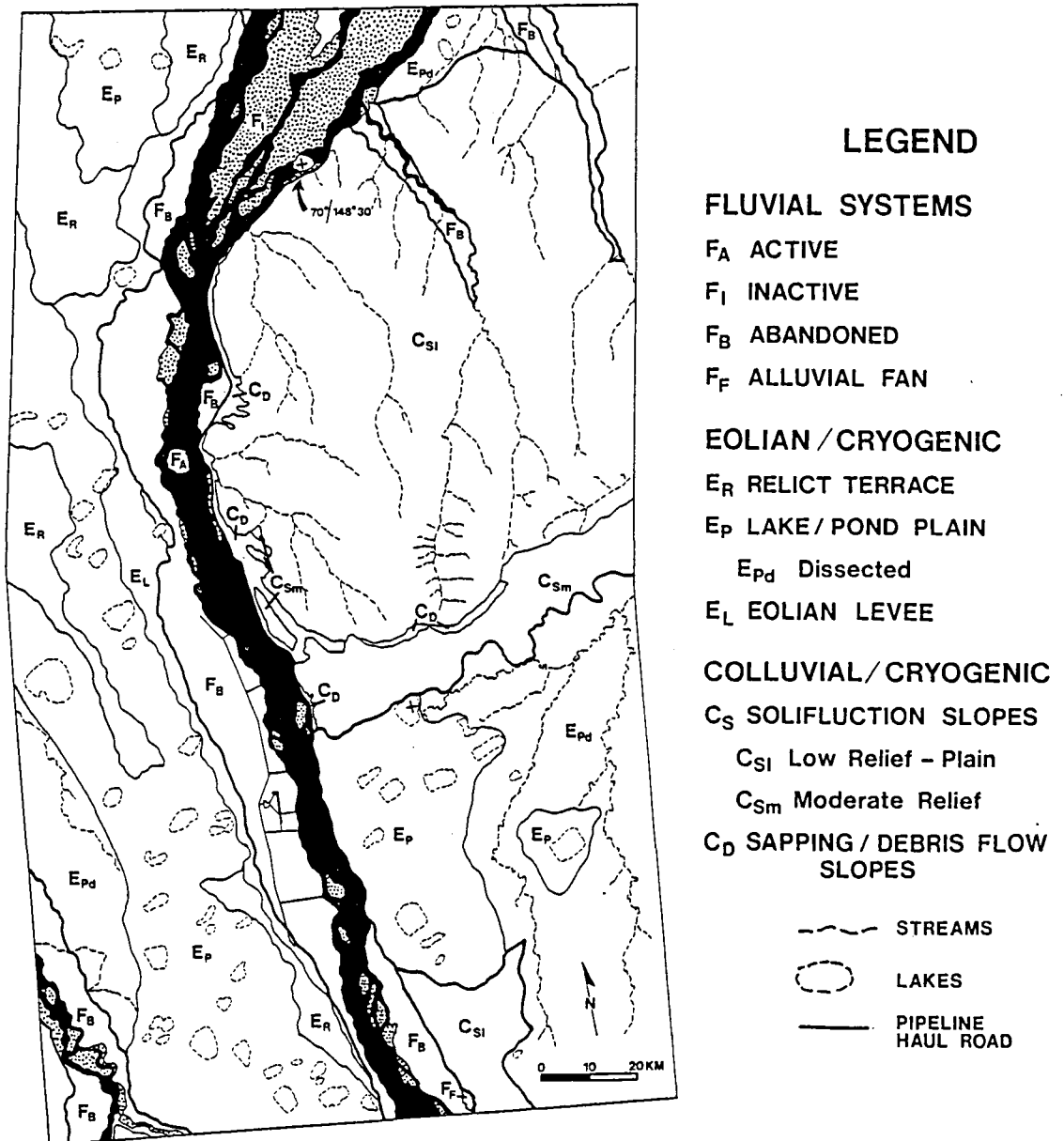


FIGURE 2

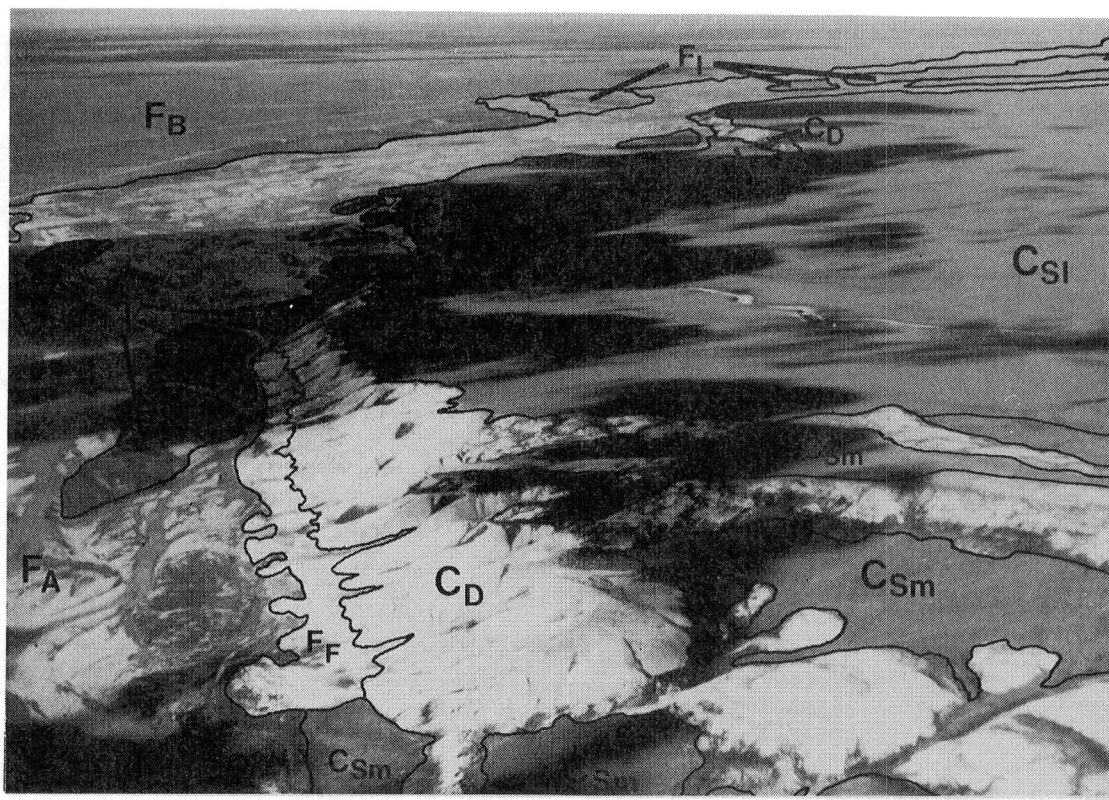


Figure 3. Low-level aerial view northwest over Franklin Bluffs erosional remnant. Symbols are keyed to Figure 2 explanation.

#### REFERENCE

Boothroyd, J.C. and Timson, B.S., 1980, Fluvial and glacial processes, Central Arctic Slope Alaska: Reports of Planetary Geology Program, 1979-1980, NASA Tech. Memo. 81776, p. 277-280.

## NETWORK PATTERNS AS RELATED TO FORMATION MECHANISMS OF MARTIAN VALLEYS

David Pieri, Jet Propulsion Laboratory, California Institute of Technology, Pasadena, CA 91103

Recent work by the author on the morphology and development of martian valley systems has emphasized the dissimilarity in morphology and planimetric pattern between them and terrestrial pluvial-fluvial systems (e.g. see Pieri, 1979; 1980a). To better illustrate the basis for these comparisons, it is useful to discuss prototype examples of patterns potentially generated by various processes. In this context the discussion is limited to very elementary examples of three fundamental modes of network development: (1) surface runoff from rainfall, (2) surface runoff from a restricted headward source region, and (3) headward-progressing basal sapping. The presence of any of these styles of network formation has very different implications regarding constraints on climatic models and upon the source location and mode of interaction of water with the martian surface.

Figure 1a represents a typical evolved dendritic network, and Figure 1b illustrates the path of fluid through the system. The emphasis is on interfluvial drainage throughout the system, indicative of a source of fluid which is areally uniform over the characteristic timescale for erosional modification of the network pattern. These systems are characterized by a wide range of tributary junction angles which vary systematically (Pieri, 1980b).

Figure 2a represents a network formed by introduction of fluid at a headward source region. Figure 2b shows the fluid paths. Junction angles are very low and major trunk intersections tend to occur near the mouth. Network patterns are typically parallel or digitate. Interfluvial drainage is typically absent. Good terrestrial examples of this type of network occur on the new Mt. St. Helens ash sheets (Malin, 1980).

Figure 3a is a schematic sketch of canyons formed by basal sapping (e.g. Colorado Plateau, Laity, 1981; Laity *et al.*, 1980). Figure 3b is another schematic illustrating fluid movement below a resistant and undermined layer. Fluid movement in this mode occurs in the subsurface and tends to be facilitated by structure (dotted lines in sketch). Often, angular networks with chaotic junction angle systematics are observed. Valleys typically display amphitheater terminations.

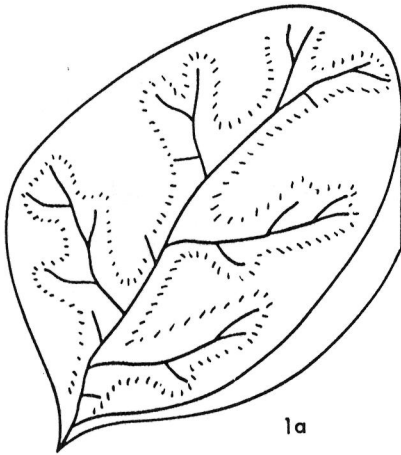
Dendritic systems have not been seen on Mars, whereas parallel and digitate networks with little apparent interfluvial erosion are common, as are deep angular networks with cusped terminations. While more detailed studies of the oldest valley systems may yield insights into how the groundwater system was originally charged, perhaps by rainfall, there is as yet no compelling evidence of erosion by rainfall on Mars.



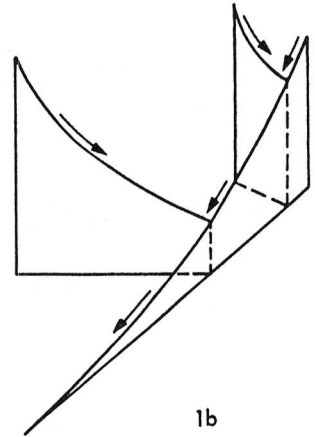
#### REFERENCES:

- Malin, M.C. (1980), manuscript in preparation.
- Laity, J.E. (1981), Groundwater sapping in the Colorado plateau, this volume.
- Laity, J.E., D.C. Pieri, and M.C. Malin, (1980), Sapping processes in tributary valley systems, p. 295, in Reports of Planetary Geology Program, 1979-1980, NASA TM-81776, NASA, Wash. D.C.
- Pieri, D.C. (1979), Geomorphology of martian valleys, Ph.D. Thesis, Cornell University, Ithaca, N.Y., 280 pgs.
- Pieri, D.C. (1980a), Junction angles in drainage networks, to be submitted to Jour. of Geology.
- Pieri, D.C. (1980b), Martian valleys: Morphology, distribution, age, and origin, Science, in press.

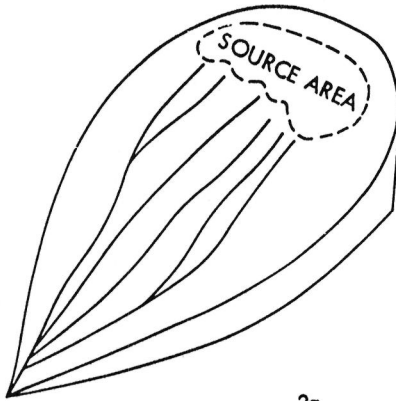
This research was carried out under NASA Contract 7-100.



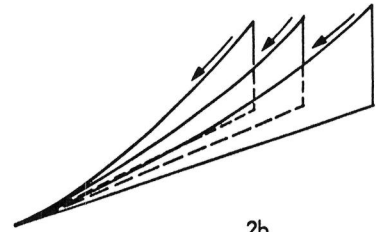
1a



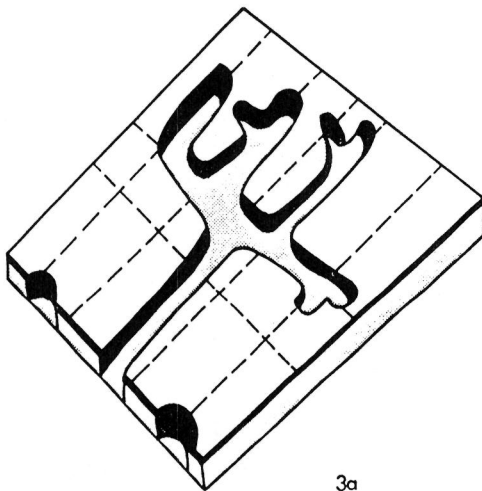
1b



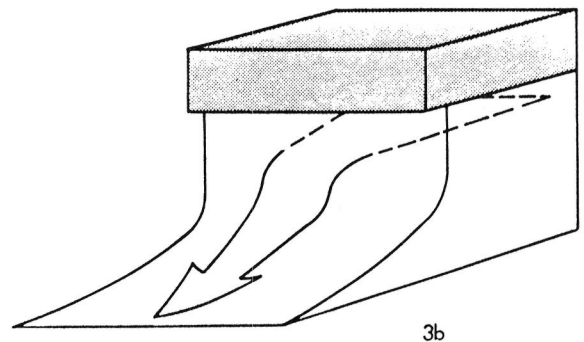
2a



2b



3a



3b

Low Energy Cavitation in Martian Floods, David Pieri,  
 Jet Propulsion Laboratory, Pasadena, California 91103 and  
 Carl Sagan, Cornell University, Ithaca, New York, 14853

Cavitation is the phenomenon of bubble formation and nearly instantaneous collapse associated with extreme erosive damage by a flowing fluid on obstacles in the flow. Cavitation bubbles occur when the fluid pressure is reduced dynamically below its vapor pressure. On the Earth, cavitation under natural conditions is an interesting but relatively rare phenomenon. It has been suggested as a mechanism for pothole initiation in glacial meltwater streams (1), (4). Baker (2) suggested cavitation as an active erosion mechanism for the channeled Scabland floods. Subsequently, it has been suggested (3), (5) that cavitation would be an active erosion process on Mars for catastrophic flooding under the present low pressure atmospheric conditions. A rough calculation, however, of cavitation bubble maximum collapse pressure (6) shows that under present martian atmospheric conditions, even though the velocity to initiate cavitation is far lower than the terrestrial value due to the lower atmospheric pressure (3) (5), cavitation collapse pressures are far lower than in terrestrial flows of comparable discharge. Thus, a low energy, and probably less erosive form of cavitation would be associated with breakout flooding on Mars under most conditions.

Cavitation bubble pressure is calculated from the simple equation

$$P_R = C' (\zeta g D + \rho_o) \frac{R_o^3}{R^3} \quad (1)$$

where  $P_R$  is the pressure generated by collapse,  $\rho_o$  is the atmospheric pressure, and  $\zeta g D$  is the hydrostatic pressure for a fluid of density  $\zeta$  and depth  $D$  under gravitational acceleration  $g$ .  $R_o$  is the original bubble diameter and  $R$  is the bubble diameter when collapse is nearly complete.  $C'$  is fluid dependent and equals 0.20 (cgs units) (7) for water. The effective pressure transmitted to an obstacle,  $P_r'$  is usually about 0.005  $P_r$  at about two bubble radii (7) and this value is used here. Figure (1) shows  $P_r$  and  $P_r'$  as a function of depth for both Earth and Mars, for  $R_o/R = 100$  (cited in (7) as a reasonable value). Values of yield strengths for various materials are shown and are referenced to the right ( $P_r'$ ) abscissa. Though  $P_r$  and  $P_r'$  are approximate only, from figure 1 it is clear that martian cavitation bubble pressure comes into the range of natural terrestrial cavitation pressure only for uncovered flows deeper than 27 meters.

#### References:

- (1) Barnes, H.L., 1956, Amer. J. Sci., 254, p. 493-505.
- (2) Baker, V.R., 1971, Geol. Soc. Am. Spec. Paper, 144, 79 p.
- (3) Baker, V.R., 1978, NASA Tech. Memo, 79729, p. 248-249.
- (4) Embleton C, and C.A.M. King, 1968, Glacial and Periglacial Geomorphology, S. Martin's Press, New York, 608 p.

- (5) Pieri, D. and C. Sagan, 1978, NASA Tech. Memo, 79729, p.268.
- (6) Pieri, D., 1979, PhD. Thesis, Cornell University, Geomorphology of Martian Valleys, 288 p.
- (7) Knapp, R.T. et al., 1970, Cavitation, McGraw Hill, New York, 578 p.

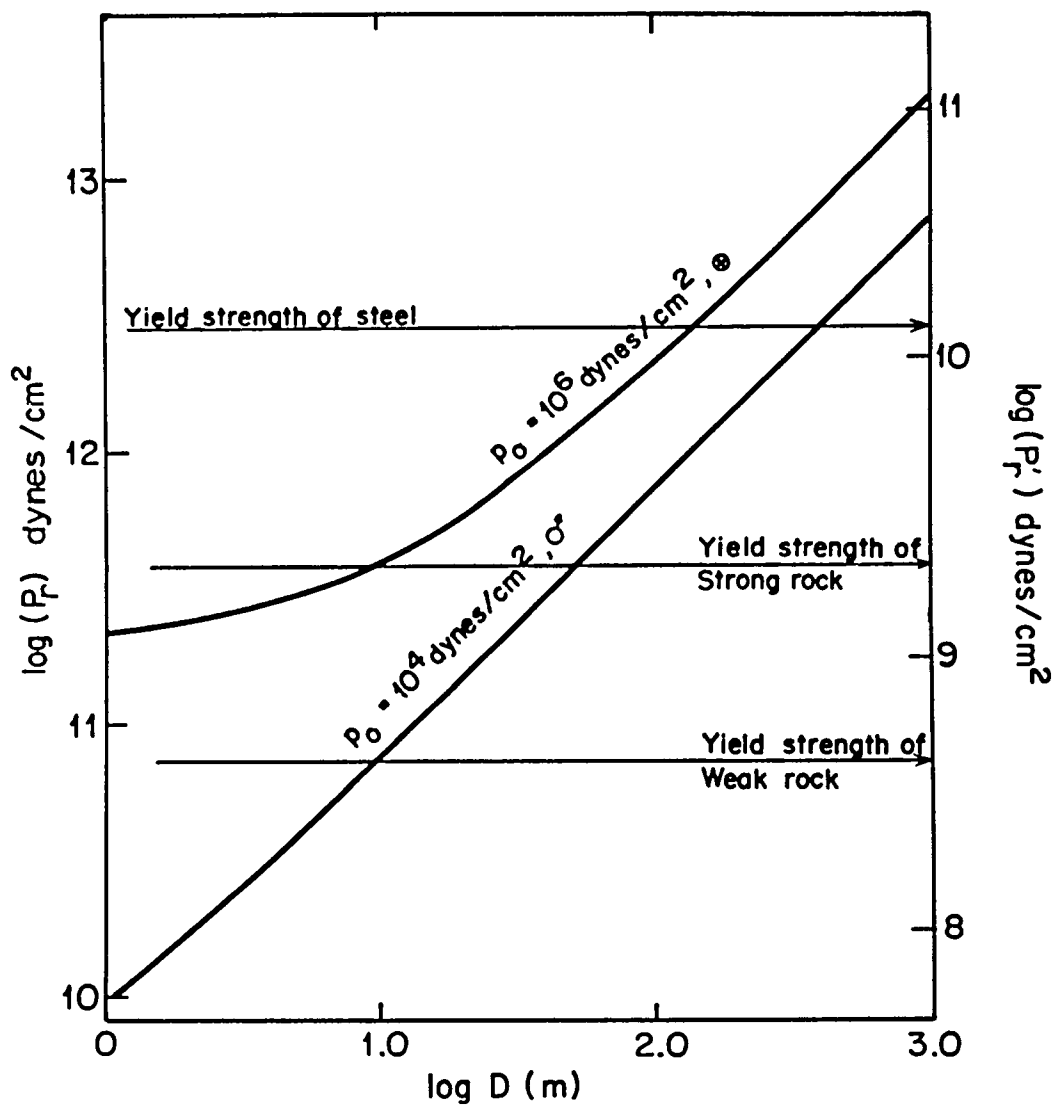


Figure 1.

## GROUNDWATER SAPPING ON THE COLORADO PLATEAU

Laity, Julie E., Jet Propulsion Laboratory, California Institute of Technology, Pasadena, CA 91103

Tributary valley systems on the Colorado Plateau are being compared to morphologically analogous martian valley systems whose features indicate either formation or modification by sapping processes. Sapping is a process by which valleys extend headward or slopes retreat owing to the collapse of valley walls following the undermining of basal support. The terrestrial systems are comparable to those on Mars based on a similarity of network pattern, amphitheater terminations of first order tributaries, large scale and evident structural control. Not all sedimentary lithologies on the Colorado Plateau exhibit valleys with these characteristics. Particularly well-developed examples are found in the Navajo sandstone, to which our research is presently limited. The Navajo is a massive fine-grained eolian sandstone which is sufficiently exposed to allow examination of valley development at several scales and under varying structural conditions. Spring sapping occurs in the Navajo because of its high permeability, excellent aquifer properties, and the presence of an underlying aquitard. Discharge of groundwater at seeps and springs enlarges cavities and alcoves, undercutting the cliff face and causing massive slab failures and vertical cliff recession (Laity, 1980). Although the constituent materials, climate, scale, structure, and groundwater conditions cannot be replicated for Mars in any earth analog, the striking form similarities suggest that at least gross geomorphic processes may be similar.

Studies of regional transmissivity of sedimentary rocks on the Colorado Plateau by Jobin (1956) show the Navajo to be the most transmissive of all rocks as a function of its permeability and geometrical configuration and continuity. The recharge potential of the aquifer is high because of generally widespread exposure at low dip angles, essentially uniform permeability of the sandstone, and pervasive fracturing of the rock. The saturated thickness of the Navajo is not known for the study area, but in neighboring areas it attains a thickness of 200 feet with a porosity which is a conservative 15 percent (Goode, 1965). The occurrence of sapping is related to the outcropping of springs and surface seepage at canyon heads and sidewalls localized by the presence of an aquitard (the Kayenta Formation), by vertical variations in the lithology of the Navajo which result in perched water tables (Gates, 1965), and by horizontal and vertical variations in permeability resulting from fractures. Dominant regional joints are vertical, or nearly so, and are essentially normal to the bedding planes. The hydrologic role of the fractures is: (1) to funnel local runoff into the canyons; (2) to increase the overall permeability of the sandstone of the upper plateau and further, to act as a course for plateau streamflow allowing considerable inflow to the subsurface through a porous bed; and (3) to serve as a pathway for laterally flowing groundwater at depth. Fractures warp the groundwater table to concentrate water flow and pipe it towards the canyon heads. As groundwater flow lines are also more concentrated around the headwalls than the canyon sidewalls, lateral growth is always less than headward growth and in time the canyon heads attain an amphitheater form.

Drainage patterns in the Navajo exhibit many characteristics which indicate structural control (allied to groundwater sapping) rather than topologic randomness. Amongst these are topologic asymmetry in which the networks are notably right- or left-handed, unusual constancy of tributary junction angles into the mainstream, and a pervasive parallelism of tributary orientation. For valleys which exhibit "sapped" characteristics, stream orientations can be explained by the interrelationship of groundwater flow direction and fracture orientation. Joint trend and density, channel frequency, orientation, and length, and predominant bed dip and directions were measured for five drainage basins near Glen Canyon and plotted on rose diagrams. The azimuthal distributions indicate that the systematic joint trends strongly affect the pattern of network growth. For the five basins examined, 50-80 percent of all tributary length is oriented in a direction which is along the joint trend most closely corresponding to the predominant up dip direction. Topologically asymmetric networks are developed on shallow dipping monoclinal limbs where topography mirrors bed dip and tributary growth is up dip in response to groundwater seepage at the canyon head: in the down dip direction groundwater flow is away from the mainstream and no tributaries develop. Constancy of junction angle is a function of parallelism in the regional jointing pattern. In these networks, sapping is the most important process in determining the directionality and pattern of network growth. Ephemeral surface runoff acts primarily to cut relatively shallow channels on the plateau and to remove the products of disintegration from wall collapse in the canyons.

Valley form is also strongly tied to the hydrogeologic properties of the drainage basin. Bed dip of the impermeable boundary relative to the mainstream is critical because it determines in large part the direction of groundwater flow. Another factor which influences canyon form is the proportion of drainage basin area comprised of lithologies which are less permeable than the Navajo. As surface runoff forms a larger percentage of all runoff it acts to degrade the canyon headwalls and smooth the longitudinal profile. These conditions are exemplified in a study of the contrasting profiles of east-flowing and west-flowing tributaries to the lower Escalante River. Sapping processes are dominant in the west-flowing tributaries which are formed entirely in the Navajo. Groundwater flow is down dip towards the Escalante River and intersects the tributary headwalls. The headwall is a steep cliff 400-500 feet or more in height which appears as a distinctive step in the longitudinal profile and as an amphitheater in planimetric view. The canyons appear to be migrating headward along the Navajo/Kayenta interface. In contrast, eastward-flowing tributaries exhibit form characteristics which suggest the dominance of overland flow in their formation. Longitudinal profiles are concave in the upper reaches and straight to slightly convex in the lower reaches: amphitheater valley heads or profile steps have not developed. These form differences may be explained by differences in the hydrologic budget of the sub-basin. The upper one-third of the basin is formed in lithologies other than the Navajo which contribute considerable surface runoff. Additionally, the bed dip on this side of the Escalante routes subsurface runoff away from the sub-basin axis so that the longitudinal profile does not intersect the groundwater table.

Amphitheater terminations and steps in the longitudinal profile

might be explained as "knickpoint retreat" in a fluvial system swing to climatic change, baselevel lowering of perennial rivers, or differential tectonism. None of these processes, however, serve to explain the profile asymmetries developed along the Escalante River. Sapping accounts for this asymmetry and is a more reasonable explanation for steps of such height than fluvial erosion. Field relationships such as the very small stream-cut notches at canyon heads relative to the headwall height and the absence of sizeable plunge pools at the headwall base obviate waterfall erosion as a significant agent in the development of amphitheater-headed canyons. In conclusion, valleys which exhibit certain network and form similarities to those on Mars can be shown to be formed primarily by sapping processes. A detailed examination of the interaction of surface and subsurface runoff, lithologic properties and local structure provide many clues as to their origin.

#### REFERENCES:

- Gates, J.S., 1965, Groundwater in the Navajo Sandstone at the east entrance of Zion National Park: in Geology and resources for south-central Utah, Utah Geol. Soc. Guidebook 19, p. 151-160.
- Goode, H.D., 1965, Sources of water to supply coal-fired electric power plants in Kane County, Utah: in Geology and resources for south-central Utah, Utah Geol. Soc. Guidebook 19, p. 143-150.
- Jobin, D.A., 1956, Regional transmissivity of the exposed sediments of the Colorado Plateau as related to distribution of uranium deposits: U.S. Geol. Survey Prof. Paper 300, p. 207-211.
- Laity, J.E., D.C. Pieri, and M.C. Malin, 1980, Sapping processes in tributary valley systems: Reports of Planetary Geology Program, 1979-1980, NASA TM 81776, p. 295-297.



## CHANNEL MEANDERING AND BRAIDING: ARE EMPIRICAL EQUATIONS BASED ON TERRESTRIAL RIVERS APPLICABLE TO MARS?

Komar, Paul D., School of Oceanography, Oregon State University,  
Corvallis, Oregon 97331

Terrestrial river channels are rarely straight for distances greater than about ten channel widths (Leopold and Wolman, 1960). Instead, they tend to meander or to develop into a complex braided system. Meandering channels on Mars are rare, Nirgal Vallis being the best known example (Sharp and Malin, 1975). Meandering tends to be better developed in some of the small channels than in the large outflow channels. Both show stretches of braiding.

Data from terrestrial rivers and laboratory "streams" have demonstrated that the wavelength,  $L_m$ , of meandering is controlled mainly by the discharge,  $Q$ , and many empirical relationships have been proposed relating the two. One example is that of Inglis (1947) and Leopold and Wolman (1957, 1960),

$$L_m = 36Q^{0.5} \quad (1)$$

where the discharge  $Q$  is in cfs units and  $L_m$  is feet. Although the values of the empirical coefficients in such a relationship vary from study to study (Carlston, 1965; Ackers and Charlton, 1977), all demonstrate the control of  $Q$  on the meander length in both rivers and laboratory results, with little dependence on other flow or channel variables.

Sagan (1976) has estimated the discharge that carved Nirgal Vallis from its meander characteristics, apparently employing a relationship such as equation (1), concluding that the discharge must have been approximately equal to that of the contemporary Mississippi River. Since equation (1) is empirically based on terrestrial data, and is not dimensionally correct, the question arises as to whether it is applicable to martian channels with a gravity field one-third that of earth. The dimensional analysis approaches of Shahjahan (1970) and

Ackers and Charlton (1977), and the instability analyses of Anderson (1967) and Parker (1976) provide relationships that include the acceleration of gravity as well as other pertinent flow and channel parameters. For example, Anderson (1967) obtains

$$L_m = 72 \left( \frac{Q}{\sqrt{gh}} \right)^{1/2} \quad (2)$$

where  $h$  is the flow depth. This relationship indicates a dependence on  $g$ , but only a relatively weak one since it is included to the one-fourth power.  $Q$  and  $h$  being the same for flows on Mars and earth, the reduced martian gravity would produce a factor  $(981/372)^{1/4} = 1.27$  increase in the resulting meander length. In the opposite direction, the estimate by Sagan (1976) of the discharge in Nirgal Vallis would be reduced by a factor  $1/1.27 = 0.78$ , still leaving a very substantial flow according to the observed meander wavelength. As seen in equation (2), the mean flow depth could also affect the estimate. Any analyses employing the empirical equation (1) or the semi-empirical equation (2) inherently have a high uncertainty in the estimates obtained, both equations being based on log-log data plots.

The instability analyses of Parker (1976) also lead to a better understanding of the conditions under which channels remain straight or braid rather than meander, and to the expected number of braids. The relationships indicate a stronger dependence on gravity, so differences between Mars and earth can be expected. These relationships together with the laboratory results on the rate at which meandering can develop from an initially straight channel are being used to interpret the non-meandering channels on Mars.

More refined analyses of channel meandering can be obtained through spectral analysis, although the interpretations of the results are not always certain (Speight, 1965, 1967; Toebes and Chang, 1967; Chang and Toebes, 1971; Surkan and Van Kan, 1969; Ferguson, 1975). Such analyses are being conducted on select terrestrial rivers, including those employed by Leopold and Wolman (1957, 1960) to obtain equation (1),

as well as on martian channels, but our results to date are insufficient to warrent definite conclusions.

#### References

- Ackers, Peter, and F.G. Charlton (1977) Meandering of small streams in alluvium: Rept. INT77, Hydraulics Res. Station, Wallingford, England, 78pp.
- Anderson, A.G. (1967) On the development of stream meanders: Proc. 12th Cong. IAHR, Fort Collins, Col., v.1, p. 370-378.
- Carlston, C.W. (1965) The relation of free meander geometry to stream discharge and its geomorphic implications: Amer. Jour. Sci., v. 263, p. 864-885.
- Chang, T.P., and G.H. Toebes (1971) Geometric parameters for alluvial rivers related to regional geology: Proc. 14th Cong. IAHR, v.3, p. 193-201.
- Ferguson, R.I. (1975) Meander irregularity and wavelength estimation: Jour. Hydrology, v. 26, p. 315-333.
- Inglis, Sir Calude (1947) Meanders and their bearing on river training: Maritime and Waterways Engr. Div. Meeting, Inst. Civil Engrs., London.
- Leopold, L.B., and M.G. Wolman (1957) River channel patterns: braided, meandering and straight: USGS Prof. Paper 282-B, p. 37-86.
- Leopold, L.B., and M.G. Wolman (1960) River meanders: Geol. Soc. Amer. Bull., v. 71, p. 769-794.
- Parker, G. (1976) Cause and characteristic scales of meandering and braiding in rivers: Jour. Fluid Mech., v. 76, p. 457-480.
- Sagan, Carl (1976) Preliminary investigations of the physics of martian channels: Reports of Accomplishments of Planetology Programs, 1975-1976, NASA TM X-3364, p. 166-168.
- Shahjahan, M. (1970) Factors controlling the geometry of fluvial meanders: Bull. Internat. Assoc. Sci. Hydr., v. 15, n. 3, p. 13-24.
- Sharp, R.P., and M.C. Malin (1975) Channels on Mars: Geol. Soc. Amer. Bull., v. 86, p. 593-609.
- Speight, J.G. (1965) Meander spectra of the Anabunga River: Jour. Hydrol. v. 3, p. 1-15.
- Speight, J.G. (1967) Spectral analysis of meanders of some Australasian Rivers: in Landform Studies from Australia and New Guinea, eds. Jennings and Mabbutt, Canberra, Austral. Natl. Univ. Press, p.48-63.
- Surkan, A.J., and J. Van Kan (1969) Constrained random walk meander generation: Water Resour. Res., v. 5, p. 1343-1352.
- Toebes, G.H., and T.P. Chang (1967) Planform analysis of meandering rivers: Proc. 12th Congr. Int. Assoc. Hydraul. Res., v.1, p.362-369.

## Preliminary Analysis of Energy in the Martian Geomorphic System

Lisa A. Rossbacher and Sheldon Judson, Department of  
Geological and Geophysical Sciences, Princeton  
University, Princeton, NJ 08540

A planetary geomorphic system can be assessed in terms of the sources and rates of energy consumption by various agents. This is the most fundamental way to integrate our understanding of the overall system. The relationship between geomorphic work and available energy is only approximately understood for Earth (Bloom, 1978). Although additional assumptions must be made to formulate an energy budget for the martian geomorphic system, such an analysis is valuable for understanding the relative significance of individual agents.

The major energy source on Mars is solar radiation; the sun provides approximately 99.98% of the available heat energy on Mars. The average solar constant for Mars is  $0.857 \text{ ly/min}$ . The total solar energy received is about  $2.175 \times 10^{16} \text{ W}$ . The geothermal contribution, based on the martian heat flow estimates of Toksöz and Hsui (1978), supplies only about  $5.07 \times 10^{12} \text{ W}$  (0.02% of the solar contribution). The rotational energy of the solar system also adds some energy to the system; for Earth, the quantity is the same order of magnitude as the geothermal heat flow. It is reasonable to expect that the rotational energy for Mars is similar to Earth's. Because this source is so much less than the solar input, it will not be quantified further in this preliminary analysis. Solid planet tides may also provide a notable energy source; we are investigating this possibility.

Energy input is not distributed evenly over the surface of the planet. The distribution of geothermal heat varies somewhat with the composition of the underlying material. The incident solar radiation is clearly not distributed uniformly; the energy received at the equator is more than twice that at the poles (Sellers, 1965). On a smaller scale, the incident radiation varies according to the slope angle and orientation. Variations in the Sun-Mars distance will also have an impact on the available energy, and thereby on the temperature and climate (Ward, 1974).

Not all of the solar energy that reaches Mars is available for geomorphic work. The planetary albedo reflects approximately 17% of the incoming radiation. Of the remaining energy ( $\sim 1.8 \times 10^{16} \text{ W}$ ), nearly all is sensible heat that enters the atmosphere, and only about 0.2% is expended in the latent heat of vaporization of

atmospheric water (based on a diurnal atmospheric water-vapor variation of 20 ppm [Flasar and Goody, 1976]).

Wind is the most active geomorphic agent on Mars, and most of the energy used in geomorphic work must be funneled into wind. Energy is consumed in all stages of aeolian activity: entrainment, transportation, and deposition. The threshold energy required for entrainment is a function of the fluid threshold velocity; for saltation of fine particles, this is about 2 m/sec at the grain surface level (Sagan and Pollack, 1969). The threshold velocities on Mars are considerably higher than those on Earth, largely because of the decreased atmospheric density on Mars, but settling velocities are remarkably similar between the two planets (Arvidson, 1972). Thus, the energy used by entrainment will be far more significant than that needed for transportation or impact. The rate of energy flow (power) of wind is related to the cube of the wind velocity (Merriam, 1978). The Viking landers recorded average surface wind velocities of a few meters per second, but the velocities ranged between  $\sim 2$ -150 m/sec (Hess et al., 1977). As the wind velocity increases from the lower to the upper part of this range, the power per unit area rises by a factor of  $10^6$ .

When a particle falls and strikes a target, energy is dissipated in several ways: heat, plastic deformation, non-recoverable strain, fracturing, and the kinetic energy of subsequent motion. For a particle with a density of  $2 \text{ g/cm}^3$  moving at a typical martian threshold velocity of 2 m/sec, the dissipated energy density is about  $2 \times 10^4 \text{ dyne/cm}^2$  (Sagan et al., 1977).

The freeze-thaw cycle of water on Mars is significant for mechanical weathering. The amount of energy used is difficult to determine because (1) it overlaps with the sublimation-precipitation of atmospheric water, (2) the amount of water - or ice - available on Mars is unknown, and (3) the process occurs primarily beneath the surface, where it cannot be directly observed. If large amounts of water exist on Mars, the phase changes of water may provide or consume available energy.

Tectonism on Mars creates potential geomorphic energy in gravity; this energy is dissipated very slowly through mass movements toward a local base level. Other available non-gravitational energy is used instantaneously, as by wind. The martian geomorphic system can be divided into two temporal loops: (1) short-lived energy that is dissipated rapidly (wind, phase changes, surface-temperature changes) and (2) long-term potential energy that is dissipated slowly (mass movements).

We are continuing to refine this integrated evaluation of the martian geomorphic system. This work is supported by NASA grant NSG-7568.

# REFERENCES CITED

- Arvidson, R.E., 1972, Aeolian processes on Mars: erosive vehicles, settling velocities, and yellow clouds: Geological Society of America Bulletin, v. 83, p. 1503-1508.
- Bloom, A.L., 1978, Geomorphology: A Systematic Analysis of Cenozoic Landforms: Prentice-Hall (Englewood Cliffs, NJ), 510 p.
- Flasar, F.M., and R.M. Goody, 1976, Diurnal behavior of water on Mars: Planetary and Space Science, v. 24, p. 161-181.
- Hess, S.L., R.M. Henry, C.B. Leovy, J.A. Ryan, and J.E. Tillman, 1977, Meteorological results from the surface of Mars: Viking 1 and 2: Journal of Geophysical Research, v. 82, p. 4559-4574.
- Merriam, M.F., 1978, Wind, waves, and tides: Annual Review of Energy, v. 3, p. 29-56.
- Sagan, C., and J.B. Pollack, 1969, Windblown dust on Mars: Nature, v. 223, p. 791-794.
- Sagan, C., D. Pieri, P. Fox, R.E. Arvidson, and E.A. Guinness, 1977, Particle motion on Mars inferred from the Viking Lander cameras: Journal of Geophysical Research, v. 82, p. 4430-4438.
- Sellers, W.D., 1965, Physical Climatology: The University of Chicago Press (Chicago), 272 p.
- Toksz, M.N., and A.T. Hsui, 1978, Thermal history and evolution of Mars: Icarus, v. 34, p. 537-547.
- Ward, W.R., 1974, Climatic variations on Mars. I. Astronomical theory of insolation: Journal of Geophysical Research, v. 79, p. 3375-3386.

## GEOMORPHIC PROCESSES IN ICELAND'S COLD DESERTS: MARS ANALOGS

Malin, Michael C., Department of Geology, Arizona State University,  
Tempe, Arizona 85281

One of the more challenging problems in Mars geomorphology is distinguishing the relative importance of winds and floods in producing landforms seen in the large outflow channels. As both agents act through fluid erosion, often larger landforms are not characteristic of the process and agent of formation. The intent of this study is to examine an area where both processes have acted on materials in a manner similar to that on Mars, and where competing processes (e.g., normal fluvial runoff, etc.) are minimized.

The area under study is in north-central Iceland, adjacent to Jökulsá á Fjöllum (fig. 1). The area was subjected to an intense flood ( $\sim 5 \times 10^5 \text{ m}^3/\text{sec}$ ) some 2500 years ago, eroding about  $0.7 \text{ km}^3$  of rock and tephra, including the 2900 year old H<sub>3</sub> Hekla tephra (Tómasson, 1973). This flood created the features most often cited as analogues to the Washington State Scablands and to martian channels (see, e.g., Masursky et al., 1977). Superimposed on the channel is Hekla tephra less than 2000 years old. Other, smaller floods have occurred in the area, and also show inter-fingered time relationships between lava extrusion, tephra deposition and eolian redistribution, flooding, and subsequent tephra redistribution.

There are two major aspects of this research: 1) delineation of the "damage" done to basalts and tephra by the flood(s), including structural control of erosional landforms, and 2) examination of eolian activity as an indication of the vigor of eolian processes on wholly volcanic materials.

A two week field reconnaissance of the southern portion of the flood area in August, 1980 had two main goals: 1) to examine small (cm) to moderate (10 m) erosional and depositional landforms created by the flood, and 2) to locate sites for future wind test plots patterned after Sharp's Garnet Hill station.

Of particular interest were the distribution and caliber of debris transported by the flood, and the scale of relief associated with erosional and depositional landforms. Erosion appears to have been limited to abrupt but local topographic gradients. Grooving occurred dominantly on pahoehoe surfaces. Aa flows provided sites of enhanced deposition, and flow fronts facing downstream provide sites for point bar formation.

Eolian processes of three kinds were noted. "Lag" surfaces were ubiquitous in areas where lava flows provided coarse debris. The origin of these "lag deposits" (enrichment through deflation of fines, or heaving of larger particles from below) will be explored at the test sites. Ripples, composed of coarse gravels and, near Askja, pumice fragments, were found in several environments. Their mode of formation and movement, as well as that of lag surfaces, will be studied to gain insight into reasons for their weak expression on Mars. Finally, grooving, pitting, and fluting of materials transported by the flood show the strong influence of eolian processes on the surface since flooding. Variations in size of these features can be linked to sediment caliber and volume, target rock vesicle size, orientation, and abundance, and to density and strength.

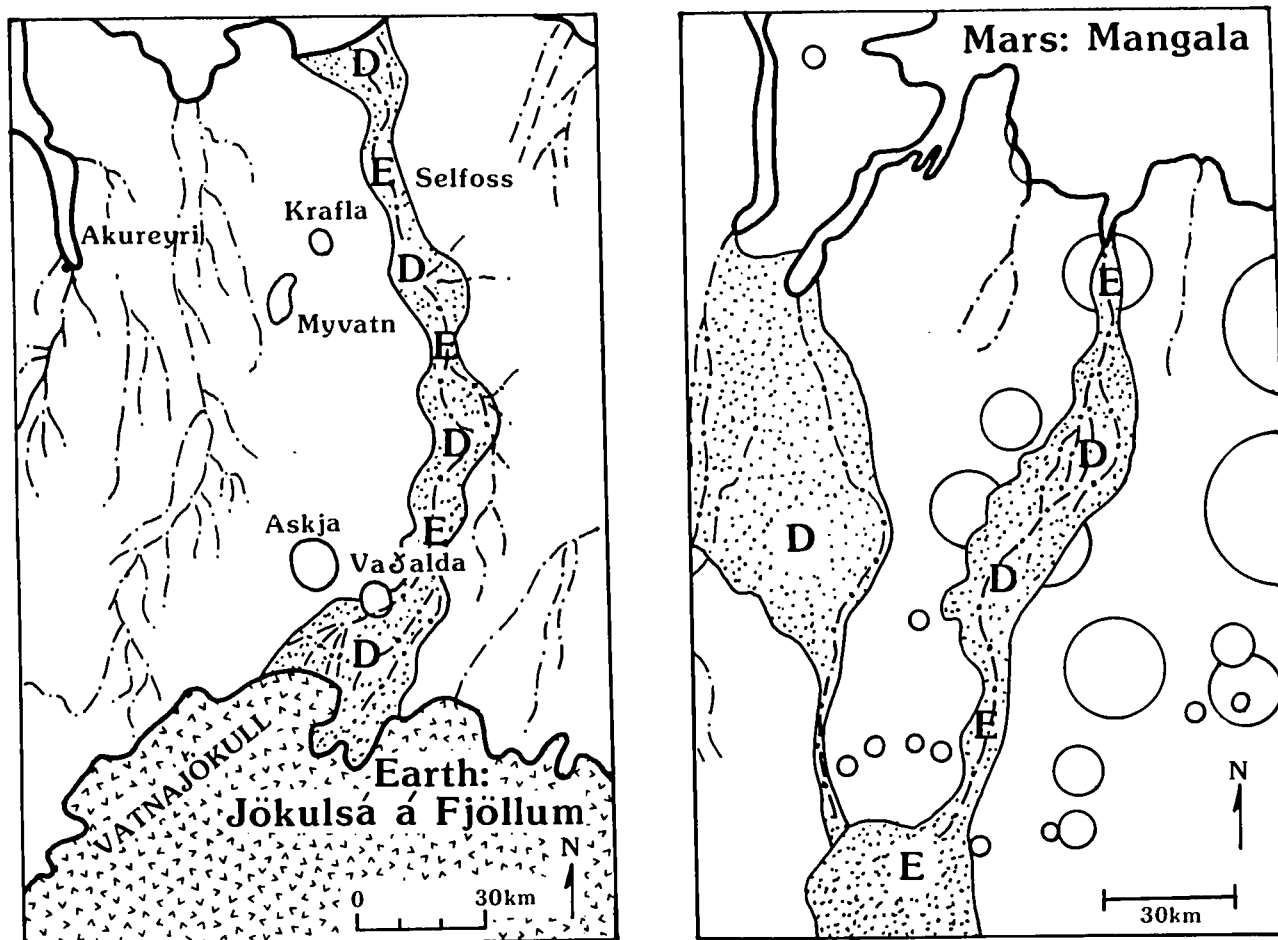


Figure 1  
 Sketch maps of areas on Earth (left) and Mars (right) where catastrophic floods have occurred, portrayed at the same scale. The terrestrial example is the 2500 year old remnant of a flood in north central Iceland, caused by the meltwater from a sub-glacial volcanic eruption. The martian example presents part of Mangala Vallis, which extends several hundred kilometers farther south than shown here. Areas of deposition are indicated by D; areas of deep scour and erosion, E. As expected, deposition occurs in areas where the flow broadens, shallows and slows, whereas erosion occurs where flow narrows, deepens and increases in speed. Jökulsá á Fjöllum map after Tómasson, 1973.



## THE MARTIAN FRETTED TERRAINS: EXAMPLES OF THERMOKARST LABYRINTH TOPOGRAPHY

Brook, George A., Department of Geography, University of Georgia, Athens,  
GA 30602

Sharp (1973) has described fretted terrain as being characterized by smooth, flat, lowland areas separated from a cratered upland by abrupt escarpments of complex planimetric configuration. Landforms range from isolated buttes and mesas to large plateau regions divided by narrow, flat-floored, intersecting valleys (Fig. 1). Sharp suggests that the material of the upland plateaus is a thick blanket of regolith containing a substantial amount of frozen water and that scarp recession occurs as a result of undermining by evaporation of exposed ground ice or by ground water sapping. Soderblom and Wenner (1978) have noted that erosional processes in fretted terrains have operated to a roughly uniform depth in materials of widely different relative age. They have postulated the existence of a major lithologic discontinuity at 1-2 km below the original upland surface which coincided with the H<sub>2</sub>O freezing point. In the liquid water environment below the interface diagenesis occurred, which increased the resistance to erosion. In the ice regime above, any natural weakness of near-surface material was preserved in the absence of chemical alteration. Subsequently, a variety of erosional processes stripped the ice-laden zone away. Carr and Schaber (1977) have identified flows they interpret as being produced by frost creep or gelifluction. Squyres (1978) interprets the same flows as rock glaciers.

Although several workers favor a thermokarst origin for fretted terrain there is no obvious terrestrial analog to support such a view. However, two terrestrial landscapes do bear a striking resemblance to this Martian topographic type although developed at a smaller scale. The first is labyrinth karst, a landform type discovered in 1972, it contains closed depressions up to 300 m deep (Brook and Ford, 1978). The pit, street, platea, and marginal plain stages of labyrinth karst development have also been identified in areas of fretted terrain where relative relief exceeds 1 km (Brook, 1979, 1980; Figs. 1 and 2).

In the second landscape, ice-wedge thermokarst, relative relief rarely exceeds 10-20 m. As described by Soloviev (1962, 1973), development begins with the formation of high-centered polygons and intersecting networks of trough-like depressions as the polygonal system of ice wedges begins to thaw. Further melting deepens the troughs causing the sides of the polygons to slump and to form conical mounds called baydjarakhs. As degradation continues the baydjarakhs collapse and decay with the formation of uneven-floored depressions (dujodas) within the baydjarakh field. Continued collapse ultimately produces circular to oval depressions with steep sides and flat floors (alases).

Photographs of degrading ice-wedge polygons on eastern Banks Island in the Canadian arctic (French, 1976, Fig. 3.4, p. 22) and in the Yenisei River valley near Krasnoyarsk, U.S.S.R. (Academy of Sciences, USSR, Moscow 1961, Fig. 80, p. 273) reveal that before the high-centered polygon stage of

Soloviev, elliptical subsidence pits develop along melting ice wedges, particularly at ice wedge intersections. Summer meltwater creates 'beaded drainage' with pools up to 3 m deep and 30 m long parallel to the melting ice wedges (Hopkins *et al.*, 1955). Further melting with coalescence of the collapse pits forms a field of high-centered polygons.

The pit, high-centered polygon, baydjarakh, dujoda, and alas sequence of ice-wedge thermokarst development broadly parallels the pit, street, and platea sequence in labyrinth karst evolution. Furthermore, the ice-wedge thermokarst equivalent of the marginal plain has been identified on eastern Banks Island (French, 1974, Figs. 3-5, p. 792). In one area dissected by two small streams, an amphitheater-like hollow 0.5 km in diameter with outlier baydjarakhs has formed by escarpment retreat into a flat-topped interfluve. Thermal melting acting preferentially along ice wedges in lake silts has isolated baydjarakhs more than 8 m high. Once isolated in front of the retreating scarp the baydjarakhs are subject to thawing from all sides and quickly degrade. The processes that have produced the ice-wedge thermokarst of eastern Banks Island are almost identical to those postulated by Sharp (1973) as having produced the Martian fretted terrains.

Labyrinth karst resembles Martian fretted terrain more than any other terrestrial landscape and yet it is doubtful if these topographies have similar modes of origin. Karst labyrinths are produced by solution and there is no evidence of extensive areas of soluble rocks on Mars or evidence that solution was ever an important weathering process. The resemblance between labyrinth karst and ice-wedge thermokarst, and widespread evidence of near-surface permafrost on Mars, tend to support the postulated thermokarst origin for the Martian fretted terrains. By this interpretation these areas are Martian examples of thermokarst labyrinth topography.

#### References

- Academy of Sciences, U.S.S.R. (1961). *Polevye Geokriologicheskie (Merzlotnye) Issledovaniya*. Akademiya Nauk SSSR, Moskva 1961.
- Brook, G. A. (1979). Terrestrial and Martian Rock Labyrinths. NASA Tech. Mem., 80339: 42-46.
- Brook, G. A. (1980). Pits, Streets, Platea, Towers, and Marginal Plains on Mars. NASA Tech. Mem., 81776: 57-59.
- Brook, G. A. and Ford, D. C. (1978). The Origin of Labyrinth and Tower Karst and the Climatic Conditions Necessary for Their Development. *Nature*, 275: 493-496.
- Carr, M. H. and Schaber, G. G. (1977). Martian Permafrost Features. *J. Geophys. Res.*, 82: 4039-4054.
- French, H. M. (1974). Active Thermokarst Processes, Eastern Banks Island, Western Canadian Arctic. *Can. J. of Earth Sci.*, 11: 785-794.
- French, H. M. (1976). *The Periglacial Environment*. Longman Inc., New York.
- Sharp, R. P. (1973). Mars: Fretted and Chaotic Terrains. *J. Geophys. Res.*, 78: 4073-4083.

Soderblom, L. A. and Wenner, D. B. (1978). Possible Fossil H<sub>2</sub>O Liquid-Ice Interfaces in the Martian Crust. *Icarus*, 34: 622-637.

Soloviev, P. A. (1962). Alasnye Relyef Centralnoj Jakutii i ego Proiskhozhdenie, in *Mnogoletne-merzlyye Porody i Sopotstvuyuhchiye yim Yavleniya na territorii JASSR*, Izdatelstvo AN SSSR, Moscow: 38-53.

Soloviev, P. A. (1973). Thermokarst Phenomena and Landforms Due to Frost Heaving in Central Yakutia, *Biuletyn Peryglacjalny*, 23: 135-155.

Squyres, S. W. (1978). Martian Fretted Terrain: Flow of Erosional Debris. *Icarus*, 34: 600-613.

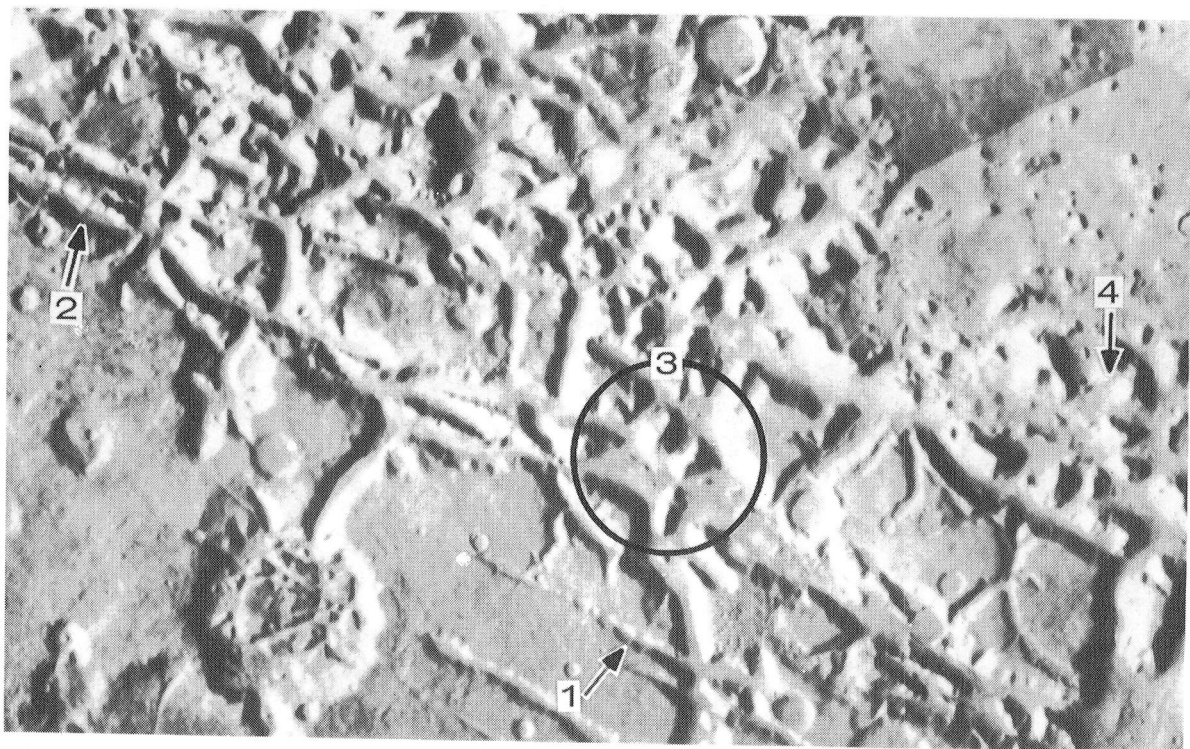


Fig. 1 Martian fretted terrain at Nylosyrtis Mensae. The pits (1), streets (2), platea (3), and marginal plains with residual towers (4) resemble the landforms of terrestrial labyrinth karst.

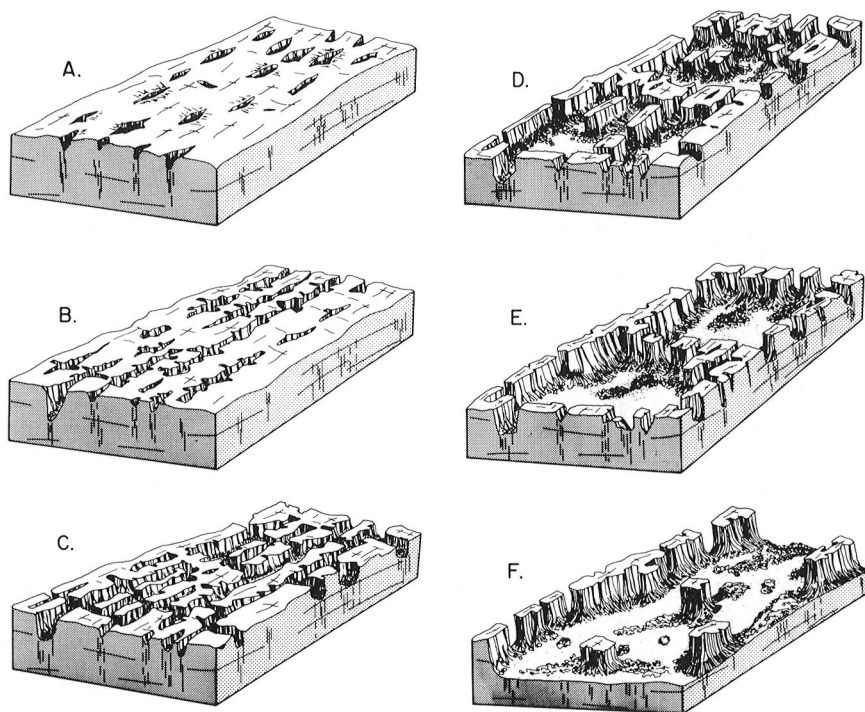


Fig. 2 Stages in the evolution of labyrinth karst. During early stages strings of pits develop in vertical fractures (A). By enlargement and coalescence along the fractures strings of pits are converted to intersecting networks of streets (B and C). As streets deepen and widen the intervening rock ridges are dissected and ultimately destroyed. Replacing them are large closed depressions called platea (D and E). As platea expand rock towers are left which rise from a marginal plain (F).

Martian Fractured Terrain: Possible Consequences of Ice-Heaving  
 Paul Helfenstein, Department of Geological Sciences, Brown University,  
 Providence, RI 02912

Fractured terrain occurs over extensive areas of the Martian northern hemisphere, poleward of 25°N latitude in Acidalia Planitia, Utopia Planitia, Elysium Planitia, and near the pole. Characteristically, fractures form roughly polygonal patterns in cratered and smooth plains materials at elevations of 0 to 3 km below mean Mars datum. Three types of fractured terrain have been identified: open polygons, incompletely surrounded by fractures; closed polygons, totally enclosed by fractures; and twin-concentric fractures with locally depressed floors and terraces.

Measurements of size, shape and frequency of closed polygons in Acidalia, Utopia and the North Polar region (Helfenstein and Mouginis-Mark, 1980) have revealed that closed polygons having five to six sides and typical diameters of 2 to 6 km are most uniform in size and symmetry. Martian polygons may attain diameters up to 20 km, but these larger polygons are generally asymmetric and tend to have variable numbers of sides.

The polygonal nature of fractured terrain suggests that the troughs are normal faults produced by a horizontally isotropic tensile stress (Lachenbruch, 1962). A major objection to proposed terrestrial-type mechanisms of origin is that the scale of Martian fractured terrain exceeds that of the largest terrestrial examples by two orders of magnitude. Pechmann (1980) has demonstrated that the mechanisms of dessication, seasonal periglacial thermal contraction, and basaltic thermal contraction are not likely to produce polygons of the scale observed on Mars. Helfenstein and Mouginis-Mark (1980) suggest that large polygons (greater than 6 km in diameter) may evolve by the coalescence of smaller (~2 km) diameter polygons and that Martian polygons can form at diameters 50% larger than terrestrial analogs due to the lower gravity of Mars. Applying the fracture theory of Lachenbruch (1961), the depth of fracture propagation required to yield trough separation of about 2 km is approximately 150 to 200 m (assuming tensile strengths of 70 to 50 bars as in frozen-silt (Haynes and Karalius, 1977) and crystalline rocks (Pechmann, 1980), respectively. Thus, a key requirement of the mechanism of formation is that tensile stresses (and hence, fractures) must operate to depths of at least several hundred meters.

To account for the discrepancy in polygon scale, it has been proposed that periodic permafrost contraction having cycle times much longer than seasonal may result in polygons of the dimensions observed on Mars. Coradini and Flamini (1979) have suggested that secular variations in temperature arising from changes in the obliquity of the martian orbit (Ward et al., 1974) may induce the required depth of stress. To test this hypothesis, the time variation in obliquity,  $\theta$ , was modeled from Ward's fig. 4c according to:

$$\theta = \theta_0 \cos(2\pi t/\lambda_1 + \epsilon_1) \cos(2\pi t/\lambda_2 + \epsilon_2) + 24^\circ$$

where  $\theta_0$  is the amplitude of obliquity change (~18°),  $t$  is time,  $\lambda_1$  and  $\lambda_2$  are wavelengths of  $1.25 \times 10^5$  years and  $2.5 \times 10^6$  years, respectively, and  $\epsilon_1$  and  $\epsilon_2$  are phase adjustment parameters. A history of yearly average temperature  $\langle T \rangle$  was calculated for different latitudes using:

$$\langle T \rangle = \left[ \frac{(1-A)S}{2\pi^2 \sigma (1-e^2)^{0.5}} \int_0^{2\pi} \left\{ 1 - (\sin \delta \cos \theta - \cos \delta \sin \theta \sin \phi)^2 \right\}^{0.5} d\phi \right]^{0.25}$$

which follows from Ward's equation 44 and the Stephen-Boltzmann law. A is the albedo to the surface ( $\sim 0.15$ ), S is the solar flux normalized to 1.52 A.U.,  $\sigma$  is the Stephen-Boltzmann constant, e is the eccentricity of the Martian orbit (0.093), and  $\phi$  is integrated over one rotation of the planet on its axis. This model ignores atmospheric effects as well as conduction of heat into the planet's surface. The results, shown in fig.1, demonstrate that secular variations, although large at the poles, become negligible at about  $45^\circ$  latitude. Since fractured terrain is observed at  $45^\circ$  latitude, and secular thermal variations are apparently not large there, we conclude that Martian fractured terrain is probably not caused by secular changes in temperature. The secular variations may, however, be responsible for upturned edges of Martian North Polar polygons (Helfenstein and Mougini-Mark, 1980).

It is proposed that the formation of Martian fractured terrain is a periglacial process which involves ice-heaving from aquifers buried at least 150-200 m under frozen-silt. Progressive downward freezing of the aquifer and volumetric expansion of freezing water would result in vertical updoming, horizontal tensile stressing, and polygonal fracturing of the frozen-silt above the aquifer. If the tensile properties of surficial materials can be established, then variations in average regional polygon diameters may be used to estimate the depth of buried aquifers. More refined mechanical models will have to be examined, however, before this can be accomplished with confidence.

#### References:

- Coradini and Flamini, 1979. J. Geophys. Res., 84, 8115-8130.  
 Haynes and Karalius, 1977. CRREL Report 77-3.  
 Helfenstein and Mougini-Mark, 1980. Submitted to Icarus.  
 Lachenbruch, 1961. J. Geophys. Res., 66, 4273-4292.  
 Lachenbruch, 1962. GSA Special Paper, 70, 69 p.  
 Ward et al., 1974. J. Geophys. Res., 79, 3387-3395.

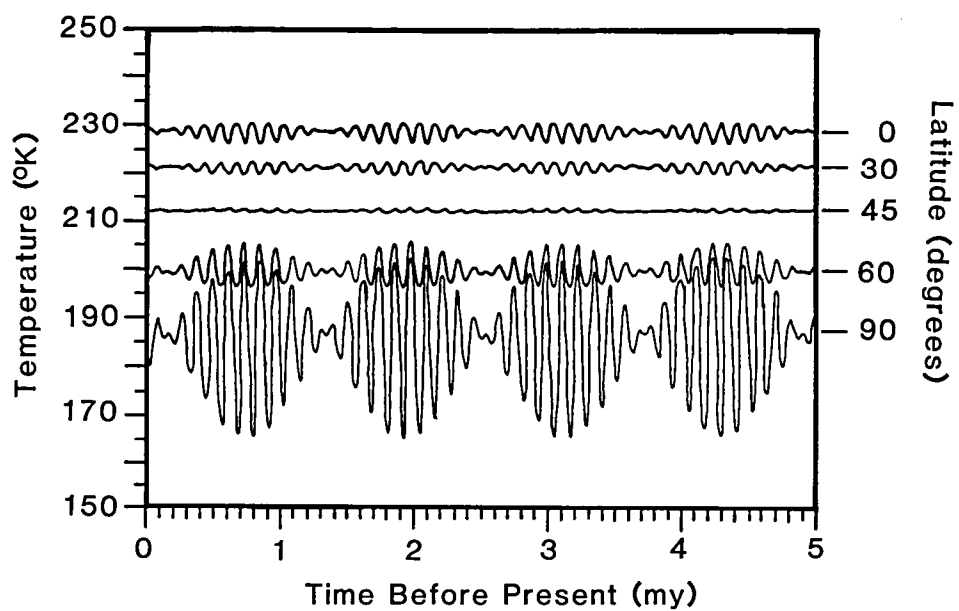


Fig 1: Variations in average annual temperature over the past 5 million years on Mars for various latitudes.

THE LAST PICTURE SHOW: SMALL-SCALE PATTERNED GROUND IN LUNAE PLANUM.

Nancy Evans, Jet Propulsion Laboratory, California Institute of Technology, Pasadena, CA 91103, and Lisa A. Rossbacher, Department of Geological and Geophysical Sciences, Princeton University, Princeton, NJ 08540.

The final sequence of images taken by the Viking I Orbiter cameras on revolution 1485, 31 July 1980, was centered at  $17.6^{\circ}\text{N}$ ,  $57.0^{\circ}\text{W}$  in Lunae Planum. This same area was examined four (Earth) years earlier upon Viking's arrival at Mars during the Lander I site certification activities. A synoptic view of the area is provided in Fig. 1, Viking mosaic 211-5190, obtained during that period at a range of 1700 km (resolution 42.5 m per pixel). The footprint spotlights the location of the final images. From the last sequence, 485S01-24, one image (485S16) was selected as Figure 2a. The entire sequence has an average slant range of 600 km; it was taken using image-motion compensation techniques, and its effective resolution is 15 m per pixel. Because the image reproduction in Fig. 2a may not show the polygonal features described here, Figure 2b is a tracing of the patterned ground within the outlines of Frame 485S16.

Major features in the 485S coverage are readily identifiable in the lower-resolution site certification mosaic. Distinct polygonal patterns, invisible at lower resolutions, can be observed throughout the high-resolution mosaic. Polygonal features that are outlined by ridges, rather than the often-observed troughs, seem to form a net-like structure strikingly similar to stone polygons seen in periglacial terrains on Earth. Structures on Mars resembling patterned ground have been previously described (1,2,3,4); these features range up to an order of magnitude larger than analogous terrestrial patterns. The small-scale patterned ground in Lunae Planum, however, ranges in diameter from 400 m to 1000 m. These diameters are comparable to those seen on Earth (5,6,7).

The primary significance of these features is as the first reported martian patterned ground of a scale similar to terrestrial patterns. Other polygonal ground on Mars (mid-latitude and polar) is defined by troughs or fractures; the ridges outlining the Lunae Planum polygons suggest periglacial stone circles on Earth. The topography in Lunae Planum is not sufficiently defined to determine the relationship between slope and polygon size or shape, which is an important characteristic of terrestrial patterned ground (8).

At this time, images which most clearly indicate the presence of these features are undergoing custom processing in the Image Processing Laboratory of Jet Propulsion Laboratory to improve the discriminability of the polygonal structures. Analysis of these data will include mapping to determine spatial and geological relationships and evaluation of the origin of the patterns. With the results from the preliminary analysis, pre-existing Viking images will be re-examined to determine the presence of similar patterns at the same and lower resolutions.



Hypotheses to explain the size of the polygons include the reduced martian gravitational acceleration, the lower atmospheric pressure, and the high frequency of the freeze-thaw cycle. Using the Viking Thermal Model (9), having established the thermal inertia value to be 6.5 at 17°N, 57°W, and the albedo value to be 1.27, it was determined that diurnal temperature fluctuations cross 273°K during 190 sols (L 125-225) (10). The frequency of the freeze-thaw cycle is directly correlative with the development of patterned ground (11). The presence of patterned ground does not necessarily imply the existence of permafrost; patterned ground is a periglacial feature.

The results of these investigations will be reported at the January Planetary Geology Principal Investigators meeting. This work is supported by NASA grants NAS7-100 (NE) and NSG-7568 (LAR).

#### REFERENCES CITED

- (1) Carr and Scaber, 1977, J. Geophys. Res., v. 82, p. 4039-4054.
- (2) Morris and Underwood, 1978, Repts. Planet. Geol. Prog., NASA TM 79729, p. 97-99.
- (3) Helfenstein and Mouginis-Mark, 1980, Lunar Planet. Sci. XI, p.429-431.
- (4) Pechmann, 1980, Icarus, v. 42, p. 185-210.
- (5) Pratt, 1958, AAPG Bull., v. 42, p. 2249-2251.
- (6) Willden and Mabey, 1961, Science, v. 133, p. 1359-1360.
- (7) Neal et al., 1968, Geol. Soc. America Bull., v. 79, p. 69-90.
- (8) Small, 1970, The Study of Landforms, Cambridge Univ. Press, 486 p.
- (9) Kieffer et al, 1977, J. Geophys. Res., v. 82, p. 4281-4287.
- (10) Christensen, P., personal communication.
- (11) Washburn, 1980, Geocryology, John Wiley and Sons, 160 p.

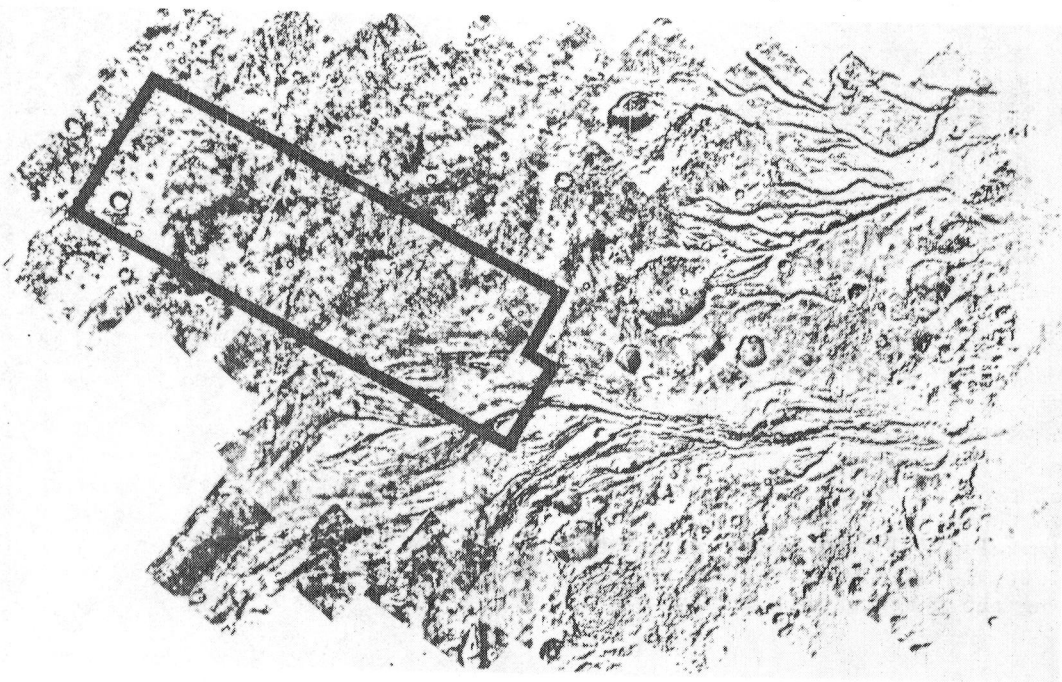
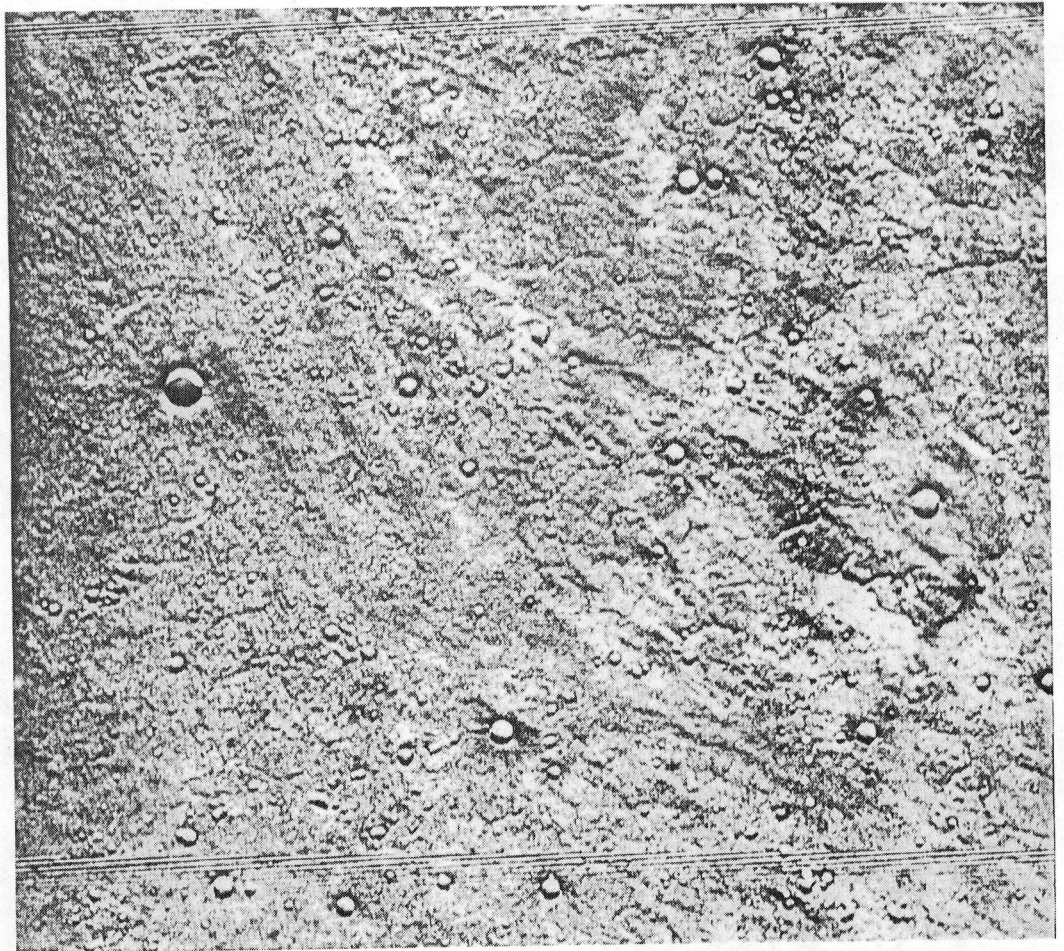
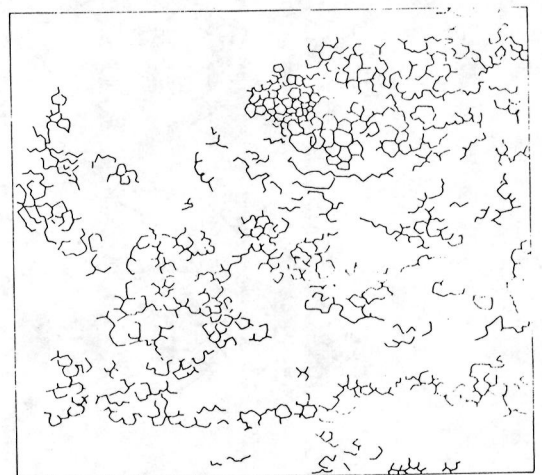


Figure 1. Viking mosaic 211-5190 including footprint of 485S01-24.



2a

Figure 2. Viking I Orbiter frame 485S16; the resolution is 15 m per pixel. (2a), above, is an example of the small-scale patterned ground in Lunae Planum, located at approximately  $17.36^{\circ}$  N,  $56.56^{\circ}$  W. (2b), left, is a tracing of 2a emphasizing the patterned features.



2b

SURVEY OF POSSIBLE GLACIAL OR PERIGLACIAL FEATURES ON ORTHOPHOTOMOSAIC  
SUBQUADRANGLES OF MARS AT SCALE 1:2,000,000, B. K. Lucchitta and H. M.  
Ferguson, U.S. Geological Survey, Flagstaff, AZ 86001.

A global inventory of features whose origin can be attributed to permafrost or ice is in progress. Major morphologic entities under consideration are mass-wasting features, patterned ground, apparent collapse structures possibly due to thermokarst, and forms resulting from the interaction of volcanism and ice.

A survey of all available orthophotomosaic subquadrangles at a scale of 1:2,000,000 was conducted in order to identify and map possible ice related morphologies. Forty subquadrangles are in the equatorial area (MC-9, 10, and MC-16 through 23), and seven in the south (MC-25 and part of MC-26). The resolution of the images (130 to 300 m per pixel) precludes recognition of all but major features. The only mass-wasting features apparent at this scale are large debris blankets flanking the martian volcanoes (1), some landslides in the Valles Marineris (2,3), and grooved channel floors, whose origin may be due to scouring of creeping ice or rockglacial masses (4). Intensely gullied slopes that were mapped may also be due to mass wasting; but small channels and gullies on level ground were not included in this study because they are the subject of other investigations. Patterned ground found in this survey of the equatorial area is characterized by polygonal or irregular fracture sets, which are probably not related to periglacial ice-wedge phenomena.

Most conspicuous and abundant at the scale of the orthophotomosaics are collapse features possibly due to thermokarst. They include pits along grabens, erosionally enlarged and widened grabens, irregular clusters of pits, shallow depressions, and the regional disintegration features associated with chaotic and fretted terrains (5). These features are polygonally fractured areas, mesas, buttes, knobs, hummocks, scalloped scarps, canyon-like flat-floored channels, and stubby cirque-like valley heads.

The survey shows that pits along grabens are most common in the fractured terrain south of Alba Patera and in the vicinity of the Tharsis volcanoes. In the older fractured terrains of the Claritas and Thaumasia Fossae pits are scarce and associated only with younger fractures. Large pits also parallel the Valles Marineris grabens. Pitted grabens are nearly absent in ridged plains and in the southern highlands, except for some that are developed along young grabens of Memnonia Fossae. The survey supports Rossbacher and Judson's (6) contention that pits may result from thermokarst due to volcanic heating.

Polygonally fractured ground is most abundant near the chaotic and fretted terrains. It also occurs along the courses of some of the larger outflow channels, particularly Kasei Vallis. With the exception

of polygonal cracks in a few floor-fractured craters, polygonally fractured ground is absent in the southern highlands. The association of the polygonally fractured ground with obvious disintegration features such as the chaotic and fretted terrains, or with erosional features such as channels, suggests that the fractures are enlarged by erosion; the common lack of outside drainage suggests widening by collapse and interior drainage. Notable is the occurrence of some polygonal fractures on raised bulges in the vicinity of the chaotic terrain, which suggests local swelling of the ground prior to disintegration.

Scarps, mesas, knobs, and channels of the fretted terrain were attributed to possible ice disintegration processes by Sharp (5). Conspicuous fretted terrain with high scarps occurs only along the highland border, but smaller mesas, buttes, and scalloped scarps are found in patches within the highlands, and locally appear to result from intensive erosion along dendritic channel networks. The observation that fretted terrain, which may result from ice sapping (5), is associated with small channels corroborates Pieri's (7) suggestion that the small-channel networks may be due to ground-sapping runoff.

The collapse structures associated with the Noctis Labyrinthus troughs, the Valles Marineris grabens and the chaotic terrain were also attributed to possible disintegration of ground ice by Sharp (5,8). The collapse apparently occurred along linear structural patterns toward the west, and along circular structural patterns due to buried craters toward the east. The reason for this equatorial belt of apparently warmed ground causing the melting of postulated ice could be due to a combination of internal and external processes, and is not yet well understood.

#### REFERENCES

- (1) Carr, M. H., Greeley, R., Blasius, K. R., Guest, J. E., and Murray, J. B., 1977, Some martian volcanic features as viewed from the Viking Orbiter: *Jour. Geophys. Res.*, 82, 3985-4015.
- (2) Lucchitta, B. K., 1978, A large landslide on Mars: *Geol. Soc. of Am. Bull.*, 89, 1601-1609.
- (3) Lucchitta, B. K., 1979, Landslides in Valles Marineris: *Jour. Geophys. Res.*, 84, 8097-8113.
- (4) Lucchitta, B. K., 1980, Did ice streams carve martian outflow channels?: *Third Colloquium on Planetary Water, Niagara Falls, NY*, in press, and submitted to *Science*.
- (5) Sharp, R. P., 1973, Mars: Fretted and chaotic terrain: *Jour. Geophys. Res.*, 78, 4073-4083.
- (6) Rossbacher, L. A., and Judson, S., Ground ice on Mars: Inventory, distribution, and resulting landforms. Submitted to *Icarus*.
- (7) Pieri, D. C., Martian valleys: Morphology, distribution, age and origin. Submitted to *Science*.
- (8) Sharp, R. P., 1973, Mars troughed terrain: *Jour. Geophys. Res.*, 78, 4063-4072.

GLACIALLY GROOVED VALLEY FLOORS ON EARTH AND MARS, B. K. Lucchitta, U.S. Geological Survey, Flagstaff, AZ 86001.

Conspicuous on the floors of all large martian outflow channels are longitudinal grooves that somewhat resemble terrestrial hydraulic chutes above cataracts in catastrophic flood terrains (1). The origin of these grooves has been attributed to roller vortices in giant floods (2,3). This origin remains controversial because no flood-related grooves are seen on Earth that rival the width, depth, and longitudinal extent of the grooves on Mars, nor grooved terrain that rivals the width of grooved martian channel floors. Moreover, no flood-caused grooved terrain is recognized on terrestrial satellite images that have resolutions similar to Viking images. Yet, grooved terrain, whose dimensions are comparable to those on Mars, does exist on Earth; it is known as fluted ground and formed at the base of continental ice sheets, and associated grooves can be clearly seen on Landsat images.

A survey of terrestrial glacial terrain and areas formerly covered by Pleistocene ice was conducted on Landsat images in order to locate such fluted ground. It was found in valleys up to 20 km wide in northern Iceland; in the Anchorage Basin of Alaska, where the Chulitna-Susitna and Yentna valleys merge to form a vast grooved region 80 km wide; and in the Northwest Territories of Canada, where fluted ground extends across 180 km south of the Great Bear Lake. This width is comparable to the widest area of grooved terrain on Mars on the floor of Kasei Vallis.

On Mars and Earth the groove sets may be hundreds of kilometers long, forming broadly sweeping curves. On a local scale some curve more tightly where obstacles are encountered, and in places groove sets intersect. The width and depth of individual grooves vary. Grooves nearly 30 m deep in Kasei Vallis and in the Yentna River valley of Alaska are nearly 600 m wide. However, many grooves on Mars are much deeper and wider than presently exposed terrestrial counterparts. This contrast should not be surprising, as on Earth, where vigorous fluvial erosion readily obliterates topography, the terrain records mostly the effects of the last glaciation; on channel floors on Mars, craters reflecting various amounts of abrasion suggest that the grooves record the passage of several ice sheets.

Glacially fluted ground on Earth is developed in till, bedrock, and stratified drift (4). Some of the grooves in till are separated by ridges that have knobs of bedrock at the upstream ends and are mostly very elongated drumlins. Those in bedrock are developed best in soft or mechanically weak rock types, and are essentially independent of bedrock structures (4). On Mars the material forming the valley floors is unknown, and in most areas it is difficult to determine whether the grooves are developed in poorly consolidated deposits of the channel floor or in resistant bedrock. In some areas, however, such as the Chryse Basin, grooves cut across lava plains (5) and resistant wrinkle-

ridge structures. Breaching of resistant units by ice streams also occurs in the Northwest Territories of Canada (6).

The origin of glacial grooves on Earth is still controversial. Boulton (7) suggested that grooves formed where ice, diverging around obstacles, concentrated plucked boulders towards adjacent lows, thus increasing abrasion. Smith (6) thought that plucking of boulders was of greater importance than abrasion for the generation of grooves that scoured bedrock in the McKenzie Valley of Canada. On Mars, either process may have operated.

In summary, the morphologic resemblance of glacially fluted terrain on Earth to grooves on the floors of martian outflow channels is striking, and sculpturing by ice may well have been a dominant mechanism.

#### REFERENCES

- (1) Baker, V. R., 1978, Large-scale erosional and depositional features of the channeled scabland, in Baker, V. P., and Nummedal, D., eds., The Channeled Scabland, NASA, Office of Space Sci., Planet. Geol. Program, Washington, D.C., 81-115.
- (2) Baker, V. R., 1973, Erosional forms and processes for the catastrophic Pleistocene floods in eastern Washington, in Morisawa, M., ed., Fluvial geomorphology. Published in Geomorphology, State University of New York, Binghamton, NY., 123-148.
- (3) Thompson, D. E., 1979, Origin of longitudinal grooving in Tiu Vallis, Mars: Isolation of responsible fluid types: Geophys. Res. Letts., 6, 735-738.
- (4) Flint, R. F., 1971, Glacial and quaternary geology, John Wiley and Sons, Inc., New York, 892 p.
- (5) Greeley, R., Theilig, E., Guest, J. E., Carr, M. H., Masursky, H., and Cutts, J. A., 1977, Geology of Chryse Planitia: Jour. Geophys. Res., 82, 4093-4109.
- (6) Smith, H. T. U., 1948, Giant glacial grooves in Northwest Canada: Am. Jour. Sci., 246, 503-514.
- (7) Boulton, G. S., 1979, Processes of glacier erosion on different substrata: Jour. Glaciology, 23, 15-38.

INVENTORY OF NORTH POLAR ICE, MARS, Harold Masursky, A. L. Dial and M. H. Strobell, U.S. Geological Survey, 2255 North Gemini Drive, Flagstaff, Arizona 86001

Geologic mapping of the north polar region of Mars has been completed, including the outlining of all residual ice deposits. Detailed profiles of the ice-covered areas are being compiled photogrammetrically from Viking images by Francis Schafer (USGS). Ice volumes are being calculated for two types of deposits, one overlying the other. The upper deposit--residual ice--is layered and exhibits differential reflectivity that probably represents varied amounts of contained eolian debris. This debris is estimated (Hugh Kieffer, USGS, personal communication) as only 1-3% of total volume, the remainder being water ice. The underlying deposit consists dominantly of eolian material in generally continuous layers; we therefore infer that ice is confined to the voids. We calculate the volume of water ice in this deposit as 33%. The basal contact of the eolian material is irregular, as it overlies cratered and mantled terrain.

Additional planetwide sources of water are perennially frozen ground--frozen to the depth where the thermal gradient has raised temperature above the melting point--and water contained in the regolith. Our measurements do not improve significantly on previous estimates of these water volumes.

## MECHANICS OF FLOW AND EROSION POTENTIAL OF ROCK GLACIERS AND GLACIERS IN COMPRESSING FLOW

David E. Thompson, Jet Propulsion Laboratory, California Institute of Technology, Pasadena, CA 91103.

An analytic and computer model has been initiated to study the flow characteristics, erosion potential, and development of surface compression ridges on rock glaciers (Thompson and Laity, 1980). The goal of the study is to understand the mechanics of flow and erosion and transport of debris over large distances by rock glaciers. This model should eventually correlate with climate cycling and its relation to debris storage and transport in glaciated mountain valleys. As pertains to Mars, the model is an attempt to clarify the potential role or existence of rock glaciers for debris transport. Squyres (1978, 1979) has demonstrated that the distribution of lobate debris deposits on Mars seems concentrated in regions of high frost deposition which might allow for debris concentrations to become charged with interstitial ice over long times, and thereby begin to flow as rock glaciers. On Earth, there appears to be a cycling between rock glaciers and ice glaciers in debris basins, and this cycle may not necessarily be in phase with climate cycles. A detailed rock glacier response model will help decipher both Earth and Martian paleoclimates, and also the possibility of free surface ice on Mars. The distances over which much of the lineated valley fill occurs on Mars is enormous with respect to possible rock glacier flow known on Earth. It is thus imperative to understand the possibilities of long distance debris transport by rock glaciers or ice-cored debris moving in compressive flow.

The models being developed in this analysis consist of basically two approaches to rock glacier flow rheology, coupled with extensive variation of parameters to determine the erosive effect of stress field variations in compressing flow along the base of rock glaciers where the shear strain-rate is the highest. This analysis is guided in part by similar analysis for ice glaciers (for example, Nye and Martin, 1968). The models consist of: 1) modeling of rock glacier flow as a perfectly plastic fluid with the upper layers of the rock glacier which do not deform modeled as a plug (analysis following Nye, 1951, 1967); 2) modeling of rock glacier flow as a stratified fluid of variable viscosity and density (analysis in part akin to Nye, 1957) whereby three layers are identified in the rock glacier: a basal ice layer with fine debris, an upper ice free layer, and a transition region wherein the debris becomes ice-charged rheologically. Stress and flow distributions are being developed for these models, but the flow is confined to compressing flow so that analysis allows for thrust-fault type slip planes in the plastic case or for compression and amplification of surface waves in the quasi-viscous case. This constraint helps identify the origin of large "compression" features on rock glaciers and to test their stability against variations in the stress field. It is of interest to further determine the amount of ice per volume necessary to allow initiation of flow in debris, and specifically a flow which can be maintained as a continuum flow over very long distances with forces originating from internal deformation of the medium rather than just from upstream compression.



The analysis is further constrained by a detailed field program on selected rock glaciers in the Sierra Nevada with some comparison to debris lobes observed in the foothills of the St. Elias Mountains, Kluane Park, Yukon Territory. In the Sierra, a rock glacier of roughly 2 km long has been selected for detailed field work. This rock glacier exhibits a high density of compression ridges as well as a lichen-free rock front indicating probable current activity and flow. In 1979 a strain-net of 52 stations was established on the upper two-thirds of the rock glacier using a vertical subtense bar and a Wild T-2 theodolite. Strike and dip measurements were made on large target boulders (also visible on air photos) so that both downslope flow and block rotation can be identified following subsequent surveys. This strain-net has now been transferred onto a map of the rock glaciers on which flow can be plotted. This season, a longitudinal profile of the surface of the rock glacier has also been made. This profile indicates the possibility of an ice-free snout even though the debris appears fresh and hence mobile. The profile is not diagnostic by itself of the health of the glacier, but it does give a clue on the mass balance (both ice and debris) of the rock glacier. The snout shows a steep front preceded immediately upglacier by a region of collapse and sinking. A large compression wave or perhaps thrust fault along slip planes rises high above this sunken region. If the rock glacier is indeed ice-free in the snout, compressive flow into this region could be allowing the bulk of the rock glacier to ride up over this blockage to flow, with surficial debris tumbling down the steep front to maintain its fresh appearance. In this case, the transition of flow into or over the blocked region is of high interest in that the response of this downstream region will determine the future behavior of the rock glacier, and indeed its life expectancy. If ice sublimates or melts and drains freely out of this snout region, and if the ice-charged rock glacier upstream cannot overcome this blockage to flow, then the rock glacier length is intimately tied to the local climate and will not be able to advance beyond a certain distance even if most of the ice core is protected from the ameliorating climate. Continuing field work should provide data on flow in this transition region and thereby constrain the theoretical models and tie them to a testable field area.

This research was carried out under NASA Contract 7-100.

#### REFERENCES:

- Nye, J.F., 1951, The flow of glaciers and ice-sheets as a problem in plasticity: Proc. Royal Soc., A, vol. 207, p. 554-572.
- Nye, J.F., 1957, The distribution of stress and velocity in glaciers and ice-sheets: Proc. Royal Soc., A, vol. 239, p. 113-133.
- Nye, J.F., 1968, Plasticity solution for a glacier snout: Jour. Glaciology, vol. 6, no. 47, p. 695-715.
- Nye, J.F. and P.C.S. Martin, 1968, Glacier Erosion: in W.Ward, ed., Reports Commission of Snow and Ice, General Assembly of Bern, IASH publication no. 79, p. 78-86.
- Squyres, S.W., 1978, Martian fretted terrain: flow of erosional debris: Icarus, vol. 34, p. 600-613.
- Squyres, S.W., 1979, The distribution of lobate debris aprons and similar flows on Mars: Jour. Geophys. Res., vol. 84, no. B14, p. 8087-8096.
- Thompson, D.E. and J.E. Laity, 1980, Origin of Mars fluvial features: analysis for fluids of stress and temperature dependent rheology: Reports of Planetary Geology Program, NASA TM-81776, p. 268-270

PRE-SURGE CHARACTERISTICS AND WATER STORAGE IN TRAPRIDGE GLACIER,  
YUKON, 1980

David E. Thompson, Jet Propulsion Laboratory, California Institute of Technology, Pasadena, CA 91103.

Field work during the summer of 1980 has indicated that Trapridge Glacier is in a pre-surge flow condition and should begin to surge within the year. Trapridge Glacier is a 7 km long subpolar glacier on the flank of Mt. Wood, St. Elias Mountains, in southwestern Yukon Territory. Two other surge glaciers flow in its immediate vicinity, Rusty and Backe Glaciers, and all three drain into Hazard Creek, thence, into the Steele Valley by subglacial water flow under Steele Glacier. Trapridge last surged in the early 1940's and thus, apparently has a quiescent phase lasting about 40 years between surges. Extensive studies of Trapridge, Backe, and Rusty have been carried out over the past decade to decipher flow characteristics of these glaciers while they are not surging and to gain an understanding of the cause of surging there (Collins, 1972; Goodman, et al., 1975; Jarvis and Clarke, 1975; Clarke, 1976).

As recently as 1976, additional work carried out on Trapridge by Jarvis and Clarke did not indicate development of any pre-surge characteristics: thermal profiles were not anomalous, and equipment could be sledged over the relatively uniform surface slope. Air photos taken over the past few years indicate the development of a slight bulge occurring in the ice, roughly mid-glacier, but the bulge was not a gross surface feature until observed in summer 1980.

Trapridge Glacier now has a steep ice front bulge (40 meters in height) running completely across the glacier about midway downglacier. The bulge could not be traversed except by use of fixed-line and crampons. A field program was initiated with G.K.C. Clarke (UBC-Geophysics) to study the pre-surge characteristics of Trapridge. Thirty 10 foot electrical conduit tubes were painted and numbered, then set into the glacier in a survey network across the bulge, down the ice front, and in front of and behind the bulge. This network was surveyed, using a Wild T-2 theodolite, multiple times during the summer from several fixed bedrock survey stations. Several of the stations were those used during studies of previous years. Hence, large airphoto targets were also set up at these stations and airphoto flights contracted so that this year's survey of Trapridge can be tied back to that of previous years, providing a long time-base over which to study ice flow and profile changes.

Longitudinal profiles of the ice surface across the bulge were taken by leveling with the T-2 and a vertical subtense bar. Selected stations corresponded to the fixed survey poles set in the ice. In addition, seven holes were drilled in the ice using a propane-driven hot-water drill. These holes all went to bedrock and were located along the centerline profile below, across and above the bulge. Immediately upon completion of drilling of each hole, thermistors were lowered into the waterfill hole and allowed to freeze in place. Thermistors were spaced on the cable at an interval to allow 6 to 10 thermistors per cable depending on the hole depth. Ice thicknesses above the bulge reached 60 meters, whereas below the bulge, the ice was only 15-20 meters thick.

However, the high density of thermistors has allowed very detailed thermal profiles and hole freezing histories to be developed.

It has been found that all the thin ice below the bulge is several degrees below freezing, even at the bed, but the ice across the bulge front and above the bulge is temperate at the bed and only below freezing in the upper layers of the glacier. The bulge itself corresponds exactly to the transition between the warm ice core of this subpolar glacier and the surrounding sheath of subzero ice. This characteristic helps explain not only the current surface profile of Trapridge but also the cause of its surge behavior (Thompson, 1980). Essentially the bulge and warm ice core is sliding into and up against the frozen ice tongue below the bulge. The surge will occur as soon as the stresses built up at the ice front are great enough to overcome the blockage of the cold ice dam.

All seven drill holes were waterfilled during drilling because of the hot water drill-medium. However, even within 12 hours, the holes in cold ice had refrozen solid and had to be reamed and redrilled for installation of thermistors and hydrophones. The holes in warm ice remained open, but waterfilled. The deepest, uppermost hole drained rapidly during drilling at about 30m depth, indicating communication with open intra-glacial channels at that depth. Upon further drilling the hole again refilled, but then as basal ice and silt was encountered at about 62 meters, the hole drained again. Sounding showed the piezometric water level to be at 30 meters above the bed, but below the initial drainage level. The water was thus at pressure and communicating with open water or channels at the bed. A combination of thermal profile data, freezing and hole closure data, and water level data in boreholes above the bulge has allowed development of a simplified water storage model in Trapridge Glacier. The core of temperate ice allows for buildup of water behind the slip/non-slip boundary at the glacier bed. A theory is now being developed which details that this water can propagate subglacially in conjunction with stress discontinuities in the basal ice, allowing for possible jokulhlaup release of the water. The propagation of the stress discontinuity and water front must enhance if not control the glacier surge itself. An understanding of the water surge mechanism in association with the ice surge provides better understanding of the source of water for catastrophic floods in glaciated areas wherein water may be protected from the open atmosphere environment, as required on Mars, so that floods can be derived from mechanisms other than free-surface ice-dammed lakes. However, the study also provides information on how an ice-dammed lake may leak and communicate with subglacial or intraglacial channel networks, and subsequently break out.

This research was carried out under NASA Contract 7-100.

REFERENCES:

- Collins, S.G., 1972, Survey of the Rusty Glacier area, Yukon Territory, Canada, 1967-1970: Jour. Glaciology, vol. 11, no. 62, p. 235-253.
- Clarke, G.K.C., 1976, Thermal regulation of glacier surging: Jour. Glaciology, vol. 16, no. 74, p. 231-250.
- Goodman, R.H., G.K.C. Clarke, G.T. Jarvis, S.G. Collins, and R. Metcalfe, 1975, Radio soundings on Trapridge Glacier, Yukon Territory, Canada: Jour. Glaciology, vol. 14, no. 70, p. 79-84.
- Jarvis, G.T., and G.K.C. Clarke, 1975, The thermal regime of Trapridge Glacier and its relevance to glacier surging: Jour. Glaciology, vol. 14, no. 71, p. 235-250.
- Thompson, D.E., 1980, Surging glaciers as an oscillatory steady-state flow: Reports of Planetary Geology Program, NASA-TM, this volume, 1981.

## SURGING GLACIERS AS AN OSCILLATORY STABLE FLOW

David E. Thompson, Jet Propulsion Laboratory, California Institute of Technology, Pasadena, CA 91103

About 200 glaciers in North America exhibit periodic flow behavior, alternating between long periods of quiescent flow and stagnation and sudden surge flow. The surges usually last for one or two years, and ice flow velocities increase by hundred-to-thousand-fold to rates of kilometers per year, although the ice snout advance does not necessarily proceed at this rate. Post (1969) and Meier and Post (1969; and other articles in this symposium volume) have summarized many of the general characteristics and observations of surging glaciers. Surges occur in cirque, valley, and piedmont glaciers ranging in size from 2 to 200 km in length, and possibly in some ice sheets, in glaciers of varying surface slope, longitudinal profile, and thickness, and in glaciers in different climatic regimes and bedrock types. Surging glaciers are not uniquely correlated with areas of high tectonic activity or geothermal heat flow, and they can be either temperate throughout or of cold, subzero ice. Although accurate bed profiles are not available for most glaciers, their gross bed topography appears to be no different from that under non-surging glaciers.

Any theory for surges needs to be able to explain the roughly uniform periodicity of surges, the 2 to 3 year average duration of continuous surging, the reason why only a few glaciers of the thousands of active glaciers surge, and certain dynamical characteristics during surging. A reservoir and receiving area can always be defined for a surge, and when a surge occurs, the downstream part of the reservoir begins to swell and the ice surface gradient steepens. A surge is initiated just below this point and propagates both up- and downstream. The ice thickness in the reservoir is lowered appreciably, on the order of tens to hundreds of meters, and a large bulge of ice propagates toward the terminus throughout the duration of the surge. The bulge is distinguishable from a kinematic wave in that it does not travel unchanged down the glacier but continually envelopes more of the glacier leaving a chaotic crevasse pattern on the surface caused by the increased flow velocities (Meier and Post, 1969). A kinematic wave in glaciers is a response to a perturbation in accumulation rate (Nye, 1960), and surges do not appear to be governed by so well defined a perturbation. Rapid, erratic ice flow inhibits temperature- or velocity-at-depth measurements during a surge so that essentially nothing is known about the stress or flow fields, or about the physical properties of the ice.

Current ideas for the origin of surging have been: a) that the surge arises as a result of wide-spread lubrication of the glacier along its base from a thickening water film (Weertman, 1969; Robin and Weertman, 1973; Budd and McInnes, 1974); b) that at least for subpolar glaciers a softening of basal ice from geothermal heat flux could allow surging (Robin, 1955; Clarke, 1976); and c) that changes in longitudinal stress gradients might allow a rapid change from compressive to extensive flow (Robin, 1967, 1969). None of these theories fully explains the erratic behavior of surging glaciers as evidenced by the highly contorted medial moraines (Meier and Post, 1969, p. 809) which seem to imply a laterally

non-uniform surging. Conceptually, the surge phenomenon appears to be an oscillatory flow state whereby certain glaciers suddenly become unstable, advance catastrophically, then gradually return to their more quiet mode. Theoretical analysis carried out over the past several years has shown that it is difficult to conceive of a basic glacier flow regime which develops inherent flow instability against certain simplified flow perturbations (Thompson, 1976, 1978, 1979, 1980) but even if unstable flow regimes were readily possible in glaciers, one would still need to explain why all glaciers do not surge.

Recent, very detailed field work on Trapridge Glacier, a small surge glacier in the St. Elias Mountains, Yukon, by myself and Garry Clarke (UBC), has yield information which tends to show that the surge phenomenon may not need to be classified as a flow instability, but rather that surges represent an equilibrium stable flow which is oscillatory as a primary flow. The clue to understanding this mode of flow is one of realizing how glaciers maintain uniform ice discharge. Glaciers flow both by internal deformation and by slip at the bed. A given discharge of ice can be moved either by a thin rapidly moving glacier (high slip) or by a thick but slowly moving glacier (low slip). The degree of internal deformation depends on ice thickness and slope, but not on amount of bedslip. Trapridge Glacier has a warm ice core which is lubricated at the bed by meltwater, and an outer sheath of cold ice frozen to the bed and not slipping. Thus, a slip region is flowing into a non-slip region. As the temperate ice core flows against the cold ice down at the tongue of the glacier, it is blocked and ice begins to build up behind the non-slipping cold ice. In order for Trapridge to maintain a uniform discharge, or, in fact, not to exist in an oscillatory flow state, the downstream cold ice tongue would have to flow at the same rate as the warm ice core. But because the cold ice is frozen to the bed and not slipping, it would have to flow in terms of internal creep only, and in order for it to deform fast enough to keep pace with the warm core which is deforming and slipping, it would have to be very thick or on a very steep slope. But the Trapridge tongue is thin and long, and a glacier cannot be thickening into its terminus nor can a steep glacier be both thick and long. Therefore, the slip-region ice overtakes the non-slip region ice, the surface gradient steepens until longitudinal stresses overcome the blocking of the ice dam, a surge occurs, the ice profile thins and levels out, and the glacier then freezes to the bed throughout its length, shutting off the surge. Over time, the ice thickens again in the accumulation basin, it melts at the bed and a warm core is formed whereby the surge cycle starts again.

The important point in this scenario is that the only requirement for a surge is to have an upstream slip region and a downstream blockage to flow. If this condition exists, then the only possible flow state is an oscillatory flow which then represents the equilibrium stable flow of the glacier. The glacier is not unstable: it is always responding in a way to restore equilibrium. The requirement of change from slip to non-slip can be easily envisioned in sub-polar glaciers where the source of non-slip is the frozen basal ice with no free water. However, a temperate glacier may exhibit the same behavior if, for example, the lower reaches of the glacier flow over permeable or friable metamorphic rocks or moraine. In that case, the water at the bed can drain out into

the bedrock, under pressure, thus preventing the lubrication needed for enhanced slip. Slip may still occur, but if the downstream ice does not keep pace with the upstream discharge, an oscillatory flow state must develop.

This theory is now being made more exact by developing flow models and varying parameters to delineate specific flow response criteria, and to determine whether the surge should, in fact, activate the cold ice, override it, or just bulldoze through it.

This research was carried out under NASA Contract 7-100.

#### REFERENCES:

- Budd, W.F., and McInnes, B.J., 1974, Modelling periodically surging glaciers: Science, vol. 186, p. 925-927.
- Clarke, G.K.C., 1976, Thermal regulation of glacier surging: Jour. Glaciology, vol. 16, p. 231-250.
- Meier, M.F., and Post, A., 1969, What are glacier surges?: Canadian Jour. Earth Sci., vol. 6, p. 807-816.
- Nye, J.F., 1960, The response of glaciers and ice-sheets to seasonal and climatic changes: Proc. Roy. Soc. London A, vol. 256, p. 559-584.
- Post, A., 1969, Distribution of surging glaciers in western North America: Jour. Glaciology, vol. 8, p. 229-240.
- Robin, G. de Q., 1955, Ice movement and temperature distribution in glaciers and ice sheets: Jour. Glaciology, vol. 2, p. 523-532.
- 1967, Surface topography of ice sheets: Nature, vol. 215, p. 1029-1032.
- 1969, Initiation of glacier surges: Canadian Jour. Earth Sci., vol. 6, p. 919-926.
- Robin, G. de Q., and Weertman, J., 1973, Cyclic surging of glaciers: Jour. Glaciology, vol. 12, p. 3-18.
- Thompson, D.E., 1976, Application of fluid-instability analysis to glacier flow: Ph.D. Thesis, UCLA, Los Angeles, California.
- Thompson, D.E., 1978, Stability of glaciers against long-wavelength surface perturbations: EOS, Trans. American Geophys. Union, 59, no. 4, p. 274.
- Thompson, D.E., 1979, Stability of glaciers and ice sheets against flow perturbations: J. Glaciology, vol. 24, no. 90, p. 427-441.
- Thompson, D.E., 1980, Pre-surge characteristics and water storage in Trapridge Glacier, Yukon, summer 1980: Reports of Planetary Geology Program, NASA-TM, this volume, 1981.
- Weertman, J., 1969, Water lubrication mechanism of glacier surges: Canadian Jour. Earth Sci., vol. 6, p. 929-939.

GEOMORPHIC AND HYDRAULIC ANALYSIS OF CATASTROPHIC FLOOD FEATURES  
IN THE ALSEK RIVER VALLEY, YUKON

David E. Thompson, Jet Propulsion Laboratory, California Institute of Technology, Pasadena, CA 91103.

A geomorphic map has been constructed of the pertinent fluvial features found in the Alsek River Valley, both upstream and downstream of Lowell Glacier. About every 70 to 100 years, Lowell Glacier surges, advances, and block the drainage of Alsek River. Lake Alsek forms behind the ice dam and grows to roughly 70 km with a total volume estimated at 40 cubic kilometers of water. The lake drains catastrophically on the order of a few days by destruction of the ice dam, scouring much of the Alsek Valley below the dam and creating giant current ripples upstream of the dam during sub-critical flow over the lake bottom. The initial field program in this area dealt with profiling the giant current ripples and extensive gravel sampling of the debris which makes up these features. The goal has been to decipher flood hydraulics from recognition of the size of debris moved and to create a scenario for flooding history across the large gravel bars. Additionally now, work has begun on the more intense scour features located downstream of the Lowell Glacier dam.

The area is complex in that flooding occurs periodically over the same gravel bars, reworking the debris and the features: it is not representative of one major flooding event occurring over a pristine environment such as occurred in the Channeled Scabland or perhaps on Mars. In addition, the flooding is constricted to a previously formed river channel, and various changes of channel direction or local constrictions add major complexities to the flow pattern. Several kilometers below the Lowell Glacier dam is Fisher Glacier, and below that Tweedsmuir Glacier. Both of these glaciers also periodically surge and block the Alsek drainage, so that, for example, superposed in the downstream scour features below the Lowell dam are extensive lacustrine deposits and current ripples from Lake Fisher. This overlap has made it difficult to distinguish high-water levels of flood scour from lake storm-beaches. However, certain scour features are diagnostic of local high turbulence.

Perhaps the most common feature downstream of ice dams is the pervasive horseshoe vortex scour around obstacles in the flow. These features lie in association with massive boulders which probably have not participated in the flooding as bedload unless only during the initial dam break-up. Generally, these boulders have been ice-rafted over the lake, then dropped before the flooding begins. The horseshoe vortex scour occurs upstream of these obstacles, and the greatest density is immediately below the ice dam in regions of steep gradient. The presence of these scour features indicates that the fluid flow must be relatively of low concentration of debris in that a high debris concentration allows for a quasi-viscous diffusion of vorticity and prevents intensification necessary for this type of scour (Richardson, 1968). However, it remains to be determined at what stage in the flooding this scour is occurring in the Alsek Valley.

Large reaches of longitudinal scour and grooves appear to develop in



uniform directions only slightly correlated with the general channel topology. Reaches with small radii of curvature are generally overridden by the longitudinal grooving, and change in grooving direction only occurs with respect to large channel direction changes. Terracing and grooving seems to be well developed in finer bar material whereas scour and current ripples develop in debris of cobble-sized clasts.

More extensive field work needs to be done in reaches between ice-dam locations in order to separate out high water levels during flooding. Calculation of total lake volumes and total flood duration gives only average discharge calculations; what is needed is a development of flood hydrographs or, at least a separation of different stages of flooding in gross detail so as to identify significant periods of high erosive potential, sediment transport, and structured turbulence in the flood.

This research was carried out under NASA Contract 7-100.

#### REFERENCES:

Richardson, P.D., 1968, The generation of scour marks near obstacles: Jour. Sed. Pet., vol. 38, no. 4, p. 965-970.

Hillslope modification and evolution of the Valles Marineris wall scarps. Peter C. Patton, Department of Earth & Environmental Sciences, Wesleyan University, Middletown, Connecticut 06457, and Victor R. Baker, Department of Geological Sciences, The University of Texas at Austin, Austin, Texas 78712.

In addition to the impressive landslide modification of the walls of the Valles Marineris system (Lucchitta, 1978) there are other important slope elements developed on the canyon walls. The slope forms are modified as a function of relative scarp angle, degree of structural control and the inferred degree to which the slope base is rejuvenated by removal of accumulated regolith. This last factor can only be inferred through analogy to cliff retreat mechanisms and resulting hillslope forms on Earth. While a complete continuum of slope morphology can be proposed, it appears that slope evolution does not proceed through a continuous process but is strongly controlled by structure.

Relatively small reentrants in the form of small troughs eroded into the steep smooth scarps of the major grabens is the first major hillslope element. These slope forms are not preferentially eroded along lines of structural weakness and are essentially normal to the cliff face. They are well developed along the northern margin of Tithonium Chasma. The overall morphology of these small reentrants is similar to the scarp face dry valleys of the Chalk Escarpment in southern England (Small, 1964). Similar to the Martian scarp valleys most of the chalk dry valleys are not preferentially developed along joints or faults but have their axis perpendicular to the escarpment. The evolution of the chalk scarp valleys has been attributed to spring sapping processes (Small, 1964) and to intensified freeze-thaw activity during periglacial climates (Brown, 1969). The lack of correlation of the valleys with the joint controlled spring systems favors the periglacial hypothesis (Brown, 1969). Solifluction lobes present at the mouth of the chalk valleys indicate that periglacial processes are probably the most important mechanism in removing debris from the valley floor. This process may be equally important on Mars but debris lobes cannot be positively identified.

Small Martian scarp face valleys gradually merge with the spur and gully topography described by Lucchitta (1978). Spur and gully slope development occurs on longer lower gradient slopes as secondary scarps develop within the lengthening slope system. Spur and gully hillslopes are only extensively developed along the major scarps in the Valles Marineris system. Well developed hillslopes of this type are numerous in Ius Chasma. Based on known models of hillslope development (Carson and Kirkby, 1972) these forms require that regolith be removed from the hillslope system in order for the resistant spurs to achieve topographic expression. Removal of debris

from the slope may be accomplished by a variety of processes. Solifluction and aeolian processes are two possibilities but cannot be proven. An additional possibility is that graben subsidence has continued during slope development thereby effectively removing material from the slope base. In Ius Chasma the truncation of hillslope bases which have extensive spur and gully development by several apparent fault scarps provides partial support for this hypothesis. Therefore extensive spur and gully topography may be associated with areas of rapid subsidence.

The elongate alcove headed tributary valleys to the major grabens are the third major slope element. Numerous excellent examples can be found in Ius Chasma. These valleys are strongly structurally controlled and differ from the scarp face valleys in that pronounced spur and gully topography has not modified their slopes. Analogous planimetric valley forms exist on the Colorado Plateau where resistant cliff forming sandstones cap the hillslopes (McKnight, 1940; Baker, 1946). The valleys of the southwestern U.S. expand by slab failure of these sandstones (Schumm and Chorley, 1964). Many of these cliffs maintain vertical faces as they retreat because of the rapid disintegration of the weakly cemented sandstones. It is suggested that the slopes of the Martian valleys have evolved through similar processes but that the debris generated by slope retreat has accumulated as a mantle of talus producing smooth slope forms and parallel retreat of the slope crest (Carson and Kirkby, 1972). This would imply that proposed sediment transport processes such as solifluction may have been less important in the evolution of these slopes.

Therefore, it appears that simple rockfall - slab failure hillslope models with or without regolith storage can account for the slope forms present in the Valles Marineris system.

#### References

- Baker, A.A., 1946, Geology of the Green River Desert-Cataract Canyon region Emery, Wayne and Garfield counties Utah: U. S. Geol. Survey Bull. 951, 122 p.
- Brown, E.H., 1969, Jointing, aspect and the orientation of scarp-face dry valleys, near Ivinghoe, Buckinghamshire: Trans. Inst. British Geog., v. 48, p. 61-73.
- Carson, M.A. and Kirkby, M.J., 1972, Hillslope form and process: London, Cambridge Univ. Press, 475 p.

- Lucchitta, B.K., 1978, Morphology of the chasma walls, Mars: U.S. Geol. Survey Jour. of Research, v. 6, p. 651-662.
- McKnight, E.T., 1940, Geology of area between Green and Colorado rivers Grand and San Juan counties Utah: U.S. Geol. Survey Bull. 908, 147 p.
- Schumm, S.A. and Chorley, R.J., 1964, The fall of Threatening Rock: Am. Jour. Sci., v. 262, p. 1041-1054.
- Small, R.J., 1964, The escarpment dry valleys of the Wiltshire Chalk: Trans. Inst. British Geog., v. 34, p. 33-52.

Exhumed topography--a case study of the Stanislaus Table Mountain, California, D.D. Rhodes, Department of Geology, Whittier College, Whittier, CA 90608 (NASA Summer Faculty Fellow, Jet Propulsion Laboratory, California Institute of Technology, Pasadena, CA 91103)

Exhumed topography is one possible result of a cycle of erosion, deposition, and renewed erosion. Resurrected landforms are not only excellent evidence for episodic erosion, but the preserved landform itself is also a record of the conditions under which it formed. Certain geometrical patterns and the unusual appearance of some knobs, ridges, and craters led Sharp (1973) to suggest that some features in the south polar region of Mars were the results of exhumation. Soderblom et al. (1973) presented evidence for the erosion of a debris mantle and consequent resurrection of topography in areas distant from the martian polar regions. Both studies indicate that exhumation may be important and widespread on Mars. As a step toward a better understanding of exhumed topography, a resurrected landform in California was studied.

The landform chosen for the analog study is the Stanislaus Table Mountain of the west-central Sierra Nevada Range. Table Mountain is not a single feature, but rather a discontinuous line of flat-topped hills, which extend for more than 95 km, from the crest of the range near Sonora Pass to Knights Ferry at the edge of the Great Valley. Table Mountain was originally one of a number of Tertiary valleys cut in a blanket of pyroclastic volcanic debris that covered most of the western slope of the northern Sierra Nevada (Lindgren, 1911). Approximately 9 m.y. ago latite lava flowed down the valley and partially filled it (Bateman and Wahrhaftig, 1966). Plio-Pleistocene uplift of the Sierras rejuvenated the rivers draining the range. Uplift and base level changes were large. For example, at Parrots Ferry, the modern Stanislaus River occupies a canyon which has been cut to a depth of 400 m below the surface of the Table Mountain flow. Most of the volcanic cover was stripped from the area, but the resistant latite cap protected parts of the Table Mountain channel. Above Parrots Ferry, the flow has been heavily dissected. However, the downvalley portion of the Table Mountain flow has undergone relatively little erosion. The flow was exhumed from the surrounding pyroclastic debris, and the topography was inverted around it. The previous valley is now a ridge, which in places stands as much as 90 m above the re-exposed bedrock surface. Many of the original characteristics of the Pliocene valley are well preserved. Seen from the air (figure 1), the lower portion of Table Mountain has the sinuous path of the original meandering channel. Tributary junctions are preserved as spurs projecting from the main ridge. These details of the former topography can be used to analyze the Pliocene stream system.

An estimate of the paleo-hydrology of the channel can be made from geometrical properties of the flow. The pattern is meandering, with a rather low sinuosity (about 1.3). The meanders have radii of curvature that vary in length from about 150 m to 450 m. Meander wavelengths are also variable, ranging from approximately 320 m to 1380 m. The width of the flow averages 150-180 m. Using these geometric properties of a meandering pattern and their relationships to the discharge of modern rivers (Carlston, 1965), it was possible to estimate the mean annual flood of the Table Mountain paleo-channel. Although all measured parameters are variable, they indicate a comparatively small range of discharges, on the order of 30-140 m<sup>3</sup>/sec.

The numerous tributary junctions preserved by the lava are also informative. Nearly all of the paleo-tributaries entered the main stream at high angles, i.e. greater than 45°. High junction angles are associated with tributaries that have a significantly steeper slope than the trunk stream (Horton, 1932) and that are of much lower magnitude than the main channel (Pieri, 1979). These relationships are evidence that the relief in this portion of the Table Mountain drainage was significant and not the gently rolling surface envisioned in previous studies (Lindgren, 1911, and others).

A feature that has a form similar to the Stanislaus Table Mountain exists in the Mangala region of Mars (figure 2). The steep-sided, flat-topped ridge is sinuous and has projecting spurs remarkably like those of Table Mountain. If this landform is an inverted and exhumed valley, it is strong evidence for distinct episodes of erosion on Mars.

This study was conducted at the Jet Propulsion Laboratory under the auspices of the NASA Summer Faculty Fellowship Program. R.S. Saunders served as Research Colleague.

### References

- Bateman, P.C., and Wahrhaftig, C., 1966, Geology of the Sierra Nevada; in Bailey, E.H., ed., Geology of northern California: California Division of Mines and Geology Bulletin 190, p. 107-172.
- Carlston, C.W., 1965, The relation of free meander geometry to stream discharge and its geomorphic implications: American Journal of Science, v. 263, p. 864-885.
- Horton, R.E., 1932, Drainage basin characteristics: American Geophysical Union Transactions, v. 13, p. 350-361.
- Lindgren, W., 1911, The Tertiary gravels of the Sierra Nevada, California: U.S. Geological Survey Professional Paper 73, 226 p.
- Pieri, D.C., 1979, Geomorphology of martian valleys [Ph.D. dissertation]: Ithaca, NY, Cornell University, 280 p.
- Sharp, R.P., 1973, Mars: south polar pits and etched terrain: Journal of Geophysical Research, v. 78, p. 4222-4230.
- Soderblom, L.A., Dreidler, T.J., and Masursky, H., 1973, Latitudinal distribution of a debris mantle on the martian surface: Journal of Geophysical Research, v. 78, p. 4117-4122.



Figure 1. A portion of the Stanislaus Table Mountain, located west of Jamestown, CA. The latite cap rock preserves the meandering pattern and tributary junctions of the paleo-channel. (Photo from Fairchild Aerial Photography Collection)

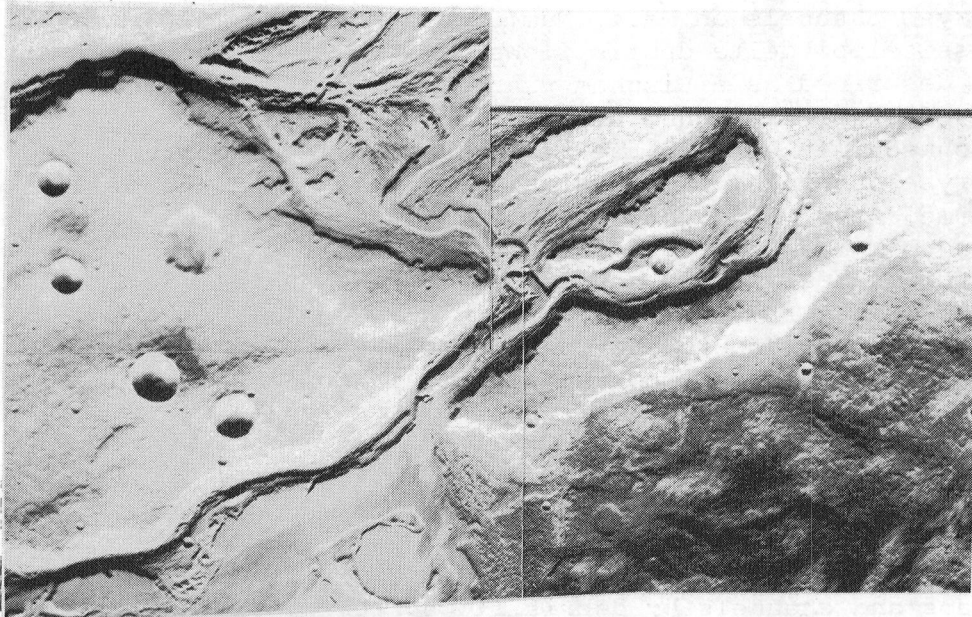


Figure 2. Photomosaic of a portion of the Mangala region of Mars. Smooth terrain, including sinuous ridge, filled crater, and table land appear to be exhumed. Center of mosaic is at approximately -6.7, 155. Scale is about 6900 m/cm. (Viking survey images 452S 19-21.)

## RHEOLOGY OF BINGHAM PLASTICS AND IMPLICATIONS FOR MARS CHANNELS.

Dag Nummedal, Dept. of Geology, Louisiana State University, Baton Rouge, LA 70803.

Channels are defined as large, elongate, erosional features containing a suite of bedforms indicative of large scale fluid flow. Many channels originate in chaotic terrains and incorporate areas which appear to be regions of older chaos modified by outflow from sources further upstream. This applies in particular to channels in the Chryse region of Mars. This sequential modification strongly suggests that the channels developed, in part, in a headward direction through processes of fluid release from the ground, followed by surface collapse.

This investigation attempts to identify the properties of the released fluid through an analysis of the rheology of a Bingham plastic. A Bingham plastic model was chosen because of the striking morphological similarities between subaqueous debris flows on the Mississippi delta and the Chryse channels on Mars (Nummedal and Prior, 1980). The Mississippi delta debris flows may, to a first approximation, be described as a Bingham plastic. By using the equations for flow of a Bingham plastic in a semi-elliptical channel (Johnson, 1970) with the proper hydraulic geometry of the Chryse channels, the shear strength for the material which formed Ares, Simud, Tiu and Shalbatana Valles, was found to range from 30 to 200 dynes/cm<sup>2</sup>, i.e. corresponding to the natural shear strength values of the Scandinavian Holocene quick clays.

The results support the contention that quick clay liquefaction may be an important factor in chaos and channel generation.

### References:

- Johnson, A. (1970): Physical Processes in Geology. Freeman Co. San Francisco.
- Nummedal, D. and Prior, D.B. (1980): Origin of Martian chaos and channels by debris flows. Icarus (in press).



### Submarine Landslides.

David B. Prior, Coastal Studies Institute, Louisiana State University, Baton Rouge, LA 70803

Geologists are beginning to appreciate that submarine slope-instability, particularly on continental shelves and shelf breaks, is a common and widespread phenomenon. Active landslides and areas of former instability, probably of late-Pleistocene age, are being identified by modern survey techniques. The significance of such processes to geologic sedimentation models and submarine slope evolution has been underestimated. Slope instability is responsible for large scale distinctive morphology, various sediment deformation structures, bed thickness inconsistencies and in some places may be the dominant method of sediment transport. The scale of activity and individual features, including rotational and planar sliding, debris flows and mudslides is impressive. It is undoubtedly true that the largest landslides on earth have occurred on the bottom of the sea.

Sediment movement in submarine settings occurs under reduced effective gravity because of the buoyancy due to ambient water. Therefore, good terrestrial analogs for channels and sediment instability features on Mars should be sought among seabed features.

## PRELIMINARY GEOMORPHIC INTERPRETATION OF THE VALLES MARINERIS, KASEI VALLES AND NOCTIS LABYRINTHUS REGIONS OF MARS

Bodard, J. (+), Pernet, E. (+), Rogeon, P. (+), Bousquet, B. (+),  
Masson, Ph. (++)

(+) Institut de Géographie et d'Aménagement Régional, Université de  
Nantes, 44 000 Nantes (France) ;

(++) Laboratoire de Géologie Dynamique Interne (ERA n° 804-02),  
Université Paris-Sud, 91 405 Orsay (France).

These studies aim to determine if, as on the Earth, it is suitable to define a morphology directly related to the structural constraints, to evaluate the importance of the erosional processes, and to define the types of the involved erosional processes. On the Earth, every erosional process is resulting of the combined actions of internal (tectonism and volcanism), external (mainly weathering) and biological agents. On Mars, the erosional processes seem to be only related to the internal and external agents. The observation of slope deposits and of the erosional landforms allow us to assume that in addition to the landforming process due to the meteorite bombardments, external agents directly related to the planet environment do have an important action on its surficial evolution.

The methodology used in this preliminary study is similar to the methodology used in terrestrial geomorphic studies :

- observation of the structures and determination of the relevant geomorphic features,
- observation of erosional and depositional features (types, groups, localization, and relationships with morphology),
- interpretation of the relationships between the morphology and the land forms. Based on the interpretation of Viking Orbiter images, sketch maps using the same geomorphic symbols as those used for terrestrial geomorphic maps, are produced.

The polygonal network observed in Labyrinthus Noctis seems to be superimposed on cracks. This network seems to be very similar to terrestrial dessication cracks. The mechanism involved in such process of formation would be related to vapor release of the humidity contained in the martian crust. The network produced by that process would have been enlarged and widened by the Tharsis updoming

movements. This process could also explain the formation of the aligned crater chains which could be related to the crack early initiation.

Some areas of Kasei Valles seem to show a similar evolution. But in the Chryse Planum western boundary, a pattern of valleys similar to the terrestrial fluvial systems is observed. It shows the same type of tributary organization, the same type of confluences, and the same type of drainage basin. The analysis of the fluvial system shows two sequences of patterns. Capture of streams produced by over flooding or by regressive erosion and by tectonic movements, have also contributed to the formation of this fluvial pattern. Although these observations seem to indicate that fluvial streams occurred in some places in Kasei Valles and in Valles Marineris, some of these landforms could be due also to turbulent streams in eolian or torrential regimes. These different types of streams could not have an atmospheric source. But they could have a phreatic origin or could be due to suddenly vapor releases.

Another question relevant to the duration of these processes has to be addressed : are these stream-like forms due to catastrophic floods occurring after a long period of endogenic preparation, as indicated by some geomorphic characteristics of the channels (e.g., transverse sections or profiles), or did these streams took place during a relatively long period of time as apparently indicated by the sinuous network of these channels ? The second hypothesis (long period of stream erosion) could be confirmed by the fact that some of these stream channels are modified by large impact craters.

In Valles Marineris these observations are implemented by the studies of the wall and slope evolution. This evolution seems to happen under two different modes :

- internal processes (tectonics) producing catastrophic landslides controlled by secondary erosional processes,
- slope deposits suggesting progressive erosional processes due to elementary fragmentation or destruction of the canyon walls.

According to the altitude of these deposits, one can admit that some of these slopes are older than the others, and that a period of humidity took place into a dry period. The catastrophic evolution of the

walls would have taken place during the period of humidity, and would have interrupted the slow evolution of the walls during the dry period. The resulting detritic materials are possibly removed by the wind and by running stream (according to the channels observed at the bottom of these deposits). It is possible that some of these processes (related to a dry period) are still active.

During the catastrophic period of landsliding, the interchannels are moving backward very rapidly. This evolution could explain the formation of the different chasmas observed in Valles Marineris. The size of these chasmas could be explained not only by the action of landslides but also by an initial fracturation.

# A MODEL FOR THE REMOVAL AND SUBSURFACE STORAGE OF A PRIMITIVE MARTIAN ICE SHEET.

Clifford, S. M., Dept. of Physics and Astronomy, University of Massachusetts, Amherst, Ma. 01003

In the martian northern plains and near the south polar cap, examination of Viking orbiter imagery has revealed a number of features which bear a strong resemblance to Iceland's table mountains (Allen, 1979; Hodges and Moore, 1979). Since table mountains are formed by subglacial volcanic eruptions, the discovery of possible analogs on Mars has led to the suggestion that an ice-rich unit once covered a significant fraction of the planet's surface; from an examination of the height of these landforms Allen (1979) has determined that the thickness of this unit may have ranged from 100 to 1200 m. In response, Arvidson *et al.* (1980) have argued that, in the absence of any obvious volatile sinks of sufficient size, the problems associated with the removal and storage of such a massive ice sheet make it difficult to support a subglacial origin of the martian 'table mountains'. However, a number of these problems can be surmounted by the hydrologic model discussed by Clifford *et al.* (1979) and Clifford and Huguenin (1980a). This model is based on the existence of a global interconnected groundwater system underlying the martian permafrost. Even a fairly conservative estimate of the storage potential of such a groundwater system still provides sufficient volume to readily accommodate a mass of H<sub>2</sub>O equivalent to that which may have been stored in an extensive primitive ice sheet.

A groundwater system is necessarily subject to certain geologic constraints - the most obvious being that there must exist a suitably porous and permeable layer in which the groundwater can reside. The existence of such a layer on Mars is expected for a number of reasons, most of which are summarized by Carr (1979) and Fanale (1976). Figure 1 is a simplified physical description of this crustal layer. For the purposes of this abstract we will assume that lithostatic pressure leads to self-compaction of fracture

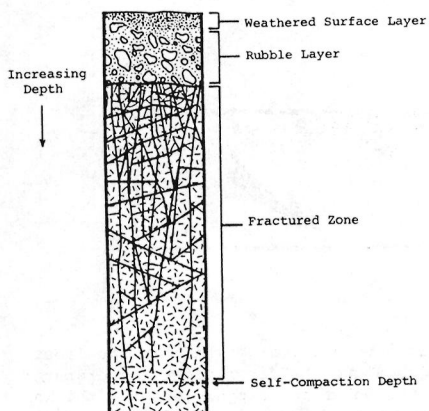


Figure 1. An idealized stratigraphic column of the martian crust. The levels illustrated are: a) the weathered surface layer, or martian "soil", a fine particulate material which is thought to have an average depth of from one to several hundred meters (est. mean porosity: ~30 - 50%) (Pollack *et al.*, 1979; Hillel, 1971); b) the rubble layer, consisting of a mantle of crater ejecta interbedded with volcanic flows (est. mean depth: several kilometers or more; est. porosity: 10 - 50%) (Fanale, 1976; Carr, 1979); c) the fractured zone, basement material fractured *in situ* by impact generated shock waves and tectonic stress (depth to self-compaction: 10 - 20 km; est. mean total intergranular and fracture porosity: ~5 - 20%) (Carr, 1979; Davis and De Wiest, 1966; Wise, 1980; Motts, 1980).

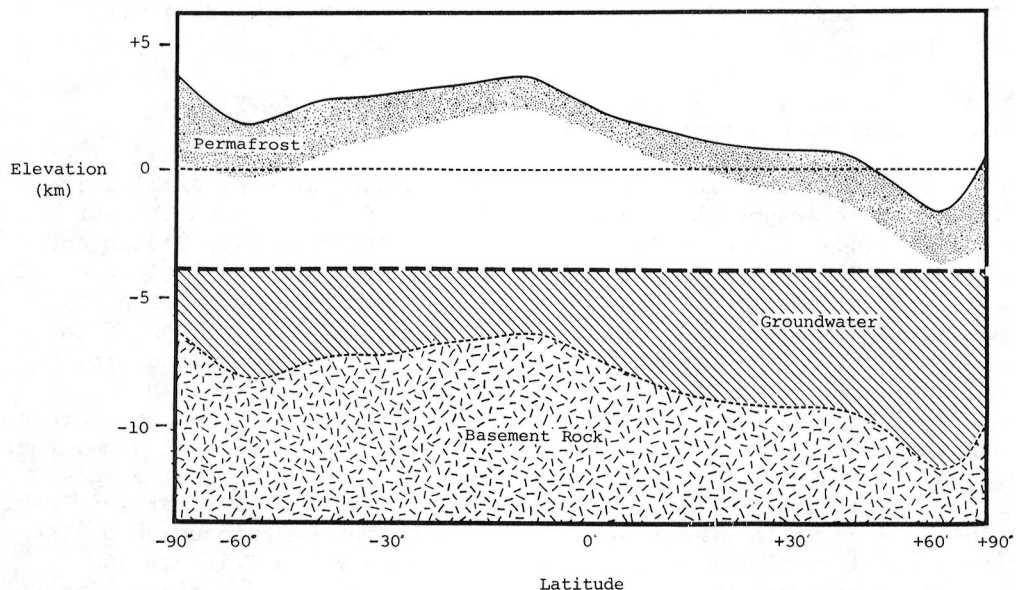


Figure 2. A pole-to-pole cross section of the martian crust illustrating the relationship between topography, permafrost and the proposed groundwater system. Surface elevations are averaged as a function of latitude after Mutch *et al.* (1976). Permafrost thicknesses are taken from Fanale (1976). The self-compaction depth is assumed to be a uniform 10 km.

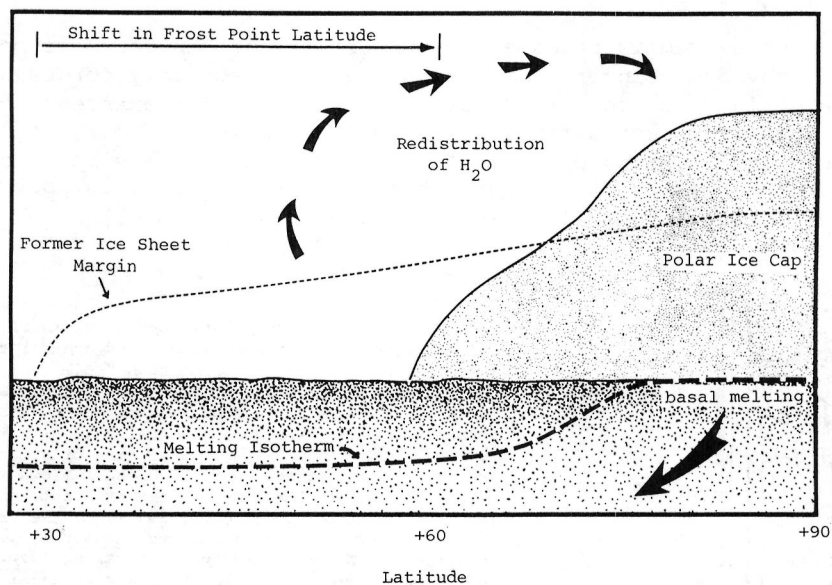


Figure 3. Retreat of a primitive martian ice sheet in response to a climatic shift in the frost point latitude. Low and mid-latitude surface temperatures rise above the frost point temperature resulting in the poleward redistribution of  $H_2O$ . Eventually the polar ice cap exceeds the thickness required for the onset of basal melting. Given the geothermal heat flux estimate of Fanale (1976), a 500 m thick ice sheet that once covered 40% of the planet could be introduced into the proposed global groundwater system in as little as ten million martian years. (Diagram is not to scale.)

and intergranular pore space at a uniform depth of 10 km below the martian surface and that the mean value of crustal porosity, down to this depth, is ~5% (Clifford and Huguenin, 1980b). These are probably conservative figures (Carr, 1979; Wise, 1980) but they serve to make the following point: Consider the amount of water contained in a hypothetical ice sheet 500 m thick and covering 40% of the martian surface. If we could somehow transform this ice into a liquid and use it to fill the available pore space in our model crust we would find that the groundwater system so formed would underly over 95% of the martian surface at a depth approximately 4 km below the planet's mean elevation (see Figure 2). Thus, even conservative choices for the depth of self-compaction and overall porosity yield a crust with a sizable groundwater storage capacity.

Given that the crust has sufficient capacity to store a primitive ice sheet as groundwater there still remains the question as to how this transformation can be physically accomplished. Figure 3 illustrates one possible approach. Ice will remain stable on the martian surface only at latitudes where the mean annual temperature remains below the frost point. Should the mean temperature rise above the frost point the ice sheet will begin to ablate and the H<sub>2</sub>O redistributed poleward. What the sheet loses in areal extent it gains in thickness at the pole. Each additional layer of ice deposited causes a readjustment of the local thermal gradient. Eventually a thickness is reached where basal melting will occur (Clifford, 1980). If the area involved in basal melting is equal to the present size of the permanent north polar cap, and if we assume the geothermal heat flux of  $22 \text{ cal cm}^{-2} \text{ yr}^{-1}$  calculated by Fanale (1976), then the entire mass of the hypothetical ice sheet described earlier could be introduced into a global groundwater system in as little as 8 million martian years.

In conclusion, we see that the hydrologic model presented by Clifford *et al.* (1979) and Clifford and Huguenin (1980a) can resolve both of the major problems cited by Arvidson *et al.* for the subglacial birth of the martian 'table mountains'. However, a true test for the existence of a global groundwater system, such as the one discussed here, must wait for some future program of seismic exploration on Mars (Tittmann, 1979).

Acknowledgement: This research has been supported under NASA grants NSG 7397, NSG 7405 and NAGW 40.

References: Allen, C.C. (1979) JGR 84, 8048; Arvidson *et al.*, Rev. Geophys. Space Phys. (in press); Carr, M.H. (1979) JGR 84, 2995; Clifford, S.M. (1980) Lunar Plan. Sci. Conf. XI (abs.), 165; Clifford *et al.*, (1979) BAAS 11, 580; Clifford, S.M. and Huguenin, R.L. (1980a) NASA TM 81776, 144; Clifford, S.M. and Huguenin, R.L. (1980b) BAAS (in press); Davis, S.N. and De Wiest, R. (1966) Hydrogeology, John Wiley & Sons, 463 p.; Fanale, F.P. (1976) Icarus 28, 179; Hillel, D. (1971) Soil Physics, Academic Press, 288 p.; Hodges, C.A. and Moore, H.J. (1979) JGR 84, 8061; Motts, W.S. (1980) personal communication; Mutch *et al.*, (1976) The Geology of Mars, Princeton Univ. Press, 400 p.; Pollack *et al.*, (1979) JGR 84, 2929; Tittmann, B.R. (1979) JGR 84, 7940; and Wise, D.U. (1980) personal communication.

LARGE LANDSLIDES IN OPHIR, CANDOR, AND MELAS CHASMATA, MARS, K. L. Kaufman and B. K. Lucchitta, U.S. Geological Survey, 2255 North Gemini Drive, Flagstaff, Arizona 86001.

Seven large landslides and their surroundings were studied in detail on Viking images and topographic maps. The deposits of these slides are banked against their break-away scarps, and large debris aprons extend onto the canyon floors below. Thus the slides are of type II in the classification scheme of Christiansen and Head (1). The combined deposits cover  $16,700 \text{ km}^2$  of the valley floor, and individual deposits range from 500 to  $6,900 \text{ km}^2$  in area. The landslide scars form reentrants 20 to 110 km wide in the chasma walls, which are 6 to 8 km high in this area. The landslide scars tower 2 to 5 km above the slide masses and are composed of talus slopes (near  $30^\circ$ ) topped by stubby ridges. Irregular, hummocky and jumbled slump blocks and Toreva blocks mark the head of the slide deposits. Within this upper part, subsidiary linear and curvilinear scarps are 5 to 15 km long and, in one place, a row of subsidiary scarps is 50 km long. This row of scarps parallels a graben on the plateau surface above the slide mass, and may be a pre-slide graben or it may consist of post-slide faults. Large debris aprons below the slump blocks extend toward the foot of the slides for distances as great as 110 km. They are longitudinally grooved, but most have some transverse ridges near the toe.

The great distances which these slides apparently traveled across the valley floors suggest high speeds. A minimum speed was ascertained in one place, where a slide deposit apparently lapped up onto a ridge to a height of 1 km. By equating the potential energy necessary to rise up on the ridge with the kinetic energy of the slide mass, a speed of about 300 km per hour was calculated for this slide at a distance of 50 km from its origin. This speed is slightly higher than that of most terrestrial catastrophic landslides (2), but below the speed (near 400 km per hour) determined for the upper reaches of the Huascarán slide in Peru (3).

All large slides in the area investigated lie on south facing slopes. The reason for this position is not known, but it could be due to a slight regional dip towards the south that would increase the shear stress (4), or it could be related to increased insolation that contributed to melting of ground ice in the chasma walls.

The landslides are relatively young. Superposition relations indicate that they post-date the tectonism that formed the chasma grabens, the formation of spurs and gullies on the chasma walls, the deposition of layered deposits within the chasmata, and the erosion of troughs between these deposits and valley walls. Also, the craters superposed on the slides have a density of 120 craters  $> 1 \text{ km}$  per  $10^6 \text{ km}^2$ , and so have a relative age slightly younger than the youngest martian channels (5) and equivalent to late eruptive activity on the Tharsis volcanoes. Locally, fault scarps appear to cut the slide deposits, suggesting that tectonic activity persisted into post-slide time.



Ophir, Candor, and Melas Chasmata, in which the landslides occur, are three separate fault troughs enlarged by mass-wasting of the walls. The plateau between the troughs was partially breached by the retreat of the walls toward one another, and an interconnected system of troughs was formed. However, the origin of the troughs as separate grabens is still evident in the elevation of their floors (6): the floor of Candor Chasma is about 1 km lower than that of Ophir Chasma to the north, and about 2 km lower than that of Melas Chasma to the south. These elevations differ from those on previous maps (7) based on Mariner images, which show a continuous gradient from Ophir to Melas. Candor Chasma thus forms a trough between Ophir and Melas Chasmata, and drainage from the slides, if they were wet, could not have been through-flowing toward the outlet through Coprates Chasma.

Study of the topographic map (6) in the region of the landslides inspired another interesting speculation. The stubby ridges at the top of slide scars are 1 to 2 km thick, and have been cited as evidence for a caprock, probably lava, underlying the plateau surface above the slides (8). The thickness of 1 to 2 km of this caprock corresponds to the thickness of the permafrost layer calculated for the equatorial region (9,10): it is possible that this caprock is not a resistant lava layer, but is ice-cemented rock of unknown composition. The caprock may now be seen as a separate layer because, on the landslide scars, the hypothetical ice-water interface was exposed by the sliding event. By contrast, in the adjacent areas of ridges and gullies on the walls where no caprock is seen, erosion may have been slow, the ground may have remained frozen parallel to newly exposed surfaces, and the ice-water discontinuity would not be seen at the surface.

#### REFERENCES

1. Christiansen, E. H., and Head, J. W., 1978, Martian landslides--classification and genesis (abs.): NASA Tech. Memo 79729, 285-287.
2. Lucchitta, B. K., 1978, A large landslide on Mars: Geol. Soc. of America Bull., 89, 1601-1609.
3. Plafker, G., and Erickson, G. E., 1978, Mechanism of catastrophic avalanches from Nevados Huascarán, Peru, *in* Rock Slides and Avalanches (Barry Voight, ed.), Elsevier, Amsterdam, 277-314.
4. Varnes, D. J., 1978, Slope movement types and processes, *in* Landslides: Analysis and Control (R. L. Schuster and R. J. Krizek, eds.), Natl. Acad. of Sci., Spec. Report 176, 11-33.
5. Masursky, H., Dial, A. L., Jr., and Strobell, M. E., 1980, Martian channels - A late Viking view (abs.), *in* Reports of the Planetary Geology Program, 1979-1980, in press.
6. Wu, S. S. C., 1980, Coprates Northwest: U.S. Geol. Survey Atlas of Mars, 1:2,000,000 Topo. Ser., in prep.
7. U.S. Geological Survey, 1976, Topographic map of Mars: U.S. Geol. Survey Misc. Inv. Map I-961, scale 1:25,000,000.
8. Scott, D. H., and Carr, M. H., 1978, Geologic map of Mars: U.S. Geol. Survey Misc. Inv. Map I-1083, scale 1:25,000,000.

9. Fanale, F. R., 1976, Martian volatiles: The ice degassing history and geochemical fate: *Icarus*, 28, 179-202.
10. Rossbacher, L. A., and Judson, S., 1981, Ground ice on Mars: Inventory, distribution, and resulting landforms. Submitted to *Icarus*.

## Chapter 8

### REMOTE SENSING OF PLANETARY SURFACES: INTERPRETATIONS AND TECHNIQUES



## VIKING LANDER IMAGING EXPERIMENT - UPDATE AND NEW OBSERVATIONS

K.L. Jones and S.K. LaVoie, Jet Propulsion Laboratory, Pasadena, CA 91103.

On February 1, 1980 (VL-2 sol 1212,  $L_S=60$ ), due to a variety of problems related to an onboard battery failure (1), Viking Lander 2 ceased useful imaging observations. At the time of failure, both cameras were fully operational - in fact, camera 2 was in the middle of acquiring real-time image 22I150. A subsequent attempt to revive the lander (April 11, sol 1281) succeeded in acquiring 10 minutes of playback of old images, but the battery problem again resulted in a premature loss of the relay-link and no new imaging data were acquired. As of the end of the 3-1/2 year mission, VL-2 had returned 2156 camera events and had just completed documenting its second complete northern hemisphere winter.

Viking Lander 1 continues operations and, primarily depending on the availability of tracking antennas, is returning an image per week. The mission is now being called the Lander Monitor Mission. Since the start of the mission (VL-1 sol 935,  $L_S=243$ ) and the time of writing (sol 1432,  $L_S=145$ ) 37 images (out of a possible 68) had been received. Most (34 images) were received between sols 1128 ( $L_S=359$ ) and 1432 ( $L_S=145$ ), corresponding to the northern hemisphere spring and summer months. Imaging return between September 1980 and September 1981 will be somewhat reduced due to the two Voyager Saturn encounters and Mars solar conjunction. Following that time, imaging return should again be fairly regular. At that time, VL-1 will be in early northern hemisphere winter.

### Data Reduction and Distribution

As of September 1, 1980, Experiment Data Record (EDR) tapes containing VL-2 images through 22I150 (final image) and VL-1 images through 12J079 (sol 1387,  $L_S=123$ ) had been distributed. Photoproducts (EDR and TDR) were in the final printing stages and distribution anticipated for the October-November time period. By January, 1981, it is anticipated that all remaining backlog Lander imaging data products will be distributed.

A major effort, the EDR Picture Catalog (2) for the Extended and Continuation Automatic missions, was in final typesetting at Langley Research Center and release planned for January, 1981. The pair of catalogs, one each for VL-1 and VL-2, are identical in format to the Primary Mission catalog prepared by Bob Tucker (3). Any investigators using Viking Lander imaging data should be aware of the existence of these catalogs.

### VL-1 and VL-2 Imaging Observations

Our abstract (4) for the January, 1980 PGPI meeting identified changes in the surface appearance around the two landers as imaged through the end of 1979. In that abstract, it was indicated that no new dust layer had accumulated at either lander site. This observation was updated at the meeting - newly acquired images (e.g. 22I111, sol 1050,  $L_S=341$ ) suggested that, at least at the VL-2 site, a new bright dust layer similar in appearance to the first year's had indeed accumulated. Other VL-2 images, especially 21I125 (sol 1150,  $L_S=341$ ) and 21I126 (sol 1170,  $L_S=352$ ) more clearly confirmed this. Recently received VL-1 images also show a surface brightening attributed to bright dust accumulation during the second

winter. For both sites, the observational evidence is, as reported in earlier papers (5,6), the decrease in apparent contrast between dark sampler arm trenches and surrounding soil. A clear example from VL-1 is a trench at  $-35^\circ$ ,  $106^\circ$  (camera 2 coordinates) as seen in color images 12H196 (sol 615,  $L_S=72$ ) and 12J053 (sol 1194,  $L_S=31$ ). A contrast reduction is apparent in all three diodes.

Wind-induced changes at both sites have been minimal or non-existent. No new slumps similar to the Big Joe or Whale Rock slumps have formed. Two images (21I135, sol 1192 and 21I136, sol 1193) show no changes of a conical soil pile created early in the mission by the surface sampler arm.

As described in (4), a condensate layer formed at the VL-2 site during the second winter. This condensate followed an almost identical pattern of formation and disappearance as observed during the first year. As of VL-2 sol 1050 ( $L_S=341$ ), small scattered patches of bright condensate remained. The next received images (sol 1138,  $L_S=26$ ) show that, by that time, all condensate had disappeared.

#### Dust and Condensates - Summary of Observations/Inferences

Based on two Mars-years' imaging observations, the following correlations can be deduced:

- a) The first condensate appearance, as well as the temperature buffering, at  $151^\circ\text{K}$  during the time of condensate formation argues for a  $\text{CO}_2$  composition.
- b) The slow disappearance of the condensate, despite increasing temperatures, argues for an  $\text{H}_2\text{O}$  composition.
- c) The reddish appearance of the condensate (6,7) is consistent with either a very thin condensate layer (frost) or a mixed condensate-dust composition (snow) (7).
- d) Dynamics of condensate formation are minimally influenced by observed year-to-year variations in the intensity of planetwide dust storm activity.
- e) Bright dust accumulated at both sites, despite the appearance of a condensate layer at VL-2 but not VL-1.
- f) Despite year-to-year variations in dust storm activity, similar amounts of bright dust accumulated at each lander site during both years.
- g) At both sites, dust accumulations occur entirely during the late autumn and winter months.

Based on these correlations (or non-correlations) the following can be deduced:

- 1) The condensate composition is a mixture of  $\text{CO}_2$  and  $\text{H}_2\text{O}$ , as concluded earlier by (5).
- 2) While we strongly suspect that dust particles must act as nucleation centers for condensate formation, this must be deduced from calculations rather than observational evidence. A directly observable correlation between condensate and dust accumulation at the VL-2 site is not yet established or precluded by imaging data alone.
- 3) The observed yearly accumulation of bright dust, as discussed in earlier papers, implies that with observable frequency that surface at both sites is swept clear by eolian activity.

- 4) Except for such eolian activity, what we have observed at the lander sites during the first two years is typical of an average year.

#### References

- 1) Miller, Don, personal communication.
- 2) Jones, K.L., M. Henshaw, C. McMenomy, A. Robles, P.C. Scribner, S.D. Wall, J.W. Wilson, Viking Lander Imaging Investigation, Picture Catalog of Extended Mission and Continuation Mission Experiment Data Record, 2 vols., NASA Reference Publication, in press.
- 3) Tucker, Robert B., Viking Lander Imaging Investigation, Picture Catalog of Primary Mission Experiment Data Record, NASA Reference Publication 1007.
- 4) Jones, K.L. and S.K. LaVoie, Two Mars Years - Viking Lander Imaging Observations, abstract in NASA TM-81776, Jan. 1980, Reports of Planetary Geology Program, 1979-1980.
- 5) Jones, K.L., R.E. Arvidson, E.A. Guinness, S.L. Bragg, S.D. Wall, C.E. Carlston and D.G. Pidek, One Mars Year: Viking Lander Imaging Observations, Science, 204, pp. 799-806, 25 May 1979.
- 6) Guinness, E.A., R.E. Arvidson, D.C. Gehret and L.K. Bolef, Color Changes at the Viking Landing Sites Over the Course of a Mars Year, J. Geophys. Res., 84, 1979.
- 7) Wall, S.D., Analysis of Condensates Formed at the Viking 2 Lander Site: The First Winter, submitted to Icarus.

SPECTRAL VARIETY OF MARTIAN SURFACE MATERIALS: COMPARISON OF  
EARTHBASED AND VIKING LANDER DATA.

Strickland, E. L., Dept. Earth, Planetary Sci., Washington Univ.  
St. Louis, Mo. 63130; R. B. Singer, Planetary Sciences, Hawaii  
Institute of Geophysics, University of Hawaii, Honolulu, Hi.  
96822

We are comparing spectral data derived from Viking Lander cameras with visible and near-infrared earthbased regional data (McCord et al., 1977). Because of the width and irregular nature of the lander cameras' bandpasses, these data cannot be plotted as single wavelengths or ranges. Additional data processing is necessary before direct comparisons are undertaken. Two independent routes are possible: (a) convolve the higher resolution earthbased data to lander bandpasses, and then make direct channel by channel comparisons; (b) use a computational technique similar to that developed by Huck, et al. (1977) to generate spectral estimates from lander and convolved earthbased spectra, and then compare the spectral estimates directly. We are employing both techniques. Additional complications for comparisons of spectral reflectances are uncertainties in calibrations and martian atmospheric effects. To circumvent these problems, we are initially comparing data ratioed to the brightest and reddest materials in each dataset (presumed to be aeolian dust deposits) as well as weighted "scene averages".

Preliminary results indicate that earthbased data show similar spectral variety to the Viking 1 site. Both relatively "red" soil and "blue" soil and rock color extremes seem represented in earthbased data, but apparently missing are analogs of "yellow" and "green" rocks described in Strickland (1979). Given the expected spectral averaging for earthbased data (Singer and McCord 1979), and the greater spectral variety of Viking Orbiter data than earthbased data (McCord et al. 1980), the implication is that the landing sites, though apparently similar to each other (Strickland 1979), contain only a subset of the spectral units which exist on the martian surface.

References cited:

- McCord et al., 1977, Icarus 31, 25-39.  
Huck et al. 1977, J. Geophys. Res. 82, 4401-4411.  
Strickland, 1979, Proc. Lunar Planet. Sci. Conf. 10th., 3055-3077  
Singer and McCord, 1979, Proc. Lunar Planet. Sci. Conf. 10th.,  
1835-1848  
McCord et al. 1980, to be submitted to JGR, 1980.



SPECTRAL PROPERTIES OF SOILS EXPOSED AT THE VIKING 1 SITE  
Guinness, Edward A., Dept. of Earth and Planet. Sci., Washington  
University, St. Louis, MO, 63130.

The intent of this paper is characterize the intrinsic range in the spectral reflectance (0.4 to 0.75 microns) of soils exposed at the VL 1 site. The theoretical photometric function derived by Hapke (1980) has been fit to reflectance data of several soil patches seen by the Lander cameras so that soil color variations due to photometry could be eliminated. Earth-based reflectance data for several bright and dark regions were degraded to the Lander camera spectral resolution. Lander soil data were then corrected to the same lighting and viewing conditions as telescopic observations so that the two data sets can be compared. The purpose of such comparisons is to place the Lander soils in the context of the global spectral variety seen on Mars. Results can be summarized as follows:

(1) The photometric function of Lander soil has a prominent opposition effect in addition to a phase function that is strongly backscattering (Figure 1). The ratio of reflectance at a 1 degree phase angle to that at a 10 degree phase angle is averages 1.25, 1.24, and 1.19 for blue, green, and red wavelengths, respectively. The photometric function has a wavelength dependence, which causes color ratios to vary by up to 33% as a function of phase angle.

(2) Viking Lander multispectral data of soil is highly correlated; that is, as the soil becomes redder, it also becomes greener and bluer. However, variations throughout the scene in blue and green reflectance are small, on the order of  $\pm 0.01$  of the mean value. The mean reflectance of Lander soil at a phase angle of 5 degrees is 0.11 and 0.17 averaged over the blue and green channels of the Lander camera, respectively. The reflectance averaged over the red channel ranges from 0.30 to 0.39 at a 5 degree phase angle. Such a result is consistent with the principal component and discriminant function analyses of Lander multispectral data, which show that much of the discriminability among the soils exposed at the VL 1 site is obtained from the red and infrared images (Guinness, 1980).

(3) The prominent soils types examined at VL 1 are a bright, red soil that appears to be a thin blanket deposit and a darker, less red soil that is exposed where the redder soil is disturbed. The color and brightness difference between these two units correlates with inferred particle size differences, with the darker, less red soil being coarser-grained than the bright, red soil. The increase in brightness and redness as particle size decreases for the VL 1 soil is the same as the color and particle size relationship of ferric oxides with particle sizes of one to several hundred microns (Hunt et al., 1971).

(4) All of the soils examined at the VL 1 site appear redder than

Martian bright regions after correcting the Lander soil reflectance for its photometric function and for the magnitude of scattered skylight (Figure 2). The difference between the Lander and Earth-based reflectance data may be due to the preferential loss of red light from the Earth-based data by scattering in the Martian atmosphere which corresponds to light that has passed through the atmosphere twice. Alternatively, the differences may be due to the spectral contribution of rocks in the Earth-based spectra since rocks are less red than soil. A patch on Big Joe, one of several dark rocks in the scene, is significantly less red than both bright regions and soils at the Viking 1 site. The decreased redness probably means that Big Joe has a smaller Fe<sup>3+</sup> content than either bright regions or Lander soil suggesting that the surface of Big Joe is relatively unaltered.

(5) Toulmin et al. (1977) proposed that the soil exposed at both Viking landing sites is part of a globally homogenized soil unit. This interpretation is based on the remarkable similarity in the composition of the soil at both landing sites even though the sites are separated by approximately 6500 kilometers. The presence of a global soil unit is further supported by the wide spread distribution of bright regions which are also spectrally very uniform from place to place (McCord et al., 1977). The similarity in composition and in color (Huck et al., 1977) of soil exposed at VL 1 and VL 2, together with the result that the color of VL 1 soil is comparable to bright regions, all suggest that the Lander soils are typical of brighter soils covering a large portion of the Martian surface.

## References

- Guinness, E., Ph. D. Thesis, Washington University, St. Louis, Missouri, 1980.
- Hapke, B., Bi-directional reflectance spectroscopy. I. Theory, J. Geophys. Res., in press.
- Huck, F., et al., Spectrophotometric and color estimates of the Viking Lander sites, J. Geophys. Res., 82, 4401-4411, 1977.
- Hunt, G., et al., Visible and near-infrared spectra of minerals and rocks: III. Oxides and hydroxides, Mod. Geo., 2, 195-205, 1971.
- McCord, T., et al., Spectral reflectance of martian areas during the 1973 opposition: Photoelectric filter photometry 0.33-1.10 microns, Icarus, 31, 25-39, 1977.
- Toulmin, P., et al., Geochemical and mineralogical interpretation of the Viking inorganic chemical results, J. Geophys. Res., 82, 4625-4634, 1977.

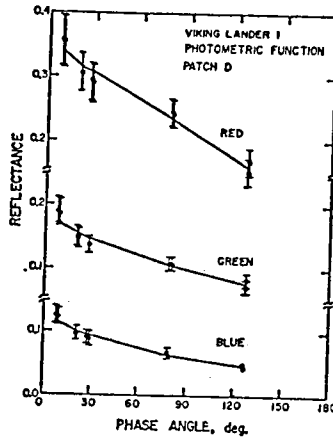


Figure 1. This is an example of the reflectance data for VL 1 soil. The solid line is the Hapke photometric function fit to the data. The deviations of the data from the Hapke function are randomly distributed with respect to reflectance and phase angle, which indicates that the Hapke photometric function is a reasonable model for the soil photometric function. The error bars are  $\pm 10\%$  of the reflectance values. Note that the slope of the photometric function is different for each color.

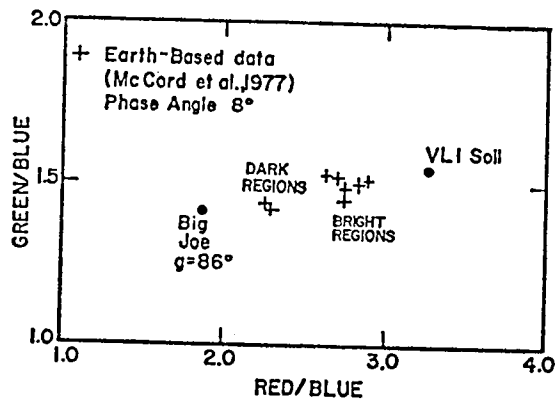


Figure 2. Color ratio data of several bright and dark regions, observed from Earth, are compared to color ratio data for Lander soil. All eight Earth-based observations have approximately the same incidence, emission, and phase angles ( $i=33$  deg.,  $e=33$  deg., and  $g=8$  deg.). The Earth-based data have been degraded to the Lander camera spectral resolution. Lander soil data have been corrected for their photometric functions to the same lighting and viewing geometry as the Earth-based data. The Big Joe datum, with a phase angle of 86 degrees, is the only point with a different lighting and viewing geometry.

## OBSERVING CHANGES WITH THE VIKING LANDER CAMERAS

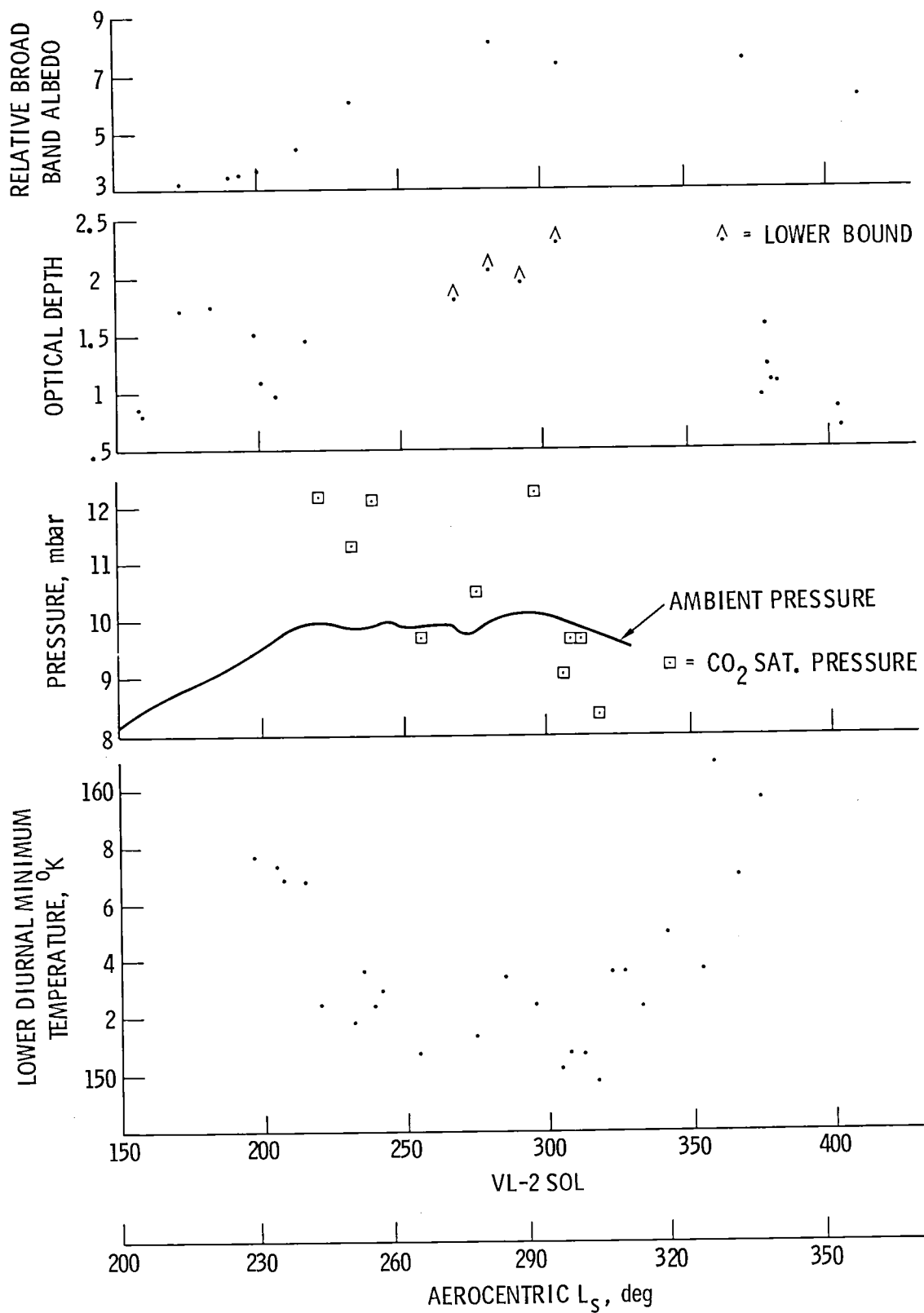
Stephen D. Wall, Jet Propulsion Laboratory  
Louise Cullen, Jet Propulsion Laboratory

After their initial characterization of the local Martian surface, the most important task of the Viking landers has been to monitor their surroundings for significant changes. Measuring changes in any quantitative radiometric way requires careful decalibration of the imagery. Internal and external calibration are provided. Internal calibration is performed by lighting a small lamp within the camera and recording the camera response to it. External calibration is by the imaging of test charts on the lander deck. The accuracy of both methods is limited. Internal calibration does not compensate for varying insolation, and external calibration is hampered by the collection of dust on the test charts. The test charts also receive an unknown amount from the lander body. The complexity of reducing these calibration has limited the enthusiasm for quantitative use of Viking lander data.

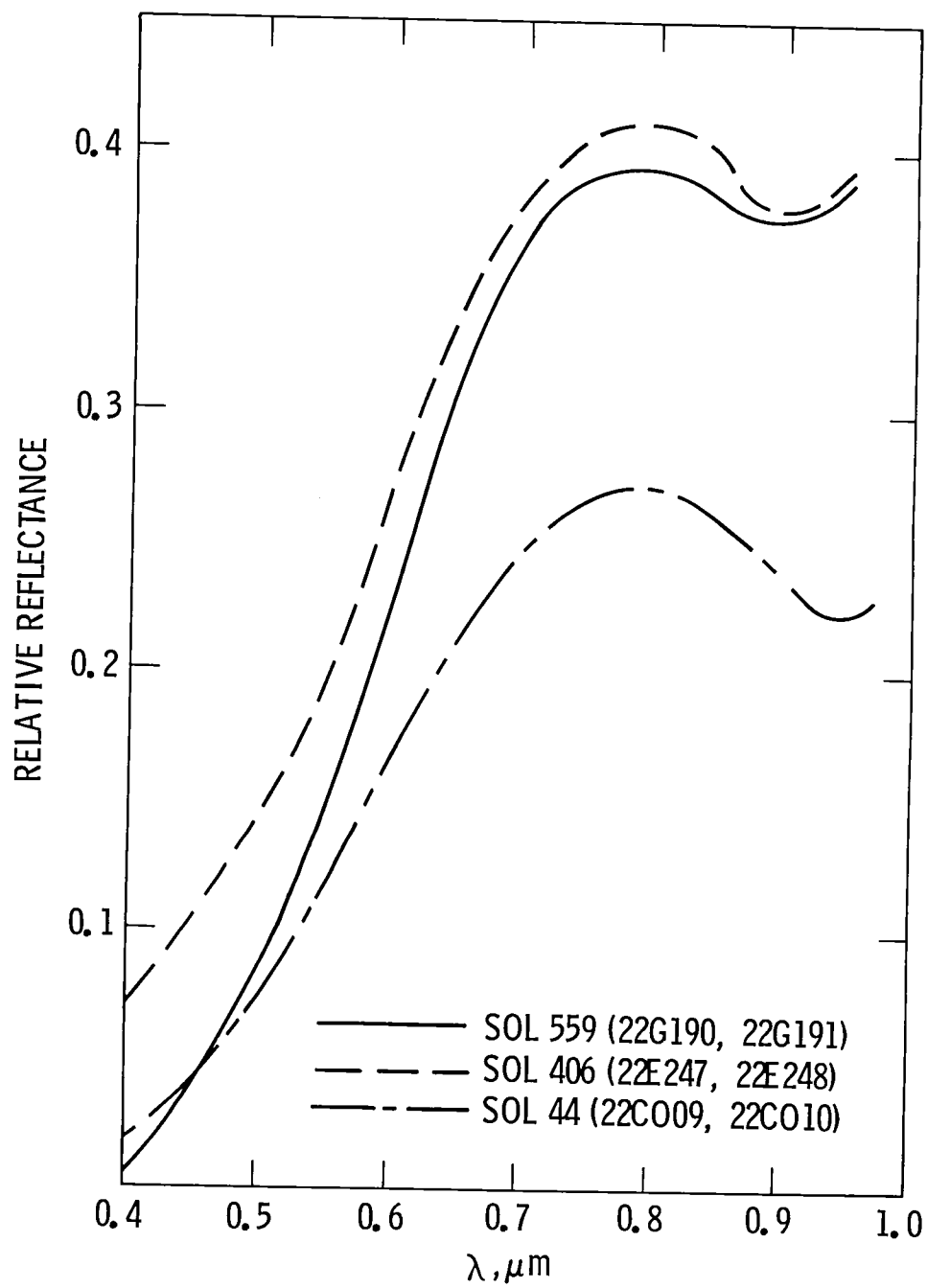
To help alleviate the calibration problems, internal calibration data are being reduced at JPL and an easily-used decalibration file is being supplied with the lander EDR data set to experimenters. External calibration has also been simplified by frequent optical depth measurements (e.g., Pollack *et al.*, 1979) and by a simple test to determine whether or not a test chart has dust on it (described by Guinness *et al.*, 1979 and Wall, 1980). With the help of these methods, comparisons can be easily made over long time periods. Application of the decalibration schemes to the first-winter condensate periods at the Viking 2 site has shown that surface albedo began to increase shortly after a major increase in optical depth near sol 165 (Figure 1) and within 50 sols of the ambient pressure falling below CO<sub>2</sub> saturation pressure. Albedo remained high long after daytime temperatures reached above 180 K. Spectral reflectance estimates, made using a technique developed by Park and Huck (1976), show that the condensate was quite red and that the surface remained redder than before the condensate appeared long after it was gone (Figure 2). These results tend to confirm earlier suggestions that the condensate was a combination of water and carbon dioxide ices which fell to the surface already condensed onto dust particles brought to the lander site by the dust storms. This work is being done under the Mars Data Analysis Program at the Jet Propulsion Laboratory, California Institute of Technology, under contract NAS7-100 with NASA.

## REFERENCES

- Guinness, E. A., Arvidson, R. E., Gehret, D. C., and Bolef, L. K. (1979). *J. Geophys. Res.* 84, 8355-8364.
- Park, S. K. and Huck, F. O. (1976). *NASA Tech. Note* D-8292.
- Pollack, J. B., Colburn, D. S., Flasar, M., Kahn, R., Carlston, C. E., and Pidek, D. P. (1979). *J. Geophys. Res.* 84, 2929-2945.
- Wall, S. D. (1980). *Icarus*, submitted.



Wall, Figure 1 407



Wall, Figure 2

The Search for Sun Dogs on Mars  
Paul Romani, University of Michigan

Sun dogs, or parhelia, are bright spots that appear on either side of the sun at the same elevation as the sun. On Earth, sun dogs are caused by H<sub>2</sub>O ice crystals in the atmosphere. Whenever there are large numbers of hexagonal plate crystals in the air, with their short sides vertical, sun dogs appear. Each crystal acts like a prism; light from the sun strikes it and is refracted. Sun dogs form at the angle of minimum deviation for a prism, which is also the point of maximum light. The equation of minimum refraction is as follows:

$$\sin\left(\frac{d+a}{2}\right) = n \left[ \sin\left(\frac{a}{2}\right) \right]$$

where  $a$  is the prism angle,  $n$  the index of refraction, and  $d$  the angle of minimum deviation. This equation for minimum refraction is valid only for rays in the principal plane of the prism. For sun dogs this only occurs when the sun is on the horizon. When the sun is above the horizon the sun's rays strike the ice crystals inclined to their principal planes. The net effect is to increase the effective index of refraction for the projection of the ray in the principal plane. Thus with higher sun elevations the angular distance from the sun dog to the sun increases. The sun dogs still appear at the same elevation as the sun. Using the above equation for H<sub>2</sub>O ice,  $n = 1.31$  (yellow light), and  $a = 60^\circ$ , thus  $d$  is  $21^\circ 50'$ . Tabular or columnar H<sub>2</sub>O crystals form with right angles, so there exist water sun ice dogs for  $a = 90^\circ$ . These form at  $45^\circ 44'$  away from the sun ( $n = 1.31$ ). Sun dogs may be colored, too, due to the change in the index of refraction with wavelength, with red closest to the sun, blue farthest away.

If there is no preferred orientation of the crystals, as in cirrus type clouds, then a halo is formed. Halos of both  $22^\circ$  and  $46^\circ$  angular radius can appear. This halo may be colored, too, with the inner part red and the outer part blue. Unlike sun dogs, the halos occur at the same angular distance regardless of how high up the sun is, as they are formed by crystals with randomly oriented principal planes.

On Mars there exists the possibility of sun dogs and halos formed by either H<sub>2</sub>O or CO<sub>2</sub> ice. Unfortunately the index of refraction of solid CO<sub>2</sub> is not well known. An approximate value from some sources is 1.38 with an uncertainty of  $\pm 0.05$ . Frozen CO<sub>2</sub> can form cubic crystals with prism angle  $90^\circ$ , so these CO<sub>2</sub> crystals would cause either sun dogs or halos at  $64^\circ 45'$ . But a slight change in the index of refraction will change the position of the sun dogs/ halos greatly. For example, if  $n = 1.40$ , they then form at  $73^\circ 44'$ , or if  $n = 1.36$ , they then form at  $58^\circ 10'$ .

Evidence of sun dogs on Mars would be useful for several reasons. It would show that large quantities of CO<sub>2</sub>/H<sub>2</sub>O crystals are present in the atmosphere at certain times. The crystal shapes would also be known.

The difference between a sun dog or a halo would indicate the crystal orientation. CO<sub>2</sub> sun dogs would provide a good value of the index of refraction of CO<sub>2</sub> under Martian conditions.

The search for sun dogs was made using Viking lander images. The Lander cameras form images by reflecting light from the scene onto one of 12 photodiodes. The photodiodes in turn convert the light into an electrical signal that is then digitized. Thus, each image is an array of numbers called picture elements. The end product is called a camera event. To make a color camera event, each line is viewed in turn by a blue, green and red photodiode. Infrared camera events are also composed of three images of the same scene, each image made by a photodiode with a different effective wavelength in the infrared. High resolution camera events are made using a broad band photodiode. All three types of camera events were used in the search.

First it was decided to look at all camera events that contained any part of the sky from 20° to 90° away from the sun when the sun elevation was lower than 15°, and that contained the elevation of the sun when the image was made. The 20 to 90 degree span was to try to catch both H<sub>2</sub>O and CO<sub>2</sub> phenomena, even with the uncertainty in the index of refraction of CO<sub>2</sub>. A low sun elevation would provide the longest path through the atmosphere and thus increase the probability of refraction. There were 60 camera events that qualified.

As time allowed, more images were searched. First high sun, morning camera events of the first summer were checked to see if the summer morning H<sub>2</sub>O ice fog was causing any sun dogs or halos. 16 images met this requirement. At the same time Lander 2 autumn camera events were included to try to catch the sun shining through the polar hood clouds. Also, refraction phenomena could possibly be caused by atmospheric ice that was deposited during the following winter. There were nine such camera events. Finally, it was decided to search all camera events that contained the right azimuth for sun dogs regardless of sun elevation or season. This last group had a total of 109 camera events in it. Due to a lack of time, not all of these images were checked.

The images were searched for sun dogs at the Computer Graphics Lab at JPL. For each horizontal line of picture elements in the image, a graph of intensity as a function of azimuth was displayed on a CRT. An increase in intensity with distance from the sun, as opposed to the normal decline of intensity, would represent a sun dog. The entire sky portion of each image was searched. A display of the numerical values of the picture elements in a given area could be done if further information was desired.

On some, images noise was a problem. Occasionally it was necessary to use a computer program that did a vertical average of the picture elements in a defined box, to see if a horizontal variation in intensity was real.



To the level of detectability of the Viking lander cameras, no sign of either sun dogs or halos were seen. A total of 110 camera events were checked. 53 of these were either totally or partially saturated. Noise was a problem in 14 camera events. In 58 camera events either the point  $22^\circ$  and/or the point  $46^\circ$  away from the sun was present; the point  $65^\circ$  away from the sun was present in 35 images. At Lander 2, eight camera events that had the desired azimuth in them were images of the back of the S-band antenna. Of the 18 summer morning camera events, nine were good for  $H_2O$  ice refraction phenomena, 12 for  $CO_2$ . There were five camera events that were useless due to missing lines.

From this search alone it is not possible to conclude that there are no sun dogs on Mars. It is possible that they are there but were not captured in Lander images. There is also the chance that the sun dogs were missed because of data saturation. That is more possible for the sun dogs at  $22^\circ$ , as they form closest to the sun of all the sun dogs.

For the  $CO_2$  sun dogs there could be two additional reasons for failing to observe them, even though the crystals are present. One could be that the index of refraction of solid  $CO_2$  is too high. If the  $CO_2$  crystal is cubic, and the index of refraction is greater than 1.414, then any ray striking the crystal will suffer total internal reflection. Another possibility is that the  $CO_2$  condenses on already formed water crystals. If the  $H_2O$  part of the crystal is significant, then no sun dogs will be seen, even though the  $CO_2$  does make the cubic crystal. Most rays striking it will go from air to frozen  $CO_2$  to frozen  $H_2O$  and out again. Thus cubic  $CO_2$  crystals may be present in large quantities without forming sun dogs.

Of course, the necessary  $H_2O$  and  $CO_2$  crystals could be not present. At least the search shows that sun dogs are not a common or easily visible phenomena on Mars. This implies that for the days good images are available an upper bound can be placed on the quantity of sun dog forming crystals.

#### Acknowledgments

This work was done while I was a participant in NASA's Planetary Geology Intern Program. Steve D. Wall was my advisor at JPL. The suggestion to search for sun dogs on Mars was made by Paul Doherty of Oakland University, Rochester Campus, Michigan. The work was performed at Jet Propulsion Laboratory, California Institute of Technology, and was supported by the Planetary Geology Intern Program and by NASA contract NAS7-100.

# BRIGHTNESS DEGRADATION OF VIKING LANDER ULTRAVIOLET CHIPS

Zent, A. P., E. A. Guinness, R. E. Arvidson, Dept. of Earth and Planetary Sciences, Washington University, St. Louis, Missouri 63130.

The ultraviolet degradable patches mounted on the Viking Landers have been examined with the intent to use these patches as dosimeters to estimate the UV flux reaching the surface of Mars. Huguenin (1976) proposed a theory of UV induced photostimulated oxidation of rocks on the martian surface, and Klien (1977) suggested UV radiation as the driving energy behind the formation of peroxides and superoxides that were possibly detected during the Viking Lander biology experiments. In view of these recent theories there is considerable interest in obtaining quantitative estimates of the UV flux currently reaching the surface of Mars.

We have tracked the brightness of the UV patches in each of the Lander multispectral channels. The data that have been reduced thus far are for VL1 through sol 700. The greatest amount of darkening should be observed when the chips are viewed at blue wavelengths because the darkening of the UV patches is due to a developing UV absorption feature that moves toward longer wavelengths with increasing UV dosage. In this report, we outline our data reduction method and examine the statistical validity of temporal changes in the reflectance of the UV patches as observed in blue, green, red and infrared light. Extensive calibration tests (extent of darkening in given wavelength versus cumulative UV dose) are currently being performed by the IITRI Corporation of Chicago, Illinois. Results from these tests will be utilized, when available, to convert our data to the equivalent UV flux reaching the surface of Mars.

Each Viking Lander is equipped with three Reference Test Charts (RTC)s. Each RTC includes two patches that darken when exposed to ultraviolet radiation and, in addition, a blue, green, red and eleven grey patches. Each grey patch is a Lambertian scatterer with a bi-directional normal reflectance that is independent of wavelength (Wall et al., 1975). Each of the two cameras views one RTC directly (i.e., the emission angle is always zero).

For the grey patches, the expression relating camera preamplifier voltage to target and system parameters is:

$$(1) V_j = C_j \rho \cos i \int_0^\infty S(\lambda) R_j(\lambda) d\lambda$$

where  $j$  represents a photodiode,  $C_j$  is the camera calibration constant,  $V_j$  is measured in volts,  $\rho$  is the bi-directional normal reflectance of the patch,  $\cos i$  is the scene photometric function,  $S(\lambda)$  is the solar illumination function and  $R_j(\lambda)$  is the responsivity of the diode. This relationship expresses the linear dependence between patch reflectance and camera output. Such a relationship has a slope of:

$$(2) m = C_j (\cos i) \int_0^\infty S(\lambda) R_j(\lambda) d\lambda$$

Slopes were obtained for the image data covering the RTC's through the use of linear regressions. It can be seen that the voltage for the UV or color patches, divided by m, is equal to:

$$(3) [\rho] = \frac{\int_{\lambda} (\rho_{\lambda}) S(\lambda) R_j(\lambda) d\lambda}{\int_{\lambda} S(\lambda) R_j(\lambda) d\lambda}$$

where  $[\rho]$  is the bi-directional normal reflectance of the UV or color patches, weighted over the solar illumination and camera transfer functions. It is assumed that the UV and color patches are also Lambertian scatterers.

Table 1 lists the data acquired from Viking Lander 1 that we employed in tracking the darkening of the UV patches. In selecting these data it should be noted that shadowed images, as well as those obtained at times when the optical depth was greater than 2.0, were neglected. The reasoning for this procedure is that we wish to eliminate all images which are illuminated by skylight.

Reflectances of the UV patches were solved for as a function of time. Solutions for the patches as seen in blue, green, red and infrared wavelengths are shown in Figure 1. There is a pronounced drop in the UV patch reflectance as a function of cumulative hours of normal illumination, a drop that is displayed most prominently in the blue and least in the infrared data. There has been little to no change in the reflectance of the color patches with time, nor is there any functional dependence of patch reflectance upon incidence angle, reinforcing the assumption of Lambertian scattering for the UV and color patches. In summary, we conclude that the UV patches have darkened in response to an incident UV flux. We expect to be able to derive the UV irradiance over the wavelength range to which the patches are sensitive once the tests at IITRI are completed.

#### REFERENCES CITED

- Huguenin, R. L., Photostimulated oxidation of magnetite, 1973, J. Geophys. Res., 78, 8481-8506.  
 Klien, H. P., The Viking biological investigation: General aspects, 1977, J. Geophys. Res., 82, 4677-4680.  
 Wall, S. D., E. E. Burcher, D. J. Jobson, 1975, Reflectance characteristics of Viking Lander camera reference test charts, NASA Tech. Memo. 72762.

TABLE I  
REFLECTANCE DATA OF UV AND COLOR PATCHES

FRAME	DIODE	REG	T	UV1	UV2	RED	GRN	BLU	i	Sol
11A038	BLU	5.05	0.50	sat b	0.811	0.103	sha	0.469	24.9	006
11A038	GRN	4.40	0.50	0.925	0.847	0.075	0.197	sha	24.9	006
11A038	RED	2.88	0.50	0.973	0.899	0.620	0.121	sha	24.9	006
11A148	IR1	2.21	0.45	0.775	0.716	0.489	0.428	0.606	66.7	026
11B089	IR1	2.30	0.40	0.793	0.741	0.578	0.557	0.755	67.5	040
11C182	BLU	2.77	1.89	0.688	0.631	0.130	0.174	0.484	40.5	246
11C182	GRN	2.93	1.89	sat b	0.686	0.096	0.279	0.189	40.5	246
11C182	RED	2.49	1.89	0.824	0.773	0.569	0.207	0.366	40.5	246
11F237	BLU	3.82	1.42	sat b	0.531	0.133	0.156	0.450	64.3	469
11F237	RED	2.96	1.42	sat b	0.718	0.516	0.199	0.333	64.3	469
11F238	IR1	2.29	1.42	0.790	0.766	0.591	0.584	0.804	64.3	469
11G008	IR1	2.45	1.87	0.793	0.767	0.583	0.584	0.805	65.0	470
11G228	IR1	2.72	0.69	0.755	0.743	0.577	0.572	sat b	58.7	542
11H015	BLU	3.69	0.50	0.518	0.509	0.129	0.156	0.448	67.0	556
11H015	GRN	3.59	0.50	sat b	0.589	0.115	0.273	0.185	67.0	556
11H015	RED	2.75	0.50	0.716	0.688	0.514	0.198	0.328	67.0	556

- 1) REG is the slope of the regression between grey patch voltage and reflectance.
- 2) T is the atmospheric optical depth
- 3) Columns 5 to 9 are the estimated bi-directional reflectances of the patches. Overexposed patches are indicated as "sat b", while "sha" refers to a shadowed patch.
- 4) The incidence angle of the RTC is listed under i.

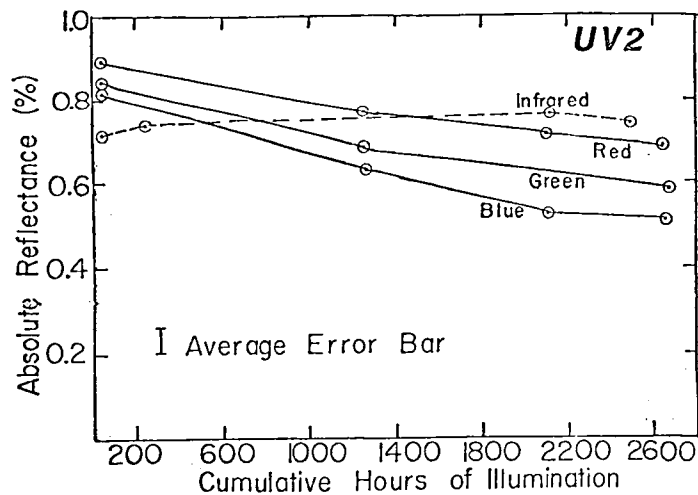


Figure 1 - Darkening of VL 1, RTC 1, UV-2 chip with time.

## COMPARISON OF VOYAGER IMAGES OF DAY AND NIGHT VIEWS OF IO

Richard J. Terrile, Jet Propulsion Laboratory, California Institute of Technology, Pasadena, CA 91103 and Allan F. Cook, Harvard-Smithsonian Center for Astrophysics, Cambridge, MA 02138

During the Voyager encounters with the Jovian system (Smith et al., 1979) a unique set of images of Io were acquired under a variety of lighting and thermal conditions. In particular, two images in the clear filter (effective wavelength of  $4770 \text{ \AA}$ ) were recorded showing nearly the same hemisphere of Io under conditions of day and night. The first image, shows the hemisphere with a sub-spacecraft point of  $21.1^\circ\text{W}$  and  $3.31^\circ\text{N}$  with a resolution of about  $56 \text{ km/line pair}$ . This image is illuminated by direct sunlight with a phase angle of  $8.6^\circ$ . Figure 1 is a version of this image which has been geometrically reprojected to the same sub-spacecraft coordinates as the second image. This second image, shown in figure 2, has a sub-spacecraft point of  $26.5^\circ\text{W}$  and  $5.4^\circ\text{S}$  with a resolution of about  $22 \text{ km/line pair}$  and a solar phase angle of  $148.3^\circ$ . The main portion of this image is illuminated by sunlight reflected off of Jupiter. Jupiter's disk presents a  $19.3^\circ$  source in the sky with a phase angle of  $26^\circ$  and provides adequate illumination to discriminate surface detail with an approximate signal to noise ratio of about 10. A comparison of these two images allows an examination of Io's surface under very different thermal conditions since the difference in day and night surface temperatures is approximately  $40^\circ\text{K}$ .

Io is now known to exhibit active volcanism on a planetary scale from a least 9 discrete sources (Strom et al. 1980). Furthermore, the Voyager Infrared Interferometer Spectrometer experiment (IRIS) has detected gaseous  $\text{SO}_2$  absorption lines over one of the active volcanic sources (Hanel et al., 1979). If concentrations of  $\text{SO}_2$  gas from volcanic effluents are high enough (locally  $10^{-7}$  to  $10^{-6}$  bar) then condensation of  $\text{SO}_2$  frosts should occur during night cycles. This would be observed as higher night-side surface albedos. Surface brightening has been looked for in the Voyager data by looking at photometry of Io as it comes out of eclipse (Veverka et al, 1980). No post-eclipse brightening was observed so it is unlikely that a large enough transient atmosphere of  $\text{SO}_2$  exists to condense during an eclipse. During an entire night cycle, however, there may be time enough for local concentrations of  $\text{SO}_2$  frost to accumulate over an area large enough to be observed by Voyager.

In general, large scale day-night albedo variations are not observed so an upper limit on the transient  $\text{SO}_2$  atmosphere of Io can be placed at about  $10^{-6}$  bar at the time of Voyager 2 encounter. Closer examination of the data does reveal a contrast decrease in some areas of about 25% during the night cycle. This contrast decrease is being investigated in terms of a calibration problem due to scattered light or possibly a real surface phenomenon due to local albedo variations near plume sources where gas concentrations are expected to be higher.

This paper represents one phase of research carried out at the Jet Propulsion Laboratory, California Institute of Technology, under contract NAS 7-100 sponsored by the National Aeronautics and Space Administration.

#### References:

- Hanel, R., Conrath, B., Flasar, M., Kunde, V., Lowman, P., Maguire, W., Pearl, J., Pirraglia, J., Samuelson, R., Gautier, D., Gierasch, P., Kumar, S. and Ponnampertuma, C. (1979) "Infrared Observations of the Jovian System from Voyager 1." *Science*, 204, 972.
- Smith, B. A., Soderblom, L. A., Johnson, T. V., Ingersoll, A. P., Collins, S. A., Shoemaker, E. M., Hunt, G. E., Masursky, H., Carr, M. H., Davies, M. E., Cook, A. F., Boyce, J., Danielson, G. E., Owen, T., Sagan, C., Beebe, R. F., Veverka, J., Strom, R. G., McCauley, J. F., Morrison, D., Briggs, G. A. and Suomi, V. E. (1979) "The Jupiter System Through the Eyes of Voyager 1." *Science*, 204, 951.
- Strom, R. G., Schneider, N. M., Terrile, R. J., Cook, A. F. and Hansen, C. (1980) "Volcanic Eruptions of Io." *J. G. R.*, in press.
- Veverka, J., Simonelli, D., Thomas, P., Morrison, D. and Johnson, T. V. (1980) "Voyager Search for Post-Eclipse Brightening on Io." *J. G. R.*, in press.

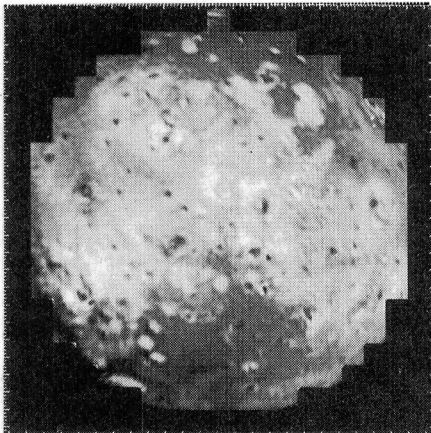


Figure 1

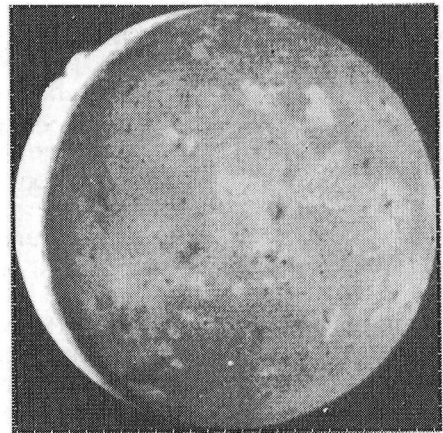


Figure 2

Figure 1: A geometrically reprojected Voyager 2 image of Io with a resolution of 56 km/line pair and a solar phase angle of  $8.6^\circ$ . The center of projection for this image corresponds to the same sub-spacecraft coordinates as figure 2.

Figure 2: Night-side image of Io with a sub-spacecraft point of  $26.5^\circ\text{N}$  and  $5.4^\circ\text{S}$  and a resolution of 22 km/line pair. The solar phase angle of this image is  $148.3^\circ$  so that the majority of visible surface is being illuminated by sunlight reflected off of Jupiter's disk.

# MARINER 10 COLOR-RATIO DATA AND THE SURFACE OF MERCURY

Bruce Hapke and Barry Rava, Department of Geology and Planetary Science,  
University of Pittsburgh, Pittsburgh, PA 15260.

The first analysis of the color-ratio map of Mercury (Hapke et al, 1980, Proc. Lunar Planet. Sci. Conf. 11th, in press) has been completed. Our preliminary conclusions are as follows.

- (1) The crust of Mercury is a low-Fe, low-Ti basic or ultrabasic silicate.
- (2) There is little correlation between the color and geological units, in particular with the smooth plains. This argues strongly that the smooth plains are not volcanic units of different composition from the rest of the crust.
- (3) This lack of correlation also implies that the color units are very old, with exogenic terrain later superimposed on ancient compositional units.
- (4) In a few instances boundaries of color units are associated with the thrust fault scarp system or with other examples of structural modification of the surface.
- (5) In the cases where a stratigraphic sequence can be established the tendency appears to be for pre-existing terrain to be covered by ancient, blue, low-Fe, magma flows.
- (6) In several isolated small areas there is evidence for late endogenic modification by red, Fe-rich volcanics.

The following sequence of events is proposed for the crust of Mercury:

- (1) formation of a primitive low-Fe crust; (2) formation of several major color units, possibly related to the last stages of differentiation and solidification of the crust; (3) contemporaneous heavy bombardment, formation of planet-wide scarp system and modification by low-Fe magmas; (4) Caloris event; (5) limited local basin filling by magmas (possibly generated by impact) of same composition as surroundings; (6) isolated late endogenic modification by high-Fe volcanic processes, possibly pyroclastic; (7) formation of young craters resulting in blue ejecta and rays.

The color-ratio data is marginally reconcilable with the smooth plains being basin ejecta, as advocated by Wilhelms. Apparently no lunar-like epoch of widespread mare flooding occurred on Mercury. This is consistent with current theories of the formation of the solar system which predict a low abundance of FeO and radioactive K in Mercury.

# IMPACT CRATERING: RELATIVE IMPORTANCE TO RADAR SCATTERING FROM LUNAR MARIA AND SYRTIS MAJOR

Richard A. Simpson, H. Taylor Howard, and G. L. Tyler  
(Center for Radar Astronomy, Stanford University, Stanford, CA 94305)

Planetary radar is used to determine altitudes, reflectivity, and roughness of target surfaces on scales of centimeters to hundreds of meters--scales largely inaccessible to other remote sensing instruments. From the basic data geophysical processes which shape the surface over geologically short periods of time may be inferred. We have reviewed data obtained from Syrtis Major over the past dozen years (at two wavelengths) and find that the basin has a unique character -- a character which, at first glance, makes Syrtis Major resemble lunar maria more closely than it does other parts of Mars. In this paper we show that any such resemblance is contrary to predictions based on impact cratering statistics. The resemblance is probably due to a coincidental morphological similarity between impact cratered terrain on the moon and wind eroded/deposited features in Syrtis Major.

The lunar surface is readily divided into two distinct units when observed at radar wavelengths  $\lambda$ . The maria are smooth relative to highlands, with typical values for surface roughness  $\sigma$  of  $4^\circ$  rms in maria and  $6$ - $8^\circ$  rms in highlands for  $\lambda = 13$  cm. No such simple distinction can be made for Mars. In plains, for example, we find both the roughest Martian surfaces and some of the smoothest. West of Tharsis Simpson *et al.* (1978a) found  $10^\circ$  rms estimates from radar data. Early (Mariner 9) imagery could not distinguish among these planar units but, Schaber (1980), from examination of high resolution Viking imagery, has identified surface structure which may be responsible for the high radar roughness values. Somewhat to the east of Tharsis is one of the smoothest surfaces on the planet; rms surface roughness less than  $1^\circ$  has been inferred (Downs *et al.*, 1973; Simpson *et al.* 1978a).

Syrtis Major, on the other hand, is a circular martian plain (at approximately  $280$ - $300^\circ$ W,  $0$ - $20^\circ$ N) which behaves in a more conventional fashion. Though inferred roughness values at  $\lambda = 13$  cm for both the basin and its surroundings are less than one might expect for comparable lunar terrains, the plain is distinctly smoother than its environs. Roughness estimates in the

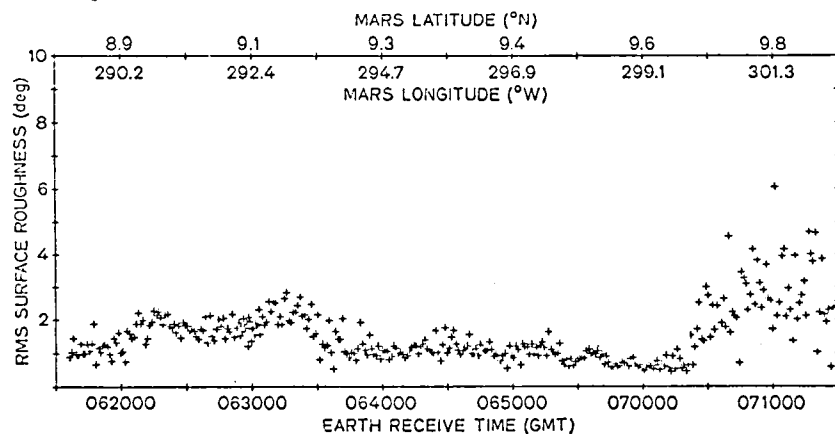


Fig. 1 - Estimates of rms surface roughness from 1978 Viking bistatic radar data (see Simpson *et al.*, 1979). High values of roughness west of  $300^\circ$ W should be considered qualitative; signals were so dispersed in frequency that echoes could not be reliably measured.



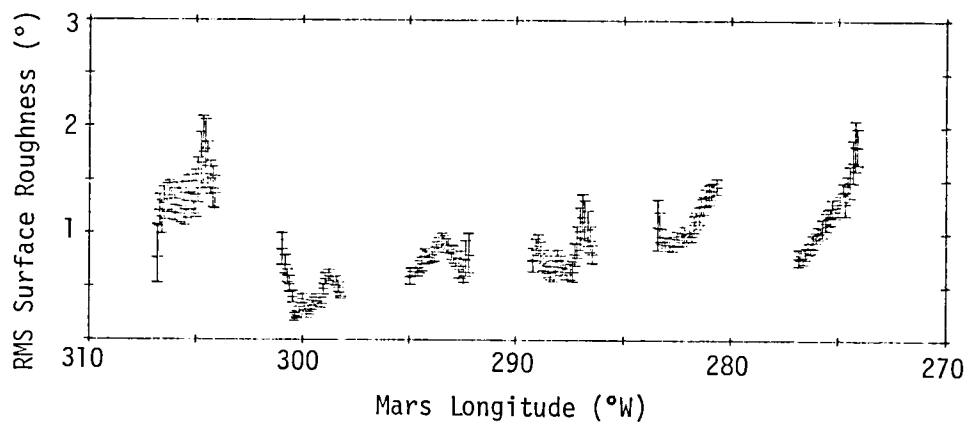


Fig. 2 - Estimates of rms surface roughness from 1978 Arecibo range-Doppler radar data. Specular point latitude was  $10.4^{\circ}\text{N}$ ; wavelength  $\lambda = 12.6$  cm. Because the experimental parameters governing operation of the radar system discriminated against observation of high angle scattering, estimates larger than  $1^{\circ}$  rms should be considered qualitative only. The  $0.25^{\circ}$  rms value near  $300^{\circ}\text{W}$  comes from the smoothest surface yet identified by planetary radar. Note reversal of horizontal (longitude) axis compared with Fig. 1.

central part of Syrtis Major have recently been obtained from 1978 observations which were made near  $15^{\circ}\text{N}$  and near  $10^{\circ}\text{N}$ . All the new data show roughness decreasing from east to west, with values  $\sigma \sim 1^{\circ}$  rms being typical (Figs. 1 and 2). Toward the east roughness rises to  $2^{\circ}$  rms in certain spots while at the western margin it may be as low as  $0.25^{\circ}$  rms. Roughness in the terrain to the west of Syrtis Major is at least  $2^{\circ}$  rms, and probably much more; however, the data are noisy and quantitative estimates are difficult to obtain. In the southern part of the basin Downs *et al.* (1978) showed that roughness over  $280\text{--}300^{\circ}\text{W}$  at  $3^{\circ}\text{N}$  averaged  $1.09^{\circ}$  rms. Along the northern margin Simpson *et al.* (1978b) reported values on the order of  $2^{\circ}$  rms, consistent with the other estimates if we recognize that the surface probed was a mix of plains and cratered terrain and that in such cases the smoother surface has an influence on the radar signature disproportionate to its fractional area.

Lunar maria show different values of  $\sigma$  when observed as a function of wavelength; Syrtis Major (alone among Mars regions to date) exhibits the same behavior. Rogers *et al.* (1970) obtained  $\sigma \sim 2^{\circ}$  rms for Syrtis Major ( $280\text{--}300^{\circ}\text{W}$ ,  $3\text{--}12^{\circ}\text{N}$ ) when using  $\lambda = 3.8$  cm wavelength. More recently, and with finer resolution, Downs *et al.* (1978) reported surface roughness estimates averaging  $1.65^{\circ}$  rms over  $280\text{--}300^{\circ}\text{W}$  at  $3^{\circ}\text{N}$  and  $\lambda = 3.6$  cm. The Downs *et al.* (1978) value of  $\sigma = 1.09^{\circ}$  rms (above) at  $12.6$  cm wavelength was over the same ground track; these imply a wavelength variation of the form  $\sigma \propto \lambda^{\alpha}$  with  $\alpha \approx -0.35$ . Downs *et al.* reported no wavelength difference in scattering from Margaritifer Sinus; Simpson *et al.* (1977) reached similar conclusions using  $\lambda = 70$  cm and  $\lambda = 12.6$  cm data acquired simultaneously from a number of locations on Mars during 1973.

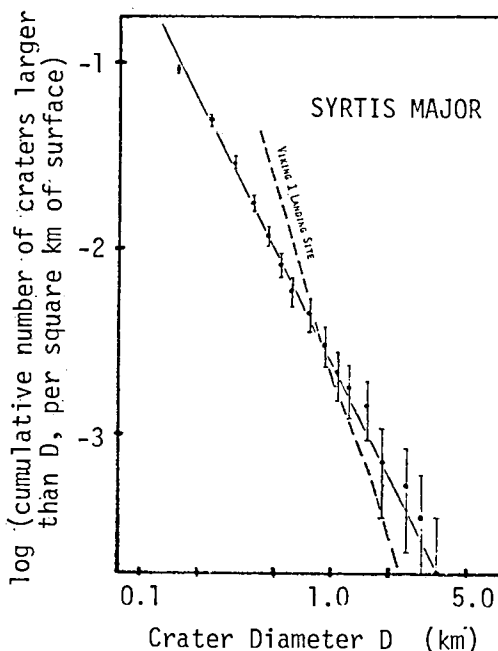
Tyler (1979), through the work of Moore *et al.* (1975, 1976) and others, has shown that roughness inferred from lunar bistatic radar data may be related to the age of the surface -- in particular, through cratering statistics. For surfaces which are mature (in equilibrium) at crater diameters several hundred times the radar wavelength, there is little wavelength dependence in the scattering. For surfaces which do not satisfy this condition, wavelength dependent scattering is observed. The mature surface is characterized by a crater density  $N$  versus diameter  $D$  of the form  $N \propto D^{-2}$ ; a younger surface has  $N \propto D^{-3}$ .

Fig. 3 - Crater distribution curve for mosaic in central Syrtis Major (Viking images 716A31 through 716A45; resolution typically 18 m/pixel). Slope of -2 would be characteristic of mature maria on the moon. Dashed line (Masursky et al., 1977) is for Viking Lander 1 site.

-----  
Meyer and Grolrier (1977) have published a crater density versus diameter curve showing  $N \propto D^{-2}$  for a large portion of Syrtis Major. The  $N \propto D^{-2}$  Meyer and Grolrier results were based on Mariner 9 imagery, which is generally inferior to that from Viking. We obtained Viking images for a small section of central Syrtis Major and constructed a mosaic; a crater count from the mosaic also gives  $N \propto D^{-2}$  (Fig. 3). Based on the crater statistics and our lunar experience, we should, therefore, have expected no wavelength dependence in scattering.

Curiously, the amplitude of the Syrtis Major  $N \propto D^{-2}$  curves is significantly lower than comparable curves for the moon -- by a factor of about 3 in the case of Meyer and Grolrier and by a factor of nearly 10 for our own curve. If there are fewer craters in Syrtis Major, then our observation that the inferred roughness is lower may follow. We can reconcile the  $N \propto D^{-2}$  behavior with the observed wavelength dependence only by concluding that some other form applies for  $D \lesssim 100$  m.

Our attempt to apply lunar experience to Mars required the implicit assumption that impact cratering is the dominant process in shaping surface forms of centimeter to 100 meter dimensions. We thereby ignored the effects of the martian atmosphere. The uniqueness of Syrtis Major in its similarity to lunar maria so far as radar behavior is concerned was some evidence in favor of that (or an equivalent assumption); we now believe that evidence to have been misleading. The absence of meter-sized craters in lander photographs from Viking 1 and Viking 2 is a strong indication that craters are relatively unimportant in determining the radar scattering properties of Mars surfaces. The highly visible windstreaks in Syrtis Major point toward aeolian processes as the dominant factor in radar scattering. We have yet to develop a model which will produce the observed behavior, but it is now clear that impact cratering should be a relatively minor factor.



REFERENCES: Downs, G.S., R.R. Green, and P.E. Reichley, *Icarus*, **33**, 441-453, 1978; Downs, G.S., and 4 co-authors, *Icarus*, **18**, 8-21, 1973; Masursky and 4 co-authors, *J. Geophys. Res.*, **82**, 4016-4038, 1977; Meyer, J.D., and M.J. Grolrier, U.S. Geological Survey, I-995 (MC-13), 1977; Moore, H.J., and 7 co-authors, U.S. Geological Survey Open File Report 76-298, 1976; Moore, H.J., and 8 co-authors, U.S. Geological Survey Open File Report 75-284, 1975; Rogers, A.E.E., and 4 co-authors, *Radio Science*, **5**, 2, 465-473, 1970; Schaber, G.G., Radar, visual and thermal characteristics of Mars: rough planar surfaces, *Icarus*, in press, 1980; Simpson, R.A., G.L. Tyler, J.P. Brenkle, and M. Sue, *Science*, **203**, 45-46, 1979; Simpson, R.A., G.L. Tyler, and D.B. Campbell, *Icarus*, **33**, 102-115, 1978a; Simpson, R.A., G.L. Tyler, and D.B. Campbell, *Icarus*, **36**, 153-173, 1978b; Simpson, R.A., G.L. Tyler, and B.J. Lipa, *Icarus*, **32**, 147-167, 1977; Tyler, G.L., *Icarus*, **37**, 29-45, 1979.

## MARS RADAR: THE SEARCH FOR RADAR-DEFINABLE SURFACE UNITS

S.H.Zisk NEROC Haystack Observatory, Westford MA 01886; and P.J.Mouginis-Mark, Dept. Geological Sciences, Brown University, Providence RI 02912.

Goldstone radar measurements of Mars during the 1971 and 1973 oppositions (1) have provided a wealth of data that has enabled the topography (2) and surface characteristics (3,4) of the planet to be investigated. Each point measurement of the radar signal contains information on the altimetry, surface roughness (C-factor, ref.5), and dielectric constant (via inherent reflectivity) for a lateral scale of 0.1-10 meters (6) with an areal resolution of  $1.3^\circ$  in latitude,  $0.16^\circ$  in longitude, and a height accuracy of about 100 meters (1). As part of an on-going program, we are currently investigating this data set with the objectives of identifying the spatial distribution of martian surface materials with similar characteristics and understanding the physical mechanisms which produce the variety of radar returns.

For a uniform surface, the usual template fitting technique (5) for the time-dependence of the observed radar signals results in a pair of independent values for the smoothness and reflectivity (as well as other parameters not considered here). In certain instances the quantitative reliability (standard error) of the computed values may be quite poor (4), but to a first approximation mechanically and chemically comparable surface materials (top meter layer) located at different areocentric positions will produce quantitatively similar radar returns. The distribution and areal extent of such surfaces with the same radar properties therefore provides complementary information for the geological characterization of surface features identified from orbital images (3,4).

As an example of the analyses we are pursuing, Fig.1 presents a 2-dimensional histogram of the frequency of radar-measured surface elements having given reflectivity and smoothness values for part of the data set (see figure caption). It is evident from the bright spots in Fig.1 that certain combinations of values occur more frequently than do others. Note that the bright spots in Fig.1 are not sharply bounded, but exhibit extended halos. This apparent imprecision of the radar characterization is probably due to several factors, including measurement error (which becomes worse as one approaches the origin of Fig.1); real homogeneity of the martian surface; and the inherent ambiguity in radar characterizations (4). We have found that the imprecision of the technique has a lesser effect if one considers small areas of the planet at a time so that the overlap effects are minimized. In Fig.2, six areas of more-numerous data points are identified for an amalgamation of three elevation slices similar to Fig.1. These areas indicate combinations of radar reflectivity and smoothness which are common in the given region of the martian surface.

Fig.3 shows, for the entire surface, the location of each radar point falling within the outlines of Fig.2. It is apparent from Fig.3 that the areas having uniform radar characteristics do, in fact, appear as large, coherent surface units rather than randomly-scattered points. Several of the radar outlines of

Fig.2 appear in more than one location on Mars: although units 3 and 5 are well-bounded, all the other units are relatively widely distributed. This either indicates that similar materials occur over much of the planet or, more likely, that different materials show similar radar characteristics. In the case of units 4 and 6, the extremely low smoothness indicates a rugged terrain, and is associated with a very low echo strength (4). It is not possible to distinguish differences in dielectric constant with any reliability, because of this low signal strength. On the otherhand, the high smoothness and reflectivity regions of units 3 and 5 are well defined and reliably measured. They are seen to correlate well with the radar anomaly associated with Solis Lacus (7).

Currently, we are continuing our analyses and interpretations of other units in Fig.2, together with a more rigorous search for possible correlations between altitude and radar characteristics.

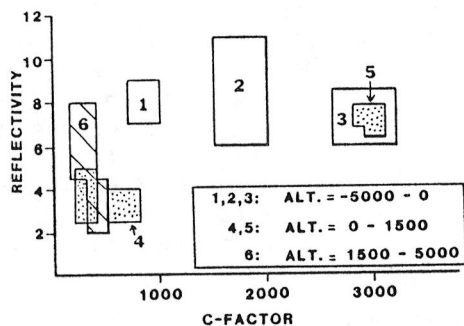
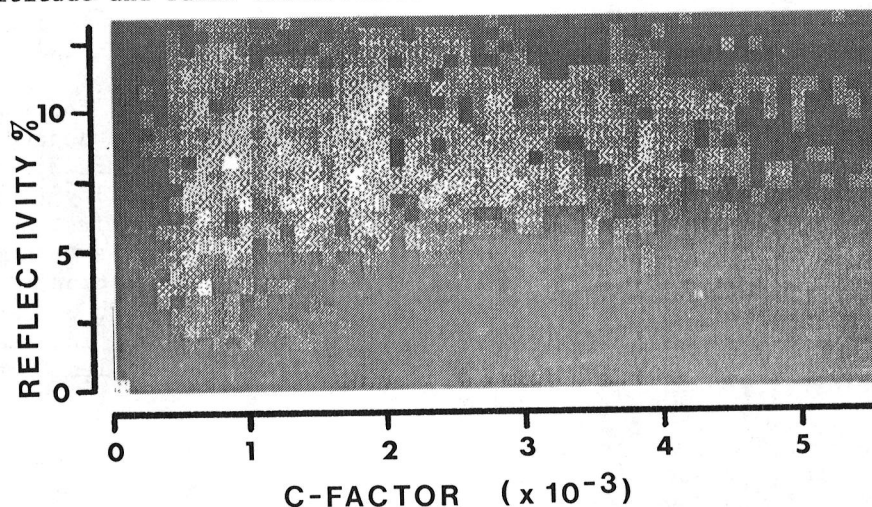


Fig.1 (above): 2-dimensional histogram of radar reflectivity vs. smoothness (C-factor). Includes all values between 60-120°W, 13-22°S at an altitude of -5 to 0 km (from ref.1). Bright areas indicate the existence of a larger number of points than do darker areas. Fig.2 (left): Locations of six "bright spots" identified from histograms similar to Fig.1 for radar data between 60-120°W, 13-22°S at all altitudes.

REFERENCES: 1) Downs G.S. et al. (1975) *Icarus* 26, 273. 2) Roth et al. (1980) *Icarus*, in press. 3) Schaber G.G. (1980) *Icarus* 42, 159. 4) Mouginis-Mark P.J. et al. (1980) *PLPSC 11th*, in press. 5) Hagfors T. (1964) *J.Geophys.Res.* 69, 3779. 6) Evans J. & Hagfors T. (1968) *Radar Astronomy*, McGraw-Hill, NY. 7) Zisk S.H. & Mouginis-Mark P.J. (1980) *Nature*, in press.

# DEGREES LATITUDE

## DEGREES LONGITUDE

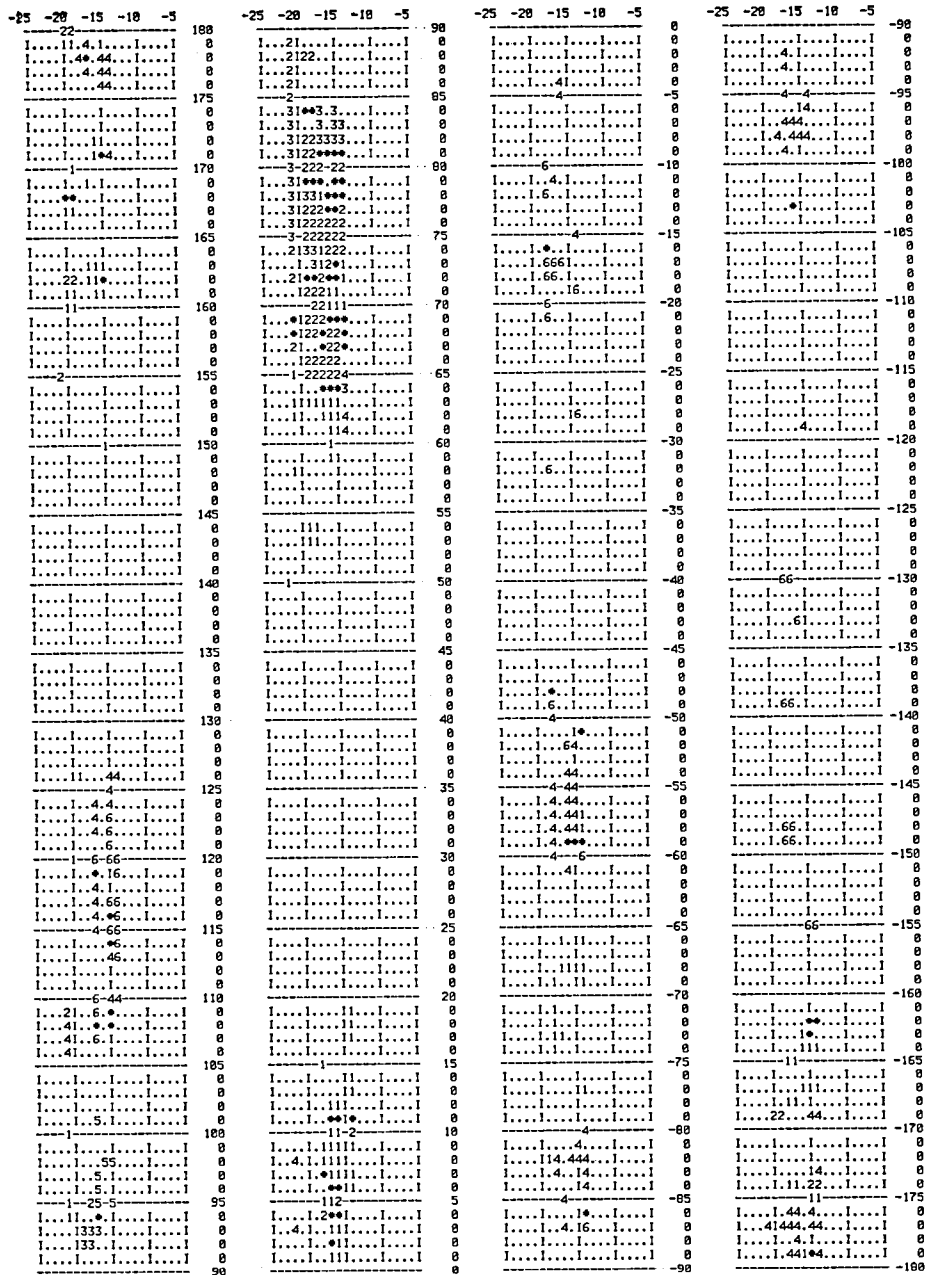


Fig.3: Distribution of radar units corresponding to the six areas identified in Fig.2 for the whole of Mars between 13-22°S. Sample bin size is 1° x 1°, giving 5-30 points per bin. "#" symbol indicates a bin that contains more than one of the radar units.

RADAR BACKSCATTER STUDIES IN NORTHERN ARIZONA: A PROGRESS REPORT,  
Gerald G. Schaber, U.S. Geological Survey, Flagstaff, AZ 86001.

Empirical models for radar backscatter developed during analysis of aircraft and Seasat spacecraft radar-image data, and calibrated radar scatterometer data of Death Valley, CA, are currently being tested in a semi-arid region of northern Arizona that is characterized by volcanic and sedimentary rocks with sparse cover of vegetation. To date, numerous radar image data sets have been collected that include K-band (0.86-cm wavelength), X-band (3-cm), and L-band (25-cm) images. Seasat L-band images have also been acquired in both optically and digitally processed formats. Four wavelength (75 cm, 18 cm, 6.3 cm, and 2.3 cm), multipolarization (VV-VH and HH-HV) radar scatterometer data, and 11-channel multispectral (.38 to 14 microns) image data were collected by the Johnson Space Center's (JSC) C-130 aircraft during 280 km of flightlines in June 1980. In October 1980, the JSC's RB57F aircraft, carrying a modified ANA/PQ 102 Goodyear X-band radar imaging system, will cover the Arizona backscatter test site in mapping format with dual incidence angles and polarization. Both the scatterometer and X-band flights by JSC have been negotiated through a cooperative program of research among the U.S. Geological Survey, NASA Planetology and Applications Programs, and the Environmental Research Institute of Michigan (ERIM).

Complete X-band and L-band radar-image coverages were acquired simultaneously over the northern Arizona backscatter test site in November 1979 by ERIM under contract to the U.S. Geological Survey. However, high-velocity upper-level winds (100 knots) resulted in poor X-band image data; the site will be reflighted by JSC for X-band data in October 1980.

Color aerial photographs at 1:3,000 scale obtained during the JSC scatterometer flight in June 1980 are presently being plotted on 1:36,000-scale aerial photographs to establish precise scatterometer footprints. Detailed surface-relief-statistics will be acquired through photogrammetric techniques and statistical analyses techniques for those surfaces selected for correlation with radar backscatter results (normalized cross-section versus surface-relief statistics at various incidence angles). Surface moisture and temperature data collected during the scatterometer overflights will be used to calibrate the radar- and thermal-image data, respectively. One published paper has resulted from this study to date [1].

Reference

- [1] Schaber, G. G., Elachi, Charles, and Farr, T., 1980, Remote sensing data of SP Mountain and SP flow in north-central Arizona: Remote Sensing of Environment, 9, 149-170.

## SEASAT RADAR LINEAMENT DETECTION: TESTING THE EFFECTS OF SHADOW ILLUSIONS

D.U. Wise, Univ. of Massachusetts, Amherst, Mass. 01003

Radar imagery is commonly used for the detection of topographic lineaments on planetary surfaces. These lineaments are presumed to represent erosional enhancement of fracture traces related to the tectonic history of a region. With the advent of the SEASAT radar system, lineament sets appeared on that imagery in bold and obvious patterns tempting many structural geologists to map and interpret these lineament patterns.

Unfortunately, any type of topographic shadowing enhances some lineament trends, suppresses others, rotates the apparent azimuths of others, and can create lineaments which do not exist (Wise, 1969, 1976). The extremely large depression angle from the horizontal of the SEASAT system makes this imagery particularly susceptible to these shadow illusions.

A test of the "observability" of lineaments on the SEASAT imagery was run using a dozen graduate students in the course on Brittle Fracture Analysis at Univ. of Massachusetts. After training the students' "eyes" in lineament mapping, each of the 12 students drew the lineaments they could see on the SEASAT imagery of an area along the Ohio River within the Huntingdon, W. Va., 1/250,000 quadrangle. The area is underlain by flat lying sediments and maturely dissected to provide erosional enhancement of any fracture traces which might be present.

Because the SEASAT system can provide imagery either on the ascending or descending leg of its orbit, two images of the same area were available, one illuminated from the SE-NW azimuth and the other from the NE-SW azimuth. Each image was analyzed by six students, their maps digitized, and azimuth frequency histograms prepared for their results with smoothing by a 10° running average. Figure 1 illustrates the variety of azimuth distribution patterns seen on the same SEASAT image (SE illumination) by six different partially trained observers. The arrow represents the illumination azimuth.

Cumulative plots of the results of these six observers are illustrated at the top of Fig. 2 and contrasted with the observations of two somewhat more experienced observers of the same imagery. In the lower part of Fig. 2 the same type of plots are presented for the results of the SW illuminated SEASAT imagery using six different student observers.

The test results show the need for considerable caution in interpreting what is "fact" on this type of imagery. The variety of trends seen or imagined by the various observers is not too far removed from the realm of random statistics. The pattern that does appear very clearly is the low level of detectability of lineaments parallel with the illumination azimuth and the enhancement (or creation) of lines approximately 30 degrees of azimuth on either side of the illumination azimuth. This phenomenon is not restricted to SEASAT radar but was described and analyzed by Wise (1969) for side illuminated relief maps. The test does not mean that the SEASAT system is impossible for lineament analysis but at the least it suggests

the need for experienced observers, multiple directions of illumination and extreme caution in interpretation of any results.

#### REFERENCES

- Wise, D.U., 1969, Pseudo-radar topographic shadowing for detection of sub-continental sized fracture systems, in Proc. of 6th Internatl. Sym. on Remote Sensing of the Environment, Univ. of Mich., p. 603-615.
- Wise, D.U., 1976, Sub-continental sized fracture systems etched into the topography of New England, in Proc. First International Conference on New Basement Tectonics, Utah Geol. Assoc. Publ. 5, p. 416-422.



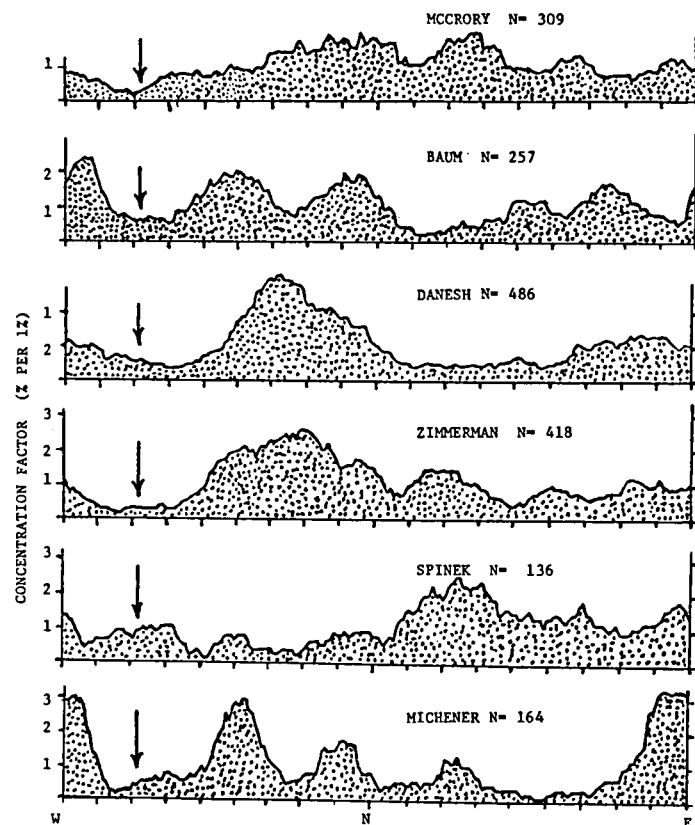


Figure 1. Azimuth-frequency histogram of lineaments detected by six different observers of the same SEASAT radar image. The arrow indicates the azimuth of radar illumination of the area, a portion of the Appalachian Plateau along the Ohio River. The data have been smoothed by a 10 degree running average.

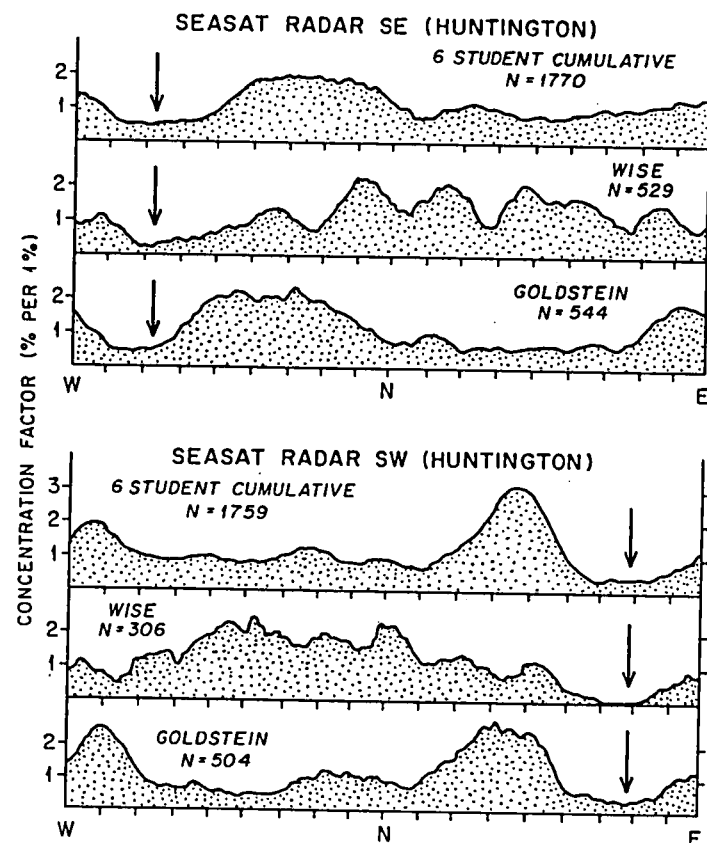


Figure 2. Contrasts of azimuth-frequency histograms of lineaments observed for the same area illuminated with different radar illumination azimuths. The arrows indicate the radar azimuth. Top illustration is a cumulative plot of the data of figure 1. All plots have been smoothed with a 10 degree running average.

THE MAETIQ DOME EGYPT - AN EARTH ANALOG STUDY OF ROCK TYPE  
DISCRIMINABILITY USING BROAD-BAND VISIBLE AND REFLECTED IR DATA.  
Jacobberger, P., R. Arvidson and E. Guinness, Dept. of Earth and  
Planetary Sciences, Washington University, St. Louis, Missouri 63130

Earth-based spectral reflectance data of Mars indicate that weathered surface materials are widely present on both bright and dark regions (Singer et al., 1979). At the Viking Lander sites, rock coatings, stains, and abundant fine-grained, weathered materials are ubiquitous (Binder et al., 1977; Strickland 1979). Singer et al., 1980a,b) has reported some success in deconvolving earth-based spectra (25 filters over 0.3 - 1.1  $\mu\text{m}$ ) of some dark areas into signatures related to major weathered and unweathered mineral components. One question that can be asked is the extent to which the Viking Orbiter VIS data (three channels, at  $0.45 \pm 0.03 \mu\text{m}$ ,  $0.53 \pm 0.05 \mu\text{m}$ , and  $0.59 \pm 0.05 \mu\text{m}$ ) can be used to characterize the proportion of weathered and pristine materials for a given location. To test such a capability we have begun an Earth analog study using Landsat multispectral scanner data over a region of known and quite variable rock type, the Maetiq gneiss dome, Eastern Egypt. The overall intent of the project is to see how well Landsat MSS data (roughly similar to VIS multispectral data in spectral resolution) can be used to discriminate intrinsic rock types where they are partially obscured by desert varnish. We also hope to gain a better understanding of the chemical and mineralogical properties of desert varnish, and a clearer understanding of the relationship between the desert varnish and the rocks on which it develops.

The Maetiq dome is composed of gneisses, mylonites, and migmatites of varying composition (Figure 1). The dome is structurally and lithologically distinct from the Precambrian oceanic-arc complex rocks which surround it (Sultan et al., 1980), and is cored by a syntectonic-late tectonic granite pluton (Sturchio et al., 1980). The entire suite of rocks comprising the dome is stained by desert varnish. The varnish tends to partially obscure the intrinsic color and albedo differences of the various rock types, much in the same way as weathered coatings and stainings may obscure such differences on Mars.

Figures 2a and 2b show the first two principal components for a Landsat scene over the dome. The first component brightness is controlled primarily by high irradiances in the 0.6 to 0.8  $\mu\text{m}$  region, while dark regions in the second component are dominated by high values of green (.5 to .6  $\mu\text{m}$ ) irradiance. Clearly, the dome is redder than the surrounding country rocks, which are composed of green schist facies sequences. Distinct brightness patterns within the dome can also be discerned and mostly correlate with mappable geologic units. Some 30 soil and rock (both weathered and pristine) samples were collected from the dome in order to test the discriminability inherent within the LANDSAT data. Spectral reflectances of these samples are being measured at Cornell University. These ground truth data (high spectral resolution) should allow us to discern just how well the LANDSAT MSS data have done in discriminating the various rock and soil types exposed in

the region. The data should also provide clues as to whether-or-not desert varnish is related to the intrinsic rock types.

#### REFERENCES CITED

- Binder, Alan B., Arvidson, Raymond E., Guinness, Edward A., Jones, Kenneth L., Morris, Elliot C., Mutch, Thomas A., Pieri, David C. and Sagan, Carl, 1977, The geology of the Viking Lander 1 site, J. Geophys. Res., 82, 4439-4451.
- Gillespie, A., 1980, Digital techniques of image enhancement, in Remote Sensing in Geology, Siegal, B. and A. Gillespie, ed., J. Wiley, 700 p.
- Singer, Robert B., McCord, Thomas B., Clark, Roger N., Adams, John B., and Huguenin, Robert L., 1979, Mars surface composition from reflectance spectroscopy: a summary, J. Geophys. Res., 84, 8415-8426.
- Singer, Robert B., 1980a, The composition of the Martian dark regions: I. Visible and near-infrared spectral reflectance of analog materials and interpretation of telescopically observed spectral shape, JGR, in press.
- Singer, Robert B., 1980b, The composition of the Martian dark regions: II. Analysis of telescopically observed absorptions in near-infrared spectrophotometry, JGR, in press.
- Strickland, Edwin L. III, 1979, Martian soil stratigraphy and rock coatings observed in color-enhanced Viking Lander images, Proc. Lunar. Planet. Science Conference 10, 3055-3077.
- Sturchio, N.C., Batiza, R., Sultan, M.I., El Shazly, E.M., and Abdul-Meguid, A.A., 1980, Geology of the Maeti q gneiss dome, central Eastern Desert of Egypt: the foliated rocks, EOS, in press (abstract).
- Sultan, M., Batiza, R., Sturchio, N.C., El Shazly, E.M., and Abdul-Meguid, A.A., 1980, Geology of the Maeti q gneiss dome, central Eastern Desert of Egypt: granite and granodiorite, EOS, in press (abstract).

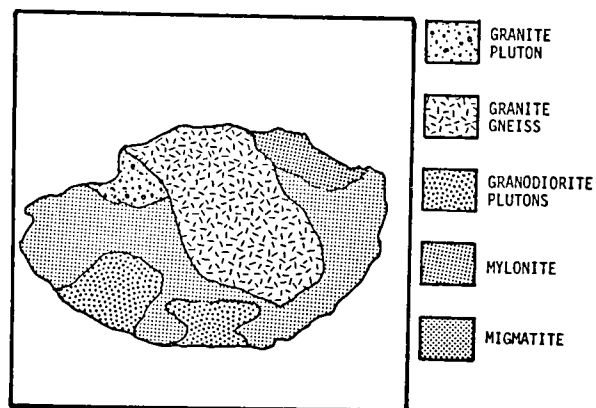
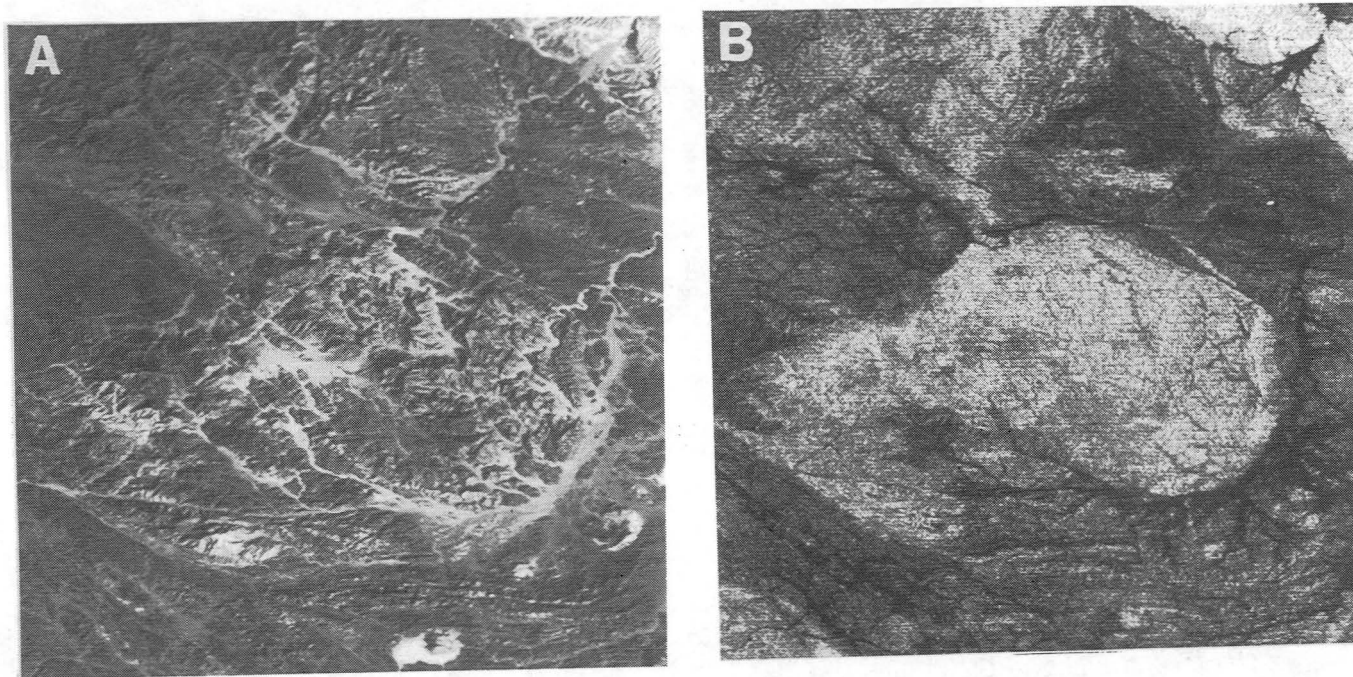


Figure 1 - Sketch map of Maeti q dome, Egypt. The dome is surrounded by green schist facies metamorphic rocks. The dome is located at 26° N. Latitude, 34° E. Longitude, and is about 30 km wide. Based on mapping by Batiza (pers. com.).



Figures 2A, 2B - First and second principal components image of Landsat frame, covering the Maeti dome. The first component displays 96% of the variance in the 4 channels, while the second component displays 2.9%. The variance weighted eigenvectors for the two components indicate that bright regions in the first component have high irradiances in the 0.6 to 0.8  $\mu\text{m}$  region, while dark areas in the second component have high irradiances in the 0.5 to 0.6  $\mu\text{m}$ . A discussion of principal component techniques can be found in Gillespie (1980).

## DIFFUSE REFLECTANCE SPECTRA OF PARTICULATE (SUBMICRON) IRON OXIDES AND SELECTED MIXTURES THEREOF

Richard V. Morris, SN7, Geochemistry Branch, NASA-JSC, Houston, TX 77058  
Stanley C. Neely, University of Oklahoma, Norman, OK 73019

### INTRODUCTION

Previous laboratory investigations into the spectral properties of particulate iron oxides have concentrated predominantly on samples having either relatively large ( $>1\text{-}10\mu\text{m}$ ) or undocumented mean particle sizes (e.g., 1,2). These and similar studies have proven to be valuable in inferring compositional information about the Martian surface from reflectance spectra obtained mainly by telescopic observation (e.g., 3). However, it has also been shown in laboratory experiments that the nature of the reflectance spectra of particulate materials (such as the surface of Mars) can be a strong function of mean particle size, especially at very small mean particle sizes (e.g., 4,5). Thus, in order to properly interpret the reflectance spectra of the Martian surface, it is important to also have a detailed knowledge of the dependence of the spectral properties of iron oxides on mean particle size. To this end, we are conducting an investigation of the spectral properties of particulate iron oxides having submicron mean particle sizes. In this abstract, we report results for hematite ( $\alpha\text{-Fe}_2\text{O}_3$ ), maghemite ( $\gamma\text{-Fe}_2\text{O}_3$ ), goethite ( $\alpha\text{-FeOOH}$ ), lepidocrocite ( $\gamma\text{-FeOOH}$ ), and magnetite ( $\text{Fe}_3\text{O}_4$ ) and a few selected mixtures thereof.

### SAMPLE DESCRIPTION AND EXPERIMENTAL PROCEDURES

The iron oxides were obtained in particulate form as commercially available reagents; all were synthetically prepared. The particle shape and mean grain size were determined from TEM photomicrographs. The results are compiled in Table 1. The iron oxides were combined into intimate mixtures (blends) by means of ultrasonic agitation in ultra-pure freon; after blending, the freon was evaporated at  $\sim 30^\circ\text{C}$ .

The diffuse reflectance spectra were recorded on a Cary 14 spectrophotometer having a 25 cm integrating sphere. With a  $\text{N}_2$  gas purge, the available spectral range is  $\sim 0.35\mu\text{m}$  to  $\sim 2.20\mu\text{m}$ . Halon powder was used as the reference material.

### RESULTS AND DISCUSSION

#### Pure Oxides

The diffuse reflectance spectra of the pure oxides are shown in Figures 1A and 1B. The spectrum of hematite ( $\alpha\text{-Fe}_2\text{O}_3$ ; HMS3) is similar to those published by other workers (e.g., 1,6). The spectrum is characterized by a band at  $\sim 0.86\mu\text{m}$ , an inflection centered near  $0.62\mu\text{m}$ , and strong absorption shortward of  $\sim 0.55\mu\text{m}$ . The spectrum of goethite ( $\alpha\text{-FeOOH}$ ; GTS2) is somewhat different from those published in the geologic literature (e.g., 1,6) but is similar to those published by the paint industry (e.g., 7). Bands are centered near  $\sim 0.65\mu\text{m}$  and  $\sim 0.92\mu\text{m}$ , the former of which is not observed in the spectra published in the geologic literature. The strong absorption occurs shortward of  $\sim 0.43\mu\text{m}$ . The presence or absence of the 0.65 band may reflect relative chemical purities

(7,8). The goethites studied by (1) and (6) are naturally occurring and may contain significant impurities; major element analyses of GTS2 (not shown) showed it was nearly chemically pure. The spectrum of lepidocrocite ( $\gamma$ - $\text{FeOOH}$ ; LPS2) is similar to that of goethite except the two bands occur at slightly longer wavelengths ( $\sim 0.68$  and  $\sim 0.97 \mu\text{m}$ ). This spectrum suggests lepidocrocite as a possible alternative to pyroxene for the  $0.93$ - $0.97 \mu\text{m}$  band in the 1969 Martian bright area spectra reported by (9).

The spectrum of magnetite ( $\text{Fe}_3\text{O}_4$ ; MTS4) is similar to those published by others for magnetite samples having a small mean particle size (e.g., 6). The reflectance of magnetite MTS4 is 2-4%. The spectrum of maghemite ( $\gamma$ - $\text{Fe}_2\text{O}_3$ ; MHS3) is characterized by a weak band centered at  $\sim 0.93 \mu\text{m}$ , a shoulder near  $0.63 \mu\text{m}$ , and strong absorption shortward of  $\sim 0.45 \mu\text{m}$ . Maghemite has been suggested by (10) to be present on the Martian surface as a minor (1-7%) component in or on most of the surface particles. Comparison of the spectrum for MHS3 to those for the bright areas of Mars (3) shows no strong spectral indication for maghemite, assuming the spectrum of MHS3 is representative of maghemites in general. However, this test for the presence of maghemite is probably not very sensitive because MHS3 has no distinctive strong bands longward of  $\sim 0.80 \mu\text{m}$  and because the gradual increase in absorption from  $\sim 0.80$  to  $\sim 0.45 \mu\text{m}$  could be masked by other  $\text{Fe}^{3+}$  oxides such as hematite.

### Blends

In Figure 2 are the diffuse reflectance spectra of the blends of hematite (HMS3), maghemite (MHS3), and goethite (GTS2) with 10 wt. % magnetite (MTS4). Such blends might approximate, in an optical sense, a rock, a rock coating, or a soil which is a mixture of a  $\text{Fe}^{3+}$ -bearing phase and an opaque phase such as magnetite. All three spectra have the same general form. There is a moderate to steep positive slope from the UV-blue to the reflectance maximum which is at  $\sim 0.58$ ,  $\sim 0.75$ , and  $\sim 0.76 \mu\text{m}$  for the GTS2, HMS3, and MHS3 blends, respectively. Longward of the reflectance maximum, the slope is negative with some superimposed structure for the GTS2 and HMS3 blends. The GTS2 blend is olive green in color; the HMS3 blend is red-brown; and the MHS3 blend is dark brown.

The hematite blend spectrum closely resembles the Martian dark region spectrum as represented by the spectrum of a dark region in Iapygia with the effects of atmospheric  $\text{CO}_2$  and 20% surface coverage by bright material numerically removed (11). Both have a reflectance maximum at  $\sim 0.75 \mu\text{m}$  and an apparent band minimum at  $\sim 0.89 \mu\text{m}$ . The magnitude of the negative slope in the near-IR is greater in the blend but still compares favorably. In addition, an absorption at  $\sim 0.99 \mu\text{m}$  is present in the Mars spectrum but not the blend, presumably because of an  $\text{Fe}^{2+}$ -bearing silicate phase present in the Martian case but not in our blend.

The reflectance maximum of  $\sim 0.58 \mu\text{m}$  for the GTS2 blend clearly renders it a poor spectral analogue for the Martian dark region spectrum. However, appropriate blends of GTS2, HMS3, and MTS4 would provide a way of shifting the reflectance peak between  $0.58$  and  $0.75 \mu\text{m}$ . The MHS3 blend is not a good spectral analogue, primarily because it does not have the  $\sim 0.89 \mu\text{m}$  band. In addition, the prominent shoulder near  $\sim 0.62 \mu\text{m}$  is not readily apparent in the Martian dark region spectrum.

(2) has published spectra of mixtures of limonite and a much coarser-grained magnetite, and these spectra have a negative slope in the near-IR.

He suggests that the finer-grained limonite can be thought of as forming a coating on the larger magnetite grains and regards that his spectra reflect this physical situation. This picture does not seem physically realistic for our blends because the mean particle diameters are not too dissimilar (cf., Table 1). Thus, we suggest that a negative slope in the near-IR may not necessarily be indicative only of a coating phenomenon.

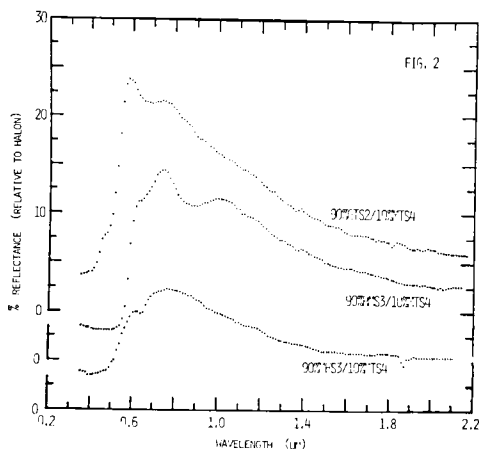
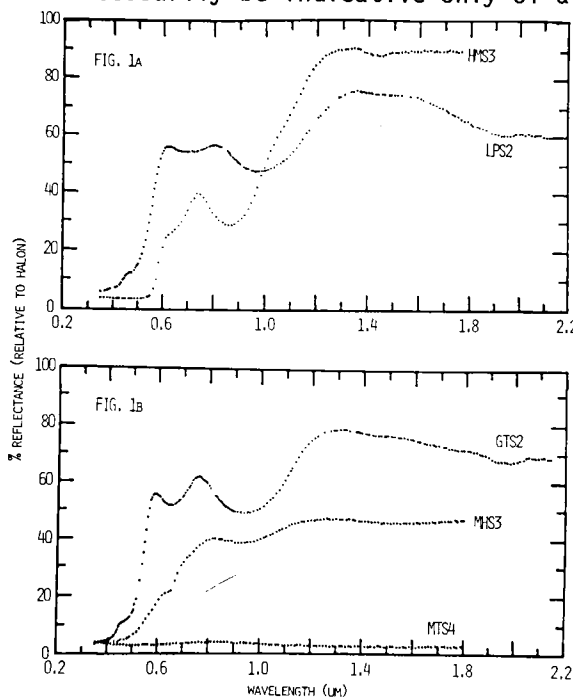


Fig. 1 (left). Reflectance vs. wavelength for pure oxides.

Fig. 2 (up). Reflectance vs. wavelength for oxide mixtures. Spectra are offset for clarity.

Table 1. Selected properties

Property	Unit	GTS2	HMS3	LPS2	MHS3	MTS4
Nominal Comp.		$\alpha$ -FeOOH	$\alpha$ -Fe <sub>2</sub> O <sub>3</sub>	$\gamma$ -FeOOH	$\gamma$ -Fe <sub>2</sub> O <sub>3</sub>	Fe <sub>3</sub> O <sub>4</sub>
Shape		acicular	nodular	acicular	acicular	cubical
M <sub>Z</sub>	μm	0.05x0.4	0.2	0.03x0.9	0.05x0.3	0.5
M <sub>Z</sub> + σ	μm	0.07x0.5	0.3	0.04x1.2	0.06x0.4	0.7
M <sub>Z</sub> - σ	μm	0.03x0.3	0.1	0.02x0.5	0.03x0.2	0.4

M<sub>Z</sub> = mean grain size; σ = standard deviation

REF.: (1) Adams (1975) In *Infrared and Raman Spectroscopy of Lunar and Terrestrial Minerals*, p.91; (2) Singer (1980) LPS XI, 1045; (3) Singer et al. (1979) JGR 84, 8415; (4) Wendlandt and Hecht (1966) *Reflectance Spectroscopy*; (5) Vincent and Hunt (1968) *App. Optics* 7, 53; (6) Hunt et al. (1971) *Mod. Geol.* 2, 195; (7) Hancock (1975) In *Industrial Minerals and Rocks*, p.335; (8) Bell et al. (1975) In *Infrared and Raman Spectroscopy of Lunar and Terrestrial Minerals*, p.1; (9) Huguenin et al. (1977) LS VIII, 478; (10) Hargraves et al. (1979) JGR 84, 8379; (11) Singer and McCord (1979) *PLPSCI* 10, 1835.





## Chapter 9

### PLANETARY CARTOGRAPHY, GEODESY AND GEOLOGIC MAPPING



# VOYAGER CARTOGRAPHY

Batson, R. M., U. S. Geological Survey, Flagstaff, Arizona 86001

Maps of the four Galilean satellites of Jupiter are being made with image data from the Voyager 1 and 2 spacecraft (Batson and others, 1980). These maps are being made in range of scales and in several versions. The following table shows the number of sheets being made at each scale:

	<u>Io</u>	<u>Europa</u>	<u>Ganymede</u>	<u>Callisto</u>
1:25M Prelim. Pictorial Maps	1	1	1	1
1:25M Color Maps	1	1	1	1
1:15M Planetwide	1	1	1	1
1:5M Quadrangles	3	1(+1?)	11	8(+1?)
Special Maps	5	0	0	0
Total	<u>11</u>	<u>4(+1?)</u>	<u>14</u>	<u>11(+1?)</u>

Mapping priorities at 1:5M have been established as follows, on the basis of scientific interest and data availability:

## Io

Ji 2  
Ji 4  
Ji 3 / total 3 sheets

## Europa

either 2-sheet standard format, or 1-sheet special format, to be determined .

## Ganymede

Jg 7  
Jg 8, 9  
Jg 12  
Jg 15  
Jg 13  
Jg 14 / total 11 sheets

Jg 3  
Jg 10, 6  
Jg 5, 2  
Jg 1  
Jg 4

## Callisto

Jc 6  
Jc 2  
Jc 1  
Jc 3  
Jc 4

Jc 5  
Jc 9, 8  
Jc 10  
Jc 13(?) / total, 8 possibly 9 sheets

Total for program 23 - 35 sheets.

Cartographic image-processing for the mapping is at three levels. Level one includes all preprocessing, artifact removal and general cleanup

if Voyager pictures. Level two includes photometric and geometric correction of each picture. Levels one and two are complete for all frames. Level three includes mosaicking in appropriate formats on appropriate projections. This last processing is underway. At least two versions of each mosaic will be distributed with filters at different spatial frequencies. Airbrush versions will show both relief only and relief with surface markings superposed.

#### REFERENCE

Batson, R. M., Bridges, P. M., Inge, J. L., Isbell, Christopher, Masursky, Harold, Strobell, M. E., and Tyner, R. L., 1980, Mapping the Galilean satellites of Jupiter with Voyager data: Photogrammetric Engineering and Remote Sensing (in press).

## THE CONTROL NETWORKS OF THE GALILEAN SATELLITES

Davies, Merton E., The Rand Corporation, Santa Monica, California 90406

Geodetic control networks are being computed for all of the Galilean satellites using pictures from the Voyager 1 and 2 encounters at Jupiter. Points have been identified on the satellites and their coordinates computed by single-block analytical triangulations. The status of the control nets is summarized in the following table:

<u>Satellite</u>	<u>Points</u>	<u>Pictures</u>	<u>Measurements</u>	<u>Normal Equations</u>	<u>Overdeterminations</u>	<u><math>\sigma</math> (mm)</u>
Io	478	234	8330	1658	5.02	0.01827
Europa	112	115	2534	569	4.45	0.01488
Ganymede	1329	204	11386	3270	3.48	0.02258
Callisto	402	182	5594	1350	4.14	0.02053

The systems of longitude on Europa, Ganymede, and Callisto are now defined by small craters. On Io, the IAU (1975) definition of longitude is still in use since it is doubtful that a small permanent feature can be found which will still be identifiable on future missions, considering the high rate of volcanism. On Europa, the crater Cilix (point 52) defines 182° longitude; on Ganymede, the crater Anat (point 1000) defines 128° longitude; and on Callisto, the crater Saga (point 400) defines 326° longitude.

The angle W is measured from the ascending node of the satellite's equator on the standard Earth equator (1950.0) along the satellite's equator to the satellite's prime meridian. When the system of longitudes is defined by a surface feature, the angle W is measured by the planetwide control net. At this time, the equations for W are

$$\begin{aligned} \text{Europa} & \quad W = 157^\circ 39' 21'' + 101^\circ 37' 47'' 235d \\ \text{Ganymede} & \quad W = 196^\circ 43' 63'' + 50^\circ 31' 76081d \\ \text{Callisto} & \quad W = 157^\circ 89' 33'' + 21^\circ 57' 10715d \end{aligned}$$

where  $d = \text{JED} - 2433282.5$ .

The control net computations can be used to measure the mean radii of the satellites, which give at this time--Io,  $1815 \pm 5$  km; Europa,  $1569 \pm$  km; Ganymede,  $2631 \pm 10$  km; and Callisto,  $2400 \pm 10$  km.

### Bibliography

- Davies, Merton E., Thomas A. Hauge, Frank Y. Katayama, and James A. Roth, Control Networks for the Galilean Satellites: November 1979, The Rand Corporation, R-2532-JPL/NASA, November 1979.
- Davies, Merton E., and Frank Y. Katayama, Coordinates of Features on the Galilean Satellites, The Rand Corporation, P-6479, June 1980.

## IMPROVED ACCURACY OF COORDINATES OF FEATURES ON MARS

Davies, Merton E., The Rand Corporation, Santa Monica, California 90406

The objective of this program is to improve the accuracy of the coordinates of the control points on Mars in the region between and beyond the Viking 1 lander site and the small crater, Airy-0. This is accomplished by tying photogrammetric strips of Viking mapping frames (with resolutions about one-half kilometer) between these points. The strips will be designed to form triangles since they expand beyond these two points, thus forming a geodesic grid. The beginning of the grid can be seen in Figure 1. The southern strip is completed (Davies and Dole, 1980); the northern strip is in process. Additional strips are planned.

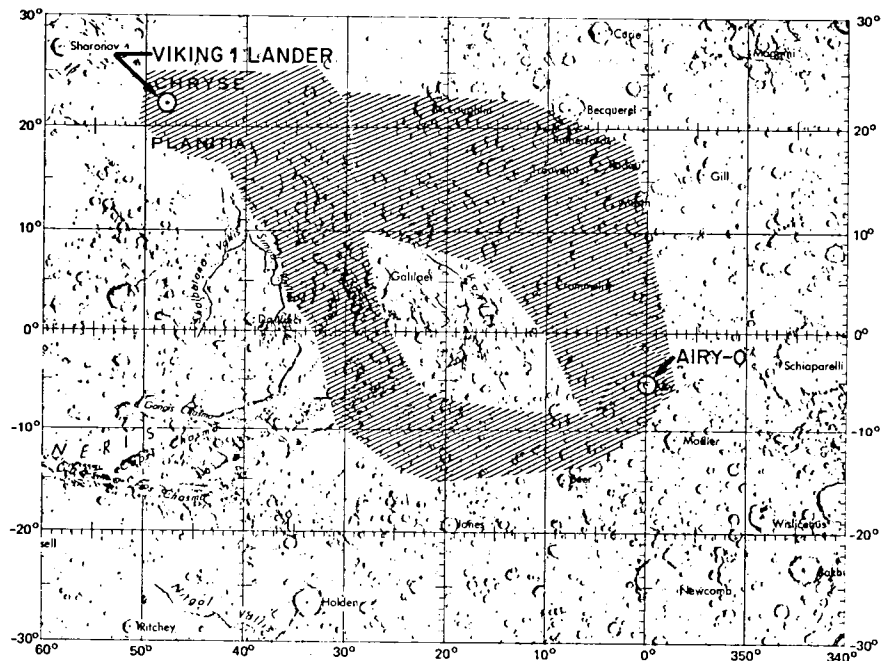


Fig. 1--Cross-hatching shows the path of the photogrammetric strips

## IMPROVED ACCURACY OF COORDINATES OF FEATURES ON MARS

Davies, Merton E.

The center of the small crater, Airy-0, defines the prime meridian on Mars, thus the longitudes of all points must be measured photogrammetrically relative to Airy-0. The location of the Viking 1 lander site has been identified on an orbiter picture (Morris and Jones, 1980), thus permitting a photogrammetric tie to the site. The latitude and radius of the lander site was accurately measured by the Viking Lander Radio Science Team (Mayo et al., 1977; Michael, 1979), so the Viking 1 lander site and Airy-0 are important control points on Mars that are identified on high-resolution Viking frames. For this reason, the improved accuracy grid included these points from its beginning. This grid will be included in a periodic planetwide control net update to improve the coordinates of points throughout the surface of Mars.

### References

- Davies, M. E., and S. H. Dole, Improved Coordinates of Features in the Vicinity of the Viking 1 Lander Site on Mars, The Rand Corporation, R-2600-NASA, March 1980.
- Mayo, A. P., et al., "Lander Locations, Mars Physical Ephemeris, and Solar System Parameters: Determination from Viking Lander Tracking Data," J. Geophys. Res., Vol. 82, No. 28, Sept. 30, 1977, pp. 4297-4303.
- Michael, W. H., Jr., "Viking Lander Tracking Contributions to Mars Mapping," The Moon and Planets, Vol. 20, 1979, pp. 149-152.
- Morris, E. C., and K. L. Jones, "Viking 1 Lander on the Surface of Mars: Revised Location," submitted to Icarus.

# MARS: 1:2,000,000 MAPPING

R. M. Batson and R. L. Tyner, U.S. Geological Survey, Flagstaff,  
Arizona 86001

Mars is divided into 140 quadrangles for mapping at a scale of 1:2,000,000. Most of the map sheets are controlled photomosaics tied to the Viking triangulation (1). In addition to the basic controlled photomosaics, selected quadrangles are compiled as shaded relief maps, color mosaics, and contour maps (2). Thirty-two controlled photomosaics have been published and seventeen are in press. Ten are in compilation. Copies of interim mosaics (which are incomplete pending receipt of additional data) have been distributed to Regional Planetary Image Facilities. The status of this mapping is shown in fig. 1. Publication of three of the completed shaded relief maps has been delayed because of geometric problems, including possible control-point misidentifications in MC1A and MC1B, and the necessity to correct relief distortion so that the shaded relief is consistent with the contours in MC18NW. The appropriate corrections are being made to digital versions of the maps and the publication cycle is expected to resume early in 1981.

Preparation of color mosaics was suspended during FY 1980, but will resume early in FY 1981, with expected publication of ten or more color mosaics within a year.

## REFERENCES

- (1) Davies, M. E., Katayama, F. Y., and Roth, J. A., 1979, Control net of Mars: February 1978: The Rand Corporation R-2309-NASA, 91p.
- (2) Wu, S. S. C., 1980, 1:2M contour mapping, in Proceedings of the Planetary Investigators' Conference, NASA Technical Memorandum B1776, Arizona State University, Tempe, January 14-16, 1980, p. 355,356.



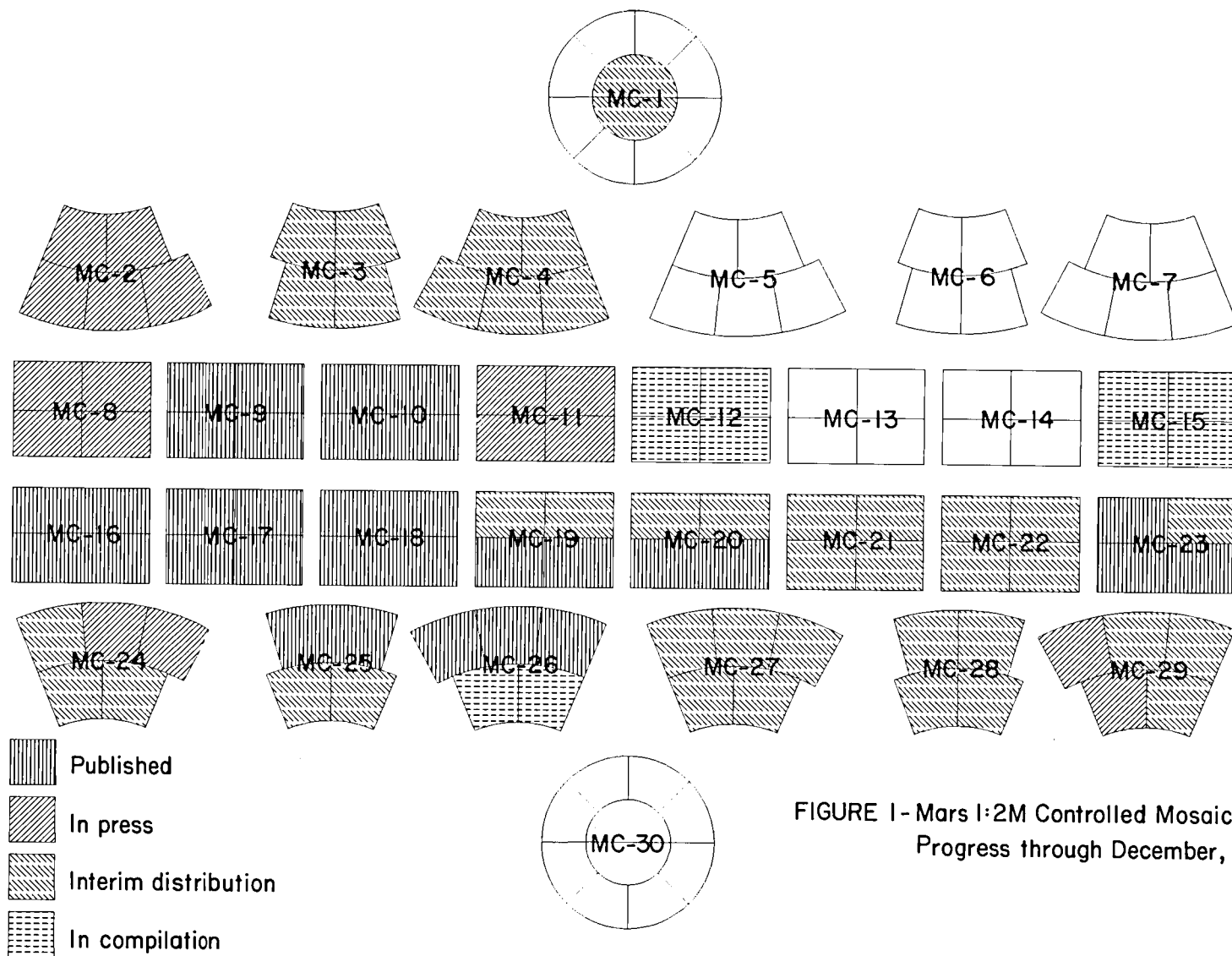


FIGURE 1 - Mars 1:2M Controlled Mosaics:  
Progress through December, 1980

TOPOGRAPHIC MAPPING OF MARS: 1:2 MILLION CONTOUR MAP SERIES,  
Sherman S.C. Wu, Francis J. Schafer and Raymond Jordan  
U.S. Geological Survey, Branch of Astrogeologic Studies, Flagstaff,  
Arizona 86001

High-quality Viking Orbiter photographs of various resolutions are being used for the systematic mapping of the planet Mars. Despite the fact that the photographs have extremely narrow fields of view, special photogrammetric techniques have been developed (1, 2, 3) that enable stereo models to be set up on an analytical plotter for photogrammetric compilation of topographic maps. Information provided by these maps is essential to understanding the geologic processes that have affected the martian surface.

For the systematic topographic mapping of Mars using photogrammetric stereoplotters, a planetwide geodetic control net was established using high-altitude Viking orbital photographs with slant ranges as high as 37,000 km. This control network, which involves about 500 photographs in an equatorial belt and 500 photographs in a polar belt, is based on an analytical aerotriangulation method through a block adjustment using the SEDR data of the Viking mission and the primary control net derived by Davies (4).

The compilation of the 1:2 million contour maps uses Viking Orbiter photographs with slant ranges between 14,000 km and 24,000 km. Resolution of the photographs is adequate for the compilation of 1-km contour lines. The format of each of these maps in the equatorial belt, which is 60° wide (30° N. to 30° S.), is a size that evenly divides each of the existing 1:5 million maps into four subquads (5), each of which covers an area of 22.5° longitude by 15° latitude. A Mercator projection is used, and the scale is true at 27.3 N. and 27.3 S. Elevations are referred to the Mars topographic datum (1,2).

Fig. 1 shows an example of these subquads. This map was compiled from six stereo models set up on the AS-11AM analytical plotter. The mapped area is a portion of Valles Marineris, the Mars canyonland, and covers both Tithonium and Ius Chasmata. In the mapped area, the depth of the canyon is about 10 km and the slope of the canyon walls ranges from 20° to 30° (6). Fig. 2 shows another subquad which includes the volcano Arsia Mons, 23 km high. This map was compiled from seven stereomodels.

We are currently compiling maps in the vicinity of Tharsis Montes and Valles Marineris. With the extensive coverage of the Viking Orbiter photographs, all 64 subquads in the equatorial band can be compiled stereoscopically. However, because of gaps in the medium-resolution coverage, some lower resolution photographs may have to be used.

#### REFERENCES

- (1) Wu, S. S. C., 1975, Topographic mapping of Mars: U.S. Geol. Survey Interagency Rept., Astrogeology 63, 191 p.
- (2) Wu, S. S. C., 1978, Mars synthetic topographic mapping: Icarus 33, no. 3, 417-440.

- (3) Wu, S. S. C., 1979, Mars photogrammetry: NASA Tech. Memo. 80339, 432-435.
- (4) Davies, M. E., Katayama, F. Y., and Roth, J. A., 1979, Control net of Mars: The Rand Corporation, R-2039-NASA, February, 1978, 91 p.
- (5) Batson, R. M., 1979, Mars cartography: NASA Tech. Memo. 80339, 413-414.
- (6) Wu, S. S. C., 1979, Photogrammetric portrayal of Mars topography: Jour. Geophys. Res., 84, no. B14, 7955-7959, 3 maps.



Fig. 1 -- TOPOGRAPHIC MAP OF COPRATES NORTHWEST QUADRANGLE OF MARS

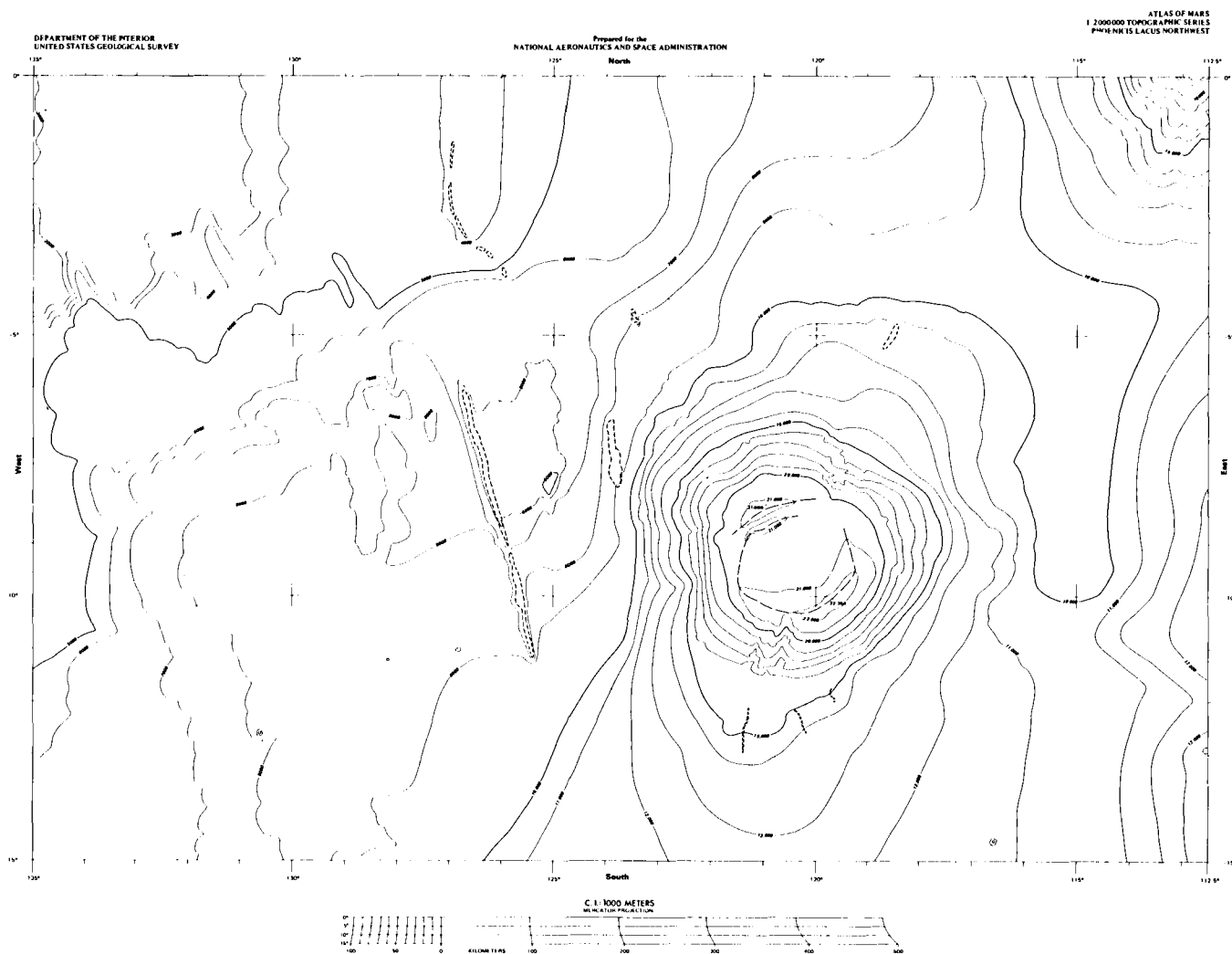


Fig. 2 - TOPOGRAPHIC MAP OF PHOENICIS LACUS NORTHWEST QUADRANGLE OF MARS

## MARS 1:15,000,000 MAPPING

Batson, R. M., U. S. Geological Survey, Flagstaff, Arizona 86001

Four sheets are contained in the Mars 1:15,000,000 series. Base materials are 1:5,000,000 maps of Mars transformed to the appropriate projection. Airbrush shaded-relief renditions incorporate additional image detail from Viking Orbiter pictures. Two versions of the maps will be published: version one will show relief only, without nomenclature; version two will have nomenclature.

Airbrushing is now complete and all four sheets are at review stage, prior to submission for publication.

## VOIR PHOTOGRAMMETRY,

Sherman S. C. Wu, Francis J. Schafer and Loretta A. Barcus  
U.S. Geological Survey, Branch of Astrogeologic Studies, Flagstaff, AZ.  
86001

VOIR photogrammetry is a research project for the extraction of three-dimensional topographic information of terrain features of Venus from VOIR stereo-radar imagery. Radar images constructed by a radar correlator-processor represent a line-scan geometry. Due to the uniqueness of radar geometry, which is affected by its method of illumination and image formation, the stereo radar mapping problem is complex (1). It is presently being solved with two approaches (2): off-line and on-line. The off-line approach uses current digital image-processing technology to computer-rectify and correct geometric distortions of side-looking radar imagery so that the analytical photogrammetric plotters presently available can be used for map compilation. The on-line approach interfaces a high-speed digital computer to the existing radar stereoplotter so that all computations for geometric corrections can be performed in real time during map compilation.

The off-line approach was experimented with by using images taken by different radar systems covering areas of Huntsville, AL, Pinedale, WY, and Phoenix, AZ. A pair of radar images of the Huntsville area taken by a UPD-4 radar system was tested (3). Computer-rectification and stereo-modeling were successfully accomplished on the AP/C analytical plotter. However, due to the fact that they were taken from the same side, the base-to-height ratio was too small for photogrammetric compilation and measurements.

A second attempt was to rectify a pair of stereo-radar images of a glacial lake at Pinedale, WY, looking from the same side but using different modes of the NASA radar system. Different modes have different depression angles; the depression angle of mode 1 is  $57^\circ$  and that of mode 2 is  $36^\circ$ . This difference makes the base-to-height ratio large, enabling compilation of a contour map from the model on the AP/C analytical plotter. However, because severe distortion occurred in the mode 1 imagery from an unknown source in the radar system, the map compiled from the model has large errors when compared with a standard U.S. Geological Survey 1:62,500 topographic map.

Because of these errors, a third test was made, in which a pair of stereo-radar, mode 2, images was rectified. These images cover the Phoenix, AZ area; they were taken from opposite sides and therefore have very strong geometry. A stereo model was set up on the AP/C analytical plotter and photogrammetric measurements were made along with a map compilation. The images were taken from an altitude of 60,000 feet and have a scale of 1:200,000. However, the scale of the rectified photographs is 1:800,000. The map was compiled at a scale of 1:250,000 to allow a comparison with the U.S. Geological Survey topographic map at the same scale. Because the area covered between Phoenix and the White Tank Mountains is very flat, only planimetry was compiled from the model (Fig. 1), but ground coordinates and elevations of about 150 discrete points were also measured.

The planimetry compiled from the rectified radar model on the AP/C analytical plotter matches the U.S. Geological Survey topographic map fairly well. Of the 88 elevations measured from the model and compared with the map, about one-third differ by less than 5 m, 50% by less than 10 m, 68% by less than 20 m, 86% by less than 30 m, and 92% by less than 40 m. However, a comparison of the horizontal coordinates from the model with those on the map shows that about 60% of the displacements are less than 250 m and 90% less than 400 m; these distances are 0.3 and 0.5 mm at the scale of the model (4, 5).

The on-line approach uses a Modcomp Computer that is interfaced to the radar stereoplotter (6). Because the Modcomp Computer is Fortran programmable, all rectification and correction for geometric distortions can be programmed into the plotter and performed in real time. Interface hardware is near completion and software development is currently in progress.

#### REFERENCES

- (1) LebreI, Franz, 1979, Accuracy analysis of stereo side-looking radar: Photogr. Engr. and Remote Sensing, 14, no. 8, 1083-1096.
- (2) Wu, S. S. C., 1979, Stereo mapping with side-looking radar imagery: The International Symposium of the Problem of Accuracy Improvement of Photogrammetric Models, International Society for Photogrammetry, Commission III, July 31-August 5, 1979, Moscow, USSR, p. 54.
- (3) Wu, S. S. C., 1979, Radar photogrammetry: NASA Tech. Memo. 80339, 426-428.
- (4) Wu, S. S. C., 1980, Topographic mapping with side-looking radar imagery, presented at the 14th International Congress of the International Society for Photogrammetry, July 13-25, 1980, Hamburg, Germany, p. 44.
- (5) Wu, S. S. C., and Schafer, F. J., 1980, Side-looking radar using analytical plotters, in Proceedings of the 1980 Analytical Plotter symposium and workshop sponsored by the American Society of Photogrammetry, April 20-25, 1980, Reston, Virginia, 442-444.
- (6) Miranda, F. F., 1971, Radar stereo equipment program: Final rept., Goodyear Aerospace Corp., GERA-1712, 42 p.



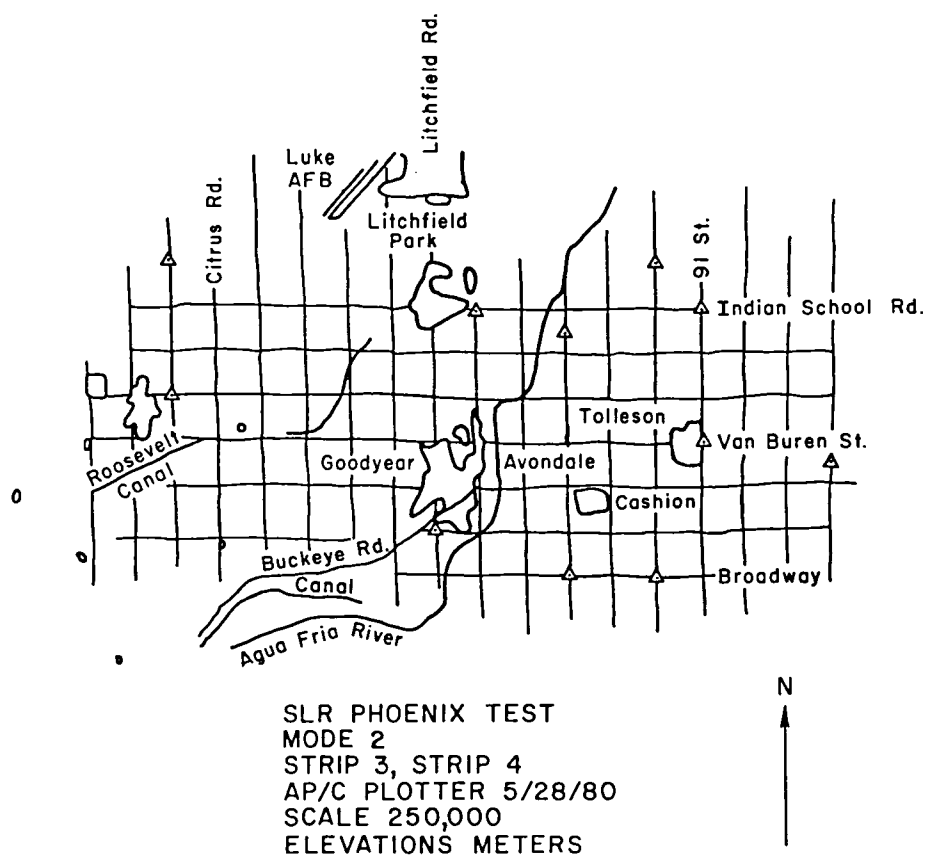
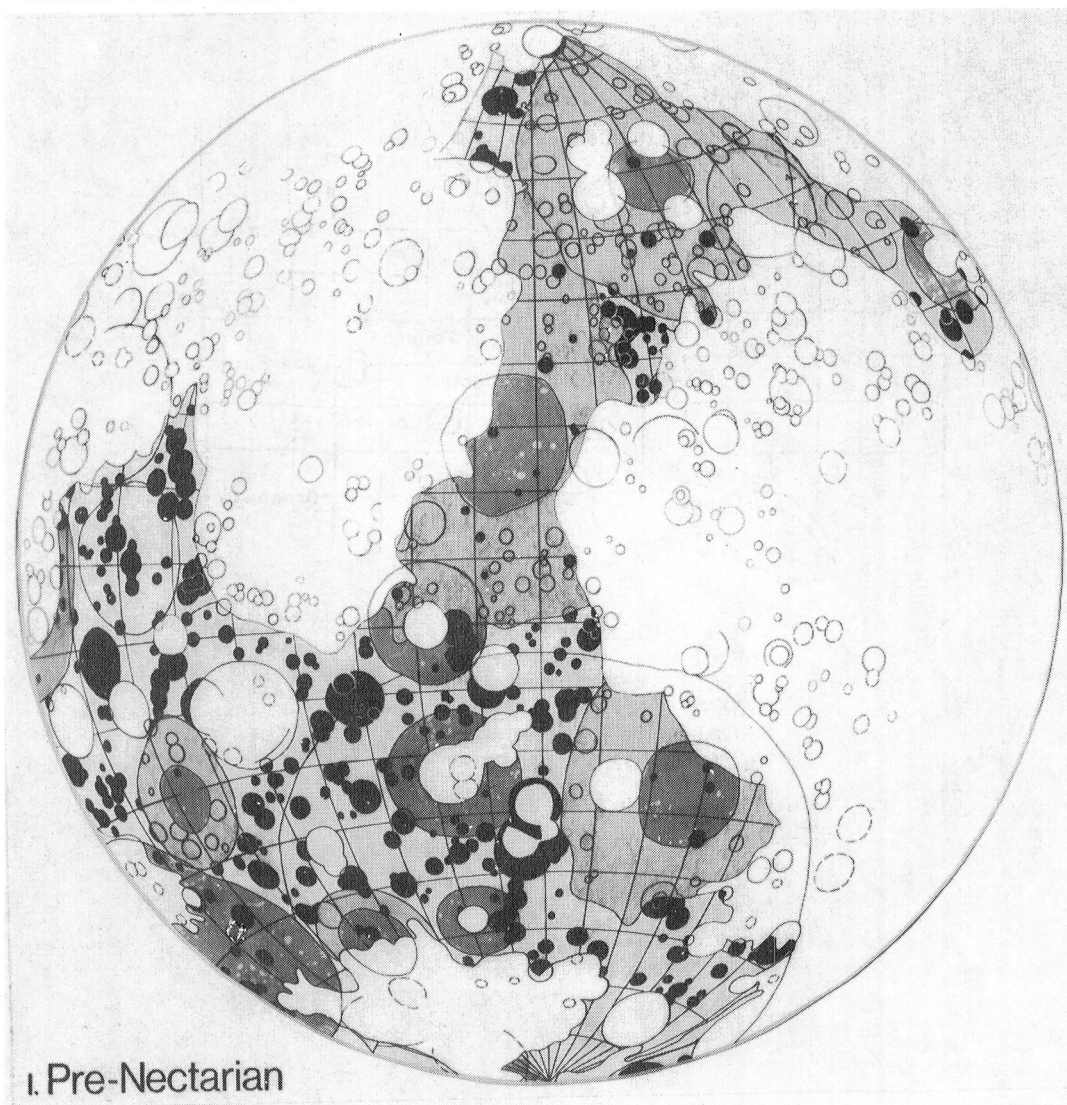


Fig. 1. Planimetric map of Phoenix, AZ, area compiled from a model of NASA radar images.

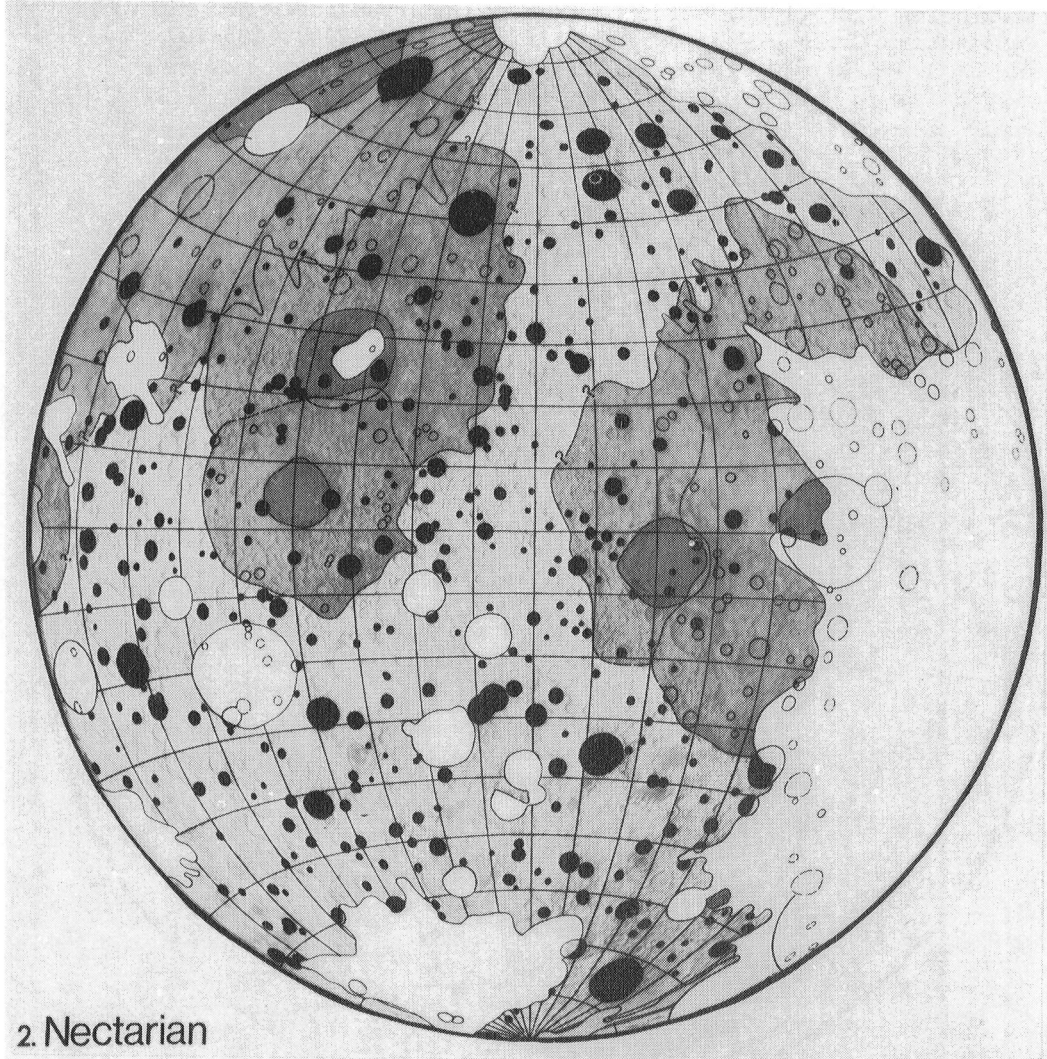
## PALEOGEOLOGIC MAPS OF THE FAR SIDE OF THE MOON

Don E. Wilhelms, U.S. Geological Survey, Menlo Park, CA 94025

Three maps show the major geologic units formed on the Moon's far side in about the first 0.7 aeons of its history (figs. 1-3). The map representing one of the three time intervals shows only features formed in that time. Terranes older than the one being portrayed are shown by the air-brush rendition of the base map without further shading (base by J. L. Inge, U.S. Geological Survey; equal-area projection). Younger terranes are blank.

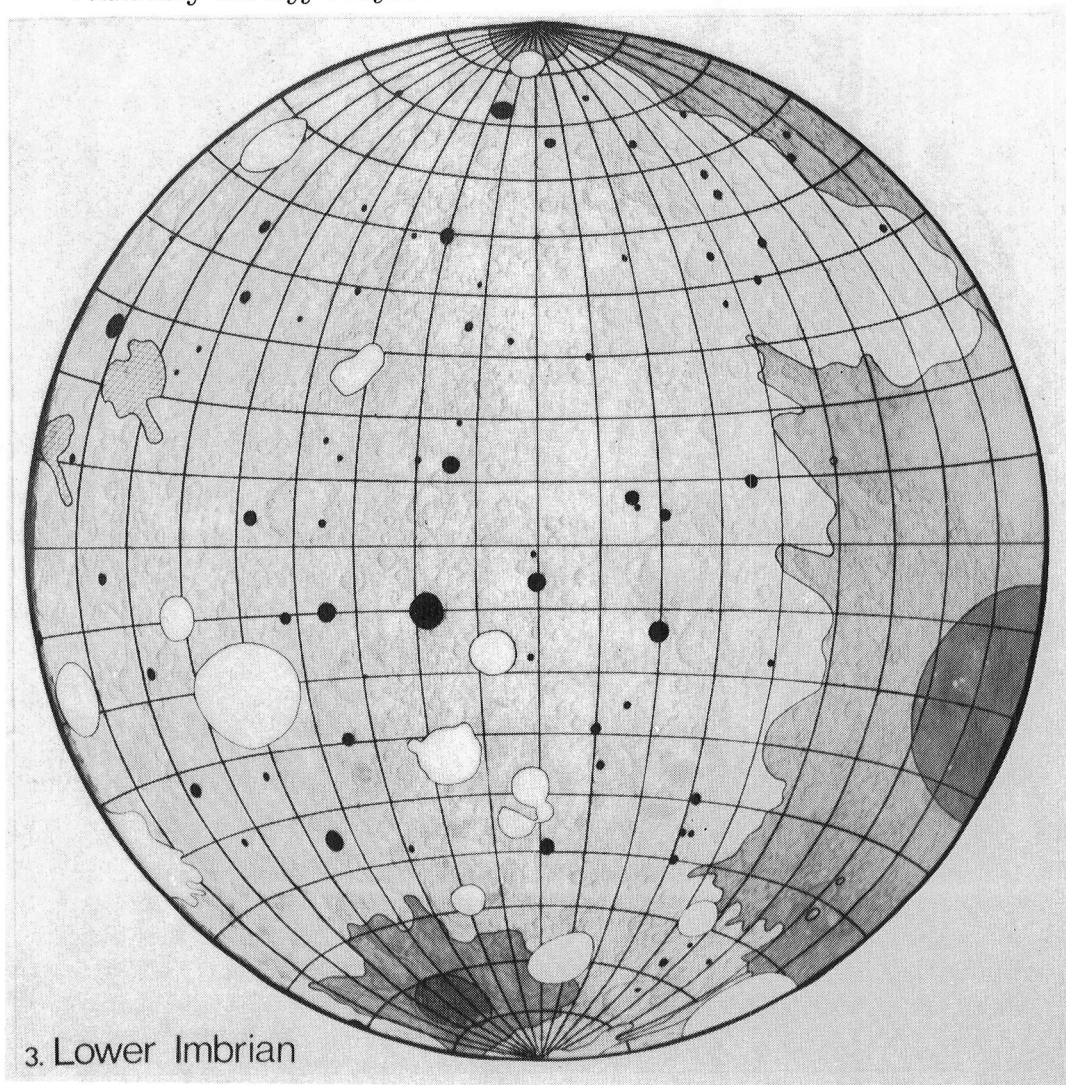


Craters  $\geq 30$  km and all known or suspected basins [1] are mapped. Exposed interiors of craters are shown in black and those of definite basins in medium gray, where the interior is defined as the depression inside a crater's rim crest or a basin's topographic rim (as interpreted by [1]). Rim crests or topographic basin rims that are buried by deposits of the age being portrayed or younger are outlined, dashed where of doubtful age. Deposits are visible around many craters but are left unmapped for clarity. Imbrian, Nectarian, and late pre-Nectarian basins [2] are surrounded by mappable deposits and secondary craters (light gray). Middle and early pre-Nectarian basins undoubtedly once had visible deposits also, but only the interiors are mapped here (shaded except for the huge South Pole-Aitken basin and indefinite basins).



The dominance of basins and craters in these early scenes is clear; little area remains that could be extensively inundated by volcanic materials. Two light-plains deposits of possible volcanic origin are shown by a rhomb pattern in fig. 3. Others could be present but undetected in basin and crater interiors and perhaps other depressions. The falloff in lunar far-side activity with time is also illustrated. Very few blank areas indicating subsequent deposits of any type remain in fig. 3, even though the early Imbrian epoch ended with the Orientale impact before deposition of the visible maria.

- [1] Wilhelms D.E. (1979) Geologic map of lunar ringed impact basins. *Abstracts, Conference on Multi-ringed Basins*. Lunar Sci. Inst. (inpress)
- [2] Wilhelms D.E. (1980) Relative ages of lunar basins. *Reports of Planetary Geology Program 1979-1980*. NASA TM 80339, 135-137.



Chapter 10  
WORKSHOPS AND SPECIAL PROGRAMS



PLANETARY GEOLOGY UNDERGRADUATE RESEARCH PROGRAM (PGUR)  
Marjorie M. Eagan, State University of N.Y. at Buffalo

A total of eighty-three (83) applications were received from undergraduates interested in participating in the program during the summer of 1980. This was twice the number received last year. The ratio of male/female applicants was two to one. A corresponding increase in requests from Principal Investigators for intern placement also occurred. The following twenty (20) students were selected and assigned to work with PI's at locations indicated.

Richard P. Binzel, senior at Macalester College, MN  
Hosted by Dr. Eugene Shoemaker/Eleanor Helin at Cal Tech,  
Pasadena, CA. Program dates - June 2 through July 25, 1980

Stephen H. Brown, senior at Univ. of Massachusetts, Amherst  
Hosted by Dr. James Head, Brown University, Providence, RI  
Program dates - June 23 through August 15, 1980

James D. Giglierano, junior at Eastern Kentucky Univ.  
Hosted by Mrs. Carol S. Breed, USGS, Flagstaff, AZ  
Program dates - June 28 through August 9, 1980

Marilyn Ginberg, sophomore at Franklin & Marshall College, PA  
Hosted by Dr. Stephen Saunders, JPL, Pasadena, CA  
Program dates - June 15 through August 8, 1980

Peter C. Gustafson, junior at California State Univ. at Fresno  
Hosted by Dr. Elliot Morris, USGS, Flagstaff, AZ  
Program dates - June 2 through July 25, 1980

Silvia M. Heinrich, senior at Univ. of Massachusetts, Amherst  
Hosted by Dr. Robert E. Strom, University of Arizona  
Program dates - June 16 through August 8, 1980

Charles T. Herzig, junior at Dickinson College, PA  
Hosted by Dr. Farouk El-Baz, Smithsonian Inst, Washington, DC  
Program dates - June 2 through July 25, 1980

Melinda L. Hutson, junior at University of Minnesota  
Hosted by Dr. Robert Wolfe, Smithsonian Inst., Washington, DC  
Program dates - June 16 through August 8, 1980

John M. Japp, senior at University of Nebraska, Lincoln  
Hosted by Dr. Stephen Saunders, JPL, Pasadena, CA  
Program dates - June 30 through August 22, 1980

Tony Johnson, junior at Georgia Southwestern College  
Hosted by Mrs. Camilla K. McCauley, Museum of No. Arizona,  
Flagstaff. Program dates - June 23 through August 15, 1980

Jeffrey D. Kenney, senior at Bates College, Maine  
Hosted by Dr. Stephen Saunders, JPL, Pasadena, CA  
Program dates - June 16 through August 8, 1980

Kathleen A. Malone, senior at San Jose State University  
Hosted by Dr. Ronald Greeley, NASA Ames Research Center, CA  
Program dates - June 2 through July 25, 1980

Fernando Martinez, senior at City College of New York  
Hosted by Dr. James Head, Brown University, Providence, RI  
Program dates - June 30 through August 22, 1980

Leo G. Matthews, senior at Hofstra University, NY  
Hosted by Dr. Duwayne M. Anderson, S.U.N.Y. at Buffalo  
Program dates - June 2 through July 25, 1980

Lynn Muradian, junior at Massachusetts Inst. of Technology  
Hosted by Dr. Stephen Saunders, JPL, Pasadena, CA  
Program dates - June 30 through August 22, 1980

Christina A. Neal, junior at Brown University, RI  
Hosted by Dr. Elliot Morris, USGS, Flagstaff, AZ  
Program dates - June 2 through July 25, 1980

Paul N. Romani, junior at University of Michigan  
Hosted by Dr. Stephen Saunders, JPL, Pasadena, CA  
Program dates - June 16 through August 8, 1980

Marianne Stam, senior at Univ. of California, Berkeley  
Hosted by Dr. James Head, Brown University, Providence, RI  
Program dates - June 30 through August 22, 1980

Randii Wessen, senior at S.U.N.Y. at Stony Brook  
Hosted by Dr. Chas. Stembridge w/Patricia Cates, JPL, Voyager  
Science Office. Program dates - July 7 through August 29, 1980

Deborah L. Young, senior at S.U.N.Y. at Oneonta  
Hosted by Dr. Chas. Stembridge w/Patricia Cates, JPL, Voyager  
Science Office. Program dates - Oct. 1 through Nov. 25, 1980

Intern and host reports at the completion of the summer assignments were positive, indicating strong support for continuance of the program.



## THE PLANETARY GEOLOGY ADJUNCT INVESTIGATORS PROJECT: A PROGRESS REPORT

D'Alli, Richard E., Department of Geology, Arizona State University, Tempe, AZ 85281

The Planetary Geology Adjunct Investigators Project (formerly the Associates Project) has now been in operation for 21 months. The objectives of the Project continue to be one of increasing communications between Principal Investigators in the Planetary Geology Program and the general community of geologists, and the infusion of planetary program results into the geologic curriculum. As outlined previously (D'Alli, 1980), the objectives are implemented by means of faculty development, scientific communications, and special educational materials.

A summer workshop in Planetary Geology was conducted at Arizona State University August 11–16, 1980. The workshop was a six day, intensive introduction to the fundamentals of planetary geology. The workshop was announced by brochures mailed to departments of geology in the Pacific northwest and the northern tier of states. The workshop interspersed formal lectures with "hands-on" laboratory activities during the first two days at Arizona State. The remaining four days were spent at the U. S. Geological Survey, Astrogeology Branch, and in the field, Flagstaff, Arizona. The Project wishes to gratefully acknowledge the Planetary Geology Principal Investigators who served as instructional staff, providing stimulating lectures and discussion. Activities included an aerial tour of planetary analogs in northern Arizona, a day-long field trip to Meteor Crater, and an optical mineralogy laboratory using the lunar thin section educational packages from the Johnson Spacecraft Center.

The nationwide Planetary Geology Speakers Bureau will be in full operation by January 1, 1981. Twelve Planetary Geology Principal Investigators have agreed to deliver colloquia at colleges and universities in their vicinity. The Project will coordinate host requests and speaker scheduling.

Videotapes in planetary geology are now in production. They will be 20 minutes in length, in color, and feature Planetary Geology Principal Investigators dealing with concepts in their area of expertise. The first tape is an overview of impact cratering, touching on mechanics, crater degradation processes, and surface chronology. It has been completed and is ready for distribution. The second tape, now in production, presents a synopsis of the development of planetary geology as a discipline and strategies in solar system exploration. For information regarding the use and availability of the tapes, contact the Planetary Geology Program at Arizona State University. The tapes have been designed for use at the undergraduate and graduate level.

### REFERENCE

D'Alli, Richard E. (Abstract), 1980. The Planetary Geology Associates Project: A Progress Report, Rep. Plan. Geol. Prgm. 1979–1980, NASA TM 81776, p. 377.

# PLANETOLOGY IN ROME, 1980

R.Bianchi, A.Carusi, P.Cerroni, A.Coradini, M.Coradini, C.Federico, E.Flamini, M.Fulchignoni, G.Magni, M.Poscolieri and G.B.Valsecchi.

Istituto di Astrofisica Spaziale del C.N.R. - Reparto di Planetologia  
Viale dell'Università 11, 00185 ROMA, ITALY.

During the past year the research work of the Planetology Group of Rome covered the following topics:

- a) A study of the morphological evolution of fresh impact craters has been developed and applied to approximately one hundred lunar craters. The model makes it possible to compute erosion rates due to gravity mass movements, under the assumption that the initial shapes of the impact craters were conical, as shown by topographic investigations of the lunar craters.
- b) Statistical techniques for image processing have been developed further and calibrated using Lansat images of Southern Italy. This makes it suitable for the analysis of images of non terrestrial surfaces.
- c) A study of the thermal evolution of the Galileian satellites has been initiated on the basis of theoretical models of planetary accretion developed by Safronov, Ruskol and Kaula.
- d) The study of close encounters between Giant Planets and fictitious minor bodies has been developed further by including the effects of Saturn, Uranus and Neptune on the evolution of chaotic orbits in the outer Solar System.
- e) Computer programs of stellar evolution have been adapted to the case of gaseous planets and the equation of state governing the evolution of these planets has been formulated theoretically.

PLANETARY NOMENCLATURE, Harold Masursky and M. H. Strobell, U.S. Geological Survey, 2255 North Gemini Drive, Flagstaff, AZ 86001

A list of feature names for the satellites of Jupiter has been assembled; these names appear on the published preliminary maps. More names will be applied soon to the high-resolution photomosaics of Io and Ganymede now in preparation, and still more will be added to the formal 1:5 million-scale geologic maps of all the Galilean satellites prior to publication.

A similar list of feature names has been assembled for the satellites of Saturn. These names will be applied in November 1980 if Voyager's photographic observations are successful.

Preliminary radar maps of Venus have been completed, including Venus-Pioneer altimetry and images and also ground-based radar data from Arecibo and Goldstone. These maps contain selected names from the list of feature names compiled for Venus. More names will be applied to the formal maps and globe of Venus now in preparation.

For Mars, new names have been applied to the revised 1:5 million-scale maps, to the 1:2 million-scale photomosaic series, and to the preliminary maps of high-resolution observations made by Viking Survey Missions 1 and 2.

#### Outer Solar System Nomenclature

Owen, Tobias, Earth and Space Sciences, State University of New York,  
Stony Brook, NY 11794

The IAU Task Group on Outer Solar System Nomenclature met twice in 1980: in May at the Hawaii Colloquium (IAU 57) on the Satellites of Jupiter and in June at the COSPAR meetings in Budapest. Participating U.S. scientists supported by this grant were M. E. Davies, H. Masursky, T. Owen, and B. A. Smith. Other attending members were K. Aksnes (Norway), A. Brahic (France), and N. P. Erpylev (USSR). V. Teifel' (USSR) and M. Bobrov (USSR) were unfortunately unable to attend.

The following decisions were reached at these meetings:

- 1) Newly Discovered Satellites: Names shall be consistent with existing tradition in each case (e.g., giants and Titans for Saturn, Shakespearean characters for Uranus). No new names were approved pending refinement of orbits.
- 2) Longitude-Defining Features on Jovian Satellites: EUROPA-Cilix (Europa's brother): 182°long., +1°lat. GANYMEDE-Anat (Goddess of Dew (Assy.-Baby.)): 134°long., 0°lat. CALLISTO-Saga (Wife of Odin): 326° long., 0°lat. (No feature was selected for Io, since long-term survival is unlikely!)
- 3) Categories for Names of Surface Features on Jovian Satellites: Specific sources of names were defined for each type of feature on each satellite. This scheme is being used in the preparation of maps.
- 4) Categories for Names of Surface Features on Satellites of Saturn: We shall continue to draw names from the mythologies of various cultures, as we have done in the case of the Jovian satellites. Distinctly different myths and/or legends will be used for the different satellites.

Planetary Data at the National Space Science Data Center

Robert W. Vostreys, National Space Science Data Center, Code 601  
Goddard Space Flight Center, Greenbelt, Maryland 20771

The National Space Science Data Center/World Data Center A for Rockets and Satellites (NSSDC/WDC-A-R&S) is the repository for reduced data from planetary mission investigations. These data are available for additional studies beyond those conducted by the investigators and teams involved with each mission. Data are available to researchers throughout the world.

Pioneer Venus data are expected to be archived at the Data Center during the coming year. Plans for the nature and form of the data are now being developed.

Virtually all of the expected data for the Viking missions are available from NSSDC/WDC-A-R&S. An updated Catalog of Mission Data and Data User's Note (DUN) for the Orbiter Imaging are expected to be released in the near future. A portion of the Lander digital image data on magnetic tape have been archived and are available to interested researchers.

Voyager 1 and 2 Jupiter encounter imagery are available. Data submission plans for the other investigations have been received. In some cases these data are archived and ready for distribution.

For information on the availability of specific data sets from lunar and planetary missions, please consult the NSSDC Planetary Data Listing. It contains the spacecraft, experiment, and data set names. Included are the time period covered, form of the data, and quantity. This Data Listing is available here at the meeting.

FREQUENCY-ENCODED STORAGE OF DIGITAL IMAGE DATA ON VIDEODISKS.  
Bolef, L.K. and R.E. Arvidson, Dept. of Earth and Planetary Sciences,  
Washington University, St. Louis, Missouri 63130

Nearly a trillion bits of Viking data now exist. Comparable amounts of data may be returned during the Galileo and VOIR missions. The magnitude of these data sets create problems during data analysis, problems in addition to those associated with reproduction and dissemination of the information. For instance, only about  $3.7 \times 10^{18}$  bits of information can be stored on a single 2400' tape recorded at 1600 BPI. That equates to approximately 2700 tapes to store all Viking data. The sheer number of tapes present problems to users involved in topical analyses - problems with storage and with the time involved in finding and mounting the tapes. Comparable mass storage disk recorders using magnetic media are prohibitively expensive for most users. Digital storage using optically-read media are currently in prototype stages at a number of companies, although RCA, for instance, does not expect to have a commercially available read-only unit before 1985.

One way to solve problems caused by vast amounts of data is the storage of frequency-encoded digital data on videodisks that can be read with commercially available, and relatively cheap videodisk players. Such encoding schemes in relatively inefficient form are currently used on commercially available systems for storing digital data on videotape as part of a disk back-up capability. With the broad bandwidth typical of videodisk players (~12 MHz) a maximum recording rate of about 20 megabits/second is possible. With a playing time of  $\sim 7 \times 10^3$  seconds, we expect that about  $10^{11}$  bits of data can be recorded on one disk. Thus, only about 10 disks are needed to hold all the Viking data. The compression ratio (number tapes/number disks) is approximately 270:1. The expected storage density is about  $10^{18}$  bits/cm<sup>2</sup>, which favorably compares with  $\sim 10^{14}$  bits/cm<sup>2</sup> for tape and  $5 \times 10^{15}$  bits/cm<sup>2</sup> for magnetic disk media. The actual storage capacity for a single videodisk would depend on the frequency encoding scheme used, and on the data source characteristics supplying the recording device. The frequency encoded data could then be read back with a player and converted to a digital data stream through the use of relatively simple decoder electronics. We are currently attempting to have Viking Lander digital image data stored on a test disk.

VIKING ORBITER IMAGING MOSAIC CATALOG. Nancy Evans, Jet Propulsion Laboratory, California Institute of Technology, Pasadena, CA 91103.

This collection of nearly 500 Viking imaging mosaics was prepared and edited at Jet Propulsion Laboratory during the last two years of the Viking imaging operations. Published in two volumes, the set includes all "211-" designated mosaics distributed to NSSDC and the regional planetary imaging facilities between the numbers 211-4983 through 211-5788. Mosaics having numbers greater than 5788 will be contained in a third volume of several hundred mosaics and will be published at the completion of image reduction activities.

Mosaics contained in these volumes should be considered the correct or corrected version. Many errors in identification, orientation, and location were discovered in the preparation of this document. These have been corrected, and in all cases the original 211- number was retained to identify the mosaic. However, upon ordering a negative or enlargement you may discover that the entire lay out of the page has been altered. The Mark IV Listing for mosaics has been changed to reflect these corrections.

An introduction provides all of the information necessary for the use of the catalog. The format consists of a reference image of the mosaic and a footprint plot of that mosaic on facing pages. Each frame in the footprint has been identified by PICNO and the roll and file designation necessary to order the individual image from NSSDC. Ordering instructions have been included.

The Viking Orbiter Imaging Mosaic Catalog provides a handy and concise reference tool for using the Viking Orbiter imaging data set. As the mosaics are more or less chronologically arranged, the collection serves as an overview of the various imaging objectives throughout the many Viking Mission phases. The original of this publication has been used extensively at JPL throughout the preparation period to aid in the location of data for studies of surface features, terrain types, seasonal variations in the surface and atmosphere, and for viewing the same area from different aspects or altitudes. It has also been used to select illustrations for articles and books, slides for lectures, and coverage to be included in television specials. Copies will be distributed at the meeting if publication is completed.

This work is supported by NASA grant NAS7-100.

LOCATION AND PLOTTING OF HIGH RESOLUTION VIKING ORBITER IMAGE SEQUENCES.  
N. Evans, P. Scribner, Jet Propulsion Laboratory, California Institute  
of Technology, Pasadena, CA 91103.

A major task conducted during FY 1980 consisted of the location and plotting of the Viking Orbiter high resolution sequences. Due to timing errors, the result of orbit uncertainties, the near periapsis images were displaced from several to many degrees in latitude, longitude, or both in directions predictable within an individual load but erratic from load to load or from orbit determination to orbit determination. Images at these high resolutions; 7.5 to 25m per pixel, are interesting but scientifically non-useful unless relatable to structures on a grander scale.

A total of 220 events were identified as having been obtained from a slant range of 1000Km or less. All were then examined and those sequences which were badly degraded by atmospheric opacity, inadequate lighting, or smear were eliminated, leaving a total of 112 events from VO 1 and 84 events from VO 2. These sequences were mosaicked, sorted by MC sub-sub quad per USGS-Flagstaff definition, and stored.

The USGS map series at a scale of 1:2 million provided an ideal base for the foot-printing endeavor. As maps of this series were published, the high resolution sequences were plotted as a footprint on the base map. Later we were able to obtain interim mapping products (prior to their release for checking) and this speeded up our operation considerably. Some sequences were directly locatable using only the map products and the Viking images from which the maps were rendered. Other sequences required the use of images at a scale between the mapping resolution (150-250m per pixel) and the high resolution images (7.5-25m per pixel). Rarely, it was necessary to put a sequence aside, unlocated, to await the reduction of better mapping frames, location of intermediate resolution coverage of the area, another pair of eyes, or sometimes just another day. At the present time 58 sequences (69%) have been located and plotted at the 1:2 million scale.

Figure 1 reflects in terms of sub-sub quadrangle maps those areas in which the high resolution coverage has been located and plotted. Table 1 is a listing of each sequence which has been identified as high resolution and the sub-sub quad in which it has been located. Blank locations indicate sequences which are not yet plotted. Figure 2 is an inset of a high resolution sequence mosaic with the footprint plot of that coverage on a portion of the 1:2 million base map. Until the completion of the 1:2 million map series makes possible the final publication of this effort, we will gladly supply xerox copies of particular areas of coverage to experimenters, upon request. This work is supported by NASA grant NAS7-100.



TABLE 1. HIGH RESOLUTION VIKING SEQUENCES

360A31	MC-9,NW	768A21	MC-16,NE	405B01
691A41		768A41	MC-16,NE	406B01
695A01	MC-9,SW	769A01		407B43
697A31	MC-9,SE	771A41	MC-17,NW	408B01
697A61	MC-9,SE	772A01		409B01
699A31	MC-9,SE & NW	773A01	MC-17,NW	410B01
701A51	MC-10,SW	775A01	MC-18,SW	411B01
702A01	MC-10,SE	776A61	MC-18,NW & SE	411B41
705A01		778A01	MC-18, SE & MC-19,SW	412B41
706A01		779A		416B31
708A01		781A01		419B01
709A01		782A01	MC-19,NE	424B01
713A41		784A		425B01
717A51		786A41	MC-20,SE	427B71
718A01		789A21		428B01
719A01		790A01		429B01
720A21		791A01		430B01
721A01		794A01		432B31
724A01	MC-23,NW	795A01		433B01
725A01		796A01		442B21
727A21		797A51		444B21
728A51	MC-16,NW	800A51		445B01
729A75		801A51	MC-23,SE	446B01
730A01	MC-16, NE	803A01	MC-16,SW	446B21
730A51	MC-16,NE	804A63	MC-16,SW & SE	452B01
731A01	MC-17,NW	806A51	MC-16,SE	455B21
732A51		808A41	MC-17,SE	456B01
733A01	MC-9,SW	809A01	MC-16,SE	457B01
733A51	MC-17,NW	811A41	MC-18,SW	459B61
734A01	MC-9,SW	813A01	MC-18,SW	459B01
737A51		815A61	MC-18,SE	461B01
738A51		817A21	MC-19,SW	466B81
738A75		818A21	MC-26,NE	477B01
739A01	MC-18,NE	819A01		487B01
740A01	MC-10,SE	822A		488B01
741A31	MC-19,NW	824A		488B21
742A01		826A		494B01
742A51		826A51		499B01
743A01	MC-19,NW	829A		500B01
743A51	MC-19,NW	830A		524B01
744A41		831A41		525B01
745A01		834A		531B01
746A01		835A		531B21
746A51		837A		532B01
747A31	MC-20,NW	846A		538B01
748A01		867A		551B51
748A21	MC-20,NW	919A01	MC-20,SW	560B01
749A01		920A51	MC-20,SE	565B61
750A51		921A51	MC-20,SE	572B61
751A01		922A51	MC-20,SE	575B61
752A01		936A01	MC-20,SW	585B23
753A41		944A01	MC-20,SW	
754A01		960A01		
756A51		960A41	MC-16,NE & MC-17,SW	
758A01		364B31	MC-18,SE	
758A51		366B01		
759A11		367B01		
759A31		372B01		
760A01	MC-23,NW	380B71		
762A41	MC-23,NW	388B01		
763A01		392B01		
764A01		394B01		
765A41	MC-16,NW	401B01		
766A01		404B01		
767A01	MC-16,NE	403B31		

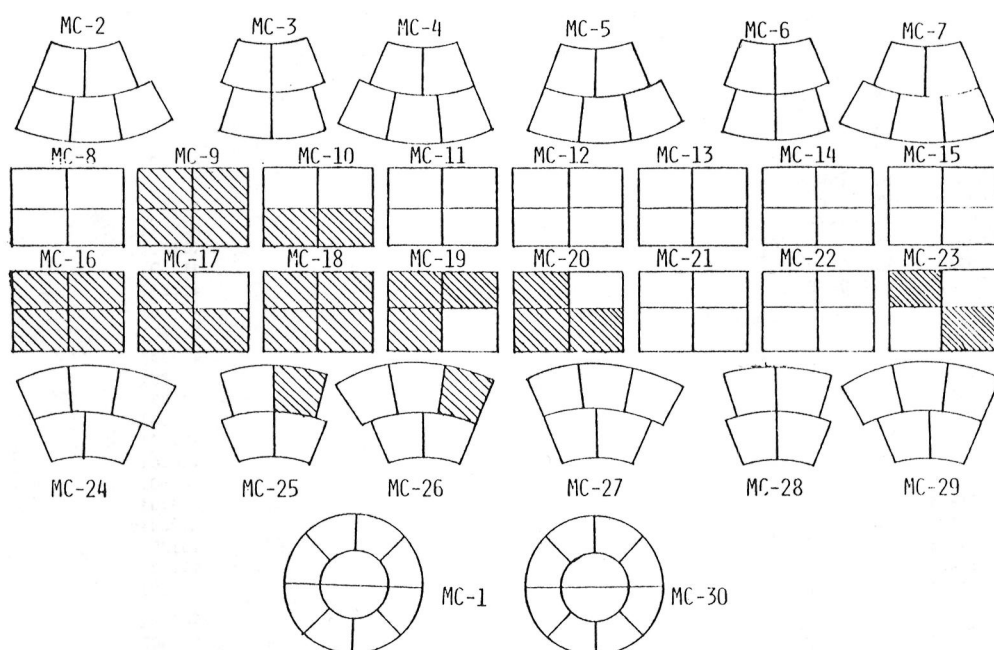


Figure 1. USGS 1:2 million map series sub-subquad layout. High-resolution footprinting is complete in cross-hatched areas.

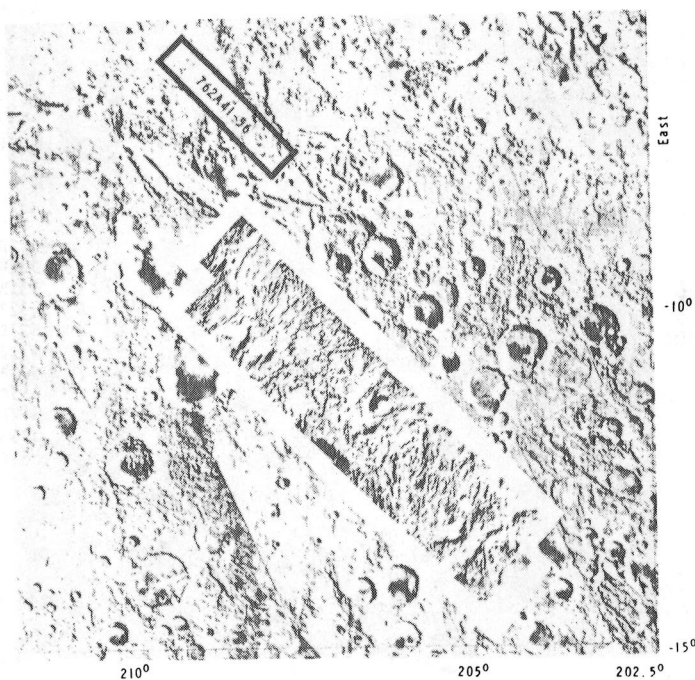


Figure 2. High-resolution sequence 624A41-56, inset and footprint, on MC-23NW.

VIKING ORBITER SURVEY MISSIONS I AND II; COVERAGE AND DATA REDUCTION.  
Nancy Evans, Jet Propulsion Laboratory, California Institute of Technology,  
Pasadena, CA 91103.

Two opportunities to obtain higher resolution mapping images (1600-2500) km slant range) were capitalized upon during the later operations of the Viking I Orbiter. The first, a period of roughly 50 days, extending through September and October of 1979 was Survey I; the second, Survey II, lasted for a period of 40 days from late May through early July of 1980.

Survey I contiguous coverage, Figure 1, began on revolution 1176 at a range of 1600 km and continued until revolution 1225. The slant range at this time was at 2500 km, the higher range of our resolution requirements. The resulting swath of mapping, some 100° in length and varying from 5° to 8° in width, covers the northern reaches of Arabia. Due to a fortuitous "windfall" through the MTIS/MTPS processing facilities, 80% of these data were processed in the shading-corrected, rectilinear version, and perhaps 20% of those were processed in the orthographically projected version. Errors in the SEDR and reduced processing opportunities severely hampered this effort. Table I indicates the processing states of these data.

Survey II, Figure 2, began on revolution 1427 at a range of approximately 2500 km and continued through revolution 1467 at 1000 km slant range. Sequences included four basic blocks of coverage: Al Quahira, Ma'adim, Memmonia, and Mangala. Later blocks were added at increasingly higher resolutions which continued, northward, up the Mangala Vallis toward Olympus Mons. Of these sequences, the Mangala Block, revolutions 1448-1453, has been processed, and only in the shading corrected, rectilinear version. Two sequences of the Ma'adim block, 1434 and 1435, have been similarly processed. This reflects approximately 10% of the total Survey II coverage.

Prior to the Survey II Mission, revolutions 1406 through 1426, a block of stereographic coverage was obtained extending eastward from Hellas Planitia, as shown in Figure 3. Very little of this data, perhaps 12 frames have been reduced.

At the time of this writing all SEDR data for the later missions (after revolution 1122) have been examined, corrected, and checked to assure the integrity of the pointing information. This insures the eventual production of orthographic projections for all of this data as well as the mapping data obtained between Survey I and Survey II. Some 13,000 frames of Viking I Orbiter data remain to be processed. The present plan is to continue the data processing effort over a period of four years. It is hoped that a more finalized schedule of production can be established prior to the meeting in January.

Work on these data has been supported through NASA grant NAS7-100.

TABLE I

	SCR	NGF		SCR	NGF		SCR	NGF
1176S01-24	x		193	x	x	210		
177	x	x	194	x	x	211		
178	x		195	x	x	212		
179	x		196	x	x	213	x	
180	x		197	x		214		
181	x		198	x		215		
182	x		199	x		216		
183	x		200	x		218	x	x
184	x		201	x		219		
185	x		202	x	x	220		
186	x		203	x	x	221		
187	x		204	x	x	222		
188	x		205	x	x	223		
189	x	x	206	x	x	224S41-64		
190	x	x	207	x	x	225S01-24		
191	x	x	208	x	x			
192	x	x	209	x				

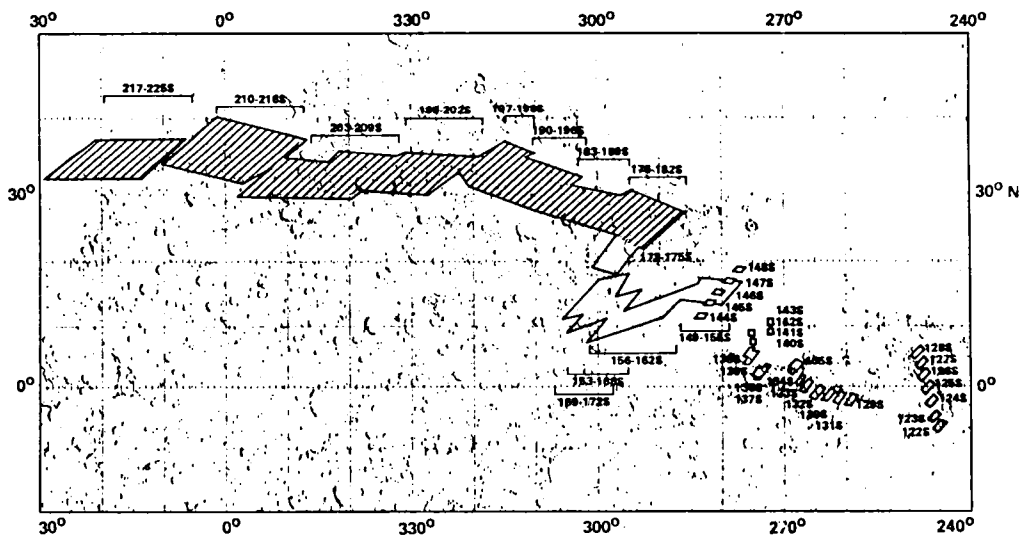


Figure 1. High-resolution contiguous mapping coverage obtained during the Survey I Mission is indicated on this plot of total coverage by shading.

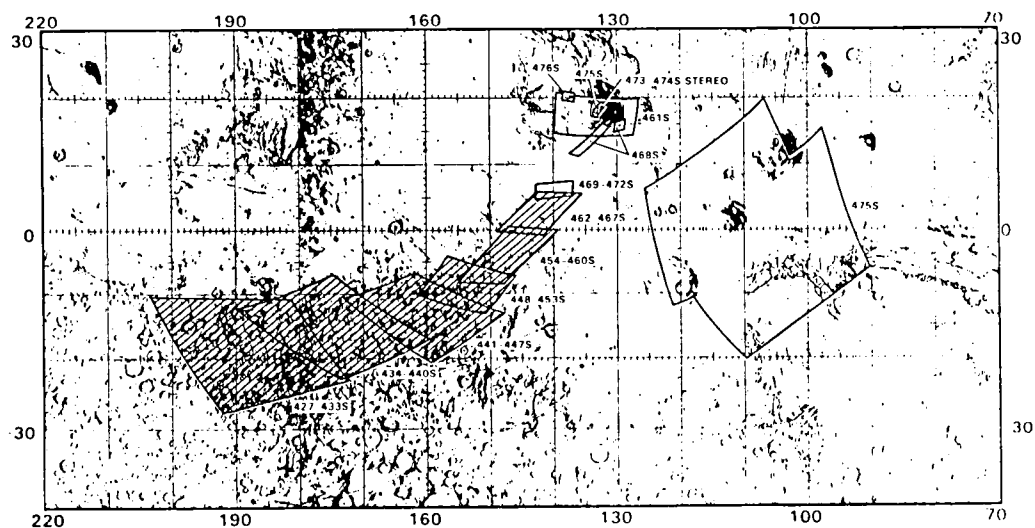


Figure 2. The Survey II high resolution contiguous mapping coverage is indicated in this plot of later mission sequences by shading.

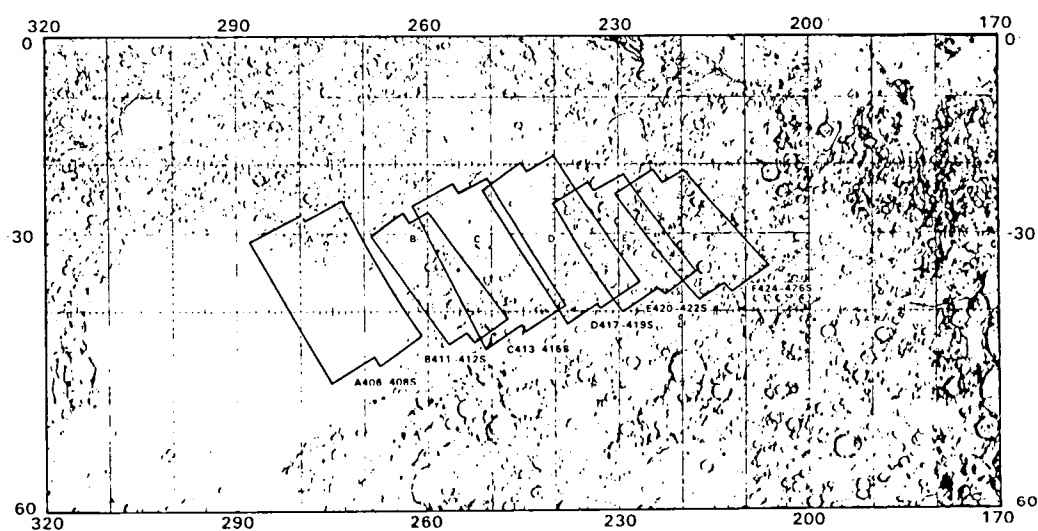


Figure 3. This block of stereographic coverage was obtained to the east of Hellas Planitia prior to the beginning of Survey II.

## THE SECOND MARS CHANNEL WORKSHOP: A REPORT.

Victor R. Baker, Dept. of Geological Sciences, University of Texas at Austin, Austin TX 78712.

Dag Nummedal, Dept. of Geology, Louisiana State University, Baton Rouge, Louisiana 70803

Elongate depressions on Mars have been classified in three major categories: channels, valleys and troughs.

Channels are large, elongate, erosional features containing a suite of bedforms indicative of large scale fluid flow.

Examples of channels include Ares and Maja Valles.

Valleys are elongate troughs, or systems of troughs indicative of erosion by fluid flow, but without a bedform suite to establish a more precise characterisation of the erosive event.

Two categories of valleys have been identified: trunk valleys and valley networks. Trunk valleys have one (or a few) dominant troughs with small tributaries. Examples of this valley type would be Nirgal and Nanedi Valles. Valley networks have more completely developed tributary systems. Examples would include the many valley networks in Thaumasia and Margaritifer Sinus.

Troughs are elongate topographic depressions with no indications of erosion by fluid flow.

Water is identified as a necessary ingredient in the primary formation of both channels and valleys. However, at the scale of resolution at which features can be seen on Mars, flows as diverse as glaciers and catastrophic floods produce similarly appearing features. Although some processes can be ruled out as of major importance in the primary erosion of the channels, this similarity of large scale features has prevented complete agreement on channel origin.

Channels appear to have formed by relatively high discharges over short periods of time. The diagnostic evidence for this includes the great lengths and widths of the channels, their low sinuosity, streamlined islands and grooves. The morphological evidence also strongly suggests multiple erosional events in each channel. Groundwater release with ensuing surface collapse and headwards channel growth has played an important role in channel formation. Therefore, the volume of a channel is not a measure of the amount of material removed by a through-flowing fluid. Neither does the channel cross-section bear any direct relationship to the cross-sectional area of any instantaneous flow. Water released by upstream collapse has repeatedly sculpted older channel flow features further downstream. All channels have been subject to extensive secondary modification operating over time spans of many hundred million years.

These processes include mantling with lava flows and sedimentary deposits as well as eolian removal of selected materials. Mass movement, probably aided by water, played an important role in long-term landscape degradation.

The dominant process of valley formation appears to have been headward erosion by sapping as indicated by the ubiquitous existence of theatre-headed tributaries. The overall graded appearance of most valley networks suggests that water was an important agent in removal of material mobilized by the sapping process. Other agents of sediment removal may have been dominant in local areas.

The evidence presented in this summary suggests that groundwater played a dominant role in the evolution of the martian landscape. This groundwater appears to have been released from a planet-wide reservoir in the regolith. Recharge of this reservoir must have required atmospheric pressure and temperature conditions sufficient to induce precipitation. Primary formation of channels appears to have occurred throughout a large part of martian geologic history. Many channels are incised into heavily cratered terrain. Valleys are ubiquitous in this unit. Some channels are also incised into the Lunae Planum surface, and some intercrater plains units are incised by channels as well as valley networks. Channels are clearly older than cross-cutting geologic units, some of which include some Chryse Planitia lava flows.

This summary represents a consensus reached by the participants at the second Mars Channel Workshop, held at Flagstaff, Arizona, Sept. 29 through Oct. 1, 1980.

Participants were: Victor Baker, Jon Boothroyd, Jim Cutts, Paul Komar, Julie Laity, Baerbel Lucchitta, Mike Malin, Harold Masursky, Dag Nummedal, Dave Pieri and Dave Thompson.

## PLANETARY GEOLOGY ACTIVITIES AND DEVELOPMENTS IN FRANCE

Masson, Ph., Mercier, J. L., Laboratoire de Géologie Dynamique Interne (ERA n° 804-02), Université Paris-Sud, 91 405 Orsay, France

The Laboratoire de Géologie Dynamique Interne (LGDI) of the Université Paris-Sud (UPS) at Orsay began to get involved in the NASA Planetary Geology Program in 1974. At that time a research program of comparative planetary tectonics (Earth and Mars) was initiated at UPS-Orsay after a scientific visit of one of its members at the USGS-Branch of Astrogeologic Studies, Flagstaff, Az. Since that date, the LGDI Planetology Group increased, developed its activities, cooperated to the organization of the European Planetary Geology Consortium (EPGC), and organized a Planetary Data Library at UPS-Orsay.

Due to the organization of the Planetary Data Library, several french scientific groups or individuals decided to initiate comparative planetology research programs in cooperation with the LGDI Planetology Group, in the geologic and geomorphic fields. The Planetary Data Library is managed by a librarian under the responsibility of a NASA PGPI. The library contains about 43 000 images (negative and positive films, paper prints, microfiches) of Mars (Mariner 9 and Viking missions), Mercury (Mariner 10), Jupiter and its satellites (Voyager), plus complete sets of the already published maps (topographic, shaded relief, geologic) of the Moon, Mars, Mercury and the Galilean Satellites. The library offers several facilities for in situ image retrieval or analysis, as microfiche reader, light table, image analyzer, and dark room. The Planetary Data library is connected to an Image Processing Facility (Centre de Dépouillement et de synthèse des Images, Institut d'Optique) also located at Orsay, for image computerized processes and color video enhancements. The library contains also a wide collection of earth satellite images (Landsat and Skylab) for terrestrial comparisons with planetary surfaces (meteorite craters and large tectonic features). These images are available under different formats : negative and positive films, paper prints). A multispectral viewer is available for false colour compositions, enlargements and reproductions of the Landsat MSS images. The data available at the LGDI Planetary Data Library are provided by the World Data Center A for Rockets and Satellites (NASA Goddard Space Flight Center, Greenbelt, Md.) and the Planetary Data Facility of the USGS Branch of Astrogeologic Studies (Flagstaff, Az.) under the auspices of NASA Office of Space Science, Planetary Division (Washington, D. C.), and by the USGS-EROS Data Center (Sioux Falls, S. D.). The library organization and its technology developments are supported by grants provided by the Institut National d'Astronomie et de Géophysique (INAG, Paris, France) and the Centre National d'Etudes Spatiales (CNES, Paris, France).



The research programs developed or under developments at Orsay or in cooperation with the LGDI Planetology Group, are mainly conducted in the framework of the NASA Mars Data Analysis Program (MDAP) and the Jupiter Data Analysis Program (JDAP). At the moment, three main groups of studies are conducted :

- structural analysis of Mars and Mercury,
- studies of erosional landforms and processes on Mars,
- theoretical studies and laboratory simulations of ice fracturation on Ganymede.

On Mars, the structural analysis of lineaments and tectonic features are under completion at LGDI and the Institut de Physique du Globe de Paris (2 Ph.D in preparation). These studies aim to relate the tectonic features observed on the surface of Mars to the internal structure of the planet and to its structural evolution (1).

On Mercury, a general study of tectonic and volcanic features is under completion at LGDI (1 PhD under completion). This study interprets the different stages of the early evolution of this planet, and shows the significance of Caloris basin formation on the structural evolution of Mercury. Based on this study an estimation of the crust thickness is attempted (2).

Erosional landforms and processes on Mars, are under study. Comparative studies of eolian processes with terrestrial analogs and wind tunnel experiments are developed by the Laboratoire de Géographie Physique Zonale at the Université de Reims (2 PhD in preparation) (3). Geomorphic studies of channels and fluvial-like features are under completion at the Institut de Géographie et d'Aménagement Régional, Université de Nantes (3 MS under completion) (4).

Theoretical studies and laboratory simulation of ice fracturation are initiated at the Institut de Physique du Globe de Paris and at LGDI, in order to understand the grooved and faulted pattern observed on Ganymede .

In addition to these research programs, the LGDI Planetology group and the Planetary Data Library contributed this year to :

- . the organization of a public exhibit devoted to Astrophysic and Planetology (this exhibit which took place during one week at UPS-Orsay was visited by more than 3000 participants, mainly under graduate students) ;
- . the coordination of a european working group on Mars surface Exploration Program, sponsored by the European Space Agency (ESA) (5).

## References

- (1) Fernandez-Chicarro, A., Masson, Ph. - A possible origin of the ridged plains of Mars (this issue).
- (2) Thomas, P., Carey, E., Fleitout, L., Masson, Ph. - Large tectonic effects of Caloris impact on Mercury (this issue).
- (3) Mainguet, M., Bordes, J. M., Cossus, L., Masson, Ph. - Dynamical signification of different types of dunes in the sandseas around the North polar ice cap of Mars : comparison with terrestrial analogs (this issue).
- (4) Bodard, J., Pernet, E., Rogeon, P., Bousquet, B., Masson, Ph. - Preliminary geomorphic interpretation of the Valles Marineris, Kasei Valles and Noctis Labyrinthus regions of Mars (this issue).
- (5) Blamont, J., Borderies, N., Coradini, M., Dubois, J., Fulchignoni, M., Guest, J. E., Hiller, K., Lopes, R., Masson, Ph., Wänke, H. - Mars Ball Project - Preliminary Scientific Report, ESA, Paris, Mars-June 1980.

## LATE ABSTRACTS



THE ORIGIN OF MARE RIDGES: Sharpton, V. L. and Head, J. W.,  
Dept. of Geological Sciences, Brown University, Providence, RI 02912.

Introduction: A decade of post-Apollo analysis has advanced the understanding of lunar mare ridges and yet has not fully resolved the long standing dilemma of whether these features are of volcanic or tectonic origin. Table I summarizes the various lines of evidence presented in support of the volcanic and tectonic models. An analysis of these data was undertaken following the results of recent investigations of small scale features associated with mare ridges (Sharpton and Head, 1980).

Discussion: The first part of Table I lists factors suggesting volcanic involvement in mare ridge formation. Since none of this evidence precludes a tectonic origin for mare ridges we will examine several points in detail to determine what the relative significance of these factors should be in theories of ridge formation.

(1) The results of Sharpton and Head (1980) suggest that the manner in which the 'flow-like' lobes of lunar mare ridges modify small adjacent impact craters, is inconsistent with any type of lateral transport including volcanism or mass wasting. Instead these mare ridge lobes appear to be material that has been structurally uplifted along nearly vertical fractures associated with previous impact-induced brecciation. Thus a major argument for the volcanic model (V-1, Table I) now appears more consistent with a tectonic origin.

(2) The ropy, braided or overlapping patterns mare ridges exhibit in plan view are suggestive of the influence of volcanic processes (V-2). However, detailed mapping strongly suggests that this extrusive-like appearance is due to a combination of: 1) the presence of the lobate features discussed above, and 2) the complex patterns formed by the arrangement of mare ridge segments within linear zones where mare ridge formation is concentrated. These zones of concentrated mare ridge development could be zones of weakness where stresses associated with regional tectonism might be concentrated. The close association of these zones with flooded pre-mare topography such as basin rings and crater rims (T-7) suggests that zones of weakness occur in areas where the basaltic fill is relatively thin; 3) deformation within the locally thinned basaltic layer could be transmitted to the surface through displacements along the network of fractures induced by impact bombardment thus producing the complex patterns characteristic of mare ridge systems. Faults associated with these zones of weakness might then be surficially expressed along the pre-existing network of fractures induced by impact bombardment thereby resulting in the ropy, braided or overlapping patterns characteristically manifested by mare ridge systems.

(3) The occasional association of mare ridges and the source depressions of volcanic sinuous rilles does not require a genetic relationship between the two. The ascent of magma occurs preferentially along zones of weakness or fracture in planetary crusts. Tectonic deformation is also associated with such zones. There is abundant evidence for mare ridge formation postdating most sinuous rilles (Young et al., 1973). Thus, a more plausible explanation for this occasional association is simply the well-established, but non-genetic, correlation in space of tectonic and volcanic features.

(4) The association of positive gravity anomalies over some mare ridges (V-4) is interpretive. Scott (1974) identified extended linear gravity anomalies, both positive and negative, in Oceanus Procellarum. These anomalies, which trend NW-SE, roughly parallel major systems of mare ridges in the area. The interpretation that these data suggest that mare ridges "are the surface expressions of deep-seated systems of basaltic dikes" (Scott, 1974) is based on shifting the observed anomalies westward as much as 100 km "to produce a

better correspondence, in places, between the positive gravity trends and some of the larger or more dense clusters of mare ridges" (Scott, 1974). The fact that mare ridges in this area (and elsewhere) are confined to mare basalt units and do not modify the frequent 'islands' of highland-type material disfavor the hypothesis that mare ridges are related to "basaltic dikes which have intruded fractures and faults in less dense crustal rocks" (Scott, 1974). An alternate explanation suggests that the elongate gravity anomalies represent regional variations in the thickness of the mare fill due to subsurface topography. To test this model, the gravity map of Oceanus Procellarum (Scott, 1974) was compared to the isopach map of the western mare basins developed by DeHon (1980). Results show that zones where the maximum basalt thickness exceeds 1 km can be connected to form NW-SE trends which correlate favorably with the observed positive gravity anomalies. The negative gravity anomalies are observed in areas where basalts are thinner. These results appear to strengthen the hypothesis that the elongate gravity characteristics of Oceanus Procellarum are being primarily influenced by thickness variations of the basalt fill. These thickness variations also determine the local strength of the mare layer and therefore assert a control over the location of mare ridge systems. This results in a general parallelism between the basalt fill, the trends of major mare ridge systems and observed gravity anomalies.

(5) The broad arch often associated with mare ridges has suggested to some investigators the presence of a shallow laccolithic-type intrusion (V-5). The associated mare ridges would then be viscous extrusions of laccolithic material out of extensional fractures along the crest of the arch. However the morphology of the broad arch appears inconsistent with this model in several ways: 1) mare arches often follow regional topographic trends (T-12) implying that the arches, like the variations in regional topography (T-1), result from tectonic deformation; 2) ridges and arches often occur separately and when found together the ridge segments may not trend parallel to the arch, rather they may crisscross along the arch or run beside instead of on the arch (Hodges, 1973; Lucchitta, 1977) suggesting only an indirect relation between the two features, and; 3) there is often a significant topographic variation on opposite sides of the arch implying a tectonic rather than volcanic origin for these features (T-5).

(6) The auto-intrusive or 'squeeze-up' hypothesis (V-6) is somewhat similar to the laccolithic model above. Here the morphology of mare ridges (disregarding monumental differences in scale) has been compared to small-scale features associated with the solidification of terrestrial lava lakes. As the upper portion solidifies it tends to fracture and sink, squeezing partially solidified material up from below and creating small linear welts on the surface of the lava lake. However, in addition to the obvious difficulties with scale differences, several observations seem to discount the applicability of this analogy: 1) the presence of boulder patches on mare ridges plus the modification of very fresh appearing impact craters by mare ridges - if mare ridges are squeeze-up features they should all be coated with the same dark powdery regolith that mantles the mare surface and fresh appearing craters should not show ridge-like modification, and; 2) ridges are observed crossing distinct volcanic unit boundaries (T-2).

Analysis of the lines of evidence supporting a tectonic origin for mare ridges reveals two independent observations that apparently preclude the possibility that mare ridges are predominantly volcanic in origin. The first is the investigation revealing that the lobate or ropy extensions ubiquitous to mare ridges modify adjacent features in a manner that is inconsistent with volcanic emplacement (Sharpton and Head, 1980). The second is an expansion on the observation that mare ridges cross known volcanic unit boundaries.

Apollo photograph AS17-2313 (P) shows a ridge which crosses distinct volcanic unit boundaries in Southeastern Mare Serenitatis. For this observation to be consistent with volcanic emplacement of the ridge, the volcanic event forming the ridge must be younger than the mare units it crosses. However the ridge segment that modifies the light mare unit to the west is itself light and distinct, but when the ridge crosses into the dark eastern unit it assumes the same dark, subdued nature as that unit. Also vidicon images of Mare Serenitatis (Johnson *et al.*, 1975) show that mare ridges have the same spectral character as the mare units they modify - even through the spectral character of various mare units are distinctly different. Thus the surface character, albedo, and spectral character of mare ridges imply they are fundamentally related to the individual mare units in which they occur but because mare ridges cross stratigraphic boundaries they must be unrelated to the emplacement of these mare units. The volcanic model appears unable to resolve this dilemma; however these observations are consistent with the tectonic model for the origin of mare ridges.

**Conclusion:** Although lunar mare ridges possess various morphological characteristics which might suggest an origin through volcanic processes, compilation and analysis of the observations in Table I reveal serious inconsistencies with the volcanic model. Results of this analysis clearly support the alternative model that mare ridges and their characteristic morphology are the expressions on the mare surface of tectonic deformation within the lithosphere and that associated volcanic features are of minor importance and unrelated to the basic genesis of mare ridge structures.

TABLE I

ORIGIN	EVIDENCE
Volcanic (V)	<ol style="list-style-type: none"> <li>(1) Ridges modify adjacent craters by a flow-like mechanism (1-5).</li> <li>(2) Braided, discontinuous, overlapping or ropy patterns suggest extrusive origin (1,3,5).</li> <li>(3) Some ridges are associated with sinuous rilles and other volcanic landforms (1,4).</li> <li>(4) Ridges are sometimes associated with positive gravity anomalies suggesting basalt extrusion from dikes (6).</li> <li>(5) Broad arch suggests possibility of shallow laccolithic-type intrusions (1).</li> <li>(6) Ridges show similarities to "squeeze-up" features associated with the cooling of terrestrial lava lakes (3).</li> </ol>
Tectonic (T)	<ol style="list-style-type: none"> <li>(1) The maria have undergone tectonic modification as evidenced by large topographic variations on the present surface (7).</li> <li>(2) Ridges cross volcanic unit boundaries (4,8-10).</li> <li>(3) Several ridges extend into adjacent highlands (4,11).</li> <li>(4) Some ridges continue as fault scarps (4,9,11).</li> <li>(5) Measurable elevation difference in terrain on opposite sides of many ridges strongly suggests vertical offset (13).</li> <li>(6) Latest ridge formation postdates the last regional volcanic episode as evidenced by crater deformation (9,11,14,15).</li> <li>(7) Ridges are often associated with pre-mare buried topography (3,16-18).</li> <li>(8) Ridges sometimes deform post-mare craters as evidenced by crater shortening (2,9).</li> <li>(9) Close correlation exists between ridge location and changes in basalt thickness where stresses might be localized (13,16,18,19).</li> <li>(10) Regional trends of mare ridges are consistent with global fracture patterns (16,20,21).</li> <li>(11) Circular basin trends are consistent with deformation due to loading (18,21).</li> <li>(12) Local ridge trends may parallel the strike of regional slope (13).</li> </ol>

References: (1) Strom RG (1972) *The Moon* 47, 187; (2) Howard KA *et al.* (1973) NASA SP 330, 3-22; (3) Hodges CA (1973) NASA SP 330, 31-12; (4) Young RA *et al.* (1973) NASA SP 330, 31-1; (5) Scott DH (1973) NASA SP 330, 31-25; (6) Scott DH (1974) *PLSC* 5, 3025; (7) Scott DH *et al.* (1978) *PLPSC* 9, 3527; (8) Howard KA *et al.* (1973) NASA SP 330, 29-1; (9) Lucchitta BK (1975) *PLSC* 5, 2761; (10) El-Baz F (1978) *In Apollo Over the Moon*, NASA SP 362, 89; (11) Wolfe EW *et al.* (1972) *Geotimes* 17, 11, 14; (12) Colton GW (1978) *In Apollo Over the Moon*, NASA SP 362, 94; (13) Lucchitta BK (1977) *PLSC* 8, 2691; (14) Muehlberger WR (1974) *PLSC* 5, 101; (15) Howard KA (1978) *In Apollo Over the Moon*, NASA SP 362, 88; (16) Maxwell TA *et al.* (1975) *GSA Bull.* 86, 1273; (17) Peeples WJ *et al.* (1978) *JGR* 83, 3459; (18) Maxwell TA (1978) *PLPSC* 9, 3541; (19) DeHon RA *et al.* (1976) *PLSC* 7, 2729; (20) Raftala J (1978) *The Moon and Planets* 19, 457; (21) Solomon SC and Head JW (1979) *JGR* 84, 1667; (22) Fagin SW *et al.* (1978) *PLPSC* 9, 3473; (23) Bryan WB (1973) *PLPSC* 9, 93.

Text References: De Hon RA (1980) *Lun. Planet. Sci.* XI (Abst), 229; Hodges CA (1973) NASA SP 330, 31-12; Johnson TV *et al.* (1975) *PLSC* 6, 2677; Lucchitta BK (1977) *PLSC* 8, 2691; Scott DH *et al.* (1974) *PLSC* 5, 3025; Sharpton VL and Head JW (1980) *Lun. Planet. Sci.* XI (Abst), 1024; Young RA *et al.* (1973) NASA SP 330, 31-1.

## CHEMICAL WEATHERING IN THE DRY VALLEYS OF ANTARCTICA: PRELIMINARY RESULTS OF A SEM STUDY

D. S. McKay, SN6, NASA Johnson Space Center, Houston, TX 77058  
D. Prestell, Lockheed, NASA Johnson Space Center, Houston, TX 77058

### INTRODUCTION

Workers at JSC have begun a program of studying a set of samples collected in the Dry Valleys of Antarctica by E. K. Gibson during the field season of 1979-80 (1,2). The major purpose of this investigation is to understand some important regolith processes involving chemical weathering, mineral formation, and transport of material in a cold dry region containing ice and permafrost. Increased understanding of these regolith processes may give us insight into similar processes which might be operating on Mars.

### APPROACH

Samples used in our preliminary study are from a soil pit near Lake Vanda in Wright Valley. These samples have been previously analyzed for water content, and various water soluble species by E. Gibson and Co-workers (2). Using the Scanning Electron Microscope (SEM) with energy dispersive X-ray analyzer, we examined quartz grains from three different depths in the soil pit: sample WV 219 from the upper 2 cm, sample WV 238 from a horizon described as salt-rich (2) and sample WV 221 from the depth interval of 44-48 cm. We have initially concentrated on quartz sand grains in order to compare their surfaces with quartz grains from the desert sands of Egypt which we have found to be covered with a thin coating of complex mineralogy (3).

### RESULTS

In each of the Wright Valley samples investigated, the quartz grains had adhering coatings of variable thickness and complex mineralogy. The coating material was firmly enough attached that it was not dislodged by ultrasonic cleaning in liquid Freon.

We found that the quartz grains from WV 238 (the salt-rich horizon) contains abundant adhering NaCl (halite) present as both intergrown euhedral crystalline masses and as anhedral irregular mounds (Fig. 1). This halite is intergrown with small fragments of plagioclase, unidentified clay minerals, and small (micron-size) euhedral crystals of a sulfate mineral.

Other minerals found on the surface of the quartz grains include gypsum (or anhydrite) and platy mineral fragments containing (in addition to Si) Al, Mg, Na, and K. These minerals appear to be clays, probably smectite, but positive identification must await X-ray or electron diffraction work. Some areas of the quartz grains contain abundant small (0.1-1 micrometer) euhedral to sub-hedral crystals containing Na, Mg, and S. This mineral is tentatively identified as bloedite.



Quartz grains from the uppermost sample (WV 219) are similar but tend to be less covered with adhering coating minerals. Euhedral calcite is present on some quartz surfaces (Fig. 2). Some surfaces are fresh appearing with sharp conchoidal fractures suggesting relatively recent fracturing. The uppermost soils may be subject to considerable mechanical reworking, primarily by wind (2).

Quartz grains from the lowermost sample (WV 221) are relative free of halite, corresponding to the much lower content of soluble Cl (2). These quartz grains contain partial coatings which closely resemble the clay-rich coatings found on the Egyptian sand grains. For sample WV 221 these coatings contain (in addition to Si) Al, Mg, Fe, K, Ca, and Na in approximately that order of abundance. This chemistry is suggestive of montmorillonite. The most striking feature seen on these quartz grains is the presence of small euhedral crystals of K-feldspar. These crystals (Fig. 3, 4) are very fresh and appear to have grown in-situ on the surface of the quartz grains. They are well crystallized and show no sign of fracturing and abrasion. They overlie a coating of fine grained material but also may have some adhering coating (Fig. 4). These crystals apparently are authigenic and not detrital. The presence of authigenic feldspar,  $\text{CaCO}_3$ , halite, gypsum, and other sulfates in this soil profile, along with the chemical data (2), reinforces the interpretation that significant chemical weathering is taking place with attendant mobility of many chemical species. An understanding of such weathering in Antarctica may lead to a better understanding of the Viking results from Mars.

#### REFERENCES:

- (1) E. Gibson (this volume);
- (2) E. Gibson, B. Ransom and R. Ingraham (this volume);
- (3) D. McKay, J. Constantopoulos, D. Prestel and F. El-Baz (this volume).

(Figures on next page)

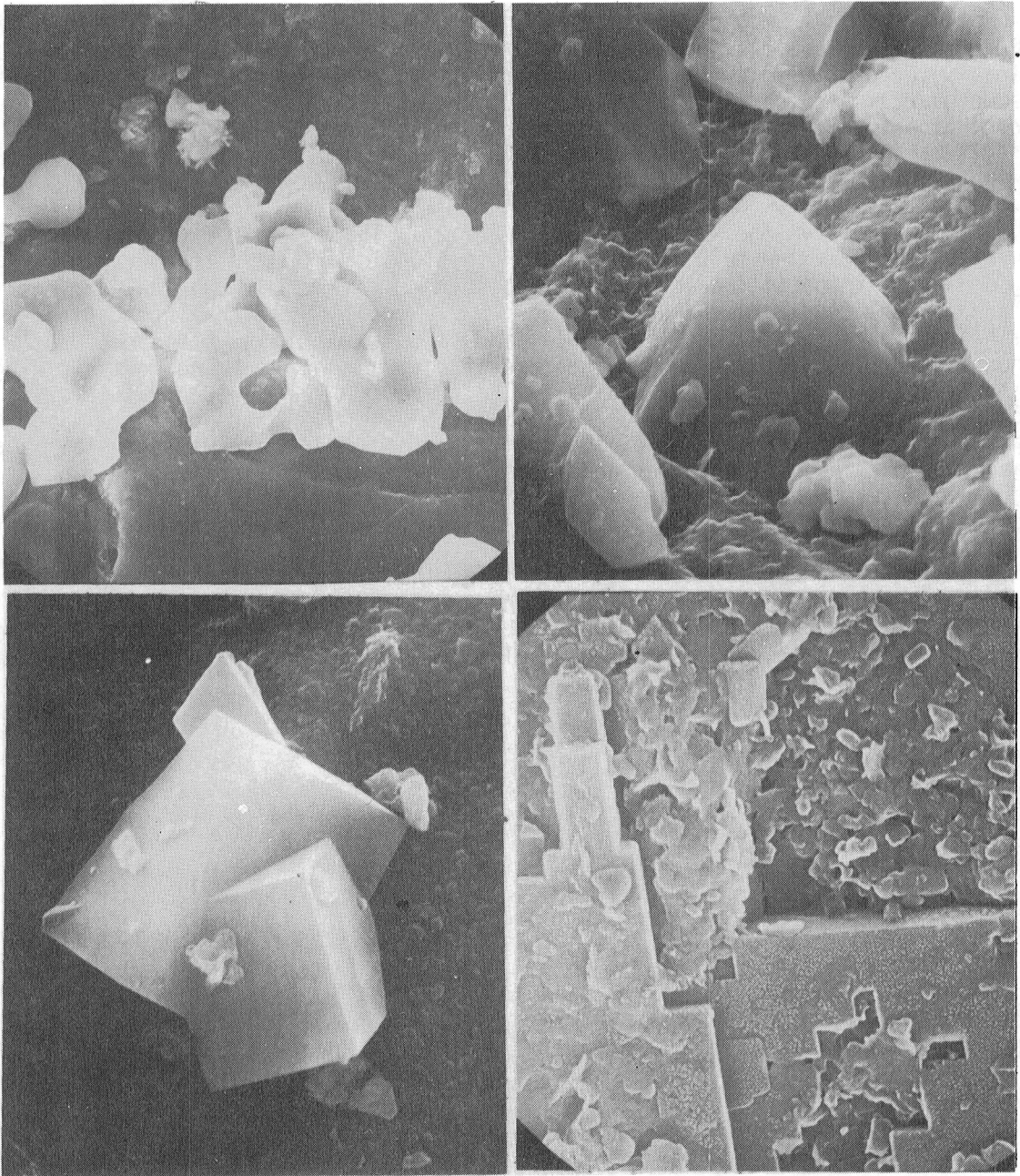


Fig. 1. (top left) Irregular mounds of halite on the surface of quartz sand grains. Width of field = 100 micrometers.

Fig. 2. (top right) Calcite crystals growing on surface of quartz grain. Width of field = 10 micrometers.

Fig. 3. (bottom left) Authigenic K-feldspar twinned crystals growing on surface of quartz grain. Width of field = 10 micrometers.

Fig. 4. (bottom right) Closeup of surface of another authigenic K-feldspar showing growth steps. Width of field = 3 micrometers.

#### CRATERING RECORDS OF GANYMEDE AND CALLISTO.

Robert G. Strom, Alex Woronow and Michael C. Gurnis, Lunar and Planetary Laboratory, University of Arizona, Tucson, Arizona 85721

The crater populations of Ganymede and Callisto are markedly different from those on the terrestrial planets. The surface of Callisto is dominated by impact craters as large as 600 km in diameter. No extensive areas of smooth plains or other types of non-impact related topography have been seen. The craters on Ganymede appear to have a larger spectrum of morphological characteristics than those on Callisto. This is probably due in part to the higher resolution coverage ( $\sim 1$  km/lp) and in part to the more complex surface history of Ganymede. In general Ganymede's craters show a range of freshness from sharp rimmed with rays and well developed ejecta blankets to very low-rimmed, flat-floored with no discernable ejecta deposits. There appears to be an abundance of central pits, but central peaks are also common.

Because of uncertainties in such fundamental parameters as the source and composition of the impacting bodies, the reaction of icy targets to hypervelocity impacts, and the diversity and vigor of crater degradation and removal processes, the interpretations presented here must be considered preliminary. Many of the uncertainties are currently under investigation and the result of those investigations will provide feedback to analyses such as these.

Several striking features are immediately apparent in the crater curves of Ganymede and Callisto (Figure 1). The size-density curves for the heavily cratered terrains on Ganymede and Callisto differ markedly in both shape and crater density. Being deeper in Jupiter's gravity field, Ganymede should have experienced about twice the impact-flux rate of Callisto (Smith, et al., 1979). However, the most heavily cratered and therefore oldest terrain on Ganymede is actually less densely cratered than the most cratered terrain on Callisto. Although the two curves nearly parallel between about 50 and 130 km diameter, at smaller diameters considerable differences occur. Finally, neither of the crater populations on Ganymede or Callisto resembles those encountered on the terrestrial planets.

Figures 1 through 3 show that four different crater curves, representing vastly different crater densities, on different terrains and even different satellites all possess the same steep-slope ( $\sim 4.7$ ) distribution function at large diameters. If the paucity of craters in that diameter range was solely due to obliteration by relaxation, then one would expect a very different distribution function between, for example, the fresh craters preserved over long time periods in rigid ice, and the degraded craters perhaps formed at a time when the ice was more able to flow. Therefore the observed large variations in crater densities, but similarities in slope among the many different terrains, ages, degradational classes, and even satellites, argue against this curve in this diameter range being shaped by equilibrium. Therefore, the production function in the Jupiter region was vastly different from that in the inner Solar System.

We do not believe that these curves truly represent attainment of equilibrium, but even if we accept such a conclusion, we can still make strong arguments that the crater production function recorded on the Galilean satellites was not the same one recorded in the inner Solar System as follows: adjust the total crater flux at Callisto so that the minimum amount of crater obliteration would be required in order to ultimately evolve the observed Callisto curve from the lunar highlands' production function by assuming that no craters in the 8 to 11 km diameter range were obliterated on Callisto and none were obliterated at any diameter on the lunar highlands. If, for each diameter bin, we now calculate the percentage of all craters which would have to be obliterated in order to evolve the Callisto curve, we obtain the solid line in Figure 4. The other curves are for varying degrees of crater enlargement. Such a calculation is conservative not only because it assumes that no 8 km craters were obliterated, but also because it assumes that craters on the Moon and Callisto follow the same scaling relationship. If, as Boyce (1979) has suggested, craters in ice will be larger than their equivalents formed in rocky substrates, then the degree of obliteration required to develop the observed Callisto curve from that of the Moon is also greater. The dotted and dashed lines in Figure 18 show cases for enlargement factors of 1.4x and 2x for craters on Callisto. The most conservative case requires that more than 90% of all craters larger than 80 km diameter would have to have been obliterated by relaxation. This is far more obliteration than is consistent with the appearance of the surface. If so many of these large impact structures and their ejecta deposits were totally obliterated by relaxation, some would still have left easily recognizable scars in the form of circular areas depleted in craters. Only if essentially all of the large bodies all impacted very early in the cratering history would their crater scars now all be cratered to densities indistinguishable from the average background; but accepting such a scenario would immediately concede that the cratering histories of the terrestrial planets and of the Galilean satellites were different.

One may contend that low crater-density scars do exist; the best example being the Valhalla basin. However, our statistics include Valhalla and all degraded basins with measurable diameters. Therefore, these are not yet obliterated by relaxation and count among the observed craters and not among the low crater-density scars. We are forced to accept, therefore, that we can not subject Callisto to the lunar highlands' cratering history, add the phenomenon of crater relaxation and develop a surface such as the one actually observed. Consequently, we conclude that the crater production functions were different for the inner Solar System and the jovian region.

#### REFERENCES:

Smith, et al. (1979). The Galilean Satellites and Jupiter: Voyager 2 Imaging Science Results, Science, 206, 927-950.

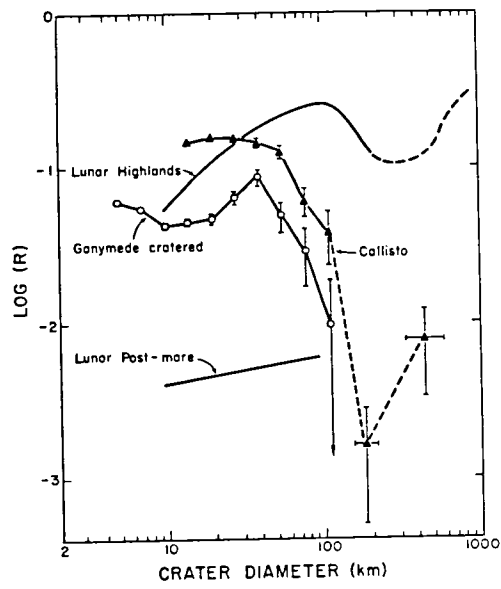


Figure 1

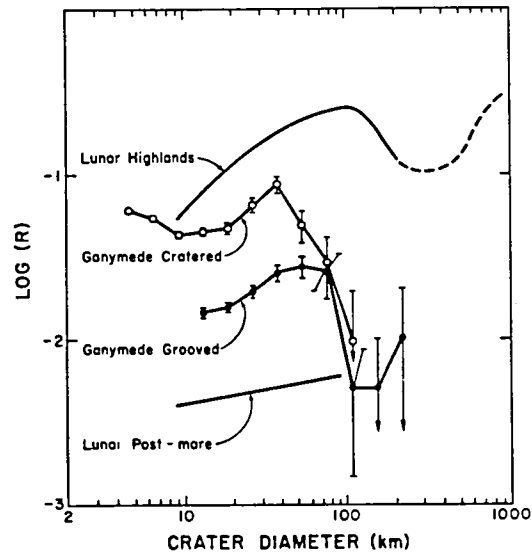


Figure 2

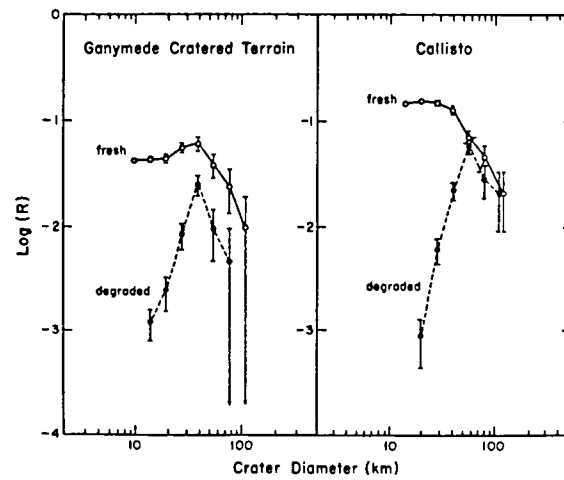


Figure 3

## POSSIBLE SOURCE OF THE MARTIAN SALTS

Robert L. Huguenin, Dept. Physics/Astronomy, Hasbrouck, University of Massachusetts, Amherst, MA 01003

It has been proposed by us (Huguenin et al., 1979; Huguenin and Clifford, 1980) that near-surface liquid  $H_2O$  may occur in several regions on Mars, most notably Solis Lacus, Noachis-Hellespontus, and near Syrtis Major. This was based on observations of anomalous  $H_2O$  condensates forming in and around these regions throughout much of the martian year. Independent radar corroboration of this was recently published by Zisk and Moriginis-Mark (1980) for Solis Lacus and Noachis-Hellespontus, and additional support from Viking orbiter colorimetric imagery has been cited by McCord et al. (1980) for Noachis-Hellespontus.

We have argued that the  $H_2O$  may migrate into these regions from below and be lost at the surface by evaporation (Clifford and Huguenin, 1980). It was proposed that the evaporation/replenishment process may be part of a planetwide cycle in which  $H_2O$  vapor migrates from the near equatorial evaporation sites to the poles, where it is returned to an interconnected global subsurface reservoir of  $H_2O$  through basal melting of the cap. It was argued by Clifford (1980) that upward transport of the  $H_2O$  to the surface in the Solis Lacus and other evaporation sites may occur via  $H_2O$  vapor and thin film migration toward a near-surface freezing front. Here a layer of tempofrost may accumulate during the colder martian months, and then undergo melting and enhanced evaporation during the warmer months (Huguenin, Clifford, and Greely, 1980). It was argued that melting of this layer by the penetrating thermal wave near perihelion could produce relatively high subsurface  $H_2O$  vapor pressures due to the diffusion-inhibiting effects of the overburden soil, and that the vapor may escape as jets of steam and aerosol dust. This we suggested may be the mechanism by which the periodic dust storms develop within these anomalous regions.

Migration of the  $H_2O$  through the rock and soil matrix would be expected to produce extensive leaching and highly saline solutions. If true, evaporation of the brines should induce the precipitation of salts at or near the surface. Laboratory studies and theoretical phase modeling by Brass (1980) suggest that as much as 250-300 mg of chloride salts and 25 mg of sulfates per gram of water may precipitate out at the surface. With evaporation rates from Solis Lacus estimated to be a minimum of  $10^{-1} \text{ km}^3$  of  $H_2O$  per year (based on estimates of the minimum volume of  $H_2O$  necessary to produce the observed condensates), this would correspond to the production of  $10^{13}$  g of salts at Solis Lacus per year.

Rapid evaporation of this brine film, such as we have proposed occurs near perihelion, may produce extremely fine salt particles that would be carried into the atmosphere as aerosols. Jetting processes, similar to the ones that may produce the dust storms, may periodically produce high aerosol salt concentrations during the year. These aerosols could serve

as catalysts for a variety of atmospheric chemical reactions (particularly if they contained ferrous iron impurities), such as those described by Huguenin, Prinn, and Maderazzo (1977). It is possible, for example, that during these 'salt storms'  $O_2$  and CO abundances could decrease due to enhanced catalytic  $CO + \frac{1}{2}O \rightarrow CO_2$  reaction rates. Other reactions discussed by Huguenin et al. (1977) could also be enhanced. These aerosols could also serve as nuclei for condensate precipitation such as that observed at the VL2 site and proposed for deposition at the poles.

In addition to the atmospheric effects, these aerosol salts may have had some significant effects on interpretations of soil composition and mineralogy. With salt production rates at Solis Lacus estimated to be as high as  $10^{13}$  g yr<sup>-1</sup>, as much as  $10^{-5}$  g cm<sup>-2</sup> salt could be deposited each year at the Viking sites, assuming adequate transport rates and horizontal mixing efficiencies. It is therefore possible that much of the salt detected by the XRF experiments at the two Viking lander sites may have been deposited during the proposed salt storms. Many of the elements included in the analyses may have been transported to the sites from a few small regions, and some of the interpretations and theories based on the XRF data may therefore need to be reexamined. The possibility that the salts contain Fe<sup>2+</sup> and/or Fe<sup>3+</sup> impurities may have an effect on some of the interpretations based on reflectance spectra as well. These will be subjects of future investigation.

#### ACKNOWLEDGMENT

This research was supported by grants NSG 7397, NSG 7405 and NAGW 40 from NASA.

#### REFERENCES

- Brass, G., *Icarus*, 42, 20-28, 1980.
- Clifford, S.M., *Proc. 3rd Colloq. Plan. Water* (in press), 1980.
- Clifford, S.M. and Huguenin, R.L., NASA TM 81776, 144, 1980.
- Huguenin, R.L., Prinn, R.G., and Maderazzo, M., *Icarus*, 270, 1977.
- Huguenin, R.L., Clifford, S.M., Sullivan, C.A., and Miller, K.J.  
NASA TM 80339, 208, 1979.
- Huguenin, R.L., and Clifford, S.M., NASA TM 81776, 153, 1980.
- Huguenin, R.L., Clifford, S.M., and Greely, R., NASA TM 81776, 215, 1980.
- McCord et al. (Planetary Remote Sensing Consortium), *J. Geophys. Res.*, in press.
- Zisk, S.H. and Morigines-Mark, P., *Nature*, in press.

# QUANTITATIVE MEASUREMENTS OF THE TOPOGRAPHY OF THE NORTH POLAR LAYERED DEPOSITS

James A. Cutts and Karl R. Blasius, Science Applications, Inc., Planetary Science Institute, 283 S. Lake Ave., Suite 218, Pasadena, CA 91101

In work reported last year (Cutts, 1980) we performed simulations of the thicknesses of sequences of strata in the north polar layered deposits on Mars. Our model incorporated various kinds of climatic modulation of the thicknesses of individual layers which were tied to long-term variations in the planet's obliquity and eccentricity. Currently, we are engaged in efforts to measure thicknesses of individual layers in a sequence using Viking Orbiter images. Measurements of adequate precision and accuracy would enable us to test the hypothesis of climatic control of layer thicknesses and identify those aspects of long term climate variation that are most critical. The investigation involves a collaboration with Dr. Alan Howard of the University of Virginia: we define elevation differences between control points using stereophotogrammetric techniques; Howard analyzes relief differences with photoclinometric methods (Howard, 1980).

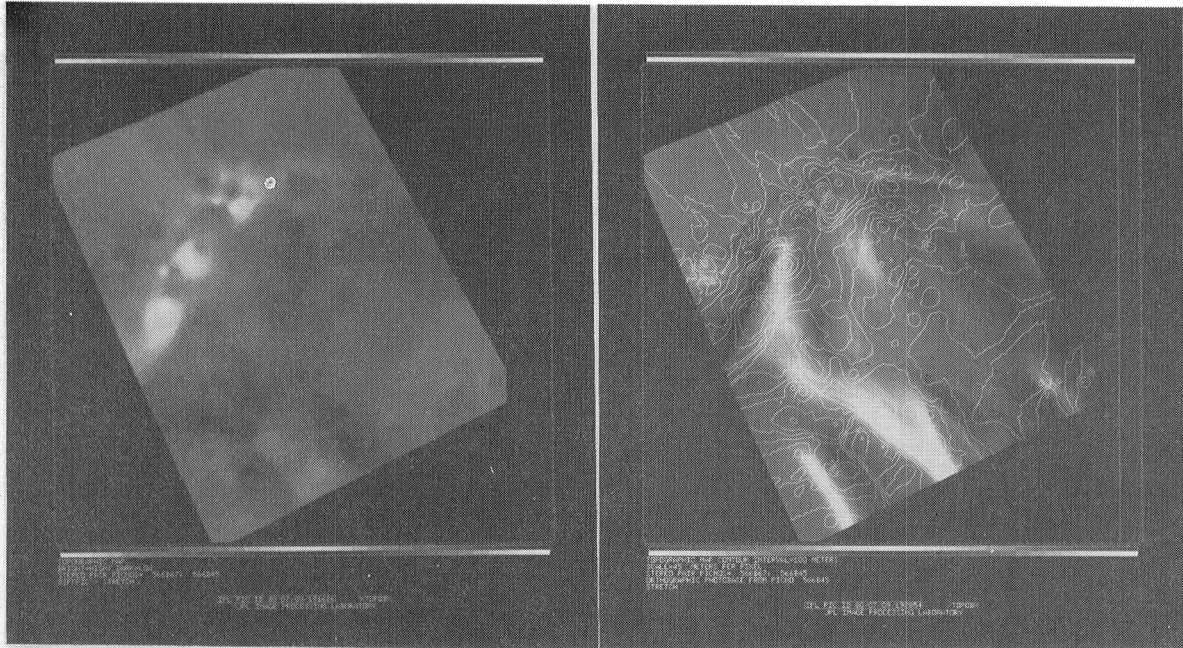
Two areas have been chosen for the initial investigation: the first area near  $79^{\circ}\text{N}$   $332^{\circ}\text{W}$  includes a marginal scarp of convoluted plan form separating the layered deposits from a cratered substrate (stereo images 566B75 and 566B53). Layers are well-defined along most of the length of this scarp. The second area near  $79^{\circ}\text{N}$   $350^{\circ}\text{W}$  lies entirely within layered deposit materials and includes complexly dissected surfaces (stereo images 566B67 and 566B45). We report here preliminary results of the stereo analyses.

Approximately 500 features (small areas) have been identified in each pair of images of the largely featureless layered deposits. Elevations have been measured using computer correlation/digital mapping techniques developed by us in conjunction with IPL, JPL (Ruiz *et al.*, 1977 and Blasius and Cutts, 1980) and Benesh (1978). Preliminary digital map products generated from these analyses are displayed in Fig. 1. The number of parallax measurements was higher than we expected to achieve, but the areal resolution of the data still does not permit us to directly measure the thickness of individual layers; rather, we measure relief across series of layers and use these results to calibrate higher resolution photoclinometric profiles over precisely the same slopes.

Both the stereo and the photoclinometric data have systematic errors stemming from uncertainties in parameters of the various models -- spacecraft pointing, surface photometric function and atmospheric backscatter. However, because the stereo and photoclinometric observations are affected differently by these parameters we can constrain the parameter values by forcing the two types of measurements to agree as well as demanding that all measurements yield topographic closure. Results of these parameter fitting efforts are discussed.



A



B

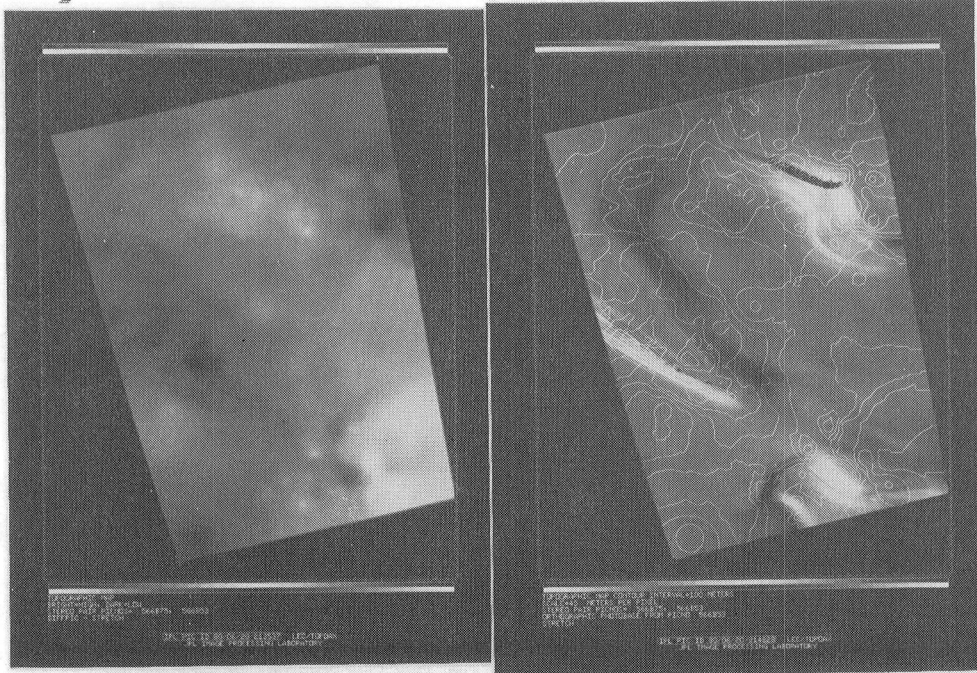


Figure 1. Preliminary (unedited) topographic mapping materials compiled from two high resolution stereo pairs of the north polar region of Mars. Topographic control points will be selected from augmented and edited data.

REFERENCES:

- Benesh, M., 1978, Viking Orbiter Stereophotogrammetry, Photogram. Eng. Rem. Sens. 44, 265.
- Blasius, K.R., and Cutts, J.A., 1980, Topography of Martian Central Volcanoes, submitted to Icarus.
- Cutts, J.A., 1980, Simulations of Stratigraphy of Martian Polar Layered Deposits, in Reports of Planetary Geology Program, 1979-80, NASA TM-81776, 63-65.
- Howard, A.D., 1980, Studies of the Martian Polar Caps, ibid., 60-62.
- Ruiz, R.M., et al., 1977, IPL Processing of the Viking Orbiter Images of Mars, J. Geophys. Res. 82, 4189-4202.

## Status of Planetary Image Processing at Munich

G. Neukum, J. Henkel, K. Hiller, and W. Lüders

Institut für Allgemeine und Angewandte Geologie, Ludwig-Maximilians-Universität,  
Luisenstr. 37, 8000 München 2, FRG

Efforts have been made in our group to acquire the capability of processing and evaluating planetary multispectral images. Work was done in collaboration with the US Geological Survey (Flagstaff) and in cooperation with the two German institutions, the Deutsche Forschungs- und Versuchsanstalt für Luft- und Raumfahrt (DFVLR) and the Zentralstelle für Geo-Photogrammetrie und Fernerkundung (ZGF). Our aim has been to learn about the basic problems and needs in processing planetary images in primarily using Viking imagery and to gradually build up our capabilities and develop the necessary methods for the processing and evaluation of Voyager and future Galileo multispectral imagery.

During the summer of 1979, one of us (J.H.) stayed for a three months' training period at the USGS in Flagstaff (Arizona). In this period he participated in the work for the projects "Lunar Consortium" and "Mars Consortium". Special processing of images of the near side of the Moon was performed from a series of ten pairs of images taken by a vidicon camera through a telescope at  $0.38\ \mu\text{m}$  and  $0.56\ \mu\text{m}$  (originally taken by Soderblom and Johnson). Ratio, first and second principal component of the two channels were determined and matched to one false color image showing the Titanium distribution on the lunar nearside in superior detail than in any previous processing. Several map projections have been calculated from this imagery later in Munich.

With the experience from the US training period, existing software for geometric registration of multispectral Landsat images was adapted to the problems of planetary image data processing and new software developed at the digital processing system of the ZGF. Now it is possible to match planetary multispectral images which are not generally of the same geometry. We have since concentrated on processing multispectral Viking images of the Vallis Marineris area, e.g. in the way of producing false color images from stretched Viking imagery. Linear probability tail stretches

from 0.5 % to 99.5 % relative to the number of pixels were used after registration of the components of the scenes and the components matched together. This procedure resulted in good enhancement of color differences and gave a good separation of different surface units. Additionally, a scene of the Kasei Vallis region was processed for ratio and first and second principal component determinations.

Multispectral image processing of the Viking scenes was also done at the DFVLR using the DIBIAS System. Different methods were applied, e.g. after a linear stretch of the greyscale of three channels, passpoints were determined to correct the image geometry. A mere translation between the channels was assumed. The color composite of the corrected scene yielded good results (of visual impression) when the mean and standard deviation of the greyscales were normalized to the same values for each channel. The separation of different surface units was moderately good.

The different surface units are being mapped, compared with high resolution imagery data and crater retention ages determined. Work is in progress in extracting surface details by applying different filtering techniques.

## Relative Ages of the Olympus Mons, Aureole Material

K. Hiller<sup>1)</sup>, Rosaly Lopes<sup>2)</sup>, J.E. Guest<sup>2)</sup>, and G. Neukum<sup>1)</sup>

1) Institut für Allgemeine und Angewandte Geologie, Ludwig-Maximilians-Universität, Luisenstrasse 37, 8000 München 2, FRG

2) University of London Observatory, Mill Hill Park, London NW7 2QS, GB

The aureole material of Olympus Mons has been described by various authors (e.g. refs. 1,2,3,4,5) and various origins have been suggested. Material of the aureole appears to overly the surrounding plains and post-date the Tharsis uplift (ref. 4). Overlying the aureole surface are younger Olympus Mons lavas that have flowed over the perimeter scarp (ref. 4).

Using well known crater counting techniques (refs. 6,7,8), we have attempted to determine the age of the aureole surface relative to adjacent surfaces and to the principal events in Mars history. From cratering data we assign model ages based on the curves of Neukum and Hiller (ref. 8) thus providing in a quantitative way the relative ages between different units. Based on this method, we find model ages of  $N(1)=10^{-3}/\text{km}^2$  or  $3.2 \times 10^9$  yr to  $4.0 \times 10^9$  yr for the plains underlying the aureole material. Obtaining an age for the aureole material itself is complicated by the rugged nature of the aureole surface. Two types of counts were conducted. Firstly, craters were counted on the flat plateau tops of the ridges that give the aureole its characteristic appearance (fig. 1). These surfaces give a crater retention age of  $N(1)=2.7 \times 10^{-4}/\text{km}^2$  ( $0.5$  to  $1.5 \times 10^9$  yr). Counts of the whole area, including the terrain between the ridges, give a crater retention age for the larger craters comparable to that of the plateau tops, but for smaller craters ages of about  $N(1)=3.2 \times 10^{-5}/\text{km}^2$  ( $\sim 0.2 \times 10^9$  yr) are obtained (fig. 2).

Based on previous crater counts, Olympus Mons is considered to have formed between about  $3.0 \times 10^9$  and  $<0.5 \times 10^9$  yr (ref. 8); based on our new counts we can bracket the age of the aureole material as lying between about  $3.2 \times 10^9$  and  $0.5$  to  $1.5 \times 10^9$  yr (more likely near the latter). Based on the counts made on the plateau ridge tops any major crater destruction on the aureole surface was terminated about  $0.5$  to  $1.5 \times 10^9$  yr ago corresponding to the peak in activity on Olympus Mons and the other prominent Tharsis volcanoes. However, erosion continued

until about  $0.2 \times 10^9$  yr ago in the inter-ridge regions, this erosion terminating at about the time of the youngest outpourings of lava in the calderas at the summit of the volcano (fig. 3,4 ). It is possible that this erosional episode on the aureole material is related to volcanic activity, perhaps caused by seismicity giving crater degradation in relatively unconsolidated material on steep slopes in the aureole.

#### References:

- 1) Carr, M.H., Masursky, H., and Saunders, R.S. (1973) J. Geophys. Res. 78, 4031-4036
- 2) Morris, E.C., and Dwornik, S.E. (1978) US Geol. Survey Map I-1049
- 3) King, J.S. & Rhiele (1974) Icarus 23, 300-317
- 4) Lopez, R., Guest, J.E., and Wilson, C. (1980) The Moon and the Planets 22, 221-234
- 5) Hodges, C.A., and Moore, H.J. (1979) J. Geophys. Res. 84, 8061-8074
- 6) Soderblom, L.A. et al. (1974) Icarus 22, 239-263
- 7) Neukum, G., and Wise, D.U. (1976) Science 194, 1381-1387
- 8) Neukum, G., and Hiller, K. (1980) acc. for publ. in J. Geophys. Res.

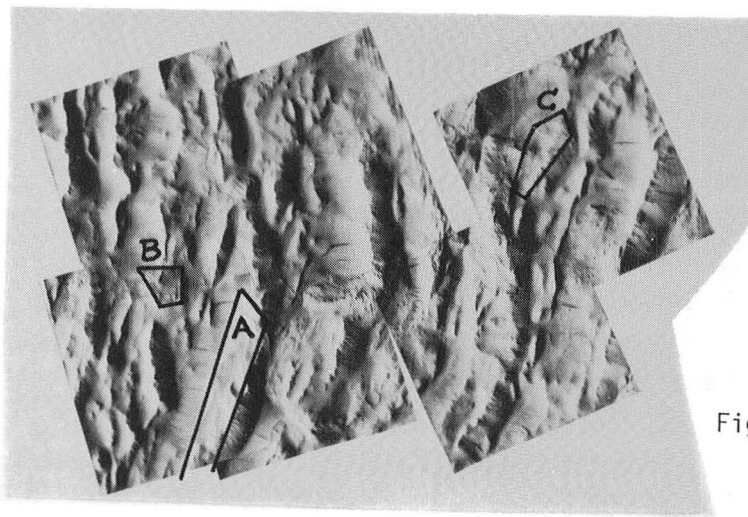


Fig. 1

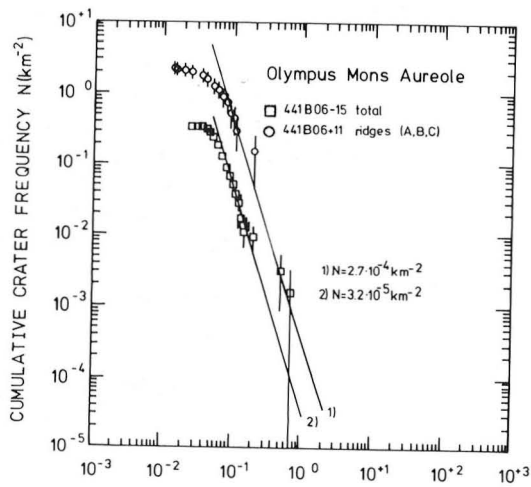


Fig. 2

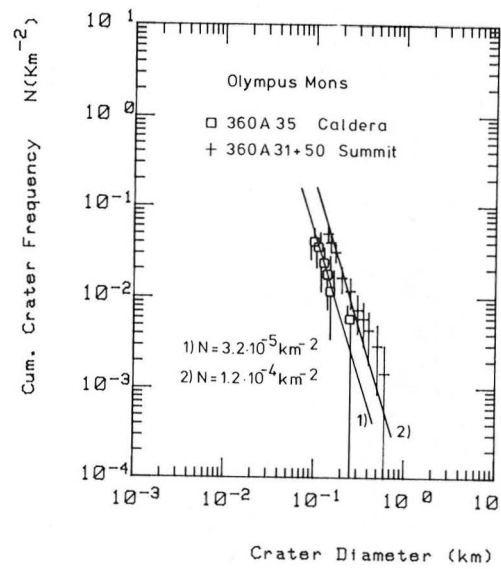


Fig. 4

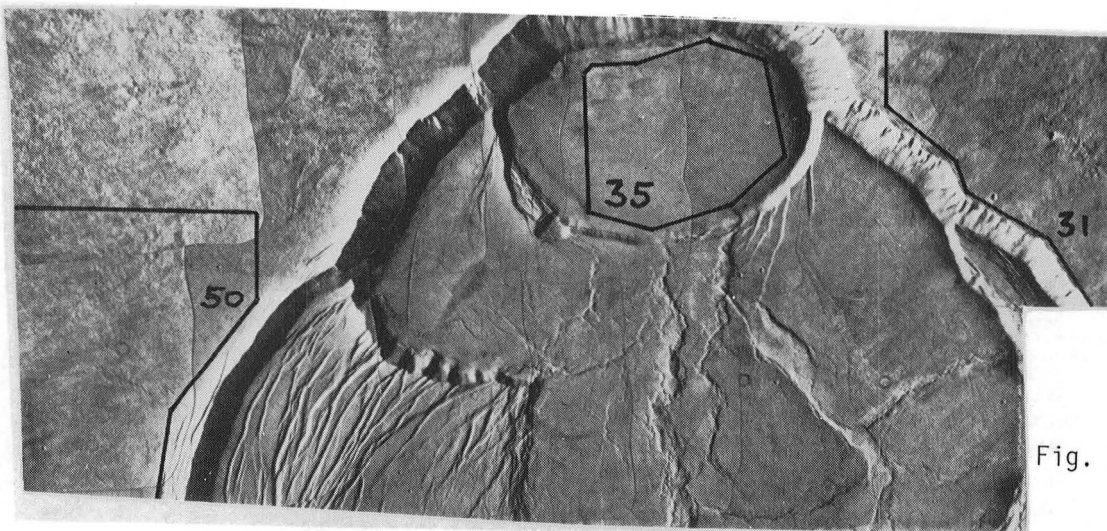


Fig. 3

## SMALL LUNAR DARK-MANTLE DEPOSITS OF PROBABLE PYROCLASTIC ORIGIN

B.R. Hawke and T.B. McCord, Hawaii Inst. of Geophys., Univ. of Hawaii, Hon. HI 96822; J.W. Head, Dept. of Geological Sciences, Brown Univ., Prov., RI 02912

Introduction: In recent years, considerable emphasis has been placed on the study of lunar samples of pyroclastic origin and the dark-mantle deposits which are thought to be composed of similar material<sup>e.g.1,2,3</sup>. The lunar dark-mantle deposits fall into two classes based on extent: (1) The large regional dark-mantle deposits, such as the Sulpicius Gallus Fm. and those on the Aristarchus Plateau, generally extend from about a hundred to several hundred kilometers across the lunar surface. (2) Small, isolated, dark-mantle deposits which generally extend only a few kilometers to tens of kilometers.

With few exceptions<sup>e.g.13</sup>, research in recent years has concentrated on the large, regional pyroclastic deposits<sup>4-7,11</sup>. Early studies considered the possibility that endogenic dark-halo craters were isolated sources of dark-mantle material and that regional dark-mantle deposits were composed of abundant and densely packed dark-halo craters and their deposits<sup>9</sup>. A recent study of the Alphonsus dark-halo craters<sup>13</sup>, however, strongly supported a vulcanian explosive eruption style for these features, in contrast to strombolian or continuous eruption styles suggested for the regional dark-mantle deposits<sup>10</sup>. This study<sup>13</sup> also suggested that the Alphonsus dark-halo crater deposits were correlative with mare deposits in adjacent Mare Nubium. Thus, the presence of spectrally distinct small dark-mantle deposits in the highlands adjacent to the maria may provide evidence concerning the presence and composition of early mare deposits which were subsequently buried by lavas of a different composition.

The present study of small dark-mantle deposits has been undertaken 1) to establish their mode of occurrence, distribution, and geologic setting; 2) to determine their compositions and relations to the composition of nearby maria; 3) to establish the geometry of the deposits and associated source vents; and 4) to assess eruption conditions that led to the emplacement of the dark-mantle deposits.

All previously mapped small dark-mantle deposits<sup>e.g.12</sup> have been investigated using a variety of photographic and remote sensing data sets in an effort to distinguish true pyroclastic deposits from dark-halo craters formed by impact and excavation of a low-albedo subsurface layer<sup>13,14</sup>. Near-infrared spectra (0.6-2.5  $\mu\text{m}$ ) have also been acquired for many deposits.

Deposit Descriptions and Compositional Affinities - J. Herschel: (62° N, 41°W) A major deposit of dark-mantling material is located on the eastern portion of the floor of J. Herschel crater (see Fig. 1), a pre-Imbrian impact structure north of Mare Frigoris<sup>15</sup>. The deposit is associated with a rille which is composed in part of coalesced craters of probable endogenic origin. While these small coalesced craters are probably the source vents for some of the dark-mantling material, deposit distribution suggests that most was ejected from four major vent systems. These vents range from four to eight kilometers in diameter, are irregular in outline, and appear related to the rille system.

The low-albedo region exhibits low 0.40/0.56  $\mu\text{m}$  values and is "redder" than its surroundings. However, the deposit is not distinct in the 0.95/



0.56  $\mu\text{m}$  image. While some portions exhibit 0.95/0.56  $\mu\text{m}$  ratio values equal to or slightly above nearby highlands, other portions are lower. The low 0.40/0.56  $\mu\text{m}$  values are similar to those exhibited by the mare basalts in nearby Mare Frigoris and are consistent with a similar composition.

Atlas: (47°N, 45°E) Two dark-mantle deposits<sup>16</sup> are located on the interior of the 85-km floor-fractured crater Atlas (see Fig. 2). The northernmost deposit is the less dark of the two and is associated with a rille and fracture system on the crater floor. The distribution of the northern deposit suggests that one large (2-6 km in dia.) elongate crater is the major source vent. Superposition relationships demonstrate that the dark-mantle deposit was emplaced prior to the formation of Hercules crater and hence the deposit is probably late Imbrian or early Eratosthenian in age. The darker, slightly more extensive southern dark-mantle deposit is associated with an elongate (5-9 km in dia.) vent on the lower portion of the Atlas wall and near the intersection of three major floor rille systems. The dark-mantling material occurs up to 14 km from the source vent. Both Atlas pyroclastic deposits are spectrally distinct in multispectral images of the region. They exhibit both high 0.40/0.56  $\mu\text{m}$  values ("blue") and high 0.95/0.56  $\mu\text{m}$  values.

Franklin: (39°N, 48°E) The deposit in the floor of Franklin appears to be associated with a series of aligned elongate craters on the eastern portion of the crater floor<sup>17</sup>. The deposit is spectrally distinct and displays relatively high 0.40/0.56  $\mu\text{m}$  and 0.95/0.56  $\mu\text{m}$  values.

The spectral characteristics of both the Atlas and Franklin dark-mantle deposits are similar to those exhibited by the Apollo 17 dark-mantle as well as other lunar "black spots" which have been interpreted as being composed of a significant component of Apollo 17 black spheres. The occurrence of deposits rich in high-Ti pyroclastic spheres may indicate an early phase of mare volcanism in the eastern Frigoris region which produced high-Ti mare basalts now covered by later "red" basalts in the region.

Additional dark-mantle deposits studied in detail thus far include: 1) those east of Aristoteles (50°N, 35°E and 50°N, 28°E)<sup>16</sup>, 2) three deposits with associated vents on the interior of Gauss crater (36°N, 79°E), 3) the Messala crater floor deposit (39°N, 60°E), 4) the dark-mantle deposit in the Rimae Fresnel region (28°30'N, 4°E), 5) the Bohnenberger crater interior deposit (16°S, 40°E), and 6) the dark-mantle deposit northeast of Grimaldi.

Conclusions: On the basis of detailed studies of ten pyroclastic deposits, the results of our previous studies of small dark-mantle deposits associated with Alphonsus crater<sup>13</sup> and the Apollo 15 region<sup>2</sup>, and a general survey of all previously mapped small dark-mantle deposits, we offer the following preliminary conclusions: 1) small dark-mantle deposits of pyroclastic origin are more abundant and widely distributed than previously realized; 2) few of the deposits studied contain contiguous mare (lava flow) deposits; 3) many of the deposits are associated with floor-fractured craters; 4) the deposits are concentrated around the lunar maria; 5) deposit ages, although not yet established in all cases, appear to lie in the period of mare emplacement; 6) the majority of deposits have compositional affinities with surrounding maria; 7) several deposits (e.g. Atlas, Franklin) have spectral characteristics distinct from adjacent mare, suggesting that they may represent deposits associated with an earlier phase of

basaltic volcanism.

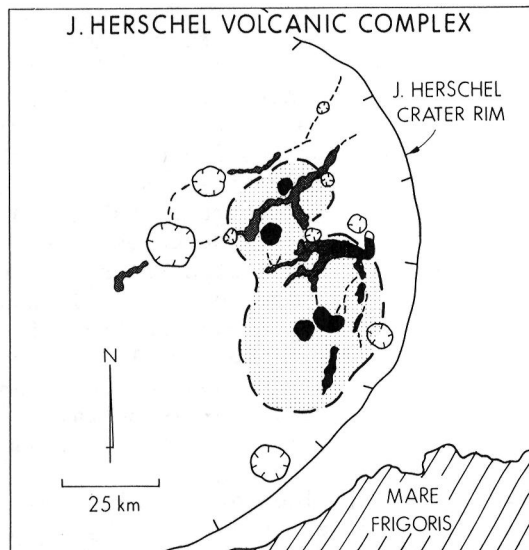


Fig. 1: Sketch map of the J. Herschel volcanic complex.

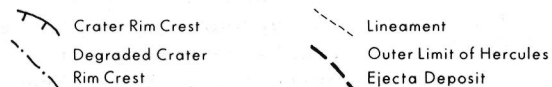
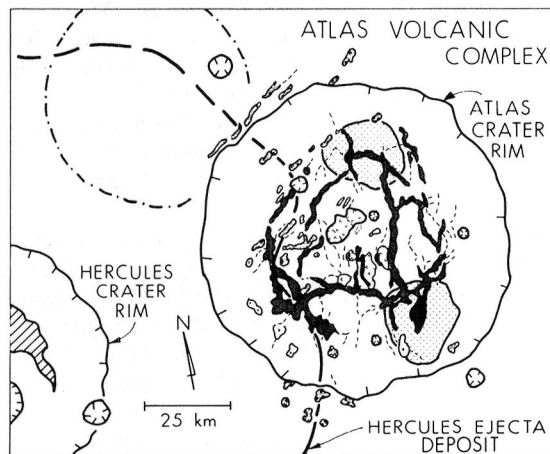
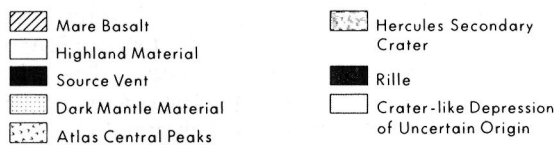


Fig. 2: Sketch map of the Atlas volcanic complex.

References: 1) P. Butler (1978) PLPSC 9, 1459. 2) B. Hawke et al. (1979) PLPSC 10, 2995. 3) J. Head et al. (1980) LPS XI, 418. 4) C. Pieters et al. (1973) JGR 78, 5867. 5) C. Pieters et al. (1974) Science 183, 1191. 6) J. Adams et al. (1974) PLSC 5, 171. 7) S. Zisk et al. (1977) The Moon 17, 59. 9) T. McGetchin and J. Head (1973) Science 180, 68. 10) L. Wilson and J. Head (1980) JGR, in press. 11) J. Head (1974) PLSC 5, 207. 12) D. Wilhelms and J. McCauley (1971) USGS Map I-703. 13) J. Head and L. Wilson (1979) PLPSC 10, 2861. 14) P. Schultz and P. Spudis (1979) PLPSC 10, 2899. 15) G. Ulrich (1969) USGS Map I-604. 16) B. Lucchitta (1972) USGS Map I-725. 17) M. Grolier (1974) USGS Map I-841.

AUTHOR INDEX



# Author Index

Alexander, C.	p 8
Anderson, D.M.	p 191
Andrawes, F.F.	p 193
Arthur, D.W.G.	p 12, 40, 180
Arvidson, R.E.	p 77, 85, 426, 442
	p 478
Aubele, J.C.	p 231
Axelrod, R.	p 317
Baker, V.R.	p 234, 345, 394, 486
Banerdt, W.B.	p 16, 215
Barcus, L.A.	p 463
Batiza, R.	p 77
Batson, R.M.	p 451, 456, 462
Bianchi, R.	p 127, 474
Blackburn, T.R.	p 193
Blasius, K.R.	p 147, 504
Bodard, J.	p 402
Bolef, L.K.	p 478
Booth, M.C.	p 196
Boothroyd, J.C.	p 348
Bousquet, B.	p 402
Boyce, J.M.	p 55, 60, 140
Bratt, S.	p 116
Breed, C.F.	p 312
Breed, C.S.	p 307
Breed, W.J.	p 317
Brook, G.A.	p 369
Brown, S.H.	p 258
Bus, S.J.	p 3
Carey, E.	p 144
Carr, M.H.	p 342
Carusi, A.	p 474
Casadevall, T.J.	p 236
Cassen, P.	p 8
Cerroni, P.	p 127, 474
Chapman, C.R.	p 23
Clifford, S.M.	p 405
Comer, R.P.	p 116
Constantopoulos, J.	p 304
Cook, A.F.	p 10, 28, 31, 429
Coradini, A.	p 474
Coradini, M.	p 127, 474
Cotera, A.S.	p 317
Craig, R.G.	p 319
Crumpler, L.S.	p 88, 231
Cullen, L.	p 420
Cutts, J.A.	p 147, 504
D'Alli, R.E.	p 473
Danielson, G.E.	p 10

# Author Index (continued)

Davies, G.F.	p 85
Davies, M.E.	p 10, 453, 454
Davis, D.R.	p 23
Davis, P.A.	p 180
De Hon, R.A.	p 128
Dial, A.L.	p 37, 184, 383
Diffendaffer, P.	p 215, 221
Downey, E.M.	p 225
Downs, G.S.	p 167
Dzurisin, D.	p 236
Eagan, M.M.	p 471
El-Baz, F.	p 161, 292, 295
	p 298, 301, 304
Ellsworth, K.	p 70
Elston, W.E.	p 231
Evans, N.	p 376, 479, 480, 483
Fanale, F.P.	p 16, 215, 221, 281
Federico, C.	p 474
Ferguson, H.M.	p 381
Ferguson, J.	p 125
Fernandez-Chicarro, A.	p 107
Fink, J.	p 113, 170, 243, 339
Finnerty, A.A.	p 43, 45
Flamini, E.	p 474
Flavill, R.	p 127
Fleitout, L.	p 144
Fulchignoni, M.	p 127, 474
Fudali, R.F.	p 125
Furin, M.X.	p 128
Garvin, J.B.	p 238
Gault, D.E.	p 113, 170
Gibson, Jr., E.K.	p 193, 199, 202
Giegengack, R.	p 314
Gierasch, P.	p 327
Gifford, A.W.	p 90
Ginberg, M.	p 95
Gooding, J.L.	p 205, 206, 209,
	p 212, 221
Gray, M.	p 317
Greeley, R.	p 113, 170, 243,
	p 245, 247, 275,
	p 278, 285, 287,
	p 290, 339
Greenberg, R.	p 23
Gregory, T.E.	p 93
Grolier, M.J.	p 307, 312
Guest, J.E.	p 509
Guinness, E.A.	p 77, 417, 426, 442
Gurnis, M.C.	p 172, 174, 499

# Author Index (continued)

Hale, W.	p 131, 158
Hamdan, A.H.	p 161
Hansen, C.	p 28
Hapke, B.	p 431
Hawke, B.R.	p 119, 152, 155, 512
Head, J.W.	p 64, 116, 119, 131
	p 158, 238, 493, 512
Helpenstein, P.	p 373
Helin, E.F.	p 3
Helm, P.J.	p 330
Henkel, J.	p 507
Herzig, C.T.	p 301
Hiller, K.	p 507, 509
Hodges, C.A.	p 266
Howard, A.	p 333
Howard, H.T.	p 432
Hoyt, B.R.	p 319
Huguenin, R.L.	p 502
Hurren, J.	p 127
Hutson, M.L.	p 164
Hutton, R.E.	p 225
Ingram, R.E.L.	p 202
Iversen, J.D.	p 275
Jacobberger, P.	p 442
Japp, J.M.	p 212
Jaques, L.	p 125
Johansen, L.A.	p 150, 215, 221, 249
Johnson, A.P.	p 317
Johnson, T.V.	p 209
Jones, K.L.	p 413
Jordan, R.	p 458
Judson, S.	p 364
Kachadoorian, R.	p 269
Kaufman, K.	p 319, 408
Kenney, J.	p 281
Komar, P.D.	p 361
Krinsley, D.H.	p 243, 285, 287
Kupferman, P.	p 10
Laity, J.E.	p 358
Laue, E.	p 221
Lauer, Jr., H.V.	p 218
LaVoie, S.K.	p 413
Leach, R.	p 275, 278, 285
Lee, S.W.	p 20
Leonard, R.	p 275, 278
Lopes, R.	p 509
Lucchitta, B.K.	p 379, 381, 408
Luders, W.	p 507
Magni, G.	p 474

# Author Index (continued)

Malin, M.C.	p 67, 81, 290, 367
Malone, K.	p 278
Manent, L.S.	p 295, 298
Marshall, J.	p 285, 287
Martelli, G.	p 127
Masson, Ph.	p 107, 144, 402, 488
Masursky, H.	p 82, 184, 383, 475
Maxwell, T.A.	p 292
McCauley, C.K.	p 317
McCauley, J.F.	p 307, 312
McCord, T.B.	p 512
McCrary, T.	p 98
McGill, G.E.	p 79
McKay, D.	p 304, 496
Mercier, J.L.	p 488
Milton, D.J.	p 125
Moore, H.J.	p 225, 266, 269
Moore, R.B.	p 269
Morris, E.C.	p 252
Morris, R.V.	p 218, 445
Morrison, D.	p 27
Mosher, J.A.	p 10
Mouginis-Mark, P.J.	p 34, 152, 155, 238
	p 258, 435
Muradian, L.	p 215
Neeley, S.C.	p 445
Neukum, G.	p 507, 509
Nummedal, D.	p 400, 486
Owen, T.	p 476
Paluzzi, P.R.	p 81
Parmentier, E.M.	p 64
Passey, Q.R.	p 3
Patton, P.C.	p 394
Peale, S.	p 8
Pernet, E.	p 402
Pieri, D.	p 43, 48, 51, 95
	p 352, 355, 401
	p 122, 272
Pike, R.J.	p 19
Pilcher, C.B.	p 55, 60, 261, 263
Plescia, J.B.	p 14, 275
Pollack, J.C.	p 127, 474
Poscolieri, M.	p 304, 496
Prestell, D.J.	p 401
Prior, D.B.	p 43, 45
Ransford, G.A.	p 202
Ransom, B.	p 431
Rava, B.	p 319
Raymondi, M.	p 8
Reynolds, R.	



# Author Index (continued)

Rhodes, D.D.	p 397
Roddy, D.J.	p 177, 180
Rogeon, P.	p 402
Romani, P.	p 423
Roszbacher, L.A.	p 364, 376
Roth, L.E.	p 167
Sagan, C.	p 355
Sanger, R.	p 215, 221
Saunders, R.S.	p 93, 150, 167, 221
	p 281
Schaber, G.G.	p 37, 40, 82, 438
Schafer, F.J.	p 458, 463
Schmidt, M.S.	p 319
Schneider, D.	p 221
Schneider, N.M.	p 28, 31
Schubert, G.	p 70, 167
Scott, D.H.	p 104, 241, 255
Scott, R.F.	p 225
Scribner, P.	p 480
Sharpton, V.L.	p 493
Sheridan, M.F.	p 134
Shoemaker, E.M.	p 3, 55, 60
Shorthill, R.W.	p 225
Sigurdsson, H.	p 245
Simonelli, D.	p 72
Simpson, R.A.	p 432
Singer, R.B.	p 416
Smith, R.S.U.	p 318, 322
Smith, P.M.	p 127
Soderblom, L.A.	p 10, 177, 180
Solomon, S.C.	p 116
Spitzer, C.R.	p 225
Squyres, S.	p 64, 68
Stewart, G.	p 290
Strickland, E.L.	p 416
Strobell, M.	p 184, 383, 475
Strom, R.G.	p 28, 31, 174, 499
Summers, A.	p 8
Tanaka, K.L.	p 104, 241, 255
Terrile, R.J.	p 28, 429
Thomas, P.	p 144, 324, 327
Thomas, P.C.	p 20
Thompson, D.E.	p 384, 386, 389, 392
Tice, A.R.	p 191
Timson, D.S.	p 348
Tyler, G.L.	p 432
Tyner, R. L.	p 456
Underwood, Jr., J.R.	p 101, 314
Valsecchi, G.B.	p 474

# Author Index (concluded)

Veverka, J.	p 68, 327
Vostreys, R.W.	p 477
Wall, S.D.	p 221, 420
Ward, A.W.	p 330
Weidenschilling, S.J.	p 23
Weisman, M.	p 330
Whipple, F.L.	p 6
White, B.R.	p 275, 278
Whitford-Stark, J.L.	p 34
Wilhelms, D.E.	p 466
Williams, S.	p 290
Wise, D.	p 98, 439
Witbeck, N.E.	p 101, 140, 330
Witteborn, F.C.	p 14
Wohletz, K.H.	p 134
Wolfe, R.W.	p 164, 319
Womer, M.	p 247
Woronow, A.	p 137, 174, 499
Wu, S.S.C.	p 458, 463
Young, V.	p 193
Zent, A.P.	p 426
Zisk, S.H.	p 435











1. Report No. NASA TM-82385		2. Government Accession No.		3. Recipient's Catalog No.	
4. Title and Subtitle Reports of Planetary Geology Program - 1980				5. Report Date December 1980	
				6. Performing Organization Code	
7. Author(s) Compiled by Henry E. Holt and Elisabeth C. Kusters				8. Performing Organization Report No.	
				10. Work Unit No.	
9. Performing Organization Name and Address Planetary Geology Program Office of Space Science Planetary Division				11. Contract or Grant No.	
				13. Type of Report and Period Covered Technical Memorandum	
12. Sponsoring Agency Name and Address National Aeronautics and Space Administration Washington, D.C. 20546				14. Sponsoring Agency Code	
15. Supplementary Notes					
16. Abstract  This is a compilation of abstracts of reports from Principal Investigators of NASA's Planetary Geology Program, Office of Space Science. The purpose is to provide a document which succinctly summarizes work conducted in this program. Each report reflects significant accomplishments within the area of the author's funded grant or contract. No attempt has been made to introduce editorial or stylistic uniformity; on the contrary, the style of each report is that of the Principal Investigator and may best portray his research. Bibliography information will be included in a separately published document. Full reports of selected abstracts will be presented to the annual meeting of Planetary Geology Principal Investigators at Louisiana State University, Baton Rouge, Louisiana, January 6 - 8, 1981.					
17. Key Words (Suggested by Author(s)) Planetary Geology Solar System Evolution Planetary Geologic Processes			18. Distribution Statement Unclassified - Unlimited  Subject Category 88		
19. Security Classif. (of this report) Unclassified	20. Security Classif. (of this page) Unclassified	21. No. of Pages 546	22. Price A23		





National Aeronautics and  
Space Administration

Washington, D.C.  
20546

Official Business

Penalty for Private Use, \$300

SPECIAL FOURTH CLASS MAIL  
BOOK

Postage and Fees Paid  
National Aeronautics and  
Space Administration  
NASA-451



**NASA**

POSTMASTER: If Undeliverable (Section 158  
Postal Manual) Do Not Return

---